SCUOLA DI DOTTORATO
UNIVERSITÀ DEGLI STUDI DI MILANO-BICOCCA

Department of Earth and Environmental Sciences

PhD program in Chemical, Geological and Environmental Sciences

Cycle XXXI - Curriculum in Geological Sciences

INTEGRATED CHRONOSTRATIGRAPHY AND TAPHONOMIC STUDIES IN MIOCENE SEDIMENTARY SUCCESSIONS OF THE EAST PISCO BASIN (PERU)

PhD candidate: BOSIO GIULIA

Registration n.: 735836

Supervisor: Prof. Elisa Malinverno

Tutor: Prof. Igor Maria Villa

Co-tutors: Prof. Anna Gioncada, Prof. Giovanni Bianucci

Coordinator: Prof. Maria Luce Frezzotti

2017-2018

Ai miei compagni
di avventure.

“But to the earth, a hundred years is nothing. A million years is nothing. This planet lives and breathes on a much vaster scale. We can’t imagine its slow and powerful rhythms, and we haven’t got the humility to try.”

John Michael Crichton

Index

Abstract (English)

Along the western side of the Ica River (Ica Desert, Peru), the Miocene Chilcatay and Pisco formations of the East Pisco Basin crop out. These units are characterized by an extraordinarily preserved marine vertebrate fossil fauna, especially cetaceans. This dissertation has the purpose of making chronostratigraphic and taphonomic studies on these formations, cropping out in the western side of the Ica River.

Despite the growing significance of the vertebrate fauna of the Chilcatay and Pisco formations, a comprehensive stratigraphic framework has not been established for a long time. Using tephra fingerprinting, ^{39}Ar–^{40}Ar dating, biostratigraphy and strontium isotope stratigraphy, the chronostratigraphy of both the units is here proposed. The Chilcatay Formation is divided into two unconformity-bounded allomembers, designated as Ct1 and Ct2. The vertebrate assemblage in the *Ct1a* facies of the Ullujaya locality comprises a coastal community, dominated by mesopredators representative of a warm-temperate, sheltered embayment connected with riverine and open-ocean environments. The chronostratigraphic framework is well constrained by integration of biostratigraphic data and isotope geochronology and suggests a Burdigalian age. The time constrains are 19.25 Ma for the base and 18.02 Ma for the top, using ^{39}Ar–^{40}Ar dating on tephra, in agreement with Sr isotope analyses in *Ct1a* suggesting Burdigalian ages, even the diatom biostratigraphy suggests a younger age for the top of the formation (17.08 Ma). The Pisco Formation is divided into three allomembers representing three transgressive cycles, P0, P1, and P2, from oldest to youngest. The vertebrate content of P0 is still scarcely known but clearly differs from that of the overlying P1, in which baleen-bearing whales are mainly represented by medium-sized cetotheriids; in contrast, in P2, balaenopterids dominate the assemblage. The chronostratigraphic framework was reconstruct with different methods. Sr isotope analyses on carbonates and phosphates suggest a Langhian – Serravallian age for the P0 allomember (from 14.80 to 12.60 Ma). ^{39}Ar–^{40}Ar dating and diatom biostratigraphy indicate a Tortonian age for the P1 allomember (from 9.46 to 8.60 Ma), and a Tortonian – Messinian age for the P2 allomember (from 8.39 to 6.71 Ma). Gaps in sedimentation, represented by unconformities, can be related to oxygen isotopic maxima indicating eustatic falls of sea level. Tephra fingerprinting has been applied to

build a high-resolution stratigraphy of P2 deposits and to correlate sediments exposed in different localities.

The preservation of both fossil vertebrates and invertebrates is truly exceptional in the East Pisco Basin deposits. Using optical and scanning electron microscopy and cathodoluminescence, the taphonomy of invertebrates was studied. In the Chilcatay Formation, mollusk shells are mainly made by Ca-carbonates and show a quite good preservation. Oysters show, in some cases, a well preserved pristine prismatic layer that suggests a low degree of alteration, and cathodoluminescence reveals that several samples are characterized by a low and homogeneous luminescence. The latter specimens are those selected for Sr isotope analyses applied for chronostratigraphic studies. For taphonomic studies, the Chilcatay barnacle facies recognized in Ct1 can be related to a relatively shallow-water, high-energy environment. The Pisco Formation mollusks are commonly preserved only as gypsum casts or dolomite/gypsum internal molds. Sr isotopic ratios indicate an early diagenetic formation for dolomite and a pre-Miocene seawater-derived brine origin for gypsum. Regarding vertebrate taphonomy, in the Chilcatay Formation bones exhibit a good preservation, due to fluctuations of euxinic and oxic-dysoxic conditions at the seafloor, suggested by the size distribution of pyrite framboid relics. In the Pisco Formation, the calculation of the sedimentation rates suggests that the good preservation of the fossil remains is not due to the rapid burial, but is related to early establishment of dysoxic/anoxic processes that allow phosphatization, and not only to the formation of carbonate nodules.

Abstract (Italiano)

Le formazioni mioceniche di Chilcatay e Pisco del Bacino Orientale di Pisco affiorano lungo la sponda occidentale del fiume Ica (Deserto di Ica, Perù). Queste formazioni sono caratterizzate da una concentrazione di fossili di vertebrati marini eccezionalmente conservati, in particolare cetacei. Questa tesi ha come scopo effettuare studi cronostratigrafici e tafonomici in queste formazioni esposte sulla sponda occidentale del fiume Ica.

Nonostante il crescente interesse per la fauna a vertebrati delle formazioni di Chilcatay e Pisco, un'esauriente quadro cronostratigrafico non è mai stato realizzato. In questa tesi viene proposta una ricostruzione cronostratigrafica di entrambe le formazioni, grazie all'applicazione dei metodi di tephra fingeprinting, datazioni ^{39}Ar–^{40}Ar, biostratigrafia e stratigrafia a isotopi dello stronzio. La Formazione Chilcatay è stata divisa in due allomembri, Ct1 e Ct2. L'associazione a vertebrati della facies *Ct1a* nella località di Ullujaya è costituita da una comunità costiera dominata da mesopredatori di acque temperato-calde. La cronostratigrafia è stata ricostruita grazie all'integrazione di risultati biostratigrafici e isotopici che attribuiscono la Formazione Chilcatay al Burdigaliano. Basandosi sulle datazioni ^{39}Ar–^{40}Ar, la deposizione è avvenuta tra i 19.25 e i 18.02 Ma, anche se la biostratigrafia a diatomee indica un'età più giovane per il top della formazione (17.08 Ma). La Formazione Pisco è divisa in tre allomembri, P0, P1 e P2. Il contenuto di vertebrati fossili dell'allomembro P0 è ancora da caratterizzare, ma si differenzia chiaramente dalla fauna dell'allomembro P1, in cui dominano cetoteridi di media taglia. Nell'allomembro P2, invece, l'associazione è dominata da balenotteridi. La ricostruzione della cronostratigrafia è stata possibile grazie a diversi metodi. Analisi degli isotopi dello stronzio su carbonati e fosfati attribuiscono l'allomembro P0 al Langhiano – Serravalliano (tra 14.80 e 12.60 Ma). Le datazioni ^{39}Ar – ^{40}Ar e la biostratigrafia a diatomee attribuiscono l'allomembro P1 al Tortoniano (tra 9.46 e 8.60 Ma) e l'allomembro P2 al Tortoniano – Messiniano (tra 8.39 e 6.71 Ma). Periodi di non sedimentazione, rappresentati dalle discordanze tra gli allomembri, possono essere messi in relazione con i massimi isotopici dell'ossigeno che indicano l'abbassamento eustatico del livello del mare. Il metodo del fingerprinting applicato ai tefra ha permesso di ottenere

una ricostruzione stratigrafica ad alta risoluzione per P2 e di correlare successioni esposte in diverse località.

La conservazione di vertebrati e invertebrati lungo questa successione è considerata eccezionale. La tafonomia degli invertebrati è stata studiata in entrambe le formazioni con microscopia ottica ed elettronica a scansione e con analisi di catodoluminescenza. Nella Formazione Chilcatay, i gusci dei molluschi sono prevalentemente costituiti da calcite e presentano una buona conservazione. Gli ostreidi, in alcuni casi, mostrano un livello prismatico perfettamente conservato e una luminescenza bassa ed omogenea, che testimoniano un basso grado di alterazione. Questi esemplari sono stati scelti per studi cronostratigrafici con gli isotopi dello stronzio. Studi tafonomici sulle facies a balani della Formazione Chilcatay indicano un ambiente di acque relativamente basse e un ambiente ad alta energia. Nella Formazione Pisco, i molluschi sono solitamente costituiti da calchi di gesso o modelli interni di dolomite/gesso. I rapporti isotopici dello stronzio indicano che la dolomite si è formata tramite diagenesi precoce, mentre il gesso deriva da salamoie pre-mioceniche in risalita. La tafonomia dei vertebrati mostra che le ossa della Formazione Chilcatay hanno un buon grado di conservazione, risultato di un'alternanza di condizioni anossiche e ossiche-disossiche al fondo, testimoniata da analisi sulla distribuzione granulometrica di framboidi relitti di pirite nel sedimento. Nella Formazione Pisco, il calcolo dei tassi di sedimentazione suggerisce che la buona conservazione dei reperti non è dovuta al rapido seppellimento, ma al precoce attuarsi di processi disossici/anossici che hanno permesso la fosfatizzazione e la formazione di noduli carbonatici.

Thesis structure

This thesis is subdivided in four parts: the Prologue, Part I, Part II and the Finale.
Several parts of this dissertation have already been published in peer review papers. A list of these papers is reported at the end of each chapter, followed by a list of the chapter references and the contribution of the candidate.
The Prologue is composed of three chapters (Chapter 1–3), which report a general introduction, a review of the Pisco Basin geology and the historical studies of the Pisco Fossil-Lagerstätte.
Part I concerns chronostratigraphy and consists of nine chapters (Chapter 4–12). Chapter 4 reports the dating background; Chapter 5 explains methods applied for chronostratigraphic studies; Chapters 6 to 8 show the stratigraphic, paleoecologic and chronostratigraphic results on the Chilcatay Formation; finally, Chapters 9 to 12 report the stratigraphic, paleoecologic and chronostratigraphic results on the Pisco Formation.
Part II regards invertebrate and vertebrate taphonomy and comprises five chapters (Chapter 13–17). Chapter 13 is an introduction on the exceptional preservation of fossils; Chapter 14 describes methods applied for taphonomic studies; Chapters 15 and 16 show taphonomic data of invertebrates from the Chilcatay and Pisco formations; finally, Chapter 17 describes vertebrate taphonomy from both formations.
The Finale is made of two chapters (Chapter 18–19) and reports the general discussion and the overall conclusions of this dissertation about chronostratigraphic and taphonomic studies in Miocene sedimentary successions of the East Pisco Basin.

PROLOGUE

Chapter 1. Introduction

This dissertation has the purpose of making chronostratigraphic and taphonomic studies on the Miocene formations of the East Pisco Basin, outcropping in the Ica Desert (Peru). In the southern Peruvian coast, the sedimentary succession of the East Pisco Basin, a sedimentary basin that was active between the Eocene and the Pliocene, crops out in the desert area of the Ica Region (Fig. 1.1). The upper Oligocene to lower Miocene Chilcatay Formation and the upper Miocene to Pliocene Pisco Formation are characterized by an extraordinarily preserved vertebrate fossil fauna (Fig. 1.2). The East Pisco Basin, indeed, hosts one of the most important cetacean-bearing Fossil-Lagerstätten worldwide, with exceptionally well-preserved fossils of marine vertebrates (Bianucci et al. 2016a, b).

In particular, along the western side of the Ica River, the Chilcatay Formation has received a wide attention in the past few years due to numerous significant discoveries of fossil cetaceans, in particular odontocetes (Bianucci et al. 2015; Lambert et al. 2014, 2015, 2017a). In the same area, strata of the Mio-Pliocene Pisco Formation are characterized by fossil remains of cetaceans, both odontocetes and mysticetes, but also of pinnipeds, sea-birds, sea-turtles, crocodiles, sharks, rays and bony fish (Lambert et al. 2009, 2017a, b; Collareta et al. 2015; Bianucci et al. 2016a, b, c and references therein; Landini et al. 2017a, b; Marx et al. 2017).

Over the last 30 years this fauna has been documented in an enormous body of literature and, since 2006, thanks to a European collaboration involving Italian, Belgian, Dutch, French, and Peruvian researchers, a large number of fossil vertebrates from new localities from both the Chilcatay and Pisco formations were collected and studied in detail (e.g. Bianucci et al. 2010, 2014, 2016a, b; Ehret et al. 2012; Lambert et al. 2008, 2009, 2010a, b, 2014, 2015, 2017a, b).

Beyond the vertebrate exceptional occurrence, invertebrate fossils also occurred in both the Miocene formations, showing interesting different modes of preservation. Differently from vertebrates, invertebrates are still poorly studied and only systematic works on mollusks were carried out (DeVries 1988, 2007, 2016).

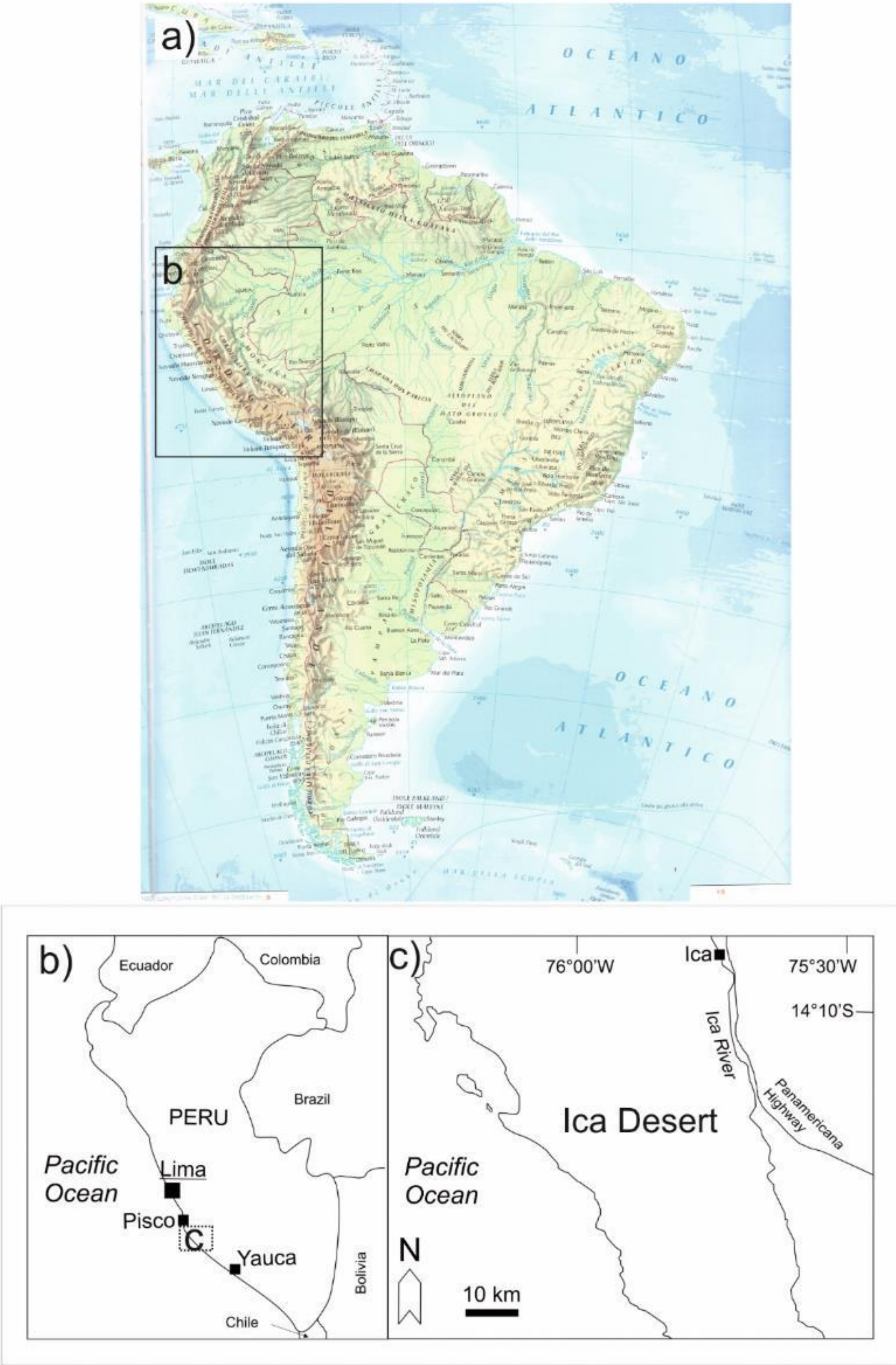

Figure 1.1. Geographic settings of the Ica desert. a) South America map. b) Sketch map of Peru. c) Location of the Ica Desert, ca. 50 km south of the Ica city. Modified from Gariboldi et al. (2015).

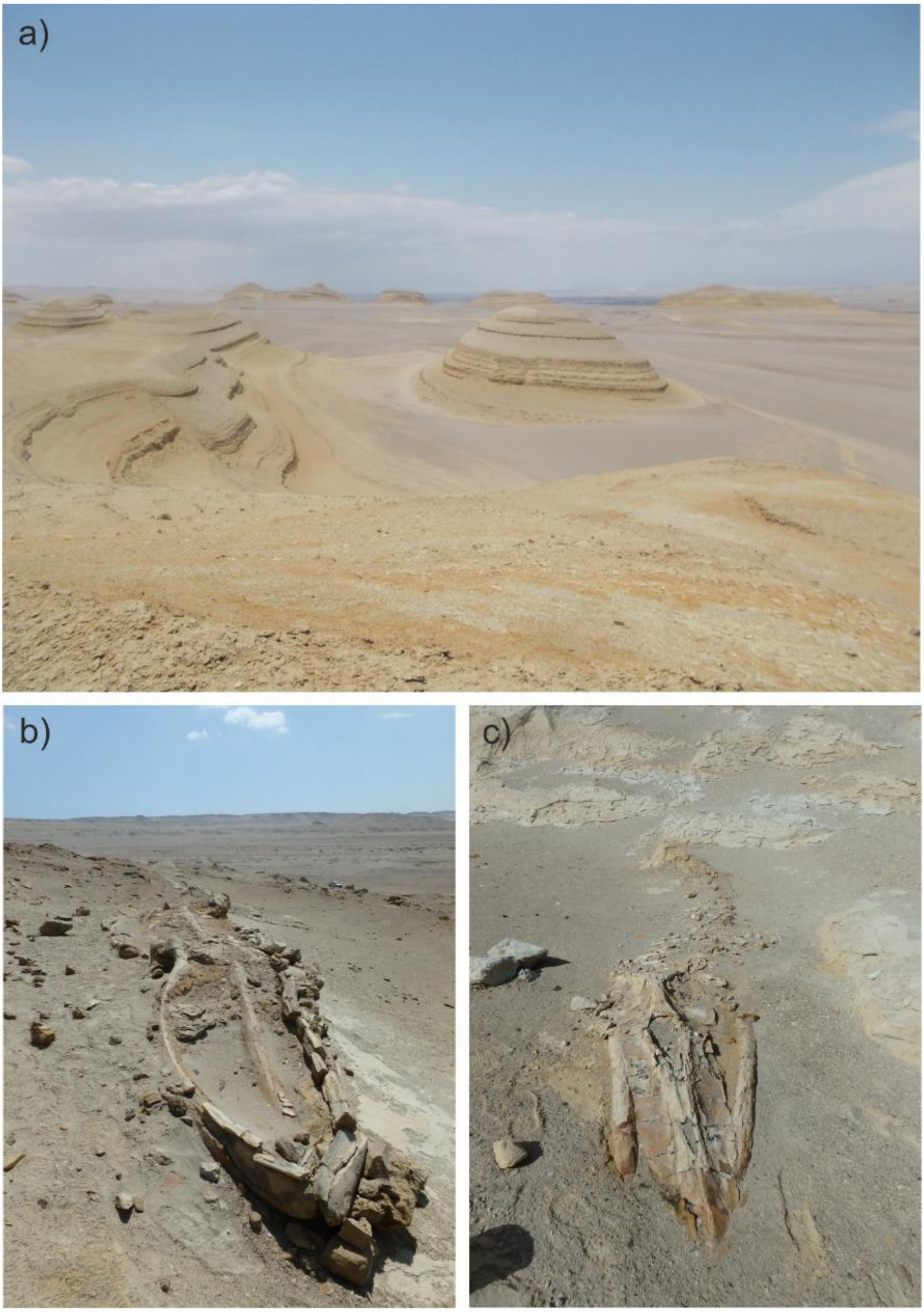

Figure 1.2. Field photos. a) Several “cerros” in the Ica desert, i.e. rounded small hills. b), c) Exceptionally preserved fossils of Mysticete found in the Pisco Formation. Bizygomatic width is 144 and ca. 70 cm, respectively.

More specifically, in the Ocucaje area, 50 km south of the Ica city, the Chilcatay and the Pisco formations crop out as a series of small (up to ca. 200 m high), rounded hills called “cerros” (Fig. 1.2), most of which represent major fossil-bearing localities. The best known “cerros” (Fig. 1.3, Fig. 1.4 and Fig. 1.5) for paleontological studies in the Pisco Formation were Cerro la Bruja (14°31'44" S; 75°40'00" W) (Lambert & Muizon 2013; Lambert et al. 2014), Cerro Ballena (14°21'22" S; 75°42'31" W) (Brand et al. 2004), Cerro Colorado (known also as Cerro Redondo) (14°21'04" S; 75°53'43" W) (Bianucci et al. 2010; Collareta et al. 2015; Lambert et al. 2010a, b, 2015; Parham & Pyenson, 2010) and the area of Cerro Los Quesos (14°30'59" S; 75°42'59" W) (Lambert et al. 2009; Esperante et al. 2015; Bianucci et al. 2016a; Di Celma et al. 2016). Other equally important fossiliferous localities, but studied only in these last years, are: Cerro Hueco la Zorra (14°26'58" S; 75°41'01" W), Cerro Blanco (14°24'57" S; 75°41'17" W), Cerro Toro Chico (14°27'36" S; 75°48'01" W), Cerro Yesera de Amara (14°35'31" S; 75°40'47" W), Cerros Cadenas de los Zanjones (14°34'21" S; 75°42'60" W) and Cerros la Mama y la Hija (14°36'17" S; 75°40'50" W) (Bosio et al. in press). The Chilcatay Formation crops out in the southernmost areas, such as Ullujaya (14°35'04" S; 75°38'19" W), near Cerro Submarino (14°35'19" S; 75°39'24" W), Mal Paso (14°36'29" S; 75°39'58" W) and the wide locality of Zamaca (14°37'37" S; 75°39'10" W). In the southern part, Chilcatay Formation crops out also in the Roca Negra locality (14°39'04" S; 75°38'54" W). All these localities are recently being studied by Di Celma et al. (2018) and Bianucci et al. (2018). At these sites, due to the arid climate and young uplift and exhumation, the stratigraphic section can be traced for several kilometers laterally, providing a unique opportunity to study how faunal assemblages changed through time, whether these changes coincided with paleoenvironmental shifts, and what their nature might be.

Unfortunately, despite the exceptional nature of the exposures and the limited structural deformation, stratigraphy and sedimentology of the important fossil-bearing localities of the Chilcatay and the Pisco formations have only received cursory study, and just a few of them have been the subject of a more accurate stratigraphic investigation in recent years (Brand et al. 2011). Published sedimentological and stratigraphical interpretations on this unit are sparse and mostly limited to preliminary studies based on selected outcrops (DeVries & Schrader, 1997; León et al. 2008; Wright et al. 1988).

Figure 1.3. Satellite image of the Ica Desert localities. Based on image © 2018 DigitalGlobe.

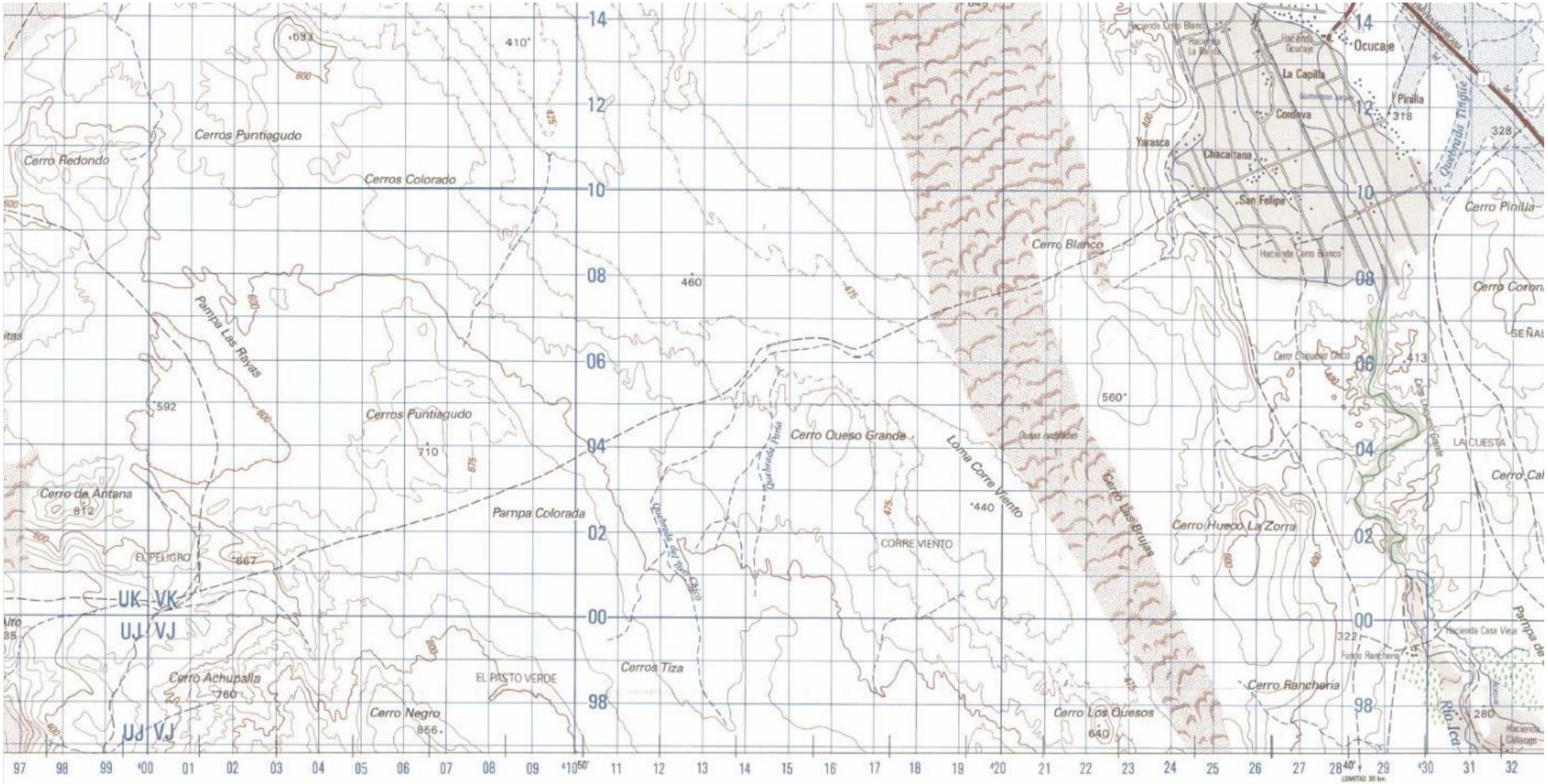

Figure 1.4. Topographic map of the northern study area, from the 1:100,000 map. © Copyright 1996 by the United States Government.

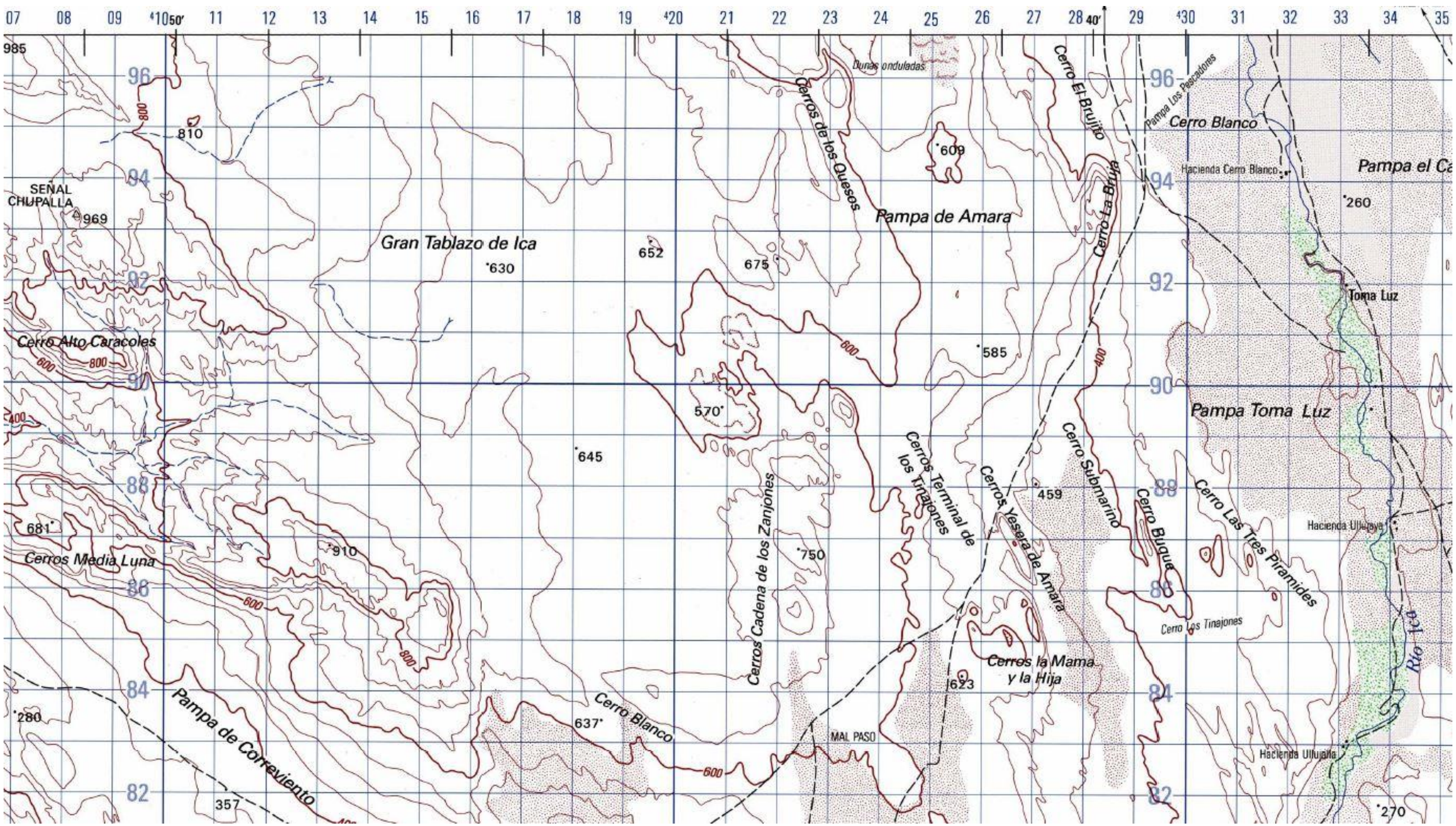

Figure 1.5. Topographic map of the southern study area, from the 1:100,000 map. © Copyright 1996 by the United States Government.

As a result, most studies of fossil vertebrates from the Chilcatay Formation have suffered from a lack of a detailed stratigraphic information and the accurate placement of these discoveries into a proper stratigraphic context remains a largely unresolved issue bearing upon uncertain intraformational correlations and poor age control. In addition, the accurate placement of the Pisco Formation discoveries into a proper stratigraphic context remains a largely unresolved issue that bears upon the general lack of robust biostratigraphic and tephrochronologic age constraints and uncertain intraformational correlations (Brand et al. 2011). During the past years, the paleontological research has mostly focused on systematic studies of single skeletons, the ecology of fossil vertebrates, and the processes governing their preservation, abundance, and taphonomy (Muizon 1988; Brand et al. 2004; Esperante et al. 2008, 2015; Lambert et al. 2009, 2010a, 2010b, 2014, 2015, 2017a, 2017b; Bianucci et al. 2010, 2016a; Collareta et al. 2015, 2017; Gariboldi et al. 2015; Gioncada et al. 2016).

Therefore, correspondence between stratigraphy and vertebrate findings has been a long-term neglected issue: fossil-bearing localities have not been correlated with the adjacent ones and a complete stratigraphic framework has not been constructed until recent works included in the Part I of this dissertation (Di Celma et al. 2016a, b, 2017, 2018; Gariboldi et al. 2017; Bosio et al. in press). In order to better understand, both qualitatively and quantitatively, the evolution of its rich marine vertebrate fauna during a pivotal time frame for the evolutionary history of marine vertebrates, such as the Miocene, the Chilcatay and the Pisco formations need the reconstruction of an accurate, high-resolution absolute and relative age framework. With its rich, but only partly described odontocete fauna (Lambert et al. 2014, 2015; Bianucci et al. 2015), the Chilcatay Formation represents an important window of the cetacean evolutionary history, providing a unique opportunity to better understand the crucial, early steps of the first radiation of crown Odontoceti. Furthermore, the late Miocene is characterized by a significant cetacean turnover outlined by the diversification of several lineages of crown neocetes (e.g. delphinidans, beaked whales and rorquals; Fordyce & Muizon 2001; Bianucci & Landini 2007; Marx et al. 2016). Accurate dating of the origin of some key taxa can also allow a better definition of several calibration points for molecular divergence among crown neocetes (e.g. Lambert et al. 2017b).

This type of study, however, requires strong spatial and temporal control over the stratigraphic succession, which can only be provided by the integration of refined stratigraphic data from section measuring, detailed geologic and structural field mapping, geochronological dating, and biostratigraphy. Throughout this work, we will present stratigraphic, geochronologic and biostratigraphic data with the aim of defining a complete stratigraphic framework, reconstructing a detailed chronostratigraphy and calculating sedimentation rates in the East Pisco Basin during the deposition of both Chilcatay and Pisco formations.

Over the past forty years several biostratigraphic and radiometric data have been published for the Chilcatay and Pisco strata, such as those provided by Muizon and Bellon (1980, 1986), Macharè and Fourtanier (1987), Schrader and Ronning (1988), Tsuchi et al. (1988), Marty (1989), Dumbar et al. (1990), Ibaraki (1993), DeVries and Schrader (1997), DeVries (1998), Brand et al. (2011), Esperante et al. (2015), and those quoted in a recent review by DeVries and Jud (2018). K-Ar ages, although well positioned along sections, are biased by the low reliability of the method, while most of the times ^{39}Ar-^{40}Ar ages are provided without any information about the analytical procedures, the measurement error, and the exact stratigraphic position. Generally, ages were used to date individual localities without any attempt to correlate them. Brand et al. (2011), by identifying different marker beds, were the first to attempt a correlation between different outcrops exposed along the Ica River but they did not provide a precise location for their dating points. Biostratigraphy, mainly based on diatoms (Mertz 1966, Macharè & Fourtanier 1987, Schrader & Ronning 1988, Tsuchi et al. 1988, Koizumi 1992), was also extensively used but many of the bioevents and species used in those works have been thoroughly revised since the 80s (Gariboldi 2016).

The first objective of this thesis, discussed in Part I, is to provide more accurate stratigraphic and age constraints for fossil-bearing localities of the East Pisco Basin. In order to develop a robust basin-wide stratigraphic framework allowing for comparisons among the various fossiliferous localities and to provide refined stratigraphic frameworks and age constraints for some of the historic fossil-bearing sites, new stratigraphic analyses of both Chilcatay and Pisco formations have been performed in parallel with geochronological studies and intensive paleontological prospecting within the Ica Desert. In this study, stratigraphic architecture of both Chilcatay and Pisco formations and fossil distribution within their strata have been constrained by the integration of geological field mapping, section measuring, facies analysis, and age estimates from both isotope geochronology and microfossil biostratigraphy.

Tephra deposits and sediments were collected along measured sections to develop the chronostratigraphic model presented in this work; this is based on new radiometric age determinations ($^{39}Ar - ^{40}Ar$ and $^{87}Sr/^{86}Sr$ dating) and micropaleontologic data. Data reported here provide a crucial background for future comparisons among Chilcatay and Pisco localities and a first picture of the spatial and stratigraphic distribution of the fossil marine vertebrates and of the quantitative and qualitative composition of the whole vertebrate assemblage.

The Part II of this dissertation is focused on the taphonomic aspects of both vertebrates and invertebrates, in order to understand the possible mechanisms that led to such a well-preserved fossil-rich deposit.

Despite numerous significant paleontological discoveries and the studies dedicated to the exceptional preservation of bones (Brand et al. 2004; Esperante et al. 2015), the reasons of the exceptional preservation of this Fossil-Lagerstätte are still not so clear. Recently, researchers have focused their attention on the rapid sinking of the carcasses in soft unconsolidated sediment is considered by different authors (Brand et al. 2004, Gariboldi et al. 2015) as a likely mechanism to explain the exceptional preservation of the vertebrate skeletons. Some authors advocated also extremely high sedimentation rates (of one or two orders of magnitude higher than in modern upwelling settings) to explain the formation of the Lagerstätte (Brand et al. 2004; Esperante et al. 2015).

In this work, taphonomic and diagenetic processes are investigated in both Chilcatay and Pisco formations, representing two very different depositional environment. Here, it is proposed that there is not an only reason for the exceptional preservation, but there are many causes that led to the formation of the Pisco Lagerstätte, one of these being the paleogeochemical conditions of the sea bottom environment at the time of the carcasses deposition.

This dissertation is carried out as part of a larger, ongoing project with a sixfold aim: (i) to provide strong stratigraphic control to some of the major fossiliferous localities of the East Pisco Basin formations through the construction of detailed geological maps and the compilation of high resolution stratigraphic sections; (ii) to set the stratigraphic cyclicity evident in the architecture of the formations within a allostratigraphic framework; (iii) to constrain the age of the unconformity-bounded allomembers through the integration of radiometric dating and biostratigraphy; (iv) to investigate vertebrate and invertebrate taphonomic and diagenetic processes; (v) to establish the depositional settings and the mechanisms that explain the exceptional preservation in the Pisco Lagerstätte; (vi) to confer accurate stratigraphic and time constraints to each fossil taxon through absolute dating and correlation of stratigraphic sections.

These developments represent a first step in facilitating correlation between scattered and geographically disparate outcrop sections and provide a sound basis for future studies of the systematics, phylogeny, evolutionary and paleoecology of East Pisco Basin fossil vertebrates and invertebrates, and the taphonomic and diagenetic factors dictating their exceptional preservation.

Some parts and figures included in this chapter are modified from different introduction paragraphs of the following published papers.

The two about the Cerro los Quesos locality: "Fossil marine vertebrates of Cerro Los Quesos: Distribution of cetaceans, seals, crocodiles, seabirds, sharks, and bony fish in a late Miocene locality of the Pisco Basin, Peru" authored by Giovanni Bianucci, Claudio Di Celma, Alberto Collareta, Walter Landini, Klaas Post, Chiara Tinelli, Christian de Muizon, Giulia Bosio, Karen Gariboldi, Anna Gioncada, Elisa Malinverno, Gino Cantalamessa, Ali Altamirano-Sierra, Rodolfo Salas-Gismondi, Mario Urbina and Olivier Lambert, published on Journal of Maps in 2016, Vol. 12, 1037-1046; and "Stratigraphic framework of the late Miocene Pisco Formation at Cerro Los Quesos (Ica Desert, Peru)" written by Claudio Di Celma, Elisa Malinverno, Gino Cantalamessa, Anna Gioncada, Giulia Bosio, Igor Maria Villa, Karen Gariboldi, Andrea Rustichelli, Pietro Paolo Pierantoni, Walter Landini, Chiara Tinelli, Alberto Collareta and Giovanni Bianucci, printed on Journal of Maps in 2016, Vol. 12, 1020-1028.

Introduction for Pisco Formation is also based on the papers "Stratigraphic framework of the late Miocene to Pliocene Pisco Formation at Cerro Colorado (Ica Desert, Peru)" authored by Claudio Di Celma, Elisa Malinverno, Karen Gariboldi, Anna Gioncada, Andrea Rustichelli, Pietro Paolo Pierantoni, Walter Landini, Giulia Bosio, Chiara Tinelli and Giovanni Bianucci, published in 2016 on Journal of Maps, Vol. 12, 515-529; "Sequence stratigraphy and paleontology of the upper Miocene Pisco Formation along the western side of the lower ica valley (Ica Desert, Peru)" written by Claudio Di Celma, Elisa Malinverno, Giulia Bosio, Alberto Collareta, Karen Gariboldi, Anna Gioncada, Giancarlo Molli, Daniela Basso, Rafael M. Varas-Malca, Pietro Paolo Pierantoni, Igor

Maria Villa, Olivier Lambert, Walter Landini, Giovanni Sarti, Gino Cantalamessa, Mario Urbina and Giovanni Bianucci, printed on Rivista Italiana di Paleontologia e Stratigraia (RIPS) in 2017, Vol. 123(2): 255-273; "Biostratigraphy, geochronology and sedimentation rates of the upper Miocene Pisco Formation at two important marine vertebrate fossil-bearing sites of southern Peru" written by Karen Gariboldi, Giulia Bosio, Elisa Malinverno, Anna Gioncada, Claudio Di Celma, Igor M. Villa, Mario Urbina and Giovanni Bianucci, published on Newsletters on Stratigraphy in 2017, Vol. 50/4 (2017), 417-444; "Chemical and petrographic fingerprinting of volcanic ashes as a tool for high-resolution stratigraphy of the upper Miocene Pisco Formation (Peru)" written by Giulia Bosio, Anna Gioncada, Elisa Malinverno, Claudio Di Celma, Igor M. Villa, Giuseppe Cataldi, Karen Gariboldi, Alberto Collareta, Mario Urbina and Giovanni Bianucci, which will be published by the Journal of the Geological Society in January 2019; "Tephrochronology and chronostratigraphy of the Miocene Chilcatay and Pisco formations (East Pisco Basin, Peru)" written by Giulia Bosio, Elisa Malinverno, Igor M. Villa, Claudio Di Celma, Karen Gariboldi, Anna Gioncada, Valentina Barberini, Mario Urbina and Giovanni Bianucci, that will be submitted to Newsletters on Stratigraphy in November 2018.

Parts regarding Chilcatay Formation are taken from the paper "Facies analysis, stratigraphy and marine vertebrate assemblage of the lower Miocene Chilcatay Formation at Ullujaya (Pisco basin, Peru)" authored by Claudio Di Celma, Elisa Malinverno, Alberto Collareta, Giulia Bosio, Karen Gariboldi, Olivier Lambert, Walter Landini, Pietro Paolo Pierantoni, Anna Gioncada, Igor Maria Villa, Giovanni Coletti, Christian de Muizon, Mario Urbina and Giovanni Bianucci and published in 2018 by Journal of Maps, Vol. 14:2, 257-268.

Chapter References

Bianucci, G., Di Celma, C., Urbina, M., Lambert, G. 2016a. New beaked whales from the late Miocene of Peru and evidence for convergent evolution in stem and crown Ziphiidae (Cetacea, Odontoceti). PeerJ 4:e2479.

Bianucci, G., Di Celma, C., Collareta, A., Landini, W., Post, K., Tinelli, C., Muizon, de C., Bosio, G., Gariboldi, K., Gioncada, A., Malinverno, E., Cantalamessa, G., Altamirano-Sierra, A., Salas-Gismondi, R., Urbina, M., Lambert, O. 2016b. Fossil marine vertebrates of Cerro Los Quesos:

Distribution of cetaceans, seals, crocodiles, seabirds, sharks, and bony fish in a late Miocene locality of the Pisco Basin, Peru. Journal of Maps, 12, 1037-1046.

Bianucci, G., Di Celma, C., Landini, W., Post, K., Tinelli, C., Muizon, de C., Gariboldi, K., Malinverno, E., Cantalamessa, G., Gioncada, A., Collareta, A., Salas-Gismondi, R., Varas-Malca, R.M., Urbina, M., Lambert, O. 2016c. Distribution of fossil marine vertebrates in Cerro Colorado, the type locality of the giant raptorial sperm whale Livyatan melvillei (Miocene, Pisco Formation, Peru). Journal of Maps, 12, 543-557.

Bianucci, G., Lambert, O., Post, K. 2010. High concentration of long-snouted beaked whales (genus Messapicetus) from the Miocene of Peru. Palaeontology, 53, 1077-1098.

Bianucci, G., Landini, W. 2007. Fossil history. In: Reproductive biology and phylogeny of cetacea: whales dolphins and porpoises, (ed. DL Miller), 35-93. Enfield, NH: Science Publishers.

Bianucci, G., Urbina, M., Lambert, O. 2015. A new record of Notocetus vanbenedeni (Squalodelphinidae, Odontoceti, Cetacea) from the Early Miocene of Peru. Comptes Rendus Palevol, 14, 5-13.

Bianucci, G., Collareta, A., Bosio, G., Landini, W., Gariboldi, K., Gioncada, A., Lambert, O., Malinverno, E., Muizon, de C., Varas-Malca, R., Villa, I.M., Coletti, G., Urbina, M., Di Celma, C. 2018. Taphonomy and palaeoecology of the lower Miocene marine vertebrate assemblage of Ullujaya (Chilcatay Formation, East Pisco Basin, southern Peru). Palaeogeography, Palaeoclimatology, Palaeoecology, 511, 256-279.

Bosio, G., Gioncada, A., Malinverno, E., Di Celma, C., Villa, I.M., Cataldi, G., Gariboldi, K., Collareta, A., Urbina, M., Bianucci, G. in press. Chemical and petrographic fingerprinting of volcanic ashes as a tool for high-resolution stratigraphy of the upper Miocene Pisco Formation (Peru). Journal of the Geological Society.

Brand, L.R., Esperante, R., Chadwick, A.V., Poma Porras, O., Alomía, M. 2004. Fossil whale preservation implies high diatom accumulation rate in the Miocene-Pliocene Pisco Formation of Peru. Geology 32, 165-168.

Brand, L.R., Urbina, M., Chadwick, A., DeVries T.J., Esperante, R. 2011. A high resolution stratigraphic framework for the remarkable fossil cetacean assemblage of the Miocene/Pliocene Pisco Formation, Peru. Journal of South American Earth Sciences, 31, 414-425.

Collareta, A., Landini, W., Chacaltana, C., Valdivia, W., Altamirano-Sierra, A., Urbina, M., Bianucci, G. 2017. A well preserved skeleton of the fossil shark Cosmopolitodus hastalis from the late Miocene of Peru, featuring fish remains as fossilized stomach contents. Rivista Italiana di Paleontologia e Stratigrafia (Research In Paleontology and Stratigraphy), 123, 11-22.

Collareta, A., Landini, W., Lambert, O., Post, K., Tinelli, C., Di Celma, C., Panetta, D., Tripodi, M., Salvadori, P.A., Caramella, D., Marchi, D., Urbina, M., Bianucci, G. 2015. Piscivory in a Miocene Cetotheriidae: first record of fossilized stomach content for an extinct baleen-bearing whale. The Science of Nature, 102, 70.

DeVries, T.J. 1988. Mollusks of the Pisco Basin. Pisco Basin Guidebook, chapter 8, 127-134.

DeVries, T.J. 1998. Oligocene deposition and Cenozoic sequence boundaries in the Pisco Basin (Peru). Journal of South American Earth Sciences, 11, 217-231.

DeVries, T.J. 2007. Cenozoic Turritellidae (Gastropoda) from Southern Peru. Journal of Paleontology, 81, 331-351.

DeVries, T.J. 2016. Fossil Cenozoic crassatelline bivalves from Peru: New species and generic insights. Acta Palaeontologica Polonica, 61, 661-688.

DeVries, T. J., Jud, N. A. 2018. Lithofacies patterns and paleogeography of the Miocene Chilcatay and lower Pisco depositional sequences (East Pisco Basin, Peru). Boletín de la Sociedad Geológica del Perú, Volumen Jubilar, 8, 124-167.

DeVries, T. J., & Schrader, H. 1997. Middle Miocene marine sediments in the Pisco Basin (Peru). Boletín de la Sociedad Geológica del Perú, 87, 1-13.

Di Celma, C., Malinverno, E., Bosio, G., Collareta, A., Gariboldi, K., Gioncada, A., Molli, G., Basso, D., Varas-Malca, R., Pierantoni, P.P., Villa, I.M., Lambert, O., Landini, W., Sarti, G., Cantalamessa, G., Urbina, M., Bianucci, G. 2017. Sequence stratigraphy and palaeontology of the upper Miocene Pisco Formation along the western side of the lower Ica valley (Ica desert, Peru). Rivista Italiana di Paleontologia e Stratigrafia (Research In Paleontology and Stratigraphy), 123, 255-274.

Di Celma, C., Malinverno, E., Gariboldi, K., Gioncada, A., Rustichelli, A., Pierantoni, P.P., Landini, W., Bosio, G., Tinelli, C., Bianucci, G. 2016a. Stratigraphic framework of the late Miocene to Pliocene Pisco formation at Cerro Colorado (Ica Desert, Peru). Journal of Maps, 12(3), 515-529.

Di Celma, C., Malinverno, E., Cantalamessa, G., Gioncada, A., Bosio, G., Villa, I. M., Gariboldi, K., Rustichelli, A., Pierantoni, P. P., Landini, W., Tinelli, C., Collareta, A., Bianucci, G. 2016b. Geological Map of the Miocene– Pliocene Pisco Formation at Cerro Los Quesos (Ica Desert, Peru). Journal of Maps, 12(5), 1020-1028.

Di Celma, C., Malinverno, E., Collareta, A., Bosio, G., Gariboldi, K., Lambert, O., Landini, W., Pierantoni, P.P., Gioncada, A., Villa, I.M., Coletti, G., Muizon, de C., Urbina, M., Bianucci, G.

2018. Facies analysis, stratigraphy and marine vertebrate assemblage of the lower Miocene Chilcatay Formation at Ullujaya (Pisco basin, Peru). Journal of Maps, 14(2), 257-268.

Dunbar, R. B., Marty, R. C., Baker, P. A. 1990. Cenozoic marine sedimentation in the Sechura and Pisco basins, Peru. Palaeogeography, Palaeoclimatology, Palaeoecology, 77, 235-261.

Ehret, D. J., McFadden, B. J., Jones, D. S., DeVries, T. J., Foster, D. A., Sala Gismondi, R. 2012. Origin of the white shark Carcharodon (Lamniformes: Lamnidae) based on recalibration of the Upper Neogene Pisco Formation of Peru. Palaeontology, 55(6), 1139–1153.

Esperante, R., Brand, L. R., Chadwick, A. V., Poma, O. 2015. Taphonomy and paleoenvironmental conditions of deposition of fossil whales in the diatomaceous sediments of the Miocene/Pliocene Pisco Formation, southern Peru - A new fossil-lagerstätte. Palaeogeography, Palaeoclimatology, Palaeoecology, 417, 337-370.

Esperante, R., Brand, L. R., Nick, K. E., Poma, O., Urbina, M. 2008. Exceptional occurrence of fossil baleen in shallow marine sediments of the Neogene Pisco Formation, Southern Peru. Palaeogeography, Palaeoclimatology, Palaeoecology, 257, 344-360.

Fordyce, R.E., Muizon de, C. 2001. Evolutionary history of cetaceans: a review. In: Mazin J.-M. & de Buffrénil V. (Eds.), Secondary Adaptation of Tetrapods to Life in Water, Proceedings of the international meeting Poitiers, 169-233.

Gariboldi, K. 2016. A note on diatom stratigraphic markers in upper Miocene sediments of the Pisco Formation, Peru, and description of Delphineis urbinai sp. nov. Diatom Research, 31, 285-301.

Gariboldi, K., Gioncada, A., Bosio, G., Malinverno, E., Di Celma, C., Tinelli, C., Cantalamessa, G., Landini, W., Urbina, M., Bianucci, G. 2015. The dolomite nodules enclosing fossil marine vertebrates in the East Pisco Basin, Peru: field and petrographic insights into the Lagerstätte formation. Palaeogeography, Palaeoclimatology, Palaeoecology 438, 81-95.

Gioncada, A., Collareta, A., Gariboldi, K., Lambert, O., Di Celma, C., Bonaccorsi, E., Urbina, M., Bianucci, G. 2016. Inside baleen: Exceptional microstructure preservation in a late Miocene whale skeleton from Peru. Geology, 44(10), 839-842.

Ibaraki, M. 1993. Eocene to early Miocene planktonic foraminifera from the south of Paracas, central Peru. Shizuoka University, Report of the Faculty of Sciences, 27, 77-93.

Koizumi, I. 1992. Diatomaceous sediments along the Pacific coastal areas of South America and their evaluation. Journal of the Faculty of Science, Hokkaido University, Ser. IV, 23(2), 227-245.

Lambert, O., Bianucci, G., Beatty, B.L. 2014. Bony outgrowths on the jaws of an extinct sperm whale support macroraptorial feeding in several stem physeteroids. Naturwissenschaften, 101, 517-521.

Lambert, O., Bianucci, G., Post, K. 2009. A new beaked whale (Odontoceti, Ziphiidae) from the Middle Miocene of Peru. Journal of Vertebrate Paleontology, 29, 910-922.

Lambert, O., Bianucci, G., Post, K. 2010a. Tusk bearing beaked whales from the Miocene of Peru: Sexual dimorphism in fossil ziphiids? Journal of Mammalogy, 91, 19-26.

Lambert, O., Bianucci, G., Muizon, de C. 2017a. Macroraptorial sperm whales (Cetacea, Odontoceti, Physeteroidea) from the Miocene of Peru. Zoological Journal of the Linnean Society, 179, 404-474.

Lambert, O., Bianucci, G., Post, K., Muizon, C. de, Salas-Gismondi, R., Urbina, M., Reumer, J. 2010b. The giant bite of a new raptorial sperm whale from the Miocene epoch of Peru. Nature, 466, 105-108.

Lambert, O., Bianucci, G., Urbina, M., Geisler, J.H. 2017b. A new inioid (Cetacea, Odontoceti, Delphinidae) from the Miocene of Peru and the origin of modern dolphin and porpoise families. Zoological Journal of the Linnean Society, 179(4), 919-946.

Lambert, O., Collareta, A., Landini, W., Post, K., Ramassamy, B., Di Celma, C., Urbina, M., Bianucci, G. 2015. No deep diving: evidence of predation on epipelagic ish for a stem beaked whale from the late Miocene of Peru. Proceedings of the Royal Society B - Biological Sciences, 282, article no. 20151530.

Lambert, O., Muizon de, C. 2013. A new long-snouted species of the Miocene pontoporiid dolphin Brachydelphis and a review of the Mio-Pliocene marine mammal levels in the Sacaco Basin, Peru. Journal of Vertebrate Paleontology, 33, 709-721.

Lambert, O., Schlögl, J., Kováč, M. 2008. Middle Miocene toothed whale with Platanista-like teeth from the Vienna Basin (Western Carpathians, Slovakia). Neues Jahrbuch für Geologie und Paläontologie, 250, 157-166.

Landini, W., Collareta, A., Pesci, F., Di Celma, C., Urbina, M., Bianucci, G. 2017a. A secondary nursery area for the copper shark Carcharhinus brachyurus from the late Miocene of Peru. Journal of South American Earth Sciences, 78, 164-174.

Landini, W., Altamirano-Sierra, A., Collareta, A., Di Celma, C., Urbina, M., Bianucci, G. 2017b. The late Miocene elasmobranch assemblage from Cerro Colorado (Pisco Formation, Peru). Journal of South American Earth Sciences, 73, 168-190.

León, W., Aleman, A., Torres, V., Rosell, W., & De La Cruz, O. 2008. Estratigrafía, Sedimentología y evolución tectónica de la cuenca Pisco Oriental. Boletín INGEMMET, Serie D, 27, 1-154, Lima, Peru.

Macharé, J., Fourtanier, E. 1987. Datations des formations tertiaires du bassin de Pisco (Pérou) à partir d'associations de diatomées. Comptes rendus de l'Académie des sciences. Série 2, Mécanique, Physique, Chimie, Sciences de l'univers, Sciences de la Terre 305(5), 407-412.

Muizon de, C. 1988. Les Vertébrés fossiles de la Formation Pisco (Pérou). Troisième partie: Les Odontocètes (Cetacea, Mammalia) du Miocène. Travaux de l'Institut Français d'Études Andines, 42, 1-244.

Marty, R. 1989. Stratigraphy and chemical sedimentology of Cenozoic biogenic sediments from the Pisco and Sechura Basins, Peru. PhD Thesis, Houston, Texas, Rice University.

Marx, F.G., Collareta, A., Gioncada, A., Post, K., Lambert, O., Bonaccorsi, E., Urbina, M., Bianucci, G. 2017. How whales used to filter: exceptionally preserved baleen in a Miocene cetotheriid. Journal of Anatomy, 231, 212-220.

Marx, F.G., Kohno, N. 2016. A new Miocene baleen whale from the Peruvian desert. Royal Society Open Science, 3, 160542.

Mertz, D. 1966. Mikropaläontologische und sedimentologische Untersuchung der Pisco-Formation Südperus. Palaeontographica B, 118, 1-51.

Muizon, C. de, Bellon, H. 1980. L'âge mio-pliocène de la formation Pisco, Pérou. Comptes Rendus de l'Académie des Sciences de Paris, tome 290, Série D, 1063-1066.

Muizon, C. de, Bellon, H., 1986. Nouvelles donn ees sur l'âge de la Formation Pisco (Pérou). Comptes Rendus de l'Académie des Sciences de Paris, 303, II, 15, 1401-1404.

Parham, J. F., Pyenson, N. D. 2010. New sea turtle from the Miocene of Peru and the iterative evolution of feeding ecomorphologies since the Cretaceous. Journal of Paleontology, 84, 231-247.

Schrader, H., Ronning, P. 1988. Diatom biostratigraphy and coastal upwelling interpretation. In: Dunbar, R. B., Baker, P. A. (Eds.), Cenozoic Geology of the Pisco Basin, IGCP no. 156 Guidebook to Field Workshop, May 1988, Lima, 135-140.

Tsuchi, R., Shuto, T., Takayama, T., Fujiyoshi, A, Koizumi, I., Ibaraki, M., Rangel, Z. C., Aldana, A. M. 1988. Fundamental Data on Cenozoic Biostratigraphy of the Pacific Coast of Peru. In: Tsuchi R. (ed.), Report of Andean studies, Shizuoka University, 3, 45-70.

Wright, R., Dunbar, R. B., Allen, M., Baker, P. 1988. Morphology of stacked marine delta lobes, East Pisco Basin, Peru. In A. W. Bally (Ed.), Atlas of seismic stratigraphy, 192-196. Tulsa: AAPG, Studies in Geology, 27, III.

Chapter 2. Geology of the Pisco Basin: a review

Since Mesozoic times, the tectono-dynamics of Peru were controlled by the convergence of the continental South American Plate and the oceanic Nazca/Farallon Plate.
The oblique subduction of the eastern edge of the oceanic Nazca Plate underneath the Peruvian portion of the South American plate (Barazangi & Isacks 1979; Coira et al. 1982; Pilger 1981; Cahill & Isacks, 1992; Gutscher et al. 2000), which began in the Cretaceous and continues today, deformed the leading edge of the South American Plate and developed a composite transform-convergent margin characterized by normal and strike-slip faults that formed extensional and pull-apart basins along the western margin of Peru, as shown in Figure 2.1 (e.g. Kulm et al. 1982; Dunbar et al. 1990; León et al. 2008; Zúñiga-Rivero et al. 2010; Viveen & Schlunegger 2018).

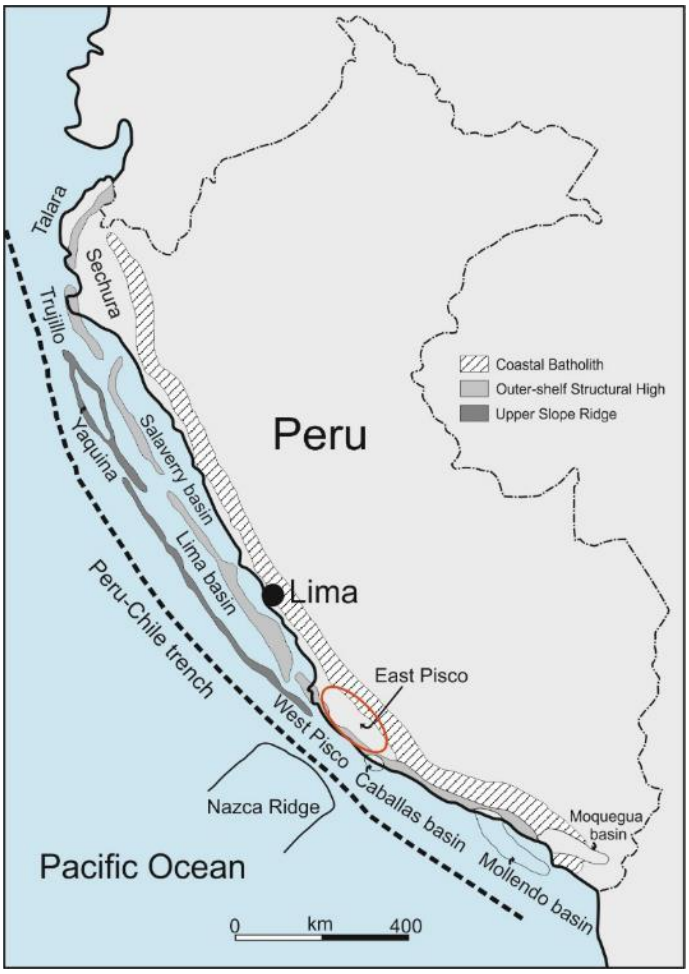

Figure 2.1. Map of the major structural trends and basins of coastal Peru, redrawn and modified from Travis et al. (1976) and Thornburg and Kulm (1981).

According to Thornburg and Kulm (1981), two long and narrow, trench parallel structural highs were formed on the continental shelf and upper slope of the Peruvian continental margin during Late Cretaceous–early Paleogene time, namely the Outer Shelf High and the Upper Slope Ridge (Fig. 2.1). These two ridges and associated shorter, transverse shelf uplifts, or local highs, subdivided the Peruvian offshore into a series of fault-bounded Cenozoic sedimentary basins, which may be separated into an inner set of shelf basins and a seaward set of slope basins. They were formed in response to prolonged extension and subsidence since the middle-late Eocene (Viveen & Schlunegger 2018).

The Pisco Basin, in southern Peru, is one of these fault-bounded basins at 14°30' S of latitude. In coastal southwestern Peru, the most easterly Outer Shelf High separates the forearc Pisco Basin into an offshore and an onshore portion, referred to as the West Pisco Basin, still submerged, and East Pisco Basin, respectively (Fig. 2.1). The East Pisco Basin, the exposed one, is a 180 × 30 km elongated sedimentary basin extending along the southern Peru from Pisco to Nazca towns.

The basement rocks are composed mostly of Precambrian gneiss and lower Paleozoic granite covered by upper Jurassic to lower Cretaceous volcanics and sediments. Within the study area, the basement rocks consists of a complex assemblage of lower Palaeozoic gabbroic to granitoid rocks forming the San Nicolás batholiths (Mukasa & Henry 1990), intruding a Precambrian metamorphic complex known as the Arequipa massif and covered by Jurassic volcano-sedimentary rocks of the Guaneros Formation. The Guaneros Formation consists of volcaniclastic rocks with andesitic to rhyolitic composition deriving from a Jurassic calcalkaline volcanic arc, interbedded with calcareous sediments (León et al. 2008). During late Cretaceous, these units formed a long and narrow structural high on the outer shelf of the Peru margin (Kulm et al. 1982; Thornburg & Kulm 1981). To the east, the basin is bounded by the Coastal Batholith, a complex of igneous rocks mostly emplaced during the late Cretaceous–early Eocene when arc magmatic activity was close to the location of the present coastline (Cobbing 1999; Mukasa 1986; Romero et al. 2013 and references therein). As such, communications of the basin with the outer ocean were restricted due to these two structural barriers. Therefore, the East Pisco Basin was a shallow water, semi-enclosed embayment protected to the west by a chain of igneous islands of the emerging Outer Shelf High (Marocco & Muizon 1988; Muizon & DeVries 1985; DeVries & Jud 2018) during the sediment deposition, as shown in Figure 2.2.

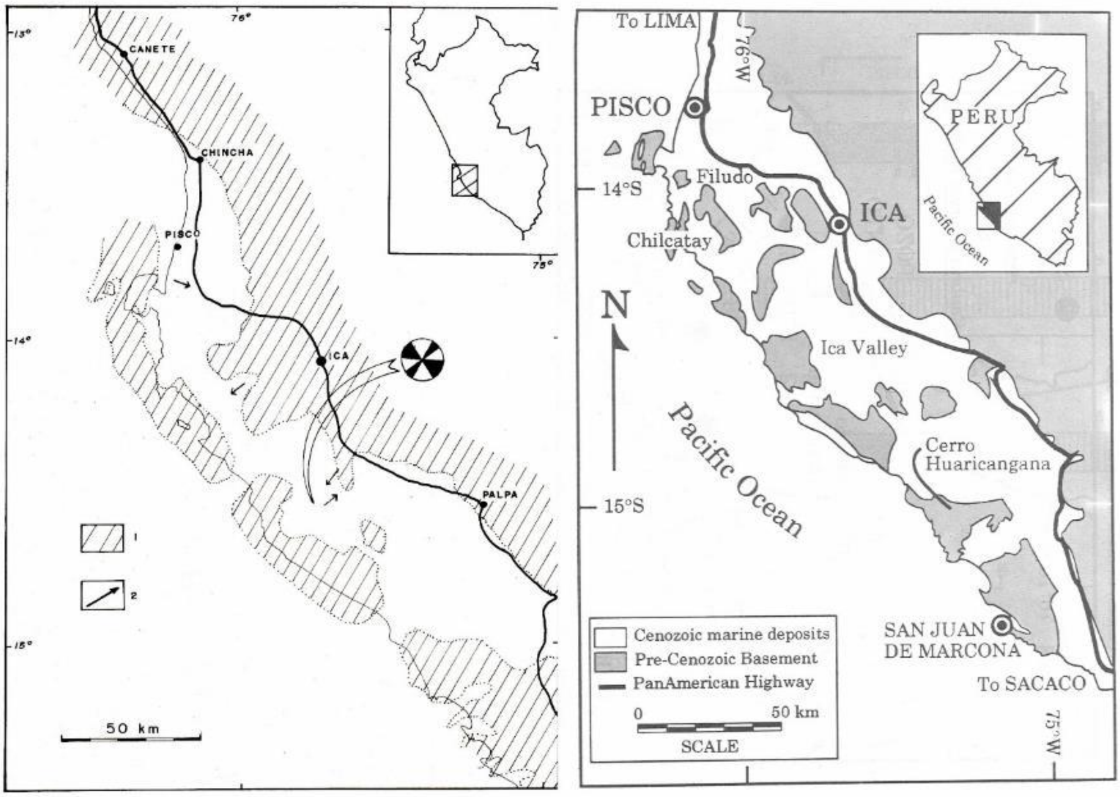

Figure 2.2. Reconstructions of the protected semi-enclosed embayment of the East Pisco Basin during the sediment deposition. From Marocco and Muizon (1988) and DeVries and Schrader (1997), respectively.

Active subduction erosion (von Huene & Lallemand 1990; Clift et al. 2003; Hampel et al. 2004) controlled a prolonged period of normal faulting and subsidence in the East Pisco Basin since at least the middle-late Eocene (Dunbar et al. 1990; León et al. 2008; Rustichelli et al. 2016a, b). This long-term subsidence driven by basal tectonic erosion allow a discontinuous deposition of large amounts of marine sediments starting from the middle-late Eocene.

The sedimentary fill of the East Pisco Basin has been described by Dunbar et al. (1990) and DeVries (1998) and consists of five lithostratigraphic units: the Eocene Caballas Formation, the middle to upper Eocene Paracas Formation (subdivided in Los Choros and Yumaque members), the uppermost Eocene-lower Oligocene Otuma Formation, the uppermost Oligocene to lower Miocene Chilcatay Formation, and the upper Miocene to Pliocene Pisco Formation (Dunbar et al. 1990; DeVries 1998, 2017; DeVries et al. 2017; DeVries & Jud 2018). Outcrops and stratigraphy of the East Pisco Basin are shown in Figure 2.3.

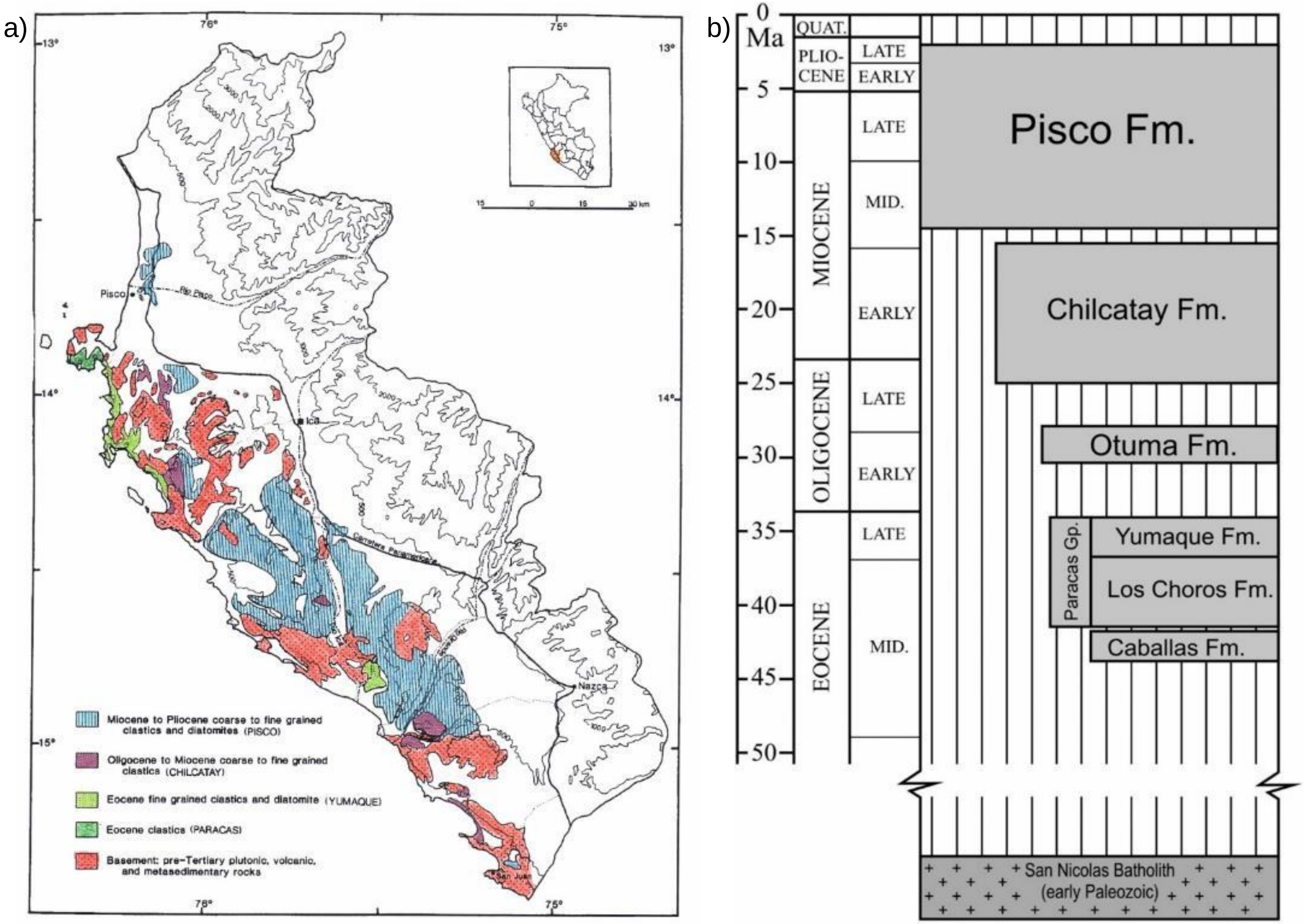

Figure 2.3. a) Geologic map of the East Pisco Basin modified from Dunbar et al. (1990).

b) Stratigraphy of the Pisco Basin modified from DeVries (1998).

These units are bounded by regionally extensive, conglomerate-mantled angular unconformities and document relatively long breaks in sedimentation. These unconformities are locally demarcated by pavements of igneous pebble to boulder clasts and could represent periods of subaerial exposure (DeVries 1998; Dunbar et al. 1990).
The Paracas Group comprises the Los Choros Formation, previously described as Paracas Formation by Petersen (1954), Newell (1956) and Balarezo et al. (1980), and the Yumaque Formation. Dunbar et al. (1990) characterized the Los Choros Formation as 700 m of nearshore and inner shelf bioclastic conglomerates, sandstones, and less amounts of siltstone and mudrock, and the Yumaque Formation as a succession of fine-grained marine mudrocks, phosphatic shales, diatomites, porcelanites and cherts. The contact between these two formations is not well defined, but appears to be gradational (Dunbar et al. 1990). The Otuma Formation is the youngest instituted unit. It is described for the first time by DeVries (1998) as 150 m of fossiliferous sandstones and siltstones deposited in an early Oligocene marine transgression and debated in detail recently by DeVries et al. (2017). The Miocene strata of the Chilcatay and Pisco formations exposed on the western side of the Ica River have been the focus of few sedimentological and stratigraphic investigations. Macharè et al. (1988) used the name "Caballas" for the upper Oligocene to lower-middle Miocene deposits belonging to the Chilcatay Formation described by Dunbar et al. (1990) as indurated siltstones and sandstones with interbedded diatomaceous intervals. Only recently, Di Celma et al. (2018) and DeVries and Jud (2018) deeply analyzed this formation, and the first is exposed in the Part I of this dissertation. Finally, the Pisco Formation was described by Dunbar et al. (1990) as an unit consists of a wide variety of lithologies, including bioclastic conglomerates and sandstones near basement highs, tuffaceous siltstones, sandstones, and ash horizons, diatomaceous siltstones, diatomites, phosphorites, dolomites, and minor limestone. Because of the coastal upwelling conditions characterizing the Peruvian shelf since the Miocene (Suess & von Huene 1988), the East Pisco Basin was characterized by continuous diatom blooms causing a high-rate biosiliceus sedimentation. Therefore, diatomaceous mudstones are the main lithology constituting the Pisco Formation, in particular in its upper portion (Brand et al. 2011). This formation is characterized by a wide spatial variability in thickness and sedimentary facies. The formation crops out for about 300 km along the coast, from Pisco to Yauca, and its thickness ranges from about 200 to 1000 m (Dunbar et al. 1990). Previous measurement of sections at different localities led to the subdivision of the Mio-

Pliocene Pisco Basin in a north (Pisco area), central (Ica River Valley) and southern (Sacaco) Basin (Marty 1989, Dunbar et al. 1990). In this dissertation, a detailed stratigraphy of the Pisco Formation is reconstruct in Part I, thanks to the accurate recent multidisciplinary studies.

The East Pisco Basin is located just landward of where the aseismic Nazca Ridge impinges on the Peru-Chile trench. The protracted extensional regime, which allows the sediment deposition, was interrupted during the middle Miocene by a widespread pulse of uplift, possibly related to the Quechua 1 tectonic event (Viveen & Schlunegger 2018). Indeed, a rapid uplift and emersion of the Cenozoic fill and underlying composite basement of the East Pisco Basin took place during the late Pliocene until now. The rapid uplift and inversion of the basin is thought to be related to the oblique subduction of the aseismic Nazca Ridge (Fig. 2.4), an area of topographically high, buoyant oceanic crust that is presently being subducted beneath the South American Plate adjacent to the Pisco Basin (Pilger 1981; Hsu 1992; Macharé & Ortlieb 1992; Hampel 2002). Subduction of the Nazca Ridge began in the Miocene (11.2 Ma) and laterally migrated south-east along the Peruvian coast, from 11°S to 15°S (von Huene et al. 1996; Hampel 2002) (Fig. 2.4).

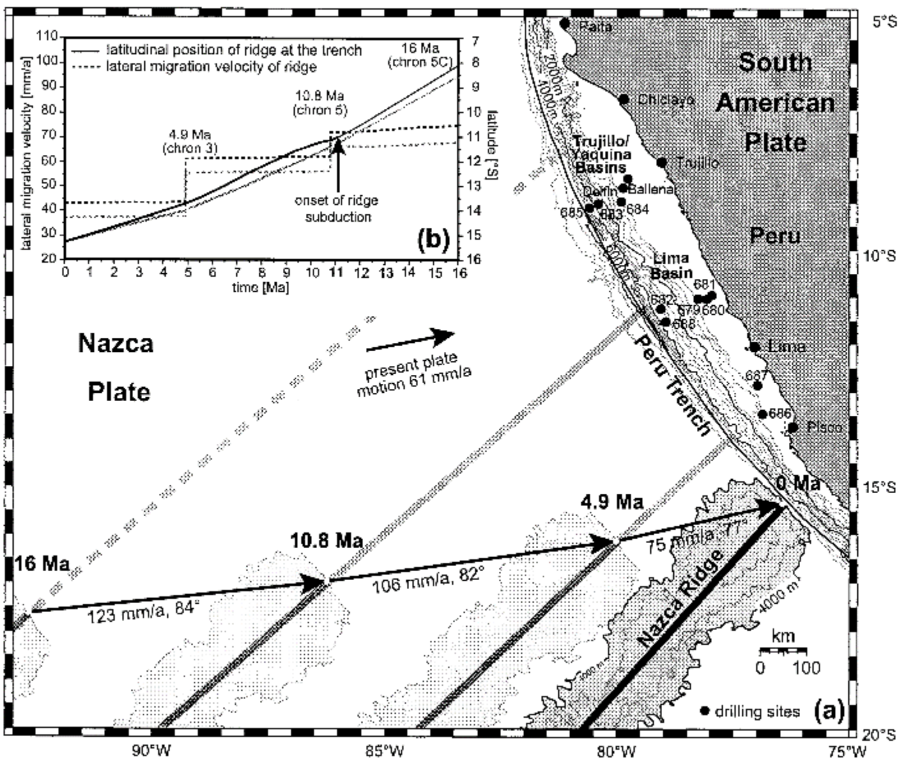

Figure 2.4. Three paleo-positions of the Nazca Ridge and displacement vectors for the present intersection point of ridge and trench. From Hampel (2002).

The result is the onland exposure of its Eocene to Pliocene sedimentary fill in a desert area such as the Ica Region coast. Conversely, areas north of the subducting Nazca Ridge (around Lima, ca. 11°S) were uplifted earlier, and the coast is currently subsiding (le Roux et al. 2000), possibly related to the transient response following the passage of oceanic ridge subduction (Saillard et al. 2011).

Nowadays, the East Pisco Basin belongs to a morphostructural unit known as "Pampas Costera" (Coastal Desert), a desert region cluttered with numerous hills with a large base and a planar top, modelled during Quaternary by marine and continental erosion phenomena (Montoya et al. 1994). Our study area, the Ica Desert, is characterized by these morphologies called "cerros", as said above.

The subduction of normal oceanic lithosphere and the collision of the aseismic Nazca Ridge beneath this part of the forearc zone have been associated with a wide range of effects on the leading edge of the overriding South America continent, including long-term subsidence driven by basal tectonic erosion, rapid crustal uplift and exhumation, and the development of a composite transform-convergent margin dominated by extensional and strike-slip tectonic activity (Kulm et al. 1982; Dunbar et al. 1990; Hsu 1992; Macharé & Ortlieb 1992; Clift et al. 2003; Hampel et al. 2004; León et al. 2008; Bishop et al. 2017). For this reason, the Pisco Formation is affected by faults with dip angles mostly comprised between 75 and 85°. Kinematic indicators suggest that all of the faults are either pure normal faults or have a minor strike-slip component (Rustichelli et al. 2016a). These faults display two main ranges of orientation, with the large majority of them having a NW–SE orientation and the remainder generally striking NE. Along these faults the displacement is generally minimal (metres to tens of metres) and also varies along strike, occasionally tipping out into a fracture with no displacement. Most of the fault zones are marked by an abundance of gypsum filled veins (Rustichelli et al. 2016b).

Marine sediments of the East Pisco Basin formations contain volcanic ash layers. Their abundance in the sedimentary succession depends on both the frequency of the volcanic activity and the conditions that allow the preservation in the sedimentary record. Tephra are largely abundant in the Pisco Formation, especially in the diatomitic portion, and less abundant in the oldest formations. The composition of its sediments is a consequence of the basin paleo-environment in the late Miocene, where the ocean circulation was dominated by an intense coastal upwelling along the Peruvian coast (Brink et al. 1983) and an intense volcanic activity affected the Central Andes in the southern Peru and northern Chile (Mamani et al. 2010). The numerous volcanic ashes interbedded with the basin-filling sedimentary succession provide a snapshot of the long-lived activity of the Central Andes volcanoes, frequently punctuated by large explosive eruptions. The dispersion of Andean tephra, as demonstrated by historical eruptions (Adams et al. 2001) as well as by off-shore drilling programs logs (Hart & Miller 2006), largely affected the margin with off-shore deposition of Plinian and of co-ignimbrite ashes.

As reviewed by Mamani et al. (2010), the Central Andean margin has a very complex subduction-related history. The late Palaeozoic to middle Cretaceous history was first characterized by tectonic stretching, allowing the formation of a marine back-arc basin. From the late Cretaceous to the middle Oligocene, a continuous relief formed, with a continental back-arc environment. The major crustal thickening typical of the Andean orogeny was developed only since the middle Oligocene as described by Mamani et al. (2010). These authors subdivide the continuous magmatic activity into four, partly overlapping, discrete phases: the Tacaza arc, from 30 to 24 Ma, the Huaylillas arc, between 24 and 10 Ma, the Lower Barroso arc, from 10 to 3 Ma, and the Upper Barroso arc, between 3 and 1 Ma (see Fig. 2.5). Voluminous Neogene and Quaternary ignimbrite deposits occur in southern Peru, testifying the main periods of intense and voluminous explosive activity of the arcs (Lebti et al. 2006; Thouret et al. 2007, 2016).

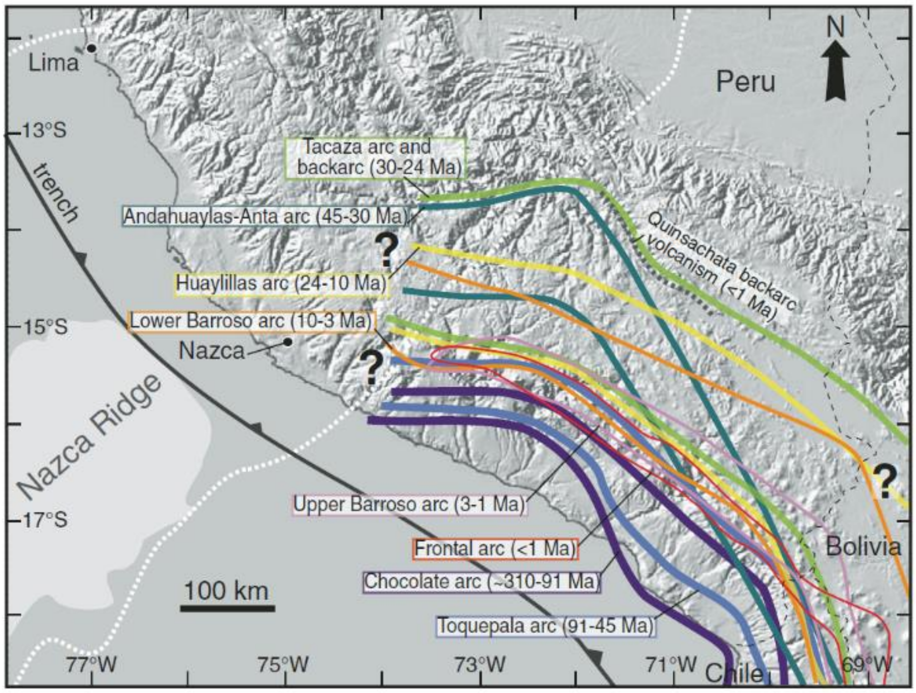

Figure 2.5. Location, extension, and age (Ma) of the volcanic arcs and backarc areas distinguished in southern Peru. From Mamani et al. (2010).

According to these authors, two major intervals of ignimbrite eruption are recognized, namely between ca. 26 and ca. 18 Ma, and between ca. 10 and ca. 1.5 Ma (Roperch et al. 2006; Thouret et al. 2007) along the western Andean slope of southern Peru. These time intervals are those in which tephra layers are more frequent in the East Pisco Basin. The present-day active volcanic arc, or Western Cordillera, lies about 230 km east of the trench. In southern Peru, the active volcanic arc ends at about 14°S, in correspondence with the subduction of the buoyant Nazca Ridge beneath Peru and with the change from "normal" to "flat" subduction, as shown in Figure 2.6 (Hampel 2002; Espurt et al. 2008; Bishop et al. 2017).

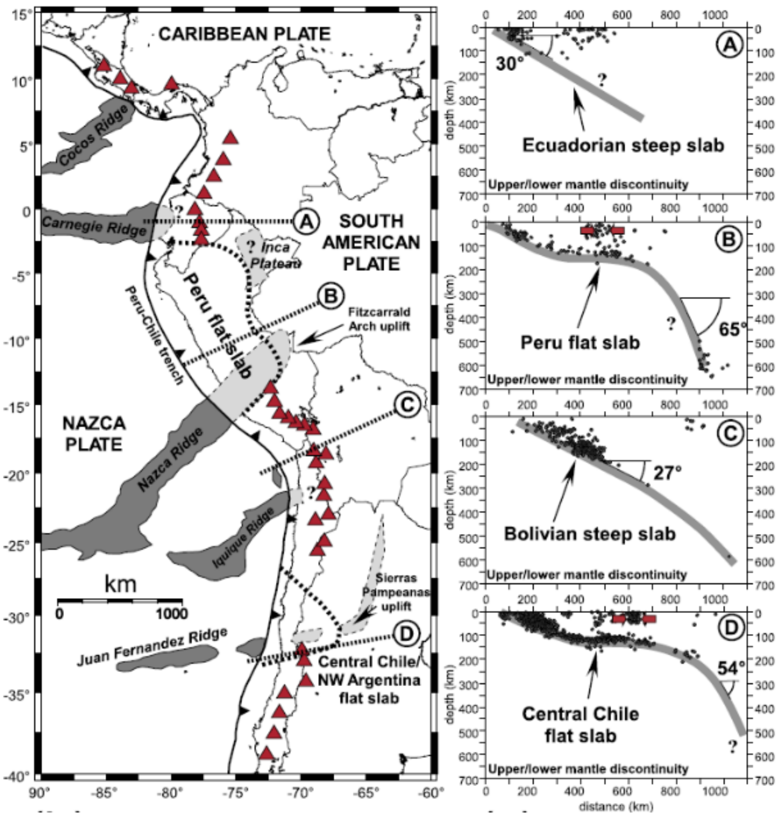

Figure 2.6. Geodynamic setting of the Nazca-South American convergence system. Flat subduction margins are not affected by volcanism. Modified from Espurt et al. (2008).

The geological setting described in this chapter is a mingling of several paragraphs of already published papers written underneath.

"The dolomite nodules enclosing fossil marine vertebrates in the East Pisco Basin, Peru: Field and petrographic insights into the Lagerstätte formation" authored by Karen Gariboldi, Anna Gioncada, Giulia Bosio, ElisaMalinverno, Claudio Di Celma, Chiara Tinelli, Gino Cantalamessa, Walter Landini, Mario Urbina and Giovanni Bianucci, published on Palaeogeography, Palaeoclimatology, Palaeoecology in 2015, Vol. 438, 81-95.

"Stratigraphic framework of the late Miocene Pisco Formation at Cerro Los Quesos (Ica Desert, Peru)" written by Claudio Di Celma, Elisa Malinverno, Gino Cantalamessa, Anna Gioncada, Giulia Bosio, Igor Maria Villa, Karen Gariboldi, Andrea Rustichelli, Pietro Paolo Pierantoni, Walter Landini, Chiara Tinelli, Alberto Collareta and Giovanni Bianucci, printed on Journal of Maps in 2016, Vol. 12, 1020-1028.

"Stratigraphic framework of the late Miocene to Pliocene Pisco Formation at Cerro Colorado (Ica Desert, Peru)" authored by Claudio Di Celma, Elisa Malinverno, Karen Gariboldi, Anna Gioncada, Andrea Rustichelli, Pietro Paolo Pierantoni, Walter Landini, Giulia Bosio, Chiara Tinelli and Giovanni Bianucci, published on Journal of Maps in 2016, Vol. 12, 515-529.

"Sequence stratigraphy and paleontology of the upper Miocene Pisco Formation along the western side of the lower ica valley (Ica Desert, Peru)" written by Claudio Di Celma, Elisa Malinverno, Giulia Bosio, Alberto Collareta, Karen Gariboldi, Anna Gioncada, Giancarlo Molli, Daniela Basso, Rafael M. Varas-Malca, Pietro Paolo Pierantoni, Igor Maria Villa, Olivier Lambert, Walter Landini, Giovanni Sarti, Gino Cantalamessa, Mario Urbina and Giovanni Bianucci, printed in 2017 on Rivista Italiana di Paleontologia e Stratigraia (RIPS), Vol. 123(2): 255-273.

"Biostratigraphy, geochronology and sedimentation rates of the upper Miocene Pisco Formation at two important marine vertebrate fossil-bearing sites of southern Peru" written by Karen Gariboldi, Giulia Bosio, Elisa Malinverno, Anna Gioncada, Claudio Di Celma, Igor M. Villa, Mario Urbina and Giovanni Bianucci, published on Newsletters on Stratigraphy, Vol. 50/4 (2017), 417-444.

"Taphonomy and palaeoecology of the lower Miocene marine vertebrate assemblage of Ullujaya (Chilcatay Formation, East Pisco Basin, southern Peru)" authored by Giovanni Bianucci, Alberto Collareta, Giulia Bosio, Walter Landini, Karen Gariboldi, Anna Gioncada, Olivier Lambert, Elisa Malinverno, Christian de Muizon, Rafael Varas-Malca, Igor Maria Villa, Giovanni Coletti, Mario Urbina and Claudio Di Celma,

published in 2018 on Palaeogeography, Palaeoclimatology, Palaeoecology, vol. 511, 256-279.

"Intraformational unconformities as a record of Late Miocene eustatic falls of sea level in the Pisco Formation (southern Peru)" written by Claudio Di Celma, Elisa Malinverno, Giulia Bosio, Karen Gariboldi, Alberto Collareta, Anna Gioncada, Walter Landini, Pietro Paolo Pierantoni and Giovanni Bianucci, published in 2018 on Journal of Maps, vol. 14(2), 607-619.

Parts on volcanism are taken from "Chemical and petrographic fingerprinting of volcanic ashes as a tool for high-resolution stratigraphy of the upper Miocene Pisco Formation (Peru)" written by Giulia Bosio, Anna Gioncada, Elisa Malinverno, Claudio Di Celma, Igor M. Villa, Giuseppe Cataldi, Karen Gariboldi, Alberto Collareta, Mario Urbina and Giovanni Bianucci, which will be published by the Journal of the Geological Society in January 2019; and from "Tephrochronology and chronostratigraphy of the Miocene Chilcatay and Pisco formations (East Pisco Basin, Peru)" written by Giulia Bosio, Elisa Malinverno, Igor M. Villa, Claudio Di Celma, Karen Gariboldi, Anna Gioncada, Valentina Barberini, Mario Urbina and Giovanni Bianucci, submitted to Newsletters on Stratigraphy in December 2018.

Chapter References

Adams, N. K., de Silva, S. L., Self, S., Salas, G., Schubring, S., Permenter, J. L., Arbesman, K. 2001. The physical volcanology of the 1600 eruption of Huaynaputina, southern Peru. Bulletin of Volcanology, 62 (8), 493-518.

Balarezo, V., E. P. R., Samame B., M., Morales, A., B. 1980. Sinopsis explicativa del mapa del Departamento de Ica. Inst. Geol., Miner. Metal. Lima, Bol. Ser. F, 2, 27.

Barazangi, M., Isacks, B. L. 1979. Subduction of the Nazca plate beneath Peru: Evidence from spatial distribution of earthquakes. Geophysical Journal of the Royal Astronomical Society, 57, 537-555.

Bishop, B.T., Beck, S.L., Zandt, G., Wagner, L., Long, M., Knezevic Antonijevic, S., Kumar, A. Tavera, H. 2017. Causes and consequences of flat-slab subduction in southern Peru. Geosphere, 13, 1392-1407.

Brand, L.R., Urbina, M., Chadwick, A., DeVries, T.J., Esperante, R. 2011. A high resolution stratigraphic framework for the remarkable fossil cetacean assemblage of the Miocene/Pliocene Pisco Formation, Peru. Journal of South American Earth Science, 31, 414-425.

Brink, K.H., Halpern, D., Huyer, A., Smith, L. 1983. The Physical Environment of the Peruvian Upwelling System. Progress in Oceanography, 12, 285-305.

Cahill, T., Isacks, B.L. 1992. Seismicity and shape of the subducted Nazca plate. Journal of Geophysical Research, 97, 17503–17529.

Clift, P.D., Pecher, I., Kukowski, N., Hampel, A. 2003. Tectonic erosion of the Peruvian forearc, Lima Basin, by subduction and Nazca Ridge collision. Tectonics, 22, 1023.

Cobbing, E. J. 1999. The Coastal Batholith and other aspects of Andean magmatism in Peru. In A. Castro, C. Fernandez, & J. L. Vigneresse (Eds.), Understanding granites: Integrating new and classical techniques (Vol. 168, pp. 111-122). London: Geological Society, London, Special Publications.

Coira, B., Davidson, J., Mpodozis, C., Ramos, V. 1982. Tectonic and magmatic evolution of the Andes of northern Argentina and Chile. Earth-Science Reviews, 18, 303-332.

DeVries T.J. 1998. Oligocene deposition and Cenozoic sequence boundaries in the Pisco Basin (Peru). Journal of South American Earth Science, 11: 217-231.

DeVries, T. J. 2017. Eocene stratigraphy and depositional history near Puerto Caballas (East Pisco Basin, Peru). Boletín de la Sociedad Geológica del Perú, 112, 39-52.

DeVries, T. J. & Jud, N. A. 2018. Lithofacies patterns and paleogeography of the Miocene Chilcatay and lower Pisco depositional sequences (East Pisco Basin, Peru). Boletín de la Sociedad Geológica del Perú, Volumen Jubilar 8, 124-167.

DeVries, T. J., Urbina, M., & Jud, N. A. (2017). The Eocene- Oligocene Otuma depositional sequence (East Pisco Basin, Peru): Paleogeographic and paleoceanographic implications of new data. Bol. Sociology Geology Perú, 112, 14-38.

Di Celma, C., Malinverno, E., Collareta, A., Bosio, G., Gariboldi, K., Lambert, O., Landini, W., Pierantoni, P.P., Gioncada, A., Villa, I.M., Coletti, G., Muizon, de C., Urbina, M., Bianucci, G. 2018. Facies analysis, stratigraphy and marine vertebrate assemblage of the lower Miocene Chilcatay Formation at Ullujaya (Pisco basin, Peru). Journal of Maps, 14(2), 257-268.

Dunbar, R. B., Marty, R. C., Baker, P. A. 1990. Cenozoic marine sedimentation in the Sechura and Pisco basins, Peru. Palaeogeography, Palaeoclimatology, Palaeoecology, 77, 235-261.

Espurt, N., Funiciello, F., Martinod, J., Guillaume, B., Regard, V., Faccenna, C., & Brusset, S. 2008. Flat subduction dynamics and deformation of the South American plate: Insights from analog modeling. Tectonics, 27, TC3011.

Gutscher, M. A., Maury, R., Eissen, J. P., Bourdon, E., 2000. Can slab melting be caused by flat subduction? Geology, 28(6), 535-538.

Hampel, A. 2002. The migration history of the Nazca Ridge along the Peruvian active margin: a re-evaluation. Earth and Planetary Science Letters, 203, 665-679.

Hampel, A., Kukowski, N., Bialas, J., Huebscher, C., Heinbockel, R. 2004. Ridge subduction at an erosive margin: The collision zone of the Nazca Ridge in southern Peru. Journal of Geophysical Research, 109, B02101.

Hart, D., Miller, D.J. 2006. Analysis and correlation of volcanic ash in marine sediments from the Peru margin, Ocean Drilling Program Leg 201: explosive volcanic cycles of the north-central Andes. In: Jørgensen, B.B., D'Hondt, S.L., and Miller, D.J. (eds), Proceedings of the Ocean Drilling Program, Scientific Results, 201, 1-43.

Hsu, J. T. 1992. Quaternary uplift of the Peruvian coast related to the subduction of the Nazca Ridge: 13.5 to 15.6 degrees south latitude. Quaternary International, 15-16, 87–97.

Kulm, L. D., Resig, J. M., Thornburg, T. M., Schrader, H. J. 1982. Cenozoic structure, stratigraphy and tectonics of the central Peru forearc. In J. K. Legget (Ed.), Trench and forearc geology: Sedimentation and tectonics on modern and ancient plate margins (pp. 151-169). London: Blackwells.

Le Roux, J.P., Tavares Correa, C., Alayza, F. 2000. Sedimentology of the Rimac-Chillon alluvial fan at Lima, Peru, as related to Plio-Pleistocene sea level changes, glacial cycles and tectonics. Journal of South American Earth Sciences, 13, 499-510.

Lebti, P.P., Thouret, J.-C., Worner, G., Fornari, M. 2006. Neogene and Quaternary ignimbrites in the area of Arequipa, Southern Peru: Stratigraphical and petrological correlations. Journal of Volcanology and Geothermal Research, 154, 251-275.

León, W., Aleman, A., Torres, V., Rosell, W., De La Cruz, O. 2008. Estratigrafía, Sedimentología y evolución tectónica de la cuenca Pisco Oriental. Boletín INGEMMET, Serie D, 27, 1-154, Lima, Peru.

Macharé, J., DeVries, T., Barron, J., Fourtanier, E. 1988. Oligo-Miocene transgression along the Pacific margin of South America: New paleontological and geological evidence from the Pisco Basin, Peru. Geodynamique, 3, 25-37.

Macharé, J., Ortlieb, L. 1992. Plio-Quaternary vertical motions and the subduction of the Nazca Ridge, central coast of Peru. Tectonophysic, 205, 97-108.

Mamani, M., Worner, G., Sempere, T. 2010. Geochemical variations in igneous rocks of the Central Andean orocline (13°S to 18°S): Tracing crustal thickening and magma generation through time and space. Geological Society of America Bulletin, 122, 162-182.

Marocco, R., de Muizon, C. 1988. Le Bassin Pisco, bassin cenozoıque d'avant arc de la còte du Pèrou central: analyse geòdynamique de son remplissage. Geòdynamique, 3, 3-19.

Marty, R. 1989. Stratigraphy and chemical sedimentology of Cenozoic biogenic sediments from the Pisco and Sechura Basins, Peru. PhD Thesis, Houston, Texas, Rice University.

Montoya, M., García, W., Caldas, J., 1994. Geologia de los cuadrangolos de Lomitas, Palpa, Nasca y Puquio. Republica del Peru, Sector Energia y Minas. Inst. Geol.Min. Metall. 53 (A).

Muizon de, C., DeVries, T. J. 1985. Geology and paleontology of late Cenozoic marine deposits in the Sacaco area (Peru). Geologische Rundschau, 74, 547-563.

Mukasa, S. B. 1986. Zircon U–Pb ages of super-units in the Coastal batholith, Peru: Implications for magmatic and tectonic processes. Geological Society of America Bulletin, 97, 241-254.

Mukasa, S. B., Henry, D. J. 1990. The San Nicolás batholith of coastal Peru: Early Palaeozoic continental arc or continental rift magmatism? Journal of the Geological Society, 147, 27-39.

Newell, N. D. 1956. Reconocimiento geologica de la region Pisco-Nazca. Bol. Soc. Geol. Peru, 30: 261-295.

Petersen, G. 1954. Informe preliminar sobre la geologia de la faja costerna del departamento de Ica: Bol. Tec. Empresa Petrol. Fisc., 1, Lima, pp. 33-61.

Pilger, R. H. 1981. Plate reconstructions, aseismic ridges, and low-angle subduction beneath the Andes. Geological Society of America Bulletin, 92, 448-456.

Romero, D., Valencia, K., Alarcon, P., Pena, D., Ramos, V.A. 2013. The offshore basement of Perú: Evidence for different igneous and metamorphic domains in the forearc. Journal of South American Earth Sciences, 42, 47-60.

Rustichelli, A., Di Celma, C., Tondi, E., Bianucci, G. 2016a. Deformation within the Pisco Basin sedimentary record (southern Peru): stratabound orthogonal vein sets and their impact on fault development. Journal of South American Earth Sciences, 65, 79-100.

Rustichelli, A., Di Celma, C., Tondi, E., Baud, P., Vinciguerra, S. 2016b. Fibrous gypsum veins as diffuse features and within fault zones: the case study of the Pisco Basin (Ica desert, southern Peru). Journal of the Geological Society, London, 173.

Saillard, M., Hall, S.R., Audin, L., Farber, D.L., Regard, V., Hérail, G. 2011. Andean coastal uplift and active tectonics in southern Peru: 10Be surface exposure dating of differentially uplifted marine terrace sequences (San Juan de Marcona, ~15.4°S). Geomorphology, 128, 178-190.

Suess, E., von Huene, R. 1988. Introduction, objectives, and principal results, Leg 112, Peru continental margin. Proc. Ocean Drilling Program, Initial Report, 112, 5-44.

Thornburg, T.M., Kulm, L.D. 1981. Sedimentary basins of the Peru continental margin: Structure, stratigraphy, and Cenozoic tectonics from 6°S to 16°S latitude. In: Kulm, L.D., Dymond, J., Dasch, E.J. & Hussong, D.M. (eds). Nazca plate: Crustal formation and Andean convergence. Geological Society of America, Memoirs, 154, 393-422.

Thouret, J.-C., Worner, G., Gunnel, Y., Singer, B., Zhang, X., Souriot, T. 2007. Geochronologic and stratigraphic constraints on canyon incision and Miocene uplift of the Central Andes in Peru. Earth and Planetary Science Letters, 263, 151-166.

Thouret, J.-C., Jicha, B.R., Paquette, J.L. & Cubukcu, E.H. 2016. A 25 myr chronostratigraphy of ignimbrites in south Peru: implications for the volcanic history of the Central Andes. Journal of the Geological Society, Collection.

Viveen, W., Schlunegger, F. 2018. Prolonged extension and subsidence of the Peruvian forearc during the Cenozoic. Tectonophysics, 730, 48-62.

von Huene, R., Lallemand, S. 1990. Tectonic erosion along the Japan and Peru convergent margins. Geological Society of America Bulletin, 102, 704-720.

von Huene, R., Pecher, I.A., Gutscher, M.-A. 1996. Development of the accretionary prism along Peru and material flux after subduction of Nazca Ridge. Tectonics 15, 19-33.

Zùniga-Rivero, F. J., Klein, G. D., Hay-Roe, H., & Alvarez-Calderon, E. 2010. The hydrocarbon potential of Peru. Lima: BPZ Exploraciòn & Producciòn S.R.L., 338.

Chapter 3. Historical studies of the Pisco Fossil-Lagerstätte

The history of the discovery and investigation of the Pisco Fossil-Lagerstätte starts at the end of the 19th century, but detailed scientific studies came later, in the second half of the 20th century (Muizon & DeVries 1985; Bianucci 2010).

Antonio Raimondi (1826-1890), an Italian-born Peruvian geographer and naturalist (Fig. 3.1a), was the first to notify the presence of fossil remains along the Peruvian coast. In 1863, he discovered several fossil remains of whales (Fig. 3.1b) and of other marine vertebrates (Libreta No.33 Archivio General de la Nación, Perù). Born in Milan, Raimondi emigrated to Peru in 1850, becoming professor of natural history at the National University of San Marcos. His studies were focused on geography, geology, botany, zoology, ethnography, archaeology and paleontology. In 1874, he started to write his volume “El Peru”, which was the first of numerous editions (Fig. 3.1c). Raimondi described and classified interesting fossil deposits in several Peruvian localities, such as Luya in the Amazon; Cajabamba, Pomabamba and Huallanca in Ancash; Angaraes and Yauli in Huancavelica; Huari in Junin; Morococha in Lima. However, the major paleontological contribution of Antonio Raimondi for the Pisco Basin history was the discovery of several marine fossils, including cetaceans, in the southern mountains of the Sacaco Desert (Acari district). His findings from the whole country were described by William More Gabb (1839-1878), an American paleontologist that classified his collection (Gabb 1877).

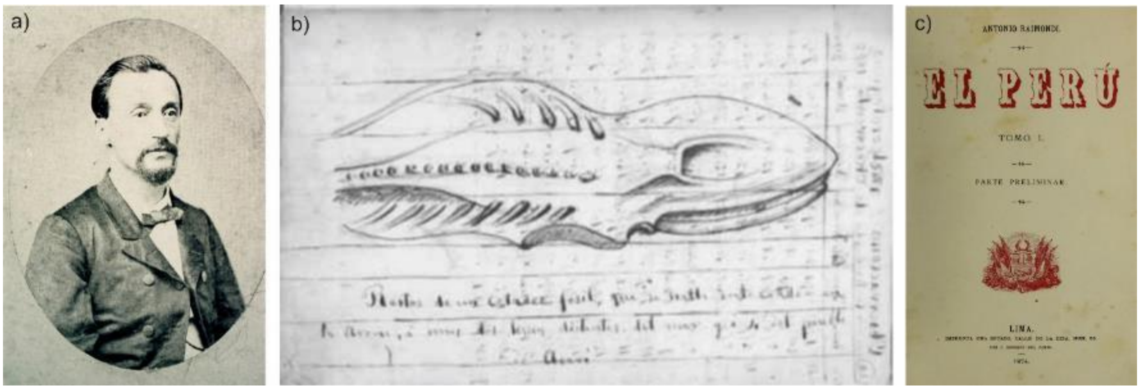

Figure 3.1. a) Antonio Raimondi. b) Drawing of a fossil whale made by Antonio Raimondi in the Sacaco Desert. Libreta No. 33. Archivo General de la Nación, Perù. From Bianucci (2010). c) Cover of “El Perù (Tomo I)” written by Antonio Raimondi.

At the very end of the 19th century, Carlos Lisson (1868-1947) was the first to mention the fossil whale remains at Ocucaje, in 1898. Lisson was a geologist with a deep interest in vertebrate and invertebrate fossils, putting efforts into collect information on local fossil remains, describing new findings.

At the beginning of the 20th century, George Irving Adams (1870-1932), an American geologist, studied and described the geology of Peru, describing for the first time the Pisco Formation. In Adams (1908) we can read the first description of this formation: "In the low hills to the north of Pisco, which is called "Cerro de Tiza" (meaning chalk), there are exposed white and yellowish rocks which have a calcareous aspect much like chalk […]. In the Ica River valley the same formation is found resting on igneous and older stratified and metamorphic rocks […]". In the same paper, he noticed the presence of fossil whales both in Cerro Blanco and on the plains to the east of the port of Lomas: "In a hill to the west of the Hacienda Ocucaje, in a hill called "Cerro Blanco" the writer saw the remains of a whale embedded in the Pisco formation. There was also some strata in which a few marine shells are found and others in which phosphate nodules occur, but to an extent so limited that they have no commercial values […]. The Pisco formation is also found in the plains to the east of the Port of Lomas, where the remains of a whale were seen by the writer, and in one of the valleys which cut the plain a conglomerate of marine shells was found […]". Adams also characterized for the first time the sediments of the Pisco Formation, asserting the presence of diatomites and volcanic deposit: "The so-called chalk material was analyzed by the Corps of Engineers of Mines and found to consist principally of silica, with small amounts of lime and alumina. A microscopic examination showed it to contain many diatoms and what appeared to be volcanic ash […]". Finally, he affirm that the fossils were still not studied and unknown, but he tried, for the first time, to attribute an age to the Pisco Formation: "Although some fossils have been found, they have not been studied, critically. The age of the Pisco formation is not surely known. The writer has assigned it to the Pliocene provisionally, since it is overlain by deposits which are probably of Pleistocene age, and there is no information which shows the necessity of assigning it to an earlier time".

The scientific interest on this exceptional site grew in the second half of the 20th century, with the studies of non-local paleontologist, such as Edwin Harris Colbert (1905-2001), an American vertebrate paleontologist. In Colbert (1944), the author scientifically described for the first time a whale from near the mouth of the Rio Ica, the new odontocete species *Incacetus broggii* (Fig. 3.2).

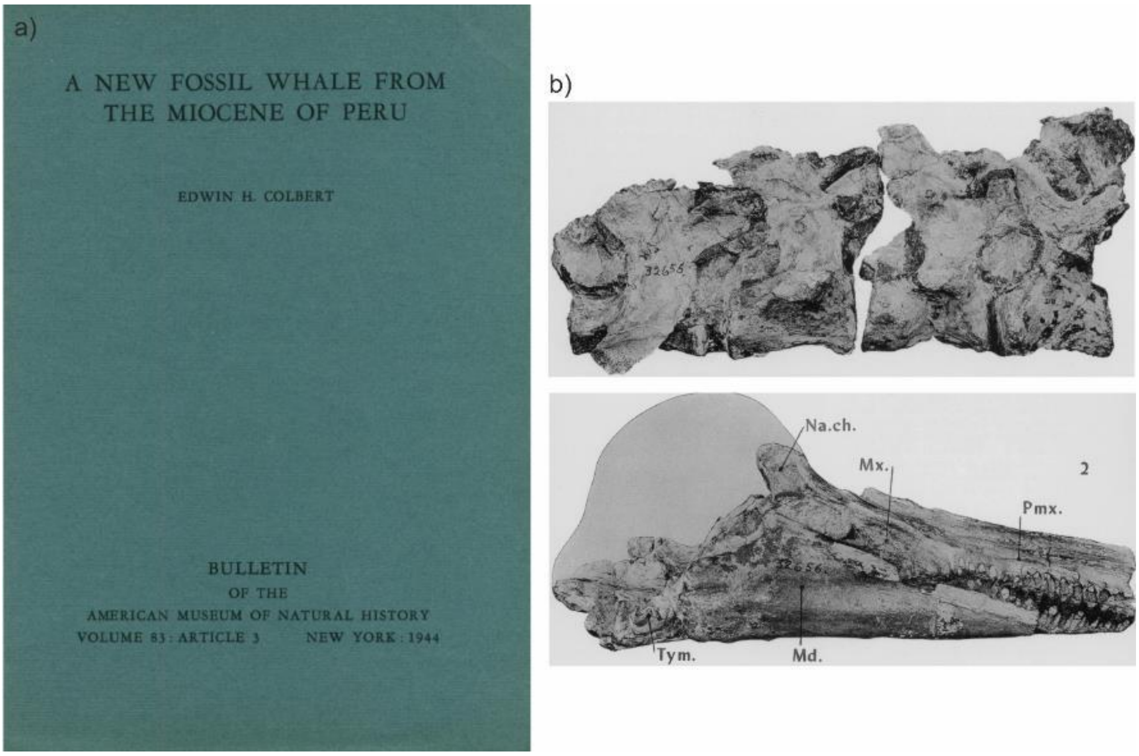

Figure 3.2. a) Cover of the first scientific paper on fossil whales from the Rio Ica area, Colbert (1944). b) Vertebrae, skull and mandible of the new species *Incacetus broggii.*

In the late Sixties, the French paleontologist Robert Hoffstetter (1908-1999) described the first fossil fauna assemblage in the Pisco Formation, investigating vertebrate-bearing sites such as the Sacaco area (Hoffstetter 1968).

But it was in the Eighties that the scientific interest in the Pisco Fossil-Lagerstätte really increased. The French paleontologist Christian de Muizon delivered several important studies on vertebrates of the Pisco Formation (Muizon 1978, 1983a, b, c, 1984; Muizon & Bellon 1980, 1986; Muizon & DeVries 1985) and the American paleontologist Thomas J. DeVries gave important contributions in the studies on fossil mollusk fauna (DeVries 1988, 1998; DeVries & Schrader 1997).

During the 2000s, scientific studies finally became international and multidisciplinary, involving scientists from different countries such as Italian, Belgian, Dutch, French, and Peruvian researchers, thanks to international and national collaborations. In 2008, the discovery of a giant new raptorial sperm whale, the *Leviathan melvillei* (Fig. 3.3), by

Klaas Post, Giovanni Bianucci, Olivier Lambert and Mario Urbina, highlighted the importance of studying in depth this Fossil-Lagerstätte. This whale, with a 3 m-long head, very large upper and lower teeth, robust jaws and a temporal fossa considerably larger than in *Physeter*, represents one of the largest raptorial predators and, to our knowledge, the biggest tetrapod bite ever found (Lambert et al. 2010).

a)

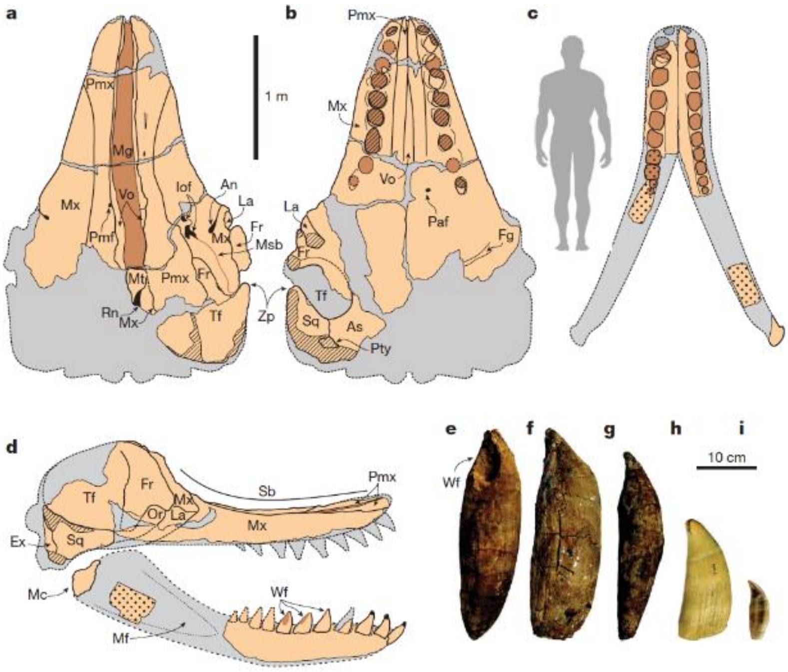

b)

Figure 3.3. a) Skull, mandible and tooth morphology of the holotype of *L. melvillei* MUSM1676. From Lambert et al. (2010). b) Illustration reconstructing *L. melvillei* features. © Alberto Gennari.

Chapter References

Adams, G.I. 1908. An outline review of the geology of Peru. Annual Reports of the Smithsonian Institutions, 385-429.

Bianucci, G. 2010. Esplorazioni e nuove scoperte nel deserto del Perù: i cetacei fossili di Cerro Colorado e Cerro los Quesos. Quaderni del Museo di Storia Naturale di Livorno, 23, 3-12.

Colbert, E.H. 1944. A new fossil whale from the Miocene of Peru. Bulletin of the American Musem of Natural History, 83, 195-216.

DeVries, T.J. 1988. Mollusks of the Pisco Basin. Pisco Basin Guidebook, chapter 8, 127-134.

DeVries, T.J. 1998. Oligocene deposition and Cenozoic sequence boundaries in the Pisco Basin (Peru). Journal of South American Earth Sciences, 11, 217-231.

Gabb, W.M. 1877. Description of a Collection of Fossils Made by Doctor Raimondi in Peru. Journal of the Academy of Natural Sciences of Philadelphia, Series II, 8, 263-336.

Hoffstetter, R. 1968. Un gisement de vertèbrés tertiaires à Sacaco (Sud-Pèrou) témoin Néogène d'une migration de faunes australes au long de la còte occidentale sudaméricaine. Comptes Rendus Hebdomadaires des Séances de l’Académie des Sciences de Paris, Série D, 267, 1273-1276.

Lambert, O., Bianucci, G., Post, K., Muizon, de C., Salas-Gismondi, R., Urbina, M., Reumer, J. 2010. The giant bite of a new raptorial sperm whale from the Miocene epoch of Peru. Nature, 466, 105-108.

Libreta No. 33., Archivo General de la Nación, Perù.

Lisson, C. 1894. Los fosfatos de Ocucaje. Boletín de Minas e Industrias de la Construcción, 14, 33-34.

Muizon de, C. 1978. Arctocephalus (Hydrarctos) lomasiensis, subgen. nov. et nov sp., un nouvel Otariidae du Mio-Pliocène de Sacaco. Bulletin de l'Institute Français d'Études Andines, 7, 169-189.

Muizon de, C. 1983a. Pliopontos littoralis un nouveau Platanistidae (Cetacea) du Pliocène de la côte péruvienne. Comptes Rendus de l’Académie des Sciences de Paris, Series II, 296, 625- 628.

Muizon de, C. 1983b. Un nouveau Phocoenidae (Cetacea) du Pliocène inférieur du Pérou. Comptes Rendus de l’Académie des Sciences de Paris, Series II, 296, 1203-1206.

Muizon de, C. 1983c. Un Ziphiidae (Cetacea) nouveau du Pliocène inférieur du Pérou. Comptes Rendus de l’Académie des Sciences de Paris, Series II, 297, 85-88.

Muizon de, C. 1984. Les Vertébrés de la Formation Pisco (Pérou). Deuxième partie: Les Odontocètes (Cetacea, Mammalia) du Pliocène inférieur de Sud-Sacaco. Travaux de l'Institut Français d'Études Andines, 27, 1-188.

Muizon de, C., Bellon, H. 1980. L'âge mio-pliocène de la Formation Pisco (Pérou). Comptes Rendus Hebdomadaires des Séances de l'Académie des Sciences de Paris, Série D, 290, 1063-1066.

Muizon de, C., Bellon, H. 1986. Nouvelles données sur l'âge de la Formation Pisco (Pérou). Comptes Rendus Hebdomadaires des Séances de l'Académie des Sciences de Paris, Série D, 303, 1401-1404.

Muizon de, C., DeVries, T. J. 1985. Geology and paleontology of late Cenozoic marine deposits in the Sacaco area (Peru). Geologische Rundschau, 74, 547–563.

PART I – CHRONOSTRATIGRAPHY

Chapter 4. Previous dating in the Pisco Basin

The chronostratigraphy of the Miocene Chilcatay and Pisco formations has been, until our contribution, poorly resolved. No high-resolution chronostratigraphic reconstruction of the Chilcatay nor the Pisco formations had been available, until now, but previous authors have tried to date these formations with different methods, starting from the end of the 20th century.

In the Eighties, some age estimations were carried out for the Chilcatay Formation, but the lack of stratigraphic information and the few scattered data led to uncertain correlations between different localities and a weak age control within the formation. The first information about the geological period, in which the Chilcatay Formation sediments were deposited, was reported by Schrader and Ronning (1988), using diatom biostratigraphy, who assigned them an upper Oligocene to lower-middle Miocene age. According to Dunbar et al. (1990), biostratigraphic results on diatoms and forams indicated an earliest middle Miocene age for the upper part, without specifying any stratigraphic position.

DeVries and Jud (2018) attributed the base of the Chilcatay Formation to the late Oligocene for the molluscan assemblage, dated at about 25 Ma in a locality 350 km south from the East Pisco Basin, and for the foram biostratigraphy by Ibaraki (1993), who proposed late Oligocene ages at Cerro las Salinas. Ibaraki (1993) also quotes unpublished biostratigraphic data by Schrader, which indicate progressively younger ages for the top of the formation (from 19.5 to 15 Ma) at the localities of Lomas Chilcatay and Cerro la Virgen.

More recently, one absolute dating has been carried out on an ash layer at the top of Chilcatay Formation, in the western side of the Ica River. It was dated through ^{39}A–^{40}Ar method by Belia and Nick (2016), giving an age of 17.70 ± 0.24 Ma. Now, in the present work, ^{39}Ar–^{40}Ar dating on tephra, and diatom and silicoflagellate biostratigraphy were applied in the Chilcatay Formation in the western side of the Ica River: the results are shown in the following chapters of Part I of this dissertation.

For the Pisco Formation, several ages were estimated starting from the Eighties, but without any chronostratigraphic reconstruction. As summarized in Table 4.1, previous authors have dated the Pisco Formation by means of different methods. K–Ar ages for the Pisco Formation were first obtained for the southern (Sacaco) Basin (Muizon & Bellon 1980, 1986; Muizon & DeVries 1985). They report late Miocene ages of 9.5 Ma (base of El Jahuay section), 8.8-8 Ma (base of Aguada de Loma section) for the basal Pisco Formation and a Pliocene age of 3.9 Ma (Sacaco section) for the upper Pisco Formation, but this estimate has been questioned by new data (Ehret et al. 2012) (Fig. 4.1). Dunbar et al. (1990) listed K–Ar dates obtained for the Pisco Formation that range from 6.89 ± 0.10 Ma in the northern Basin (Monte Caucato section), to 6.75 ± 0.18 Ma in the central Basin (Queso Grande section) to 5.49 ± 0.12 and 6.42 ± 0.12 Ma in the southern part of the central Basin (Molde de Queso and Huaracangana sections, respectively).

New ^{39}Ar–^{40}Ar ages are provided by Brand et al. (2011) and Esperante et al. (2015), ranging from 9.2 to 6.85 Ma for different localities in the Ica Valley and from 7.73 to 7.11 Ma for the site of Cerro los Quesos, respectively (Fig. 4.1). The stratigraphic position of such dated samples along their composite section is however not well constrained, as stated by the authors (see Brand et al. 2011). More recently, Ehret et al. (2012) provided ages obtained with Sr isotopic ratio (measured on mollusk shells) and zircon U–Pb dating in the southern Basin. They report age ranges of 9.03-6.51 Ma for the base of El Jahuay section and 8.79-6.45 Ma for the Montemar section; these are compatible with previous K–Ar dates provided for the same sections (Muizon & DeVries 1985). Conversely, data obtained by Ehret et al. (2012) on the Sud Sacaco and Sacaco horizons provided ages older than the 3.9 Ma tuff bed of Muizon and Bellon (1980). $^{87}Sr/^{86}Sr$ analysis yield ages spanning from 6.59 to 5.89 Ma for Sacaco and Sud Sacaco, moving those levels from the Pliocene to the late Miocene (see Ehret et al. 2012 for geographic location of the dated sections).

Biostratigraphic studies in the literature have been carried out using both macrofauna and microfossils (we report ages of First and Last Occurrences: FO and LO hereafter, preceded by “ca.” when referring to an uncalibrated age). Muizon and DeVries (1985) attempted to develop a molluscan biostratigraphy for the uppermost Miocene-lower Pliocene outcrops in the Sacaco area. DeVries (1998) used the molluscan fauna to date the Pisco Basin deposits, considering in particular the occurrence of the bivalve *Anadara sechurana* Olsson, 1932 and of the gastropod *Turritella infracarinata* Grzybowsky, 1899. As *A. sechurana* was considered not younger than middle Miocene, its occurrence was used consequently in following studies to constrain outcrops of the Pisco Formation (e.g. Bianucci et al. 2010). However, recent researches highlighted that the range of *A. sechurana* is not limited to the middle Miocene and may extend into the early Tortonian. In the Gatun Formation (Panama), for instance, this species ranges from 11.6 to 10.4 Ma (Austin Hendy personal communication) and its disappearance is likely related to local unfavorable environmental conditions rather than to a real extinction (Austin Hendy pers. comm.). As such, the use of *A. sechurana* as a reliable biostratigraphic marker for the middle Miocene is questionable.

Radiolaria, although sparsely present within silty diatomite and diatomaceous silty layers, provided a well constrained biostratigraphic framework for the Pisco Formation at different localities of the north, central and south Pisco Basin (Marty 1989; also reported in Dunbar 1990). Biozone assignment identified: a latest middle Miocene to early late Miocene interval (*Diarthus pettersonii* zone, 12.02-8.84 Ma following recent calibration for the eastern Equatorial Pacific, i.e. Kamimuri et al. 2009) limited to the north Basin (Monte Caucato section); a middle late Miocene interval (*Didymocyrtis antepenultima* zone, 8.84-7.74 Ma and *D. penultima*, 7.74-6.89 Ma) in some sections of the northern (Monte Caucato section) and central Basin (Cerro Yaparejo, Fundo Santa Rosa, Yesera de Amara sections); and a widespread younger late Miocene to early Pliocene interval (*Stichocorys peregrine* zone, 6.89-4.19 Ma) in most sections of the central and southern Basin.

Mertz (1966) was the first to describe diatoms from the Pisco Formation; beside a thorough description of the observed species and a general paleoecological framework, he also used diatoms to date the formation, concluding that it must have been Miocene in age. Macharè and Fourtanier (1987) dated the Pisco Formation referring to the Equatorial Pacific biostratigraphic scheme of Barron (1983, 1985) and to the north Pacific biostratigraphic scheme of Akiba (1985) and Akiba and Yanagisawa (1986). The need to use two different schemes resides in the occurrence of species with ranges described in the North Pacific scheme (i.e., *Denticulopsis katayamae* Maruyama, 1984 in the Akiba & Yanigasawa North Pacific scheme, 1985) rather than by Barron's 1983 Equatorial Pacific scheme. Basing their conclusions on the ranges of *Coscinodiscus plicatus* Grunow, 1878 and *Denticulopsis hustedtii* (Simonsen & Kanaya, 1961) Simonsen, 1979 (which Macharè and Fourtanier referred to as *Denticula hustedtii,* for the Equatorial Pacific), Macharè and Fourtanier (1987) dated the base of the Pisco Formation to the middle-late Miocene (14-9 Ma, as reported by the authors). However, they highlight that taking into account the North Pacific range of *D. hustedtii*, the base of the formation would be younger (11-9 Ma, as reported by the authors). Notwithstanding the general lack of marker species, they also attributed the middle part of the formation exposed in the southern part of the Basin (Sacaco area, see Plate 1 of Macharè and Fourtanier 1987 for sample locations) to the late Miocene-early Pliocene, basing their conclusion on the analogies of the association with that of the Sisquoc Formation (California). Finally, they attribute the upper part of the Pisco Formation to the Pliocene because of the occurrence of *Koizumia tatsunokuchiensis* (Koizumi, 1972) Yanagisawa, 1994 (which Macharè and Fourtanier referred to as *Rossiella tatsunokuchiensis*), *Fragilariopsis reinholdii* (Kanaya & Koizumi, 1970) Zielinski and Gersonde, 2002 (which Macharè and Fourtanier referred to as *Nitzschia reinholdii*) and *Shionodiscus oestrupii* (Ostenfeld, 1900) Alverson, Kang and Theriot, 2006 (which Macharè and Fourtanier referred to as *Thalassiosira oestrupii*). Although this attribution may still be valid, it is based on the assumption that *K. tatsunokuchiensis* and *S. oestrupii* first appear in the Pliocene, as reported by Barron (1985). More recently, the range of *K. tatsunokuchiensis* has been extended back in time and the species is now known to span from 9.0 Ma to 2.6 Ma (Barron 2003, middle-to-high-latitude planktonic diatoms in the North Pacific), while the FO of *S. oestrupii* is calibrated in the late Miocene at 5.6 Ma (Barron 2003; tropical planktonic diatoms in the Equatorial Pacific).

Diatoms were also used by Schrader and Ronning (1988) to date some stratigraphic sections of the Pisco Formation. Although they refer to Barron’s 1985 Equatorial Pacific zonation, Schrader and Ronning (1988) used the species ranges of Barron both in the Equatorial Pacific zonation and in his high latitude north Pacific zonation (Barron 1985). Schrader and Ronning (1988) and Macharè and Fourtanier (1987) used *Coscinodiscus plicatus* to date the Pisco Formation, ascribing to this species a LO older than ca. 8 Ma. We draw attention to the work of Tanimura (1996), who taxonomically reexamined specimens of plicated *Thalassiosira* from DSDP North Pacific Site 173, thus implying a revision of the attribution of specimens of the formation to *C. plicatus*.

Tsuchi et al. (1988) also used diatoms to date outcrops of the Pisco Formation exposed in the Ica River; they recognized different diatom zones of Barron (1985) low-latitude diatom zonation and referred these outcrops to the Miocene. Conversely, they attributed a late middle-late upper Miocene through Pleistocene ages for diatomaceous outcrops in the Sacaco area (see Tsuchi et al. 1988 for outcrop locations).

Finally, DeVries and Jud (2018) attributed the lower part of the Pisco Formation to the middle Miocene: in the Pisco sediments that overlie the Chilcatay type section near Cerro La Virgen, the presence *Denticulopsis hustedtii* confirms an age younger than 14.5 Ma, a conclusion supported by the absence of *Synedra jouseana*. Following the authors, the presence of both *Mediaria splendida* and *D. hustedtii* in samples near Cerro La Virgen indicates that lower Pisco sediments are older than about 11 Ma. Near Yesera de Amara, silty sandstone contains both *D. hustedtii* and *S. jouseana*, indicating an age of about 14.5 Ma.

All these previous ages for both Chilcatay and Pisco formations are reported and summarized in Table 4.2.

Methods	Authors
Molluscs	de Muizon and DeVries 1985, DeVries 1988
Radiolarians	Marty 1989, Dunbar et al. 1990.
Foraminifera	Tsuchi et al. 1988.
Diatoms	Mertz 1966, Macharé and Fourtanier 1987, Schrader and Ronning 1988, Tsuchi et al. 1988, Koizumi 1992, Di Celma et al. 2016a, 2016b
K/Ar dating	de Muizon and Bellon 1980, 1986, de Muizon and DeVries 1985, Dunbar et al. 1990
$^{40}Ar/^{39}Ar$ dating	Brand et al. 2011, Esperante et al. 2015, Di Celma et al. 2016a, 2016b
$^{87}Sr/^{86}Sr$	Ehret et al. 2012
Zircon U-Pb dating	Ehret et al. 2012

Table 4.1. List of previous dating methods in the Pisco Formation and relative literature. From Gariboldi et al. (2017).

Chilcatay Formation			
Authors	**Method**	**Age**	**Locality**
Schrader & Ronning (1988)	Diatom biostratigraphy	late Oligocene to earlier-middle Miocene	-
Dunbar et al. (1990)	Diatom and foram biostratigraphy	late Oligocene-earliest middle Miocene	Pampa Chilcatay; Quebrada Huaracangana
DeVries & Jud (2018)	Mollusc biostratigraphy	late Oligocene	East Pisco Basin
Ibaraki (1993)	Foram biostratigraphy	late Oligocene	Cerro las Salinas
Belia & Nick (2016)	^{39}Ar-^{40}Ar dating	17.70 ± 0.24 Ma	Cerro Yesera de Amara
Pisco Formation			
Authors	**Method**	**Age**	**Locality**
Muizon & Bellon (1980, 1986); Muizon & DeVries (1985)	K-Ar dating	9.5 Ma; 8.8-8 Ma; 3.9 Ma	El Jahuay section; Aguada de Loma section; Sacaco section
Dunbar et al. (1990)	K-Ar dating	6.89 ± 0.10 Ma; 6.75 ± 0.18 Ma; 5.49 ± 0.12 Ma; 6.42 ± 0.12 Ma	Monte Caucato section; Queso Grande section; Molde de Queso section; Huaracangana section
Brand et al. (2011)	^{39}Ar-^{40}Ar dating	from 9.2 to 6.85 Ma	Ica Valley
Esperante et al. (2015)	^{39}Ar-^{40}Ar dating	from 7.73 to 7.11 Ma	Cerro los Quesos
Ehret et al. (2012)	$^{87}Sr/^{86}Sr$ dating; zircon U-Pb dating	9.03-6.51 Ma; 8.79-6.45 Ma; 6.59-5.89 Ma	El Jahuay section; Montemar section; Sacaco and Sud Sacaco
DeVries (1998)	Mollusc biostratigrqaphy *(Anadara sechurana)*	middle Miocene	Ica River Valley
Marty (1989); Dunbar (1990)	Radiolaria biostratigraphy *(Diarthus pettersonii* zone; *Didymocyrtis antepenultima* zone and *D. penultima* zone; *Stichocorys peregrine* zone)	12.02-8.84 Ma; 8.84-7.74 Ma and 7.74-6.89 Ma; 6.89-4.19 Ma	Monte Caucato section; Monte Caucato section, Cerro Yaparejo, Fundo Santa Rosa, Yesera de Amara sections; central and southern Basin
Mertz (1966)	Diatom biostratigraphy	Miocene	-
Macharè & Fourtanier (1987)	Diatom biostratigraphy (*Coscinodiscus plicatus* and *Denticulopsis hustedtii; Koizumia tatsunokuchiensis, Fragilariopsis reinholdii* and *Shionodiscus oestrupii*)	14-9 Ma; late Miocene to early Pliocene	-
Schrader & Ronning (1988)	Diatom biostratigraphy (*Coscinodiscus plicatus*)	Last Occurrence older than ca. 8 Ma	-
Tsuchi et al. (1988)	Diatom biostratigraphy	Miocene; late Miocene to Pleistocene	Ica River Valley; Sacaco
DeVries & Jud (2018)	Diatom biostratigraphy (*Denticulopsis hustedtii* and *Mediaria splendida; D. hustedtii* and *Synedra jouseana*)	younger than 14.5 Ma and ca. 11 Ma; ca. 14.5 Ma	Cerro La Virgen; Yesera de Amara

Table 4.2. Summary of the previous ages of both Chilcatay and Pisco formations.

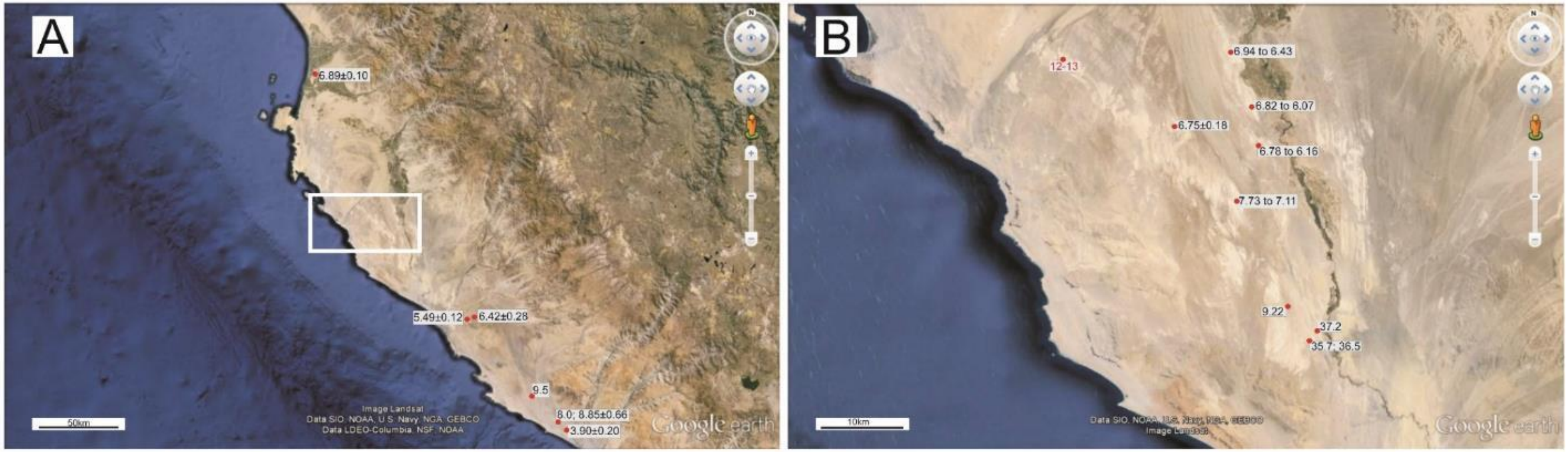

ID Ma (in figure)	Locality	Original Section/Sample Name	Lat.	Long.	Ages (Ma)	Method	Original Reference	Notes
3.90±0.20	Sacaco	A (De Muizon De Vries, 1985)	ca. 15°35'18.88"S	ca. 74°43'26.02"W	3.9	K/Ar	De Muizon and Bellon 1980	
5.49±0.12	Molde de Queso	Molde de Queso (Dunbar et al., 1980)	14°56'S	75°15'W	5.49±0.12	K/Ar	Dunbar et al. 1990	
6.42±0.28	Huaracangana	Huaracangana (Dunbar et al., 1980)	14°56'S	75°16'W	6.42±0.28	K/Ar	Dunbar et al. 1990	
6.75±0.18	Queso Grande	Queso Grande (Dunbar et al., 1980)	14°26'S	75°46'W	6.75±0.18	K/Ar	Dunbar et al. 1990	
6.78 to 6.16	Hueco la Zorra	NK	ca. 14°26'56.63"S	ca. 75°40'33.80"W	6.78 to 6.16	Ar/Ar	Esperante et al. 2015	
6.82 to 6.07	Cerro Blanco	NK	ca. 14°24'55.31"S	ca. 75°41'30.88"W	6.82 to 6.07	Ar/Ar	Esperante et al. 2015	
6.89±0.10	Monte Caucato	Monte Caucato (Dunbar et al., 1980)	13°38'S	76°11'W	6.89±0.10	K/Ar	Dunbar et al. 1990	
6.94 to 6.43	Cerro Ballena	NK	ca. 14°20'59.90"S	ca. 75°42'24.58"W	6.94 to 6.43	Ar/Ar	Esperante et al. 2015	
7.73 to 7.11	Cerro Los Quesos	NK	ca. 14°30'34.14"S	ca. 75°42'46.26"W	7.73 to 7.11	Ar/Ar	Esperante et al. 2015	
8.0	Aguada de Lomas	E (De Muizon De Vries, 1985)	ca. 15°30'22.72"S	ca. 74°47'44.72"W	7.93±0.40	K/Ar	De Muizon and Bellon 1986	
	Aguada de Lomas	E (De Muizon De Vries, 1985)	ca. 15°30'22.72"S	ca. 74°47'44.72"W	8.04±0.40	K/Ar	De Muizon and Bellon 1986	
8.85±0.66	Aguada de Lomas	E (De Muizon De Vries, 1985)	ca. 15°30'22.72"S	ca. 74°47'44.72"W	8.85±0.66	K/Ar	De Muizon and Bellon 1986	
9.22	Yesera de Amara	NK	14°37'31"S	75°40'14"W	9.22	Ar/Ar	DeVries 1998	
9.5	El Jahuay	El Jahuay (De Muizon De Vries, 1985)	ca. 15°27'5.42"S	ca. 74°52'8.36"W	9.38±0.47	K/Ar	De Muizon and Bellon 1986	
	El Jahuay	El Jahuay (De Muizon De Vries, 1985)	ca. 15°27'5.42"S	ca. 74°52'8.36"W	9.63±0.48	K/Ar	De Muizon and Bellon 1986	
12-13	Cerro Colorado	NK	ca. 14°21'4.47"S	ca. 75°53'46.47"W	12-13	*Anadara sechurana*	Bianucci et al. 2010	
35.7	12 km S Yesera de Amara	sample 87DV 509 1BSnee	14°39'45"S	75°37'44"W	35.7	Ar/Ar	DeVries 1998	1 m above s. 87DV 509 1ASnee
36.5	12 km S Yesera de Amara	sample 87DV 509 1ASnee	14°39'45"S	75°37'44"W	36.5	Ar/Ar	DeVries 1998	
37.1	7.5 km S Yesera de Amara	sample 87DV 508 1Snee	14°38'44"S	75°38'12"W	37.1	Ar/Ar	DeVries 1998	

Figure 4.1. Location of Pisco Formation previous absolute dating and *A. sechurana* used as biostratigraphic marker on the satellite map of the Ica Desert. a) Peruvian coast. b) Western side of the Ica River. From Gariboldi et al. (2017).

Text, tables and figures of this chapter are the result of modified parts from the paper "Biostratigraphy, geochronology and sedimentation rates of the upper Miocene Pisco Formation at two important marine vertebrate fossil-bearing sites of southern Peru" authored by Karen Gariboldi, Giulia Bosio, Elisa Malinverno, Anna Gioncada, Claudio Di Celma, Igor M. Villa, Mario Urbina and Giovanni Bianucci, published on Newsletters on Stratigraphy in 2017, Vol. 50/4, 417-444. In this paper, Giulia Bosio contributes to sample collection, volcanic ash analyses, ^{39}Ar–^{40}Ar geochronology, discussion on the previous dating and the new results, comparison of data and calculation of sedimentation rates.

Chapter References

Akiba, F. 1985. Middle Miocene to Quaternary diatom biostratigraphy in the Nankai Trough and Japan Trench, and modified Lower Miocene through Quaternary diatom zones for middle-to-high latitudes of the North Pacific. DSDP Initial Reports, 87, 393-480.

Akiba, F., Yanagisawa, Y. 1986. Taxonomy, morphology and phylogeny of the Neogene diatom zonal marker species in the middle-to-high latitudes of the North Pacific. DSDP Initial Reports, 87, 483-554.

Barron, J. A. 1983. Latest Oligocene through early middle Miocene diatom biostratigraphy of the eastern tropical Pacific. Marine Micropaleontology, 7(6), 487-515.

Barron, J. A. 1985. Miocene to Holocene planktic diatoms. In: Bolli, H. M., Saunders, J. B. & Perch-Nielsen, K. P. (Eds.), Plankton stratigraphy. Cambridge: Cambridge University Press, 763-809.

Barron, J. A. 2003. Planktonic marine diatom record of the past 18 my: appearances and extinctions in the Pacific and Southern Oceans. Diatom Research, 18(2), 203-224.

Belia, E. R., Nick, K.E. 2016. Early-Miocene calcareous nannofossil biostratigraphy from low-latitude, Pisco Basin, Peru. Geological Society of America Abstracts with Programs, 48, 4.

Bianucci, G., Lambert, O., Post, K. 2010. High concentration of long-snouted beaked whales (genus Messapicetus) from the Miocene of Peru. Palaeontology, 53(5), 1077-1098.

Brand, L.R., Urbina, M., Chadwick, A., DeVries, T.J., Esperante, R. 2011. A high resolution stratigraphic framework for the remarkable fossil cetacean assemblage of the Miocene/Pliocene Pisco Formation, Peru. Journal of South American Earth Sciences, 31, 414-425.

DeVries, T.J. 1998. Oligocene deposition and Cenozoic sequence boundaries in the Pisco Basin (Peru). Journal of South American Earth Sciences, 11, 217-231.

DeVries, T. J., Jud, N. A. 2018. Lithofacies patterns and paleogeography of the Miocene Chilcatay and lower Pisco depositional sequences (East Pisco Basin, Peru). Boletín de la Sociedad Geológica del Perú, Volumen Jubilar, 8, 124-167.

Dunbar, R. B., Marty, R. C., Baker, P. A. 1990. Cenozoic marine sedimentation in the Sechura and Pisco basins, Peru. Palaeogeography, Palaeoclimatology, Palaeoecology, 77, 235-261.

Ehret, D. J., McFadden, B. J., Jones, D. S., DeVries, T. J., Foster, D. A., Salas-Gismondi, R. 2012. Origin of the white shark Carcharodon (Lamniformes: Lamnidae) based on recalibration of the Upper Neogene Pisco Formation of Peru. Palaeontology, 55(6), 1139-1153.

Esperante, R., Brand, L. R., Chadwick, A. V., Poma, O. 2015. Taphonomy and paleoenvironmental conditions of deposition of fossil whales in the diatomaceous sediments of the Miocene/Pliocene Pisco Formation, southern Peru - A new fossil-lagerstätte. Palaeogeography, Palaeoclimatology, Palaeoecology, 417, 337-370.

Ibaraki, M. 1993. Eocene to early Miocene planktonic foraminifera from the south of Paracas, central Peru. Shizuoka University, Report of the Faculty of Sciences, 27, 77-93.

Kamimuri, S. I., Motoyama, I., Nishi, I., Iwai, M. 2009. Neogene radiolarian biostratigraphy and faunal evolution rates in the eastern equatorial Pacific ODP Sites 845 and 1241. Acta Paleontologica Polonica, 54 (4), 713-742.

Macharé, J., Fourtanier, E. 1987. Datations des formations tertiaires du bassin de Pisco (Pérou) à partir d'associations de diatomées. Comptes rendus de l'Académie des sciences. Série 2, Mécanique, Physique, Chimie, Sciences de l'univers, Sciences de la Terre, 305(5), 407-412.

Marty, R. 1989. Stratigraphy and chemical sedimentology of Cenozoic biogenic sediments from the Pisco and Sechura Basins, Peru. PhD Thesis, Houston, Texas, Rice University.

Mertz, D. 1966. Mikropaläontologische und sedimentologische Untersuchung der Pisco-Formation Südperus. Palaeontographica B, 118, 1-51.

Muizon, C. de, Bellon, H. 1980. L'âge mio-pliocène de la formation Pisco, Pérou. Comptes Rendus de l'Académie des Sciences de Paris, tome 290, Série D, 1063-1066.

Muizon, C. de, Bellon, H., 1986. Nouvelles donn ees sur l'âge de la Formation Pisco (Pérou). Comptes Rendus de l'Académie des Sciences de Paris, tome 303, Série II, no 15, 1401-1404.

Muizon de, C., DeVries, T. J. 1985. Geology and paleontology of late Cenozoic marine deposits in the Sacaco area (Peru). Geologische Rundschau, 74, 547–563.

Schrader, H., Ronning, P. 1988. Diatom biostratigraphy and coastal upwelling interpretation. In: Dunbar, R. B., Baker, P. A. (Eds.), Cenozoic Geology of the Pisco Basin, IGCP no. 156 Guidebook to Field Workshop, May 1988, Lima, 135-140.

Tanimura, Y., 1996. Fossil marine plicated Thalassiosira: taxonomy and an idea on phylogeny. Diatom Research, 11(1), 165-202.

Tsuchi, R., Shuto, T., Takayama, T., Fujiyoshi, A, Koizumi, I., Ibaraki, M., Rangel, Z. C., Aldana, A.M. 1988. Fundamental Data on Cenozoic Biostratigraphy of the Pacific Coast of Peru. In: Tsuchi R. (ed.), Report of Andean studies, Shizuoka University, 3, 45-70.

Chapter 5. Methods for $^{39}Ar–^{40}Ar$ dating and tephra fingerprinting, biostratigraphy, and Sr isotopes on carbonates and phosphates

5.1. Tephra characterization

An area of approximatively 300 km^2 in the western side of the Ica River was explored and mapped during several field campaigns between 2014 and 2018, in order to reconstruct the stratigraphy of this area. For the Pisco Formation, in the course of this fieldwork, more than 200 samples of volcanic ash layers and hundreds of biostratigraphic samples were collected at different localities (see Fig. 1.3, Chapter 1). The Pisco Formation crops out in Cerro los Quesos (14°30'59" S; 75°42'59" W), Cerro los Quesos west (14°31'13" S; 75°44'34" W), Cerro la Bruja (14°31'44" S; 75°40'00" W), Cerro Colorado (14°21'04" S; 75°53'43" W), Cerro Hueco la Zorra (14°26'58" S; 75°41'01" W), Cerro Blanco (14°24'57" S; 75°41'17" W), Cerro Toro Chico (14°27'36" S; 75°48'01" W), Cerros Cadena de los Zanjones (14°34'21" S; 75°42'60" W) and Cerros la Mama y la Hija (14°36'17" S; 75°40'50" W). Stratigraphic sections were measured in each locality (see Fig. 5.1 and 5.2; see the Appendix for complete and detailed stratigraphic logs), with the exception of Cerro Hueco la Zorra and Cerros la Mama y la Hija, where ash layers were stratigraphically recognized and sampled for correlation analyses with ash layers at Cerro Blanco and Cerros Cadenas de los Zanjones, respectively. For the Chilcatay Formation, stratigraphic sections were measured in the localities of Ullujaya (14°35'04" S; 75°38'19" W), Mal Paso (14°36'29" S; 75°39'58" W), Roca Negra (14°39'04" S; 75°38'54" W) and more than one section in the wide locality of Zamaca (14°37'37" S; 75°39'10" W). For each section, tephra and samples for biostratigraphic purpose were collected. In the Appendix, all the measured stratigraphic logs are reported in detail.

In the field, tephra samples were collected while measuring the section. Volcanic ash layers were described through observations on their lateral continuity, thickness, vertical grading, color, sedimentary structures and presence of phenocrysts (in particular biotite, which can be easily recognized with a hand-lens and which is of interest for age determinations). Samples were collected close to the base of the ash layer, avoiding the upper portion so as to exclude bioturbation and reworking. In order to avoid the weathered particles, the superficial parts of the tephra layers were eliminated before sampling.

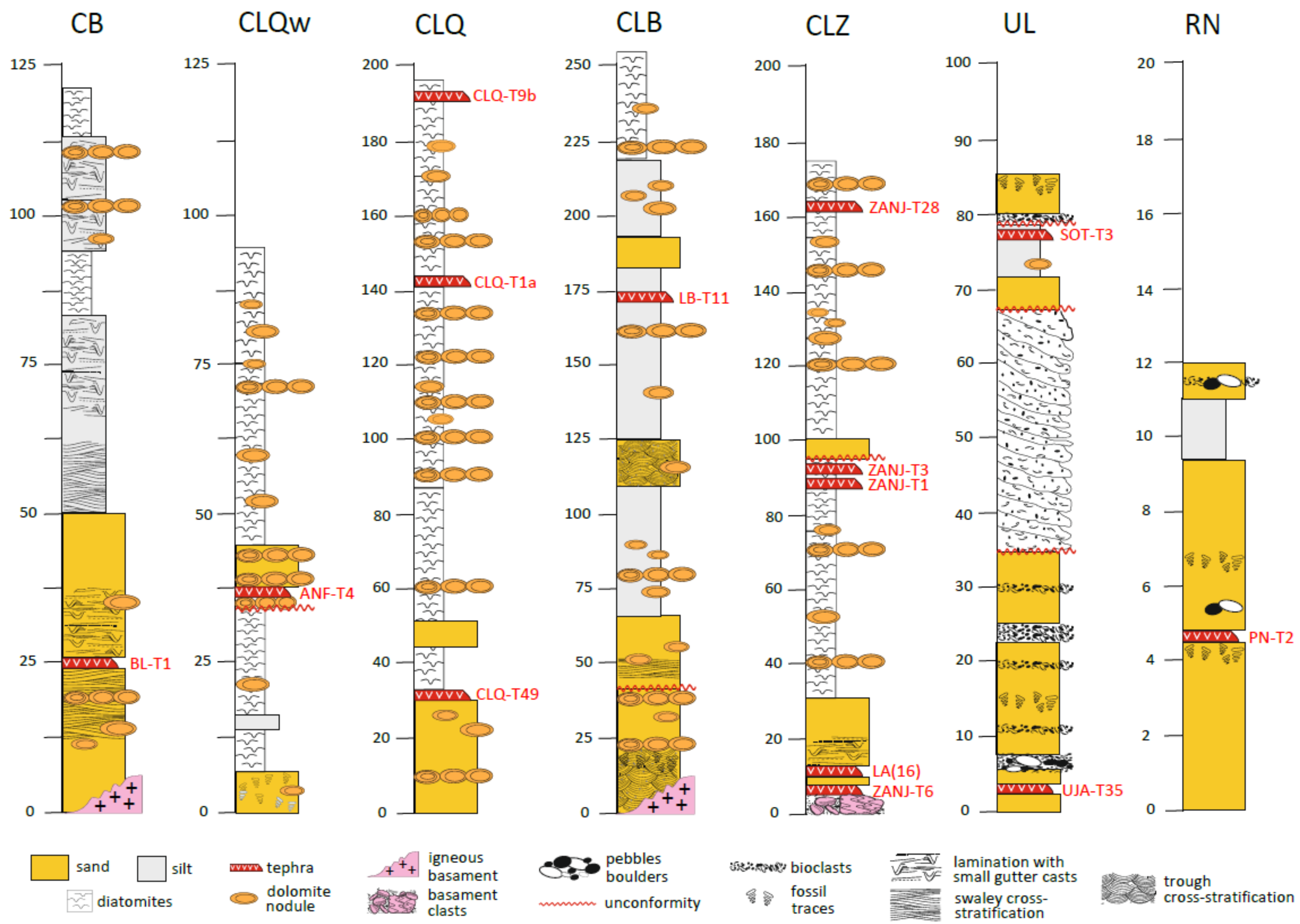

Figure 5.1. Simplified stratigraphic logs measured in the study area showing stratigraphic position of the dated tephra only.

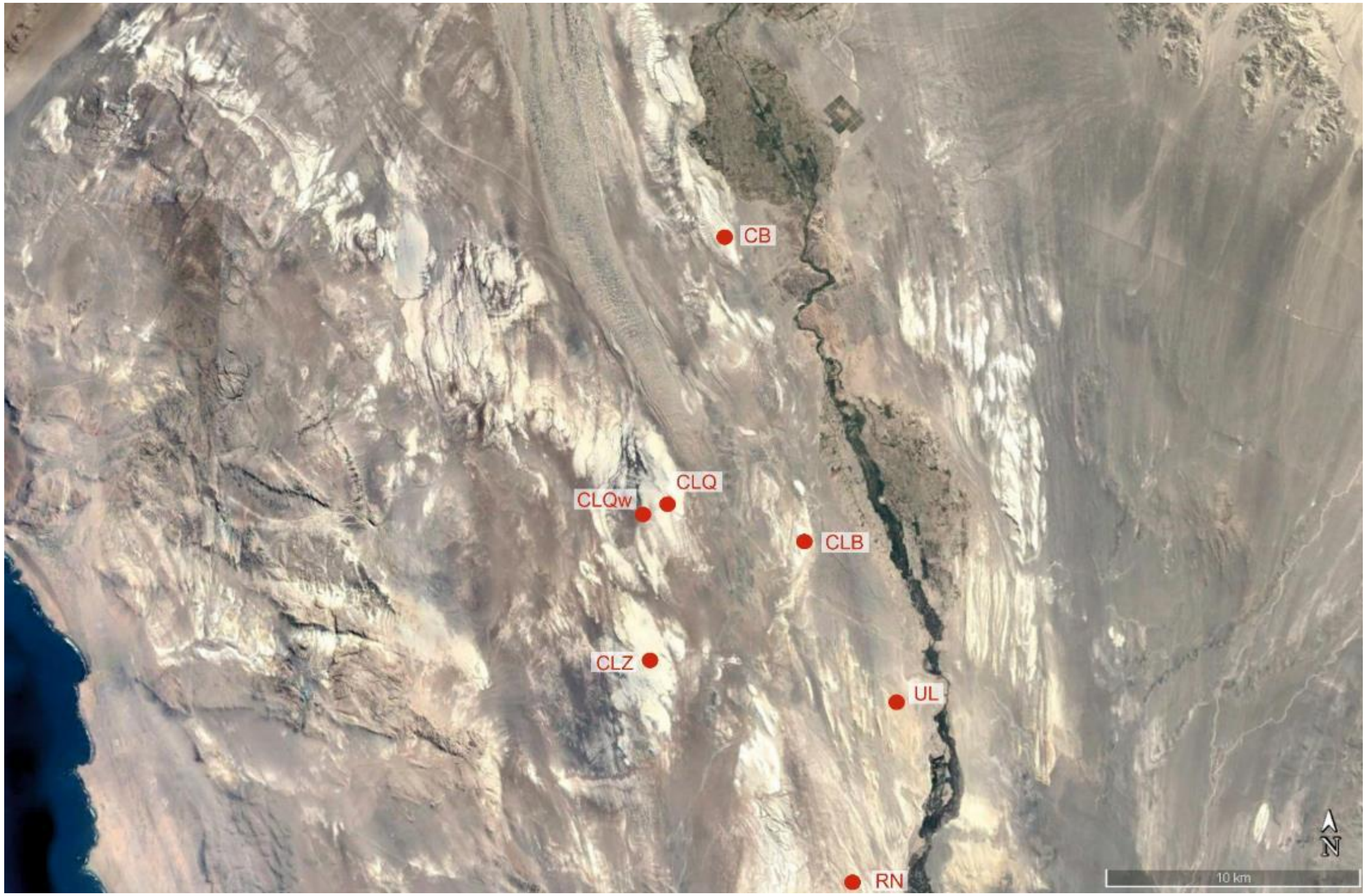

Figure 5.2. Satellite image of the localities of the measured stratigraphic logs shown in Fig. 5.1. CB = Cerro Blanco; CLQw = Cerro los Quesos west; CLQ = Cerro los Quesos; CLB = Cerro la Bruja; CLZ Cerros Cadena de los Zanjones; UL = Ullujaya; RN = Roca Negra. Based on image © 2018 DigitalGlobe.

For dating purposes, a particular attention was paid to the requirements for reducing the risk of contamination and, in order to collect as many biotite phenocrysts as possible, collection was focused at the base of the layers, where coarser biotite phenocrysts were concentrated.

The collected tephra were named with initials related to the locality, a "T" for tephra, and a number concerning the stratigraphic position along the measured section (e.g. CLQT1); small letters are used in case of sublayers recognizable in the same tephra (e.g. CLQ-T1a). The precise stratigraphic position of dated tephra sample is provided in Figure 5.1.

For tephra fingerprinting, among the collected tephra, 45 samples of the Pisco Formation were selected for petrographic and chemical investigations, focusing on the fossil-rich localities of Cerro los Quesos and Cerro la Bruja due to their paleontological relevance. They were examined under a stereomicroscope and prepared as smear slides for petrographic analysis and for a semi-quantitative component analysis, to check the presence of non-volcanic particles and evidence of alteration of volcanic components. Based on the results of this first screening, samples with more than 5% vol. of non-primary particles were interpreted as reworked/remobilized, and therefore were discarded (Tada et al. 2015; Griggs et al. 2014).

Grain size analyses were performed with the Malvern Mastersizer 2000E™ Laser Granulometer at the University of Milano-Bicocca. For each sample, three subsamples were made, and each of them was measured three times. Grain size data were processed with the Grain Size Analysis Program GRADISTAT (Blott & Pye 2001).

Samples were also wet sieved with meshes of 500, 250, 125 and 63 μm. The ashes from the 250-500 micron and 125-250 micron were mounted in resin, polished with silicon carbide and alumina, and carbon-coated. Glass shard morphology and mineral assemblages of the samples representing the product of primary deposition of ashes were observed by optical microscopy on smear slides and analyzed by scanning electron microscopy (SEM) back-scattered imaging on the carbon-coated polished mounts, to fingerprint the petrographic and textural features of the juvenile volcanic components. For the chemical composition, 32 samples were selected for biotite analyses and 35 samples were analyzed for the glass chemistry. EPMA (Electron Probe Micro Analysis) and EDS (Energy-dispersive X-ray Spectroscopy) analyses were performed on at least 10-15 representative glass shards and 10 biotite phenocrysts (core and rim) per sample, in order to obtain a chemical characterization of the tephra layers and an estimate of the weathering degree of biotite phenocrysts. SEM-EDS analyses were carried out at the University of Pisa with a Philips™ XL30 scanning electron microscope with 20 kV filament voltage, 5 nA beam current and ZAF correction, in raster mode and 10x10 or 5x5 μm-sized windows. EPMA analyses were performed with a JEOL JXA-8600™ at Consiglio Nazionale delle Ricerche in Florence and with a JEOL 8200 Superprobe™ at the University of Milan. Analytical conditions were 15 kV accelerating voltage, 5nA beam current, 3 μm beam focus for biotite and 10 μm for glass shards. Rhyolite NMNH 72854 (VG-568), basalt NMNH 111240-52 (VG-2) and basalt NMNH 113498-1 (A-99) Smithsonian Microbeam Standards (Jarosewich et al. 1980) and rhyolite SMN49 (Scaillet & McDonald 2001) were adopted as a reference material for glass analyses; phonolitic experimental glasses with known content of water obtained from Vesuvius natural materials (Scaillet et al. 2008) were used as reference for evaluating hydration in our glass analyses.

5.2. ^{39}A–^{40}Ar dating

For dating purposes, the choice was made on the basis of the stratigraphic position and the lack of a clear alteration. After petrographic analyses under a stereomicroscope and an optical microscope, mineral chemistry was quantified on biotite phenocrysts hand-picked after wet-sieving. The 250 μm biotite phenocrysts were analyzed with the JEOL 8200 Superprobe™ for Electron Probe Micro Analysis (EPMA) at the University of Milan, the same used for fingerprinting analyses, in order to analyze the chemistry of biotite, looking for weathering evidences as the loss of K content.

The selection of the datable tephra layers was made based on the stratigraphic position and the K content measured through EPMA. Fourteen samples from both Pisco and Chilcatay Formation were selected for ^{39}A–^{40}Ar analyses. Biotite phenocrysts were carefully hand-picked from 250 μm fraction under a stereomicroscope, avoiding altered crystals with corroded rims and grains with heterogeneous color or large glass inclusions. Biotite samples of 10 to 20 mg were wrapped in Al foil, producing a flat disk with 10 mm diameter and ca. 1 mm thickness. For each sample a dry aliquot of 1-2 mg was prepared in addition to the larger one.

Samples were irradiated in the McMaster University reactor (Ontario, Canada) for 30 MWh, carefully avoiding Cd shielding. In order to control the vertical flux gradient, several disk wraps of Fish Canyon sanidine (FCs) were interlayered with the sample disk wraps (Fig. 5.3a). The typical monitor mass was 2-3 mg. One monitor was placed every 6-7 samples (corresponding to 6-7 mm). The FCs age was taken as 28.172 ± 0.028 Ma (Rivera et al. 2011). The irradiation intensity factor, J, was interpolated for each sample from the parabolic equation defined by the J values of the FCs monitors. We observed, unfortunately, a problem in monitoring the irradiation intensity using the FCs monitors. In each irradiation, some of the monitors deviated from the parabolic fit by several percent, making impossible an accurate calculation of the J factor for each sample. In one instance, a vertical flux gradient of 10% in 7 mm was calculated, an unreasonably high value. This could be caused by the impurity of the FCs monitor (Bachmann et al. 2002).

Analytical procedures were an upgrade of those in Villa et al. (2000). Before each sample, a blank measurement was followed by two successive measurements of atmospheric Ar delivered by a pipette system. Samples were step-heated in a low-blank double-vacuum furnace (Fig. 5.3b). The small aliquots were analyzed first in five heating steps, in order to optimize the choice of heating steps of the large aliquots, which were usually heated in 10-12 steps. Two SAES™ C-50 getters cleaned the gas before analysis. All five Ar isotopes, as well as hydrocarbons (mass 41) and elemental ^{35}Cl, were measured in a NuInstruments™ Noblesse® noble gas mass spectrometer (Fig. 5.2b), equipped with one Faraday (F) collector with a 1011 Ω resistor and two MasCom™ ion counters (IC0 and IC1). This configuration allows the simultaneous measurement of the Ar isotopes spaced by two mass units and the direct calibration of the F/IC0 and IC0/IC1 gains in each individual run under the (variable) analytical conditions. These gains are similar, but not necessarily equal, to those determined from the atmospheric pipettes (which also independently quantify the mass fractionation originating in the source). The measurement sequence consists of four cycles: ^{40}Ar(F), ^{38}Ar(IC0), ^{36}Ar(IC1); ^{38}Ar(F), ^{36}Ar(IC0), mass 34 (IC1); ^{39}Ar(F), ^{37}Ar(IC0), ^{35}Cl(IC1); mass 41(F), ^{39}Ar(IC0), ^{37}Ar(IC1). The fourth cycle is only active when the ^{39}Ar ion count rate is less than 1 MHz. The four cycles were repeated 25 times in order to avoid spurious results due to the time-dependent ion counter non-linearities documented by Barberini and Villa (2015).

The raw data from the mass spectrometer zero-time extrapolation were processed in the in-house CalcolAr spreadsheet (Fig. 5.3c) by correcting for mass spectrometer background, ion counter gains, blank measurements, source fractionation, and decay of ^{37}Ar since irradiation, as well as propagating all the associated uncertainties.

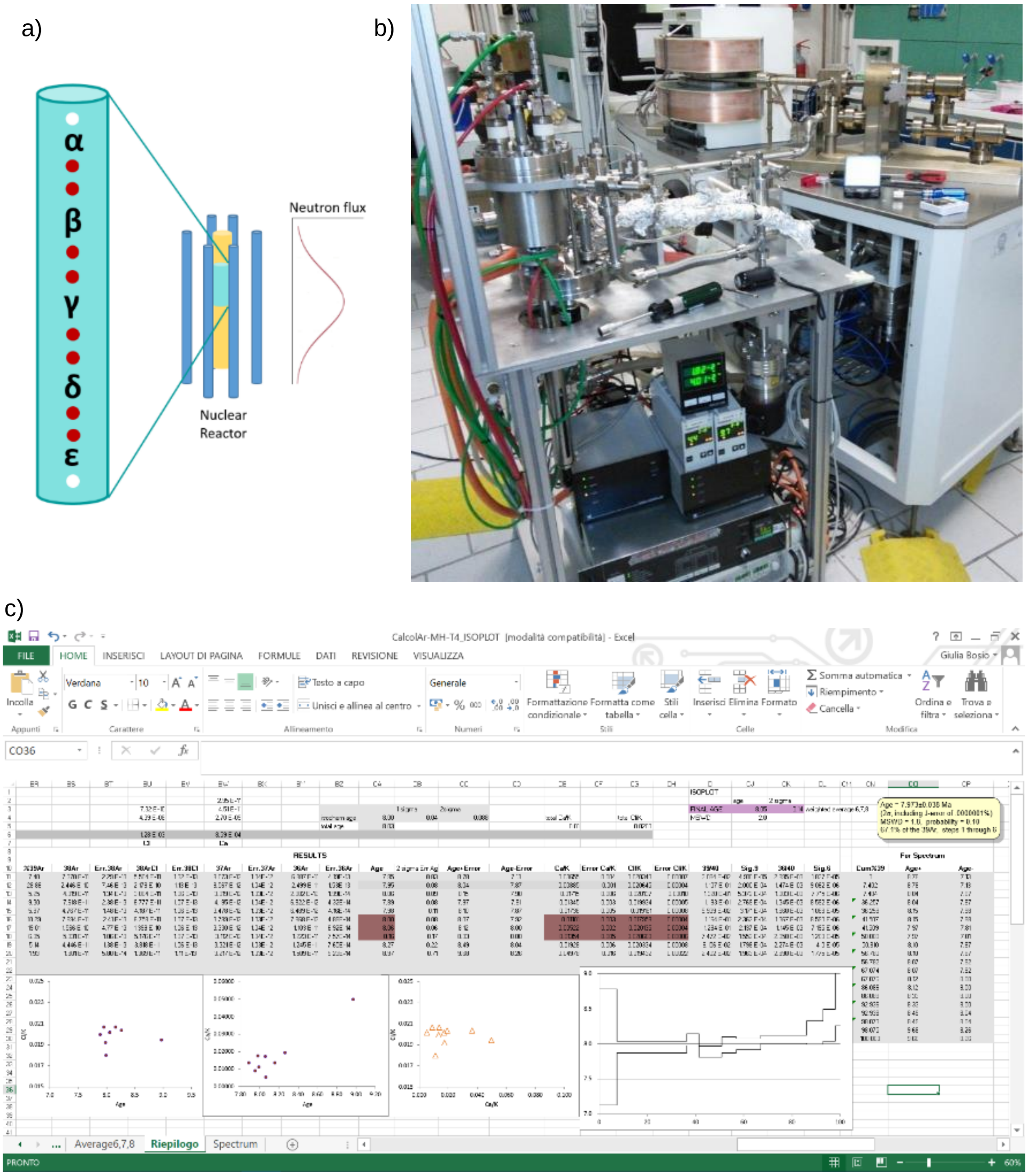

Figure 5.3. a) Scheme of the cylinder with the Fish Canyon sanidine (FCs) interlayered with the sample disk wraps in the nuclear reactor, put in order to control the vertical flux gradient. b) The low-blank double-vacuum furnace and the NuInstruments™ Noblesse® noble gas mass spectrometer at the back. c) In-house CalcolAr spreadsheet example for the age extrapolation.

The total concentrations of ^{39}Ar, ^{38}Ar and ^{37}Ar were converted to absolute concentrations of K, Cl and Ca, respectively, so as to control stoichiometry, and to provide the Ca/K and

Cl/K ratios. The ^{40}K decay constant used for the age calculation was 5.543 x 10^{-4} Ma^{-1} (Steiger & Jäger 1977), even if it is very probably incorrect (Min 2000; Naumenko-Dèzes et al. 2018), in order to make intercomparisons with literature data less cumbersome. The isochron calculations, weighted averages, and estimates of excess scatter (via the MSWD parameter) were calculated with Isoplot (Ludwig 2012). The final age estimate is given with a 2σ uncertainty, whereby different levels of uncertainty must be taken into account. The internal concordance/discordance of step ages is assessed basing on in-run uncertainties only. The intercomparison of samples analyzed in one and the same laboratory requires compounding the in-run uncertainty with that on the neutron flux gradient. Finally, the intercomparison of the present samples with those reported in the literature requires inclusion of the systematic uncertainties on the age of the irradiation monitor (if the information is provided at all) and of the uncertainty of the ^{40}K decay constant, where necessary.

5.3. Biostratigraphic analyses

Planktonic microfossils were studied from the samples collected along the measured sections, with a vertical spacing of few meters. For biostratigraphic purposes, smear slides were prepared from the fine-grained sediment.

Observations were made by means of a Leitz Diaplan™ light microscope at 630x and 1000x, and an Olympus BX50 polarized optical microscope at 1000x.

The presence and relative abundance of different diatom species were tabulated. The total abundance of diatoms relative to the remaining sediment (glass shards and other minerals) was assessed according to Koç and Scherer (1996):

D = dominant; > 60% valves.

A = abundant; ~ 20% - 60% valves.

C = common; ~5% - 20% valves.

F = few; 2% - 5% valves.

R = rare; < 2% valves.

B = barren; no diatoms present.

The relative abundance of each diatom, silicoflagellate and nannofossil taxon was estimated using the following qualitative scale:

A = abundant; > 10 valves/fields of vision (FOV).

C = common; 1 - 10 valves/FOV.

F = few; ≥ 1 valve/10 FOVs and < 1 valve/FOV.

R = rare; ≥ 3 valves/traverse of coverslip and < 1 valve/10 FOVs.

X = present; < 3 valves/traverse of coverslip, including fragments.

B = barren; no valves.

Diatom preservation categories, as reported in range charts, are described qualitatively according to Barron and Gladenkov (in Rea et al. 1993):

VG = very good (no breakage or dissolution).

G = good (majority of specimens complete, with minor dissolution and/or breakage and no significant enlargement of the areolae or a dissolution of frustule rims detected).

M = moderate (minor, but common areolae enlargement and dissolution of frustule rims, with a considerable amount of breakage of specimens).

P = poor (strong dissolution or breakage, some specimens unidentifiable, strong dissolution of frustule rims and areolae enlargement).

It is important to highlight that: (i) ages of the considered diatom bioevents are based on Equatorial Pacific diatom biostratigraphy and may therefore not be fully representative of first and last occurrences at the Pisco Basin latitudes; (ii) ages of the considered silicoflagellate biozones have not been calibrated but correlated with nannofossil biozones.

The diatom zonal scheme used here mainly follows biostratigraphic studies by Barron (1985). First and Last Occurrences (FO and LO) of species are after the works of Barron (1985, 2003) and after the Expedition 320/321 Scientists (2010). Therefore, all diatom bioevents are discussed referring to the Geochronologic and Chronostratigraphic Time Scale of Berggren et al. (1995) (the one followed by Barron 2003); the terms lower, middle, upper (chronostratigraphy) and early, middle, late (geochronology) referred to subepochs are used as in Berggren et al. (1995) as well (not recalibrated to the most recent timescale).

In this dissertation, we refer to diatom species taking into account the most up-to-date taxonomic revisions. This may create some confusion when comparing our data to older papers. In particular, many specimens, previously determined as *Coscinodiscus plicatus* in numerous biostratigraphic papers, have been moved into one of the many plicated *Thalassosira* species. We refer to Tanimura's revision (1996) to identify the plicated *Thalassiosira* specimens that we encountered in our sections, and to Yanagisawa and Akiba (1990) for the taxonomy of the species belonging to the genus *Denticulopsis*. Also,

we provide ages of FO and LO in Ma; those are proceeded by the abbreviation ‘ca.’ when referring to an uncalibrated age (i.e., when ages are only provided as ranges in illustrations of biostratigraphic schemes).
For silicoflagellate and nannofossil biozones, we refer to Bukry (1981, 1982, 1985) and Perch-Nielsen (1985).

5.4. Sr isotope analyses

During fieldwork in 2016, mollusk (i.e. ostreids and pectinids) and barnacle shells, carbonate nodules and shark teeth were collected along the measured section of the Chilcatay Formation at Ullujaya and Roca Negra, and in the P0 strata at Cerro Submarino. Samples were collected for trying another isotope technique, the Strontium Isotope Stratigraphy on carbonates (invertebrate shells) and phosphates (shark teeth).
In order to check if the shell was pristine or not, bivalve and barnacle shells were subject to petrographic, morphological, chemical and cathodoluminescence analyses, as described in Chapter 14 (Part II). It is important to avoid altered and diagenetic material that could modify the real age. The results on the invertebrate taphonomy and preservation are shown in Chapter 15 (Part II).
Once analyzed, pristine mollusk shells (i.e. ostreids and pectinids) and well-preserved barnacle sheaths (the inner upper portion made of nacre) were carefully cleaned through an ultrasonic bath in distilled water. They were bored precisely with a Dremel micro-drill to obtain shell powder from the diagenetically unaltered area. After a bath in distilled water, also the shark teeth have been scraped and the enameloid (the unaltered and non-porous material) was removed with a Dremel micro-drill. About 10-50 mg of each sample were collected, taking care to avoid contamination.
Samples from the same specimen and different taxa from the same level were selected in order to increase the statistic reliability of the data. In addition, samples of the bulk and late cements were analyzed for checking the diagenetic trend and the “fingerprint” of the terrigenous sediment. After the preliminary analyses, 15 samples were selected for the Chilcatay Formation, in the Ct1 allomember, and 8 samples for the P0 allomember.
The $^{87}Sr/^{86}Sr$ analyses were performed at Ruhr-Universität in Bochum (Germany) in the Sr isotope laboratory, where samples were dissolved in HCl and analyzed through a Finnigan MAT 262 solid source mass spectrometer, after ICP-OES analyses of the trace elements (Sr, Ca, Mg, Fe, Mn).

According to the ICP-OES Sr concentration measurements, an equivalent of carbonate sample representing 200 to 300 ng of Sr was digested with 6 M suprapure HCl for about 24 h at room temperature in closed PFA beakers, and afterwards evaporated until dryness. Subsequently, the dried samples were re-dissolved in 0.4 ml HNO_3 3M. The Sr fraction was recovered using an ion exchange Sr complexing resin (Sr-resin TRISKEM) conditioned with 0.05 M and 3 M HNO_3 applying 2 ml of distilled water. After evaporation, the dried sample material was treated with 0.5 ml of a 1:1 mixture of concentrated HNO_3:H_2O_2, removing organic remains and subsequently dried again. Finally, the samples were converted to chloride-form applying 0.4 ml 6 M HCl and dried again. For mass-spectrometry samples, they were re-dissolved in an ionization enhancing solution (after Birck 1986), and 1 µL representing 100 ng Sr was loaded on a Re single filaments. Loading blank was < 5 pg, column blank was < 1 ng, and reagent blank about < 0.01 ppb.

The mean of 34 analyses of NIST standard NBS 987 was 0.710240 with a standard deviation of 0.000023 (± 2 s.d.), whereas the mean of 24 analyses of the USGS EN-1 standard was 0.709153 with a standard deviation of 0.000019 (± 2 s.d.). The SRM measurements cover the period of Sr measurements in 2016 and 2017. The EN-1, a carbonate powder of a modern *Tridachna* shell, undergoes the same analytical procedure like all other carbonate samples from digestion to measurement and represents the reproducibility of the complete analytical process. Whereas the NBS 987 is directly loaded onto the filament and shows the stability and reproducibility of the mass spectrometry. It is possible to reduce the analytical error to a few ppm running a large number of samples in a short period of time. The seawater IAPSO (plus 5 µg/g K, Rb, Mn and Fe) was only used for the calibration of ion-exchange columns. For carbonates, the EN-1 resembles a real sample much closer than a sea water sample. The laboratory used the IAPSO primarily as an additional reference for Ca and Mg isotope analyses.

The Sr isotope measurements were performed with a TIMS refurbished MAT262 (now TiBox Spectromat Bremen) with 7 collectors. Mode of measurement was dynamic (peak-hopping), using the same exponential fractionation algorithm that is applied by Thermo for the Triton. The thermal fractionation was corrected by normalization to a $^{88}Sr/^{86}Sr$ ratio of 8,375209, and so these measurements cannot be used to calculate the stable isotope composition of Sr. The cut-off limit for a Sr-run is generally at an error of $\pm 2\ \sigma$ value $\leq 5 \times 10^{-6}$ for the $^{87}Sr/^{86}Sr$ ratio measured, and minimum of 100 ratios and maximum of 150 (200) ratios per run. The typical duration of a Sr run is 110 ratios and 2h 15’ plus the filament heating time.

No Rb- correction was applied, since for an element with two isotopes and a spectral interference on one of them a reliable correction was impossible. The thermal fractionation of Rb is very high and unpredictable und either overestimates or underestimates the impact of ^{87}Rb on ^{87}Sr during a single run. Nevertheless, Rb was monitored during the complete run. The Rb signal must be below the detection limit, otherwise the result was discarded and the measurement repeated (including the chemical separation). The single filament technique plus ionization enhancing solution allowed to heat up the Sr sample to 1300 to 1360°C for the measurement, which resulted in burning off traces of Rb during the filament heating procedure before Sr was analyzed.

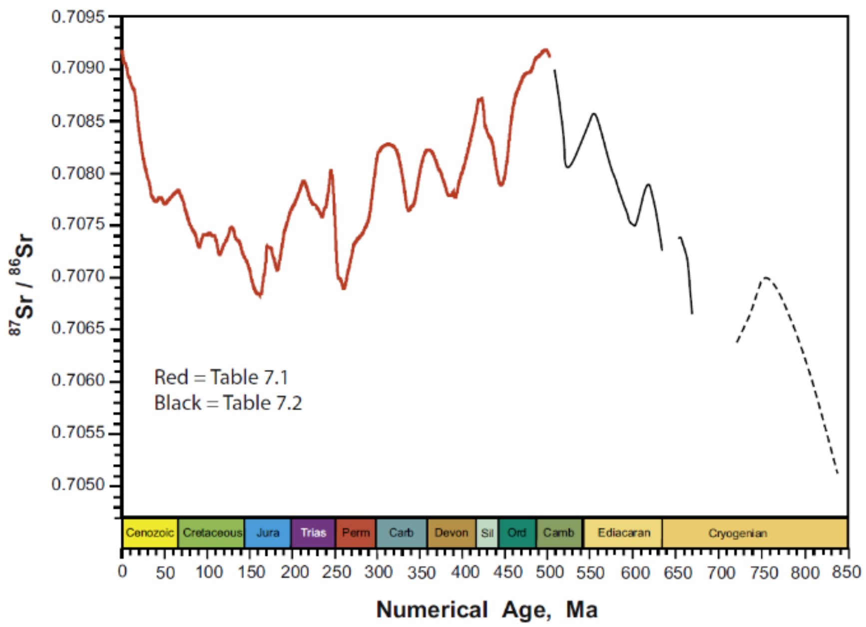

Figure 5.4. McArthur’s curve showing the variation of $^{87}Sr/^{86}Sr$ through time. From McArthur et al. (2012).

Data were interpreted applying principles learnt at the course on isotope stratigraphy held by Prof. Mariano Parente at University of Naples in 2016. The $^{87}Sr/^{86}Sr$ values were compared with the McArthur’s LOWESS table version 5 made for the GTS2012 timescale to obtain ages, following the principles of the curve realized by McArthur (McArthur 1994; McArthur et al. 2001, 2012), see Figure 5.4.

Methods explained in this chapter are the result of paragraphs of different papers. Petrographic and chemical analyses on tephra are based on the paper "Chemical and petrographic fingerprinting of volcanic ashes as a tool for high-resolution stratigraphy of the upper Miocene Pisco Formation (Peru)" written by Giulia Bosio, Anna Gioncada, Elisa Malinverno, Claudio Di Celma, Igor M. Villa, Giuseppe Cataldi, Karen Gariboldi, Alberto Collareta, Mario Urbina and Giovanni Bianucci, which will be published by the Journal of the Geological Society in January 2019.

^{39}Ar – ^{40}Ar dating and biostratigraphic methods are based on the papers: "Tephrochronology and chronostratigraphy of the Miocene Chilcatay and Pisco formations (East Pisco Basin, Peru)" written by Giulia Bosio, Elisa Malinverno, Igor M. Villa, Claudio Di Celma, Karen Gariboldi, Anna Gioncada, Valentina Barberini, Mario Urbina and Giovanni Bianucci, submitted to Newsletters on Stratigraphy in December 2018; "Biostratigraphy, geochronology and sedimentation rates of the upper Miocene Pisco Formation at two important marine vertebrate fossil-bearing sites of southern Peru" written by Karen Gariboldi, Giulia Bosio, Elisa Malinverno, Anna Gioncada, Claudio Di Celma, Igor M. Villa, Mario Urbina and Giovanni Bianucci, published on Newsletters on Stratigraphy, Vol. 50/4 (2017), 417-444. In this paper, Giulia Bosio contributes to sample collection, volcanic ash analyses, ^{39}Ar– ^{40}Ar geochronology, discussion on the previous dating and the new results, comparison of data and calculation of sedimentation rates.

Sr isotope method is that followed by the Bochum laboratory and will be published, in the next future, in the paper "Strontium Isotope Stratigraphy of the Miocene sedimentary successions in the Peruvian East Pisco Basin" in preparation.

Chapter References

Bachmann, O., Dungan, M.A., Lipman, P.W. 2002. The Fish Canyon magma body, San Juan volcanic field, Colorado: rejuvenation and eruption of an upper-crustal batholith. Journal of Petrology, 43 (8), 1469-1503.

Barberini, V., Villa., I. 2015. Ion Counter Nonlinearities. Goldschmidt 2015, Abstracts: 202.

Barron, J. A., 1985. Miocene to Holocene planktic diatoms. In: Bolli, H. M., Saunders, J. B. & Perch-Nielsen, K. P. (Eds.), Plankton stratigraphy. Cambridge: Cambridge University Press, 763-809.

Barron, J. A. 2003. Planktonic marine diatom record of the past 18 my: appearances and extinctions in the Pacific and Southern Oceans. Diatom Research 18(2), 203-224.

Berggren, W. A., Kent, D.V., Swisher, C. C., Aubry, M. P. 1995. A Revised Cenozoic geochronology and chronostratigraphy. In: Berggren, W. A., Kent, D.V., Hardenbol, J. (Eds.), Geochronology, Time Scales and Global Stratigraphic Correlation. Society of Economic Paleontologists and Mineralogists, Special Publication, Tulsa, 54, 129-212.

Blott, S.J., Pye, K. 2001. Gradistat: a grain size distribution and statistics package for the analysis of unconsolidated sediments. Earth Surface Processes and Landforms, 26, 1237-1248.

Bukry, D. 1981. Synthesis of Silicoflagellate stratigraphy for Maestrichtian to Quaternary marine sediments. In T. E. Warme, R. C. Douglas, & E. L. Winterer (Eds.), The deep sea drilling project: A decade of progress (pp. 433-444). Tulsa: SEPM, Special Publication, 32.

Bukry, D. 1982. Cenozoic Silicoflagellates from offshore Guatemala, deep sea drilling project site 495. Initial Reports, DSDP 67: 425-445. Washington: U.S. Govt. Printing Office.

Bukry, D. 1985. Correlation of late Cretaceous Arctic silicoflagellates from Alpha Ridge. In H. R. Jackson, P. J. Mudie, & S. M. Blasco (Eds.), Initial geological report on CESAR - the Canadian expedition to study the alpha ridge, arctic ocean. Geological Survey of Canada, 84-22, 125-135.

Expedition 320/321 Scientists 2010. Methods. In H. Pälike, M. Lyle, H. Nishi, I. Raffi, K. Gamage, A. Klaus, and the Expedition 320/321 Scientists, Proceedings of the integrated ocean drilling program, 320/321: Tokio: Integrated Ocean Drilling Program Management International, Inc.

Griggs, A. J., Davies, S. M., Abbott, P. M., Rasmussen, T. L., Palmer, A. P. 2014. Optimising the use of marine tephrochronology in the North Atlantic: a detailed investigation of the Faroe Marine Ash Zones II, III and IV. Quaternary Science Reviews, 106, 122-139.

Jarosewich, E., Nelen, J. A., Norberg, J. A. 1980. Reference Samples for Electron Microprobe Analysis. Geostandards Newsletter, 4, 43-47.

Koç, N., Scherer, R. P., 1996. Neogene Diatom Biostratigraphy of the Iceland Sea Site 9071. Proceedings of the Ocean Drilling Program. Scientific Results, 151, 61-74.

Ludwig, K.R., 2012. Isoplot 3.75. A geochronological toolkit for Microsoft Excel. Berkeley Geochronology Center Special Publication No. 5.

McArthur, J.M. 1994. Recent trends in strontium isotope stratigraphy. Terra Nova, 6, 331-358.

McArthur, J.M., Howarth, R.J., Bailey, T.R. 2001. Strontium Isotope Stratigraphy: LOWESS Version 3: Best Fit to the Marine Sr-Isotope Curve for 0–509 Ma and Accompanying Look-up Table for Deriving Numerical Age. The Journal of Geology, 109, 155-170.

McArthur, J.M., Howarth, R.J., Shields, G.A. 2012. Strontium Isotope Stratigraphy. In F.M. Gradstein, J.G. Ogg, Schmitz M., Ogg G. (Eds.), The Geologic Time Scale 2012 (Chapter 7, pp. 127-144). Elsevier.

Min, K., Mundil, R., Renne, P. R., Ludwig, K. R. 2000. A test for systematic errors in Ar-Ar geochronology through comparison with U-Pb analysis of a 1.1-Ga rhyolite. Geochimica et Cosmochimica Acta, 64, 73-98.

Naumenko-Dèzes, M.O., Nägler, T.F., Mezger K., Villa, I.M. 2018. Constraining the 40K decay constant with 87Rb-87Sr – 40K-40Ca chronometer intercomparison. Geochimica et Cosmochimica Acta, 220, 235-247.

Perch-Nielsen, K., 1985. Silicoflagellates. In H. M. Bolli, J. B. Saunders, K. Perch-Nielsen (Eds.), Plankton stratigraphy (Vol. 2, pp. 811–846). Cambridge: Cambridge University Press.

Rea, D. K., Basov, I. A., Janecek, T. R., Palmer-Julson, A. et al. 1993. Proceedings of the Ocean Drilling Program, Initial Reports, 145, 9–33.

Rivera, T.A., Storey, M., Zeeden, C., Hilgen, F.J., Kuiper, K. 2011. A refined astronomically calibrated 40Ar/39Ar age for Fish Canyon sanidine. Earth and Planetary Science Letters 311, 420-426.

Scaillet, B., Mcdonald, R. 2001. Phase relations of peralkaline silicic magmas and petrogenetic implications. Journal of Petrology, 42, 825-845.

Scaillet, B., Pichavant, M., Cioni, R. 2008. Upward migration of Vesuvius magma chamber over the past 20 thousand years. Nature, Nature Publishing Group, 455, 216-219.

Steiger, R.H., Jäger, E. 1977. Subcommission on geochronology: convention on the use of decay constants in geo- and cosmochronology. Earth and Planetary Sctence Letters, 36, 359-362.

Tada, R., Murray, R.W., Alvarez, Zarikian, C.A., Anderson, Jr. W.T., et al. 2015. Methods. The Expedition 346 Scientists Proceedings of the Integrated Ocean Drilling Program, 346.

Tanimura, Y. 1996. Fossil marine plicated Thalassiosira: taxonomy and an idea on phylogeny. Diatom Research, 11(1), 165-202.

Villa, I. M., Hermann, J., Müntener, O., Trommsdorff, V., 2000. 39Ar–40Ar dating of multiply zoned amphibole generations (Malenco, Italian Alps). Contributions to Mineralogy and Petrology, 140(3), 363-381.

Yanagisawa, Y., Akiba, F., 1990. Taxonomy and phylogeny of the three marine diatom genera Crucidenticula, Denticulopsis and Neodenticula. Bulletin of the Geological Survey of Japan, 41, 197-301.

Chapter 6. Stratigraphy and paleoecology of the Chilcatay Formation at Ullujaya

The Chilcatay Formation comprises marine diatomaceous and tuffaceous sandy siltstones, bioclastic sandstones and, along the base, massive sandstones, and large boulders of crystalline basement rocks. Based on planktonic foraminifera (Ibaraki, 1993) and diatoms found in Chilcatay strata exposed at Cerros Las Salinas and Cerro La Virgen, two localities about 100 and 70 km northwest of Ullujaya, a late Oligocene age has been assigned to the lowermost strata of this unit by DeVries and Jud (2018).

Chilcatay Formation crops out in the southeastern part of the study area in the western side of the Ica River, as shown in Figure 6.1. This formation is especially exposed in the locality of Ullujaya, where it reaches the maximum exposure and a large abundance of well preserved vertebrate fossils was found.

Ullujaya is a richly fossiliferous site located in the Ocucaje area, along the western side of the Ica River, in the southern coastal desert of Peru. Within the study area, the Chilcatay Formation is part of a gently dipping, northeast-facing monocline and its lower portion and base are not exposed. The Chilcatay Formation, however, a few kilometers south of Ullujaya rests on a pronounced angular unconformity on the Otuma Formation (DeVries & Jud, 2018) and disappears, possibly by onlap onto the basement rocks, a few kilometers to the north, defining a transgressive surface that becomes younger in the landward direction to the northeast. Internally, this unit has been resolved into two smaller sediment packages (allomembers) separated by a major intraformational unconformity (CE0.2) and informally designated Ct1 and Ct2 in stratigraphic order (Fig. 6.2 and 6.3a).

6.1. Ct1 allomember

The measured portion of the Ct1 allomember is about 56 m thick and comprises two distinct lithosomes: (i) a sub-horizontal package of interbedded siltstones, sandy siltstones and medium- to fine-grained sandstones (*Ct1a* facies association); and (ii) a clinobedded package of coarse-grained deposits having a mixed siliciclastic-carbonate composition (*Ct1b* facies association).

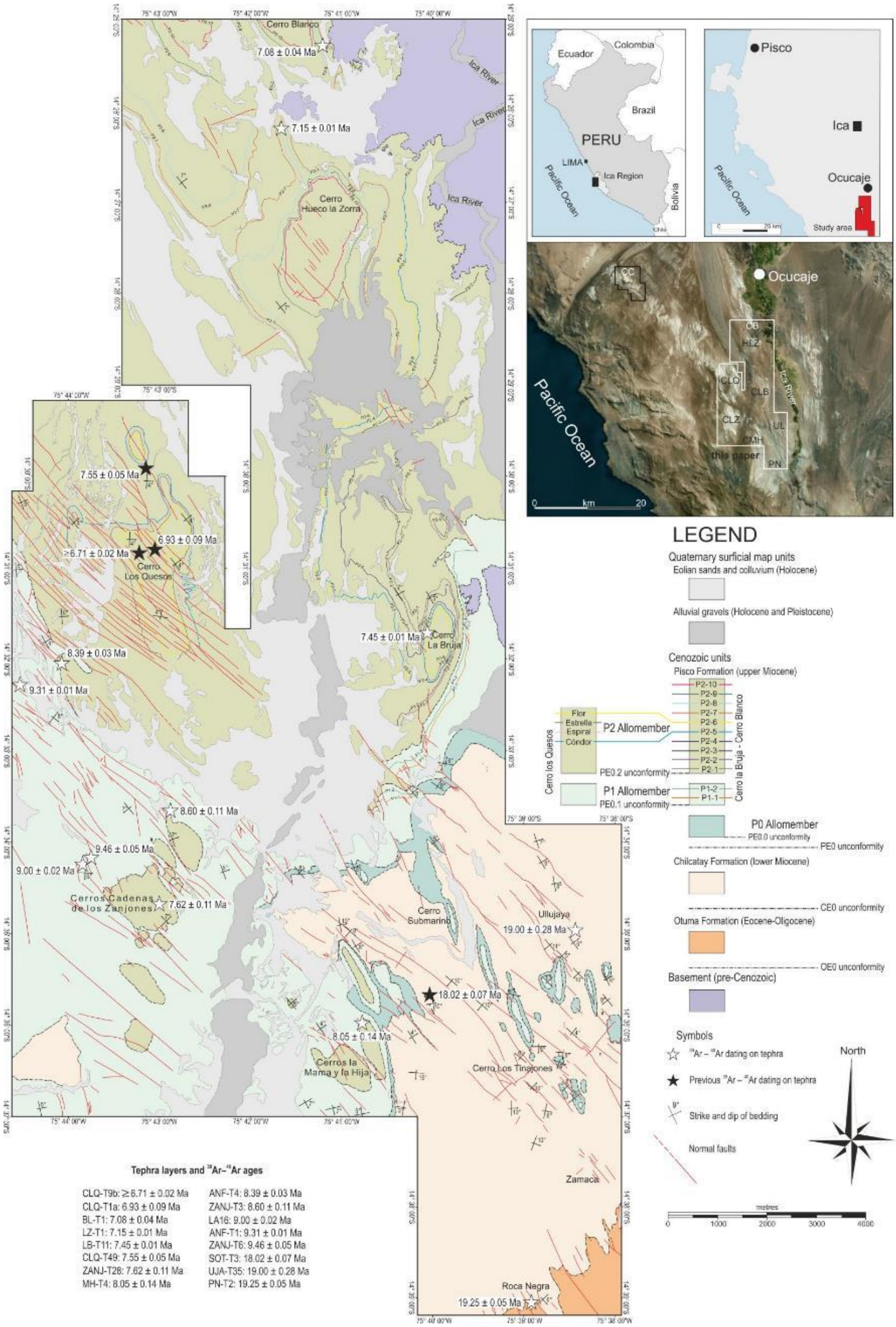

Figure 6.1. Geological map of the western side of the Ica River showing the exposure of the Chilcatay Formation in the southeastern part of the study area.

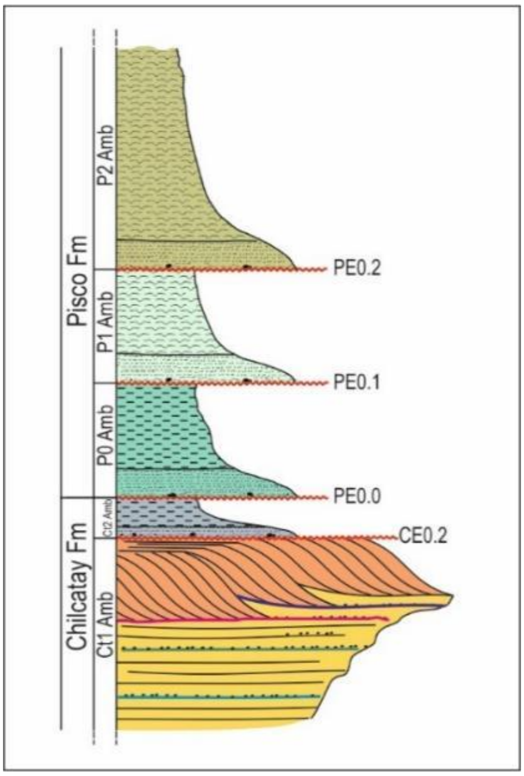

Figure 6.2. Stratigraphic column with the main units of Pisco and Chilcatay formations. From Di Celma et al. (2018).

The bulk of the *Ct1a* facies association is characterized by the dominance of massive siltstones and medium- to fine-grained siliciclastic sandstones (Fig. 6.3b). The diluted biogenic fraction is composed of small amounts of redeposited skeletal elements including barnacles and rarer calcareous tubes. Vertebrate material is abundant and includes disarticulated to partially articulated skeletons and isolated bones, and shark teeth. These fine-grained sediments are punctuated by discrete and laterally persistent beds of coarse-grained sandstones that range from 0.1 to 0.5 m in thickness and, locally, pass laterally into erosionally based granule- to boulder-sized conglomerates up to 1.5 m thick. The bases of these coarse-grained beds are sharp and display dense burrow assemblages comprising large *Thalassinoides* and subordinate *Gyrolithes* penetrating deeply into the subjacent fine-grained sediments (Fig. 6.3c, d). The composition of the granule layers is a laterally variable mixture of siliciclastic grains and skeletal elements. The latter are mainly represented by broken or whole shells of barnacles, in particular cases similar to the genus *Austromegabalanus*, and mollusk shells (mainly pectinids but also ostreids). Rare encrusting bryozoans were observed on barnacle shells. Echinoid fragments and calcareous tubes are less common; rare benthic foraminifera are also present (Fig.6.4a, b). Cobble to boulder-sized conglomerates are dominated by rounded clasts from an ash-flow tuff and the igneous basement set in a coarse-grained bioclastic matrix (Fig. 6.4c).

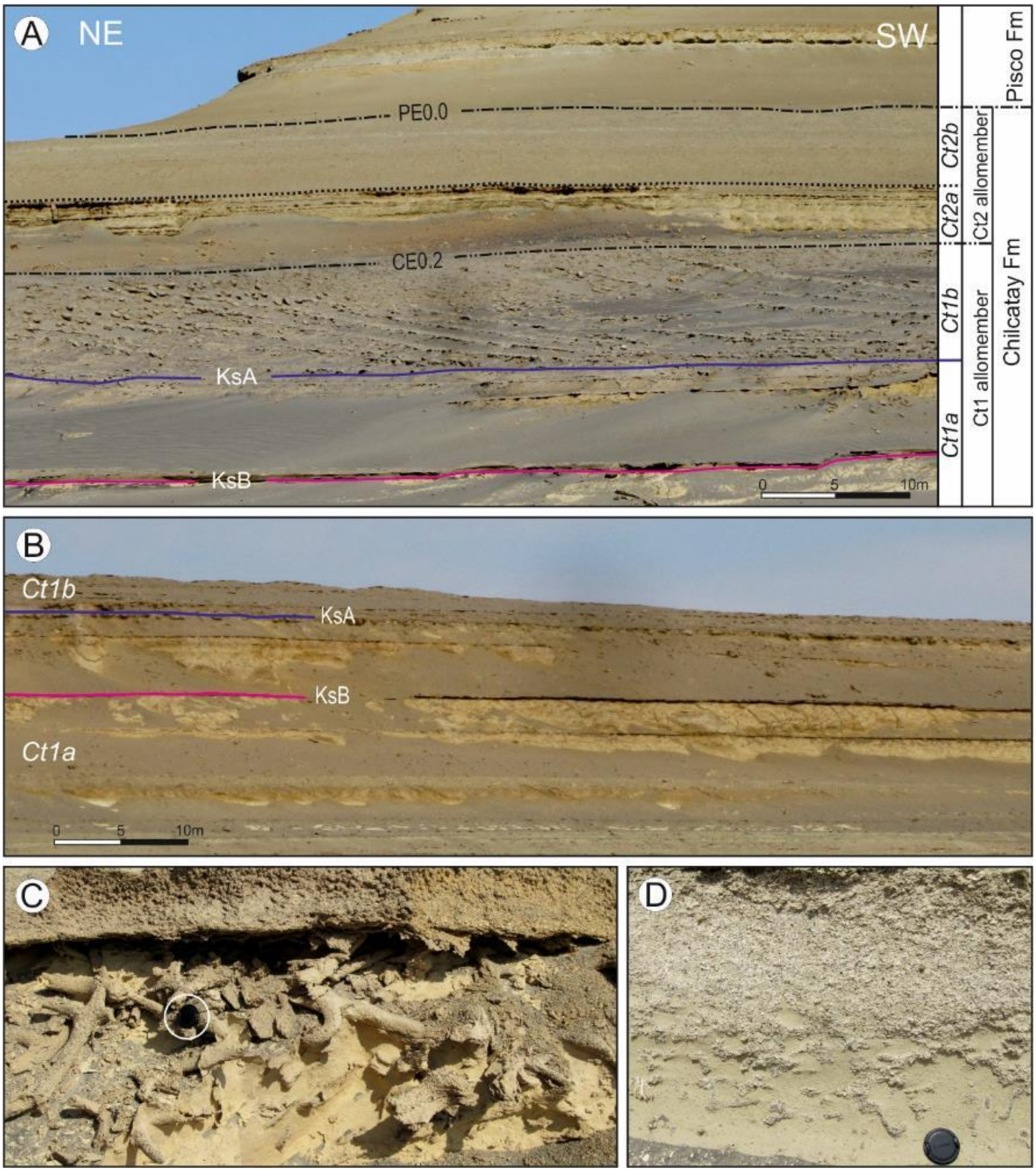

Figure 6.3. Representative outcrop views of the stratal architecture and some of the identified facies associations. a) Depositional dip oriented annotated panoramic photograph of the upper part of the Chilcatay Formation and the overlying Pisco Formation near Cerro Las Tres Piramides (14°35’22"S-75°38’20"W). The principal

surfaces used to further subdivide the Chilcatay Formation into allomembers and the internal facies architecture are indicated. At this site, the *Ct1a* and *Ct1b* facies associations of the Ct1 allomember are separated by the KsA surface. Clinoforms of the *Ct1b* facies association prograde basinward, showing truncated tops and typical downlapping basal contact onto sub-horizontal finer-grained sediments of the Ct1a facies association. The Ct2 allomember rests on the CE0.2 unconformity and exhibits a strong retrogradational (fining-upward) facies trend. The Chilcatay and Pisco strata are separated by the PE0.0 unconformity. b) Panoramic view showing the contact (KsA) between sediments of the *Ct1a* facies association and the lowermost portion of the *Ct1b* facies association at Ullujaya (14°35'03"S–75°38'36"W). KbB is a granule-size conglomerate underlain by a conspicuous assemblage of *Thalassinoides* and *Gyrolithes* burrows. c, d) Close-up views of a granule-size *Thalassinoides*-*Gyrolithes*-burrowed conglomerate beds. Note that subjacent silty strata are cut by a dense network of burrows that emanate from their bases and are passively filled with coarser-grained sediments from the immediately overlying event deposits. From Di Celma et al. (2018).

Sediments of the *Ct1a* facies association underlie and, locally, landward interfinger (from southwest to northeast) with a 20 m-thick lithosome of mixed siliciclastic-carbonate deposits (*Ct1b* facies association) showing a conspicuous SW-directed progradational pattern. Field mapping demonstrates that the *Ct1b* prograding wedge is internally composite, consisting of a multilateral stack of clinobed packages. Clinoform height attains 15-20 m and maximum declivity ranges between 15° and 20°. Individual clinobeds are between 0.2 and 0.5 m thick and are composed of coarse grained, well-sorted, skeletal-rich grainstones mixed with various amounts of granule- and small pebble sized terrigenous components (compositional mixing sensu Chiarella et al. 2017) (Fig. 6.4d). The carbonate grain association is heterozoan (sensu James 1997) and skeletal components include abundant barnacles and mollusks (Fig.6.4e, f); subordinate components are echinoids, calcareous tubes, and small benthic foraminifera. All shells show a high degree of fragmentation and disarticulation and variably abraded shapes, indicative of transport. The lower boundary of the *Ct1b* clinoformed deposit is a downlap surface characterized by a sharp and undulated lithologic contact with underlying sediments of the *Ct1a* facies association (Fig. 6.4g, h).

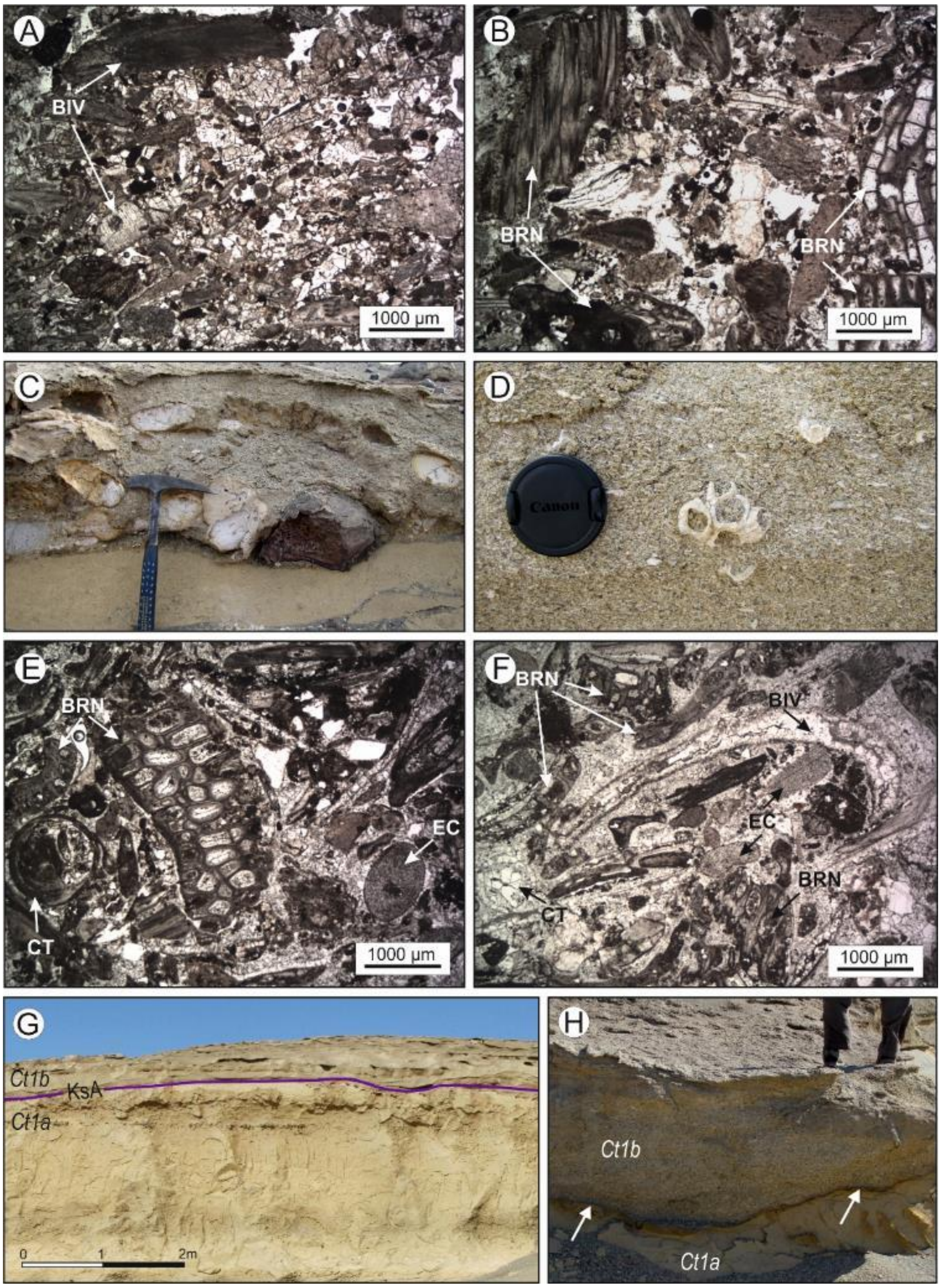

Figure 6.4. a, b) Thin-section photomicrographs of a coarse-grained bed within Ct1a showing barnacles (BRN) and bivalves (BIV). c) The conglomerates in *Ct1a* include rounded to sub-rounded, pebble- to cobble-sized clasts derived from the pre-Cenozoic basement units admixed with distinctive white-weathering, well-rounded clasts of an ash-flow tuff. Clasts are chaotically oriented and have a clast-supported texture with a skeletal-rich carbonate matrix indicating deposition by a gravity flow. A 30-cm-long rock hammer for scale. d) A striking feature of the *Ct1b* mixed siliciclastic-carbonate deposits is their extreme coarseness, and the highly fragmental nature of their

constituent particles. Macroscopically, they comprise a mixture of densely packed, gravel- and sand-sized skeletal detritus and terrigenous grains. Lens cap 6.5 cm in diameter. e, f) Thin-section photomicrographs of grain-supported fabrics in the lower portion of the Ct1b clinoforms composed of significant amounts of disaggregated barnacle plates (BRN) and bivalves (BIV), with echinoids (EC), calcareous tubes (CT) and benthic foraminifera being of secondary importance. g, h) Panoramic and close up views of the undulated erosional contact marked by a sharp break in grain size between coarse-grained grainstones (transition slope deposits, *Ct1b*) above and finer-grained sandy siltstones (offshore deposits, *Ct1a*) below. Corrected from Di Celma et al. (2018).

The general stratigraphic architecture and skeletal composition of the *Ct1b* clinobedded lithosome described here reflect the outwards dispersal of carbonate sediment and bear striking similarities with seaward-prograding heterozoan carbonate wedges documented by Pomar and Tropeano (2001) and Massari and D'Alessandro (2012). According to these interpretations, they are thought to represent entirely submerged calcarenitic wedges (infralittoral prograding carbonate wedge, IPCW) having a storm-wavegraded profile and representing the progradation of distally steepened ramps dominated by physical accommodation in the sense of Pomar and Kendall (2008) (Fig. 6.5).

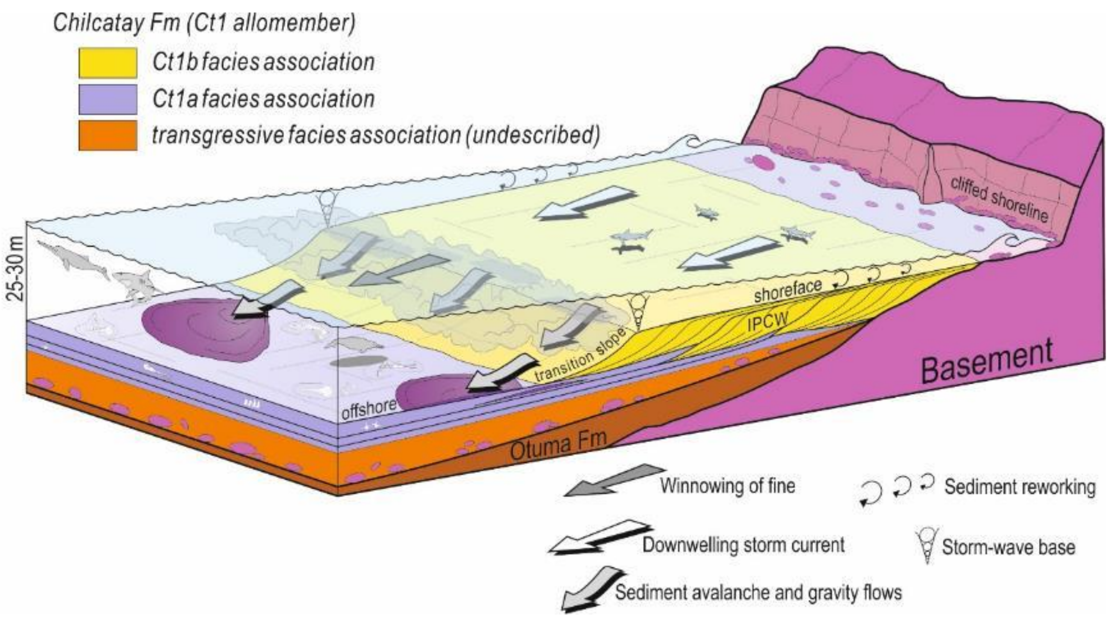

Figure 6.5. Block diagram (not to scale) illustrating interpreted depositional setting and relative positions of facies associations identified in the present study for the Ct1

allomember of the Chilcatay Formation at Ullujaya (modified from Pomar & Tropeano 2001). Along the basin margin, extensive outcrops of basement rocks and residual gravels were sites of active skeletal production, providing the rugged, rocky substrates, and coarsely particulate bottoms preferred by most sedentary benthic organisms, such as barnacles and epifaunal bivalves (mostly ostreids and pectinids). Excess skeletal material produced by the shallow-water carbonate factory was intensely reworked and winnowed out by storm-induced waves and downwelling currents and dislodged basinwards to be either deposited along the clinoform slope (transition slope) on the front of the infralittoral prograding carbonate wedge (IPCW) by avalanches processes or dispersed over the surrounding offshore settings by suspension fallout and density flows.

The formation of this type of seaward-prograding heterozoan carbonate wedge in the Chilcatay of Ullujaya was facilitated by: (i) the presence of a hard substrate (basement) that led to the development of a hard-substrate carbonate factory; (ii) stationary sea-level or sea-level decreasing, which limited the accommodation space and allowed the seaward sediment distribution and the formation of clinoforms; (iii) limited terrigenous supply.
In this context, it is inferred that clinoform progradation resulted from intermittent transport of intensely reworked and winnowed coarse-grained skeletal hash and lithogenic particles from a shallow-marine carbonate factory, which was dominated by heterozoan skeletal components, onto a depositional frontal slope below the base level of storm waves (transition-slope setting of Pomar & Tropeano 2001). Proximal to distal transport and dispersion of skeletal debris were especially active during storms by downwelling currents transforming into gravity flows at the clinoformed slope margin (Massari & Chiocci 2006). At the same time, the finer sized particles were selectively swept away (winnowed) from the high-energy top of the prograding ramp and bypassed the clinoform slope as part of the suspended load to be deposited farther downdip, into a deeper inner shelf environment. The contemporary shallow-marine carbonate factory must have been situated towards the northeast, but is no longer preserved or exposed, leaving the prograding skeletal carbonate sediments as the only evidence for its existence. Basinward, these clinoformed grainstones downlap onto and interfinger with the vertebrate fossil-bearing sediments of the Ct1a facies association. Given their downdip position with respect to the progradational carbonate wedge, the Ct1a facies association

is considered to represent deposition by suspension fallout of shoreface-derived fine-grained material in an offshore depositional setting. The sharp-based sandstone and granule- to cobble-sized conglomerate beds interbedded into these fine-grained background sediments clearly reflect periodic high-energy events in otherwise quiet marine offshore settings. Accordingly, they are interpreted as event beds resulting from storm induced, offshore-directed density currents transporting coarse-grained shoreface sediments beyond the toe of the transition slope.

The exclusive nature of distally steepened ramp such as the *Ct1b* facies in Ullujaya is due to the paleo-climatic difference between the time of deposition of the Chilcatay and the Pisco formations, the low preservation potential of the regressive deposits, and the local nature of this kind of deposits.

6.2. Ct2 allomember

The calcarenitic wedge of the Ct1 allomember is unconformably overlain by a 10.5 m-thick, fining upward unit that is virtually devoid of vertebrate fossils and is composed of basal sandstones (*Ct2a* facies association) gradually overlain by massive siltstones (*Ct2b* facies association).

The basal surface of the Ct2 allomember (CE0.2) is typically penetrated by small *Thalassinoides* burrows crossing the topmost portion of the underlying clinobedded wedge. The overlying *Ct2a* facies association is about 3.5 m thick and consists of medium- to fine-grained, massive or weakly bedded, thoroughly bioturbated sandstones (Fig. 6.3a). A thin pavement of small oysters and rare basement derived pebble- and boulder-size clasts occurs at the base. Sediments are dominated by siliciclastic materials. The *Ct2a* facies association grades upward into massive siltstones interbedded with dolomitized mudstone horizons and discrete volcanic ash layers, forming the *Ct2b* facies association. The siltstones are predominantly rich in carbonate microfossils (calcareous nannofossil and planktonic foraminifera) but become rich in siliceous microfossils (diatoms and silicoflagellates) in the upper portion.

The upward-fining pattern of the Ct2 allomember suggests an overall retrogradational (deepening-upwards) depositional trend with the basal *Ct2a* sandstones representing shoreface paleoenvironments and the finer-grained, tuffaceous, calcareous and diatomaceous *Ct2b* siltstones representing offshore paleoenvironments. The basement-derived pebble- and boulder-size clasts were probably introduced into the basin during periods of lowered sea level and imply a period of subaerial emergence prior to transgressive reworking. Accordingly, the basal CE0.2 bounding surface marks the turnaround from regression at the top of Ct1 to transgression at the base of Ct2 and is considered to represent a transgressively modified subaerial unconformity. The bioturbated nature of CE0.2 and its association with a basal oyster-bearing shelly horizon and lag gravel indicate that erosional scouring and shell concentration took place during a period of low or arrested deposition (e.g. Carnevale et al. 2011; Kidwell 1991; Kondo et al. 1998).

6.3. Overall composition of the fossil vertebrate assemblage

The vertebrate fossil assemblage of the *Ct1a* includes bony vertebrates and chondrichthyan teeth. Eighty-two marine vertebrate specimens are preserved as bony elements. Remains of Cetacea dominate this assemblage, accounting for 86.6% of the specimens, with a large number of indeterminate

specimens (56.1%). All specimens identifiable to suborder level belong to Odontoceti and no baleen whale (Mysticeti) is recorded so far.

Odontocete remains belong to Kentriodontidae (19.6%; early relatives of today's true dolphins and porpoises), Squalodelphinidae (6.1%; a family closely related to the extant South Asian river dolphin), Physeteroidea (2.4%; sperm whales), and to the genus *Chilcacetus* (2.4%; an extinct lineage of homodont, long-snouted dolphins) (Fig. 6.6). Kentriodontids belong to an undescribed species within the genus *Kentriodon* Kellogg, 1927. This kentriodontid is the most common cetacean taxon at Ullujaya, being known by several crania, some of which are associated with mandibles and partial postcranial. Seven of these crania (MUSM 586, 631, 1393, 1397, 1398, and 2431) have been collected and are now under study. Squalodelphinid remains include: 1) two specimens of *Huaridelphis raimondii* (the holotype MUSM 1396, consisting of an isolated cranium, and the referred specimen MUSM 1403, a cranium, fragmentary mandible and some associated postcranial bones) (Lambert et al. 2014); 2) a well-preserved specimen attributed to *Notocetus vanbenedeni* (MUSM 1395, consisting of a cranium with an associated cervical vertebra) (Bianucci et al. 2015); and 3) two indeterminate specimens consisting of a disarticulated partial skeleton (MUSM 1484) and an isolated tympanic bulla (MUSM 1485). Physeteroids consist of two isolated crania: 1) MUSM 3246, referred to cf. *Diaphorocetus* sp., sharing some affinities with *Diaphorocetus poucheti* from the lower Miocene Monte León Formation of Argentina; and 2) one badly damaged specimen previously regarded as an indeterminate mysticete (Lambert et al. 2014; Bianucci et al. 2015) but now confidently identified as a sperm whale (Physeteroidea indet.). Finally, the long-snouted archaic odontocete *Chilcacetus cavirhinus* is represented by two partial skeletons: 1) MUSM 1401, described by Lambert et al. (2015); and 2) MUSM 2527, currently under study.

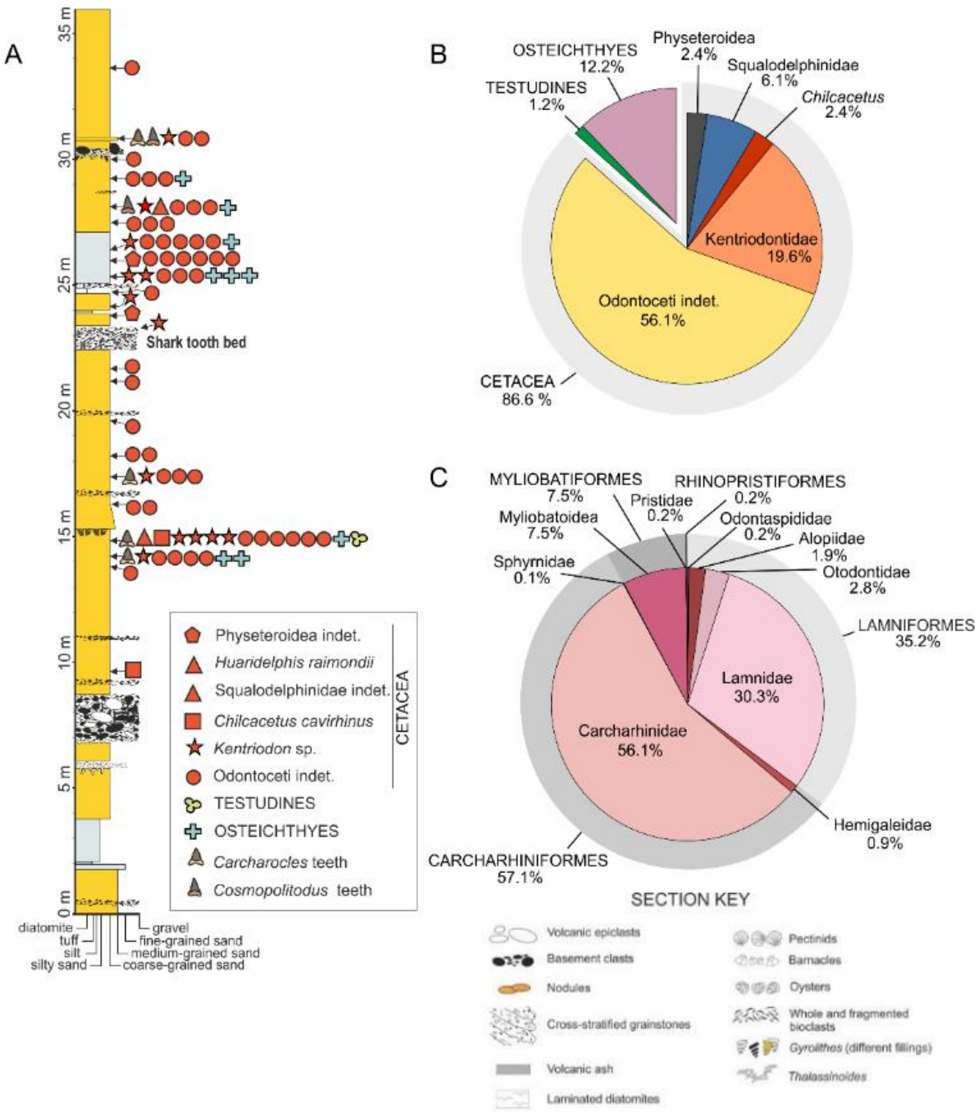

Figure 6.6. a) Stratigraphic distribution of fossil vertebrates from *Ct1a* of the Chilcatay Formation exposed at Ullujaya. b) Quantitative composition of the fossil vertebrate assemblage of *Ct1a,* based on systematic surface prospecting (teeth and spines of Elasmobranchii are not considered). c) Quantitative composition of the fossil shark and ray assemblage from the *Ct1a* facies association, based on more than one thousand isolated teeth and spines. From Bianucci et al. (2018).

More than one thousand isolated elasmobranch teeth and spines, representative of at least nine families and sixteen different species, have been collected (Fig. 6.7). These remains belong to the following four orders: i) Carcharhiniformes (57.1% of the specimen), Lamniformes (35.2%), Myliobatiformes (7.5%), and Rhinopristiformes (0.2%) (Fig. 6.6). Carcharhiniformes are represented by seven species (*Carcharhinus brachyurus*, *Carcharhinus* cf. *leucas*, *Galeocerdo aduncus*, *Hemipristis serra*, *Negaprion brevirostris*, *Physogaleus contortus*, and *Sphyrna zygaena*), Lamniformes by seven (*Alopias superciliosus*, *Anotodus agassizii*, *Carcharias* sp., *Carcharocles chubutensis*, *Cosmopolitodus hastalis*, *Isurus oxyrinchus*, and *Megalolamna paradoxodon*), Myliobatiformes by one or more (Myliobatoidea indet.), and Rhinopristiformes by one (*Anoxypristis* sp.). Almost half of the elasmobranch remains consist of teeth of *C. brachyurus* (49.4%); teeth of *C. hastalis* (22.2%) and *I. oxyrhincus* (8.1%) follow in order of decreasing abundance.

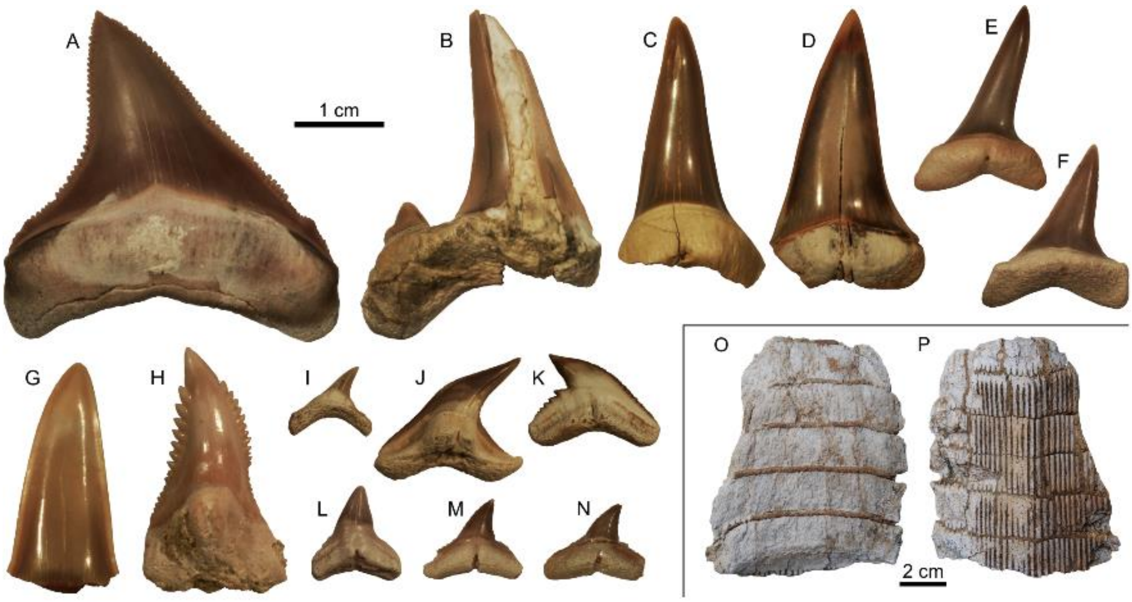

Figure 6.7. Elasmobranch remains from *Ct1a* of the Chilcatay Formation exposed at Ullujaya. A) *Carcharocles chubutensis*. B) *Megalolamna paradoxodon*. C–D) *Cosmopolitodus hastalis*. E–F) *Isurus oxyrinchus*. G) *Anotodus agassizii*. H) *Hemipristis serra*. I) *Alopias superciliosus*. J) *Physogaleus contortus*. K) *Galeocerdo aduncus*. L) *Carcharhinus* cf. *leucas*. M–N) *Carcharhinus brachyurus*. O–P) cf. *Myliobatis* sp. A–N) Lingual view. O) Occlusal view. P) Basal view. From Bianucci et al. (2018).

Bony fish are represented by an indeterminate cranium, some very fragmentary tuna-like skeletons, and the partial postcranial of a large istiophorid billfish tentatively referred to aff. *Makaira* sp. Similarly to the Pisco Formation (Collareta et al. 2015; Di Celma et al. 2017), cycloid scales consistent with those of the extant Pacific pilchard *Sardinops* are rather common in *Ct1a*. Other marine vertebrates include a large dermochelyid marine turtle, represented by a single specimen consisting of some postcranial bones.

6.4. Distribution of the fossil vertebrates

Most of the fossils of vertebrates of Ullujaya come from a 1 km^2-surface area where the *Ct1a* is exposed (Fig. 6.8); in turn, based on our field observations, both *Ct1b* and the Ct2 allomember of the Chilcatay Formation exposed in the study area seem devoid of vertebrate specimens preserved as bony elements. Vertebrate fossils have been found between 9.7 and 33.5 m abs, representing a significant portion of the 35 m-thick *Ct1a* (Fig. 6.6). Seventy-four specimens (97% of those with a stratigraphical collocation) are restricted in a 16.9 m-thick interval of sediments (13.9 to 30.8 m abs). The largest concentrations of fossil vertebrate remains are found between 14 and 15 m abs (22 specimens, 29% of the total) and from 25 to 31 m abs (36 specimens, 51%). The large majority of the chondrichthyan specimens was collected from a single fossiliferous interval located about 23 m abs, whereas a few additional remains (mostly referable to *Cosmopolitodus* and *Carcharocles*) come from different horizons within *Ct1a*. Bony fish are homogeneously distributed between 14.2 m and 29.2 m abs, whereas the dermochelyid turtle specimen was found 14.8 m abs.

6.5. Geological map and section

The combination of a high-resolution geological and stratigraphic study with the prospection and mapping of fossil vertebrates allowed the placement of all the fossils on a geological map (Fig. 6.8), and along a temporally constrained measured section (Fig. 6.9), providing an accurate spatial and temporal context to this fossil-bearing site and the individual fossil findings.

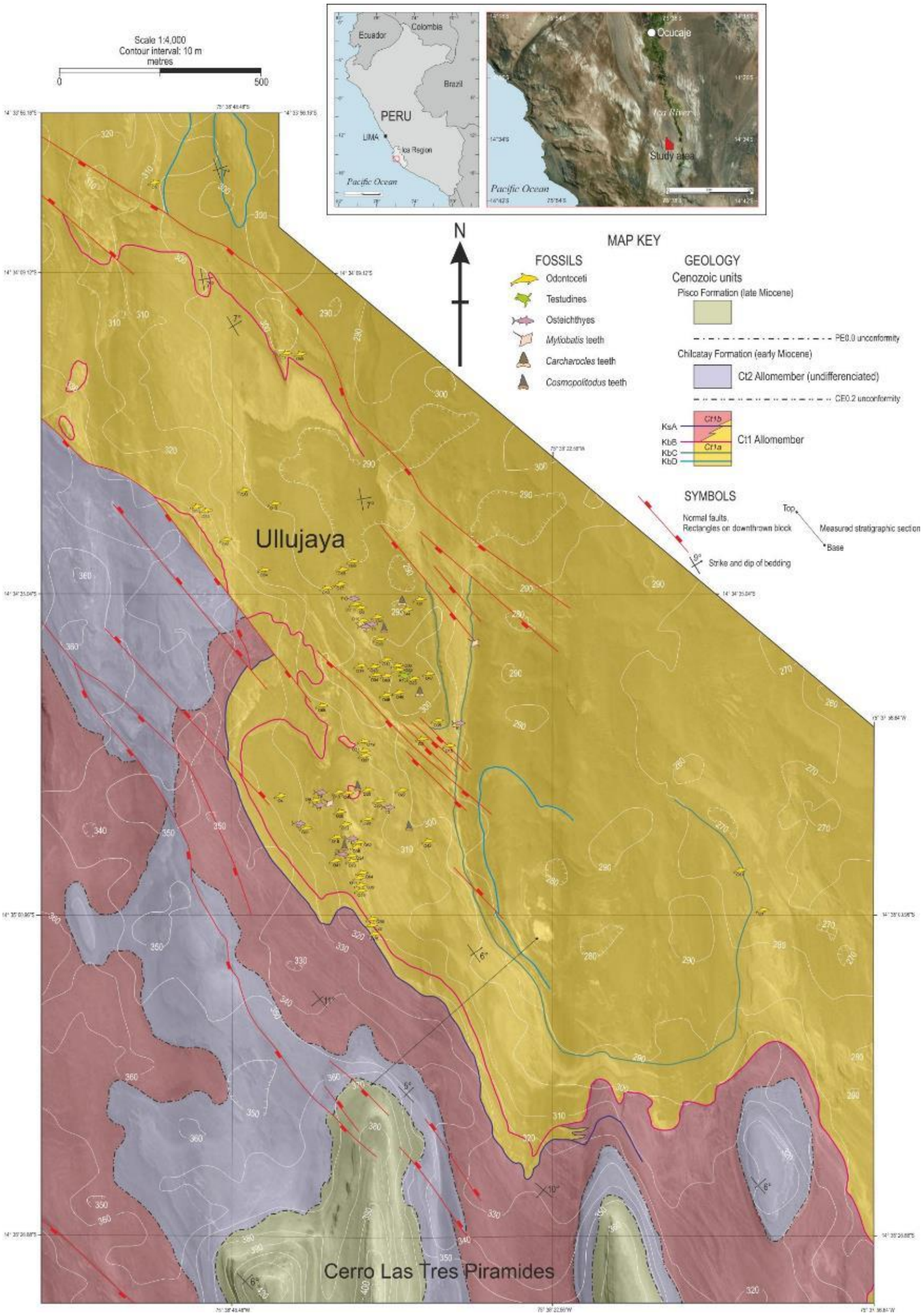

Figure 6.8. Geological map of Ullujaya and fossil spatial distribution. Modified from Di Celma et al. (2018).

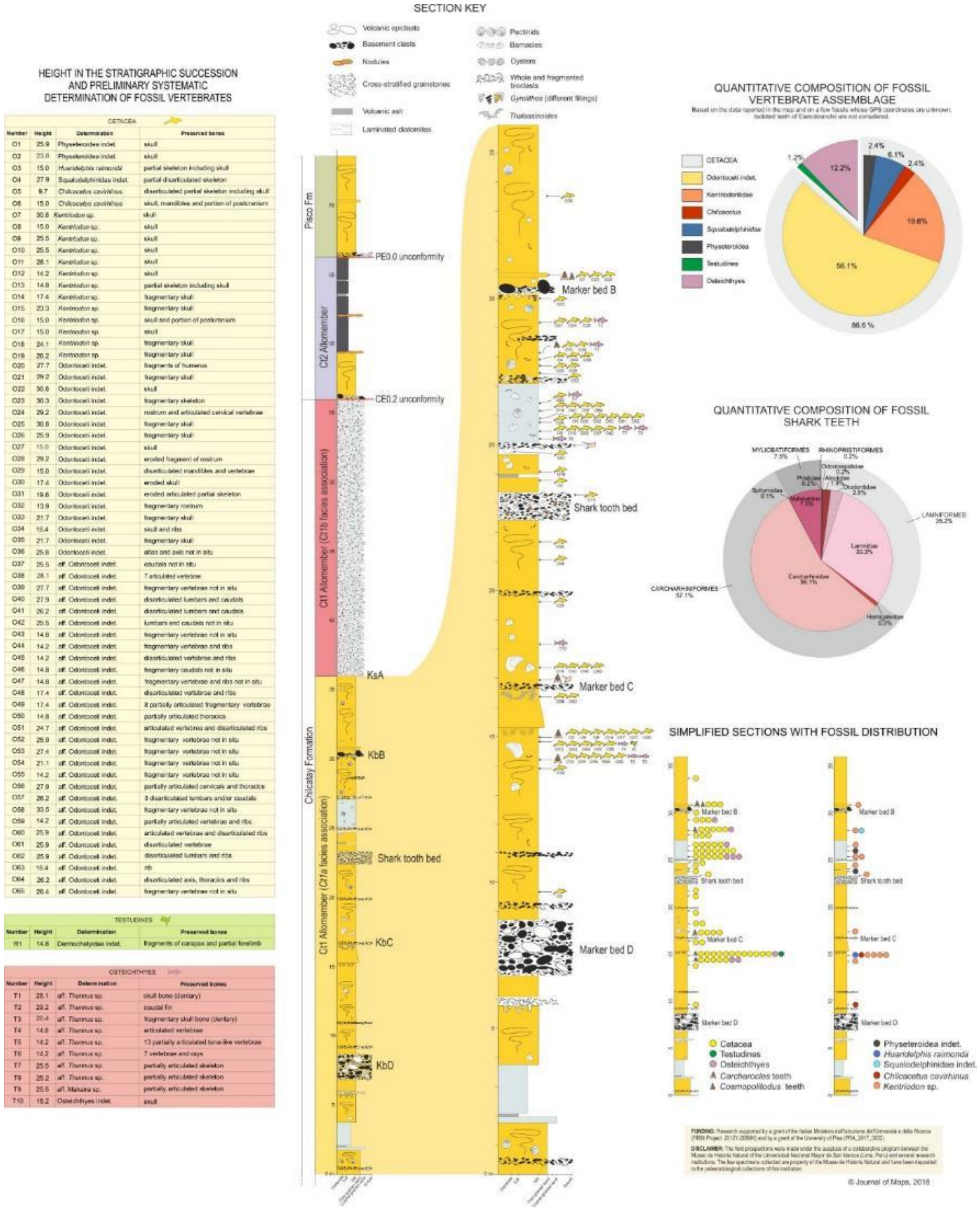

Figure 6.9. Stratigraphic measured section and fossil vertical (temporal) distribution. Modified from Di Celma et al. (2018).

6.6. Reconstruction of the depositional environment

Facies architecture, bedding patterns, and skeletal composition of the *Ct1b* clinoforms described here bear striking similarities with seaward-prograding mixed siliciclastic-carbonate wedges documented by Pomar and Tropeano (2001) and Massari and

D'Alessandro (2012) and reflect the outwards dispersal of sediment in concert with the skeletal production rate and the available physical accommodation space (sensu Pomar & Kendall 2008). According to these interpretations, *Ct1b* represents an entirely Submerged Infralittoral Prograding Wedge (ILPW; Hernández-Molina et al. 2000; Pomar et al. 2015), characterized by a storm-wave-graded profile, located at shoreface depth between the fair-weather and storm wave base, and distinctive clinoform foresets (Fig. 6.10).

In this setting, high wave-current shear-stress in shoreface environment ensures that topsets of subaqueous clinoforms are regions of dominant sediment bypass through lateral advection, erosion, and redistribution. Accordingly, it is inferred that coarse-grained skeletal hash derived from a shallow-water carbonate factory inboard of the clinoform break-points was occasionally transported seawards and deposited on the sloping front of the ILPW separating the shoreface and the offshore (transition-slope setting of Pomar & Tropeano 2001), leading to the formation of the clinoform foresets.

Downdip transport and dispersion of skeletal debris were especially active during storms by downwelling currents transforming into gravity flows at the clinoformed slope margin (Massari & Chiocci 2006). At the same time, the winnowed-out fine-grained material actively bypassed the ILPW as part of the suspended load and was deposited farther downdip, into a deeper inner shelf environment.

Basinward, these clinoformed skeletal-rich sediments interfinger with and downlap onto the vertebrate fossil-bearing siltstones and fine-grained sandstones of *Ct1a*. Given its downdip position with respect to the ILPW, Ct1a is considered to represent deposition by suspension fallout of shoreface-derived fine-grained material. The sharp-based, granule- to cobble-sized conglomerate beds interbedded into these fine-grained background sediments clearly reflect periodic high-energy events in otherwise quite marine offshore settings. Accordingly, they are interpreted as event beds resulting from tsunami backflows or storm-induced, offshore-directed density underflows transporting coarse-grained shoreface sediments beyond the toe of the transition slope.

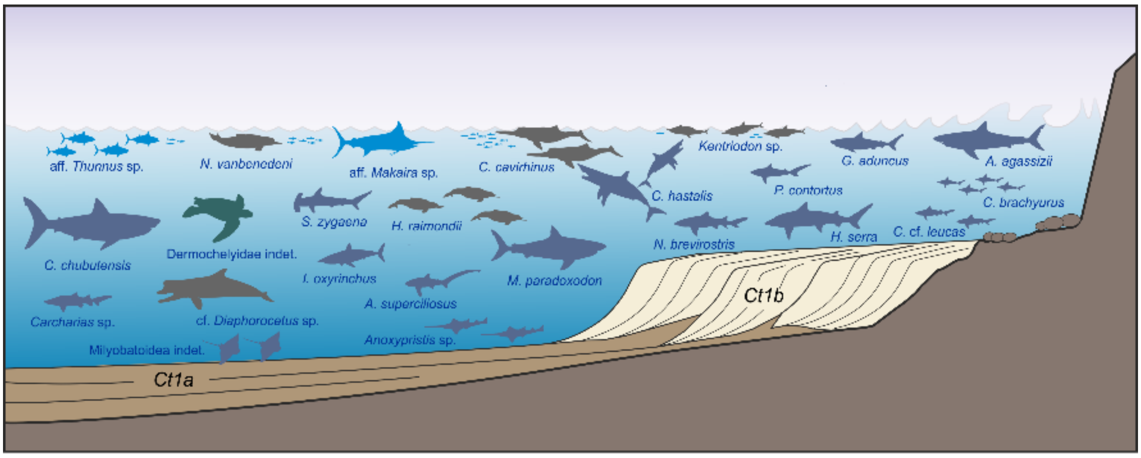

Figure 6.10. Stylized reconstruction of the early Miocene marine vertebrate fauna of Ullujaya during deposition of *Ct1a*, highlighting the diversity of the assemblage described in the present work. Different species are shown as silhouettes, and are roughly to scale. Sediments belonging to *Ct1a* and *Ct1b* are cream and brown, respectively. From Bianucci et al. (2018).

The exclusive association of discrete burrowed intervals with gravity-flow event beds intercalated in otherwise poorly bioturbated sediments and the restriction of burrow assemblages to *Thalassinoides* and *Gyrolithes* ichnogenera suggest a genetic relationship between bioturbation by decapod crustaceans and gravity flow deposition. As such, the *Thalassinoides*-*Gyrolithes*-burrowed intervals documented within *Ct1a* resemble the "doomed pioneers trace fossil assemblages" documented by Föllmi and Grimm (1990).

The record of silicoflagellates from Ullujaya helps in further refining our reconstruction of the depositional environment. The silicoflagellate assemblage from Ct1a features the temperate genus *Distephanopsis*, the warm-water genera *Corbisema* and *Naviculopsis*, and the cold-water genus *Stephanocha*. This assemblage is best interpretable as witnessing warm-temperate thermal conditions.

Finally, an approximate estimation of the paleobathymetry recorded by the toe of the slope at the transition between *Ct1a* and *Ct1b* can be obtained by summing up the depth of the break points of the clinobedded units and the thickness of the clinobeds (15-20m in *Ct1b*). The outer edge of the infralittoral wedge is naturally dependent on many different environmental factors, of which the wave climate, fetch, grain size, and general oceanographic conditions are among the most important (Mitchell et al. 2012). In the Mediterranean area, both Hernández-Molina et al. (2000) and Massari and Chiocci (2006) have found the outer edges of the breakpoints of the clinobedded units located at water depths of about 15-20 m. Due to the protected paleogeography displayed by the East Pisco Basin, the hydrodynamic conditions during deposition of the Chilcatay Formation would have been remarkably less energetic from those dictating the development of modern non-tropical skeletal carbonate sediments in oceanic settings exposed to vigorous storm-waves and probably resulted in the formation of prograding wedges at relatively shallower water depths. As a consequence, by assuming a water depth of the outer edge of the infralittoral wedge similar to that documented in the Mediterranean area, an offshore depositional setting at least 30-40 m below the sea level can be interpreted for *Ct1a* at the toe of the slope.

The bioturbated nature of the lower boundary of the Ct2 allomember and its association with a basal oyster-bearing shelly horizon and a mixture of extrabasinal pebble- to boulder-size clasts, indicate that erosional scouring and shell concentration took place during a period of sea-level fall followed by transgression (e.g., Kidwell 1991; Abbott 1998; Carnevale et al. 2011).

This chapter on the Chilcatay stratigraphy and paleoecology is the union of two published papers. The one about stratigraphy is "Facies analysis, stratigraphy and marine vertebrate assemblage of the lower Miocene Chilcatay Formation at Ullujaya (Pisco basin, Peru)" authored by Claudio Di Celma, Elisa Malinverno, Alberto Collareta, Giulia Bosio, Karen Gariboldi, Olivier Lambert, Walter Landini, Pietro Paolo Pierantoni, Anna Gioncada, Igor Maria Villa, Giovanni Coletti, Christian de Muizon, Mario Urbina and Giovanni Bianucci and published in 2018 by Journal of Maps, Vol. 14:2, 257-268. In this paper, Giulia Bosio contributes to sample collection, measurement of the stratigraphic section and field mapping, sample preparation and analyses, and isotope geochronology.

The one about paleoecology is "Taphonomy and palaeoecology of the lower Miocene marine vertebrate assemblage of Ullujaya (Chilcatay Formation, East Pisco Basin, southern Peru)" authored by Giovanni Bianucci, Alberto Collareta, Giulia Bosio, Walter Landini, Karen Gariboldi, Anna Gioncada, Olivier Lambert, Elisa Malinverno, Christian de Muizon, Rafael Varas-Malca, Igor Maria Villa, Giovanni Coletti, Mario Urbina and Claudio Di Celma, published in 2018 on Palaeogeography, Palaeoclimatology, *Palaeoecology, vol. 511, 256-279. In this paper, Giulia Bosio contributes to sample collection, measurement of the stratigraphic section and field mapping, optical microscope analyses on sediments, ex-pyrite framboid measurement, vertebrate taphonomy and microscopic analyses on bones, discussion on the paleoenvironment reconstruction and taphonomy.*

Chapter References

Abbott, S.T. 1998. Transgressive systems tract and onlap shellbeds from mid-Pleistocene sequences, Wanganui Basin, New Zealand. Journal of Sedimentary Research, 68, 253-268.

Bianucci, G., Urbina, M., Lambert, O. 2015. A new record of Notocetus vanbenedeni (Squalodelphinidae, Odontoceti, Cetacea) from the early Miocene of Peru. Comptes Rendus Palevol, 14, 5-13.

Carnevale, G., Landini, W., Ragaini, L., Di Celma, C., Cantalamessa, G. 2011. Taphonomic and paleoecological analyses (mollusks and fishes) of the Sua member condensed shellbed, Upper Onzole Formation (early Pliocene, Ecuador). PALAIOS, 26, 160-172.

Chiarella, D., Longhitano, S. G., Tropeano, M. 2017. Types of mixing and heterogeneities in siliciclastic-carbonate sediments. Marine and Petroleum Geology, 88, 617-627.

Collareta, A., Landini, W., Lambert, O., Post, K., Tinelli, C., Di Celma, C., Panetta, D., Tripodi, M., Salvadori, P.A., Caramella, D., Marchi, D., Urbina, M., Bianucci, G. 2015. Piscivory in a Miocene Cetotheriidae: first record of fossilized stomach content for an extinct baleen-bearing whale. The Science of Nature, 102, 70.

DeVries, T.J., Jud, N.A. 2018. Lithofacies patterns and paleogeography of the Miocene Chilcatay and lower Pisco depositional sequences (East Pisco Basin, Peru). Boletín de la Sociedad Geológica del Perú, Volumen Jubilar 8, 124-167.

Di Celma, C., Malinverno, E., Bosio, G., Collareta, A., Gariboldi, K., Gioncada, A., Molli, G., Basso, D., Varas-Malca, R.M., Pierantoni, P.P., Villa, I.M., Lambert, O., Landini, W., Sarti, G., Cantalamessa, G., Urbina, M., Bianucci, G. 2017. Sequence stratigraphy and paleontology of the upper Miocene Pisco Formation along the western side of the lower Ica valley (Ica Desert, Peru). Rivista Italiana di Paleontologia e Stratigrafia (Research In Paleontology and Stratigraphy), 123, 255-274.

Föllmi, K.B., Grimm, K.A. 1990. Doomed pioneers: gravity-flow deposition and bioturbation in marine dysaerobic environments. Geology, 18, 1069-1072.

Hernández-Molina, F.J., Fernández-Salas, L.M., Lobo, F., Somoza, L., Díaz-del-Río, V., Alverinho Dias, J.M. 2000. The infralittoral prograding wedge: a new large-scale progradational sedimentary body in shallow marine environments. Geo-Marine Letters, 20, 109-117.

Ibaraki, M. 1993. Eocene to early Miocene planktonic foraminifera from the south of Paracas, central Peru. Shizuoka University, Report of the Faculty of Sciences, 27, 77-93.

James, N.P. 1997. The cool-water carbonate depositional realm. In N.P. James & J.A.D. Clarke (Eds.), Coolwater carbonates. Tulsa: SEPM, Special Publication, 56, 1-20.

Kellogg, R. 1927. Kentriodon pernix, a Miocene porpoise from Maryland. In: Proceedings of the United States National Museum, 69, 1-55.

Kidwell, S.M. 1991. Condensed deposits in siliciclastic sequences: Expected and observed features. In: G. Einsele, W. Ricken & A. Seilacher (Eds.), Cycles and events in stratigraphy, 682-695. Heidelberg: Springer-Verlag.

Kondo, Y., Abbott, S.T., Kitamura, A., Kamp, P.J.J., Naish, T.R., Kamataki, T., Saul, G.S. 1998. The relationship between shellbed type and sequence architecture: Examples from Japan and New Zealand. Sedimentary Geology, 122, 109-127.

Lambert, O., Bianucci, G., Urbina, M. 2014. Huaridelphis raimondii, a new early Miocene Squalodelphinidae (Cetacea, odontoceti) from the Chilcatay Formation, Peru. Journal of Vertebrate Paleontology, 34, 987-1004.

Lambert, O., de Muizon, C., Bianucci, G. 2015. A new archaic homodont toothed cetacean (Mammalia, Cetacea, Odontoceti) from the early Miocene of Peru. Geodiversitas, 37, 79-108.

Massari, F., Chiocci, F. 2006. Biocalcarenite and mixed cool-water prograding bodies of the Mediterranean Pliocene and Pleistocene: architecture, depositional setting and forcing factors. In H.M. Pedley & G. Carannante (Eds.), Cool-water carbonates: Depositional systems and palaeoenvironmental controls, 95-120. London: Geological Society, Special Publications, 255.

Massari, F., D’Alessandro, A. 2012. Facies partitioning and sequence stratigraphy of a mixed siliciclastic-carbonate ramp stack in the Gelasian of Sicily (S Italy): A potential model for icehouse, distally-steepened heterozoan ramps. Rivista Italiana di Paleontologia e Stratigrafia (Research In Paleontology and Stratigraphy), 118, 503-534.

Mitchell, N.C., Masselink, G., Huthnance, J.M., Fernández-Salas, L.M., Lobo, F.J. 2012. Depths of modern coastal sand clinoforms. Journal of Sedimentary Research, 82, 469-481.

Pomar, L., Kendall, C.G.S.C. 2008. Architecture of carbonate platforms: A response to hydrodynamics and evolving ecology. In: J. Lukasik & A. Simo (Eds.), Controls on carbonate platform and reef development, 187-216. SEPM, Special Publication, 89.

Pomar, L., Tropeano, M. 2001. The Calcarenite di Gravina Formation in Matera (southern Italy): New insights for coarse-grained, large scale, cross-bedded bodies encased in offshore deposits. American Association of Petroleum Geologists Bulletin, 85, 661-689.

Pomar, L., Aurell, M., Bádenas, B., Morsilli, M., Al-Awwad, S.F. 2015. Depositional model for a prograding oolitic wedge, Upper Jurassic, Iberian basin. Marine and Petroleum Geology, 67, 556-582.

Chapter 7. Chronostratigraphy of the Chilcatay Formation in the western side of the Ica River

7.1. Chilcatay microfossils biostratigraphy

Planktonic microfossils were studied from the samples collected along the measured section at Ullujaya locality and in the nearby area of Cerro Yasera de Amara. Microfossils are very rare in these sediments, dominated by terrigenous silt and carbonate fragments of macroinvertebrates. Anyway, in some samples they were found. It is important to highlight that: (i) ages of the considered diatom bioevents are based on Equatorial Pacific diatom biostratigraphy and may therefore not be fully representative of first and last occurrences at the Pisco Basin latitudes; (ii) ages of the considered silicoflagellate biozones have not been calibrated but correlated with nannofossil biozones.

For the *Ct1a* facies association, diatoms include rare occurrences of *Rhaphidodiscus marylandicus* and *Triceratium pileus*, the latter constrained between 18.27 and 17.35 Ma (Expedition 320/321 Scientists 2010) or between 18.06 and 17.89 (Barron 2005). Rare occurrences of a form of *Coscinodiscus rhombicus*, possibly a transitional form to *C. lewisianus*, point to an age close to its last occurrence, dated at 18.44 Ma (Expedition 320/321 Scientists 2010). Following diatom stratigraphy, samples from the *Ct1a* facies association are therefore assigned to the *Craspedodiscus elegans* zone (Expedition 320/321 Scientists 2010), see Table 7.1. Silicoflagellates and diatoms only occur in six samples collected at 24-27 m from the base of the section. Overall, silicoflagellates are rare but represented by a varied assemblage, assigning the samples to the upper part of the *Naviculopsis ponticula* zone (Bukry 1981, 1985; Perch-Nielsen 1985) (see Table 7.1), which was dated at 18-19 Ma by correlation with calcareous nannofossil NN3 biozone (Bukry 1982). Among nannofossils, rare occurrences of *Discoaster druggi* support this age assignment.

These ages are consistent with those provided by DeVries (1998). At Roca Negra, a locality about 7 km south of Ullujaya, recent investigations (Lambert et al. 2017) have documented the occurrence of a biostratigraphically informative silicoflagellate assemblage from the basal portion of the Chilcatay Formation. This assemblage, assigned to the *Naviculopsis ponticula* zone of Bukry (1981), contains species that are typical of the lower part of this biozone, thus implying a slightly older age then the strata outcropping in our study area. This new early Miocene age assignment for the base of the Chilcatay Formation is not in conflict with the late Oligocene age provided by DeVries and Jud (2018). From a basin-wide perspective, indeed, this chronostratigraphic reconstruction implies a time-transgressive nature of the formation boundary throughout the region, ranging from late Oligocene to early Miocene, when the maximum flooding of the shelf basin was reached. Accordingly, due to the diachronous character of the basal boundary and the marginal position of the study area along the eastern, internal flank of the basin, the base of the Chilcatay strata exposed at Ullujaya can be significantly younger than in other parts of the basin.

		Diatoms					Silicoflagellates								Calcareous nannofossils											Biozones		
		Coscinodiscus lewisianus var. *similis* (17.8 - 15.35 Ma)***	*Coscinoduscus rhombicus* (28.17-18.44)***	*Delphineis lineata* (19-14.5)**	*Rhaphidodiscus marylandicus* (? - 16.49 Ma)***	*Triceratium pileus* (18.27 - 17.35 Ma)*** (19.29-17.89)*	*Corbisema triacantha* s.l. (Late Eocene - ~11.5 Ma)°	*Distephanopsis crux* var. *parva* (~19 - ~7 Ma)°	*D. crux* var. *scutulata* (~19 - ~ 11.5 Ma)°	*N. obtusarca* (~23 - ~ 18 Ma)°	*N. ponticula* subsp. *ponticula* (~19 - ~ 18 Ma)°	*N. ponticula* subsp. *spinosa* (~19 - ~ 18 Ma)°	*S. speculum* var. *speculum* (Oligocene-present)	*S. speculum* var. *triommata* (~19 - ~ 11.5 Ma)°	*Coccolithus pelagicus* (45.4-0 Ma)@	*Cyclicargolithus floridanus* (46.29-12.1 Ma)@	*Discoaster deflandrei* (50.50-10.89 Ma)@	*D. druggii* (22.82-17.95 Ma)@	*Helicosphaera carteri* (23.13-0 Ma)@	*H. euphratis* (37.32 - 14.91 Ma)@	*H. scissura* (19-14.91 Ma)@	*Reticulofenestra minuta* (50.50-2.59 Ma)@	*Sphenolithus belemnos* (19-18 Ma)@	*S. conicus* (23.13 - 17.95) Ma@	*S. moriformis* (61.61-8.29 Ma)@	Diatom biozones***	Silicoflagellate biozones°	Calcareous nannofossil biozones***
	SOT-7	R	R	C			C	C	C				R	R			R											
	SOT-6			R			R	R	R								R											
Ct2b	SOT-5		R	C			C	C	C				R	R			R									*T. pileus*	*C. triacantha*	
	YA23														C	C	R	R	R	R	R	C	R	R	C			NN3
	YA16														C	C	R					R			R			
	UJA-50						C	C	C	R		R		R														
	UJA-49						R					R		R														
	UJA-48						C	C	C	R		R	R	R												*C. elegans*	*N. ponticula*	
Ct1a	UJA-47		R			R																						
	UJA-46						R																					
	UJA-45				X			R																				

*Barron, 2006; **Barron et al., 2013; ***Expedition 320/321 Scientists, 2010; ° Perch-Nielsen, 1985; @Nannotax3

Table 7.1. Distribution of diatom, silicoflagellate and nannofossil marker species in the Chilcatay formation samples at Ullujaya. The two facies *Ct1a* and *Ct2b* are respectively attributed to the *C. elegans* and *T. pileus* biozones of Expedition 320/321 Scientists (2010); to the *N. ponticula* and *C. triacantha* biozones of Perch-Nielsen (1985); and to the calcareous nannofossil NN3 biozone of Bukry (1982). Therefore, the boundary between the two biozones cannot be identified for certain (dashed line). From the Supplementary Material of Di Celma et al. (2018).

The *Ct1b* and *Ct2a* facies associations are barren in microfossils. The *Ct2b* facies association indeed contains nannofossils. Apart from abundant longranging species, the calcareous nannofossil assemblage is characterized by rare occurrences of *Sphenolithus belemnos*, constraining the age of the samples to 19.01-17.96 Ma. In the upper 4 m of *Ct2b*, as measured east of Cerro Yasera de Amara, silicoflagellates show a well-preserved assemblage and the notable absence of *Naviculopsis*, indicating that the samples are located above the LO of this genus, occurring at ca. 18 Ma, and therefore are assigned to the *Corbisema triacantha* zone (see Table 7.1). Rare specimens of *Coscinodiscus lewisianus* var. *similis* occur in the uppermost sample, which would restrict the age of the sample to younger than 17.08 Ma (*C. rhombicus* here is rather a transition form to *C. lewisianus* var. *similis*). We interpret the *Ct2b* diatom association as belonging to the *T. pileus* zone (18.18-17.49 Ma) (see Table 7.1).

7.2. Chilcatay tephrochronology

In the western side of the Ica River, the exposed Chilcatay strata exposed contain very few volcanic ash layers compared to those of the Pisco Formation. Tephra layers can be easily recognized in the field. They usually have a gray to light gray color, and a thickness mainly ranging between 5 and 15 cm. Tephra usually have a normal grading and a sharp base, and phenocrysts are concentrated at the base of the layer. This reflects the deposition of subaerial fallout tephra, in which size and density sorting of particles occurs within the column, because particles of least settling velocity are carried to greater heights and spread over greater distances than those with large settling velocities (Fisher & Schmincke 1984), without any reworking by marine currents (Carey 1997). The four ash layers selected for dating had a lateral continuity, sharp boundaries, lack of sedimentary structures suggesting reworking, normal grading with accumulation of biotite phenocrysts at the base and no evidence of cements or crusts of secondary minerals.

Petrographic analyses revealed that most tephra are constituted by > 95% in volume by glass shards and a variable quantity of juvenile phenocrysts of feldspar, biotite and amphibole. EPMA analyses on glass shards show prevalently rhyolitic and dacitic compositions. Glasses show very low totals and scattered element concentrations; several samples were considered altered and excluded from further consideration.

Locality	Sample	Field observations		Grainsize				Glass morphology	Crystals	Glass chemistry (wt%)													
		Thickness (cm)	Color and notes	Folk (1954)	White and Houghton (2006)	median (phi)	sorting (phi)			mean, SD [n]	SiO_2	TiO_2	Al_2O_3	FeO^T	MnO	MgO	CaO	Na_2O	K_2O	P_2O_5	Cl	sum	A/CNK
Roca Negra	PN-T2	-	Light grey ash with visible biotite	unimodal, very poorly sorted, very fine sand	fine ash	3.0	2.1	bubble-wall shards; low vesiculated shards	bt, feldspar	mean [20]	74.90	0.15	14.39	1.17	0.07	0.13	0.61	3.52	5.03	0.02	-	92.37	1.17
										SD	0.24	0.03	0.13	0.06	0.03	0.02	0.02	0.13	0.15	0.02	-		
Ullujaya	UJA-T35	5	Yellowish ash with visible fine biotite	bimodal, very poorly sorted, very fine sand	very fine ash	4.0	2.3	shards with microlites; poorly vesiculated	bt, feldspar, other min.	mean[10]	76.55	0.01	14.75	0.11	0.00	1.35	2.32	2.12	2.76	0.03	0.02	87.97	1.39
										SD	0.89	0.01	0.65	0.13	0.01	0.37	0.22	0.53	0.32	0.07	0.04		
nearby Cerro Colorado	CHILC-AT1	10	White ash with visible biotite	unimodal, poorly sorted	very fine ash	3.4	1.9	platy shards; bubble-wall shards; low vesiculated shards	bt, feldspar, pumice	mean [20]	75.16	0.15	14.38	1.19	0.09	0.13	0.60	3.76	4.51	0.02	-	92.51	1.18
										SD	0.27	0.03	0.14	0.07	0.02	0.01	0.02	0.11	0.25	0.02	-		
Los Dos Cerritos	SOT-T3	10	Light grey ash with visible biotite	unimodal, poorly sorted	extremely fine ash	5.5	1.5	high vesiculated shards; bubble-wall shards	bt, feldspar	mean[19]	75.64	0.16	14.02	1.15	0.09	0.14	0.63	3.22	4.90	0.04	-	92.88	1.20
										SD	0.81	0.04	0.31	0.10	0.04	0.04	0.11	0.11	0.24	0.03	-		

Table 7.2. Field observations, grain-size classification, petrographic composition, EPMA analyses of glass shards of the Chilcatay dated tephra. Grain size parameters obtained with Blott & Pye (2001), Folk (1954), White and Houghton (2006).

Key for the “crystals” column: bt = biotite, sa = sanidine, pl = plagioclase.

Numbers between square brackets in the "[n]" column correspond to the number of analyzed points.

Figure 7.1. Satellite image of the localities of the Chilcatay dated tephra. Based on image © 2018 DigitalGlobe.

All the characteristics for dated tephra are described in Table 7.2. Biotite does not show massive evidence of alteration, such as clay minerals along cleavages. Biotite phenocrysts are enclosed by a rim of glass that prove their primary formation. Occasionally they contain inclusions of glass, apatite and zircon. EPMA analyses of biotite mostly reveal a rather homogeneous major element composition with only slight differences between core and rim.

All the dated tephra were classified as calcalkaline based on the biotite chemistry. Analyzed biotite phenocrysts have Mg/Mg+Fe+Mn ranging from 0.370 to 0.690 and Al from 2.264 to 2.972 atoms per formula unit. Al-rich compositions characteristic of strongly peraluminous magmas are absent. Biotites show a variable K content: the ones that show a low K content and a low alkali site occupancy have probably lost cations in the interlayers during alteration. On the basis of these observations and analyses, four ash layers were selected for ^{39}Ar–^{40}Ar dating in the Chilcatay Formation.

Estimating the age of the Chilcatay Formation had the added difficulty of a very limited choice of suitably unaltered ash layers. Two ash layers were selected at the base of the Chilcatay Formation, at Roca Negra and Ullujaya, one near an important new species of squalodelphinid about 3 km south of the fossiliferous Cerro Colorado locality, and one at the top of the formation in a locality informally named Los Dos Cerritos (see Fig. 7.1).

Tephra PN-T2 was sampled at Roca Negra 5 m above the CE0.1 unconformity. EPMA of biotite revealed a low alkali content, ranging from 1.78 to 1.90 apfu (atoms per formula unit), confirmed by the total ^{39}Ar concentration, which translates to a low K concentration of 5.84%. Even if the age spectrum is quite flat (Fig. 7.2a), the MSWD remains excessively high for isochrons and for weighted step age averages that only take into account isochemical steps. Therefore, we consider only the step with the lowest Ca/K (step 9), which gives an age of 19.25 ± 0.05 Ma. This step age is concordant with high-MSWD isochron and weighted average ages. Ar results are shown in Table 7.3.

Tephra UJA-T35, collected 2 m above the base of the section measured at Ullujaya (abbreviated: abs), is presumably only a short distance above the unconformity. EPMA analyses of biotite reveal a very scattered composition with a very low alkali site occupancy, from 1.50 to 1.91 apfu. The loss of K, Na and Ca in the interlayers of biotite is a result of the alteration. Also, the glass analyses are variably low in alkali. The trend in Figure 7.2b shows a parallel decrease of K content with the totals, supporting the evidence of significant alteration. By selecting isochemical steps 4-6 (having Ca/K <

0.050 and constant Cl/K), we obtain a weighted average age of 19.00 ± 0.28 Ma, with a MSWD of 1.5. Despite the evidence of alteration and the high uncertainty shown in the age spectrum (Fig. 7.2c), this age agrees with the age of PN-T2 the base of the Chilcatay Formation. Ar results for UJA-T35 are shown in Table 7.4.

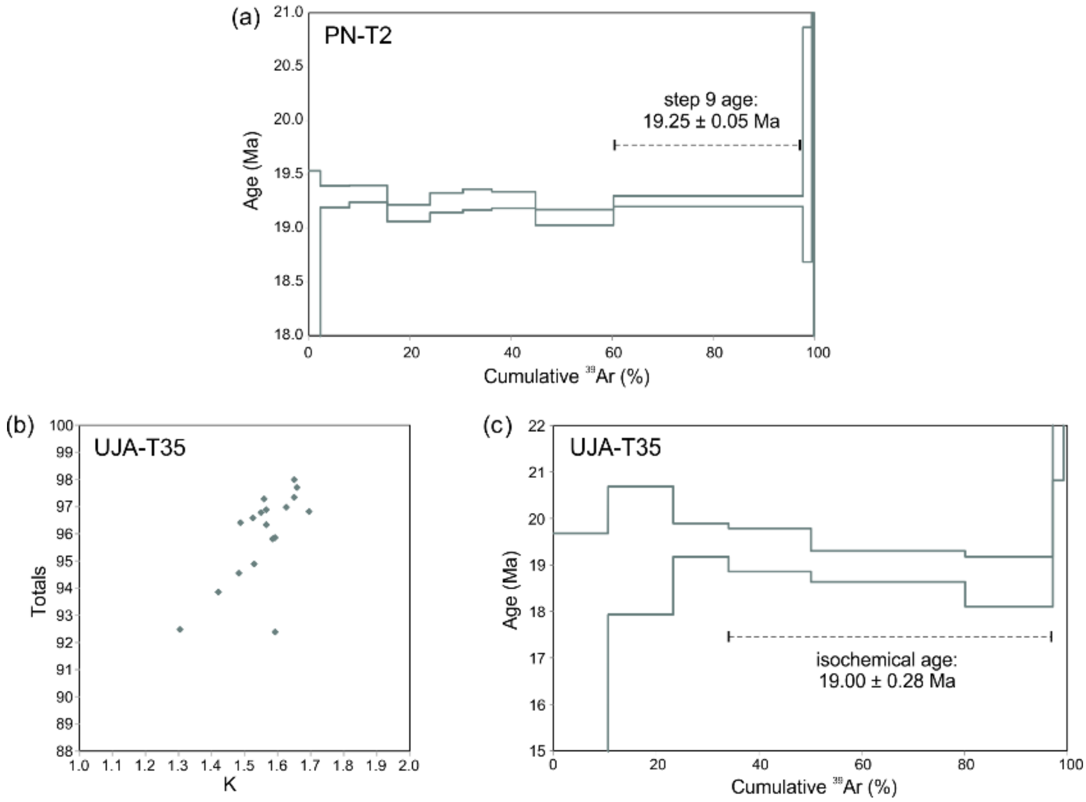

Figure 7.2. a) PN-T2 age spectrum. The calculated age from step 9 is 19.25 ± 0.05 Ma. All uncertainties are shown as 2σ. b) Biotite totals vs K content diagram of tephra UJA-T35 showing an alkali loss. K values are shown as atoms per formula unit, totals as percentage. c) UJA-T35 age spectrum. Dashed line show the steps considered for the isochemical age (i.e. weighted average age of isochemical steps), giving 19.00 ± 0.28 Ma. All uncertainties are shown as 2σ.

In the Chilcatay Formation, another tephra layer (CHILC-AT1) was dated through ^{39}Ar–^{40}Ar method, in order to attribute an age to a new species of platanistoid, collected from a locality near Cerro Colorado, where the overlying Late Miocene Pisco Formation is well known for its rich fossil content (Bianucci et al. 2016). This new specimen from the Chilcatay Formation belongs to a new squalodelphinid, *Macrosqualodelphis ukupachai*, differing from all the other genera of the family in several characters, including size, the more robust rostrum and the larger temporal fossa.

PN-T2

Step	T (°C)	^{40}Ar total	Err. ^{40}Ar	^{40}Ar*	^{39}Ar	Err. ^{39}Ar	% ^{39}Ar	^{38}Ar	Err. ^{38}Ar	^{38}Ar$_{Cl}$	^{37}Ar	Err. ^{37}Ar	^{36}Ar	Err. ^{36}Ar	Age	Error age	Ca/K	Err. Ca/K	Cl/K	Err. Cl/K	^{39}Ar/^{40}Ar	Sig. 9	^{36}Ar/^{40}Ar	Sig. 6
1	704	2.15E-08	1.08E-11	1.42E-09	1.26E-10	4.84E-13	2.26	3.94E-11	8.48E-14	2.53E-11	1.32E-11	1.09E-12	6.72E-11	2.65E-13	17.55	0.99	0.2032	0.0168	0.0356	0.0002	5.88E-03	2.27E-05	3.13E-03	1.24E-05
2	746	5.23E-09	3.13E-12	3.98E-09	3.22E-10	6.19E-13	5.76	4.51E-11	9.71E-14	4.05E-11	5.72E-12	1.08E-12	4.18E-12	2.08E-14	19.29	0.05	0.0345	0.0065	0.0224	0.0001	6.16E-02	1.24E-04	8.00E-04	4.02E-06
3	800	6.08E-09	4.04E-12	5.15E-09	4.16E-10	6.70E-13	7.44	5.58E-11	1.18E-13	5.03E-11	5.56E-12	1.08E-12	3.10E-12	1.61E-14	19.32	0.04	0.0259	0.0051	0.0215	0.0000	6.85E-02	1.19E-04	5.10E-04	2.67E-06
4	879	7.01E-09	4.72E-12	5.84E-09	4.76E-10	7.32E-13	8.52	6.29E-11	1.33E-13	5.66E-11	6.19E-12	1.09E-12	3.90E-12	1.95E-14	19.14	0.04	0.0252	0.0044	0.0212	0.0000	6.80E-02	1.14E-04	5.57E-04	2.81E-06
5	933	5.89E-09	3.71E-12	4.47E-09	3.63E-10	5.85E-13	6.49	4.82E-11	1.03E-13	4.30E-11	6.26E-12	1.09E-12	4.77E-12	2.27E-14	19.24	0.05	0.0335	0.0058	0.0211	0.0000	6.15E-02	1.07E-04	8.09E-04	3.88E-06
6	967	5.13E-09	2.49E-12	3.94E-09	3.19E-10	6.18E-13	5.71	4.21E-11	8.87E-14	3.76E-11	5.95E-12	1.08E-12	3.98E-12	1.95E-14	19.26	0.05	0.0362	0.0066	0.0210	0.0001	6.23E-02	1.24E-04	7.75E-04	3.81E-06
7	1023	7.35E-09	4.04E-12	5.96E-09	4.83E-10	7.36E-13	8.64	6.44E-11	1.33E-13	5.79E-11	7.60E-12	1.09E-12	4.67E-12	2.19E-14	19.26	0.04	0.0305	0.0044	0.0213	0.0000	6.57E-02	1.06E-04	6.35E-04	3.00E-06
8	1066	1.22E-08	1.01E-11	1.06E-08	8.63E-10	1.28E-12	15.44	1.14E-10	2.57E-13	1.03E-10	1.01E-11	1.09E-12	5.51E-12	2.50E-14	19.10	0.04	0.0227	0.0024	0.0213	0.0000	7.07E-02	1.20E-04	4.51E-04	2.08E-06
9	1099	2.86E-08	1.08E-11	2.58E-08	2.10E-09	2.33E-12	37.48	2.72E-10	5.51E-13	2.46E-10	1.55E-11	1.09E-12	9.27E-12	4.05E-14	19.25	0.02	0.0144	0.0010	0.0209	0.0000	7.32E-02	8.59E-05	3.24E-04	1.42E-06
10	1124	9.81E-09	5.06E-12	1.27E-09	1.00E-10	5.11E-13	1.80	1.88E-11	4.16E-14	1.22E-11	1.07E-11	1.09E-12	2.86E-11	1.14E-13	19.77	0.54	0.2075	0.0210	0.0217	0.0002	1.02E-02	5.23E-05	2.91E-03	1.17E-05
11	1156	2.46E-09	7.75E-13	2.20E-10	1.31E-11	5.35E-13	0.23	3.63E-12	1.13E-14	2.06E-12	5.90E-12	1.08E-12	7.50E-12	3.20E-14	26.31	1.57	0.8764	0.1652	0.0281	0.0018	5.31E-03	2.18E-04	3.05E-03	1.31E-05
12	1169	2.81E-09	9.44E-13	1.80E-10	7.84E-12	5.35E-13	0.14	3.16E-12	1.11E-14	1.40E-12	5.31E-12	1.08E-12	8.82E-12	3.76E-14	35.74	3.31	1.3150	0.2832	0.0318	0.0035	2.79E-03	1.90E-04	3.13E-03	1.34E-05
13	1308	5.46E-09	3.71E-12	3.20E-10	5.67E-12	3.68E-12	0.10	7.95E-12	2.17E-14	4.63E-12	1.53E-11	1.09E-12	1.72E-11	6.96E-14	86.52	56.43	5.2467	3.4246	0.1453	0.0943	1.04E-03	6.73E-04	3.15E-03	1.29E-05

UJA-T35

Step	T (°C)	^{40}Ar total	Err. ^{40}Ar	^{40}Ar*	^{39}Ar	Err. ^{39}Ar	% ^{39}Ar	^{38}Ar	Err. ^{38}Ar	^{38}Ar$_{Cl}$	^{37}Ar	Err. ^{37}Ar	^{36}Ar	Err. ^{36}Ar	Age	Error age	Ca/K	Err. Ca/K	Cl/K	Err. Cl/K	^{39}Ar/^{40}Ar	Sig. 9	^{36}Ar/^{40}Ar	Sig. 6
1	702	2.45E-08	1.08E-11	1.22E-09	1.16E-10	6.84E-13	10.63	3.67E-11	9.63E-14	2.06E-11	6.60E-12	1.12E-12	7.81E-11	3.91E-13	16.51	1.59	0.1108	0.0187	0.0317	0.0003	4.71E-03	2.80E-05	3.18E-03	1.60E-05
2	815	1.37E-08	5.06E-12	1.70E-09	1.38E-10	5.62E-13	12.68	3.30E-11	8.71E-14	2.39E-11	7.20E-12	1.11E-12	4.00E-11	2.02E-13	19.31	0.69	0.1014	0.0157	0.0308	0.0002	1.01E-02	4.13E-05	2.93E-03	1.48E-05
3	925	3.58E-09	1.18E-12	1.46E-09	1.17E-10	5.55E-13	10.77	2.32E-11	6.26E-14	2.04E-11	4.07E-12	1.11E-12	7.09E-12	3.82E-14	19.53	0.18	0.0675	0.0185	0.0311	0.0002	3.27E-02	1.55E-04	1.98E-03	1.07E-05
4	1036	6.97E-09	4.38E-12	2.15E-09	1.74E-10	5.46E-13	16.02	3.51E-11	9.12E-14	3.00E-11	4.22E-12	1.11E-12	1.61E-11	8.22E-14	19.32	0.23	0.0471	0.0124	0.0307	0.0001	2.50E-02	8.00E-05	2.31E-03	1.19E-05
5	1125	1.01E-08	5.39E-12	3.96E-09	3.26E-10	1.11E-12	30.02	6.48E-11	1.69E-13	5.71E-11	4.92E-12	1.11E-12	2.06E-11	1.06E-13	18.97	0.17	0.0293	0.0066	0.0312	0.0001	3.22E-02	1.11E-04	2.04E-03	1.05E-05
6	1212	8.28E-09	4.38E-12	2.21E-09	1.85E-10	5.82E-13	17.05	3.77E-11	9.92E-14	3.17E-11	4.70E-12	1.11E-12	2.03E-11	1.03E-13	18.64	0.27	0.0492	0.0117	0.0304	0.0001	2.24E-02	7.13E-05	2.45E-03	1.25E-05
7	1261	3.51E-09	1.15E-12	3.40E-10	2.27E-11	5.36E-13	2.09	5.93E-12	1.85E-14	3.65E-12	3.43E-12	1.11E-12	1.06E-11	5.52E-14	23.34	1.26	0.2928	0.0954	0.0287	0.0011	6.46E-03	1.53E-04	3.03E-03	1.57E-05
8	1311	4.33E-09	1.35E-12	1.82E-10	7.96E-12	5.02E-13	0.73	4.06E-12	1.41E-14	1.35E-12	3.37E-12	1.11E-12	1.39E-11	7.08E-14	35.54	4.70	0.8208	0.2762	0.0301	0.0033	1.84E-03	1.16E-04	3.21E-03	1.64E-05

Tables 7.3, 7.4. Ar results of the tephra layers PN-T2 and UJA-T35.

The tephra layer CHILC-AT1, sampled 1.7 km SE of the holotype of *M. ukupachai*, near an uncollected squalodelphinid skeleton most likely belonging to the same taxon, is composed of 90% glass shards and 10% juvenile crystals, mainly biotite, as estimated by optical microscopy. EPMA analyses on volcanic glasses show a rhyolitic composition, whereas the biotite crystals suggest a calcalkaline origin. Biotite analyses reveal a slight loss of K in the interlayer occupancy, but the petrological composition, the chemical homogeneity of the biotite population and the lack of sedimentary evidence suggest that this tephra layer is a primary air-fall. The level of post-eruptive marine alteration was low. Considering the "isochemical steps" (Villa et al. 2006) as the heating steps most closely reflecting the degassing of biotite crystals, we calculated the ^{39}Ar–^{40}Ar age from steps 4-9 with the lowest Ca/K and Cl/K ratios, obtaining a weighted average of 18.80 ± 0.06 Ma (2σ), with a mean square weighted deviation (MSWD) value of 12, and an isochron age of 18.70 ± 0.13 Ma (2σ), with an MSWD value of 7.3 (Fig. 7.3).

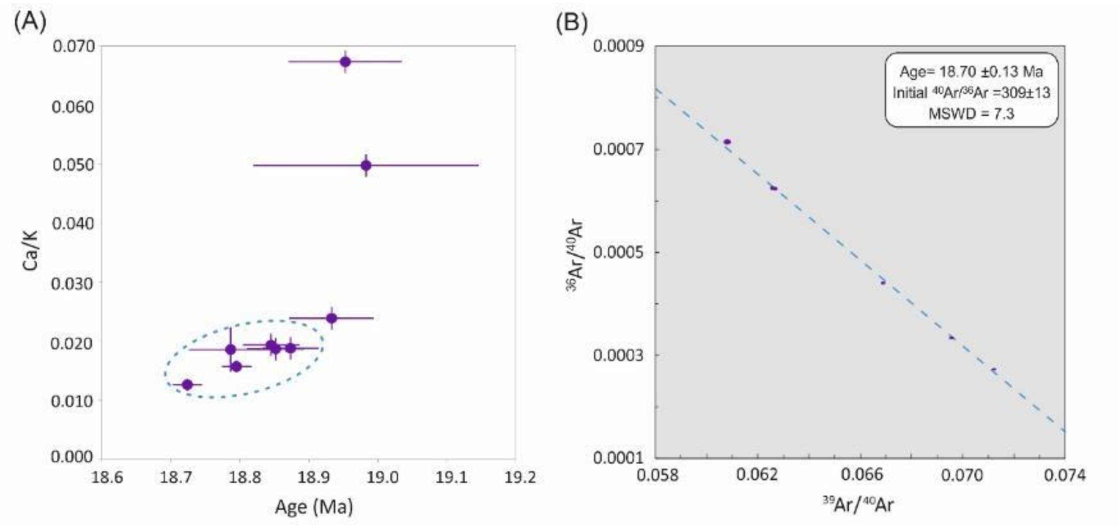

Figure 7.3. a) Ca/K versus age correlation diagram of the CHILC-AT1 biotite separate obtained by ^{39}Ar–^{40}Ar analyses. The dashed ellipse includes the isochemical heating steps 4-9 considered for the age calculations. Step 9 is the one with the lowest Ca/K ratio and the youngest age. Other steps with a high Ca/K ratio have been considered as a result of alteration and not taken into account in the age calculation. All uncertainties are given as 2σ. b) Isochron of the CHILC-AT1 biotite crystals, considering only the isochemical heating steps 4-9. The age obtained is 18.70 ± 0.13 Ma, with an MSWD of 7.3. The sizes of the ellipses representing points are the 2σ uncertainties. From Bianucci et al. (2018a).

However, both these dispersion values are too high, which points to a systematic bias, such as suggested by the substoichiometric K concentration of 6.8% calculated from the total ^{39}Ar release. For this reason, we can consider only the age given by step 9, which is the most gas-rich step (greater than 30%) and the one with the lowest Ca/K: the age calculated is 18.72 ± 0.02 Ma (2σ), which overlaps with the weighted average, as shown in Figure 7.4. The most conservative age estimate covers the entire 2σ confidence interval between 18.70 and 18.86 Ma. If this confidence interval was symmetrical and Gaussian, it would correspond to an age of 18.78 ± 0.08 Ma, which can be considered as the age of this tephra layer. Ar results are available in Table 7.5.

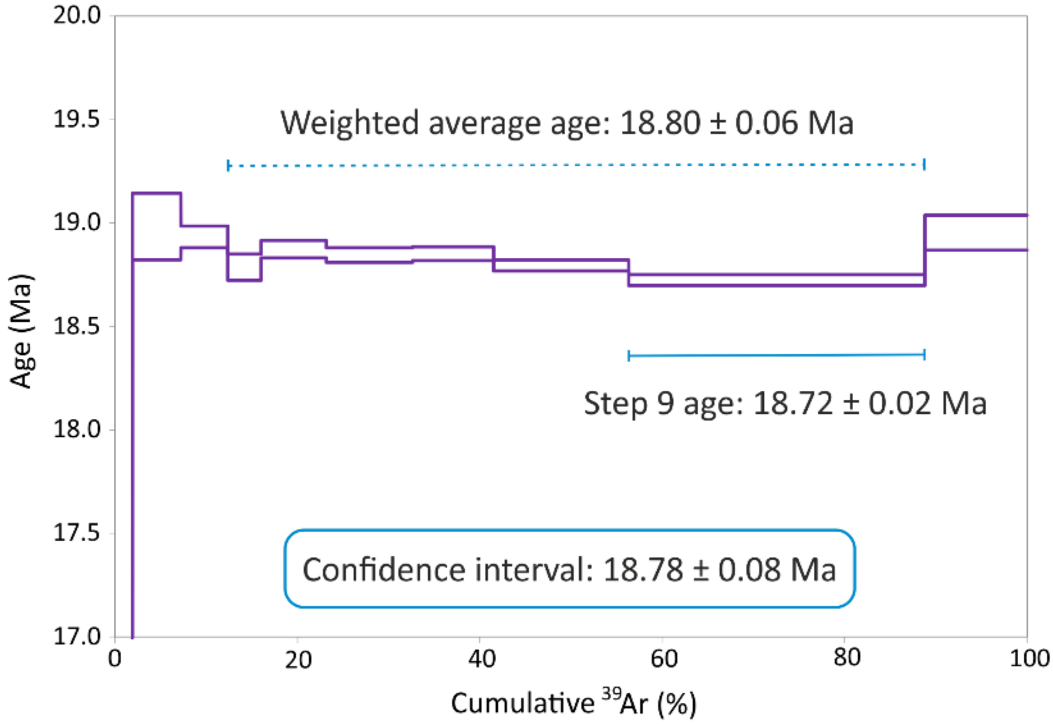

Figure 7.4. ^{39}Ar–^{40}Ar age spectrum of the biotite separate of the tephra layer CHILC-AT1. The most conservative age assignment, taking into account interpretive ambiguities at the 0.4% level, is 18.78 ± 0.08 Ma. All uncertainties are shown as 2σ. From Bianucci et al. (2018a).

For dating the top of the Chilcatay Formation in the western side of the Ica River, an ash layer (SOT-T3) was collected in the upper part of *Ct2b* facies association, just 1 m below the erosional contact with the overlying Pisco Formation (14°35’40.83"S; 75°40’4.70"W) at Los Dos Cerritos, a locality between Cerro Yesera de Amara and Cerro Submarino.

Electron probe micro-analyses on biotite crystals exhibit a homogeneous population and do not show any K loss in the interlayer occupancy. The most reliable estimate of the biotite age is provided by the steps with the lowest Ca/K ratios, as the stoichiometry of biotite is Ca-free. A strict adherence to the definition of "isochemical steps" (Villa et al. 2006) requires only considering steps 3-5, with Ca/K < 0.035. These steps give a mean weighted age of 17.99 ± 0.10 Ma and an isochron with atmospheric intercept (see Fig. 7.4). This age is nearly identical to that obtained by Belia and Nick (2016) with the ^{39}Ar–^{40}Ar method on the same ash (i.e. 17.70 ± 0.24 Ma).

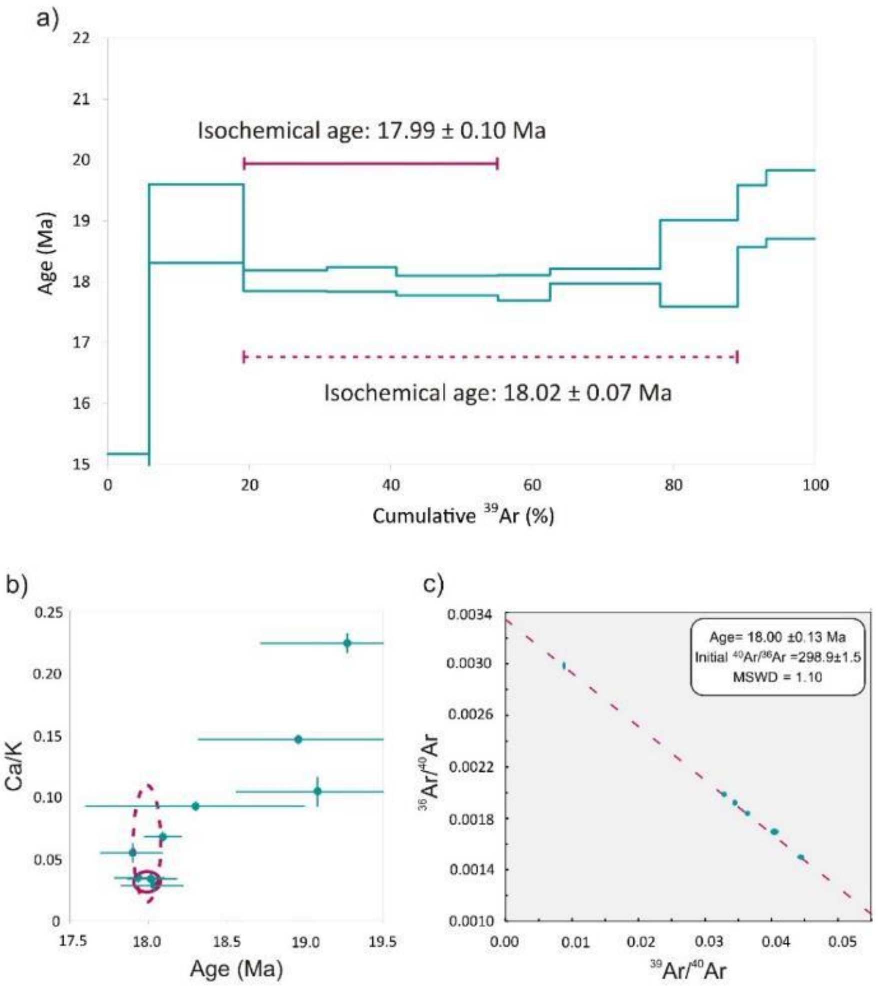

Figure 7.5. a) Age spectrum of the biotite separate of the tephra SOT-T3. The most conservative age assignment, taking into account steps 3-8, is 18.02 ± 0.07 Ma. All uncertainties are shown as 2σ. b) SOT-T3 Ca/K vs age diagram. Ellipses show the steps considered for the final age calculation. All uncertainties are given as 2σ. c) SOT-T3 Ar isochron. The sizes of the ellipses representing points are the 2σ uncertainties. From Di Celma et al. (2018).

CHILC-AT1

Step	T (°C)	^{40}Ar total	Err. ^{40}Ar	^{40}Ar*	^{39}Ar	Err. ^{39}Ar	% ^{39}Ar	^{38}Ar	Err. ^{38}Ar	^{38}ArCl	^{37}Ar	Err. ^{37}Ar	^{36}Ar	Err. ^{36}Ar	Age	Err. age	Ca/K	Err. Ca/K	Cl/K	Err. Cl/K	^{39}Ar/^{40}Ar	Sig. 9	^{36}Ar/^{40}Ar	Sig. 6
1	712	3.44E-08	1.35E-11	1.17E-09	1.46E-10	3.70E-13	1.91	5.94E-11	6.71E-14	3.67E-11	2.01E-11	2.29E-13	1.11E-10	2.14E-13	11.70	0.65	0.2682	0.0031	0.0448	0.00013	4.24E-03	1.09E-05	3.24E-03	6.35E-06
2	818	1.61E-08	4.94E-12	5.32E-09	4.07E-10	3.64E-13	5.32	6.37E-11	6.74E-14	5.21E-11	1.04E-11	2.25E-13	3.62E-11	7.16E-14	18.98	0.08	0.0498	0.0011	0.0228	0.00002	2.52E-02	2.39E-05	2.24E-03	4.50E-06
3	903	6.83E-09	1.27E-12	5.12E-09	3.92E-10	4.07E-13	5.14	5.05E-11	5.51E-14	4.48E-11	4.84E-12	2.24E-13	5.75E-12	1.53E-14	18.93	0.03	0.0239	0.0011	0.0203	0.00002	5.74E-02	6.05E-05	8.41E-04	2.24E-06
4	942	4.60E-09	9.62E-13	3.62E-09	2.79E-10	3.86E-13	3.66	3.44E-11	4.08E-14	3.05E-11	2.68E-12	2.29E-13	3.28E-12	1.15E-14	18.79	0.03	0.0186	0.0016	0.0194	0.00003	6.08E-02	8.49E-05	7.14E-04	2.50E-06
5	995	8.73E-09	2.31E-12	7.10E-09	5.46E-10	4.87E-13	7.15	6.74E-11	7.05E-14	6.00E-11	5.30E-12	2.29E-13	5.46E-12	1.39E-14	18.87	0.02	0.0188	0.0008	0.0195	0.00002	6.26E-02	5.81E-05	6.25E-04	1.60E-06
6	1035	1.15E-08	1.46E-12	9.39E-09	7.23E-10	4.95E-13	9.46	8.83E-11	9.31E-14	7.84E-11	7.22E-12	2.30E-13	7.21E-12	1.97E-14	18.85	0.02	0.0194	0.0006	0.0193	0.00001	6.27E-02	4.36E-05	6.24E-04	1.71E-06
7	1076	1.01E-08	1.38E-12	8.81E-09	6.79E-10	4.81E-13	8.88	8.28E-11	8.86E-14	7.39E-11	6.55E-12	2.29E-13	4.47E-12	1.44E-14	18.85	0.02	0.0187	0.0007	0.0194	0.00002	6.69E-02	4.83E-05	4.41E-04	1.42E-06
8	1117	1.63E-08	3.12E-12	1.47E-08	1.13E-09	6.86E-13	14.82	1.38E-10	1.45E-13	1.24E-10	9.17E-12	2.31E-13	5.43E-12	1.53E-14	18.80	0.01	0.0157	0.0004	0.0195	0.00001	6.96E-02	4.42E-05	3.34E-04	9.41E-07
9	1163	3.49E-08	9.88E-12	3.20E-08	2.48E-09	1.47E-12	32.48	3.02E-10	3.09E-13	2.71E-10	1.62E-11	2.33E-13	9.54E-12	2.45E-14	18.72	0.01	0.0126	0.0002	0.0194	0.00001	7.12E-02	4.67E-05	2.74E-04	7.07E-07
10	1289	2.29E-08	3.90E-12	1.12E-08	8.55E-10	5.74E-13	11.19	1.14E-10	1.14E-13	9.65E-11	2.97E-11	2.37E-13	3.94E-11	7.78E-14	18.95	0.04	0.0673	0.0005	0.0201	0.00001	3.73E-02	2.59E-05	1.72E-03	3.41E-06

SOT-T3

Step	T (°C)	^{40}Ar total	Err. ^{40}Ar	^{40}Ar*	^{39}Ar	Err. ^{39}Ar	% ^{39}Ar	^{38}Ar	Err. ^{38}Ar	^{38}ArCl	^{37}Ar	Err. ^{37}Ar	^{36}Ar	Err. ^{36}Ar	Age	Err. age	Ca/K	Error Ca/K	Cl/K	Error Cl/K	^{39}Ar/^{40}Ar	Sig. 9	^{36}Ar/^{40}Ar	Sig. 6
1	706	3.60E-08	1.53E-11	4.10E-10	5.48E-11	3.12E-13	5.84	5.78E-11	7.31E-14	3.47E-11	1.38E-11	1.25E-13	1.19E-10	2.67E-13	10.87	2.15	0.4899	0.0052	0.1129	0.0007	1.52E-03	8.70E-06	3.31E-03	7.55E-06
2	832	1.37E-08	3.12E-12	1.64E-09	1.25E-10	3.18E-13	13.35	3.12E-11	3.97E-14	2.21E-11	9.44E-12	1.23E-13	4.04E-11	9.19E-14	18.96	0.32	0.1464	0.0019	0.0314	0.0001	9.13E-03	2.33E-05	2.95E-03	6.75E-06
3	873	3.04E-09	4.94E-13	1.38E-09	1.11E-10	3.42E-13	11.80	1.95E-11	2.62E-14	1.72E-11	1.94E-12	1.22E-13	5.58E-12	1.58E-14	18.02	0.08	0.0340	0.0021	0.0277	0.0001	3.64E-02	1.13E-04	1.83E-03	5.20E-06
4	915	2.81E-09	5.72E-13	1.15E-09	9.23E-11	3.40E-13	9.84	1.61E-11	2.18E-14	1.39E-11	1.35E-12	1.22E-13	5.57E-12	1.56E-14	18.04	0.10	0.0284	0.0026	0.0269	0.0001	3.28E-02	1.21E-04	1.98E-03	5.57E-06
5	965	3.95E-09	7.54E-13	1.67E-09	1.35E-10	3.70E-13	14.38	2.36E-11	3.16E-14	2.06E-11	2.42E-12	1.22E-13	7.64E-12	2.01E-14	17.94	0.08	0.0349	0.0018	0.0271	0.0001	3.41E-02	9.38E-05	1.93E-03	5.11E-06
6	995	1.72E-09	4.42E-13	8.54E-10	6.90E-11	3.13E-13	7.36	1.22E-11	1.85E-14	1.08E-11	1.95E-12	1.24E-13	2.90E-12	1.05E-14	17.90	0.10	0.0549	0.0035	0.0279	0.0002	4.01E-02	1.82E-04	1.69E-03	6.14E-06
7	1029	3.31E-09	6.50E-13	1.83E-09	1.46E-10	3.46E-13	15.60	2.66E-11	3.45E-14	2.39E-11	5.11E-12	1.25E-13	4.96E-12	1.41E-14	18.09	0.06	0.0678	0.0017	0.0291	0.0001	4.42E-02	1.05E-04	1.50E-03	4.28E-06
8	1082	1.21E-08	2.86E-12	1.30E-09	1.03E-10	3.16E-13	10.95	2.51E-11	3.20E-14	1.71E-11	4.89E-12	1.25E-13	3.63E-11	8.26E-14	18.30	0.35	0.0925	0.0024	0.0296	0.0001	8.47E-03	2.61E-05	2.99E-03	6.85E-06
9	1133	2.42E-09	4.68E-13	5.02E-10	3.81E-11	3.11E-13	4.06	7.99E-12	1.32E-14	6.33E-12	2.05E-12	1.24E-13	6.42E-12	1.77E-14	19.08	0.25	0.1046	0.0064	0.0296	0.0003	1.58E-02	1.29E-04	2.65E-03	7.32E-06
10	1292	5.63E-09	1.14E-12	8.52E-10	6.40E-11	3.13E-13	6.82	1.63E-11	2.25E-14	1.25E-11	7.39E-12	1.26E-13	1.60E-11	3.89E-14	19.27	0.28	0.2240	0.0040	0.0348	0.0002	1.14E-02	5.56E-05	2.84E-03	6.93E-06

Tables 7.5, 7.6. Ar results of the tephra layers CHILC-AT1 and SOT-T3.

However, if one considers also steps 6-8, which have slightly higher Ca/K and Cl/K ratios (in any case Ca/K < 0.093), the resulting weighted average age is 18.02 ± 0.07 Ma, indistinguishable from the strict isochemical age, with a statistically acceptable dispersion (MSWD = 0.90), and also corresponding to an isochron with atmospheric intercept. The 18.02 ± 0.07 Ma estimate for SOT-T3 includes a higher number of steps and is slightly more precise than the 17.99 ± 0.10 Ma age estimate reported by Di Celma et al. (2017) for the same layer. The age spectrum displaying both options, the isochron and the Ca diagram are shown in Figure 7.5. Ar results are available in Table 7.6.

7.3. Chilcatay Formation chronostratigraphy

In the Chilcatay Formation, tephra are much less frequent and, in general, more altered than those of the P2 and P1 allomembers in the Pisco Formation. Differences in the depositional environment probably account for their preservation in the stratigraphic record and degree of alteration. The relatively deeper (60 to 100 m) environment (Gariboldi et al. 2017) represented by diatomaceous siltstones of P1 and P2 allomembers is more suitable for the preservation of ash layers than the shallow water environment of the Chilcatay strata (15 to 20 m) (Bianucci et al. 2018b). The longer exposure of the older strata to the acid interstitial water could also play a role in preservation.

Chilcatay tephra selected for ^{39}Ar–^{40}Ar dating show a slight alteration. As most dated biotite phenocrysts were subject to a slight loss of soluble cations in the interlayer, we consider the ^{39}Ar–^{40}Ar ages on near-stoichiometric biotite more reliable than those on clearly sub-stoichiometric ones.

In this thesis, ^{39}Ar–^{40}Ar dating on tephra were undertaken to define the time constraints of the Chilcatay Formation in different localities, Ullujaya, Roca Negra, Los Dos Cerritos and a locality nearby Cerro Colorado. Despite some problems caused by a variable alteration of the biotite phenocrysts, both samples give Burdigalian ages (early Miocene). The PN-T2 tephra, 5 m above the CE0.1 unconformity in Roca Negra, gives an age of 19.25 ± 0.05 Ma, which agrees with that in Ullujaya, where the lowest ash layer (UJA-T35) of *Ct1a* is dated at 19.00 ± 0.28 Ma. These ^{39}Ar–^{40}Ar results agree with the silicoflagellates biostratigraphic data reported recently by Di Celma et al. (2018a), who assigned an age of 18-19 Ma, in the *Naviculopsis ponticula* zone (Bukry, 1981), to the lower portion of the Chilcatay strata exposed at Ullujaya. The Roca Negra assemblage is probably slightly older than that encountered at Ullujaya, as it is enriched in older species of the *N. ponticula* zone (Lambert et al. 2017). This is also compatible with the modest age difference between UJA-T35 and PN-T2. Another Burdigalian age was obtained from an ash layer near an important specimen of a new squalodelphinid from the Chilcatay Formation outcropping in the south area of Cerro Colorado, scarcely correlated with other localities; the ash layer was dated at 18.78 ± 0.08 Ma. The top of the Chilcatay Formation was dated at 18.02 ± 0.07 Ma, an age given by the ash layer SOT-T3, 1 m below the PE0.0 unconformity sampled at Los Dos Cerritos, which is close to biostratigraphic data, obtained through both diatoms and silicoflagellates.

Microfossil biostratigraphy is concordant with these radiometric ages, attributing the *Ct1a* facies association to the *C. elegans* biozone of Expedition 320/321 Scientists (2010) and to the *N. ponticula* biozone of Perch-Nielsen (1985); and the *Ct2a* facies association to the *T. pileus* biozone of Expedition 320/321 Scientists (2010), to the *C. tracantha* biozone of Perch-Nielsen (1985) and to the calcareous nannofossil NN3 biozone of Bukry (1982). At the very top of the Ct2 allomember, diatom biostratigraphy suggests an age younger than 17.08 Ma for the top of the formation, which is quite younger than the SOT-T3 ^{39}Ar–^{40}Ar age.

The ^{39}Ar–^{40}Ar ages presented here constrain the Chilcatay Formation between 19.25 ± 0.05 Ma and 18.02 ± 0.07 Ma, assigning a Burdigalian age to the entire formation exposed in the study area. The Oligocene estimated age for the base of the Chilcatay Formation proposed by DeVries and Jud (2018) for a different locality was not confirmed in the study area. The base of the Chilcatay Formation can be diachronous in other localities of the East Pisco Basin, possibly due to the time-transgressive character of its basal boundary (Fig. 7.6).

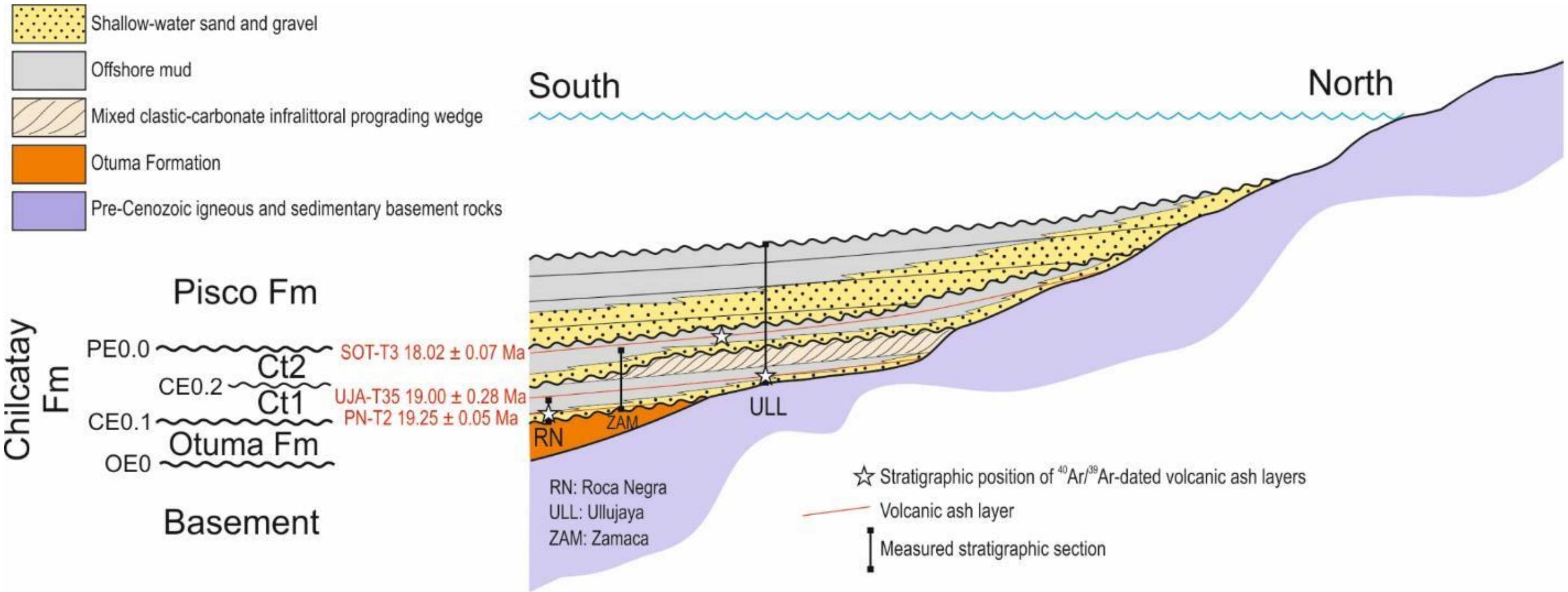

Figure 7.6. Schematic, dip-oriented stratigraphic diagram for the Chilcatay Formation and the surrounding Otuma and Pisco formations showing both the position of measured stratigraphic sections (vertical black lines) and the stratigraphic position of dated tephra layers (stars). Pisco Formation shows only one of the three transgressive cycles. Red lines show dated volcanic ash layers. ^{39}Ar–^{40}Ar ages are reported for each tephra. Modified from Di Celma et al. (2017).

Different papers have contributed to this chapter: the first is "Tephrochronology and chronostratigraphy of the Miocene Chilcatay and Pisco formations (East Pisco Basin, Peru)" written by Giulia Bosio, Elisa Malinverno, Igor M. Villa, Claudio Di Celma, Karen Gariboldi, Anna Gioncada, Valentina Barberini, Mario Urbina and Giovanni Bianucci, submitted to Newsletters on Stratigraphy in December 2018.
The second is "Facies analysis, stratigraphy and marine vertebrate assemblage of the lower Miocene Chilcatay Formation at Ullujaya (Pisco basin, Peru)" authored by Claudio Di Celma, Elisa Malinverno, Alberto Collareta, Giulia Bosio, Karen Gariboldi, Olivier Lambert, Walter Landini, Pietro Paolo Pierantoni, Anna Gioncada, Igor Maria Villa, Giovanni Coletti, Christian de Muizon, Mario Urbina and Giovanni Bianucci and published in 2018 by Journal of Maps, Vol. 14:2, 257-268. In this paper, Giulia Bosio contributes to sample collection, measurement of the stratigraphic section and field mapping, sample preparation and analyses, and isotope geochronology.
The last one is "A new large squalodelphinid (Cetacea, Odontoceti) from Peru sheds light on the Early Miocene platanistoid disparity and ecology" written by Giovanni Bianucci, Giulia Bosio, Elisa Malinverno, Christian de Muizon, Igor M. Villa, Mario Urbina and Olivier Lambert, and published in 2018 on Royal Society Open Science, 5: 172302. In this paper, Giulia Bosio contributes to give an age constraint to the new species Macrosqualodelphis ukupachai.

Chapter References

Barron, J.A. 2005. Diatom biochronology of the early Miocene of the equatorial Pacific. Stratigraphy, 2, 281-309.

Belia, E. R., Nick, K. E. 2016. Early-Miocene calcareous nannofossil biostratigraphy from low-latitude, Pisco Basin, Peru. Geological Society of America Abstracts with Programs, 48, 4.

Bianucci, G., Di Celma, C., Landini, W., Post, K., Tinelli, C., de Muizon, C., Gariboldi, K., Malinverno, E., Cantalamessa, G., Gioncada, A., Collareta, A., Salas-Gismondi, R., Varas-Malca, R.M., Urbina, M., Lambert, O. 2016. Distribution of fossil marine vertebrates in Cerro Colorado, the type locality of the giant raptorial sperm whale Livyatan melvillei (Miocene, Pisco Formation, Peru). Journal of Maps, 12, 543-557.

Bianucci, G., Bosio, G., Malinverno, E., de Muizon, C., Villa, I.M., Urbina, M., Lambert, O. 2018a. A new large squalodelphinid (Cetacea, Odontoceti) from Peru sheds light on the Early Miocene platanistoid disparity and ecology. Royal Society open science, 5, 172302.

Bianucci, G., Collareta, A., Bosio, G., Landini, W., Gariboldi, K., Gioncada, A., Lambert, O., Malinverno, E., de Muizon, C., Varas-Malca, R., Villa, I.M., Coletti, G., Urbina, M., Di Celma, C. 2018b. Taphonomy and palaeoecology of the lower Miocene marine vertebrate assemblage of Ullujaya (Chilcatay Formation, East Pisco Basin, southern Peru). Palaeogeography, Palaeoclimatology, Palaeoecology, 511, 256-279.

Blott, S.J., Pye, K. 2001. Gradistat: a grain size distribution and statistics package for the analysis of unconsolidated sediments. Earth Surface processes and Landforms, 26, 1237-1248.

Bukry, D. 1981. Synthesis of Silicoflagellate stratigraphy for Maestrichtian to Quaternary marine sediments. In T. E. Warme, R. C. Douglas, & E. L. Winterer (Eds.), The deep sea drilling project: A decade of progress (pp. 433-444). Tulsa: SEPM, Special Publication, 32.

Bukry, D. 1982. Cenozoic Silicoflagellates from offshore Guatemala, deep sea drilling project site 495. Initial Reports, DSDP 67: 425-445. Washington: U.S. Govt. Printing Office.

Bukry, D. 1985. Correlation of late Cretaceous Arctic silicoflagellates from Alpha Ridge. In H. R. Jackson, P. J. Mudie, & S. M. Blasco (Eds.), Initial geological report on CESAR - the Canadian expedition to study the alpha ridge, arctic ocean. Geological Survey of Canada, Paper 84-22, 125-135.

Carey, S. 1997. Influence of convective sedimentation on the formation of widespread tephra fall layers in the deep sea. Geology, 25, 9, 839-842.

DeVries, T. J. 1998. Oligocene deposition and Cenozoic sequence boundaries in the Pisco Basin. Journal of South American Earth Sciences, 11, 217-231.

DeVries, T.J., Jud, N.A. 2018. Lithofacies patterns and paleogeography of the Miocene Chilcatay and lower Pisco depositional sequences (East Pisco Basin, Peru). Boletín de la Sociedad Geológica del Perú, Volumen Jubilar 8, 124-167.

Di Celma, C., Malinverno, E., Bosio, G., Collareta, A., Gariboldi, K., Gioncada, A., Molli, G., Basso, D., Varas-Malca, R.M., Pierantoni, P.P., Villa, I.M., Lambert, O., Landini, W., Sarti, G., Cantalamessa, G., Urbina, M., Bianucci, G. 2017. Sequence stratigraphy and paleontology of the upper Miocene Pisco Formation along the western side of the lower Ica valley (Ica Desert, Peru). Rivista Italiana di Paleontologia e Stratigrafia (Research In Paleontology and Stratigraphy), 123, 255-274.

Di Celma, C., Malinverno, E., Collareta, A., Bosio, G., Gariboldi, K., Lambert, O., Landini, W., Pierantoni, P.P., Gioncada, A., Villa, I.M., Coletti, G., de Muizon, C., Urbina, M., Bianucci, G. 2018. Facies analysis, stratigraphy and marine vertebrate assemblage of the lower Miocene Chilcatay Formation at Ullujaya (Pisco basin, Peru). Journal of Maps, 14, 2, 257-268.

Expedition 320/321 Scientists 2010. Methods. In H. Pälike, M. Lyle, H. Nishi, I. Raffi, K. Gamage, A. Klaus, and the Expedition 320/321 Scientists, Proceedings of the integrated ocean drilling program, 320/321: Tokio: Integrated Ocean Drilling Program Management International, Inc.

Fisher, R.V., Schmincke, H.-U. 1984. Pyroclastic Rocks. Springer-Verlag. Berlin, Heidelberg, New York, Tokyo.

Folk, R.L. 1954. The distinction between grain size and mineral composition in sedimentary-rock nomenclature. Journal of Geology, 62, 344-359.

Gariboldi, K., Bosio, G., Malinverno, E., Gioncada, A., Di Celma, C., Villa, I.M., Urbina, M., Bianucci, G. 2017. Biostratigraphy, geochronology and sedimentation rates of the upper Miocene Pisco Formation at two important marine vertebrate fossil-bearing sites of southern Peru. Newsletters on Stratigraphy, 50, 4, 417-444.

Lambert, O., de Muizon, C., Malinverno, E., Di Celma, C., Urbina, M., & Bianucci, G. 2017. A new odontocete (toothed cetacean) from the early Miocene of Peru expands the morphological disparity of extinct heterodont dolphins. Journal of Systematic Palaeontology, 16(12), 981-1016.

Perch-Nielsen, K. 1985. Silicoflagellates. In H. M. Bolli, J. B. Saunders, K. Perch-Nielsen (Eds.), Plankton stratigraphy (Vol. 2, pp. 811-846). Cambridge: Cambridge University Press.

Villa, I. M., Ruggieri, G., Puxeddu, M., Bertini, G. 2006. Geochronology and isotope transport systematics in a subsurface granite from the Larderello-Travale geothermal system (Italy). Journal of Volcanology and Geothermal Research, 152, 20-50.

White, J.D.L., Houghton, B.F. 2006. Primary volcaniclastic rocks. Geology, 8, 677-680.

Chapter 8. Sr-isotope stratigraphy on fossil shells of the lower Miocene Chilcatay Formation

The $^{87}Sr/^{86}Sr$ isotope ratio in the oceans has varied through geological time (Fig. 5.3, Chapter 5) and the Sr isotopic composition can be used to date marine minerals and to correlate stratigraphic sections of marine deposits (Faure & Mensing 2005).

Sr-isotope analyses were performed on marine carbonates and phosphates for investigating the P0 allomember age because of the lack of both microfossils and datable tephra in this allomember (see Chapter 11). In order to ensure the results of these analyses, several samples of the Chilcatay Formation, whose age is now well-known in the western side of the Ica River, were analyzed together.

Chilcatay carbonate samples were first analyzed for investigating the taphonomy and the diagenesis that affected them during and after the precipitation. Diagenetic processes or weathering, indeed, could altered the pristine $^{87}Sr/^{86}Sr$, falsifying the final age of the mineral formation (Scasso et al. 2001; Brand et al. 2012; Ullmann & Korte 2015). All the taphonomic and diagenetic studies through optical microscope, SEM and cathodoluminescence allowed to select samples suitable for analyses. They are reported in Chapter 15 (Part II).

For comparing results along the stratigraphic section and among different organisms, different levels were selected from the same localities, and for each level several carbonate shells were selected, usually from diverse organisms (e.g. oysters, barnacles and pectinids). Some bulk or cement samples were also analyzed for better understanding the diagenetic path and the changes of $^{87}Sr/^{86}Sr$ values.

After discarding the badly-preserved shells (e.g., oysters from level UL-D18 at the base of the *Ct1b* facies association), fifteen samples were selected for $^{87}Sr/^{86}Sr$ analyses (Table 8.1). Three oyster samples were chosen for the base of the Chilcatay Formation (*Ct1a* facies association) at the locality of Roca Negra (see Fig. 8.1): PN-OST, PN-GIO1, PN-GIO2. They come from the same level (PN Oyster level), ten meters above the ash layer PN-T2, dated in this thesis at 19.25 ± 0.05 Ma (see Chapter 7). All these samples have been drilled from oysters: PN-OST is obtained from different nacre levels of an oyster (mother-of-pearl portion); PN-GIO1 is from the same nacre level of a different oyster; PN-GIO2 is from a darker nacre level of another oyster.

Samples	Weight (g)	Locality	Formation	Level	Meters abs (m)	Description
PN-OST	0.0523	Roca Negra	Chilcatay	Base Chilc	11	Oyster, mother-of-pearl, different levels
PN-GIO1	0.0293	Roca Negra	Chilcatay	Base Chilc	11	Oyster, mother-of-pearl, same level
PN-GIO2	0.0443	Roca Negra	Chilcatay	Base Chilc	11	Another oyster, dark gray mother-of-pearl
UJA-2a	0.0364	Ullujaya	Chilcatay	Liv B	30	Oyster, white levels
UJA-2b	0.0263	Ullujaya	Chilcatay	Liv B	30	Same oyster, gray levels
UL-D4a	0.1258	Ullujaya	Chilcatay	UL-D4	25	Oyster, mother-of-pearl
UL-D4b	0.1513	Ullujaya	Chilcatay	UL-D4	25	Barnacle sheath
UL-D4c	0.0893	Ullujaya	Chilcatay	UL-D4	25	Bulk (inside the barnacle)
UL-LIVa	0.0157	Ullujaya	Chilcatay	Liv moll e bal	9	Barnacle sheath
UL-LIVb	0.1441	Ullujaya	Chilcatay	Liv moll e bal	9	Pectinids (2 specimens)
UL-LIVd	0.1550	Ullujaya	Chilcatay	Liv moll e bal	9	One pectinid
UJA-LIVC1	0.1030	Ullujaya	Chilcatay	Liv C	17	Oyster (number 2), mother-of-pearl portion
UJA-LIVC2	0.1481	Ullujaya	Chilcatay	Liv C	17	Bulk outside the oyster (number 1)
UJA-LIVC3	0.0365	Ullujaya	Chilcatay	Liv C	17	Oyster (number 1), mother-of-pearl portion (light, not brownish)
UJA-LIVC4	0.0176	Ullujaya	Chilcatay	Liv C	17	Barnacle sheath

Table 8.1. List and description of the analyzed samples.

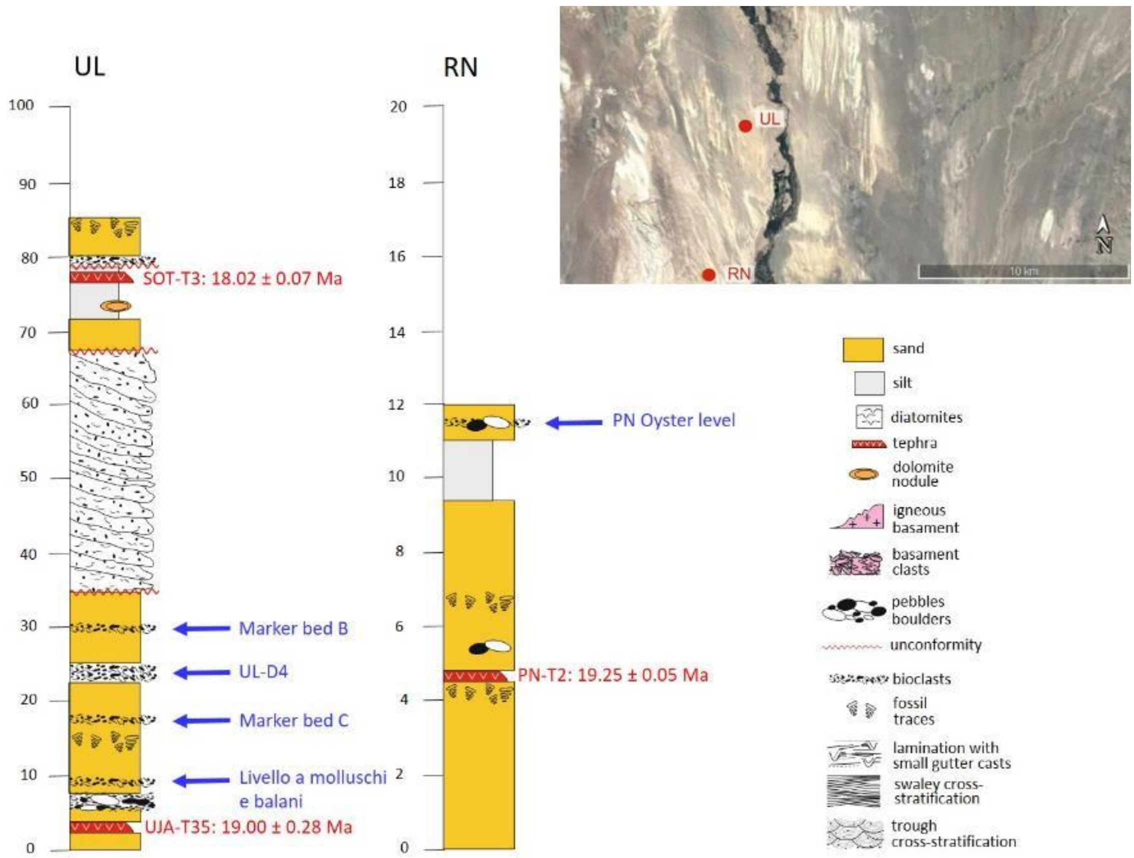

Figure 8.1. Simplified stratigraphic logs measured at the localities of Ullujaya and Roca Negra, and detail of the satellite map showing the locality geographical position. ^{39}Ar–^{40}Ar ages on tephra are shown in red, whereas levels selected for Strontium Isotope Stratigraphy are shown in blue.

Twelve samples were selected for the locality of Ullujaya (see Fig. 8.1), all in the *Ct1a* facies association, where the base below the measured section is dated at 19.00 ± 0.28 Ma by dating tephra UJA-T35 (represented in the section in Fig. 8.1 for simplicity) and the top of the formation is dated at 18.02 ± 0.07 Ma (SOT-T3, see Chapter 7). Three samples were chosen for the level at 9 m abs, here informally named “Livello a molluschi e balani” (Fig. 8.1): UL-LIVa, from a barnacle sheath, usually the non-porous and best preserved part in a barnacle; UL-LIVb, from two specimens of pectinids; and UL-LIVc, entirely from one pectinid. At 17 m abs, in the marker bed C (Fig. 8.1), four samples were selected for Sr-isotope analyses: one from the nacre part of an oyster (UJA-LIVC1); the second one is a bulk cemented in the outer part of another oyster (UJA-LIVC2); the third is from the same oyster, the nacre portion (UJA-LIVC3); and the last one is from a barnacle sheath (UJA-LIVC4). Three samples were selected for the UL-D4 level (Fig. 8.1), a layer enriched in carbonates at 25 m abs: UL-D4a, from an oyster with nacre layers; UL-D4b, from a barnacle sheath; UL-D4c, the bulk with diagenetic cement inside the barnacle. Finally, two samples were drilled from the same oyster of the marker bed B (Fig. 8.1) (i.e. UJA-2a and UJA-2b), at 30 m above the base of the section (abbreviated: abs); the first is from a light gray nacre level, the second one is from a darker nacre level.

The complete measured sections of both the localities are shown in the Appendix.

$^{87}Sr/^{86}Sr$ analyses, made at the Institute für Geologie, Mineralogie und Geophysik of the Ruhr-Universität of Bochum, gave the results shown in Table 8.2. We chose the results of $^{87}Sr/^{86}Sr$ sample corrected to difference: USGS EN-1 value McArthur and USGS EN-1 Bochum mean value. Then, we used the LOWESS Table 5 made for the GTS2012 timescale (McArthur et al. 2012), given by Professor John M. McArthur, for calculating the corresponding ages.

The LOWESS Table 5 is still incomplete, therefore the mean results were rounded off to the closest value and the values ± 2σ were rounded off overestimating the age error. Because of the uncertainty (± 2σ), we obtained three different age for each analysis: the preferred age, the minimum and the maximum (see Table 8.3).

#	sample name or number	$^{87}Sr/^{86}Sr$ measured	± 2 S $_{mean}$	$^{87}Sr/^{86}Sr_{sample}$ corrected to difference: NBS 987 value McArthur and NBS 987 measured with sample	$^{87}Sr/^{86}Sr_{sample}$ corrected to difference: USGS EN-1 value McArthur and USGS EN-1 measured with sample	$^{87}Sr/^{86}Sr$ sample corrected to difference: NBS 987 value McArthur and NBS 987 Bochum mean value	$^{87}Sr/^{86}Sr_{sample}$ corrected to difference: USGS EN-1 value McArthur and USGS EN-1 Bochum mean value
1	NIST NBS 987	0.710252	0.000006	0.710247	0.710254	0.710258	0.710268
2	PN-OST	0.708498	0.000005	0.708493	0.708500	0.708504	0.708514
3	PN-GI01	0.708513	0.000007	0.708508	0.708515	0.708519	0.708529
4	PN-GI02	0.708536	0.000005	0.708531	0.708538	0.708542	0.708552
6	UJA-2a	0.708541	0.000005	0.708536	0.708543	0.708547	0.708557
7	UJA-2b	0.708523	0.000005	0.708518	0.708525	0.708529	0.708539
8	UL-D4a	0.708506	0.000004	0.708501	0.708508	0.708512	0.708522
9	UL-D4b	0.708617	0.000005	0.708612	0.708619	0.708623	0.708633
10	UL-D4c	0.708444	0.000005	0.708439	0.708446	0.708450	0.708460
11	UL-LIVa	0.708516	0.000005	0.708511	0.708518	0.708522	0.708532
12	UL-LIVb	0.708512	0.000005	0.708507	0.708514	0.708518	0.708528
13	USGS EN-1	0.709173	0.000005	0.709168	0.709175	0.709179	0.709189
14	NIST NBS 987	0.710235	0.000005	0.710247	0.710250	0.710241	0.710251
15	UL-LIVd	0.708514	0.000005	0.708526	0.708529	0.708520	0.708530
16	UJA-LIVC1	0.708535	0.000005	0.708547	0.708550	0.708541	0.708551
17	UJA-LIVC2	0.708340	0.000005	0.708352	0.708355	0.708346	0.708356
18	UJA-LIVC3	0.708542	0.000005	0.708554	0.708557	0.708548	0.708558
19	UJA-LIVC4	0.708521	0.000005	0.708533	0.708536	0.708527	0.708537
20	SUB-5	0.708804	0.000005	0.708816	0.708819	0.708810	0.708820
21	SUB-2	0.708557	0.000005	0.708569	0.708572	0.708563	0.708573
22	USGS EN-1	0.709160	0.000005	0.709172	0.709175	0.709166	0.709176
23	NIST NBS 987	0.710244	0.000005	0.710247	0.710252	0.710250	0.710260
24	SUB-8bis1	0.708811	0.000005	0.708814	0.708819	0.708817	0.708827
25	SUB-8bis2	0.708273	0.000005	0.708276	0.708281	0.708279	0.708289
26	SUB-8bis3	0.708650	0.000005	0.708653	0.708658	0.708656	0.708666
27	Dente1	0.708803	0.000005	0.708806	0.708811	0.708809	0.708819
28	Dente2	0.708778	0.000005	0.708781	0.708786	0.708784	0.708794
29	Dente3	0.708784	0.000005	0.708787	0.708792	0.708790	0.708800
32	USGS EN-1	0.709167	0.000005	0.709170	0.709175	0.709173	0.709183

Table 8.2. Rough $^{87}Sr/^{86}Sr$ results of both Chilcatay Formation and P0 allomember analyzed samples.

The age results, shown in Table 8.3, confirm a Burdigalian age for the Chilcatay Formation, at both Roca Negra and Ullujaya.

At Roca Negra, the calculated age range for the oyster PN-OST is from 18.55 to 18.85 Ma, with a preferred age of 18.70 Ma. PN-GIO1 has a range between 18.35 to 18.70 Ma, with a preferred age of 18.50 Ma and PN-GIO2 gives a minimum age of 18.10 Ma and a maximum age of 18.40 Ma. Therefore, the entire oyster level age range is from 18.10 to 18.85 Ma, with a mean preferred age of 18.48 Ma, in agreement with the older ages of 19.25 Ma at the base of the measured section at Roca Negra about ten meters below.

At Ullujaya, in the lower level, “Livello a molluschi e balani”, the barnacle sample UL-LIVa gives a minimum age of 18.30 Ma and a maximum age of 18.65 Ma, with a preferred age of 18.50. Accordingly, the pectinid samples UL-LIVb and UL-LIVd give a preferred age of 18.50 Ma and an age range from 18.35 to 18.70 Ma and from 18.35 to 18.65 Ma, respectively. This level can be dated at 18.50 Ma as preferred age, with a range between 18.30 and 18.70 Ma.

At 17 m abs, the considered samples are: the oyster sample UJA-LIVC1, giving a preferred age of 18.25 Ma and an age range between 18.10 and 18.40 Ma; the oyster UJA-LIVC3, with a preferred age of 18.20 Ma and a range from 18.05 to 18.35 Ma; the barnacle sample UJA-LIVC4, with an age from 18.25 to 18.60 Ma. The sample UJA-LIVC2 was a bulk sample of the level that shows a lower value of $^{87}Sr/^{86}Sr$ ratio and gives older ages, suggesting an ageing caused by diagenesis. The age range of the marker bed C is between 18.05 and 18.60 Ma, with a preferred age of 18.28 Ma; considering the oldest UJA-LIVC4 as aged by diagenesis, the final age of the level can be 18.22 Ma, with a range from 18.05 and 18.40 Ma.

Going up in the measured section, in the UL-D4 level (25 m abs), the oyster sample UL-D4a gives a preferred age of 18.60 Ma, with a minimum age of 18.45 Ma and a maximum age of 18.75 Ma. The barnacle sample UL-D4b, instead, has a surprisingly young age of 17.25 Ma, with an age range between 17.10 and 17.40 Ma. The bulk sample, UL-D4c, shows a lower $^{87}Sr/^{86}Sr$ value and an older age, indicating that diagenesis has an ageing effect on the shells. So, the young age of the barnacle sheath is not explained with the diagenesis effect. Because the ages of the two samples from the same level are very different, we must choose one of the two specimens, because the mean of the preferred ages, 17.92 Ma, is not the proper age. The ages of the oyster UL-D4a are probably the most reliable ages, because the high-Mg calcite of barnacles is more instable than the low-Mg calcite of oysters, despite some filled cavities that characterized this oyster (see Chapter 15). The fact that has an older age than the underlying samples is probably due to the diagenesis effect that decreased the $^{87}Sr/^{86}Sr$ original value of the shell.

Finally, in the upper level of the *Ct1a* faces, the marker bed B (30 m abs), the two oyster samples UJA-2a and UJA-2b give similar preferred ages of 18.20 and 18.40 Ma respectively, with age ranges from 18.05 to 18.35 Ma and from 18.25 to 18.55 Ma. The mean preferred age for this level is 18.30 Ma, with a minimum age of 18.05 and a maximum age of 18.55 Ma.

Samples	**plus 2σ**	**$^{87}Sr/^{86}Sr$ corrected value**	**minus 2σ**	**Min age (Ma)**	**Preferred age (Ma)**	**Max age (Ma)**
PN-OST	0.708519	0.708514	0.708509	18.55	**18.70**	18.85
PN-GI01	0.708536	0.708529	0.708522	18.35	**18.50**	18.70
PN-GI02	0.708557	0.708552	0.708547	18.10	**18.25**	18.40
UJA-2a	0.708562	0.708557	0.708552	18.05	**18.20**	18.35
UJA-2b	0.708544	0.708539	0.708534	18.25	**18.40**	18.55
UL-D4a	0.708526	0.708522	0.708518	18.45	**18.60**	18.75
UL-D4b	0.708638	0.708633	0.708628	17.10	**17.25**	17.40
UL-D4c	0.708465	0.708460	0.708455	19.20	19.35	19.60
UL-LIVa	0.708537	0.708532	0.708527	18.30	**18.50**	18.65
UL-LIVb	0.708533	0.708528	0.708523	18.35	**18.50**	18.70
UL-LIVd	0.708535	0.708530	0.708525	18.35	**18.50**	18.65
UJA-LIVC1	0.708556	0.708551	0.708546	18.10	**18.25**	18.40
UJA-LIVC2	0.708361	0.708356	0.708351	21.00	21.25	21.45
UJA-LIVC3	0.708563	0.708558	0.708553	18.05	**18.20**	18.35
UJA-LIVC4	0.708542	0.708537	0.708532	18.25	**18.40**	18.60

Table 8.3. Sr-isotope ages obtained for each sample of the Chilcatay Formation. Cells in grey reported the selected reliable final ages.

All these Burdigalian ages are perfectly in agreement with the ^{39}Ar–^{40}Ar ages of tephra and with the biostratigraphy results gave by diatoms and silicoflagellates for the localities of Ullujaya and Roca Negra. A Burdigalian age between 19.25 and 18.02 Ma is therefore confirmed for the Chilcatay Formation in the western side of the Ica River.

This chapter is entirely unreleased. Results will be discussed and published, in the next future, in the paper "Strontium Isotope Stratigraphy of the Miocene sedimentary successions in the Peruvian East Pisco Basin" in preparation.

Chapter References

Brand, U., Jiang, G., Azmy, K., Bishop, J., Montanez, I.P. 2012. Diagenetic evaluation of a Pennsylvanian carbonate succession (Bird Spring Formation, Arrow Canyon, Nevada, U.S.A.) — 1: Brachiopod and whole rock comparison. Chemical Geology 308-309, 26-39.

Faure, G., Mensing, T.M. 2005. Isotopes: Principles and Applications. Ed: John Wiley & Sons, New York.

McArthur, J.M., Howarth, R.J., Shields, G.A. 2012. Strontium Isotope Stratigraphy. In F.M. Gradstein, J.G. Ogg, Schmitz M., Ogg G. (Eds.), The Geologic Time Scale 2012 (Chapter 7, pp. 127-144). Elsevier.

Scasso, R.A., McArthur, J.M., del Río, C.J., Martínez, S., Thirlwall, M.F. 2001. 87Sr/86Sr Late Miocene age of fossil molluscs in the "Entrerriense" of the Valdés Peninsula (Chubut, Argentina). Journal of South American Earth Sciences, 14, 319-329.

Ullmann, C.V., Korte, C. 2015. Diagenetic alteration in low-Mg calcite from macrofossils: a review. Geological Quarterly, 59(1), 3-20.

Chapter 9. Stratigraphy and paleoecology of the Pisco Formation in the western side of the Ica River

The study area where the Pisco Formation crops out is an area of approximately 300 km^2 that stretches for 22 km along the western side of the Ica River, from Cerro Blanco in the north, to Cerros las Tres Piramides in the south (Fig.9.1). Thanks to the stratigraphic investigations, a geological map was built (Fig. 9.2).

Within the study area, the slightly-deformed and richly fossiliferous Pisco Formation forms a northeastward dipping monocline possibly developed in response to subduction of the Nazca Ridge beneath the region during the Quaternary (Hampel 2002).

Integration of several partial stratigraphic sections indicates that the composite thickness of the Pisco Formation in the study area is about 470 m. Owing to lateral thickness and facies variations and the limited capacity of lithostratigraphic mapping to reveal the genetic and depositional history of the Pisco Formation, field mapping has been carried out through the construction of a detailed allostratigraphic framework measuring stratigraphic sections in several localities (see the Appendix for the detailed logs).

Based on the occurrence of three widespread erosional surfaces, designated PE0.0, PE0.1, and PE0.2 from oldest to youngest, the strata can be subdivided into three genetic packages (allomembers) that have been named P0, P1, and P2 for their lower bounding surface (see Fig. 9.3). These three unconformities converge and merge landwards into a single surface (informally referred to as PE0) representing the composite lower boundary of the Pisco Formation.

Strata between successive unconformities exhibit a deepening-upward, transgressive trend, in which deep facies associations step up over shallow facies associations. Regressive facies successions are lacking, either because regression was non-depositional or because regressive deposits were eroded during the phase of subaerial exposure and/or during the transgression. Sequence bounding unconformities are of basinal extent and indicate abrupt seaward shifts in facies (Fig. 9.2a). These surfaces are commonly demarcated by a *Glossifungites* ichnofacies (Fig. 9.2b, c) dominated by *Thalassinoides* and flask-shaped *Gastrochaenolites* that are excavated into a semiconsolidated (firmground) substrate and reflect a break in sedimentation, generally accompanied by erosion (Pemberton et al. 1995).

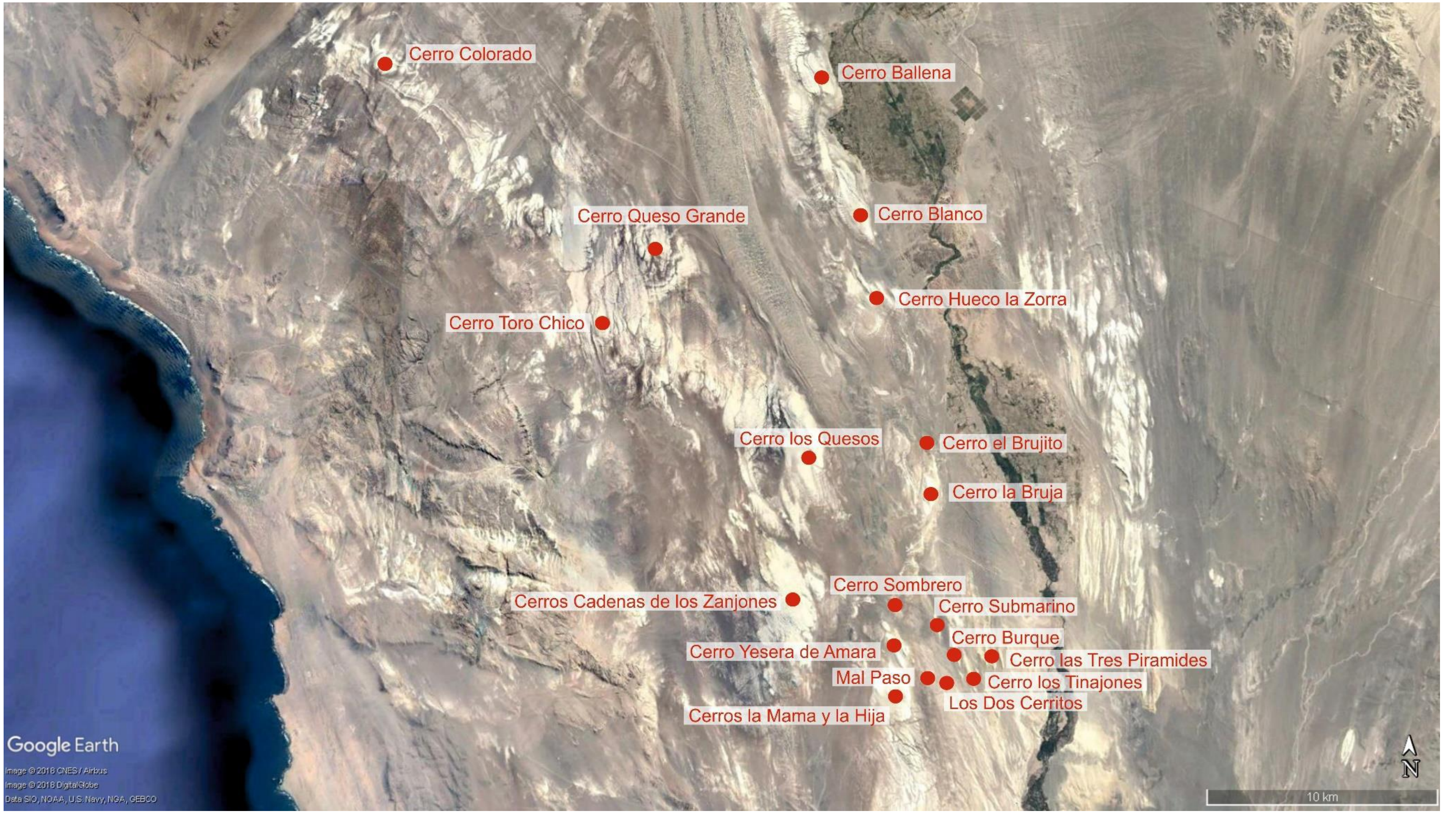

Figure 9.1. Satellite image of the Ica Desert localities where the Pisco Formation crops out. Based on image © 2018 DigitalGlobe.

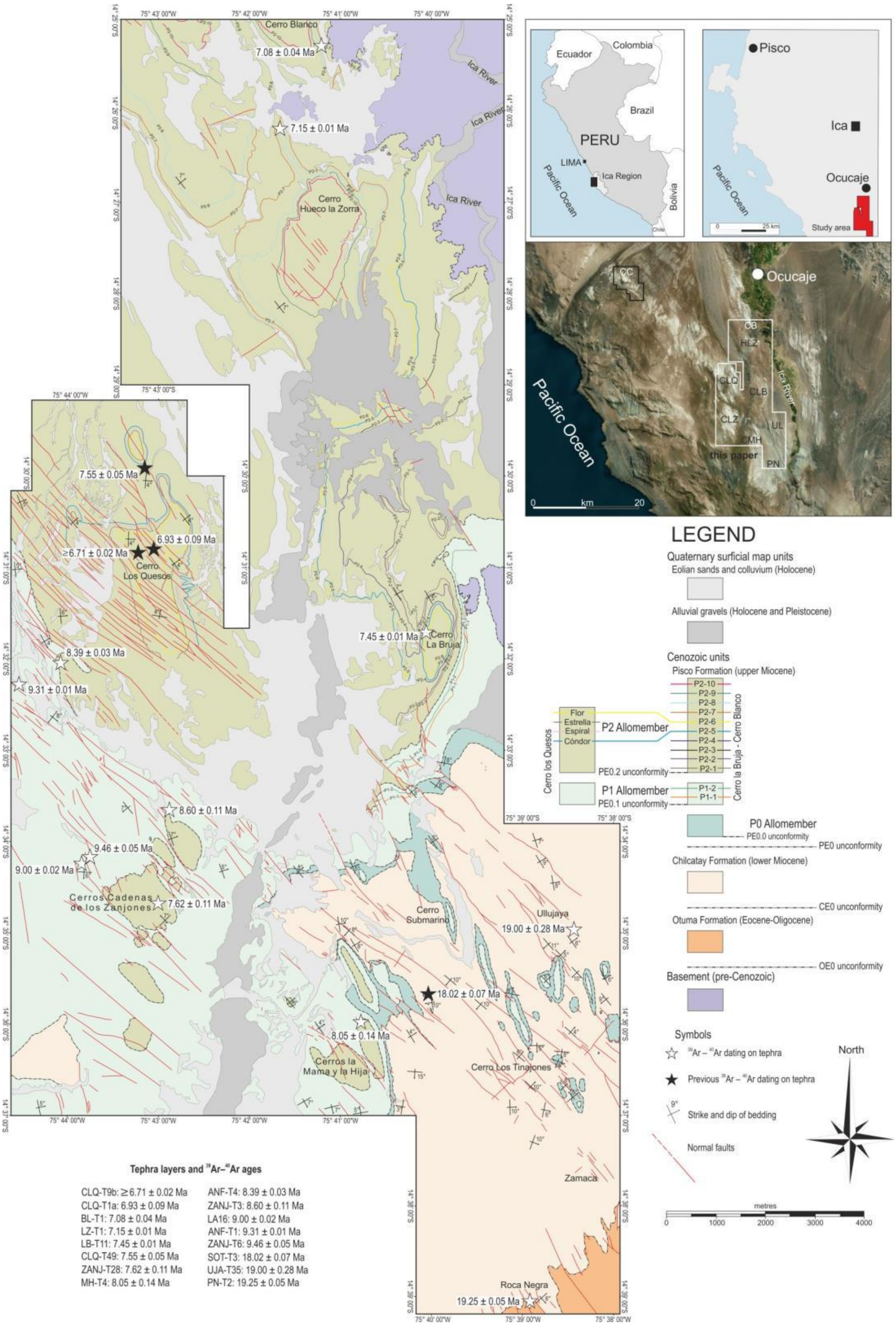

Figure 9.2. Geological map of the western side of the Ica River. The Google Earth image shows the present study area (white frame) and location of the four stratigraphic sections measured at Cerro las Tres Piramides (CTP), Cadenas de los Zanjones (CZ), Cerro La Bruja (CLB), and Cerro Blanco (CB). The areas in the black frame (Cerro

Colorado, CC) and in the red frame (Cerro los Quesos, CLQ) have been mapped by Di Celma et al. (2016b) and Di Celma et al. (2016a), respectively. The composite map is from Di Celma et al. (2017).

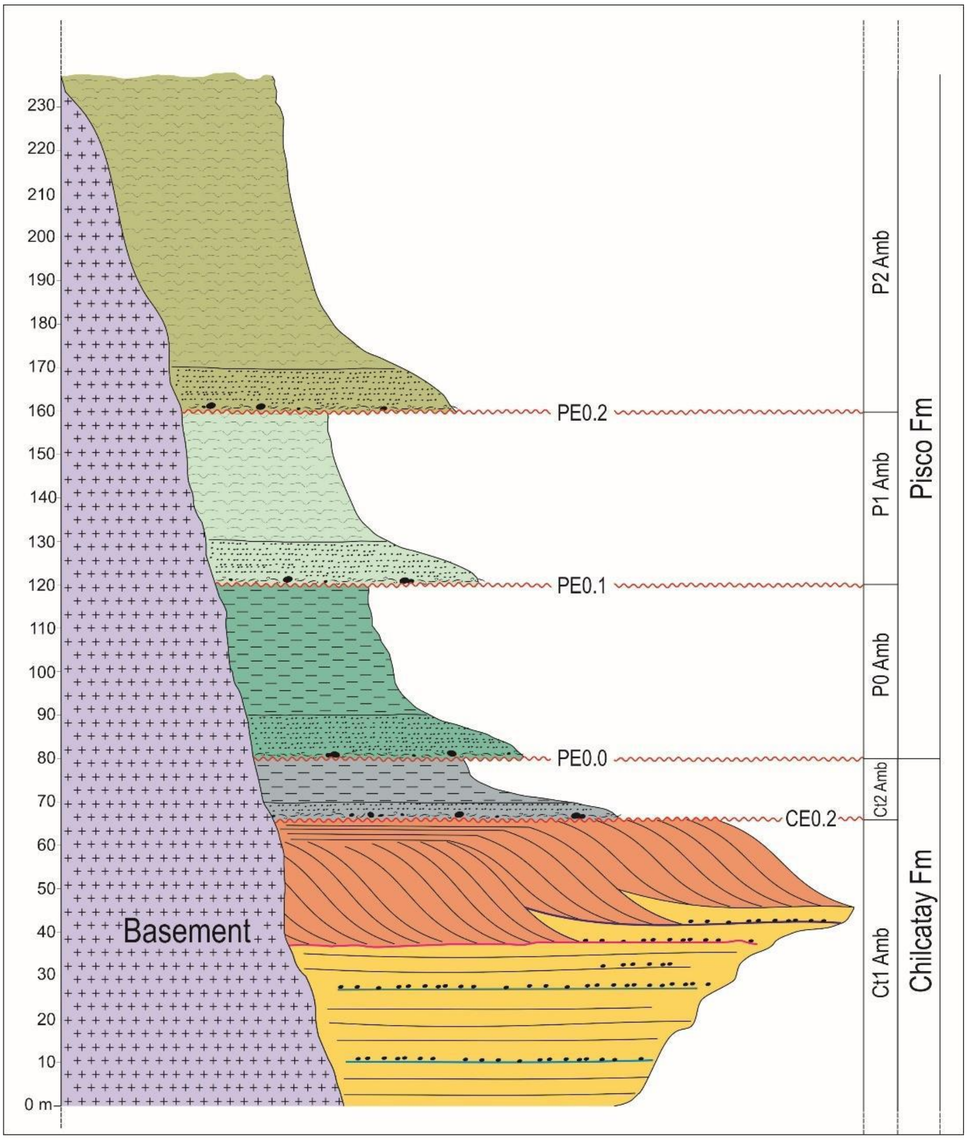

Figure 9.3. Schematic stratigraphic section of Pisco Formation and adjacent rocks. For simplicity, erosion surfaces have been designated “E” with a preceding letter indicating the relevant formation (C = Chilcatay, P = Pisco) and numbers designating successively higher stratigraphic surfaces. Accordingly, PE0.0, PE0.1, PE0.2 indicate successively younger erosion surfaces in the Pisco Formation. These three unconformities converge and merge landward into a single surface (informally referred to as PE0) representing the composite lower boundary of the Pisco Formation. The resulting allomembers (Amb) have been named for their lower bounding surface. Thus, the P0 allomember

refers to strata lying between the PE0.0 unconformity and the next higher unconformity (PE0.1). The vertical scale is only indicative of thickness of sediment packages between unconformity surfaces. From Di Celma et al. (2018).

The *Glossifungites*-demarcated erosional discontinuities are mantled by coarse grained, relatively thin (up to 0.4 m thick) intervals including a variable mixture of pebble- to boulder size lithic clasts, pebble-sized phosphatic nodules, cobble-sized dolomite clasts showing bivalve borings, internal molds of gastropods and articulated bivalves, shark teeth, polished bone fragments, and partially articulated skeletons of marine mammals (Fig. 9.4). This coarse-grained facies rests below deposits indicative of marine flooding and above a surface indicating abrupt seaward shift in facies and, therefore, it is regarded as a transgressive lag representing erosion and low net sedimentation rates during shoreface retreat (e.g., Grimm 2000; Boessenecker et al. 2014; Föllmi 2016). A subaerial origin for the basal unconformities is also corroborated by the presence of basement clasts, which were probably introduced into the basin during periods of lowered sea level and reworked by waves and currents during subsequent marine transgression.

The transgressive lag is directly overlain by a sand rich unit comprising yellow-weathering, fine- to very fine-grained sandstones and coarse siltstones that are typically moderately to highly bioturbated and, locally, showing unidirectional cross-bedding, swaley cross-stratification, and wave ripples. Vertebrate material is locally abundant and includes disarticulated to partially articulated marine mammal skeletons. The array of primary sedimentary structures represents unidirectional- or combined-low erosion and waning oscillatory low and indicates lower shoreface deposition above fair-weather wave base. The diatomaceous mudstones consist of finely laminated gray-white diatomite, rich in planktonic diatoms characteristic of a highly productive marine environment. Subordinate lithologies include volcanic ash layers, dolomitized mudstone horizons, and thin, fine- to medium-grained sandstone beds. These sediments are sparsely fossiliferous and vertebrate fossils vary in preservation from disarticulated to fully articulated skeletons. Macroinvertebrate body fossils are rare and usually limited to internal molds lacking calcium carbonate skeletal material. The diatomaceous mudstones are reflective of deposition from suspension of organic-rich mud in a low-energy offshore shelf environment.

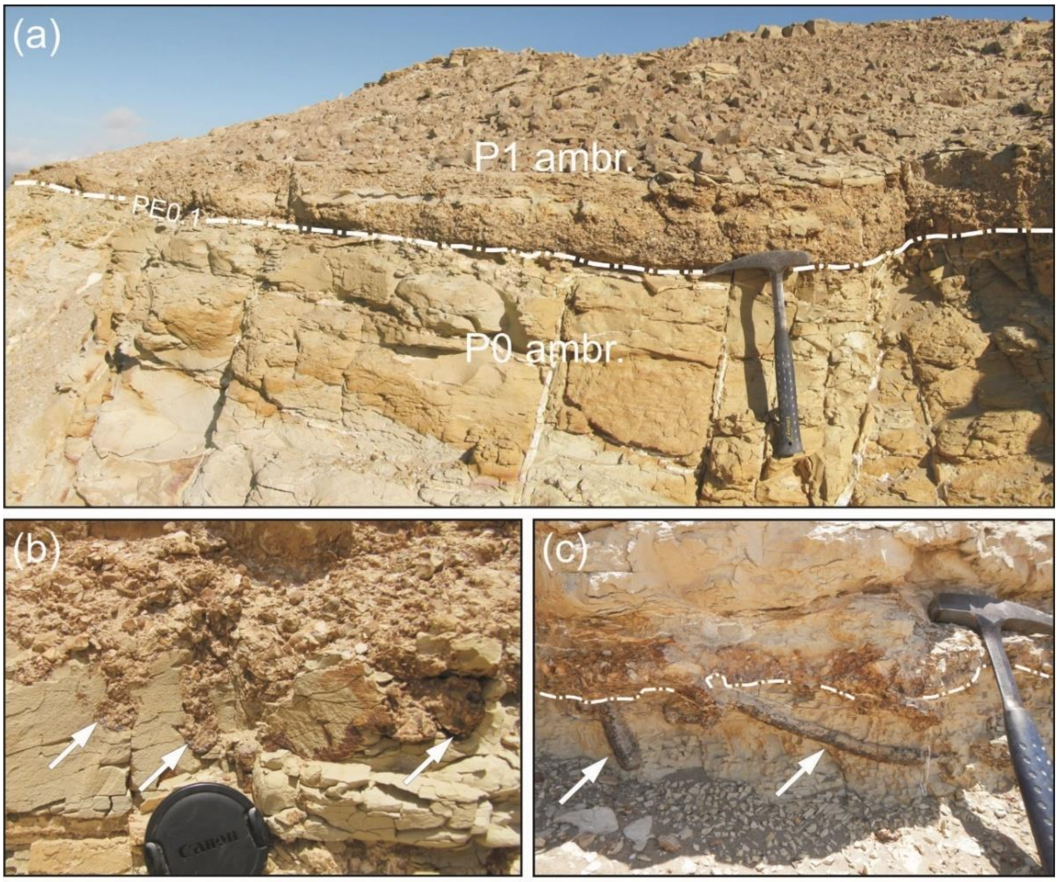

Figure 9.4. Details of the intraformational unconformities. A lens cap (6.5 cm in diameter) and a hammer (0.3 m long) are used for scale. a) Outcrop photograph of PE0.1 at Cerro las Tres Piramides (14°35'15"S - 75°38'38"W). This surface is overlain by a lag comprised of rounded phosphate and igneous pebbles, reworked shells, and bones. b) The surface itself is generally sharp and undulating, bored and penetrated by robust *Thalassinoides* burrows (arrowed), which pipe dark phosphate pebbles of the P1 allomember for 0.3 m into the underlying P0 allomember. c) Detail of PE0.0 (14°35'41"S - 75°40'5"W) showing inclined, smooth-walled *Thalassinoides* shafts weathering out in positive relief (arrowed) and passively filled with granular phosphorite infiltrated from the overlying pebble lag. From Di Celma et al. (2017).

Facies composition of a single allomember changes predictably up depositional dip, so that when traced towards the northeast, the offshore diatomaceous mudstones grade laterally into a sandstone-dominated succession comprising abundant swaley cross-stratification and unidirectional cross-bedding with occasional phosphate pebble beds overlying sharp, gutter-casted erosion surfaces. This assemblage of sedimentary structures is indicative of deposition in a shoreface setting strongly influenced by storms (Leckie & Walker 1982; Chiocci & Clifton 1991; Myrow 1992). As a consequence, the bounding unconformities that in more distal areas are demarcated by abrupt basinward shift of facies, become subtle sand-on-sand contacts in more proximal areas.

9.1. P0 allomember

Sediments of the P0 allomember are best exposed in the southeastern corner of the mapped area, where they crop out in the lower half of a series of small, isolated cerros or hills (namely, Cerro Yesera de Amara, Cerro Submarino, Cerro Buque, Cerro las Tres Piramides, Cerros los Tinajones, Los Dos Cerritos, Fig. 9.1) and rest with angular unconformity on variably deformed rocks of the Chilcatay Formation (Fig. 9.5a). At Mal Paso, immediately to the southeast of Cerro Yesera de Amara, the PE0.0 basal unconformity is characterized by truncation of the underlying strata and is marked by a prominent marine transgressive surface indicated as the M1 marker bed by Brand et al. (2011). In this area, however, our correlation of the P0 outcrop belt differs somewhat from that proposed by Brand et al. (2011). At Cerro Submarino and Cerro Buque these authors correlated our PE0.0 surface to their similar, but stratigraphically higher, M2 stratigraphic marker. We argue that the interpretation proposed by Brand et al. (2011) should be revised and that at these two localities the M2 marker defined by Brand et al. (2011) at the base of the hills is, in fact, their M1 marker (PE0.0 surface in our terminology).

This unit is strongly wedge-shaped, thinning from 40 m in the southeastern portion of the study area (Cerro las Tres Piramides, Fig. 9.5a), to a zero-edge in the vicinity of Cerro la Bruja over approximately 6 km. Rather than elimination at the top by erosion, it seems more likely that the primary reason for gross stratal thinning is progressive onlap and loss of successively younger beds at the base. Between Cerro las Tres Piramides and Cerro la Bruja this unit also shows pronounced lateral facies changes with offshore mudstones dominating the unit in the south rapidly replaced northwards by fine- to very coarse grained, cross-stratified, fossil-rich nearshore calcarenites.

The vertebrate content of this unit is less well known than that from P1 and P2 and most of the observations come from the on-going study of three localities (Mal Paso, Yesera de Amara and north of Cerro Submarino). Mysticetes (baleen bearing whales) are common and represented by at least three species: a large-sized stem balaenopteroid

(Balaenopteroidea, rorquals and relatives) similar to *Pelocetus*, a smaller *Parietobalaena*-like form, and a rare cetotheriid (Cetotheriidae) that shares some similarities with the species recognized in P1 (see below). Odontocetes (toothed whales) consist of a few specimens belonging to at least one physeteroid species and two kentriodontid-like delphinidan species. A single indeterminate pelagornithid skeleton is the only bird specimen found up to now. Fragmentary remains attributed to chelonioid sea turtles and long-snouted crocodylians are also recorded. Shark tooth-rich horizons have not been recognized to date, nevertheless, teeth attributed to the giant mega-toothed shark *Carcharocles megalodon* and to *Cosmopolitodus hastalis* occur in this unit along with abundant remains of Myliobatiformes (including the eagle ray *Myliobatis*). Moreover, teeth belonging to the extinct snaggletooth shark *Hemipristis serra* are relatively common in P0; this fossil shark species is present in the underlying deposits of the Chilcatay Formation, whereas it is absent from the younger P1 and P2 allomembers. Several associated rostral spines of a pristid sawish were also collected from strata belonging to the P0 allomember.

9.2. P1 allomember

This allomember is bounded by PE0.1 at the base and PE0.2 at the top (Fig. 9.5a, b). The PE0.1 basal surface has been indicated as the M2 marker by Brand et al. (2011) and can be traced from the south (Cerro Yesera de Amara, Cerro Submarino, Cerro Buque, Cerro las Tres Piramides, Cerro los Tinajones, Cerros la Mama y la Hija) to the central part of the study area, near the southern end of the lower slopes of Cerro el Brujito (see Fig. 9.1). The P1 allomember attains a maximum thickness of about 80 m in the southwest (Cerros Cadenas de los Zanjones) and thins towards northeast to about 40 m at Cerro la Bruja, beyond which it is supposed to pinch out by progressive onlap onto basement rocks.

The vertebrate content of this highly fossiliferous unit is known from various localities of the Ica Desert, including Cerro Colorado outside of the study area (“lower allomember” of Di Celma et al. 2016b; Bianucci et al. 2016c) and Cerro la Bruja and Cerros Cadenas de los Zanjones within it. A significant fraction of the vertebrates detected in this unit is found enclosed in more or less developed dolomite concretions (Gariboldi et al. 2015). Mysticetes are abundant and consist of several skeletons belonging to an undescribed large-sized cetotheriid species, and of a few other remains belonging to two indeterminate balaenopterid species (Collareta et al. 2015; Gioncada et al. 2016).

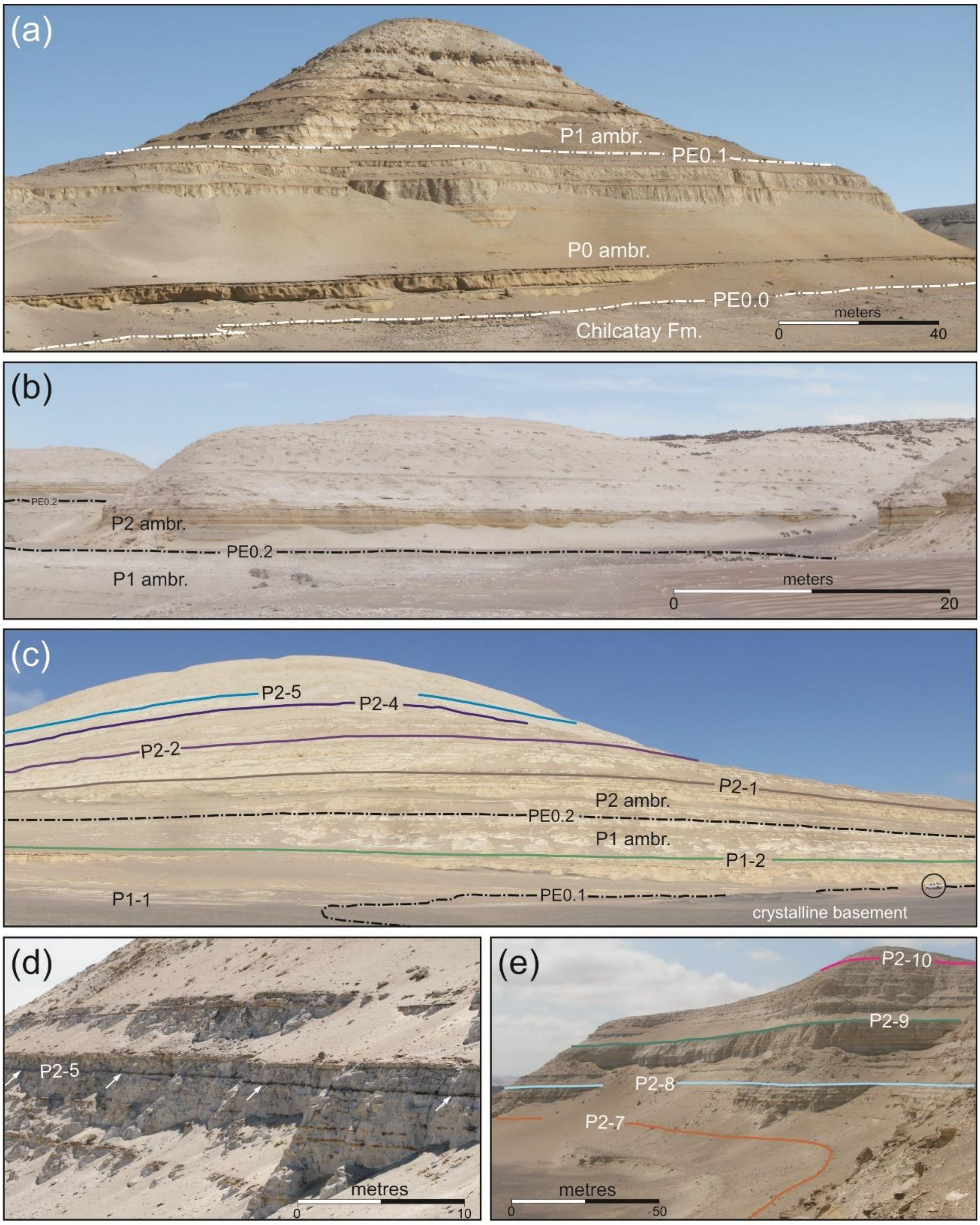

Figure 9.5. Outcrop photos showing some of the marker beds and the three key surfaces that have been mapped in the study area. The three erosive surfaces, referred to as PE0.0, PE0.1, and PE0.2 in ascending order, are readily recognizable in the field based on a seaward shift in facies from outer shelf diatomaceous mudstones to nearshore sandstones. a) Panoramic view of the Cerro las Tres Piramides section (14°35’30”S - 75°38’45”W), near the southeastern end of the study area, showing two Pisco

allomembers (namely P0 and P1) and their two bounding surfaces (PE0.0 and PE0.1). View is to the south. Note that the basal sand-rich units of the two allomembers pass conformably upsection into finer-grained diatomaceous siltstones marking deepening from the underlying nearshore facies into offshore facies. b) View of the contact between the P1 and P2 allomembers at Cerros Cadenas de los Zanjones (14°34’55”S - 75°42’56”W). Diatomaceous mudstones form gentle slopes whereas thick resistant sandstones at the base of the P2 allomember form a wide ledge and a vertical cliff between the slopes. c) Panoramic view of the eastern side of Cerro la Bruja (14°31’55”S - 75°39’46”W); circled car for scale. Here, the P1-1 marker bed is on the valley floor and onlaps the crystalline basement, whereas the P1-2 forms a prominent ledge at the base of the cliff. The PE0.2 bounding surface is at the base of the yellowish, cliff-forming basal sandstone unit correlative of “La Bruja vertebrate level”. The P2-1 marker bed is the uppermost of a set of visually distinct brown very fine-grained sandstones alternating with softer siltstones (M3 marker bed of Brand et al. 2011). The P2-2 marker bed forms a wide terrace-like ledge at the northern end of Cerro la Bruja (14°31’17”S - 75°39’50”W). At this site, P0 is not present, having lapped out northwards onto surface PE0.0. Traced northeastward, P2 oversteps P1 strata thinning and onlapping onto crystalline basement. d) Close view of the western side of Cerro la Bruja (14°31’39”S - 75°40’1”W) showing the P2-5 marker bed (arrowed), a characteristic blackish vitric tuff with soft-sediment deformed laminae. e) Panoramic view showing some of the marker beds traced along the cliff-slope profile of the eastern side of Cerro Hueco la Zorra (14°26’40”S - 75°41’20”W). The P2-8 marker bed (M 10 of Brand et al. 2011) is about 0.5 m thick and includes a phosphate pebble bed overlain by a relatively resistant, ledge-forming, thinly-bedded sandstone. Both P2-9 and P2-10 are prominent and laterally continuous ledges at the top of sheer cliff faces. From Di Celma et al. (2017).

Among the odontocetes, the stem physeteroids include the holotype and only known specimen of the giant raptorial sperm whale *Livyatan melvillei* and several *Acrophyseter*-like specimens (Lambert et al. 2010a; Lambert et al. 2017; pers. obs). The ziphiids (beaked whales) are represented by two stem species: the very common *Messapicetus gregarious* and *Chimuziphius coloradensis* (only known for the holotype skull) (Bianucci et al. 2010, 2016a; Lambert et al. 2010b). Delphinidans consist of two pontoporiids (the abundant *Brachydelphis mazeasi* and a less common, undescribed species somewhat resembling *Pliopontos littoralis*), one inioid (*Brujadelphis ankylorostris*) known for a single specimen described by Lambert et al. (2017), and several specimens of kentriodontid-like delphinidans (belonging to at least two species). Birds are known from well-preserved skeletons referred to two medium- and large-sized sulids (boobies: *Sula brandi* and *S. figueroae*) and fragmentary remains referred to indeterminate phalacrocoracids (cormorants) and procellariids (Stucchi et al. 2016). The pancheloniid sea turtle *Pacifichelys urbinai* is represented by various well-preserved specimens (Parham & Pyenson 2010). Indeterminate crocodilian remains have also been recognized. Shark teeth are common all along the studied section, although they particularly concentrate in two intervals. The chondrichthyan assemblage is well diversified but dominated by Carcharhiniformes (mostly represented by teeth belonging to *Carcharhinus* spp.); Lamniformes (including the large species *Carcharocles megalodon* and *Cosmopolitodus hastalis*) and Myliobatiformes are also well represented, whereas pristids and squatinids are present but overly rare (Landini et al. 2017). Bony fish include ubiquitous cycloid scales referred to the Pacific pilchard *Sardinops* sp. cf. *S. sagax*; sciaenids drums), and scombrids (aff. *Thunnus* sp.) were also detected. Among the Ica Desert localities in which P1 strata are exposed, Cerro Colorado features some examples of exceptional fossil preservation, such as the stomach contents of two cetaceans (a specimen of *Messapicetus gregarius* and a medium-sized cetotheriid), revealing predation upon *Sardinops* (Collareta et al. 2015; Lambert et al. 2015), and the fossilized baleen of a balaenopteroid whale (Gioncada et al. 2016).

9.3. P2 allomember

The PE0.2 surface at the base of the P2 allomember is exposed from Cerros Cadenas de los Zanjones in the southwest (Fig. 9.5b), through Cerros la Mama y la Hija and Cerro Yesera de Amara in the south, to Cerro Blanco in the north. At Cerro La Bruja (Fig. 9.5c) the overlying, richly fossiliferous interval is sometimes referred to as the "La Bruja vertebrate level" (Muizon & DeVries 1985; Muizon 1988). Due to onlap and loss of successively younger beds at the base, P2 forms a northeastward-thinning wedge with a general dip of strata between 4° and 7° to the northeast. For mapping purposes, ten distinctive stratigraphic markers consisting of distinctively weathering units of varying lithology, informally designated P2-1 to P2-10, have been traced with reasonable confidence between Cerro la Bruja and Cerro Blanco (Fig. 9.5c, d, e). In this study, the P2-1, P2-7, and P2-8 marker beds correspond with M3, M9, and M10 of Brand et al. (2011), respectively. Lateral tracing of these marker beds shows that the shallow-water strata of the P2 allomember onlap an unconformity surface cut across the P1 allomember, which they overstep north of Cerro el Brujito to onlap onto basement crystalline rocks. The PE0.2 bounding surface can be traced into outcrop belts to the west (Cerro los Quesos) and northwest (Cerro Colorado) of the present study area, where detailed stratigraphic frameworks were already established by recent studies (Di Celma et al. 2016a, 2016b). At Cerro los Quesos, the PE0.2 unconformity can be traced into a prominent lithological contact documented by Di Celma et al. (2016a) at the 29 m level in their measured outcrop section, showing that the stratigraphic interval described in that study can be assigned to P1 and P2 allomembers. Similarly, at Cerro Colorado the PE0.2 surface is correlative with the prominent intraformational unconformity interposed between a "lower allomember" and an "upper allomember" that, accordingly, are stratigraphically equivalent to allomembers P1 and P2, respectively. This correlation is supported by biostratigraphic and radiometric dating.

The vertebrate content of this unit is known from various localities of the Ica Desert, including Cerro Colorado ("upper allomember" of Di Celma et al. 2016b; Bianucci et al. 2016c), Cerro los Quesos (members C-F of Di Celma et al. 2016b; Bianucci et al. 2016b), Cerro la Bruja ("La Bruja vertebrate level" of Muizon & DeVries 1985; Muizon 1988), Cerro Hueco la Zorra, Cerro Blanco, and Cerro Ballena (see Fig. 9.1). Some of the vertebrates detected in this unit are preserved within dolomite nodules, although this phenomenon is observed to a lesser extent than in the P1 allomember (Gariboldi et al. 2015). Mysticetes are represented by at least three medium- to large-sized species of balaenopterids including a form similar to extant *Megaptera* (humpback whale), and a diminutive cetotheriid (*Piscobalaena nana*). The toothed whales are well diversified. At least three different stem physeteroids are recognized thanks to a small number of specimens: *Acrophyseter robustus*, *Acrophyseter* sp., and an undescribed large-sized taxon (Muizon 1988; Lambert et al. 2014, 2017). *Scaphokogia* and a new *Scaphokogia*-like kogiid (pygmy sperm whale) are also present in this unit with a few skulls. Ziphiids are uncommon but include at least four different species (all known from single specimens): the holotypes of *Chavinziphius maxillocristatus* and *Nazcacetus urbinai*, plus two other unnamed species based on more fragmentary remains (Lambert et al. 2009;

Bianucci et al. 2016a, 2016b). Delphinidans are relatively common, including the pontoporiid *Brachydelphis mazeasi* (also present in P1; known from the P2 allomember thanks to few specimens found near the PE0.2 unconformity), a phocoenid (cf. *Lomacetus ginsburgi*), and two kentriodontid-like delphinidans (*Atocetus iquensis* and *Belonodelphis peruanus*) (Muizon 1988). Pinnipeds are also present with at least one indeterminate species of monachine phocid (Muizon 1988; pers. obs.), whose remains (including some complete skeletons) are very common near the base of P2. Among marine reptiles, a few specimens of a large undescribed chelonioid sea turtle and fragmentary remains referred to the gavialoid crocodylian aff. *Piscogavialis jugaliperforatus* have been detected. Birds are represented by a *Phalacrocorax*-like indeterminate cormorant; suliids and spheniscids (penguins) have also been reported (Muizon & DeVries 1985; Göhlich 2007; Stucchi 2007). Among the cartilaginous fish, *Carcharocles megalodon* and *Cosmopolitodus hastalis* are present besides a few other smaller sized species (including *Carcharhinus leucas* and *Myliobatis* sp.) (Muizon & DeVries 1985; Bianucci et al. 2016b; Landini et al. 2017). Remains of bony fish are also present in this unit; whereas most of them are still indeterminate, the presence of various well-preserved skulls of billfish (istiophorids and xiphiids) is remarkable (pers. obs.; Muizon & DeVries 1985). Cases of exceptional fossil preservation in the deposits referred to the P2 allomember include the phosphatized baleen of *Piscobalaena nana* (Marx et al. 2017).

9.4. The Pisco Formation stratigraphy and paleoecology

The recognition of three unconformity-bounded sediment units that can be correlated among different parts of the basin has been used to elucidate the allostratigraphic framework of the Pisco strata exposed in the study area. Viewed as a whole, the Pisco Formation comprises a wedge of sediment that thins to the northeast, a trend also apparent within each of the three component allomembers (Fig. 9.6). These unconformity-bounded sediment packages, representing landward-stepping retrogradational events, onlap onto the underlying Chilcatay strata and basement rocks and progressively overstep them from southwest to northeast. Consequently, the basal contact of the Pisco Formation is an angular unconformity where it overlies older sediments of the Chilcatay Formation, or a nonconformity where it rests on crystalline basement rocks.

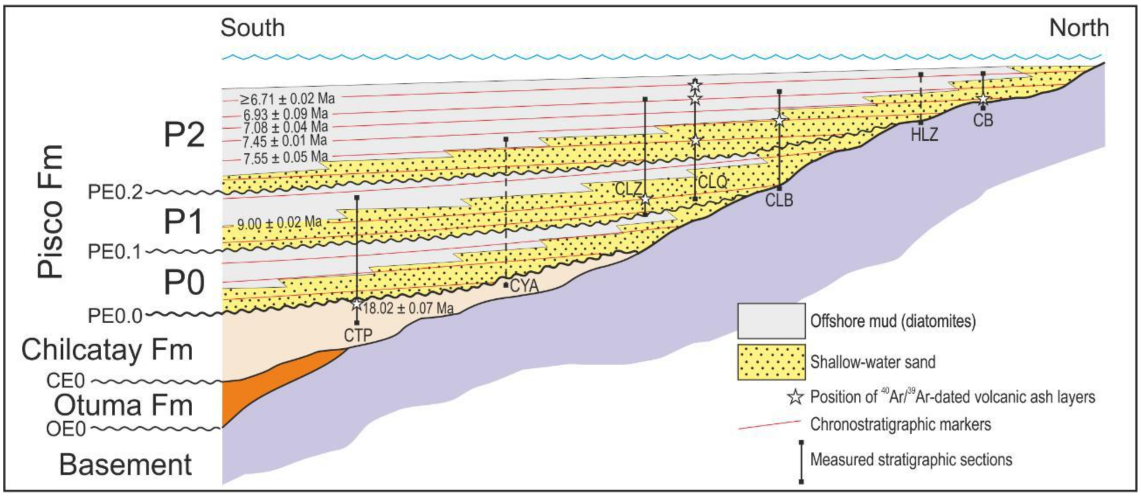

Figure 9.6. Schematic, dip-oriented stratigraphic diagram for the Pisco Formation (not in scale) showing the position of the stratigraphic sections on which the diagram is based (vertical black lines). The Pisco Formation exhibits pronounced thinning to the northeast with component sequences onlapping onto the basal composite surface PE0 and arranged in a retrogradational pattern, progressively offset to the northeast. The marine erosion surfaces that bound Pisco allomembers, namely PE0.0, PE0.1, and PE0.2, formed as a result of wave erosion in a transgressing shoreline following sea-level lowstand, and in consequence will be close to planar, and inclined slightly seaward. Red lines indicate chronostratigraphic markers (e.g., volcanic ash layers). Modified from Di Celma et al. (2017).

Our survey for fossil vertebrates outlines the outstanding paleontological value of the Pisco Formation, which stands out among Neogene marine deposits worldwide as a true Fossil-Lagerstätte. As reported above, the vertebrate content of P0 is still scarcely known; nevertheless, based on our preliminary investigations, it clearly differs from that of the overlying P1 allomember, especially with regard to the cetacean assemblage. In P1, baleen-bearing whales are mainly represented by medium-sized cetotheriids, whereas larger balaenopterids are much less abundant; in contrast, in P2, balaenopterids dominate the mysticete assemblage, and cetotheriids are represented by a small number of specimens (assigned to *Piscobalaena nana*). With regard to the odontocetes, the PE0.2 surface records the disappearance of the stem beaked whale species *Messapicetus gregarius* (one of the most common taxa in P1), replaced in P2 by other species of ziphiids (including *Chavinziphius maxillocristatus* and *Nazcacetus urbinai*); a turnover in the species of kentriodontid-like delphinidans is also observed. Stem physeteroids are present in both P1 and P2 with *Livyatan melvillei* only found in P1 and *Acrophyseter* spp. common in P2 and possibly already present in P1. The pontoporiid *Brachydelphis*, very common in P1, survives in the lower strata of the P2 allomember. Within P2, phocoenids and kogiids make their first appearance in the East Pisco Basin. The P2 allomember also records the first occurrences of pinnipeds from the Pisco Basin, represented by abundant specimens concentrated in the basal beds of this unit. Furthermore, disappearance of stem Sphenisciformes and first occurrences of crown penguins (Spheniscidae) are also documented in P2. The shark assemblage seemingly records a decline in diversity and disparity above the PE0.2 surface, with most selachian remains detected above this unconformity being referred to a few large species of Lamniformes.

This chapter is modeled on the paper "Sequence stratigraphy and paleontology of the upper Miocene Pisco Formation along the western side of the lower ica valley (Ica Desert, Peru)" written by Claudio Di Celma, Elisa Malinverno, Giulia Bosio, Alberto Collareta, Karen Gariboldi, Anna Gioncada, Giancarlo Molli, Daniela Basso, Rafael M. Varas-Malca, Pietro Paolo Pierantoni, Igor Maria Villa, Olivier Lambert, Walter Landini, Giovanni Sarti, Gino Cantalamessa, Mario Urbina and Giovanni Bianucci, printed in 2017 on Rivista Italiana di Paleontologia e Stratigraia (RIPS), Vol. 123(2): 255-273. In this paper, Giulia Bosio contributes to measurement of the stratigraphic section and field mapping, sample collection, classification and description of the invertebrate fauna, reconstruction of the chronostratigraphic framework and discussion.

Chapter References

Bianucci, G., Di Celma, C., Urbina, M., Lambert, G. 2016a. New beaked whales from the late Miocene of Peru and evidence for convergent evolution in stem and crown Ziphiidae (Cetacea, Odontoceti). PeerJ, 4:e2479.

Bianucci, G., Di Celma, C., Collareta, A., Landini, W., Post, K., Tinelli, C., de Muizon, C., Bosio, G., Gariboldi, K., Gioncada, A., Malinverno, E., Cantalamessa, G., Altamirano-Sierra, A., Salas-Gismondi, R., Urbina, M., Lambert, O. 2016b. Fossil marine vertebrates of Cerro Los Quesos:

Distribution of cetaceans, seals, crocodiles, seabirds, sharks, and bony fish in a late Miocene locality of the Pisco Basin, Peru. Journal of Maps, 12, 1037-1046.

Bianucci, G., Di Celma, C., Landini, W., Post, K., Tinelli, C., de Muizon, C., Gariboldi, K., Malinverno, E., Cantalamessa, G., Gioncada, A., Collareta, A., Salas-Gismondi, R., Varas-Malca, R.M., Urbina, M., Lambert, O. 2016c. Distribution of fossil marine vertebrates in Cerro Colorado, the type locality of the giant raptorial sperm whale Livyatan melvillei (Miocene, Pisco Formation, Peru). Journal of Maps, 12, 543-557.

Bianucci, G., Lambert, O., Post, K. 2010. High concentration of long-snouted beaked whales (genus Messapicetus) from the Miocene of Peru. Palaeontology, 53, 1077-1098.

Boessenecker, R.W., Perry, F.A., Schmitt, J.G. 2014. Comparative taphonomy, taphofacies, and bonebeds of the Mio-Pliocene Purisima Formation, Central California: strong physical control on marine vertebrate preservation in shallow marine settings. PLoS ONE, 9(3), e91419.

Brand, L.R., Urbina, M., Chadwick, A., DeVries, T.J., Esperante, R. 2011. A high resolution stratigraphic framework for the remarkable fossil cetacean assemblage of the Miocene/Pliocene Pisco Formation, Peru. Journal of South American Earth Sciences, 31, 414-425.

Chiocci, F.L., Clifton, H.E. 1991. Gravel-illed gutter casts in nearshore facies - indicators of ancient shoreline trend. In: From Shoreline to Abyss: Contributions in Marine Geology in Honor of Francis Parker Shepard. Osborne, R.H. (Ed.) - SEPM Special Publication, 46, 67-76.

Collareta A, Landini W., Lambert O., Post K., Tinelli C., Di Celma C., Panetta D., Tripodi M., Salvadori, P.A., Caramella, D., Marchi, D., Urbina, M., Bianucci, G., 2015. Piscivory in a Miocene Cetotheriidae: irst record of fossilized stomach content for an extinct baleen-bearing whale. Science of Nature, 102, 70.

DeVries, T.J., Frassinetti, D. 2003. Range extensions and biogeographic implications of Chilean Neogene mollusks found in Peru. Bol. Mus. Nacion. Hist. Nat., Chile, 52, 119-135.

Di Celma, C., Malinverno, E., Cantalamessa, G., Gioncada, A., Bosio, G., Villa, I.M., Gariboldi, K., Rustichelli, A., Pierantoni, P.P., Landini, W., Tinelli, C., Collareta, A., Bianucci, G. 2016a. Stratigraphic framework of the late Miocene Pisco Formation at Cerro Los Quesos (Ica Desert, Peru). Journal of Maps, 12, 1020-1028.

Di Celma, C., Malinverno, E., Gariboldi, K., Gioncada, A., Rustichelli, A., Pierantoni, P.P., Landini, W., Bosio, G., Tinelli, C., Bianucci, G. 2016b. Stratigraphic framework of the late Miocene to Pliocene Pisco Formation at Cerro Colorado (Ica Desert, Peru). Journal of Maps, 12, 515-557.

Föllmi, K.B. 2016. Sedimentary condensation. Earth-Science Reviews, 152, 143-180.

Gariboldi, K., Gioncada, A., Bosio, G., Malinverno, E., Di Celma, C., Tinelli, C., Cantalamessa, G., Landini, W., Urbina, M., Bianucci, G. 2015. The dolomitic nodules enclosing fossil marine vertebrates in the East Pisco Basin, Peru: field and petrographic insights into their genesis and role in preservation. Palaeogeography, Palaeoclimatology, Palaeoecology, 438, 81-95.

Gioncada, A., Collareta, A., Gariboldi, K., Lambert, O., Di Celma, C., Bonaccorsi, E., Urbina, M., Bianucci, G. 2016. Inside baleen: Exceptional microstructure preservation in a late Miocene whale skeleton from Peru. Geology, 44, 839-842.

Göhlich, U.B. 2007. The oldest fossil record of the extant penguin genus Spheniscus-a new species from the Miocene of Peru. Acta Palaeontologica Polonica, 52, 285-298.

Grimm, K.A. 2000. Stratigraphic condensation and the redeposition of economic phosphorite: Allostratigraphy of Oligo-Miocene shelfal sediments, Baja California Sur, Mexico. In C.R. Glenn, L. Prévôt-Lucas and J. Lucas (Eds), Marine Authigenesis: From Microbial to Global, SEPM Special Publication, 66, 325-347.

Hampel, A. 2002. The migration history of the Nazca Ridge along the Peruvian active margin: a re-evaluation. Earth and Planetary Science Letters, 203, 665-679.

Lambert, O., Bianucci, G., Beatty, B.L. 2014. Bony outgrowths on the jaws of an extinct sperm whale support macroraptorial feeding in several stem physeteroids. Naturwissenschaften, 101, 517-521.

Lambert, O., Bianucci, G., Post, K. 2009. A new beaked whale (Odontoceti, Ziphiidae) from the Middle Miocene of Peru. Journal of Vertebrate Paleontology, 29, 910-922.

Lambert, O., Bianucci, G., Post, K. 2010a. Tusk bearing beaked whales from the Miocene of Peru: Sexual dimorphism in fossil ziphiids? Journal of Mammalogy, 91, 19-26.

Lambert, O., Bianucci, G., Muizon, C. de. 2017. Macroraptorial sperm whales (Cetacea, Odontoceti, Physeteroidea) from the Miocene of Peru. Zoological Journal of the Linnean Society, 179, 404-474.

Lambert, O., Bianucci, G., Post, K., Muizon, C. de, Salas-Gismondi, R., Urbina, M., Reumer, J. 2010b. The giant bite of a new raptorial sperm whale from the Miocene epoch of Peru. Nature, 466, 105-108.

Lambert, O., Collareta, A., Landini, W., Post, K., Ramassamy, B., Di Celma, C., Urbina, M., Bianucci, G. 2015. No deep diving: evidence of predation on epipelagic fish for a stem beaked whale from the late Miocene of Peru. Proceedings of the Royal Society B - Biological Sciences, 282, 20151530.

Landini, W., Altamirano-Sierra, A., Collareta, A., Di Celma, C., Urbina, M., Bianucci, G. 2017. The late Miocene elasmobranch assemblage from Cerro Colorado (Pisco Formation, Peru). Journal of South American Earth Sciences, 73, 168-190.

Leckie, D.A., Walker, R.G. 1982. Storm- and tide-dominated shorelines in Cretaceous Moosebar-Lower Gates interval: Outcrop equivalents of Deep Basin gas trap in western Canada. American Association of Petroleum Geologist Bulletin, 66, 138-157.

Marx, F., Collareta, A., Gioncada, A., Post, K., Lambert, O., Bonaccorsi, E., Urbina, M., Bianucci, G. 2017. How whales used to ilter: exceptionally preserved baleen in a Miocene cetotheriid. Journal of Anatomy, 231(2), 212-220.

Muizon, C. de, DeVries, T.J. 1985. Geology and paleontology of late Cenozoic marine deposits in the Sacaco area (Peru). Geologische Rundschau, 74, 547-563.

Muizon, C. de. 1988. Les vertébrés fossiles de la Formation Pisco (Pérou). Troisièmepartie: Les Odontocètes (Cetacea, Mammalia) du Miocène. Travaux de l'Institut Français d'Études Andines, 42, 1-244.

Myrow, P.M. 1992. Pot and gutter casts from the Chapel Island Formation, southeast Newfoundland. Journal of Sedimentary Petrology, 62, 992-1007.

Parham, J.F., Pyenson, N.D. 2010. New sea turtle from the Miocene of Peru and the iterative evolution of feeding ecomorphologies since the Cretaceous. Journal of Paleontology, 84, 231-247.

Pemberton, S.G., MacEachern, J.A. 1995. The sequence stratigraphic significance of trace fossils: examples from the Cretaceous foreland basin of Alberta, Canada. In: J.C. Van Wagoner & G. Bertram (Eds). Sequence stratigraphy of foreland basin deposits-outcrop and subsurface examples from the Cretaceous of North America. AAPG Memoir, 64, 429-475.

Smith, C.R., Glover, A.G., Treude, T., Higgs, N.D., Amon, D.J. 2015. Whale-fall ecosystems: recent insights into ecology, paleoecology, and evolution. Annual Review of Marine Science, 7, 571-596.

Stucchi, M. 2007. Los pingüinos de la Formación Pisco (Neógeno), Perú. In: Díaz-Martinez E., Rábano I. (Eds) - 4th European Meeting on the Palaeontology and Stratigraphy of Latin America, Madrid, España. Cuadernos del Museo Geominero, 8, 367-373.

Stucchi, M., Varas-Malca, R.M., Urbina-Schmitt, M. 2016. New Miocene sulid birds from Peru and considerations on their Neogene fossil record in the Eastern Paciic Ocean. Acta Palaeontologica Polonica, 61, 417-427.

Chapter 10. Chronostratigraphy of the Pisco Formation in the western side of the Ica River

10.1. Diatom biostratigraphy at Cerro Colorado and Cerro los Quesos

Both P1 and P2 allomembers are exposed in Cerro Colorado (abbreviated: CC) and the P2 allomember dominates the Cerro los Quesos stratigraphic section (see Fig. 10.1).

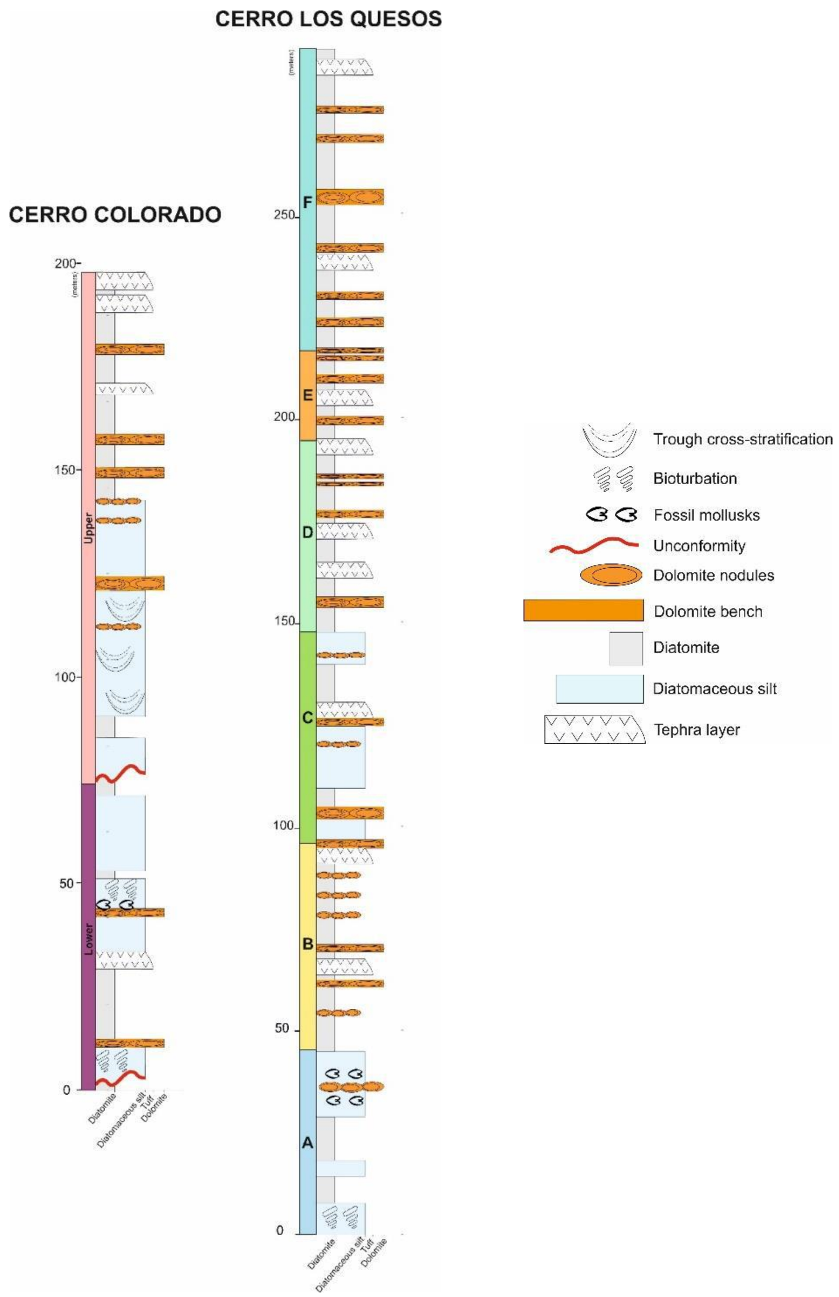

Figure 10.1. Simplified stratigraphic sections of Cerro Colorado and Cerro los Quesos. The complete sections are shown by Di Celma et al. (2016a, b).

In the Cerro Colorado section (see the Appendix for the complete and detailed stratigraphic log), only few samples are useful for biostratigraphic purposes. In the P1 allomember (0-75 m abs, the old "Lower Allomember" Di Celma et al. 2016b), stratigraphically useful species are: *Koizumia tatsunokuchiensis*, found at 35.7 m abs, with FO = 9.0 and LO = 2.6 Ma (Barron 2003, middle-to-high-latitude planktonic diatoms in the North Pacific; Fig. 10.2a, b); *Denticulopsis praekatayamae* from 1.0 m to 62.5 m abs, with FO = 9.5 Ma and LO = 8.5 Ma (Barron 2003, middle-to-high-latitude planktonic diatoms in the North Pacific, Fig. 10.2c, d); and *Lithodesmium reynoldsii*, from 11.5 m to 51.5 m abs, with FO = 9.9 Ma and LO = 8.9 Ma (Barron 2003, middle-to-high-latitude planktonic diatoms in the North Pacific, Fig. 10.2e, f, g). Apparently, *L. reynoldsii* is only present in the P1 allomember, while probably reworked *D. praekatayamae* appears sporadically also in the sediments of Cerro los Quesos (abbreviated: CLQ). At 153.3 m (P2 Allomember) rare specimens of *Thalassiosira antiqua* (Grunow 1884) Cleve-Euler, 1941 (FO = 8.5, LO = 1.6 Ma, Barron 2003, middle-to-high-latitude planktonic diatoms in the North Pacific) are present (Fig. 10.2h).

Similarly to Cerro Colorado, biostratigraphically useful species are rare along the Cerro los Quesos measured section. Although diatomites are common, genera typical of upwelling environments, such as *Chaetoceros*, *Coscinodiscus* and *Thalassionema* dominate the assemblages. Nonetheless, specimens of marker species are present and help to constrain the age of the section. Specimens of *Thalassiosira antiqua* are present from 72.9 to 96.5 m abs (Fig. 10.2i, j). Some of these specimens are smaller than those of *T. antiqua* at Cerro Colorado and their central rosette are more regular than those of the Cerro Colorado specimens (Gariboldi 2016). *Fragilariopsis reinholdii*, with FO at 7.6 Ma and LO at 0.62 Ma (Barron 2003; tropical planktonic diatoms in the Equatorial Pacific), is observed from 61.2 m abs throughout the section up to 286.8 m abs (Fig. 10.2k). Also *Koizumia tatsunokuchiensis*, with a FO at 9.0 Ma and a LO at 2.6 Ma (Barron 2003, middle-to-high-latitude planktonic diatoms in the North Pacific), is pervasive in the section (from 113.1 m to 236.8 m abs, Fig. 10.2a, b). *Nitzschia porteri*, with a FO at 12.2 Ma and a LO at 7.1 Ma (Barron 2003; tropical planktonic diatoms in the Equatorial Pacific, Fig. 10.2l, m), is observed starting from 27.8 m abs up to 277.4 m abs. Its distribution is crossing the intraformational unconformity; in addition, *Fragilariopsis miocenica*, with a FO at 7.3 Ma and a LO at 6.1 Ma (Barron 2003; tropical planktonic diatoms in the Equatorial Pacific; Fig. 10.2n), is observed from 213.4 m up to 277.4 m abs, therefore co-occurring with *N. porteri* from 213.4 m abs to 277.4 m abs.

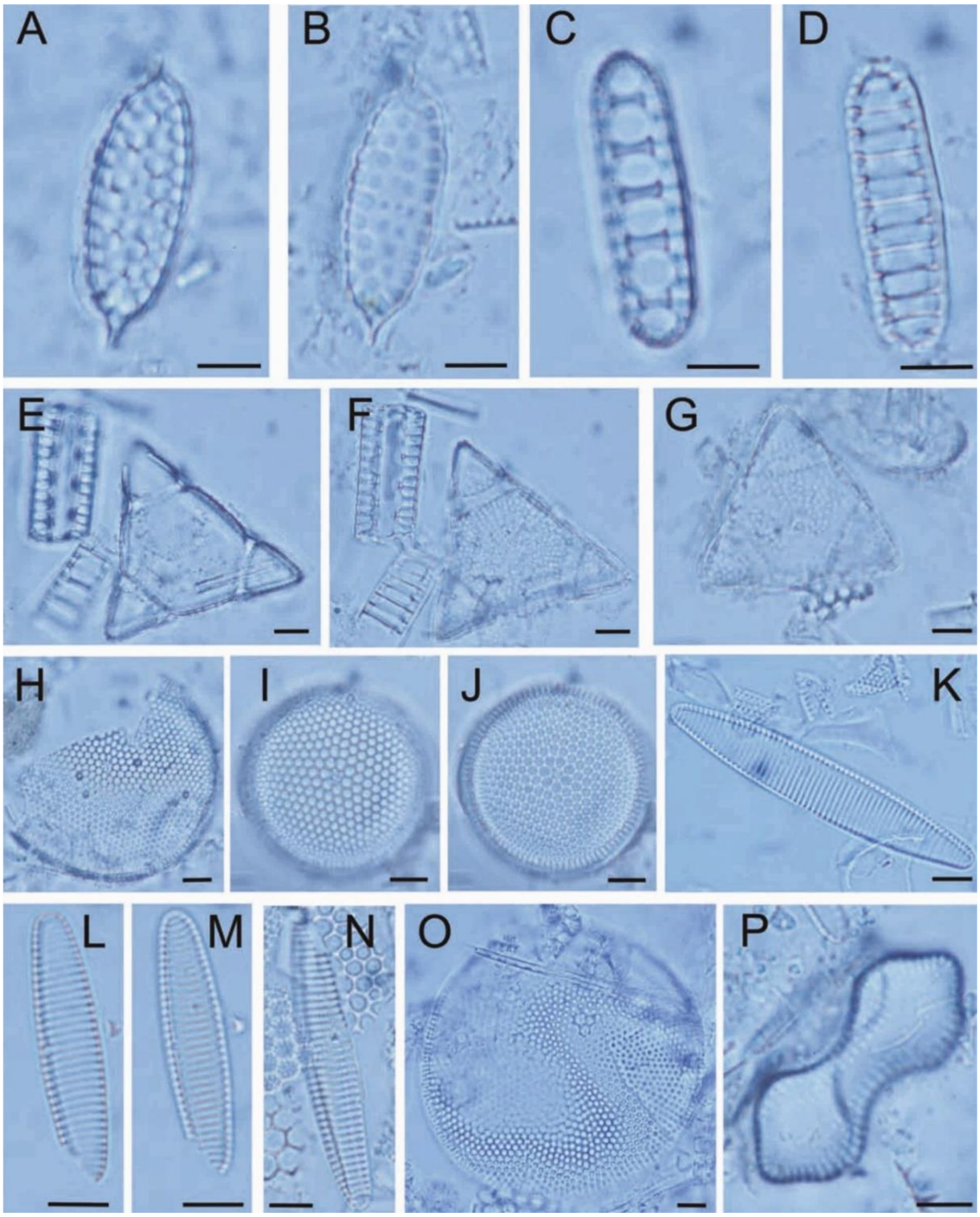

Figure 10.2. Diatom stratigraphic markers at Cerro Colorado and Cerro Los Quesos. a, b) *Koizumia tatsunokuchiensis*, same specimen at different focuses. c, d) *Denticulopsis praekatayamae*, same specimens at different focuses. e, f, g) *Lithodesmium reynoldsii*; e and f are the same specimens at different focuses. h) *Thalassiosira antiqua*, large specimen from CC with irregular central rosette. i, j) *Thalassiosira antiqua*, same specimen at different focuses. This specimen from CLQ is small and has a regular

central rosette. k) *Fragilariopsis reinholdii*. l, m) *Nitzschia porteri*, same specimen at different focuses. n) *Fragilariopsis miocenica*. o) *Thalassiosira* cf. *flexuosa*. p) *Delphineis urbinae*. All scale bars are equal to 5 µm. From Gariboldi et al. (2017).

Plicated *Thalassiosira* specimens (Fig. 10.2o) are present from 27.8 m abs up to 289.5 m abs, their distribution crossing the intraformational unconformity. SEM imagery have revealed morphological affinities of some of these specimens with *Thalassiosira flexuosa* (Brun, 1894) Akiba and Yanagisawa, 1986 as described by Tanimura (1996); those have been identified as *Thalassiosira* cf. *flexuosa* (Gariboldi 2016).

The absolute ages of many LO and FO of diatom markers that we observed are well known in the Pacific. However, specimens of stratigraphically useful pelagic species are rare in the sediments of both CC and CLQ, mainly due to dilution by abundant neritic and/or upwelling-characteristic species. Moreover, the timing of marker species ingression in the basin may have been related to the flow of oceanic currents into it. As a consequence of these two phenomena, bioevents can appear delayed (FO) or anticipated (LO) in the basin if compared to pelagic settings. Integration with ^{39}A–^{40}Ar data validates our biostratigraphic results.

At Cerro Colorado, the Pisco Formation lies directly on the Chilcatay Formation and the base of our CC section is also the base of the Pisco Formation. However, the base of this formation is diachronous throughout the basin and could be older or younger at other sites. The co-occurrence of *L. reynoldsii* (FO = 9.9 Ma, LO = 8.9 Ma, Barron 2003) and of *D. praekatayamae* (FO = 9.5, LO = 8.5 Ma, Barron 2003) from 11.5 m to 51.5 m abs constrains the age of this part of the section between 9.5 and 8.9 Ma (Barron 2003), corresponding to the *Thalassiosira yabei* zone (Fig. 10.3) of the Pacific low Latitude zonation of Barron (1985). Our results differ from previous younger and older age assignments for *L. reynoldsii* (respectively ca. 6.5-5.7 Ma, Schrader & Ronning 1988 and ca. 10-11 Ma, Macharè & Fourtanier 1987) but agree with the ^{39}A–^{40}Ar age that we obtained at 30.6 m abs (9.10 ± 0.04 Ma, see below). Our combined data thus confirm a late Miocene (Tortonian) age for Cerro Colorado P1 allomember and amend previous age assignment to the middle Miocene (Bianucci et al. 2010, Lambert et al. 2010a, b, Parham & Pyenson 2010, Pimiento & Balk 2015) based on the occurrence of *Anadara sechurana*, a bivalve that was typically found in the middle Miocene of the Pisco Basin (DeVries 1998).

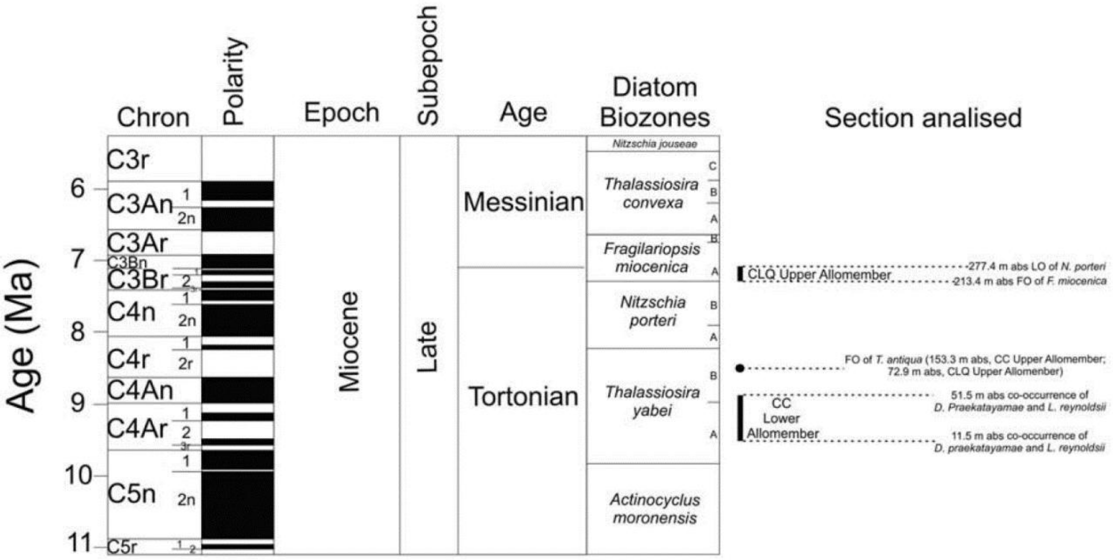

Figure 10.3. Analyzed sections plotted against Berggren's 1995 late Miocene Geochronologic and Chronostratigraphic Time Scale. Chron C5r is not completely represented. Diatom Biozones are those of the Equatorial Pacific Biostratigraphic Scheme of Barron 1985; bioevents used by Barron (1985) to define top and bottom of different biozones have been adapted to Berggren's 1995 Geologic Time Scale following Barron 2003. Bioevents of *D. praekatayamae*, *L. reynoldsii*, *T. antiqua*, *F. miocenica* and *N. porteri* are those adapted to Berggren's 1995 by Barron 2003 as well. From Gariboldi et al. (2017).

Important biostratigraphic markers do not occur in the CC P2 allomember, apart from *Thalassiosira antiqua*, which is present at 153.3 m abs. Specimens of *T. antiqua* are also present at CLQ from 72.9 m to 96.5 m abs. This observation, coupled with the finding of the same internal unconformity at CC and CLQ, leads us to state that the CC P2 allomember correlates with the portion of CLQ section above 29 m abs. The range of *T. antiqua* is calibrated to the middle to high-latitude North Pacific and its range spans from 8.5 Ma to 1.6 Ma (Barron 2003), suggesting that sediments of CC above 153.3 m abs and sediments of CLQ above sample 72.9 m abs are younger than 8.5 Ma. Although First and Last Occurrences of the cold-water *T. antiqua* should be considered with caution as bioevents along the CLQ section, the 7.55 ± 0.05 Ma radiometric age obtained for the CLQ-T49 tephra (127.5 m abs, see below) is in agreement with a calibrated age of 8.5 Ma for the FO of *T. antiqua*. The occurrence of *T. antiqua* at 153.3 m abs and the consequent correlation with the CLQ 72.9-96.5 m abs interval allow us to infer that the age range of the CC P2 Allomember is very close to a range between 8.5 Ma and 7.55 ± 0.05 Ma. At CLQ, in the stratigraphic interval spanning from 213.4 to 277.4 m abs, the co-occurrence of *Nitzschia porteri* and *Fragilariopsis miocenica* constrains the age between 7.3 Ma (FO of *F. miocenica*) and 7.1 Ma (LO of *N. porteri*), corresponding to the *Fragilariopsis miocenica* zone (Fig. 10.3) of the Pacific low Latitude zonation (Barron 1985). *Fragilariopsis miocenica* was previously reported in the Pisco Formation by Macharé and Fourtanier (1987) and Koizumi (1992) as *Nitzschia miocenica*. On the contrary, *N. porteri* was only reported by Koizumi (1992). The disappearance of *T. antiqua* in the CLQ sediments well before the 7.3-7.1 Ma interval confirms that the range of the species in the Pisco Formation does not reflect its full range observed in the high-latitude North Pacific. We therefore confirm that the sedimentary succession exposed at Cerro Los Quesos is late Miocene in age, as stated by Di Celma et al. (2016a) and in contrast to what suggested by previous authors who placed Cerro Los Quesos in the middle Miocene (Lambert et al. 2009).

10.2. Diatom biostratigraphy at Cerros Cadenas de los Zanjones

Diatom biostratigraphy was employed in the P1 allomember exposed at Cerros Cadenas de los Zanjones to supplement the problematic $^{39}Ar–^{40}Ar$ ages for the top of P1. The measured section at Cerros Cadenas de los Zanjones consists of the P1 and P2 sediments, separated by the PE0.2 unconformity. Both allomembers are characterized by sandstones at the base and diatomaceous siltstone at the top, with ash layers interspersed (Fig. 10.4a). Although marine diatoms are predominantly present and well preserved in the analyzed succession, only few samples are useful for biostratigraphy.

As shown in Table 10.1, in the P1 allomember the stratigraphic marker species *Lithodesmium reynoldsii* Barron (1976) (see Fig. 10.4b) is found at the base of the section (15-27 m abs). This species has the FO at 9.9 Ma and the LO at 8.9 Ma (Barron 2003) and was common at the base of P1 (11.5 to 51.5 m abs) in Cerro Colorado. From 15 m abs throughout the section up to 76.5 m abs, below the PE0.2 unconformity, the species *Denticulopsis praekatayamae* Yanagisawa and Akiba (1990) occurs (see Fig. 10.4c); its FO and LO are calibrated respectively at 9.5 Ma and 8.5 Ma (Barron 2003).

Above the PE0.2 unconformity, most of the identified diatom species are not useful for biostratigraphic purposes.

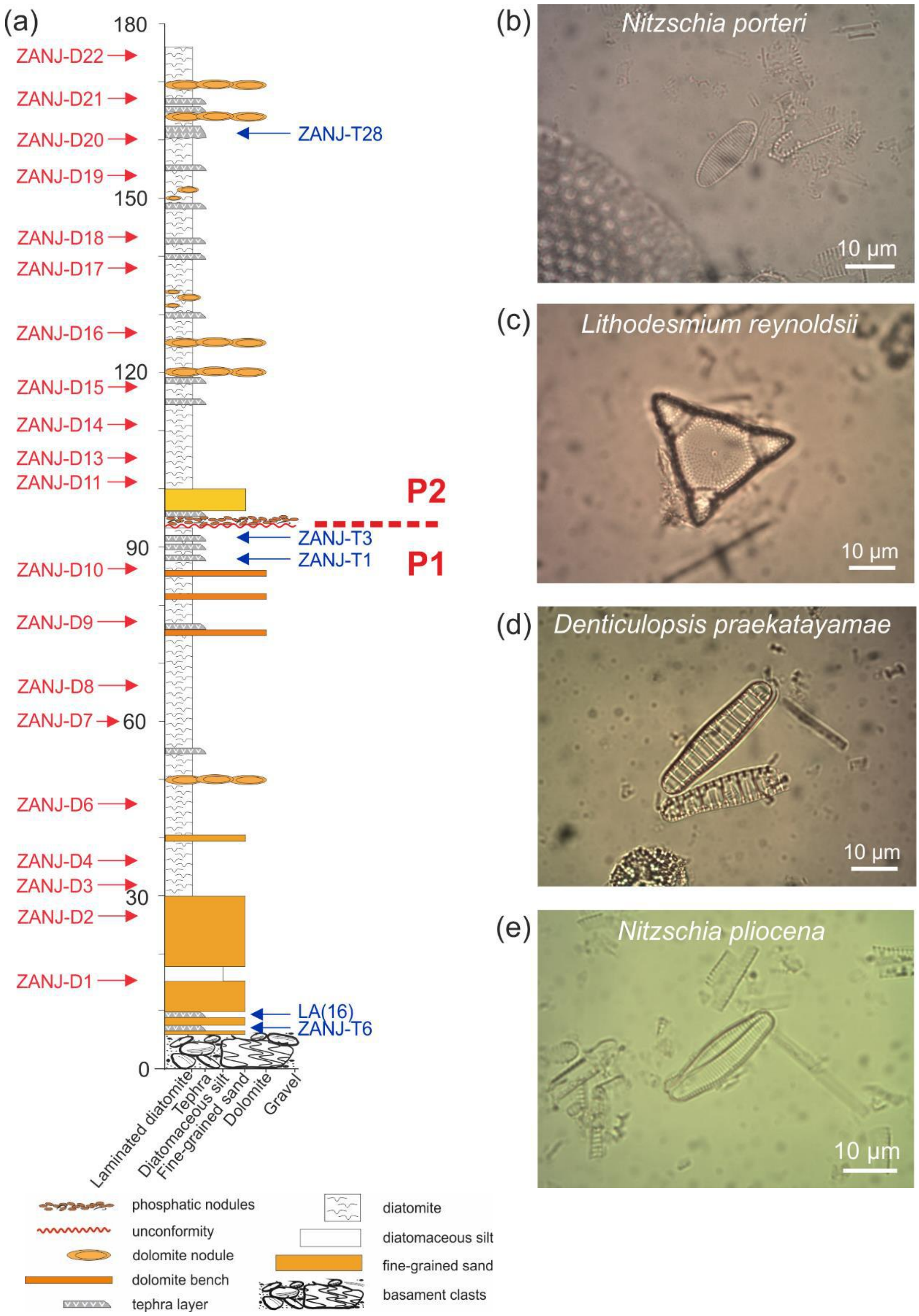

Figure 10.4. a) Measured stratigraphic section at Cerros Cadenas de los Zanjones with tephra (blue) and sediment (red) sample position. b) *Nitzschia porteri* marker species. c) *Lithodesmium reynoldsii* marker species. d) *Denticulopsis praekatayamae* marker species. e. *Nitzschia pliocena* marker species.

Cycle	Meters above base of the section	Sample	*Nitzschia porteri* (12.11 - 7.53 Ma)*	*Lithodesmium reynoldsii* (9.9 - 8.9 Ma)°	*Denticulopsis praekatayamae* (9.5 - 8.5 Ma)°	*Nitzschia pliocena* (8 - 6.8/6.7 Ma@; FO 7.8 Ma~)	**Diatom biozones (Barron, 1985)**
P2	161.5	ZANJ-D20	X			X	***Nitzschia porteri***
	127	ZANJ-D16	X			X	
P1	76.5	ZANJ-D9			C		***Thalassiosira yabei***
	60	ZANJ-D7			R		
	46	ZANJ-D6	X		F		
	36.5	ZANJ-D4			C		
	31	ZANJ-D3	X		F		
	27	ZANJ-D2	X	F			
	15	ZANJ-D1		F	C		

Table 10.1. Distribution of diatom marker species in the Pisco formation P1 and P2 allomembers at the Cerros Cadenas de los Zanjones. The two cycles are tentatively attributed to the *Thalassiosira yabei* and *Nitzschia porteri* biozones of Barron 1985. The FO and LO ages of different species are those from: *Expedition 320/321 Scientists, 2010; °Barron, 2003; @Akiba and Yanagisawa, 1986; ~Barron, 1980. The broken line in the "Cycle" column represents the PE0.2 unconformity. Therefore, the boundary between the two biozones cannot be identified for certain (dashed line).

The only marker species identified exclusively in the P2 allomember is *Nitzschia pliocena* Mertz (1966) (Fig. 10.4d), found at 127 and 161.5 m abs. *Nitzschia pliocena* was assigned to the Miocene-Pliocene in the Pisco sediments by Mertz (1966). This species is also described in the North Pacific (Northeastern Japan) by Barron (1980), who placed the FO at 7.8 Ma, and by Akiba and Yanagisawa (1986), who attributed a range between ca. 8 Ma and 6.8-6.7 Ma to *Nitzschia pliocena* in the North Pacific.

From 27 to 161.5 m abs, the presence of the *Nitzschia porteri* Frenguelli sensu Burckle (1972) (Fig. 10.4e) indicates a time period between 12.11 Ma (FO) and 7.53 Ma (LO) (Expedition 320/321 Scientists 2010) for almost the entire succession.

Therefore, the co-occurrence of the marker species *Lithodesmium reynoldsii* and *Denticulopsis praekatayamae* in the first 15 m of the section, constrains the base of the

P1 allomember between 9.5 and 8.9 Ma (respectively FO of *D. praekatayamae* and the LO of *L. reynoldsii*). The occurrence of *D. praekatayamae* in the 15-76.5 m stratigraphic interval of the section allow the attribution of the P1 allomember to the *Thalassiosira yabei* biozone (Expedition 320/321 Scientists 2010). In the P2 allomember, instead, the co-occurrence of *Nitzschia pliocena* and *Nitzschia porteri* constrains the 127-161.5 m section interval between 8.0-7.8 Ma and 7.53 Ma. Using this marker species, we tentatively assign the P2 allomember to the *Nitzschia porteri* biozone (Expedition 320/321 Scientists 2010).

10.3. ^{39}A–^{40}Ar dating on the Pisco Formation tephra

The Chilcatay strata and the Pisco strata of the P0 allomember exposed west of the Ica River contain sparse and poorly preserved volcanic ash layers. Instead, in the P1 and P2 allomembers of Pisco Formation tephra are frequently encountered, especially in the diatomitic portion, where about 10–30 tephra layers thicker than 2–3 cm are found in 100 m of section.

In the field, tephra layers have a gray to light gray color, in a few cases dark gray, and a thickness between 5 and 15 cm (Fig. 10.5a). The ash layers selected for dating had lateral continuity, lack of sedimentary structures suggesting reworking, sharp base and normal grading with accumulation of biotite crystals at the base and no cements or crusts of secondary minerals, such as gypsum.

The analyzed tephra, described in Table 10.2, consist of > 90% in volume of glass shards with the rest made of feldspar, biotite, rare amphibole and in one case muscovite (see Fig. 10.5b). Glass shards are prevalently rhyolitic and dacitic, infrequently andesitic, with high-K calcalkaline affinity (see Fig. 10.5c).

Biotite phenocrysts are coated by glass, proving their volcanic origin. Occasionally they contain inclusions of glass, apatite and zircon. They do not show evidence of alteration, such as clay minerals along cleavages. The major element composition ranges between the phlogopite to siderophyllite end-members and is rather homogeneous within each sample, with slight differences between core and rim (Table 10.3 and 10.4; Fig. 10.5d), but some samples contain two well-resolved, distinct populations and were thus discarded from dating.

The stratigraphic position of the sampled tephra layers is shown in the Appendix, where the measured stratigraphic logs are reported.

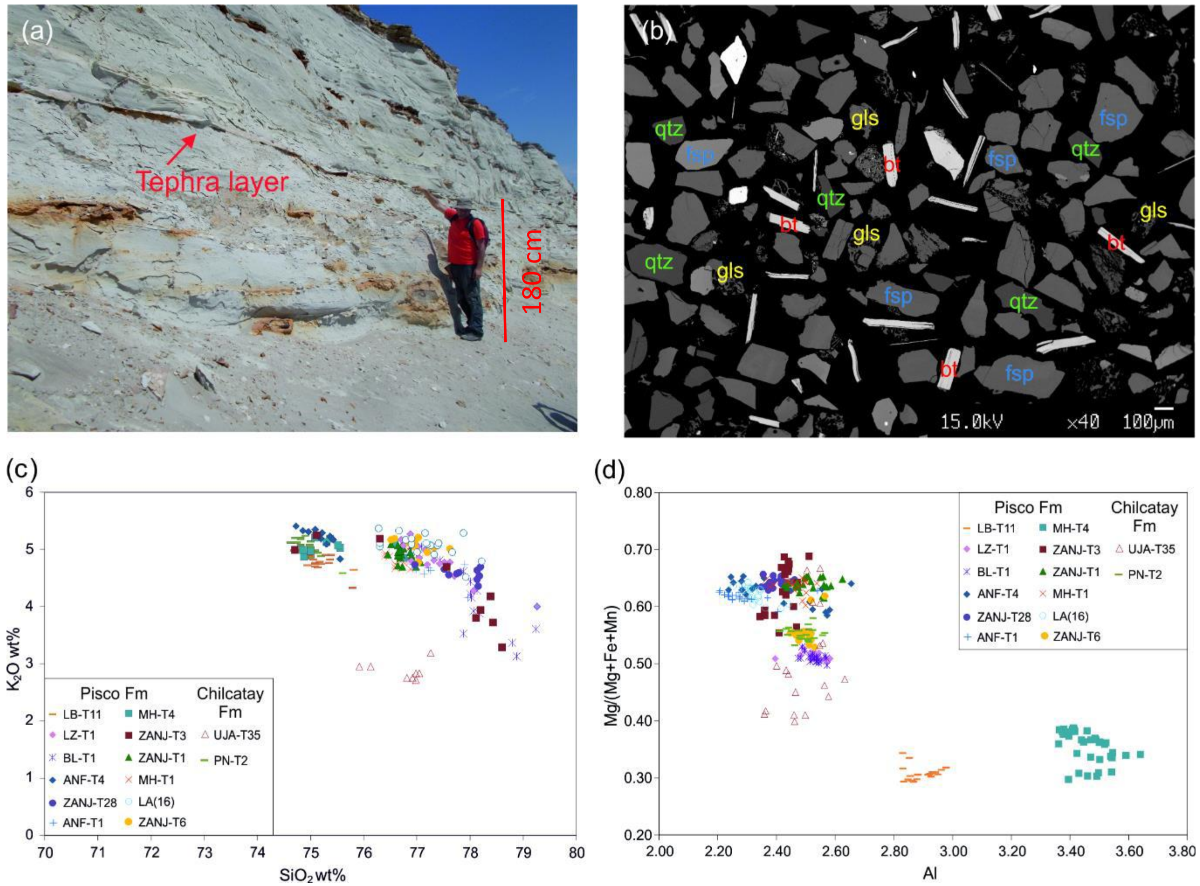

Figure 10.5. a) Field photo of BL-T1 tephra layer in the Pisco Formation at Cerro Blanco. b) BSE image of 250-500 μm fraction of BL-T1 tephra layer showing biotite (bt) and feldspar (fds) phenocrysts, quartz (qtz) and glass shards (gls). c) Volcanic glass K_2O vs SiO_2 diagram showing the glass composition of the dated tephra. Fields for arc-related volcanic rocks follow Peccerillo and Taylor (1976). d. Biotite Mg/(Mg+Fe+Mn) vs Al diagram of the dated ash layers. Values are shown as atoms per formula unit.

Locality	Sample	Field observations		Grainsize[1]				Glass morphology	Crystals	Glass chemistry (wt%)													
		Thickness (cm)	Colour and notes	Folk (1954)	White and Houghton (2006)	median (phi)	sorting (phi)			mean, SD [n]	SiO_2	TiO_2	Al_2O_3	FeO^T	MnO	MgO	CaO	Na_2O	K_2O	P_2O_5	Cl	sum	A/CNK
Anfiteatro	ANF-T1	10	White ash with visible biotite	unimodal, poorly sorted, fine sand	fine ash	2.3	1.3	platy shards; low vesiculated shards	bt, feldspar	mean [9]	77.23	0.11	12.75	0.74	0.09	0.07	0.48	3.87	4.65	0.01	0.19	93.43	1.04
										SD	0.42	0.04	0.12	0.06	0.04	0.02	0.04	0.15	0.22	0.02	0.02		
	ANF-T4*	-	Light grey ash with visible fine biotite	unimodal, poorly sorted, very coarse silt	extremely fine ash	4.3	1.4	bubble-wall shards; high vesiculated shards	bt, feldspar, px	mean [10]	70.07	0.18	12.75	1.06	0.04	0.14	0.65	3.43	4.86	0.02	na	93.21	1.06
										SD	0.14	0.03	0.11	0.07	0.02	0.02	0.02	0.13	0.17	0.03	-		
Cerro la Bruja	LB-T11*	10	Light grey ash, with abundant bt	bimodal, very poorly sorted, very fine sand	very fine ash	3.2	2.1	platy shards; high vesiculated shards	bt, feldspar	mean [26]	69.70	0.05	13.86	1.42	0.05	0.09	0.83	3.25	4.26	0.08	na	93.59	1.21
										SD	1.97	0.03	2.42	0.29	0.03	0.03	1.00	1.08	0.84	0.03	-		
Cerros Cadenas de los Zanjones	ZANJ-T1	10	White ash with visible biotite	bimodal, very poorly sorted, very coarse silt	extremely fine ash	4.3	2.2	high vesiculated and stretched shards	bt, feldspar	mean [20]	76.75	0.15	12.99	0.92	0.04	0.16	1.03	3.03	4.92	0.02	na	92.63	1.07
										SD	0.16	0.04	0.07	0.05	0.02	0.02	0.02	0.15	0.13	0.02	-		
	ZANJ-T3	5	Light grey ash with fine biotite	unimodal, very poorly sorted, very fine sand	very fine ash	3.4	2.2	platy shards; high vesiculated shards	bt, feldspar	mean [10]	77.41	0.17	13.18	0.83	0.02	0.12	0.85	3.22	4.17	0.02	na	92.78	1.17
										SD	1.49	0.06	0.51	0.18	0.02	0.06	0.14	0.14	0.85	0.02	-		
	ZANJ-T6	15	Light grey ash with visible biotite	unimodal, poorly sorted, very coarse silt	extremely fine ash	4.8	1.4	bubble-wall shards; high vesiculated shards	bt, feldspar	mean [10]	77.01	0.09	12.98	0.61	0.03	0.08	0.80	3.31	5.06	0.01	na	93.89	1.05
										SD	0.33	0.03	0.22	0.06	0.03	0.02	0.07	0.20	0.13	0.02	-		
	ZANJ-T28*	-	White ash with visible biotite	bimodal, very poorly sorted, very fine sand	very fine ash	3.4	2.1	platy shards; low vesiculated shards; bubble-wall shards	bt, feldspar	mean [10]	72.54	0.16	11.51	0.74	0.04	0.12	0.85	2.95	4.27	0.01	0.14	93.33	1.05
										SD	0.82	0.03	0.20	0.04	0.02	0.02	0.03	0.11	0.11	0.02	0.01		
	LA(16)	10	White ash with visible biotite	unimodal, poorly sorted, fine sand	fine ash	2.9	1.5	platy shards; low vesiculated shards; bubble-wall shards	bt, feldspar	mean [19]	77.14	0.10	13.01	0.71	0.08	0.07	0.44	3.34	5.08	0.01	na	93.63	1.10
										SD	0.55	0.03	0.41	0.04	0.04	0.02	0.02	0.19	0.20	0.01	-		
Cerros la Mama y la Hija	MH-T1	10	White ash with visible biotite	bimodal, very poorly sorted, very coarse silt	extremely fine ash	4.7	2.1	high vesiculated and stretched shards; bubble-wall shards	bt, feldspar	mean [20]	76.68	0.14	13.10	0.90	0.04	0.16	1.01	3.12	4.83	0.01	na	92.63	1.07
										SD	0.35	0.03	0.21	0.07	0.03	0.02	0.03	0.17	0.12	0.02	-		
	MH-T4	5	White ash with visible fine biotite	unimodal, poorly sorted, very coarse silt	extremely fine ash	4.7	1.6	high vesiculated shards	bt, feldspar, muscovite	mean [10]	75.49	0.05	14.62	0.63	0.04	0.09	0.47	3.29	5.04	0.27	na	91.72	1.26
										SD	0.67	0.02	0.22	0.13	0.03	0.02	0.09	0.71	0.12	0.09	-		
Cerro Blanco	BL-T1*	10	White ash, with visible biotite	unimodal, poorly sorted, very fine sand	very fine ash	3.6	1.4	platy shards; low vesiculated shards	bt, pl, sa	mean [15]	77.97	0.07	12.90	0.56	0.03	0.05	0.90	3.30	4.20	0.02	na	100.00	1.11
										SD	0.67	0.02	0.25	0.06	0.02	0.02	0.05	0.14	0.63	0.02	-		
Cerro Hueco la Zorra	LZ-T1*	10	White ash with visible biotite	bimodal, very poorly sorted, coarse silt	extremely fine ash	5.1	2.1	platy shards; high vesiculated shards	bt, feldspar	mean [15]	77.37	0.07	13.15	0.56	0.05	0.05	0.90	3.06	4.79	0.01	na	100.00	1.11
										SD	0.65	0.01	0.31	0.04	0.03	0.01	0.07	0.09	0.33	0.01	-		

Table 10.2. Field observations, grain-size classification, petrographic composition, EPMA analyses of glass shards of the Pisco dated tephra.

Grain size parameters obtained with Blott & Pye (2001), Folk (1954), White and Houghton (2006). Key for the "crystals" column: bt = biotite, sa = sanidine, pl = plagioclase. Numbers between square brackets in the "[n]" column correspond to the number of analyzed points.

	PN-T2		UJA-T35		ZANJ-T6		LA(16)		ANF-T1		MH-T1		ZANJ-T1	
	mean	SD	mean	SD	mean	SD	mean	SD	mean	SD	mean	SD	mean	SD
SiO_2	36.62	0.43	36.03	0.93	37.22	0.18	38.17	0.44	37.41	0.74	37.43	0.31	37.48	0.52
TiO_2	4.77	0.18	4.12	1.47	4.45	0.12	4.34	0.13	4.41	0.10	4.05	0.30	4.04	0.25
Al_2O_3	13.99	0.21	12.57	3.93	14.05	0.19	13.19	0.19	12.84	0.44	13.95	0.29	14.26	0.30
FeO^T	18.07	0.44	20.44	3.19	17.63	0.75	14.98	0.46	15.43	0.30	14.97	0.40	14.80	0.46
MnO	0.26	0.04	0.22	0.07	0.28	0.05	0.63	0.04	0.62	0.08	0.17	0.04	0.15	0.02
MgO	12.73	0.35	10.32	3.88	12.56	0.59	14.41	0.45	14.57	0.28	14.92	0.42	14.85	0.32
CaO	0.02	0.02	0.07	0.05	0.02	0.02	0.01	0.01	0.01	0.01	0.01	0.01	0.02	0.02
Na_2O	0.86	0.10	0.65	0.26	0.39	0.05	0.53	0.04	0.52	0.04	0.56	0.03	0.55	0.05
K_2O	8.26	0.13	7.99	0.49	8.96	0.11	8.89	0.07	8.91	0.07	8.81	0.09	8.80	0.08
Cl	0.10	0.03	0.18	0.08	0.09	0.01	na	na	0.16	0.01	0.11	0.02	0.11	0.01
BaO	na	na	0.62	0.32	0.75	0.16	na	na	0.50	0.21	0.48	0.11	0.43	0.13
Total	95.70	0.59	93.23	8.53	96.40	0.39	95.16	0.49	95.41	0.72	95.47	0.71	95.51	0.53
Mg_V	0.55	0.01	0.45	0.16	0.56	0.02	0.62	0.01	0.62	0.01	0.64	0.01	0.64	0.01
K+Na+Ca	1.85	0.03	1.84	0.21	1.84	0.02	1.85	0.02	1.87	0.02	1.85	0.01	1.84	0.03

Table 10.3. Electron microprobe analyses of biotite phenocrysts (wt%) of the Chilcatay and Pisco dated tephra. Mg_V ratio is $Mg/(Mg+Fe^T+Mn)$. "na" is not analyzed.

	ZANJ-T3		MH-T4		ANF-T4		ZANJ-T28		LB-T11		BL-T1		LZ-T1	
	mean	SD	mean	SD	mean	SD	mean	SD	mean	SD	mean	SD	mean	SD
SiO_2	37.97	0.43	34.89	0.56	37.46	0.77	36.74	1.20	34.30	0.43	37.11	0.32	36.96	0.95
TiO_2	4.07	0.23	3.43	0.28	4.75	0.24	4.36	0.10	4.15	0.40	3.64	0.09	3.53	0.12
Al_2O_3	13.87	0.36	18.98	0.42	13.62	0.76	13.35	0.43	15.59	0.29	14.08	0.16	13.94	0.32
FeO^T	15.41	1.70	21.04	0.59	15.05	0.82	14.61	0.26	25.65	0.51	19.40	0.34	18.95	0.28
MnO	0.19	0.06	0.17	0.06	0.26	0.05	0.18	0.04	0.15	0.05	0.34	0.03	0.33	0.05
MgO	14.82	1.30	6.59	0.62	14.37	0.61	14.87	0.34	6.45	0.28	11.53	0.22	11.43	0.30
CaO	0.03	0.05	0.01	0.01	0.03	0.02	0.01	0.01	0.02	0.02	0.02	0.02	0.05	0.02
Na_2O	0.56	0.15	0.34	0.04	0.65	0.12	0.52	0.04	0.60	0.11	0.33	0.03	0.34	0.04
K_2O	8.80	0.24	9.05	0.10	8.70	0.15	8.70	0.08	8.16	0.12	9.20	0.08	9.07	0.24
Cl	0.12	0.03	0.12	0.05	0.15	0.04	0.14	0.01	0.18	0.09	na	na	na	na
BaO	0.36	0.22	0.10	0.08	0.73	0.31	0.47	0.11	na	na	na	na	na	na
Total	96.22	0.52	94.74	0.92	95.79	0.92	93.99	1.82	95.27	0.71	95.66	0.53	94.61	1.91
Mg_V	0.63	0.05	0.36	0.03	0.63	0.02	0.64	0.01	0.31	0.01	0.51	0.01	0.51	0.01
K+Na+Ca	1.83	0.03	1.89	0.03	1.86	0.04	1.85	0.05	1.82	0.04	1.89	0.02	1.89	0.02

Table 10.4. Electron microprobe analyses of biotite phenocrysts (wt%) of the Pisco dated tephra. Mg_V ratio is $Mg/(Mg+Fe^T+Mn)$. “na” is not analyzed.

Tephra layers suitable for ^{39}Ar–^{40}Ar dating were not found in the relatively thin exposure of the oldest allomember of the Pisco Formation, P0, in the western side of the Ica River. The few identified layers were ill preserved and intermingled with the adjacent sediment, and thus could not provide a reliable time constraint.

The P1 allomember was investigated in different places, but most dated tephra were sampled at Cerros Cadenas de los Zanjones, where P1 is entirely exposed. We dated one ash layer from Cerro Colorado, CC-T1b, located 30.5 m abs. Figure 10.6 shows the age spectrum obtained from ^{39}A–^{40}Ar analyses on biotite separates. The weighted average of the steps 5-10 gives an age of 9.10 ± 0.04 Ma (2σ error).

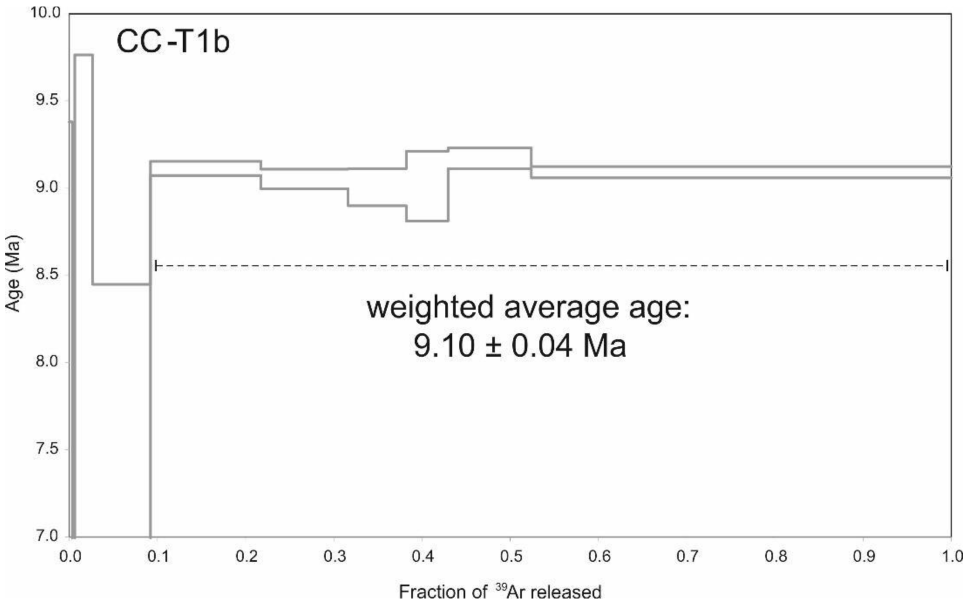

Figure 10.6. CC-T1b age spectrum. The weighted average age is 9.10 ± 0.04 Ma. Uncertainties are shown as 2σ.

In Cerros Cadenas de los Zanjones, the two lowermost tephra were dated: ZANJ-T6 (3 m abs) and LA(16) (8 m abs). The ash layer ZANJ-T6 biotite composition does not overlap with any other layers. The alkali site occupancy for biotite is comparatively high (1.81-1.88 apfu) and the K concentration calculated from total ^{39}Ar is acceptable (K = 6.83 wt%). Considering only steps 2-8 with Ca/K < 0.022, the isochron gives an age of 9.46 ± 0.05 Ma, with a MSWD of 1.5. The age spectrum is shown in Figure 10.7a. Biotite analyses of tephra LA(16) reveal a rather homogenous K concentration and an acceptable alkali site occupancy (1.82-1.90 apfu). The steps selected for calculating the isochemical age have Ca/K < 0.013 (steps from 3 to 7) and give an age of 9.00 ± 0.02 Ma (Fig. 10.7b).

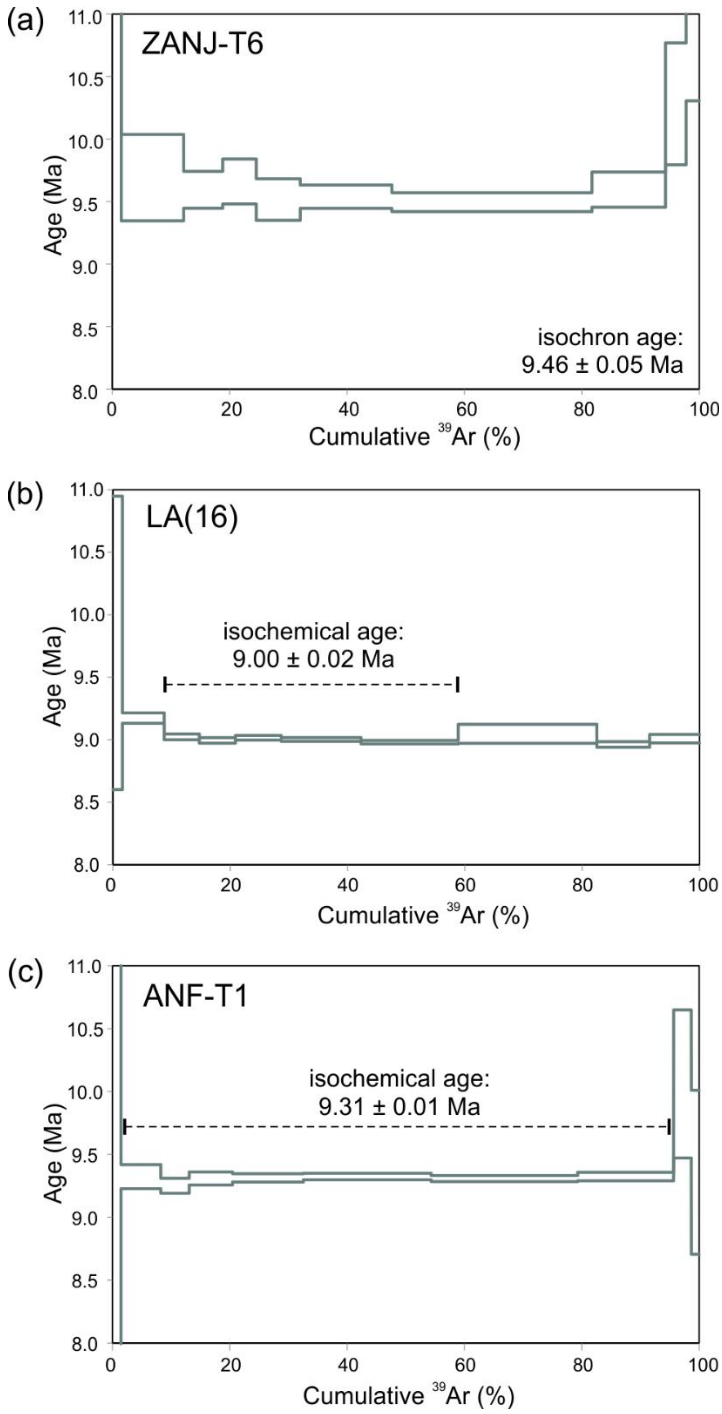

Figure 10.7. a) ZANJ-T6 age spectrum. b) LA(16) age spectrum; dashed line shows an isochemical age of 9.00 ± 0.02 Ma. "Isochemical age" is the weighted average age of isochemical steps. c) ANF-T1 age spectrum showing an isochemical age of 9.31 ± 0.01 Ma. All uncertainties are shown as 2σ.

In a locality nearby Cerro los Quesos, Anfiteatro, the ash layer ANF-T1 was sampled few meters above the PE0.1. The biotite composition has an alkali occupation between 1.83

and 1.93 apfu. The Ca content calculated from ^{37}Ar is extremely high, about 0.3%. The Ca/K ratio of the individual steps suggests two different mineral phases, one with Ca/K about 0.044 and one with Ca/K around 0.024. As all the step ages are around 9.3 Ma, it is likely the two phases have the same age; a plateau is recognizable in the age spectrum (Fig. 10.7c). The weighted average age of the steps from 2 to 8, with a low MSWD (= 0.96), is 9.31 ± 0.01 Ma, very similar to the isochron ages obtained for different step combinations. This age also agrees with the ages obtained for the P1 base in the nearby Cerros Cadenas de los Zanjones.

At the top of the allomember, one tephra was recognized in two different localities, Cerros Cadenas de los Zanjones and Cerros la Mama y la Hija, 6 km apart: ZANJ-T1 (Cerros Cadenas de los Zanjones, 90 m abs) and MH-T1 (Cerros la Mama y la Hija, few meters below the PE0.2 unconformity). The identity of the tephra was recognized from the stratigraphic position and confirmed by tephra fingerprinting analyses (Bosio et al. 2019). ZANJ-T1 biotite has a very variable alkali site occupancy, with values between 1.78 and 1.90 apfu by EPMA and a 6.11 wt% K concentration calculated from total ^{39}Ar. The age spectrum has a clear hump towards older ages between 20 and 40% of ^{39}Ar released (Fig. 10.8a). In addition, Cl/K vs age diagram shows a clear trend with a slope corresponding to an atomic ratio ^{40}Ar/Cl = 1 (see Fig. 10.8b). According to Di Vincenzo et al. (2003), these characteristics are due to sub-µm intergrowths of a K-free phase (in our case probably alteration clays) and the least unreliable age is calculated by averaging the hump steps with the neighboring ones. The weighted average of steps 4-10 yields 9.47 ± 0.09 Ma, with MSWD = 24. Even if the petrographic and chemical composition of ZANJ-T1 coincides with that of MH-T1, the gas release of the two samples is quite differently distributed (Fig. 10.8c). This is probably due to the lower abundance of clay in the interlayers of the MH-T1 biotite, which shows a higher K concentration of 6.97 wt% (from total ^{39}Ar). The final age was calculated with the weighted average of the steps 6, 7 and 8, selected for the low Ca content, with Ca/K < 0.016, and a constant Cl/K. The age confirmed the correlation: MH-T1 gives an age of 9.48 ± 0.02 Ma (MSWD = 1.04), overlapping with the ZANJ-T1 age. The ZANJ-T1/MH-T1 age is in contrast with the ages of the stratigraphically lower ash layers, which provide younger ages.

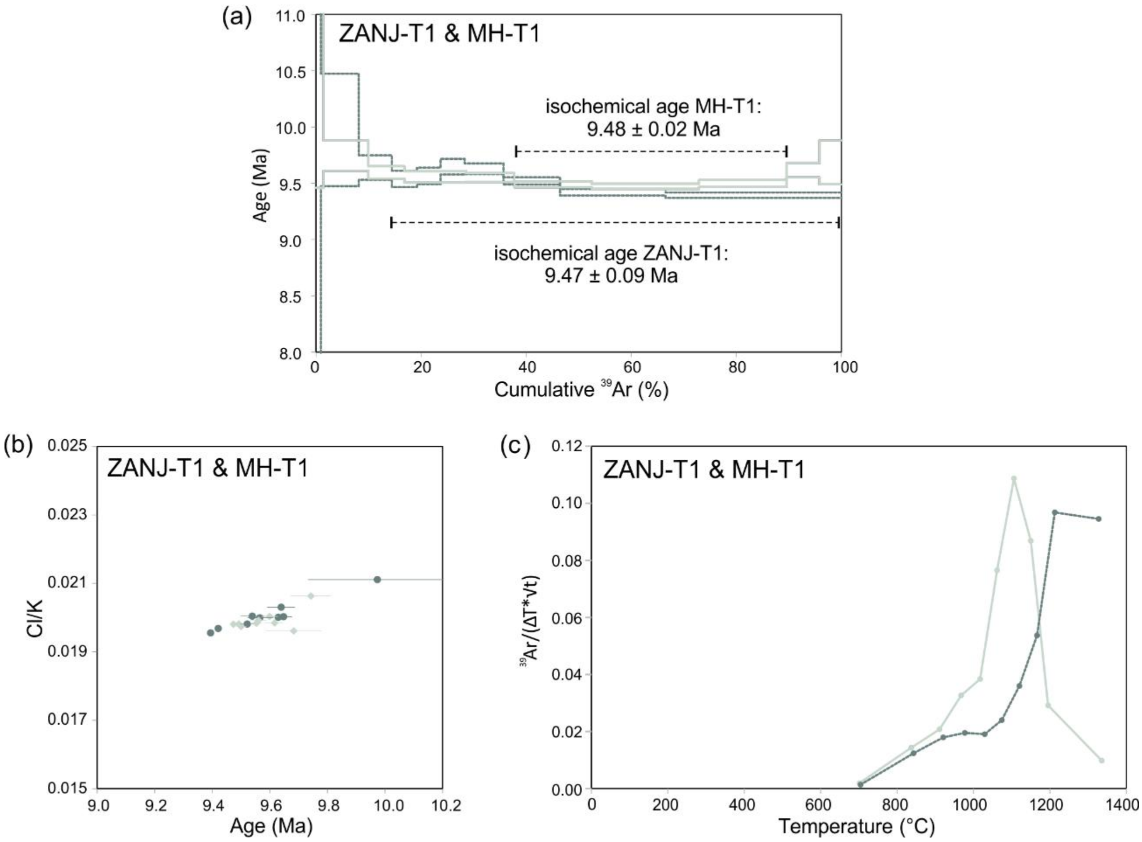

Figure 10.8. a) ZANJ-T1 (dark dotted lines) and MH-T1 (light continuous lines) age spectra. Isochemical ages (i.e. weighted average ages of isochemical steps) are 9.47 ± 0.09 Ma and 9.48 ± 0.02 Ma, respectively. All uncertainties are shown as 2σ. b) Cl/K vs age diagram of ZANJ-T1 (dark rounds) and MH-T1 (light diamonds) tephra. Uncertainties are shown as 1σ. c) Cumulative ^{39}Ar degassing (T=temperature; t=time) of both ZANJ-T1 (dark dotted line) and MH-T1 (light continuous lines) depending on the temperature.

One meter above the ZANJ-T1 ash layer, another tephra was analyzed to confirm or reject the 9.5 Ma age. Tephra ZANJ-T3 shows a younger age with respect to the underlying ZANJ-T1, as shown in the age spectrum (Fig. 10.9a). Its biotite chemical composition shows a great variability: the sum of the alkali content ranges from 1.79 to 1.89 apfu, anticorrelating with the Mg_V value, suggesting a primary variability rather than simple alteration. Moreover, the isochrons calculated with different combinations of steps all show a $^{40}Ar/^{36}Ar$ intercept lower than the atmospheric one, an artefact that points to mixing of isotopically unequilibrated and/or non-isochronous reservoirs, in particular steps with the lowest Ca content. If we also include the results of ZANJ-T3sm (the small aliquot used to optimize the heating schedule), the isochron that includes the five low Ca/K steps of the large sample (2, 3, 6, 7, 8) and the lowest Ca/K step of the small sample has an intercept closer to the atmospheric intercept than other combinations (Fig. 10.9b, c). The calculated age is 8.60 ± 0.11 Ma with a MSWD of 2.2.

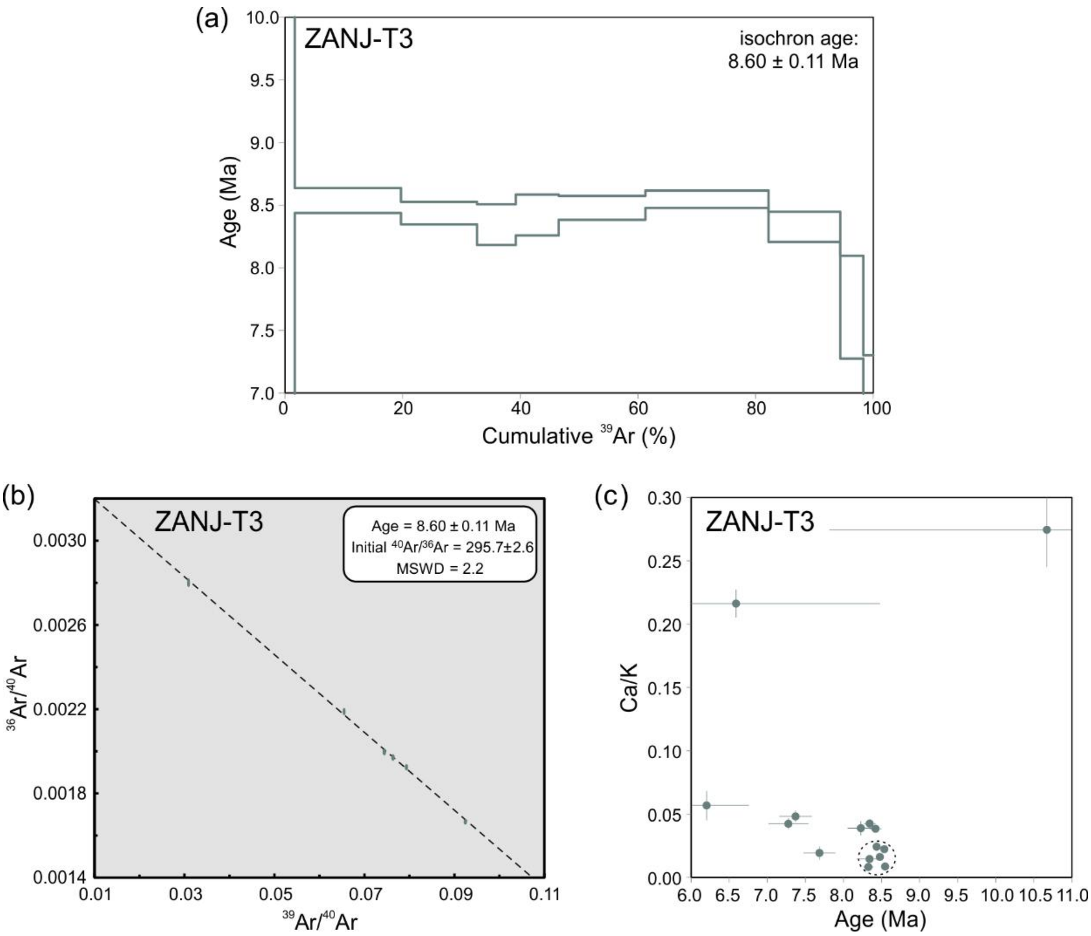

Figure 10.9. a) ZANJ-T3 age spectrum. All uncertainties are shown as 2σ. b) ZANJ-T3 Ar isochron. $^{40}Ar/^{36}Ar$ intercept is lower than the atmospheric one. The isochron age is 8.60 ± 0.11 Ma. The sizes of the ellipses representing points are the 2σ uncertainties. c) ZANJ-T3 Ca/K vs age diagram. The dashed ellipse surround the lowest Ca/K steps. Uncertainties are shown as 1σ.

The P2 allomember crops out in several areas in the western side of the Ica River. The investigated localities are those with an abundant fossil content and an extensively exposed stratigraphic succession. The PE0.2 surface was traced at different localities and two ash layers were sampled for dating the base of the P2 allomember, one at Cerros la

Mama y la Hija, 3 m above the PE0.2 unconformity (MH-T4) and one near Anfiteatro, 1 m above the PE0.2 unconformity (ANF-T4).

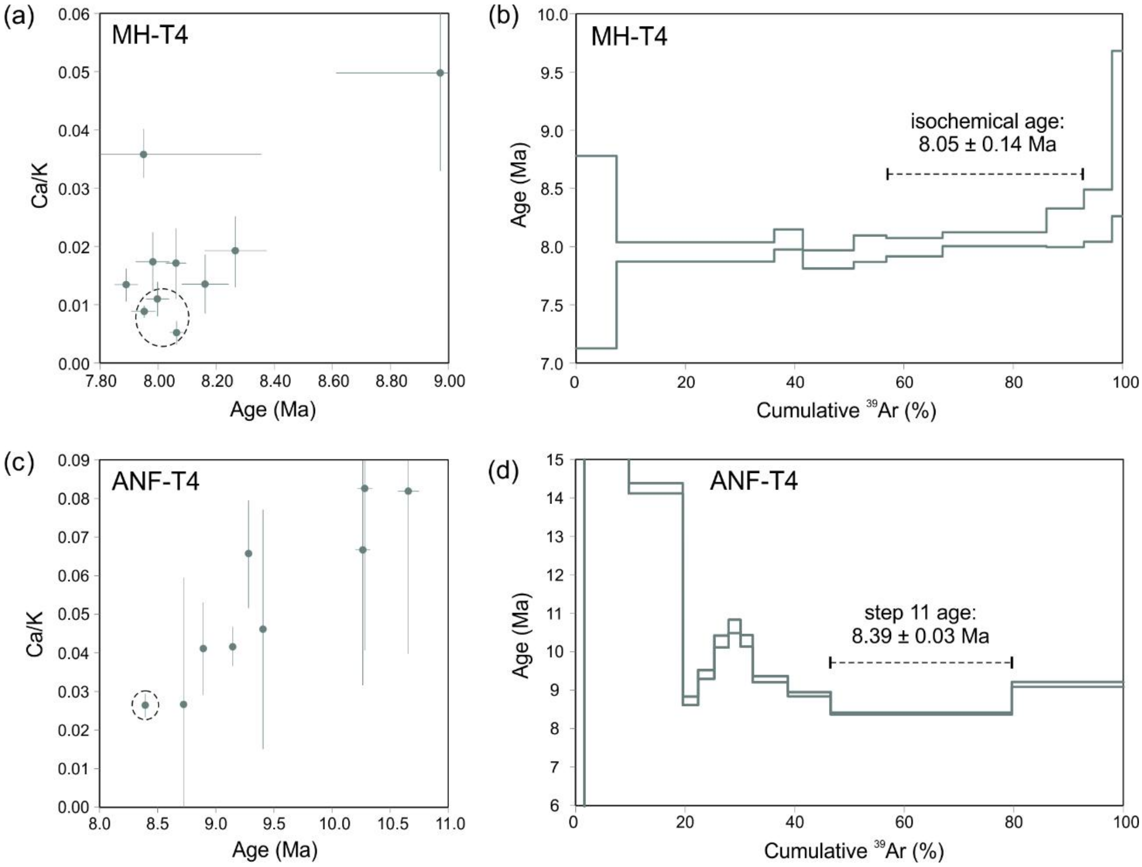

Figure 10.10. a) MH-T4 Ca/K vs age diagram. The dashed ellipse includes the lowest Ca/K steps. Uncertainties are shown as 1σ. b) MH-T4 age spectrum. The isochemical age (i.e. weighted average age of isochemical steps) is 8.05 ± 0.14 Ma. All uncertainties are shown as 2σ. c) ANF-T4 Ca/K vs age diagram, showing a too high Ca/K for a mica. The dashed ellipse includes the lowest Ca/K step. Uncertainties are shown as 1σ. d) ANF-T4 age spectrum. The calculated age from the step 11 is 8.39 ± 0.03 Ma. All uncertainties are shown as 2σ.

MH-T4 has a relatively high alkali site occupation, 1.83 to 1.95 apfu, indicating a moderate alteration. All the isochrons obtained from different step combinations show a very high MSWD and were not considered reliable. The preferred solution is to consider three isochemical steps with Ca/K < 0.014 (steps 6, 7, 8; see Fig. 10.10a) and calculate the weighted average, obtaining a final age of 8.05 ± 0.14 Ma (MSWD = 2.0), as shown in Figure 10.10b. This age estimated for the base of P2 is supported by the second dated ash layer sample, ANF-T4. Unfortunately, EPMA analyses reveal a large variability in the alkali occupancy, ranging from 1.81 to 1.97 apfu, and the K concentration, calculated from the ^{39}Ar release, is 6.46 wt%, far from the stoichiometric value. In addition, the Ca/K is always excessively high (> 0.026) for a mica (Fig. 10.10c). The isochrons calculated from different subset choices of steps with low Ca/K all give 40/36 intercepts higher than the atmospheric value. However, the clear evidence of clay interbedded with biotite (Di Vincenzo et al. 2003) and associated ^{39}Ar recoil, discourage the use of steps 9-12 to calculate an isochron, as in these steps ^{39}Ar and ^{40}Ar were disproportionated by recoil. These features explain the presence of the hump in the age spectrum (Fig. 10.10d) and the difficulties in calculating the final age. Because of these problems, we propose to consider as the most probable age that of step 11, with the lowest Ca/K ratio, i.e. 8.39 ± 0.03 Ma.

The locality of Cerros Cadenas de los Zanjones offers a continuous outcrop of P2 and P1 allomembers. It was studied in order to find a correlation between Cerro los Quesos and other localities, such as Cerro la Mama y la Hija. At the top of the outcrop section, a tephra layer was selected for ^{39}Ar–^{40}Ar dating in the P2 allomember, the ZANJ-T28 sample (161.5 m abs). EPMA analyses on biotite show an alkali content ranging from 1.79 to 1.93 apfu, and a homogeneous biotite composition. Choosing steps from 3 to 8 as isochemical steps, with similar Ca/K and Cl/K ratios, the final age was calculated with the isochron, which shows an atmospheric ^{40}Ar/^{36}Ar intercept and a low MSWD (1.13) as shown in Figure 10.12a, b. An age of 7.62 ± 0.11 Ma was calculated, in agreement with the age of 7.68 ± 0.05 Ma obtained from the step 7 with the lowest Ca/K ratio of 0.011.

Three ash layers from the succession of Cerro los Quesos were selected for dating the P2 allomember: CLQT49 (127.5 m abs, located on top of the Ballena marker bed); CLQ-T1a (the Mono marker bed, 238.5 m abs); CLQ-T9b, the highest ash layer of the succession (289.5 m abs) (see Di Celma et al. 2016a, b). Age spectra were either concordant (when several consecutive steps have the same "plateau" age, usually taken as the accurate age of the sample) or discordant (when step ages give no plateau, in which case the sample's age can be difficult to estimate). In Figure 10.11a the age spectra obtained from ^{39}A–^{40}Ar analyses on biotite separates show that samples CLQ-T49 and CLQ-T1a gave ages of 7.55 ± 0.05 Ma and 6.93 ± 0.09 Ma, respectively. In these cases, ages were calculated as weighted average age only considering the isochemical steps (taking into account both Ca/K and Cl/K ratios); steps with anomalously high Ca/K and Cl/K ratios were attributed to contamination and/or alteration phases, and not considered. For sample CLQ-T9b a discordant age spectrum was obtained, with step ages increasing steadily from 3.2 ± 0.7 Ma to 6.71 ± 0.02 Ma (Fig. 10.11a). Figure 10.11 (b, c) shows that the biotite separate of CLQ-T9b contains two different biotite populations. Figure 10.11b shows a linear trend, evidence of a mainly binary mixing between one Ar reservoir having a high Cl/K ratio (and also a low Ca/K ratio) and an age 6.71 Ma, and one Ar reservoir having an age 3 Ma, low Cl/K and high Ca/K. We interpret the former Ar reservoir as the magmatic biotite and assign an age of 6.71 ± 0.02 Ma. The bimodal distribution of phases in the analyzed separate is confirmed by Figure 10.11c where we can identify a cluster with a higher Mg/(Mg+Fe_{tot}+Mn) and lower alkali; the substoichiometric Na+K+Ca interlayer occupancy is evidence that this population consists of non-primary, altered biotite that gives inaccurately low apparent ages.

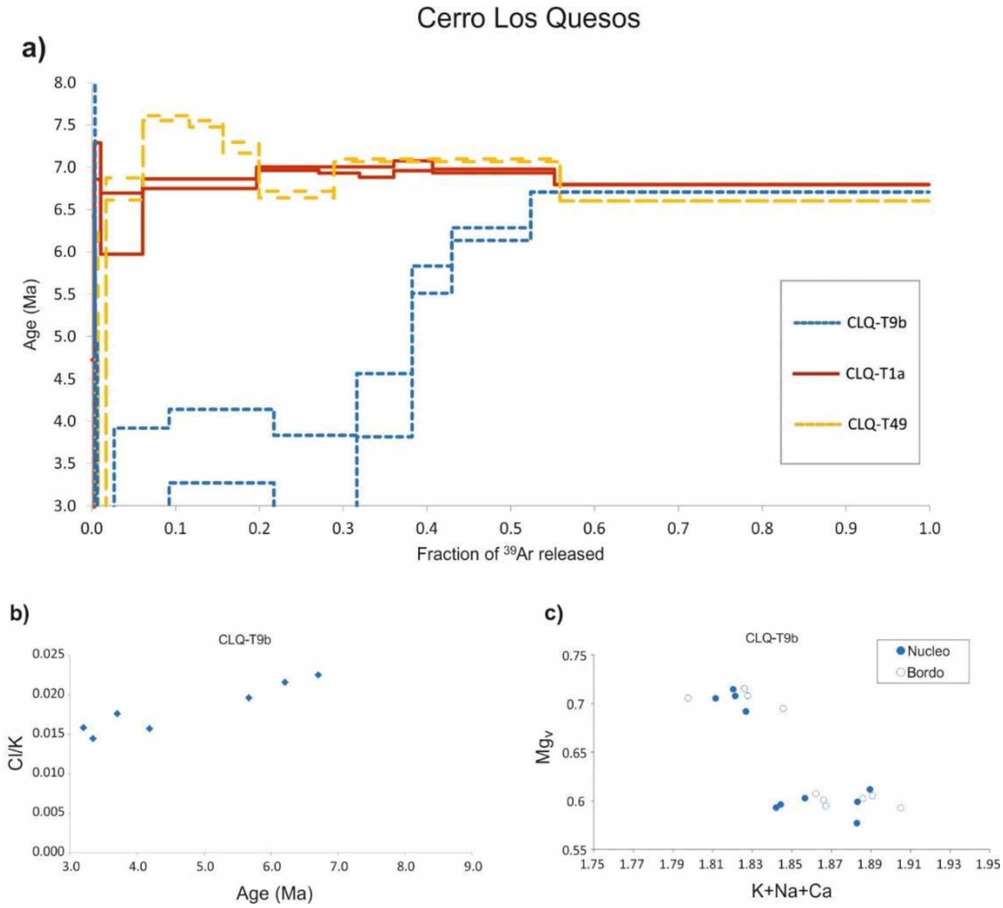

Figure 10.11. a) Age spectra of biotite phenocrysts from ash layers CLQ-T49, CLQ-T1a and CLQ-T9b from the Cerro Los Quesos site. Their ages are 7.55 ± 0.05 Ma, 6.93 ±

0.09 Ma and ≥ 6.71 ± 0.02 Ma, respectively. Uncertainties are shown as 1σ. b) Cl/K vs age correlation diagram of CLQ-T9b biotite phenocrysts. Chemical results are obtained by electron microprobe analysis. Two populations with different Cl/K ratios that are recognizable. c) Mg_v vs K+Na+Ca for sample CLQ-T9b. Chemical compositions were obtained by electron microprobe analysis; all cations are given in atoms per formula unit. Mgv is calculated as Mg/(Mg+Fetot+Mn) by microprobe analysis. K+Na+Ca represents interlayer occupancy. Two clusters are clearly seen.

Modified from Gariboldi et al. (2017).

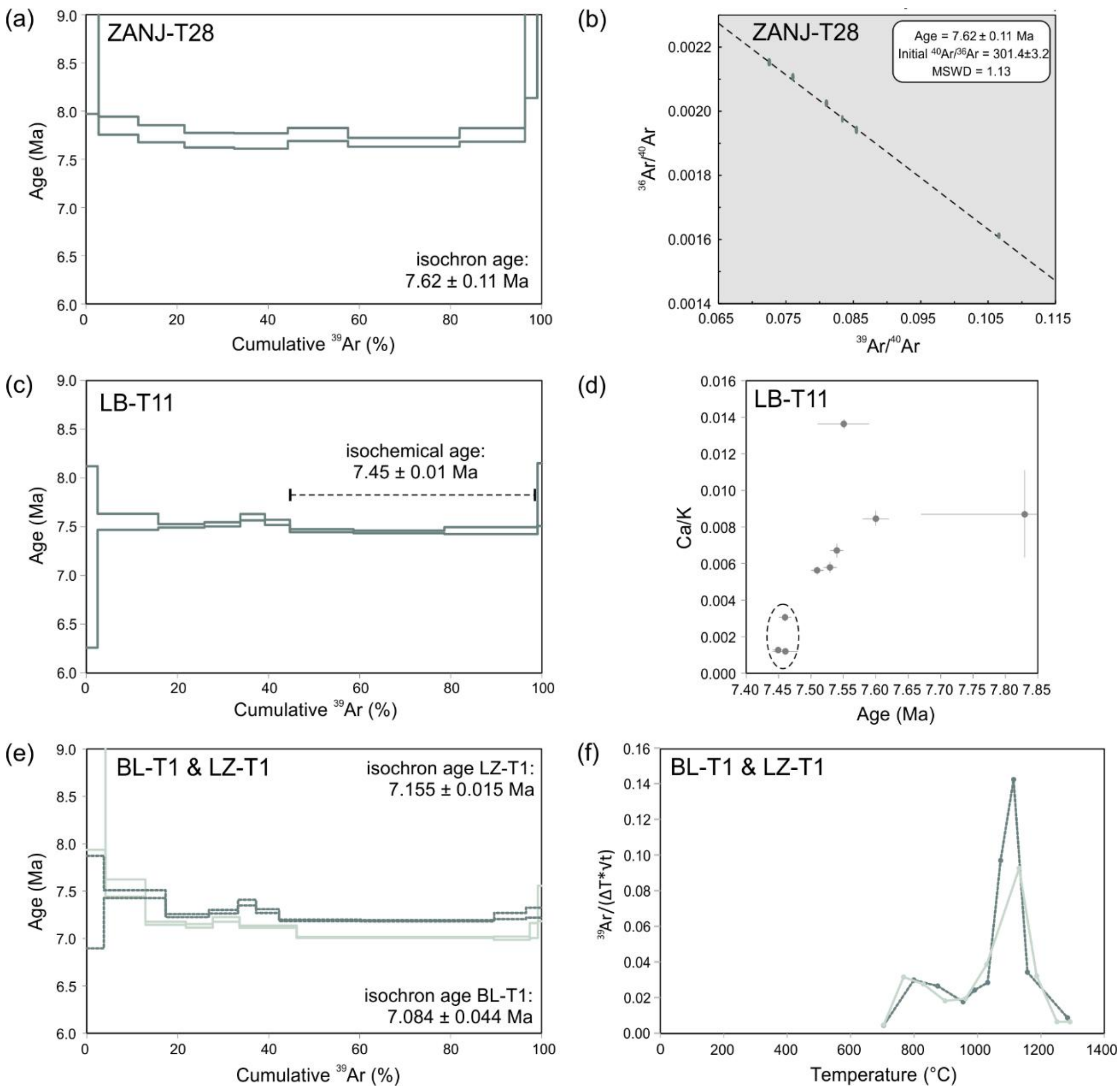

Figure 10.12. a) ZANJ-T28 age spectrum. All uncertainties are shown as 2σ. b) ZANJ-T28 Ar isochron. The isochron age is 7.62 ± 011 Ma. The sizes of the ellipses

representing points are the 2σ uncertainties. c) LB-T11 age spectrum. Dashed line shows the steps considered for the isochemical age (i.e. weighted average age of isochemical steps) of 7.45 ± 001 Ma. All uncertainties are shown as 2σ. d) LB-T11 Ca/K vs age diagram. The dashed ellipse includes the lowest Ca/K steps considered in calculating the final age. Uncertainties are shown as 1σ. e) BL-T1 (light continuous lines) and LZ-T1 (dark dotted lines) age spectra that shows the same pattern. All uncertainties are shown as 2σ. f) BL-T1 (light continuous lines) and LZ-T1 (dark dotted line) cumulative ^{39}Ar degassing (T=temperature; t=time) depending on the temperature following the same pattern.

At Cerro la Bruja, the basal sandy beds of the P2 allomember host the "CLB vertebrate level" (sensu Muizon & DeVries 1985; Muizon 1988), constituted by strata particularly enriched in fossil vertebrates. About 100 m above it, the tephra LB-T11 (174 m abs) was selected for the stratigraphic position to correlate the section with that measured at Cerro los Quesos, already dated between 7.55 and 6.71 Ma (Di Celma et al. 2016a; Gariboldi et al. 2017). EPMA analyses reveals that biotite phenocrysts were subject to a slight loss of mobile cations: the measured K+Na+Ca occupancy ranges between 1.74 and 1.90 apfu. Three heating steps with the lowest Ca/K ratio (< 0.006) were selected to calculate the weighted average age of 7.45 ± 0.01 Ma with a statistically acceptable dispersion of MSWD = 0.9. This age is also in agreement with the age obtained from the isochron: 7.45 ± 0.02 Ma (MSWD = 1.4). The age spectrum and the Ca/K vs age diagram are shown in Figure 10.12c, d.

Two ash layers from two different localities, Cerro Blanco and Cerro Hueco la Zorra, correlated in the field and through tephra fingerprinting (Chapter 12), were dated: BL-T1 and LZ-T1. EPMA analyses on biotite of both these samples suggest a moderate alkali loss in the interlayers, with an alkali site occupancy between 1.85 and 1.93 apfu. For the BL-T1 sample, four isochemical heating steps were selected for the low Ca/K ratio (< 0.029) and the constant Cl/K; the isochron defined by these steps gives an age of 7.084 ± 0.044 Ma with a statistically acceptable dispersion (MSWD = 1.17). We selected four isochemical steps also for the sample LZ-T1, with a Ca/K lower than 0.014; the isochron age is 7.155 ± 0.015 Ma, with a MSWD of 0.3. As shown in Figure 10.12e, the age spectra obtained are very similar but not overlapping, as the final ages, probably due to small chemical differences. From the total $^{38}Ar_{Cl}$ and ^{39}Ar concentrations we calculate the absolute K and Cl content: the results show that BL-T1 has a slightly greater K content and a lower Cl content than sample LZ-T1, suggesting that the latter might be slightly altered (and therefore slightly less accurately dated). The cumulative ^{39}Ar degassing diagram of the two samples show the same gas release, confirming that they belong to the same tephra (Fig. 10.12f). Although the overall age confidence interval ranges between 7.040 and 7.170 Ma, we propose that the BL-T1 age of 7.084 ± 0.044 Ma is closer to the eruption age.

The top of the P2 depositional allomember is not exposed in the sites studied in this work, therefore its upper boundary is not time-constrained.

10.4. Pisco Formation chronostratigraphy

Marine sediments in the East Pisco Basin are characterized by the occurrence of multiple volcanic ash layers, of mainly rhyolitic and minor andesitic composition.

In the western side of the Ica River, tephra are concentrated in the fine-grained diatomaceous sediments and less frequently in the sandstones. They are particularly frequent in the youngest Pisco Formation, especially in the diatomaceous sediments of the P1 and P2 allomembers. The P0 allomember, instead, only shows few and ill-preserved ash layers. In the Chilcatay Formation, tephra are much less frequent and, in general, more altered than those of the P2 and P1 allomembers in the Pisco Formation. Differences in the depositional environment probably account for their preservation in the stratigraphic record and degree of alteration. The relatively deeper (60 to 100 m) environment represented by diatomaceous siltstones of P1 and P2 allomembers is more suitable for the preservation of ash layers than the shallow water environment of the P0 and the Chilcatay strata (15 to 20 m). The longer exposure of the older strata to the acid interstitial water could also play a role in preservation.

Both Chilcatay and Pisco tephra selected for ^{39}Ar–^{40}Ar dating show a slight alteration. As most dated biotite phenocrysts were subject to a slight loss of soluble cations in the interlayer, we consider the ^{39}Ar–^{40}Ar ages on near-stoichiometric biotite more reliable than those on clearly sub-stoichiometric ones.

The ^{39}Ar–^{40}Ar ages presented here confirm and further refine the chronostratigraphy of the Pisco strata exposed along the western side of the Ica River.

Sediments of the P0 allomember are not extensively exposed in the investigated localities. The lithology is dominated by sandstones, and only one volcanic ash was observed, but it was discarded for the high abundance of non-volcanic materials and the very heterogeneous biotite composition. Because of the lack of both microfossils and tephra, no ages of the P0 allomember are currently available in the study area. In other localities, a middle Miocene age is reported by DeVries and Jud (2018) for the lower part of the Pisco Formation. At present, the time boundaries of the P0 allomember are bracketed by the upper age limit of the Chilcatay Formation and the lower age limit of the P1 allomember. P0 is younger than 18.02 ± 0.07 Ma and older than 9.46 ± 0.05 Ma, obtained from the ash layer at Los Dos Cerritos (SOT-T3), 1 m below the PE0.0 unconformity, and from the lowest tephra encountered at the base of the P1 allomember (ZANJ-T6), respectively.

The P1 allomember is entirely Tortonian, as suggested by ^{39}Ar–^{40}Ar age of 9.10 ± 0.04 Ma obtained in P1 at Cerro Colorado. At the base of the P1 allomember, ash layers (ZANJ-T6, LA(16)) provide ages of 9.46 ± 0.05 Ma and 9.00 ± 0.02 Ma few meters above the PE0.1 unconformity (Fig. 10.13). Therefore, the base is not likely to be older than 9.5 Ma, as also supported by diatom biostratigraphy in the measured section of Cerros Cadenas de los Zanjones. The co-occurrence of the marker species *Lithodesmium reynoldsii* and *Denticulopsis praekatayamae* in the first 15 m of the section, constrained the base of the P1 allomember between 9.5 and 8.9 Ma (respectively FO of *D. praekatayamae* and the LO of *L. reynoldsii*). The occurrence of *D. praekatayamae* in the 15-76.5 m stratigraphic interval of the section allow the attribution of the P1 allomember to the *Thalassiosira yabei* biozone (Expedition 320/321 Scientists 2010). The top of the P1 allomember was dated at two localities, Cerros Cadenas de los Zanjones and Cerro la Mama y la Hija. Despite alteration, the uppermost ZANJ-T3 tephra at Cerros Cadenas de los Zanjones gives a final age of 8.60 ± 0.11 Ma. However, the paired tephra ZANJ-T1 and MH-T1 show a surprisingly old age of 9.47 ± 0.09 Ma and 9.48 ± 0.02 Ma, respectively. This age for the top of the P1 allomember is off-sequence as compared with the other ^{39}Ar–^{40}Ar ages from ash layers along the measured section. This age is contrast with the biostratigraphic results, which require a long time duration for P1 to accommodate the observed floral changes. We propose that tephra ZANJ-T1/MH-T1 yields a reproducible but incorrect age, for reasons that are not understood at present, as all options seem all implausible (a reworked tuff, an ash-fall that remobilized an older layer, excess ^{40}Ar, removal of 10% of the total K). We choose to neglect this latter sample and assess that the P1 allomember is constrained between 9.46 ± 0.05 Ma and 8.60 ± 0.11 Ma.

The P2 allomember is constrained between the upper Tortonian and the early Messinian in the late Miocene. In the present thesis, the ages of MH-T4 and ANF-T4 ash layers suggest that the base of the P2 allomember has an age between 8.05 ± 0.14 Ma and 8.39 ± 0.03 Ma. The ^{39}Ar–^{40}Ar age in the P2 allomember cropping out at Cerro la Bruja supports the correlation between this locality and Cerro los Quesos by tephra fingerprinting (Chapter 12). The dated LB-T11 tephra, correlated with an ash layer at 172 m abs at Cerro los Quesos between the layers of 7.55 ± 0.05 Ma and 6.93 ± 0.09 Ma in Chapter 12, gives the reliable age of 7.45 ± 0.01 Ma. The P2 allomember is also exposed at Cerros Cadenas de los Zanjones, where one of the uppermost ash layers in the section, ZANJ-T28, gives an age of 7.62 ± 0.11 Ma. This establishes the correlation between the top of the P2 section measured at Cerros Cadenas de los Zanjones and the lowest part of the P2 section at Cerro los Quesos, which, in turn, is correlated to Cerro la Bruja (Fig. 10.13). ^{39}Ar–^{40}Ar ages in the P2 allomember exposed at Cerro Blanco and Cerro Hueco la Zorra give 7.084 ± 0.044 Ma and 7.155 ± 0.015 Ma respectively, and confirm the field-based correlation between these localities proposed in Chapter 12. Because along the western side of the Ica River the top of the P2 allomember has not been sampled yet, we can only assess that it is older or equal to 6.71 ± 0.02 Ma and younger than 6.93 ± 0.09 Ma, the youngest ages obtained so far for the P2 allomember. Biostratigraphic data at Cerros Cadenas de los Zanjones agree with the ^{39}Ar–^{40}Ar ages. The co-occurrence of *Nitzschia pliocena* and *Nitzschia porteri* constrains the 127-161.5 m section interval between 8.0-7.8 Ma and 7.53 Ma. Using this marker species, we tentatively assign the P2 allomember to the *Nitzschia porteri* biozone (Expedition 320/321 Scientists 2010), supported by the ^{39}Ar–^{40}Ar age of 7.62 ± 0.11 Ma provided by a tephra just above the considered interval (ZANJ-T28). We can assess that strata of the P2 allomember exposed in the study area were thus deposited between 8.39 ± 0.03 Ma and 6.71 ± 0.02 Ma.

Younger strata belonging to this unit, however, are exposed outside (to the north), of the study area and further work is required to establish the age of its top.

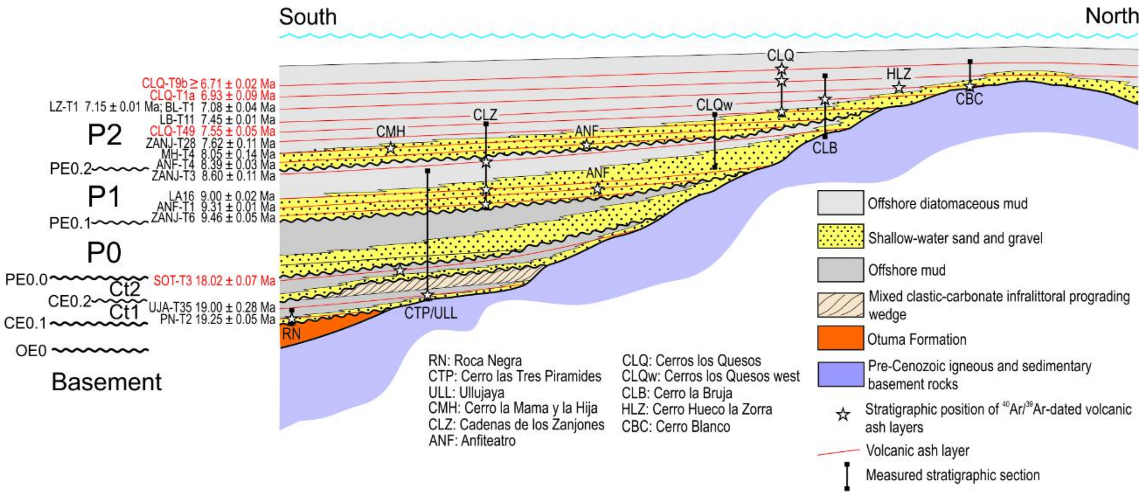

Figure 10.13. Final chronostratigraphic reconstruction of the basin. Schematic, dip-oriented stratigraphic diagram for the Chilcatay and Pisco formations showing both the position of measured stratigraphic sections (vertical black lines) and the stratigraphic position of dated tephra layers (stars). Red lines show dated volcanic ash layers. ^{39}Ar–^{40}Ar ages are reported for each tephra. Modified from Di Celma et al. (2017).

10.5. Origin and timing of erosional unconformities and correlation to global events

Diatom biostratigraphy combined with available ^{39}Ar–^{40}Ar radiometric ages indicate that strata of the P1 allomember in the study area were deposited between about 9.5 and 8.9 Ma, whereas those of the P2 allomember are younger than 8.5 Ma. A comparison between the estimated ages of allomember-bounding unconformities in the Pisco Formation and a glacio-eustatic proxy afforded by deep-sea oxygen isotopic records indicates that, within the resolution of our age model, PE0.2 approximates the drop in sea level recognized as the Mi7 event of Miller et al. (1991), an isotopic maximum dated at 8.7 Ma by Miller et al. (1998) and Westerhold et al. (2005). The PE0.1 unconformity correlates reasonably well with the Mi6 oxygen isotope maximum dated at 10.3 Ma by Miller et al. (1998) and astronomically dated at 10.4 Ma by Turco et al. (2001) and Westerhold et al. (2005). Assuming that this correlation between the studied PE0.1 and PE0.2 unconformities and the eustatic curve derived from deep-sea oxygen isotope records is correct and, therefore, that these breaks in deposition have a eustatic (global) rather than tectonic (local) origin, we speculate that the PE0.0 unconformity can reflects a previous oxygen isotope maximum event (see Chapter 18). In this frame, intermittent periods of subaerial exposure during deposition of the Pisco Formation were likely produced by recurring third-order

(0.5–3 Ma) eustatic oscillations with the rate of eustatic fall exceeding that of long-term tectonic subsidence. As a main result, the several hundred meters thick sediments of the Pisco Formation reflect accommodation space produced by a combination of a low subsidence rate and eustatic sea-level fluctuations. An additional support to the eustatic origin for these allomember-bounding surfaces would be the similar timing of the unconformities in different ocean basins. Comparison of ages of depositional breaks in the Pisco Formation with ages of seismic sequence boundaries identified and dated in the Bahamas (Eberli et al. 2002; ODP Leg 166) indicates that the timing of the PE0.1 and PE0.2 unconformities is remarkably similar with the timing of eustatic sequence boundaries lettered H (9.4 Ma) and G (8.7 Ma) along the Bahamas Transect, respectively. Considering the time represented by the erosional unconformity interposed between the youngest sediments of the Chilcatay Formation (18.02 ± 0.07 Ma) and the oldest sediments of the Pisco Formation (9.46 ± 0.05 Ma) and the modest thickness of P0 sediments, there is a long hiatus in sedimentation. This long hiatus in the stratigraphic record indicates a prolonged phase of subaerial exposure and erosion of this marginal basin and possibly reflects a widespread pulse of uplift and compression related to the Quechua 1 tectonic event (Viveen & Schlunegger 2018) exacerbating the effects of the long-term global lowering of sea level recorded during the Middle Miocene Climate Transition. The most recent estimates for the amplitude of the eustatic changes during this period indicate that the sea-level fell about 53-69 m between 16.5 and 13.9 Ma (John et al. 2011) and 50 ± 5 m between 13.6 and 11.4 Ma (John et al. 2004). As such, the Pisco Formation records a subsequent, widespread marine transgression and re-flooding of the forearc basin.

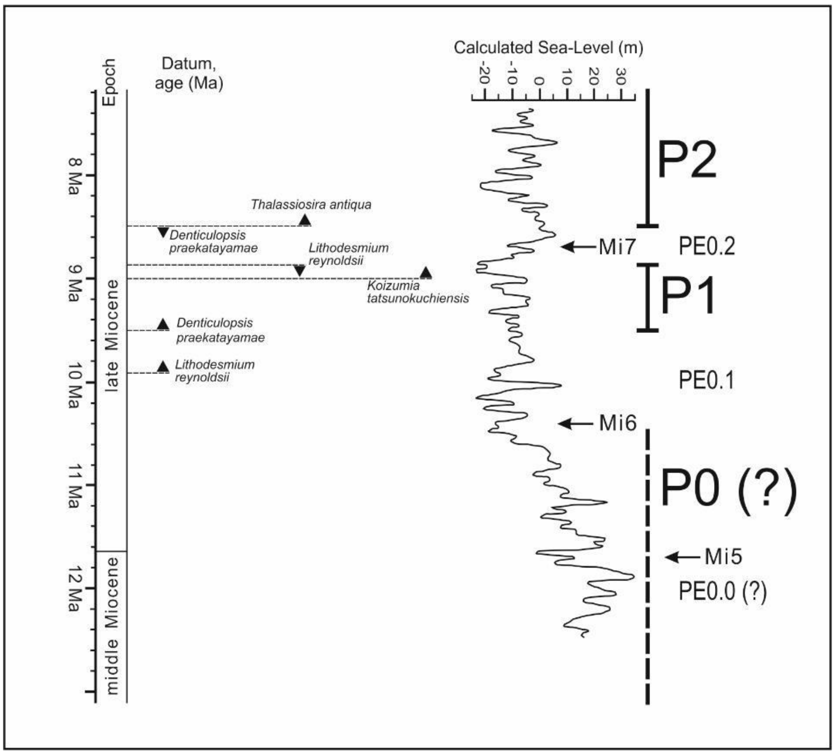

Figure 10.14. Correlation of Pisco allomembers with Late Miocene sea-level fluctuations by using integrated biostratigraphic and geochronologic data from Gariboldi et al. (2017). Diatom biostratigraphy revised following most recent publications on Equatorial Pacific diatom biostratigraphy (mostly Barron, 2003). Calculated sea-level curve from Westerhold et al. (2005). Modified from Di Celma et al. (2018).

The evidence of a eustatic origin for the allomember bounding unconformities in the Pisco Formation does, obviously, not imply that the regional tectonic activity did not affect the overall stratigraphic architecture of this unit. Within the study area, the PE0.1 and PE0.2 surfaces onlap onto the older PE0.0 surface in a broadly northeasterly direction, merging into a composite PE0 unconformity. Accordingly, the intervening P0, P1, and P2 allomembers taper progressively to the northeast and overstep each other to lap out against the pre-Cenozoic crystalline basement, forming a set of retrogradationally stacked stratal wedges. This architectural pattern, suggesting a steady increase in the accommodation space, is indicative of deposition during a long-term period of relative sea-level rise punctuated by repeated sea-level falls and is interpreted as the product of third-order eustatic sea-level changes superimposed on prolonged extension and relatively uniform subsidence (Viveen & Schlunegger, 2018).

Text, figures and tables of this chapter are taken from different papers. One is "Biostratigraphy, geochronology and sedimentation rates of the upper Miocene Pisco Formation at two important marine vertebrate fossil-bearing sites of southern Peru" written by Karen Gariboldi, Giulia Bosio, Elisa Malinverno, Anna Gioncada, Claudio Di Celma, Igor M. Villa, Mario Urbina and Giovanni Bianucci, published on Newsletters on Stratigraphy in 2017, Vol. 50/4 (2017), 417-444. In this paper, Giulia Bosio contributes to sample collection, volcanic ash analyses, ^{39}Ar–^{40}Ar geochronology, discussion on the previous dating and the new results, comparison of data and calculation of sedimentation rates.The other one is "Tephrochronology and chronostratigraphy of the Miocene Chilcatay and Pisco formations (East Pisco Basin, Peru)" written by Giulia Bosio, Elisa Malinverno, Igor M. Villa, Claudio Di Celma, Karen Gariboldi, Anna Gioncada, Valentina Barberini, Mario Urbina and Giovanni Bianucci, submitted to Newsletters on Stratigraphy in December 2018. The other paper is "Intraformational unconformities as a record of Late Miocene eustatic falls of sea level in the Pisco Formation (southern Peru)" written by Claudio Di Celma, Elisa Malinverno, Giulia Bosio, Karen Gariboldi, Alberto Collareta, Anna Gioncada, Walter Landini, Pietro Paolo Pierantoni and Giovanni Bianucci, published in 2018 on Journal of Maps, vol. 14(2), 607-619. In this paper, Giulia Bosio contributes to field mapping and measurement of stratigraphic sections, stratigraphic correlations and discussion.

Chapter References

Akiba, F., Yanagisawa, Y. 1986. Taxonomy, morphology and phylogeny of the Neogene diatom zonal marker species in the middle-to-high latitudes of the North Pacific. DSDP Initial Reports 87, 483-554.

Barron, J. A. 1976. Revised Miocene and Pliocene diatom biostratigraphy of upper Newport Bay, Newport Beach, California. Marine Micropaleontology, 1, 27-63.

Barron, J.A. 1980. Lower Miocene to Quaternary diatom biostratigraphy of Leg 57, off Northeastern Japan, Deep Sea Drilling Project. Initial Reports of the Deep Sea Drilling Project 56, 641-685.

Barron, J. A. 1985. Miocene to Holocene planktic diatoms. In: Bolli, H. M., Saunders, J. B. & Perch-Nielsen, K. P. (Eds.), Plankton stratigraphy. Cambridge: Cambridge University Press, 763-809.

Barron, J. A. 2003. Planktonic marine diatom record of the past 18 my: appearances and extinctions in the Pacific and Southern Oceans. Diatom Research, 18(2), 203-224.

Berggren, W.A., Kent, D.V., Swisher, C.C., Aubry, M.P. 1995. A Revised Cenozoic geochronology and chronostratigraphy. In: Berggren, W. A., Kent, D.V., Hardenbol, J. (Eds.), Geochronology, Time Scales and Global Stratigraphic Correlation. Society of Economic Paleontologists and Mineralogists, Special Publication, Tulsa, 54, 129-212.

Bianucci, G., Lambert, O., Post, K. 2010. High concentration of long-snouted beaked whales (genus Messapicetus) from the Miocene of Peru. Palaeontology, 53, 1077-1098.

Blott, S.J., Pye, K. 2001. Gradistat: a grain size distribution and statistics package for the analysis of unconsolidated sediments. Earth Surface Processes and Landforms, 26, 1237-1248.

Brun, J. 1894. Espèces nouvelles. Le Diatomiste, 2, 72-78.

Burckle, L. H. 1972. Late Cenozoic planktonic diatom zones from the eastern equatorial Pacific. In: R. Simonsen (Ed.), Proceedings of the First Symposium on Recent and Fossil Marine Diatoms, Bremenhaven. Beihefte zur Nova Hedwigia.

Cleve-Euler, A. 1941. Alttertiäre Diatomeen und Silicoflagellaten im Inneren Schwedens. Palaeontographica Abteilung A 92, 165-208.

DeVries, T. J. 1998. Oligocene deposition and Cenozoic sequence boundaries in the Pisco Basin (Peru). Journal of South American Earth Sciences, 11, 217-231.

DeVries, T. J., Jud, N. A. 2018. Lithofacies patterns and paleogeography of the Miocene Chilcatay and lower Pisco depositional sequences (East Pisco Basin, Peru). Boletín de la Sociedad Geológica del Perú, Volumen Jubilar 8, 124-167.

Di Celma, C., Malinverno, E., Cantalamessa, G., Gioncada, A., Bosio, G., Villa, I.M., Gariboldi, K., Rustichelli, A., Pierantoni, P.P., Landini, W., Tinelli, C., Collareta, A., Bianucci, G. 2016a. Stratigraphic framework of the late Miocene Pisco Formation at Cerro Los Quesos (Ica Desert, Peru). Journal of Maps, 12, 1020-1028.

Di Celma, C., Malinverno, E., Gariboldi, K., Gioncada, A., Rustichelli, A., Pierantoni, P.P., Landini, W., Bosio, G., Tinelli, C., Bianucci, G. 2016b. Stratigraphic framework of the late Miocene to Pliocene Pisco Formation at Cerro Colorado (Ica Desert, Peru). Journal of Maps, 12, 515-557.

Di Vincenzo, G., Viti, C., Rocchi, S. 2003. The effect of chlorite interlayering on 40Ar–39Ar biotite dating: an 40Ar–39Ar laser-probe and TEM investigations of variably chloritised biotites. Contributions to Mineralogy and Petrology, 145, 643-658.

Eberli, G. P., Anselmetti, F. S., Kroon, D., Sato, T., Wright, J. D. 2002. The chronostratigraphic significance of seismic reflections along the Bahamas Transect. Marine Geology, 185, 1-17.

Esperante, R., Brand, L. R., Chadwick, A.V., Poma, O. 2015. Taphonomy and paleoenvironmental conditions of deposition of fossil whales in the diatomaceous sediments of the Miocene/Pliocene Pisco Formation, southern Peru – a new Fossillagerstätte. Palaeogeography, Palaeoclimatology, Palaeoecology, 417, 337-370.

Expedition 320/321 Scientists 2010. Methods. In H. Pälike, M. Lyle, H. Nishi, I. Raffi, K. Gamage, A. Klaus, and the Expedition 320/321 Scientists, Proceedings of the integrated ocean drilling program, 320/321: Tokio: Integrated Ocean Drilling Program Management International, Inc.

Folk, R.L. 1954. The distinction between grain size and mineral composition in sedimentary-rock nomenclature. Journal of Geology, 62, 344-359.

Gariboldi, K. 2016. A note on diatom stratigraphic markers in upper Miocene sediments of the Pisco Formation, Peru, and description of Delphineis urbinai sp. nov. Diatom Research, 31(3), 285-301.

Grunow, A. 1884. Diatomeen von Franz Josef-Land. Denkschriften der mathematisch-naturwissenschaftlichen Classe der Kaiserlichen Akademie der Wissenschaften, 48, 53-112.

John, C. M., Karner, G. D., Browning, E., Leckie, R. M., Mateo, Z., Carson, B., Lowery, C. 2011. Timing and magnitude of Miocene eustasy derived from the mixed siliciclastic-carbonate stratigraphic record of the northeastern Australian margin. Earth and Planetary Science Letters, 304, 455-467.

John, C. M., Karner, G. D., Mutti, M. 2004. $\delta^{18}O$ and Marion Plateau backstripping: Combining two approaches to constrain late middle Miocene eustatic amplitude. Geology, 32, 829-832.

Koizumi, I. 1992. Diatomaceous sediments along the Pacific coastal areas of South America and their evaluation. Journal of the Faculty of Science, Hokkaido University, Ser. IV, 23(2), 227-245.

Lambert, O., Bianucci, G., Post, K. 2009. A new beaked whale (Odontoceti, Ziphiidae) from the Middle Miocene of Peru. Journal of Vertebrate Paleontology, 29, 910-922.

Lambert, O., Bianucci, G., Post, K. 2010a. Tusk bearing beaked whales from the Miocene of Peru: Sexual dimorphism in fossil ziphiids? Journal of Mammalogy, 91, 19-26.

Lambert, O., Bianucci, G., Post, K., Muizon, C. de, Salas-Gismondi, R., Urbina, M., Reumer, J. 2010b. The giant bite of a new raptorial sperm whale from the Miocene epoch of Peru. Nature, 466, 105-108.

Macharé, J., Fourtanier, E. 1987. Datations des formations tertiaires du bassin de Pisco (Pérou) à partir d'associations de diatomées. Comptes rendus de l'Académie des sciences. Série 2, Mécanique, Physique, Chimie, Sciences de l'univers, Sciences de la Terre, 305(5), 407-412.

Mertz, D., 1966. Mikropaläontologische und sedimentologische Untersuchung der Pisco-Formation Südperus. Palaeontographica B, 118, 1-51.

Miller, K.G., Mountain, G.S., Browning, J.V., Kominz, M., Sugarman, P.J., Christie-Blick, N.,…, Wright, J.D. 1998. Cenozoic global sea level, sequences, and the New Jersey transect; results from coastal plain and continental slope drilling. Reviews of Geophysics, 36, 569-601.

Miller, K.G., Wright, J.D., Fairbanks, R.G. 1991. Unlocking the Ice House: Oligocene-Miocene oxygen isotopes, eustasy, and margin erosion. Journal of Geophysical Research: Solid Earth, 96(B4), 6829-6848.

Muizon, C. de, DeVries, T.J. 1985. Geology and paleontology of late Cenozoic marine deposits in the Sacaco area (Peru). Geologische Rundschau, 74, 547-563.

Muizon, C. de. 1988. Les vertébrés fossiles de la Formation Pisco (Pérou). Troisièmepartie: Les Odontocètes (Cetacea, Mammalia) du Miocène. Travaux de l'Institut Français d'Études Andines, 42, 1-244.

Parham, J.F., Pyenson, N.D. 2010. New sea turtle from the Miocene of Peru and the iterative evolution of feeding ecomorphologies since the Cretaceous. Journal of Paleontology, 84, 231-247.

Pimiento, C., Balk, M. A. 2015. Body-size trends of the extinct giant shark Carcharocles megalodon: a deep-time perspective on marine apex predators. Paleobiology, 41(3), 479-490.

Schrader, H., Ronning, P. 1988. Diatom biostratigraphy and coastal upwelling interpretation. In: Dunbar, R. B., Baker, P. A. (Eds.), Cenozoic Geology of the Pisco Basin, IGCP no. 156 Guidebook to Field Workshop, May 1988, Lima, 135-140.

Tanimura, Y. 1996. Fossil marine plicated Thalassiosira: taxonomy and an idea on phylogeny. Diatom Research, 11(1), 165-202.

Turco, E., Hilgen, F. J., Lourens, L. J., Shackleton, N. J., Zachariasse, W. J. 2001. Punctuated evolution of global climate cooling during the late Middle to early Late Miocene: High-resolution planktonic foraminiferal and oxygen isotope records from the Mediterranean. Paleoceanography, 16, 405-423.

Viveen, W., Schlunegger, F. 2018. Prolonged extension and subsidence of the Peruvian forearc during the Cenozoic. Tectonophysics, 730, 48-62.

Westerhold, T., Bickert, T., Röhl, U. 2005. Middle to late Miocene oxygen isotope stratigraphy of ODP site 1085 (SE Atlantic): New constrains on Miocene climate variability and sea-level fluctuations. Palaeogeography, Palaeoclimatology, Palaeoecology, 217, 205-222.

White, J. D. L., Houghton, B. F. 2006. Primary volcaniclastic rocks. Geology, 34(8), 677-680.

Yanagisawa, Y., Akiba, F. 1990. Taxonomy and phylogeny of the three marine diatom genera Crucidenticula, Denticulopsis and Neodenticula. Bulletin of the Geological Survey of Japan, 41, 197-301.

Chapter 11. Sr-isotope stratigraphy of the P0 allomember

11.1. Sr-isotope analyses

P0 allomember age was unknown for a long time, because of the scarcity of tephra layers (only one and badly preserved tephra was found in the allomember) and the lack of microfossils in its sediments. For dating P0, several carbonate-shell invertebrates (mollusks and barnacles) and shark teeth were collected in Cerro Submarino (see Fig.11.1 and Fig. 9.1, Chapter 9 for the site position), where P0 has the maximum exposure, and analyzed for Strontium Isotope Stratigraphy (SIS).

Preventive analyses with optical microscope, SEM and cathodoluminescence were performed on mollusks and barnacles in order to identify the recrystallized material that could altered the real age of the carbonate formation. Pristine shells were chosen for the age calculation, but some recrystallized materials were also selected for $^{87}Sr/^{86}Sr$ analyses, for understanding how diagenesis changed the $^{87}Sr/^{86}Sr$ ratio (diagenesis path). Regarding shark teeth, samples were taken from the outer enameloid layer avoiding dentine, which is generally more susceptible to such alteration than enameloid (Becker et al. 2008).

For a particular level, different types of material were analyzed in order to understand how diagenesis altered the $^{87}Sr/^{86}Sr$ ratio and which ages were to be considered more reliable than others. Furthermore, several samples from the known-age Chilcatay Formation were dated for checking the reliability of the P0 results (see Chapter 8).

The samples selected for $^{87}Sr/^{86}Sr$ analyses are listed and described in Table 11.1.

Samples	Nett (g)	Locality	Formation	Level	Description
SUB-2	0.0154	Submarino	Pisco 0	SUB-2	Calcite cement in the marrow cavities of a mandibular bone
SUB-5	0.0291	Submarino	Pisco 0	SUB-5	Oyster, few mother-of-pearl portions (other parts very altered)
SUB-8bis1	0.1924	Submarino	Pisco 0	SUB-8bis	Barnacle sheat (few material, other parts very altered)
SUB-8bis2	0.0977	Submarino	Pisco 0	SUB-8bis	Bulk (inside the barnacle)
SUB-8bis3	0.0167	Submarino	Pisco 0	SUB-8bis	Recrystallized bivalve shell (outer part)
Dente1	0.0165	Submarino	Pisco 0	Base P0	Shark tooth (*Cosmopolitodus hastalis* , long one)
Dente2	0.0137	Submarino	Pisco 0	Base P0	Shark tooth (*Cosmopolitodus hastalis* , short one)
Dente3	0.0088	Submarino	Pisco 0	Base P0	Shark tooth (*Isurus oxyrinchus* , short one)

Table 11.1. List and description of the P0 analyzed samples.

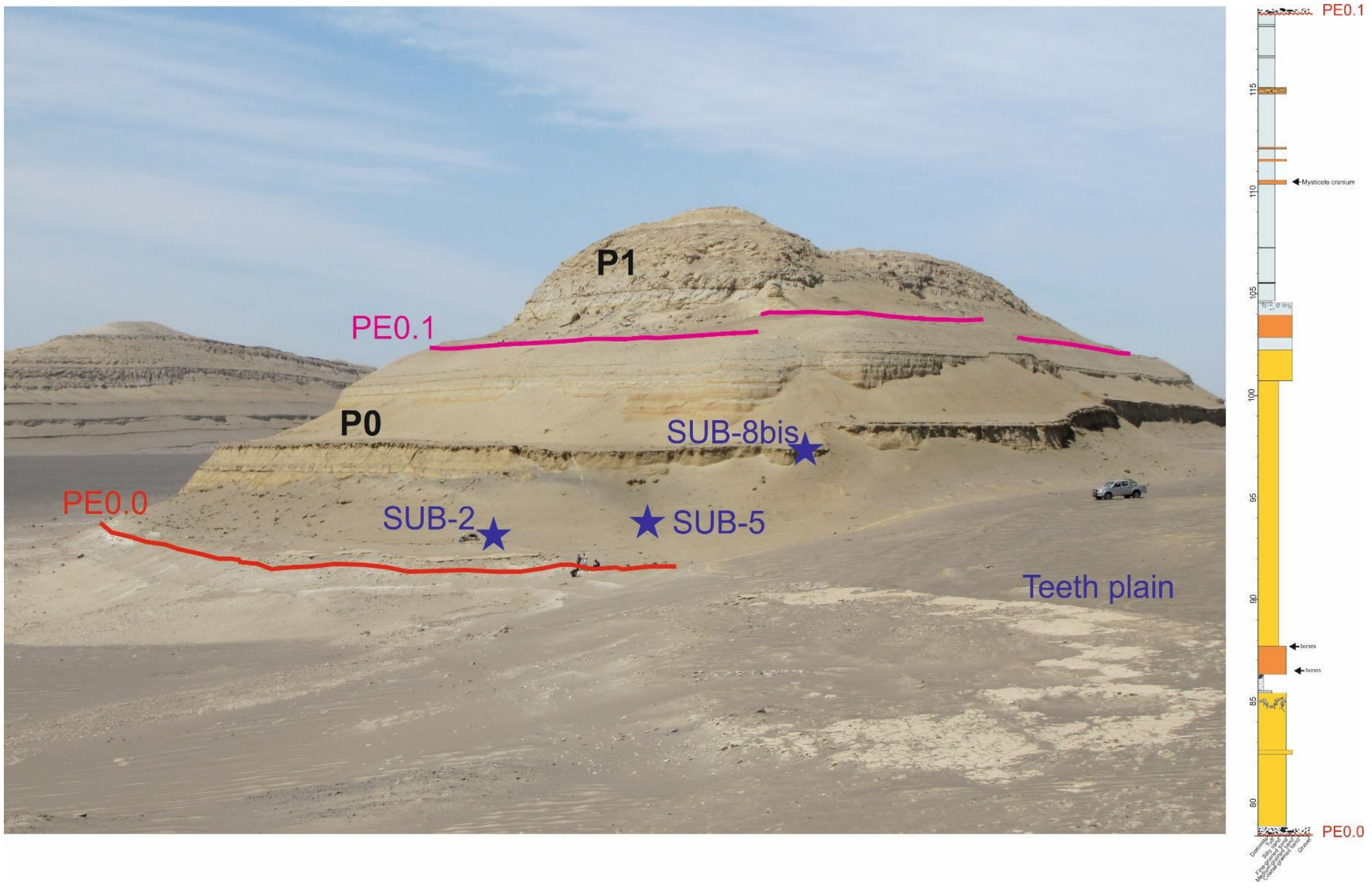

Figure 11.1. Cerro Submarino showing the PE0.0 and PE0.1 erosive surfaces, and P0 and P1 allomembers. Stars indicate the levels sampled for Sr stratigraphy. The P0 stratigraphic log on the right has been measured at a nearby locality, Ullujaya. Photo by Claudio Di Celma.

Three shark teeth were chosen at the base of P0 allomember, just above the PE0.0 unconformity, in the plain northward from Cerro Submarino (see Fig. 11.1). “Dente1” is a lower anterolateral tooth of *Cosmopolitodus hastalis*, “Dente2” is an upper tooth of *Cosmopolitodus hastalis*, and “Dente3” is a lower tooth of *Isurus oxyrinchus* (see Fig. 11.2). Even the shark teeth are not completely well-preserved, as shown by the break in the root, they show an intact outer thin enameloid layer.

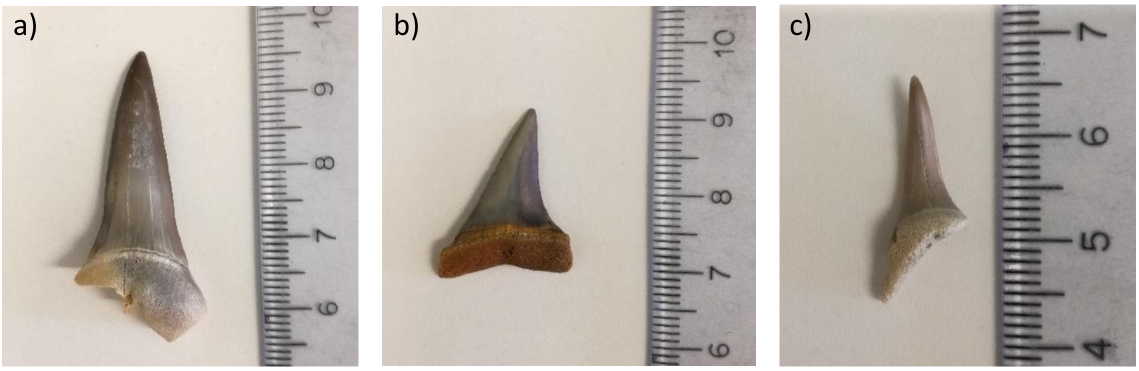

Figure 11.2. a) “Dente1” tooth of *C. hastalis*. b) “Dente2” tooth of *C. hastalis*. c) “Dente3” tooth of *I. oxyrinchus*. All images in lingual view. Scratches are the result of the sampling with micro-driller.

Few meters above the PE0.0 unconformity, a calcite nodule inside a whale mandibular arch (SUB-2, see Fig. 11.1) was first selected because we hypothesized its precipitation in the early diagenesis, as dolomitic nodules inside bone cavities in the Pisco Formation (Gariboldi et al. 2015). Actually, we realized after seeing the results that the calcite was precipitated during later diagenetic processes. Few meters above, a not very well preserved oyster was collected from the layer SUB-5 (see Fig. 11.1) and the few nacre layers were drilled as pristine calcite for $^{87}Sr/^{86}Sr$ analyses. Above ca. 5 m from SUB-5, in the level SUB-8bis (see Fig. 11.1) three samples were selected. One from the preserved calcite sheath of a barnacle (SUB-8bis1), considered pristine; one from the bulk inside the barnacle (SUB-8bis2), for looking for values related to the late cement and other components; and one from a completely recrystallized shell of a bivalve (SUB-8bis3), for understanding if the diagenesis increases or decreases the $^{87}Sr/^{86}Sr$ ratio.

#	sample name or number	$^{87}Sr/^{86}Sr$ measured	± 2 S $_{mean}$	$^{87}Sr/^{86}Sr_{sample}$ corrected to difference: NBS 987 value McArthur and NBS 987 measured with sample	$^{87}Sr/^{86}Sr_{sample}$ corrected to difference: USGS EN-1 value McArthur and USGS EN-1 measured with sample	$^{87}Sr/^{86}Sr$ sample corrected to difference: NBS 987 value McArthur and NBS 987 Bochum mean value	$^{87}Sr/^{86}Sr_{sample}$ corrected to difference: USGS EN-1 value McArthur and USGS EN-1 Bochum mean value
1	NIST NBS 987	0.710252	0.000006	0.710247	0.710254	0.710258	0.710268
2	PN-OST	0.708498	0.000005	0.708493	0.708500	0.708504	0.708514
3	PN-GI01	0.708513	0.000007	0.708508	0.708515	0.708519	0.708529
4	PN-GI02	0.708536	0.000005	0.708531	0.708538	0.708542	0.708552
6	UJA-2a	0.708541	0.000005	0.708536	0.708543	0.708547	0.708557
7	UJA-2b	0.708523	0.000005	0.708518	0.708525	0.708529	0.708539
8	UL-D4a	0.708506	0.000004	0.708501	0.708508	0.708512	0.708522
9	UL-D4b	0.708617	0.000005	0.708612	0.708619	0.708623	0.708633
10	UL-D4c	0.708444	0.000005	0.708439	0.708446	0.708450	0.708460
11	UL-LIVa	0.708516	0.000005	0.708511	0.708518	0.708522	0.708532
12	UL-LIVb	0.708512	0.000005	0.708507	0.708514	0.708518	0.708528
13	USGS EN-1	0.709173	0.000005	0.709168	0.709175	0.709179	0.709189
14	NIST NBS 987	0.710235	0.000005	0.710247	0.710250	0.710241	0.710251
15	UL-LIVd	0.708514	0.000005	0.708526	0.708529	0.708520	0.708530
16	UJA-LIVC1	0.708535	0.000005	0.708547	0.708550	0.708541	0.708551
17	UJA-LIVC2	0.708340	0.000005	0.708352	0.708355	0.708346	0.708356
18	UJA-LIVC3	0.708542	0.000005	0.708554	0.708557	0.708548	0.708558
19	UJA-LIVC4	0.708521	0.000005	0.708533	0.708536	0.708527	0.708537
20	SUB-5	0.708804	0.000005	0.708816	0.708819	0.708810	0.708820
21	SUB-2	0.708557	0.000005	0.708569	0.708572	0.708563	0.708573
22	USGS EN-1	0.709160	0.000005	0.709172	0.709175	0.709166	0.709176
23	NIST NBS 987	0.710244	0.000005	0.710247	0.710252	0.710250	0.710260
24	SUB-8bis1	0.708811	0.000005	0.708814	0.708819	0.708817	0.708827
25	SUB-8bis2	0.708273	0.000005	0.708276	0.708281	0.708279	0.708289
26	SUB-8bis3	0.708650	0.000005	0.708653	0.708658	0.708656	0.708666
27	Dente1	0.708803	0.000005	0.708806	0.708811	0.708809	0.708819
28	Dente2	0.708778	0.000005	0.708781	0.708786	0.708784	0.708794
29	Dente3	0.708784	0.000005	0.708787	0.708792	0.708790	0.708800
32	USGS EN-1	0.709167	0.000005	0.709170	0.709175	0.709173	0.709183

Table 11.2. Rough $^{87}Sr/^{86}Sr$ results of both Chilcatay Formation and P0 allomember analyzed samples, and standards.

$^{87}Sr/^{86}Sr$ analyses, made at the Institute für Geologie, Mineralogie und Geophysik of the Ruhr-Universität of Bochum, gave the results shown in Table 11.2. We chose the results of $^{87}Sr/^{86}Sr$ sample corrected to difference: USGS EN-1 value McArthur and USGS EN-1 Bochum mean value.

Then, we used the LOWESS Table 5 made for the GTS2012 timescale (McArthur et al. 2012), given by Professor John M. McArthur, for calculating the corresponding ages.

As explained in Chapter 8, the LOWESS Table 5 is still incomplete, therefore the mean results were rounded off to the closest value and the values ± 2σ were rounded off overestimating the age error. Because of the uncertainty (± 2σ), we obtained three different age for each analysis: the preferred age, the minimum and the maximum (see Table 11.3).

The age results are shown in Table 11.3. Discarding the values of diagenetic samples, all the good samples suggested a time range between the Langhian and the Serravallian, not very well constrained because of the scarcity of well-preserved specimens that allow only few dated points.

The base of the P0 allomember has a wide time range. The shark tooth "Dente1" gives a preferred age of 13.00 Ma, with an age range between 12.50 and 13.65 Ma. The tooth "Dente2" has an older preferred age of 14.80 Ma, a minimum age of 14.45 Ma and a maximum age of 15.05 Ma, the oldest age registered for the P0 allomember. Finally, the shark tooth "Dente3" gives a long time range from 13.65 to 14.90 Ma, with a preferred age of 14.60 Ma. Considering all the samples, the level cannot be dated making the mean of the preferred ages (e.g. 14.13 Ma). Because there are no reasons to prefer one tooth than another, the choice is to consider the oldest age as the one of the P0 base. This is justified because all the shark teeth are above the PE0.0 unconformity, inside a level of condensation with pebbles, bone fragments and phosphatic nodules, which can be considered result of sediment accumulation, halts in sedimentation, sediment winnowing, erosion, reworking and bypass (Föllmi 2016). Following Föllmi (2016), these condensation sediments may include amalgamated faunas of different ages. Therefore, the P0 base is dated to 14.80 Ma, with an age range from 14.45 to 15.05 Ma.

Few meters above the PE0.0 unconformity, the calcitic sample SUB-2 was discarded from the age calculation: the suspected very old age suggests a precipitation of the nodule late in the diagenesis, and not in the early diagenesis as hypothesized before. For this level, we have the confirmation that the diagenesis decreased the $^{87}Sr/^{86}Sr$ value, with a consequent ageing of the real ages.

Above this sample, the oyster sample SUB-5 gives Serravallian ages: a minimum age of 12.45 Ma and a maximum age of 13.55 Ma, with a preferred age of 12.95 Ma. This is the only specimen that preserved the pristine calcite of the level.

Finally, in the uppermost level, SUB-8bis, the pristine calcite of a barnacle confirmed that the P0 allomember belongs to the Serravallian. The pristine calcite of a barnacle gives a preferred age of 12.60 Ma, the youngest age of the succession, with an age range between 12.00 and 13.05 Ma, which can be considered the ages of the level. The other two samples (bulk and recrystallized bivalve), indeed, were analyzed for understanding the diagenetic effect: we found that the $^{87}Sr/^{86}Sr$ values are reduced and the ages are highly increased.

The P0 allomember age is now resolved, but scarcely constrained: the base of this allomember can be Langhian in age, but the rest of the unit registers Serravallian ages. Considering the preferred ages, the final age here proposed for the P0 allomember is from 14.80 to 12.60 Ma, with an error age range that extended the time range between 15.05 and 12.00 Ma.

Samples	**plus 2σ**	**$^{87}Sr/^{86}Sr$ corrected value**	**minus 2σ**	**Min age (Ma)**	**Preferred age (Ma)**	**Max age (Ma)**
SUB-5	0.708825	0.708820	0.708815	12.45	**12.95**	13.55
SUB-2	0.708578	0.708573	0.708568	17.85	18.00	18.15
SUB-8bis1	0.708832	0.708827	0.708822	12.00	**12.60**	13.05
SUB-8bis2	0.708294	0.708289	0.708284	22.15	22.35	22.60
SUB-8bis3	0.708671	0.708666	0.708661	16.65	16.80	16.95
Dente1	0.708824	0.708819	0.708814	12.50	**13.00**	13.65
Dente2	0.708799	0.708794	0.708789	14.45	**14.80**	15.05
Dente3	0.708805	0.708800	0.708795	13.65	**14.60**	14.90

Table 11.3. Sr-isotope ages obtained for each sample of the P0 allomember. Cells in grey reported the selected reliable final ages.

11.2. Age implications of the P0 cetacean assemblage

The middle Miocene age for the P0 allomember agrees with the age reported by DeVries and Jud (2018) for the lower part of the Pisco Formation and the archaic aspect of the cetacean assemblage reported by Marx et al. (2017). According to Marx et al. (2017), the P0 assemblage appears considerably more archaic than that found at the well-known Pisco localities of Cerro Colorado, Cerro Los Quesos, Cerro la Bruja and Aguada de Lomas. Therefore, a Langhian-Serravallian age for the P0 allomember agrees with this observation on the cetacean fauna.

This chapter is entirely unreleased. Results will be discussed and published, in the next future, in the paper "Strontium Isotope Stratigraphy of the Miocene sedimentary successions in the Peruvian East Pisco Basin" in preparation.

Chapter References

Becker, A.M., Seidemann, D.E., Chamberlain, J.A. Jr., Buhl, D., Slattery, W. 2008. Strontium isotopic signatures in the enameloid and dentine of upper Cretaceous shark teeth from western Alabama: Paleoecologic and geochronologic implications. Palaeogeography, Palaeoclimatology, Palaeoecology, 264, 188-194.

DeVries, T. J., Jud, N. A. 2018. Lithofacies patterns and paleogeography of the Miocene Chilcatay and lower Pisco depositional sequences (East Pisco Basin, Peru). Boletín de la Sociedad Geológica del Perú, Volumen Jubilar, 8, 124-167.

Föllmi, K.B. 2016. Sedimentary condensation. Earth-Science Reviews, 152, 143-180.

Gariboldi, K., Gioncada, A., Bosio, G., Malinverno, E., Di Celma, C., Tinelli, C., Cantalamessa, G., Landini, W., Urbina, M., Bianucci, G. 2015. The dolomitic nodules enclosing fossil marine vertebrates in the East Pisco Basin, Peru: field and petrographic insights into their genesis and role in preservation. Palaeogeography, Palaeoclimatology, Palaeoecology, 438, 81-95.

Marx, F.G., Lambert, O., de Muizon, C. 2017. A new Miocene baleen whale from Peru deciphers the dawn of cetotheriids. Royal Society open science, 4: 170560.

McArthur, J.M., Howarth, R.J., Shields, G.A. 2012. Strontium Isotope Stratigraphy. In F.M. Gradstein, J.G. Ogg, Schmitz M., Ogg G. (Eds.), The Geologic Time Scale 2012 (Chapter 7, pp. 127-144). Elsevier.

Chapter 12. Chemical and petrographic fingerprinting of Pisco Formation tephra as a tool for high-resolution stratigraphy

Due to their regional dispersion, geologically instantaneous deposition, and the common presence of minerals suitable for radiometric age determination, the value of volcanic ashes as regional chronostratigraphic markers has long been recognized (Lowe et al. 2017 and references therein).

With the aim of fully exploiting the potential of these volcanic ash layers for tephrostratigraphy, we fingerprinted tephra layers by a chemical and petrographic characterization and correlate them between different localities. Tephra fingerprinting is widely recognized as a useful method for stratigraphic reconstructions. This method is largely employed in the Quaternary (e.g. Shane et al. 2003; Lowe 2011; Smith et al. 2011; Zanchetta et al. 2011; D'Antonio et al. 2016) and has been used for correlating deposits of large eruptions of the Central Andes (De Silva & Francis 1989; Lebti et al. 2006; Breitkreutz et al. 2013). We focused on the P2 allomember, which is the youngest unconformity-bounded unit documented so far in the upper Miocene portion of the Pisco Formation with a high paleontological content (Chapter 9). We fingerprinted tephra layers of the P2 allomember by using major element chemistry of biotite and glass combined with petrographic and granulometric features. Despite the expected predominance of tephra with similar silicic composition, and the discontinuity of the record due to the shallow marine environment, we correlated ash layers in different localities largely improving stratigraphic resolution and highlight the feasibility of an approach based on major element biotite and glass chemistry.

12.1. Tephra description in the field

Tephra were collected at eight localities (see Fig. 12.1): Cerro los Quesos (14°30'59"S, 75°42'59"W), Cerro los Quesos west (14°31'13"S, 75°44'34"W), Cerro la Bruja (14°31'44"S, 75°40'00"W), Cerro Colorado (14°21'04"S, 75° 53'43"W), Cerro Hueco la Zorra (14°26'58"S, 75°41'01"W), Cerro Blanco (14°24'57"S, 75°41'17"W), Cerro Toro Chico (14°27'36"S, 75°48'01"W) and Cerros Cadenas de los Zanjones (14°34'21"S, 75°42'60"W).

Figure 12.1. Satellite image of the Ica Desert localities investigated for the P2 allomember tephra fingerprinting.

Based on image © 2018 DigitalGlobe.

Along the stratigraphic sections (detailed stratigraphic logs are shown in the Appendix), ash layers were more frequent in the P2 allomember than in the other sequences (about 10-30 tephra layers thicker than 2-3 cm in 100 m) and particularly abundant in the diatomitic portion. For the majority of the sampled tephra, thickness ranges between 5 and 15 cm. However, whereas their bases are commonly sharp and easy to recognize (Fig. 12.1a), their upper boundaries may be irregular or diffuse and not always clearly detectable, particularly in diatomite rich sediments, due to the similar light color and grain size. Some thicker tephra (up to 50 cm), organized in different sub-layers, have been found. Except for very fine-grained and crystal-free ashes, the ash beds show an evident normal grading and the lower portion is typically characterized by a higher concentration of crystals (Fig. 12.2b). Although in most cases they are unconsolidated, in some cases volcanic ash layers are cemented by secondary minerals such as gypsum and jarosite. At the base, a hard gypsum/anhydrite crust of a few mm thickness is commonly found. The color in the field is usually grey to light grey, with a "pepper and salt" appearance due to biotite, when present (Fig. 12.2b).

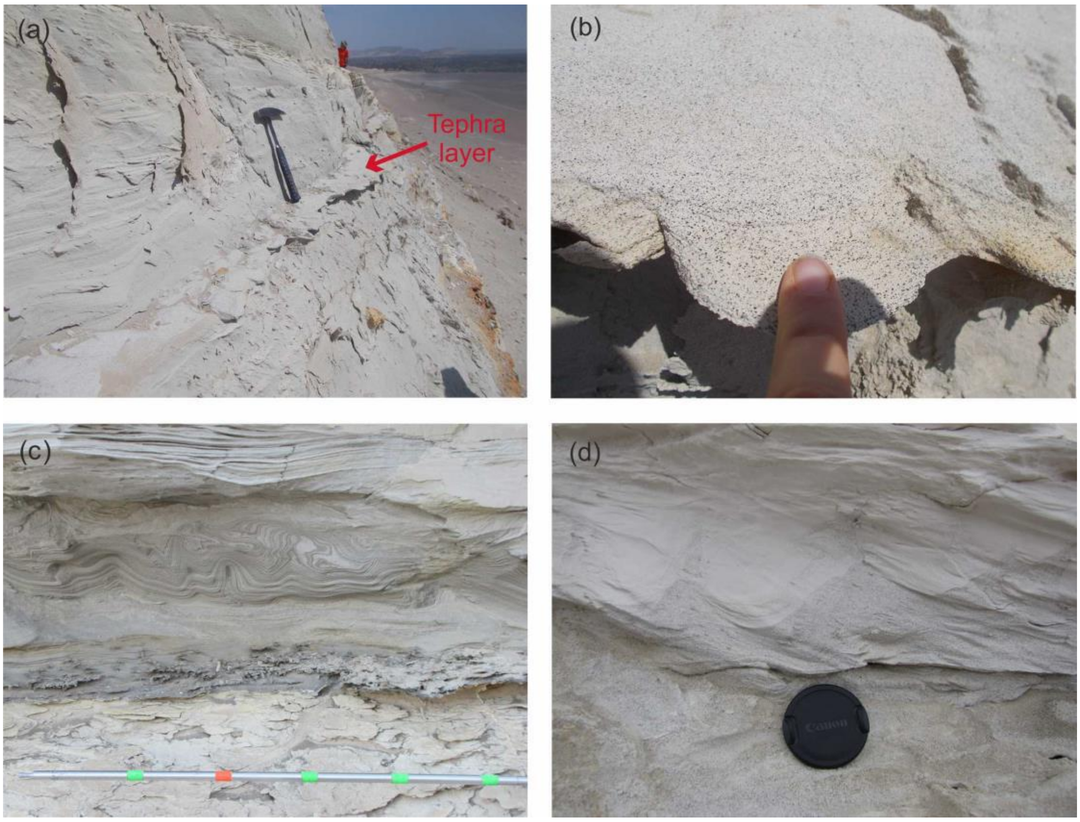

Figure 12.2. Field photos. a) Tephra layer BL-T1 interbedded with Pisco Fm diatomites at Cerro Blanco. Tephra are often revealed by the sharp bottom discontinuity

highlighted by gypsum wavy layers protruding from the outcrop. Hammer is 33 cm long. The arrow shows the tephra layer. b) Detail of the same tephra layer before cleaning the outcrop: “pepper and salt” appearance is due to the biotite concentration at the base. c) Load casts in the ash layer CLQ-T12 (Cerro los Quesos). Marks on the stick are at 10 cm of distance. d) Diapirs and flames recognizable in the tephra layer CLQ-T1 (Cerro los Quesos). Lens cap diameter is 6.5 cm. From Bosio et al. (in press).

Thin (2-3 cm) dark grey tephra were also found, although less frequently. Internally, a variety of soft-sediment deformation structures (including load casts, small-scale folding, convolutions, and dish and pillars structures) have been observed in some of the thicker layers (CLQ-T1 and CLQT-12). These deformation structures could have developed by rapid deposition of the thick ash layers on waterlogged diatom ooze, which may have started consolidation in the immediately underlying sediments (Pedersen & Surlyk 1977). Waters escaping from such layers may liquefy or fluidize the lower portion of the ash bed, resulting in sinking of the overlying denser portion into the liquidized lower portion (load casts, see Fig. 12.2c) and compensatory upward intrusion (diapirs and flames, see Fig. 12.2d) of the latter into the overlying sediment (Owen 2003). In one case, these deformation structures are recognizable in two exposures of the same tephra layer 6 km far from each other (i.e. CLQ-T12 and LB-T7).

12.2. Petrographic fingerprinting of tephra

The grain sizes of the sampled ash layers fall in the range of fine-grained sand to silt. Inspections under SEM of bulk samples of some particularly coarse tephra and of the coarser fractions of pilot wet sieved samples indicate, in some cases, a minor percentage of strongly agglomerated particles, cemented by secondary minerals. However, most of the samples consist of loose ash, nearly unaffected by secondary cements. The grain-size distribution is unimodal or bimodal and the classification is dominated by fine-grained ashes, very fine-grained ashes or extremely fine-grained ashes, mainly moderately to well sorted (White & Houghton 2006) (see Table 12.1). In case of tephra subdivided in sublayers (e.g. CLQ-T1, CC-T1), the lower sublayer is usually coarser than the upper one; only in one case (CLQ-T9), a normally graded coarser layer directly overlies a well sorted fine grained ash layer, indicating deposition of ashes of two distinct, but relatively close, eruptive events.

Locality	Sample	Field observations		Grainsize[1]				Glass morphology	Crystals	Glass chemistry (wt%)														Correlation	$^{40}Ar/^{39}Ar$ dating (Ma)
		Thickness (cm)	Colour and notes	Folk (1954)	White and Houghton (2006)	median (phi)	sorting (phi)			mean, SD [n]	SiO_2	TiO_2	Al_2O_3	FeO^T	MnO	MgO	CaO	Na_2O	K_2O	P_2O_5	Cl	sum	A/CNK		
Cerro los Quesos	CLQ-T1a*	30	Light grey ash, fining upwards, with abundant coarse biotite decreasing in abundance and size towards the top; characteristic flame-like structures protrude into the overlying finer ash sublayer (fluidization)	bimodal, very poorly sorted, very coarse silt	fine ash	3.9	2.1	high vesiculated shards	bt, sa, pl	mean [6]	76.62	0.04	13.6	0.58	0.09	0.2	0.91	2.9	4.98	0.04	na	99.96	1.15	-	6.93 ± 0.09
										SD	0.22	0.03	0.09	0.08	0.07	0.12	0.05	0.08	0.32	0.04	-				
	CLQ-T9, sublayer T9a*	8	White ash, made only of vesicular glassy clasts, massive	unimodal, moderately sorted fine silt	extremely fine ash	7.4	1.0	na	rare bt	-	na	na	na	na	na	na	na	na	na	na	na	na	na	-	na
										-	-	-	-	-	-	-	-	-	-	-	-				
	CLQ-T9, sublayer T9b*	10	Light grey ash with visible fine biotite, normally graded; directly overlies T9a	unimodal, poorly sorted, very fine sand	fine ash	2.8	1.7	high vesiculated shards	bt, sa, pl	mean [5]	76.61	0.27	13.25	0.94	0.17	0.11	0.64	2.59	5.24	na	na	99.82	1.19	-	≥ 6.71 ± 0.02
										SD	0.90	0.14	0.80	0.15	0.03	0.07	0.18	0.30	0.35	-	-				
	CLQ-T12, sublayer T12a*	20	Light brown to grey ash, overladen by a convoluted upper sublayer	unimodal, poorly sorted, coarse silt	extremely fine ash	5.2	1.1	platy shards; bubble-wall shards	pl, px	mean [18]	61.39	0.94	14.39	3.42	0.10	1.03	2.41	3.62	4.06	0.23	0.10	91.70	0.98	LB-T7a, b	na
										SD	1.04	0.09	0.22	0.22	0.03	0.10	0.21	0.79	0.18	0.05	0.02				
	CLQ-T13b	15	Light grey ash	unimodal, poorly sorted, coarse silt	extremely fine ash	6.0	1.6	na	bt, feldspar	mean [8]	74.94	0.04	14.59	1.44	0.03	0.03	0.52	2.91	5.29	0.04	0.11	99.94	1.27	LB-T10	na
										SD	0.42	0.07	0.14	0.17	0.06	0.08	0.10	0.14	0.41	0.06	0.05				
	CLQ-T14	10	Light grey ash	unimodal, poorly sorted, coarse silt	extremely fine ash	5.2	1.6	high vesiculated shards	-	mean [10]	63.93	0.46	14.81	1.74	0.08	0.45	1.12	3.47	4.57	0.06	na	90.69	1.17	-	na
										SD	0.30	0.03	0.18	0.05	0.02	0.03	0.04	0.64	0.50	0.02	-				
	CLQ-T15	10	Light grey ash	unimodal, poorly sorted, very fine sand	very fine ash	3.7	1.8	platy shards; high vesiculated shards	bt, feldspar	mean [10]	70.27	0.05	13.03	1.49	0.04	0.09	0.57	3.16	4.58	0.07	na	93.35	1.16	LB-T11	na
										SD	0.87	0.03	0.15	0.08	0.02	0.01	0.05	0.26	0.19	0.03	-				
	CLQ-T16	30	Light grey ash	bimodal, very poorly sorted, very coarse silt	extremely fine ash	4.5	2.2	bubble-wall and platy shards; high vesiculated and stretched shards	bt, feldspar	mean [10]°	63.84	0.49	14.69	1.90	0.09	0.48	1.17	4.14	4.69	0.09	na	91.58	1.05	LB-T8	na
										SD	1.13	0.03	0.39	0.13	0.05	0.05	0.10	0.79	0.29	0.03	-				
	CLQ-T17	10	Light grey-brownish ash	unimodal, poorly sorted, very coarse silt	extremely fine ash	4.4	1.2	bubble-wall shards; high vesiculated shards	bt	mean [9]	66.26	0.46	14.66	1.80	0.11	0.45	1.15	4.41	4.89	0.08	0.15	94.40	1.00	LB-T15	na
										SD	2.98	0.14	0.93	0.40	0.03	0.14	0.27	0.49	0.24	0.03	0.01				
	CLQ-T21*	20	Light grey ash, massive	unimodal, very poorly sorted, very coarse silt	very fine ash	3.9	2.0	high vesiculated and stretched shards; shards with microlites	bt, feldspar	mean [10]	66.28	0.53	14.04	1.97	0.09	0.47	1.23	4.04	4.50	0.07	0.15	93.36	1.02	LB-T17	na
										SD	0.79	0.08	0.24	0.24	0.02	0.07	0.17	0.62	0.15	0.05	0.02				
	CLQ-T23	10	Light grey ash	unimodal, poorly sorted, coarse silt	extremely fine ash	4.9	1.6	bubble-wall shards	bt	mean [14]	74.14	0.04	16.08	0.45	0.08	0.02	0.21	4.16	4.12	0.70	na	100.00	1.38	LB-T19A	na
										SD	0.65	0.02	0.23	0.06	0.03	0.01	0.02	0.11	0.80	0.05	-				
	CLQ-T32	10	Light grey ash	unimodal, very poorly sorted, very fine sand	very fine ash	3.3	2.1	na	bt	mean [3]	73.66	0.28	15.49	1.13	0.16	0.39	0.75	3.30	4.71	0.00	0.12	99.99	1.30	-	na
										SD	0.10	0.10	0.23	0.09	0.06	0.17	0.06	0.18	0.36	0.00	0.02				
	CLQ-T43	3	Dark grey ash	na	na	na	na	low vesiculated shards with microlites	pl	mean [10]	64.02	1.36	16.95	5.50	0.09	1.91	4.09	1.99	3.98	0.03	0.09	99.99	1.13	-	na
										SD	0.43	0.13	0.20	0.12	0.08	0.12	0.35	0.42	0.40	0.04	0.03				
	CLQ-T44	3	Dark grey ash	na	na	na	na	high vesiculated shards with microlites	pl	mean [10]	55.57	1.37	15.57	6.85	0.14	2.60	5.24	3.36	2.23	0.40	0.08	93.42	0.89	-	na
										SD	1.05	0.22	0.68	1.09	0.04	0.29	0.53	0.81	0.14	0.03	0.01				
	CLQ-T45	3	Dark grey ash	unimodal, poorly sorted, coarse silt	extremely fine ash	5.0	1.4	low vesiculated shards with microlites	pl	mean [8]	58.34	0.86	15.37	3.60	0.12	1.24	2.87	3.01	3.43	0.30	0.14	89.28	1.11	-	na
										SD	0.64	0.12	0.34	0.46	0.04	0.17	0.34	0.79	0.72	0.08	0.02				
	CLQ-T49*	25	Light grey ash, with very abundant coarse biotite, in normally graded sublayers	unimodal, very poorly sorted, very coarse silt	very fine ash	4.1	2.0	bubble-wall shards; high vesiculated shards	bt, sa, pl	mean [5]	77.80	0.18	12.76	0.76	0.05	0.08	0.96	2.60	4.66	0.01	0.14	100.00	1.15	-	7.55 ± 0.05
										SD	0.10	0.13	0.13	0.11	0.07	0.06	0.09	0.13	0.18	0.03	0.04				

Cerro los Quesos west	CLQ15-T4	-	White ash with visible biotite	bimodal, poorly sorted, very coarse silt	extremely fine ash	4.9	2.0	na	bt	-	na	na	na	na	na	na	na	na	na	na	na	na	na	-	na
										-	-	-	-	-	-	-	-	-	-	-	-				
	CLQ15-T5	-	Grey ash	unimodal, poorly sorted, very fine sand	very fine ash	3.2	1.2	na	bt	-	na	na	na	na	na	na	na	na	na	na	na	na	na	-	na
										-	-	-	-	-	-	-	-	-	-	-	-				
	ANF-T4	-	Light grey ash with visible fine biotite	unimodal, poorly sorted, very coarse silt	extremely fine ash	4.3	1.4	bubble-wall shards; high vesiculated shards	bt, feldspar, px	mean [10]	70.07	0.18	12.75	1.06	0.04	0.14	0.65	3.43	4.86	0.02	na	93.21	1.06	-	na
										SD	0.14	0.03	0.11	0.07	0.02	0.02	0.02	0.13	0.17	0.03	-				
	CAMPO-T-P2	-	Light grey ash with visible fine biotite	unimodal, poorly sorted, coarse silt	extremely fine ash	4.9	1.3	na	bt, feldspar	-	na	na	na	na	na	na	na	na	na	na	na	na	na	-	na
										-	-	-	-	-	-	-	-	-	-	-	-				
Cerro la Bruja	LB-T2	10	Light grey ash with scattered yellowish and reddish coarse clasts	bimodal, poorly sorted, very coarse silt	very fine ash	4.0	1.7	na	bt	-	na	na	na	na	na	na	na	na	na	na	na	na	na	-	na
										-	-	-	-	-	-	-	-	-	-	-	-				
	LB-T3	10	Light grey ash with scattered yellowish and reddish coarse clasts	unimodal, poorly sorted, very coarse silt	very fine ash	4.0	1.3	na	bt	-	na	na	na	na	na	na	na	na	na	na	na	na	na	-	na
										-	-	-	-	-	-	-	-	-	-	-	-				
	LB-T7A	5	Grey to light brown, convoluted	na	na	na	na	bubble-wall shards	pl	mean [17]	61.52	0.95	14.60	3.51	0.10	1.04	2.43	3.28	3.96	0.19	0.12	91.69	1.04	CLQ-T12	na
										SD	0.76	0.05	0.22	0.35	0.02	0.13	0.29	0.73	0.21	0.04	0.02				
	LB-T7B	10	Grey to light brown, convoluted	na	na	na	na	bubble-wall shards; low vesiculated shards	pl	mean [22]	61.93	1.04	14.70	3.73	0.09	1.17	2.57	4.28	4.09	0.31	0.10	93.99	0.91	CLQ-T12	na
										SD	0.79	0.06	0.19	0.25	0.03	0.11	0.19	0.51	0.37	0.06	0.01				
	LB-T8	5	Light grey ash with visible fine biotite	bimodal, very poorly sorted, very coarse silt	extremely fine ash	4.4	2.0	bubble-wall shards; high vesiculated and stretched shards	bt	mean [10]°	64.82	0.49	14.67	1.83	0.10	0.46	1.14	4.10	4.67	0.08	na	92.36	1.06	CLQ-T16	na
										SD	0.45	0.02	0.13	0.07	0.02	0.03	0.05	0.59	0.20	0.03	-				
	LB-T9	20	Light grey ash	unimodal, poorly sorted, coarse silt	extremely fine ash	5.6	1.4	bubble-wall shards; high vesiculated shards; shards with microlites	rare bt	mean [10]	66.14	0.56	14.44	1.91	0.09	0.46	1.21	3.47	4.46	0.13	0.14	93.01	1.13	-	na
										SD	3.17	0.29	1.34	0.81	0.03	0.28	0.65	0.94	0.52	0.12	0.03				
	LB-T10	8	White ash, massive	unimodal, poorly sorted, coarse silt	extremely fine ash	5.2	1.7	bubble-wall shards; low vesiculated shards	bt	mean [10]	69.57	0.02	13.14	1.29	0.04	0.04	0.44	3.50	4.73	0.13	na	92.89	1.12	CLQ-T13b	na
										SD	0.62	0.02	0.24	0.34	0.02	0.03	0.07	0.19	0.18	0.02	-				
	LB-T11	10	Light grey ash, with abundant bt	bimodal, very poorly sorted, very fine sand	very fine ash	3.2	2.1	platy shards; high vesiculated shards	bt, feldspar	mean [26]	69.70	0.05	13.86	1.42	0.05	0.09	0.83	3.25	4.26	0.08	na	93.59	1.21	CLQ-T15	7.45 ± 0.01
										SD	1.97	0.03	2.42	0.29	0.03	0.03	1.00	1.08	0.84	0.03	-				
	LB-T15	10	Light grey-brownish ash	unimodal, poorly sorted, very coarse silt	very fine ash	4.0	1.1	bubble-wall shards; high vesiculated shards	bt	mean [9]	66.60	0.42	14.81	1.84	0.10	0.42	1.12	4.22	5.02	0.08	0.15	94.77	1.03	CLQ-T17	na
										SD	1.15	0.14	0.61	0.19	0.03	0.12	0.21	0.50	0.36	0.02	0.02				
	LB-T17	20	White-light grey ash, massive	unimodal, poorly sorted, very coarse silt	extremely fine ash	4.6	1.9	high vesiculated shards	rare bt	mean [15]	72.01	0.57	14.22	2.17	0.09	0.52	1.43	3.99	4.90	0.10	na	100.00	0.98	CLQ-T21	na
										SD	0.36	0.02	0.18	0.08	0.02	0.03	0.07	0.42	0.21	0.02	-				
	LB-T19A	4	White yellowish ash	unimodal, poorly sorted, very coarse silt	extremely fine ash	4.6	1.5	bubble-wall shards	bt	mean [15]	73.46	0.04	16.43	0.45	0.08	0.01	0.19	4.14	4.51	0.70	na	100.00	1.37	CLQ-T23	na
										SD	0.76	0.02	0.20	0.05	0.04	0.01	0.01	0.17	0.69	0.04	-				
	LB-T30	3	Dark grey ash	unimodal, poorly sorted, coarse silt	extremely fine ash	5.2	1.5	shards with microlites	-	mean [10]	57.61	1.19	14.66	5.21	0.09	1.72	3.83	3.69	3.49	0.46	0.11	92.05	0.87	-	na
										SD	0.96	0.05	0.46	0.18	0.03	0.07	0.13	0.67	0.30	0.04	0.01				
	LB16-T1	-	Light grey-brownish ash with fine biotite	bimodal, very poorly sorted, very coarse silt	extremely fine ash	4.2	2.1	na	bt	-	na	na	na	na	na	na	na	na	na	na	na	na	na	-	na
										-	-	-	-	-	-	-	-	-	-	-	-				

										-	-	-	-	-	-	-	-	-	-	-	-				
Cerros Cadenas de los Zanjones	LA-T31A	-	White ash with visible biotite	bimodal, poorly sorted, very coarse silt	extremely fine ash	4.1	2.0	na	rare bt	-	na	na	na	na	na	na	na	na	na	na	na	na	na	-	na
										-	-	-	-	-	-	-	-	-	-	-	-				
	ZANJ-T13b	-	Light grey ash	unimodal, poorly sorted, coarse silt	extremely fine ash	4.9	1.7	shards with microlites; high vesiculated shards	-	mean [10]	59.30	0.91	15.83	3.61	0.14	1.33	2.75	3.56	3.89	0.32	0.15	91.78	1.05	-	na
										SD	0.60	0.11	0.23	0.35	0.03	0.14	0.18	0.95	0.25	0.06	0.02				
	ZANJ-T20b	-	Dark grey ash	unimodal, poorly sorted, coarse silt	extremely fine ash	5.0	1.7	high vesicualted shards; shards with microlites	-	mean [10]	59.47	0.91	15.31	3.72	0.13	1.22	2.66	3.39	4.06	0.35	na	91.21	1.03	-	na
										SD	1.08	0.05	0.17	0.21	0.03	0.18	0.32	0.97	0.47	0.03	-				
	ZANJ-T28	-	White ash with visible biotite	bimodal, very poorly sorted, very fine sand	very fine ash	3.4	2.1	platy shards; low vesiculated shards; bubble-wall shards	bt, feldspar	mean [10]	72.54	0.16	11.51	0.74	0.04	0.12	0.85	2.95	4.27	0.01	0.14	93.33	1.05	-	na
										SD	0.82	0.03	0.20	0.04	0.02	0.02	0.03	0.11	0.11	0.02	0.01				
	ZANJ-T29	-	Dark grey ash	unimodal, poorly sorted, coarse silt	extremely fine ash	4.9	1.4	bubble-wall shards	-	mean [10]	55.15	1.43	15.16	6.72	0.14	2.25	4.62	3.93	3.75	0.73	na	93.88	0.80	-	na
										SD	0.47	0.05	0.15	0.30	0.04	0.20	0.27	0.26	0.23	0.05	-				
	ZANJ-T31	-	Dark grey ash	unimodal, poorly sorted, coarse silt	extremely fine ash	5.1	1.4	bubble-wall shards; low vesiculated shards	bt	mean [10]	55.30	1.41	15.19	6.63	0.13	2.16	4.40	4.03	3.92	0.71	na	93.87	0.81	-	na
										SD	0.71	0.08	0.19	0.57	0.03	0.25	0.45	0.23	0.27	0.07	-				
Cerro Colorado	CC-T17*	10	White ash with visible biotite	bimodal, poorly sorted, coarse silt	extremely fine ash	5.7	1.8	na	bt	-	na	na	na	na	na	na	na	na	na	na	na	na	na	-	na
										-	-	-	-	-	-	-	-	-	-	-	-				
	CC-T22b*	-	White ash	unimodal, poorly sorted, very coarse silt	extremely fine ash	4.6	1.9	low vesiculated shards	bt	mean [3]	75.95	0.14	13.93	0.64	0.10	0.13	0.80	3.11	5.07	0.03	0.10	100.00	1.16	-	na
										SD	0.20	0.06	0.05	0.16	0.09	0.14	0.08	0.25	0.17	0.05	0.05				
Cerro Toro Chico	TC-T1	10	Light grey ash, with visible biotite	bimodal, poorly sorted, very fine sand	very fine ash	3.2	1.8	na	bt	-	na	na	na	na	na	na	na	na	na	na	na	na	na	-	na
										-	-	-	-	-	-	-	-	-	-	-	-				
Cerro Blanco	BL-T1	10	White ash, with visible biotite	unimodal, poorly sorted, very fine sand	very fine ash	3.6	1.4	platy shards; low vesicualted shards	bt, pl, sa	mean [15]	77.97	0.07	12.90	0.56	0.03	0.05	0.90	3.30	4.20	0.02	na	100.00	1.11	LZ.T1	na
										SD	0.67	0.02	0.25	0.06	0.02	0.02	0.05	0.14	0.63	0.02	-				
Cerro Hueco la Zorra	LZ-T1	-	White ash with visible biotite	bimodal, very poorly sorted, coarse silt	extremely fine ash	5.1	2.1	platy shards; high vesicualted shards	bt, feldspar	mean [15]	77.37	0.07	13.15	0.56	0.05	0.05	0.90	3.06	4.79	0.01	na	100.00	1.11	BL-T1	na
										SD	0.65	0.01	0.31	0.04	0.03	0.01	0.07	0.09	0.33	0.01	-				
	LZ-T19	-	Light grey ash, with fine biotite	unimodal, poorly sorted, very fine sand	very fine ash	3.3	2	na	bt, feldspar	mean [7]	71.81	0.11	14.60	0.62	0.04	0.07	1.73	3.31	2.56	0.01	na	94.86	1.28	-	na
										SD	5.77	0.04	5.36	0.09	0.03	0.04	2.74	1.52	1.32	0.02	-				

Table 12.1. Field observations, grain-size classification, petrographic composition, EPMA analyses of glass shards and ^{39}Ar-^{40}Ar dating of the P2 allomember tephra samples. (1) Grain size parameters obtained with Blott (2000), Folk (1954) and White and Houghton (2006). Key for the "crystals" column: bt = biotite, sa = sanidine, pl = plagioclase. Numbers between square brackets in the "[n]" column correspond to the number of analyzed points. * Chemical data from Gariboldi et al. (2017). °Prevalent glass composition (the sample contains shards with exotic composition). SD: standard deviation, na: not analyzed. From the Supplementary Material of Bosio et al. (in press).

The component particles are dominated by glass shards (> 85-95% in volume), without visible evidence of alteration, and variable amounts of juvenile phenocrysts (biotite, sanidine and plagioclase, in some cases amphibole, in one case muscovite) and traces of terrigenous and biogenic materials. The ash layers containing more than 5% vol. of particles extraneous to the primary volcanic material, such as diatom frustules, rock fragments, heterogeneous crystals assemblages with olivine, pyroxene, quartz and reddish aggregates probably consisting of Fe-hydroxides and clays, were interpreted as tephra modified by reworking and the samples were not further processed.

The 45 ash layers interpreted as primary tephra, sampling at eight different sites focusing on Cerro los Quesos and Cerro la Bruja, were studied for textural characteristics.

Glass shard morphology is a promising tool for distinguishing and correlating tephra layers (Lowe 2011). Optical and scanning electron microscopy allowed the study of the glass morphologies and characteristics (Fig. 12.3). Five main groups of glass shards were identified: bubble-wall shards, with round and concave sides; vesiculated shards, with variable vesicularity; stretched shards, being vesiculated shards with strongly elongate vesicles due to stretching; platy shards, without any vesicles and not stretched; shards with microlites, mainly plagioclase. Tephra were fingerprinted based on the prevalent shard features in the 125-250-micron size fraction.

The chemical composition of volcanic glass was analyzed on 35 samples (Table 12.2), avoiding the regions very close to vesicles and cracks, which could be more deeply affected by alteration, and microlites. However, BSE imaging of glass shards did not reveal, except in some cases, the formation of visible hydration cracks or of secondary minerals at the expense of the glass. As regards microlites, these are absent in most samples but are common in a few tephra having dark grey color and an andesitic composition. For each tephra, glass shards were analyzed and the mean and standard deviation of microprobe analyses was calculated to check for homogeneity. Highly heterogeneous glass analyses can indicate compositionally zoned volcanic products, but, if joined to the presence of non-volcanic clasts, could reveal a suspected non-primary ash layer. The results indicate that most of the analyzed tephra have SD lower than 1 for glass SiO_2 wt%. A few samples have a higher variability in SiO_2 wt% glass analysis (e.g. LB-T9), which could correspond to an eruption tapping a zoned reservoir, or two distinct glass populations (e.g. LB-T8), which, lacking the presence of non-volcanic clasts, could be interpreted as two eruptive events close in time or as the result of magma mixing/mingling processes. Since some hydration affected at variable degree all the analyzed ashes, resulting in microprobe totals of 89 to 95% (Table 12.2), the analyses were recalculated to 100 to allow comparing tephra with different degrees of hydration in the same diagrams (Fig. 12.4a, b, c, d).

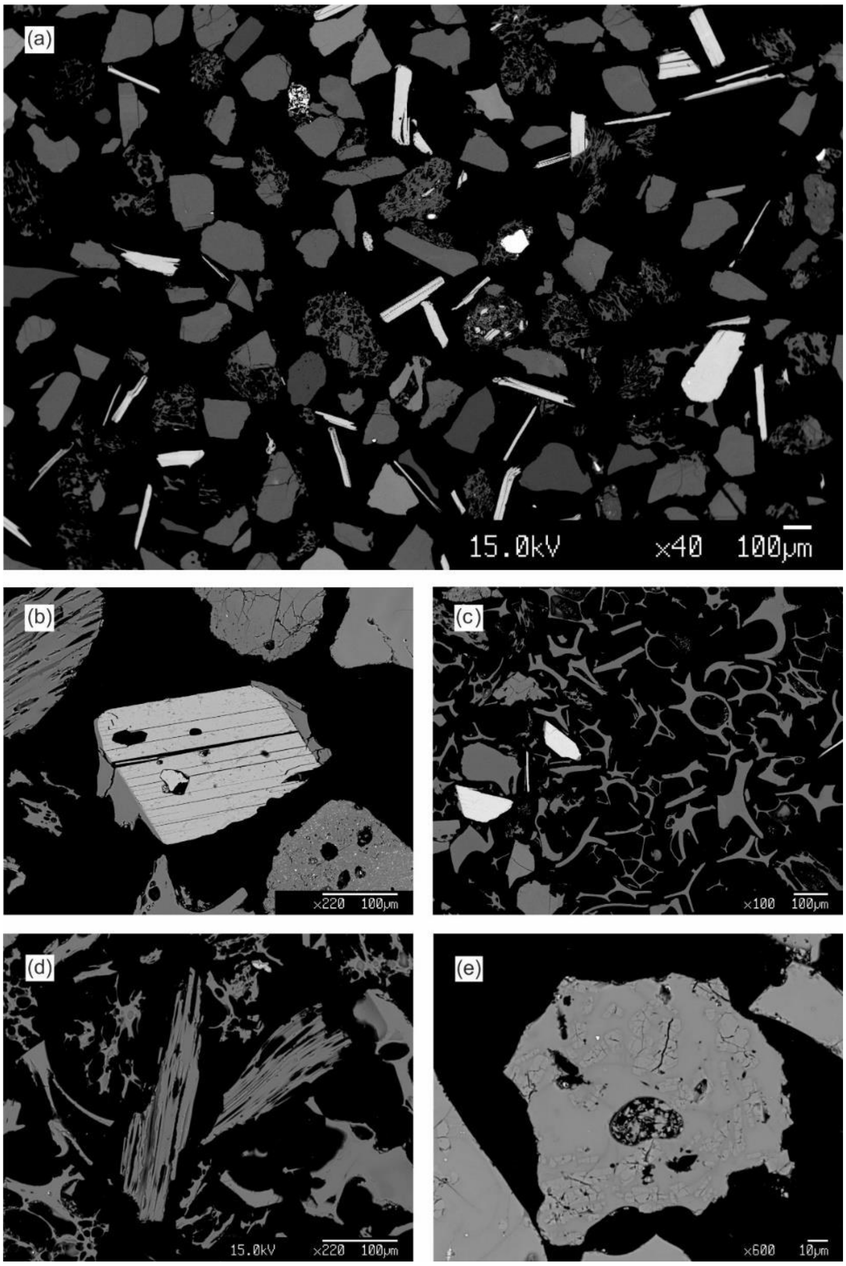

Figure 12.3. BSE images. a) 250 μm size fraction of a tephra layer. b) Biotite phenocryst showing an apatite inclusion and coated by volcanic glass. No clays along cleavages are observed. c) Example of bubble-wall glass shard morphology. d) Stretched and vesiculated glass shards, with strongly elongate vesicles due to stretching. e) Detail of a glass shard with microlites of plagioclase. From Bosio et al. (in press).

Sample	CLQ-T44		LB-T30		LB-T7A,B		LB-T15		CLQ-T21		LB-T17		LB-T11		BL-T1	
	mean [10]	SD	mean [10]	SD	mean[17]	SD	mean [9]	SD	mean [10]	SD	mean [15]	SD	mean [19]	SD	mean [15]	SD
SiO_2 wt%	59.54	1.32	62.66	0.81	66.57	0.87	69.87	0.39	71.11	1.09	72.01	0.36	75.18	0.27	77.97	0.67
TiO_2	1.47	0.24	1.30	0.05	1.07	0.05	0.49	0.03	0.57	0.08	0.57	0.02	0.06	0.03	0.07	0.02
Al_2O_3	16.68	0.67	15.94	0.34	15.80	0.21	15.82	0.17	15.06	0.17	14.22	0.18	14.28	0.14	12.90	0.25
FeO^T	7.34	1.17	5.67	0.19	3.90	0.10	2.00	0.09	2.12	0.24	2.17	0.08	1.59	0.10	0.56	0.06
MnO	0.15	0.04	0.10	0.03	0.10	0.01	0.10	0.03	0.10	0.02	0.09	0.02	0.05	0.03	0.03	0.02
MgO	2.79	0.30	1.87	0.06	1.20	0.08	0.48	0.03	0.50	0.08	0.52	0.03	0.10	0.02	0.05	0.02
CaO	5.61	0.56	4.17	0.11	2.69	0.06	1.25	0.05	1.31	0.18	1.43	0.07	0.65	0.03	0.90	0.05
Na_2O	3.60	0.84	4.00	0.70	4.06	0.70	4.56	0.33	4.33	0.62	3.99	0.42	3.23	0.15	3.30	0.14
K_2O	2.39	0.16	3.79	0.31	4.33	0.02	5.32	0.33	4.83	0.20	4.90	0.21	4.77	0.14	4.20	0.63
P_2O_5	0.43	0.03	0.50	0.04	0.27	0.09	0.08	0.02	0.07	0.05	0.10	0.02	0.09	0.03	0.02	0.02
Na_2O+K_2O	5.98	0.92	7.79	0.78	8.40	0.72	9.88	0.48	9.16	0.53	8.89	0.34	8.00	0.25	7.50	0.77
A/CNK	0.90	0.07	0.88	0.07	0.98	0.09	1.02	0.05	1.03	0.08	0.99	0.05	1.23	0.05	1.11	0.25
analytical total	93.34	1.03	91.95	1.77	92.73	1.64	94.85	0.99	93.21	1.09	93.14	0.53	93.27	0.73	94.18	1.23

Table 12.2. Electron microprobe glass analyses of some P2 tephra samples, selected to show the andesite-to-rhyolite compositional variability of tephra in the Pisco Fm. Major elements recalculated to 100% to allow comparison excluding the effect of secondary hydration, with the original analytical totals reported at the bottom. A/CNK: Alumina saturation index, $[Al_2O_3]/[CaO]+[Na_2O]+[K_2O]$. Sampling sites are reported in Table 12.1. From Bosio et al. (in press).

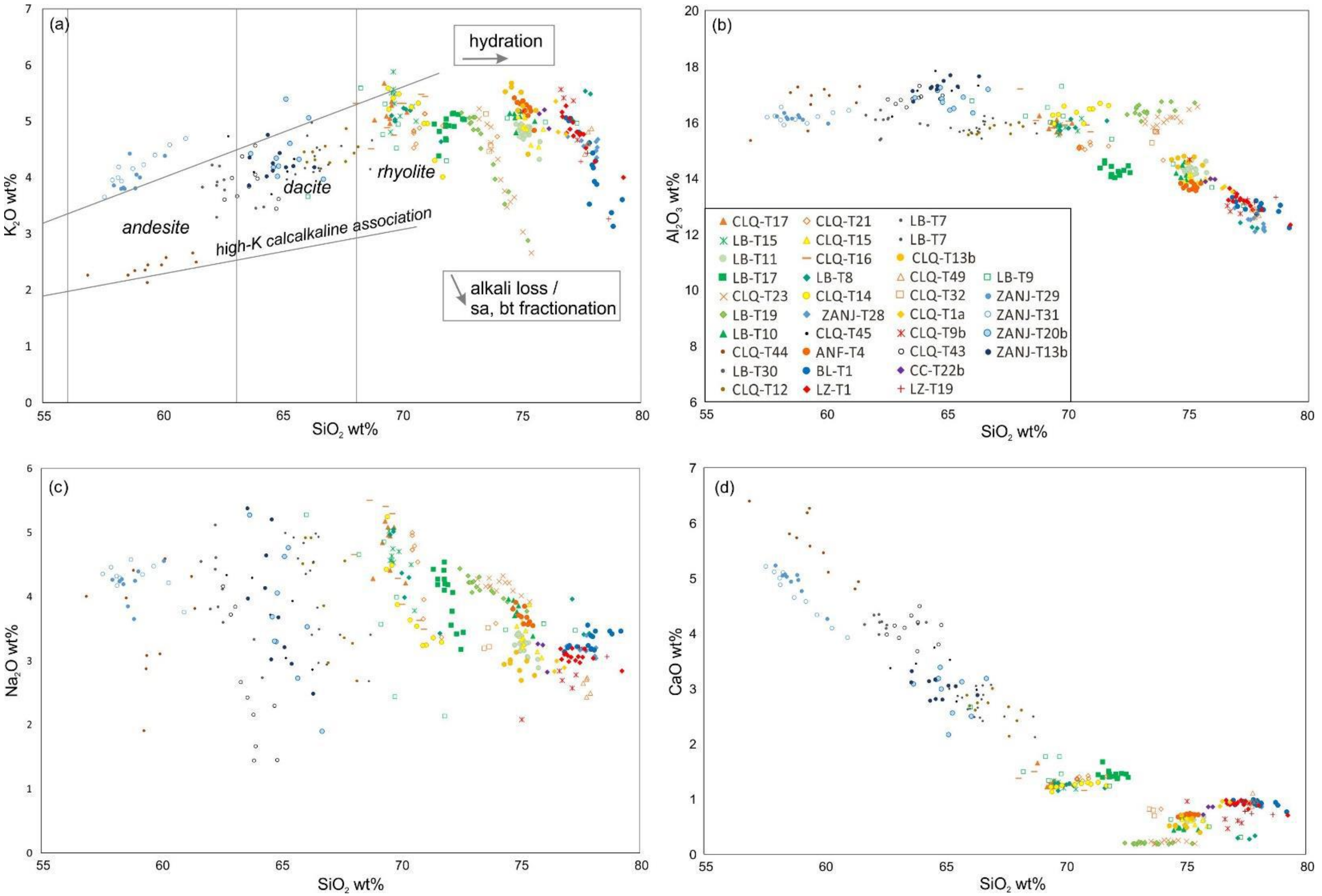

Figure 12.4. Harker diagrams. a) Volcanic glass K_2O vs SiO_2 diagram showing the glass composition of P2 allomember tephra layers. Fields for arc-related volcanic rocks following Peccerillo & Taylor (1976). b) Volcanic glass Al_2O_3 vs SiO_2 diagram. c) Volcanic glass Na_2O vs SiO_2 diagram. d) Volcanic glass CaO vs SiO_2 diagram. Elements are shown as wt% and recalculated to 100. From Bosio et al. (in press).

The results are shown in a K_2O vs SiO_2 diagram in Figure 12.4a, with fields for arc-related volcanic rocks following Peccerillo and Taylor (1976). The silica content ranges from 57 to 78 wt%, while K_2O content ranges from 2 to 6 %, with a general increase with silica. As regards the low-silica glass compositions, these belong to the few dark grey tephra (see Table 12.1). These show scattered microlites in the glass shards (Fig. 12.3e). Glass chemistry indicates for these ashes an andesitic to dacitic composition when the major elements are recalculated to 100, but the silica content of residual glass can be higher than the magma composition due to the effect of microlite crystallization and to secondary hydration. Andesitic magmas with markedly different K_2O content have been found, showing also different CaO content (e.g. CLQ-T44, ZANJ-T29, ZANJ-T31 in Fig. 12.4a, d). As regards the silicic tephra samples, the negative trends of K_2O with silica in some samples (Fig. 12.4a) could correspond to fractionation of K-bearing minerals such as sanidine and biotite, which have been observed in most silicic samples. However, since the K_2O decrease is not always accompanied by Al_2O_3 decrease (Fig. 12.4b), and considering the scattering shown by the Na_2O content of glass (Fig. 12.4c), a variable alkali loss has to be taken into account. For the silicic compositions, recalculation to 100 results in a higher silica content compared to the original erupted magma, as high as 78 wt%. However, considering that the glass shards of single tephra have a similar hydration degree, we conclude that the Pisco Formation tephra cover a large chemical variation, from andesite to rhyolite. This large chemical range is confirmed by the petrographic observation that silicic glass shards are often accompanied by biotite and sanidine, while tephra with less silicic and intermediate glass shards lack biotite. Moreover, for the purpose of fingerprinting, it is worth noting that, even if the composition of glass of most ash layers plots in the rhyolite field, it is possible to distinguish different, non-overlapping groups of tephra, all along the andesite to rhyolite compositional range (Fig. 12.4a).

Biotite phenocrysts, inspected by means of BSE imaging, did not show obvious secondary alteration minerals such as clays along cleavages (Fig. 12.3b). The composition was analyzed on 32 samples, avoiding cleavages, accessory minerals (apatite and zircon are common), as well as glass inclusions. In terms of mica classification (Rieder et al. 1999), most of the analyses plot in the biotite field, close to the phlogopite boundary, with a trend pointing to the siderophyllite end-member (Fig. 12.5a). Biotite phenocrysts are homogeneous or slightly zoned for what concerns the core-to-rim major elements compositional range (Table 12.3).

sample	CLQ-T21				CLQ-T23				BL-T1				ZANJ-T28				LB-T11				LB-T10			
crystal	1		2		6		9		7		9		2		5		2		3		5		6	
	core	*rim*	*core*	*rim*	*core*	*rim*	*core*	*rim*	*core*	*rim*	*core*	*rim*	*core*	*rim*	*core*	*rim*	*core*	*rim*	*core*	*rim*	*core*	*rim*	*core*	*rim*
SiO_2	37.26	37.36	38.02	38.11	36.07	36.66	36.44	36.56	36.66	37.51	37.16	37.03	37.34	37.88	35.55	36.28	34.49	34.95	34.24	33.68	33.16	32.78	31.80	26.87
TiO_2	5.60	5.36	5.45	5.51	2.46	2.41	2.56	2.55	3.63	3.63	3.62	3.78	4.31	4.54	4.28	4.25	3.87	3.39	4.50	4.20	1.75	1.78	1.35	1.34
Al_2O_3	13.25	13.03	13.34	12.61	21.57	21.26	20.57	20.72	13.95	14.04	13.95	14.14	13.37	13.60	12.91	12.85	15.36	15.69	15.35	15.29	17.04	17.26	18.21	20.43
FeO^T	10.96	11.03	10.98	10.57	20.85	20.89	21.40	21.29	18.91	19.27	19.47	19.61	14.68	14.16	15.02	14.73	25.78	26.53	25.99	25.92	31.23	31.20	31.05	30.44
MnO	0.16	0.16	0.16	0.19	0.16	0.19	0.19	0.19	0.36	0.37	0.30	0.33	0.18	0.20	0.24	0.12	0.18	0.08	0.22	0.08	0.09	0.12	0.13	0.15
MgO	16.87	16.91	16.52	16.52	4.98	4.73	4.99	4.91	11.30	11.57	11.27	11.35	15.01	15.28	14.54	14.49	6.34	6.56	6.22	6.18	2.56	2.42	2.77	3.27
CaO	0.06	0.04	0.03	0.05	0.05	0.07	0.02	0.04	0.02	0.02	0.01	0.02	bd	bd	0.02	0.01	bd	bd	bd	0.05	0.05	0.04	0.08	0.13
Na_2O	1.06	0.94	0.95	0.99	0.37	0.38	0.42	0.39	0.35	0.27	0.31	0.34	0.57	0.53	0.53	0.48	0.65	0.62	0.73	0.56	0.50	0.55	0.49	0.70
K_2O	8.23	8.27	8.16	8.26	9.05	8.98	9.01	8.94	9.00	9.17	9.13	9.17	8.70	8.66	8.69	8.67	8.19	8.31	8.21	8.26	8.24	8.43	7.97	7.92
Cl	0.10	0.07	0.07	0.08	na	na	na	na	na	na	na	na	0.14	0.13	0.16	0.13	0.29	0.31	0.13	0.13	0.53	0.53	0.56	0.54
BaO	0.87	0.75	1.02	0.70	na	na	na	na	na	na	na	na	0.33	0.50	0.34	0.37	na	na	na	na	0.25	0.27	0.76	0.63
Total	94.43	93.94	94.70	93.60	95.59	95.58	95.60	95.60	94.18	95.85	95.22	95.78	94.63	95.48	92.28	92.38	95.18	96.45	95.63	94.37	95.42	95.44	95.17	92.43
Ions on the basis of 22 oxygens																								
Si	5.56	5.60	5.65	5.71	5.47	5.55	5.54	5.55	5.66	5.69	5.68	5.64	5.63	5.64	5.54	5.62	5.44	5.45	5.39	5.38	5.37	5.32	5.20	4.58
Ti	0.63	0.60	0.61	0.62	0.28	0.27	0.29	0.29	0.42	0.41	0.42	0.43	0.49	0.51	0.50	0.50	0.46	0.40	0.53	0.50	0.21	0.22	0.17	0.17
Al	2.33	2.30	2.34	2.23	3.85	3.79	3.69	3.71	2.54	2.51	2.51	2.54	2.38	2.39	2.37	2.35	2.86	2.88	2.85	2.88	3.25	3.31	3.51	4.10
Fe	1.37	1.38	1.36	1.32	2.64	2.64	2.72	2.70	2.44	2.44	2.49	2.50	1.85	1.76	1.96	1.91	3.40	3.46	3.42	3.46	4.23	4.24	4.24	4.34
Mn	0.02	0.02	0.02	0.02	0.02	0.02	0.02	0.02	0.05	0.05	0.04	0.04	0.02	0.03	0.03	0.02	0.02	0.01	0.03	0.01	0.01	0.02	0.02	0.02
Mg	3.75	3.78	3.66	3.69	1.12	1.07	1.13	1.11	2.60	2.61	2.57	2.57	3.37	3.39	3.38	3.35	1.49	1.52	1.46	1.47	0.62	0.59	0.67	0.83
Ca	0.01	0.01	bd	0.01	0.01	0.01	bd	0.01	bd	bd	bd	bd	bd	bd	bd	bd	bd	bd	bd	0.01	0.01	0.01	0.01	0.02
Na	0.31	0.27	0.27	0.29	0.11	0.11	0.12	0.11	0.10	0.08	0.09	0.10	0.17	0.15	0.16	0.15	0.20	0.19	0.22	0.17	0.16	0.17	0.16	0.23
K	1.57	1.58	1.55	1.58	1.75	1.73	1.75	1.73	1.77	1.77	1.78	1.78	1.67	1.65	1.73	1.71	1.65	1.65	1.65	1.68	1.70	1.75	1.66	1.72
Cl	0.02	0.02	0.02	0.02	na	na	na	na	na	na	na	na	0.04	0.03	0.04	0.03	0.08	0.08	0.04	0.03	0.15	0.15	0.15	0.16
Ba	0.05	0.04	0.06	0.04	na	na	na	Na	na	na	na	na	0.02	0.03	0.02	0.02	na	na	na	na	0.02	0.02	0.05	0.04
sum	15.63	15.61	15.54	15.53	15.25	15.21	15.26	15.23	15.59	15.57	15.58	15.60	15.63	15.58	15.74	15.66	15.60	15.64	15.59	15.61	15.73	15.78	15.84	16.22
X	1.93	1.91	1.89	1.92	1.86	1.86	1.87	1.85	1.88	1.86	1.88	1.89	1.86	1.83	1.91	1.88	1.85	1.84	1.87	1.87	1.89	1.94	1.88	2.02
Y	5.67	5.69	5.64	5.59	5.39	5.35	5.39	5.38	5.71	5.72	5.71	5.72	5.74	5.72	5.78	5.74	5.67	5.71	5.68	5.70	5.70	5.69	5.81	6.04
Mg_v	0.73	0.73	0.73	0.73	0.30	0.29	0.29	0.29	0.51	0.51	0.50	0.50	0.64	0.65	0.63	0.63	0.30	0.31	0.30	0.30	0.13	0.12	0.14	0.16

Table 12.3. Electron microprobe analyses of biotite phenocrysts (wt%) of some P2 tephra samples, selected to show the compositional variability of tephra in the Pisco Fm. Mineral formula based on 22 oxygens. Mg_v ratio is $Mg/(Mg+Fe^T+Mn)$. Abbreviations: bd is below detection; na is not analysed. From the Supplementary Material. of Bosio et al. (in press).

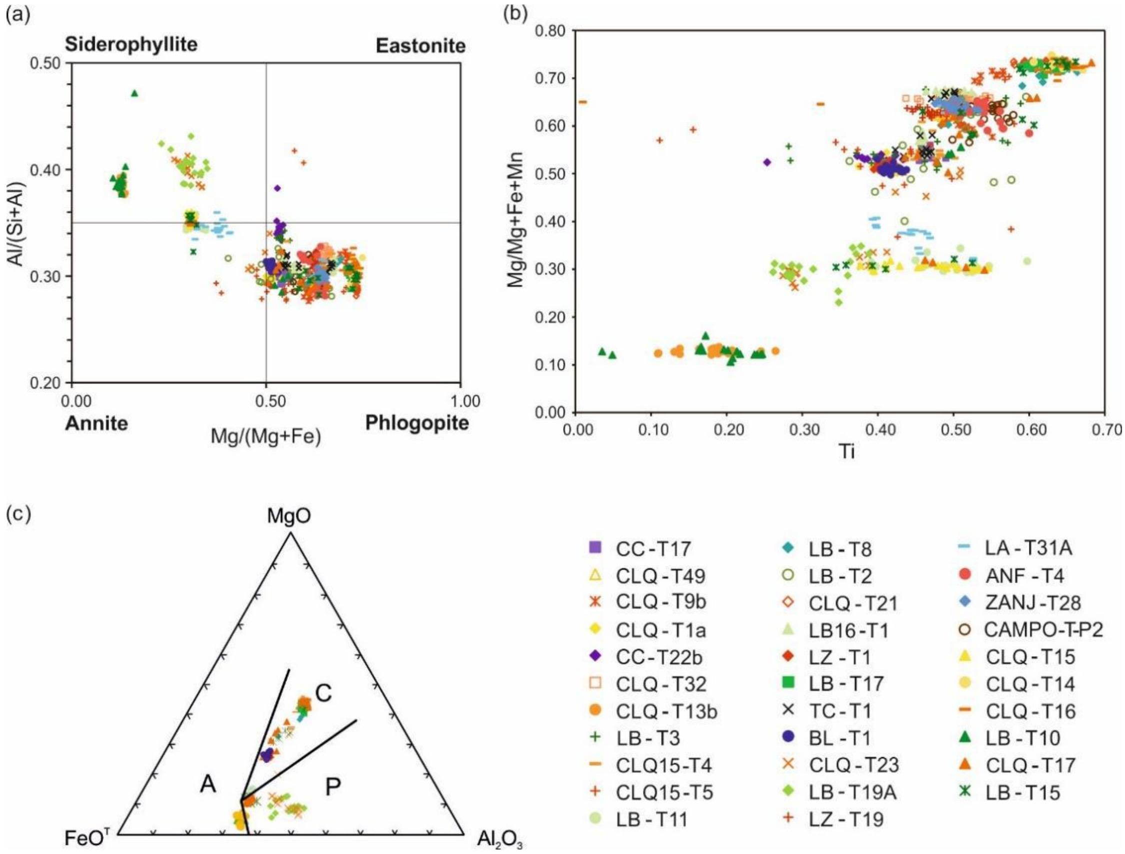

Figure 12.5. a) Classification diagram of biotite phenocrysts from P2 tephra layers. b) Biotite Mg/Mg+Fe^T+Mn vs Ti diagram of P2 ash layers. Values shown as atoms per formula unit. c) Chemical ternary diagram of biotite phenocrysts from the correlated tephra. Biotite discrimination diagram: fields from Abdel-Rahman (1994). C= calcalkaline orogenic suites; P= peraluminous suites; A= anorogenic alkaline suites. From Bosio et al. (in press).

The intra-sample compositional variability is moderate in most cases (Fig. 12.5), and a few samples present some outliers (biotite phenocrysts with very different composition, which can be interpreted as foreign crystals entrained within the ash layer or xenocrysts in the erupted magma. A few samples show bimodal (e.g. CLQ-T9b) or very heterogeneous biotite chemistry (e.g. LB-T2). As a whole, the collected data reveal a large variation in Mg_v (Mg/Mg+Fe^T+Mn), Al, Ti (Fig. 12.5a, b) as well as in Mn (see Fig. 12.6). The loss of alkali in respect to stechiometry is in most cases very low. The high Al content of the siderophyllite-rich biotite compositional data suggests to check for peraluminous compositions. When the chemical composition of biotite is plotted in the ternary discrimination diagram of Abdel-Rahman (1994), as shown in Figure 12.5c, two clusters are evident: one in the calcalkaline field and the latter in the peraluminous one.

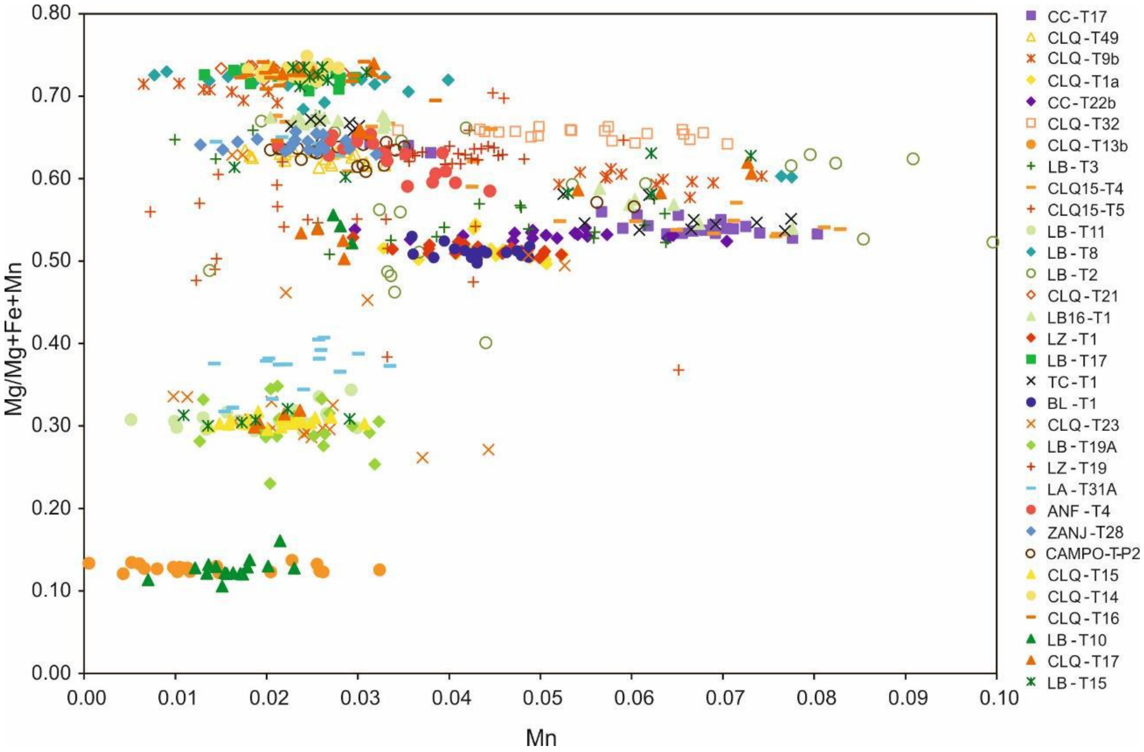

Figure 12.6. Biotite Mg/Mg+Fe+Mn vs Mn diagram of P2 ash layers. Values shown as atoms per formula unit. From Bosio et al. (in press).

12.3. Tephra of the Pisco Formation

Tephra consisting of over 95% volcanic glass and a few % crystals are particularly frequent in the diatomaceous portions of the upper Miocene Pisco Formation. Probably, the diatomaceous mudstones represent a relatively deeper (60-100 m), low hydrodynamism environment in the basin, well suitable for tephra preservation. These fine-grained ashes can be interpreted to represent the distal, crystal-depleted ashes of large explosive eruptions, being dispersed westwards either from the eruption column or from a co-ignimbrite ash-cloud (Fisher & Schmincke 1984). By following observations of Engwell et al. (2014), the rather frequent bimodal grain-size distribution within the tephra may be interpreted as to represent the coarse-grained and the fine-grained modes of the Plinian ash and the co-ignimbrite ash, respectively. Ash layers consisting of sublayers can be explained with subsequent and close in time eruptions of the same or different volcanoes (e.g. CLQT9a, b). Particularly thick layers of fine ash can be explained, instead, with a high input of ash deposited on land and then transported to the sea after a large explosive eruption (e.g. CLQ-T16). The off-shore deposition of tephra in forearc basins could, potentially, provide a more complete record of the explosive activity of Central Andes compared to on-land outcrops. The upper Miocene Pisco Formation corresponds to a period characterized by intense volcanic activity in the Central Volcanic Zone (Tosdal et al. 1981; Thouret et al. 2007, 2017; Kay et al. 2010). In particular, the stratigraphic interval studied in this Chapter (from 8.5 to 7 Ma), temporally comprised in the activity of the Lower Barroso arc (Mamani et al. 2010), slightly precedes the 5-6 Ma peak in the presence of tephra in the marine record off the coast of Peru at 10 to 11°S, found during Ocean Drilling Program (ODP) Leg 201 by Hart & Miller (2006). Several large silicic eruptions have occurred in the Central Andes during upper Miocene-Pliocene, including some in the Altiplano-Puna region with a volcanic explosivity index (VEI, Newhall & Self 1982) of 8 or greater (Salisbury et al. 2011). Moreover, nearer to the latitude of the East Pisco Basin, the Macusani region (southeast Peru) produced several large ignimbrites between 10 and 7 Ma (Pichavant et al. 1988; Cheilletz et al. 1992). Noteworthy, the Macusani ignimbrite eruptions, as well as only a few others in the Central Andes, involve magmas with strongly peraluminous composition, representing a suitable source for the peraluminous tephra identified in the Pisco Formation.

12.4. Applying tephra fingerprinting

Biotite and volcanic glass have already been used for Andean tephrostratigraphy, as well as amphibole (De Silva & Francis 1989, Lebti et al. 2006). Biotite is rather frequent in form of phenocrysts in the products of explosive eruptions of Central Andes volcanoes. The distal ashes dispersed by these eruptions are often enriched in this mineral, due to the fact that the biotite crystals are much better transported along with glass shards than those of other minerals (e.g., feldspars or amphibole) (Rose & Chesner 1987). Additionally, the relative ease with which nonstoichiometric mica compositions reveal alteration means that unaltered mica can be confidently recognized as juvenile in primary ash layers.

Both biotite and glass chemistry was used in the Pisco Formation for fingerprinting ashes and making correlations among them. The significant differences in the major element composition of biotite found in the Pisco Formation ashes, especially the large range in Mg/Fe ratio and Al content, cannot be ascribed to alteration (see Table 12.3). Alteration of biotite by weathering may result in Fe oxidation, loss of Mg resulting in low Mg_V, loss of interlayer K, while Al and Ti are retained (Gilkes & Suddhiprakarn 1979). The physical and mineralogical evidence corresponding to these chemical transformations are lacking in the studied samples, thus indicating that biotite is pristine. Instead, the large chemical variations in Mg_V uncorrelated to the K content, as well as the differences in minor elements as Ti, Al, Ba and Mn, can be ascribed to the physico-chemical features (chemistry, temperature, oxygen fugacity) of the magma from which biotite crystallized and, therefore, can be used for discriminating biotites from different eruptions.

Generally speaking, based on the composition of biotite, different samples or groups of samples gather in well-defined and non-overlapping compositional clusters in one or more bivariate diagrams (e.g. Fig. 12.5). This possibility to apply such feature for correlating tephra is particularly evident in the diagram of Figure 12.7a, constructed with respect to the fossil-rich localities of Cerro los Quesos and Cerro la Bruja, 6 km apart, showing several perfectly overlapping tephra pairs, well distinguished from each other: CLQ-T23/LB-T19a, CLQ-T21/LB-T17, CLQ-T16/LB-T8, CLQ-T15/LB-T11 and CLQT13b/LB-T10. The composition of biotite for each pair is in most cases well clustered (e.g. CLQT15/LB-T11), while in some cases it covers a wider field. For instance, two biotite populations can be distinguished in both samples LB-T19a and CLQ-T23 (Fig. 12.7a). This feature, which is not correlated to alteration evidence (i.e. low totals, low K), could be interpreted as coeval eruption of two different volcanoes, two events close in time by the same volcano, or eruption of a mingled magma (Lebti et al. 2006; Shane et al. 2008), and is, thus, an additional characteristic useful for unequivocal identification of a tephra layer. A wide field of biotite composition is also covered by the tephra pair CLQ-T17/LB-T15, which shows a very dispersed mica composition unsuitable for a single magma batch. This situation can be interpreted with (primary or secondary) mixing of ashes from different eruptions, even if the glass composition seems to be overlapping. Figure 12.7a also demonstrates the chemical identity of samples BL-T1/LZ-T1 from Cerro Blanco and Cerro Hueco la Zorra respectively. In this case, chemical analyses confirm the correlation between an ash layer placed in a stratigraphic log (BL-T1, see stratigraphic position Fig. 5.1, Chapter 5 or in the Appendix) and another one at 3 km distance (LZ-T1), previously correlated to BL-T1 based on field evidences. Strong variations in Al content of biotite crystals embedded in similarly silicic glasses indicates remarkable chemical differences of the silicic magmas. Indeed, biotite major element chemistry allowed to identify peraluminous tephra compositions, as the CLQ-T23/LB-T19a pair. The use of the major element composition of mica grains is more robust than that of glass due to the high reactivity to alteration of the latter. In the case of glass, the removal of mobile cations results in an apparent increase of immobile elements (Al, Ti), which may simulate peraluminous compositions. Therefore, while in the case of glass analysis the peraluminous character is in most cases apparent, biotite chemical analyses allow to unequivocally identify the tephra with peraluminous chemistry in the Pisco Formation.

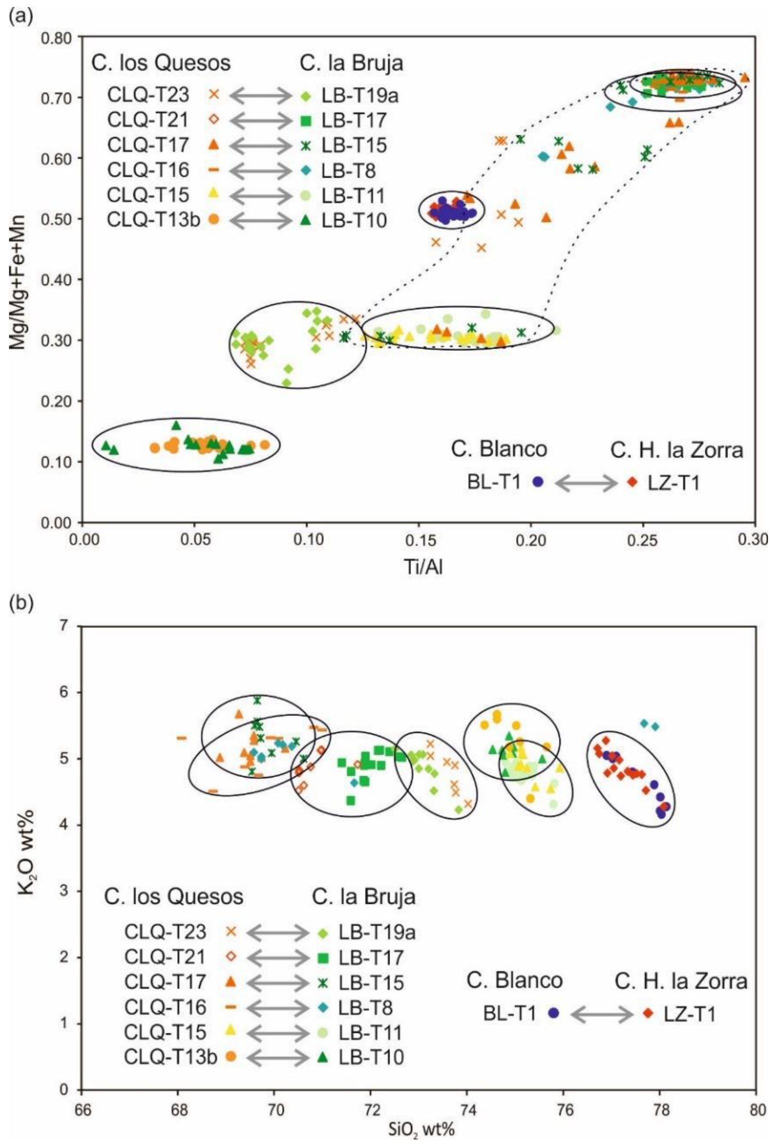

Figure 12.7. a) Ti/Al vs Mg$_V$ (Mg/Mg+Fe^T+Mn) diagram of biotite phenocrysts from correlated tephra. Six correlations using biotite chemistry are possible at the localities of Cerro los Quesos and Cerro la Bruja, and one correlation between Cerro Blanco and

Cerro Hueco la Zorra. Circles made of continuous line highlight the correlations; dashed line surround the scattered points of two correlated tephra with two different biotite populations. b) SiO_2 vs K_2O diagram of volcanic glass of correlated samples from Cerro los Quesos and Cerro la Bruja, and one pair from Cerro Blanco and Cerro Hueco la Zorra. Circles made of continuous line highlight the correlations. From Bosio et al. (in press).

Glass composition was also employed for fingerprinting ash layers and making correlations between stratigraphic sections in different localities. Indeed, notwithstanding the susceptibility of glass to alteration, an overlap in the glass composition confirms the identification of the layers correlated based on biotite chemistry. As shown in Figure 12.7b, the same tephra pairs are overlapping and can be easily distinguished from each other: CLQ-T23/ LB-T19a, CLQ-T21/LB-T17, CLQ-T17/ LB-T15, CLQT16/LB-T8, CLQ-T15/LB-T11 and CLQ-T13b/LB-T10 for the localities of Cerro los Quesos and Cerro la Bruja, and the BL-T1/LZ-T1 pair at Cerro Blanco and Cerro Hueco la Zorra.
The compositional correlation of these layers is also supported by glass clast morphology and vesicularity that give a further characterization useful for fingerprinting tephra: pairs of correlated tephra show similarities in the vesicularity, stretching, presence of microlites and clast glass shape (see Table 12.1). In many cases, grain size validates the correlation, showing a correspondence between the grain-size distribution curves of the correlated pairs (see Fig. 12.8). Compared to the chemical composition and morphology, the employment of grain size distribution for fingerprinting and correlating tephra in the Pisco Basin may be limited by the effect of marine currents in redistributing the component particles during deposition.

12.5. High-resolution stratigraphy and paleontological implications in the Pisco Formation

The mineral chemistry data recently presented for a few tephra of the Pisco Formation by Gariboldi et al. (2017) showed compositionally different sanidine-plagioclase pairs in different rhyolitic tephra, suggesting that mineral chemistry could be used to fingerprint ash layers in the Pisco Formation for long-distance correlation purposes. In the present Chapter, the overall silicic calcalkaline tephra in the upper Miocene portion of the Pisco Formation have revealed a variety of features useful for identification, including not only biotite and glass chemistry, but also grain size distribution, mineral assemblage and shard morphology. These features, joined to the frequency of tephra along the successions, allow detailed stratigraphic correlations among localities at several kilometers of distance, which can highly improve the current stratigraphic frame.

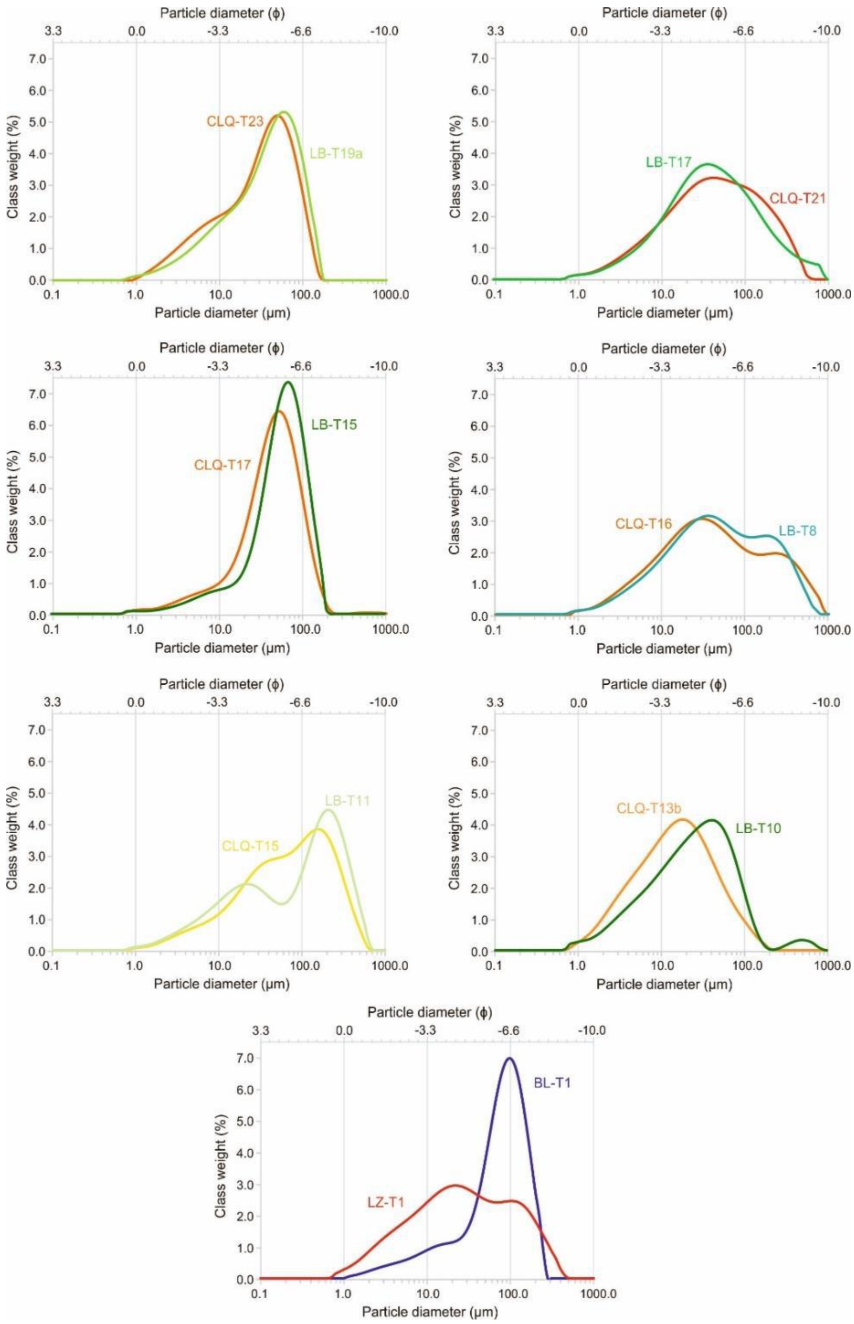

Figure 12.8. Grain-size distribution curves of correlated tephra pairs from Cerro los Quesos and Cerro la Bruja, and one pair from Cerro Blanco and Cerro Hueco la Zorra. Distribution is unimodal or bimodal, particle diameter is from extremely fine-grained to very fine-grained. Particle size is shown as both µm and ϕ. From Bosio et al. (in press).

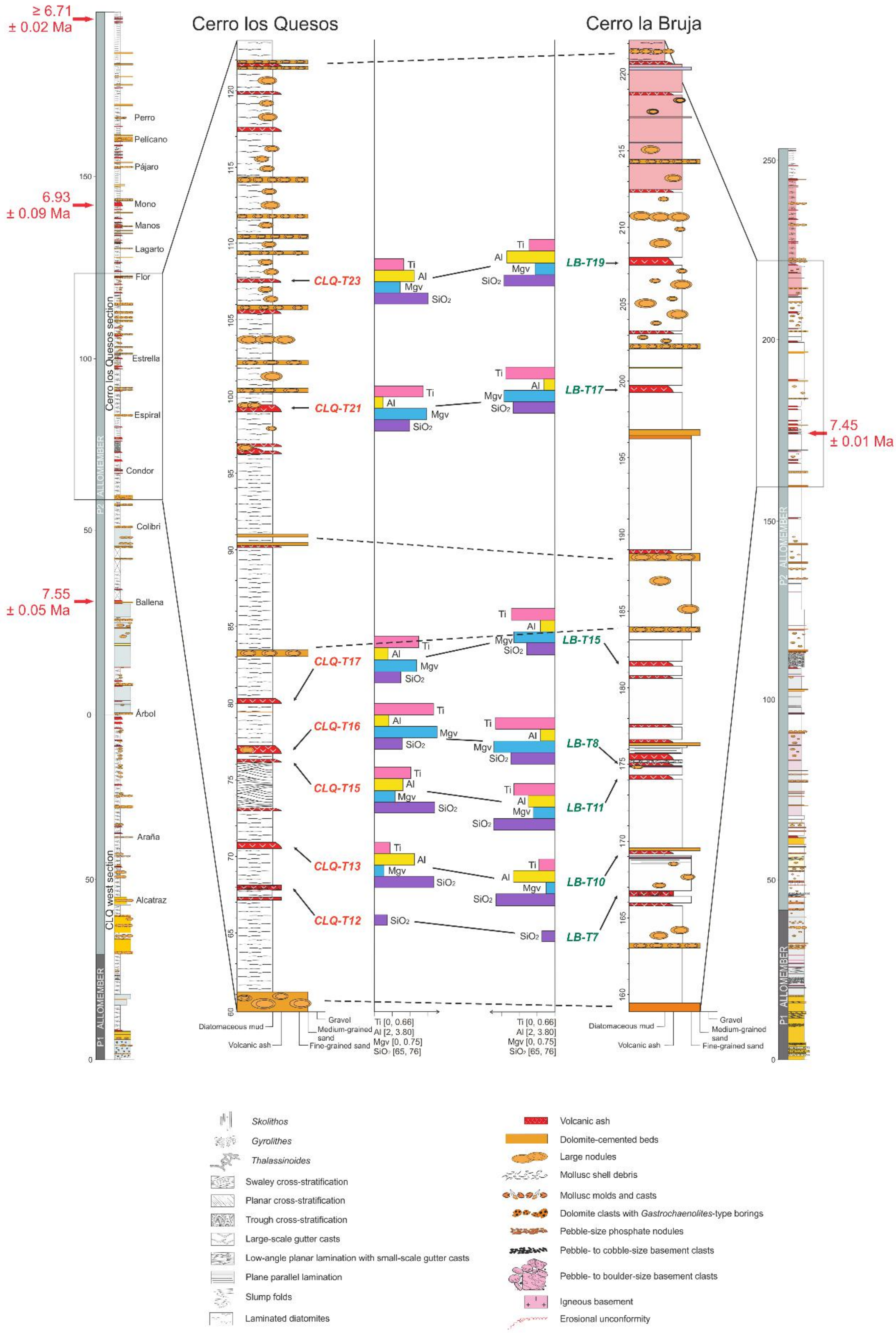

Figure 12.9. Correlation between the stratigraphic sections measured at Cerro los Quesos and Cerro la Bruja. Scaling up of the sections shown the accurate stratigraphic position of tephra layers chemically correlated (colored and in bold). Dashed lines

connect correlations based on stratigraphic position of marker beds in Di Celma et al. (2017). Tephra layers are highlighted in red. Biotite and glass chemistry is shown in the central diagrams: Ti and Al biotite contents are expressed as atoms per formula unit; Mg_V is the ratio $Mg/Mg+Fe^T+Mn$ measured on biotite phenocrysts; SiO_2 is shown as wt% and recalculated to 100. Ages written in red referred to $^{39}Ar–^{40}Ar$ ages obtained from selected ash layers: the age of 7.45 ± 0.01 Ma at Cerro la Bruja agrees with ages of 7.55 ± 0.05 Ma and 6.93 ± 0.09 Ma at Cerro los Quesos, and therefore supports the correlation based on biotite and glass chemistry. From Bosio et al. (in press).

In Figure 12.9, specific parts of the measured stratigraphic sections at the localities of Cerro los Quesos (between 60 and 120 m abs) and Cerro la Bruja (between 160 and 220 m abs), dated from 7.55 to 6.71 Ma based on $^{39}Ar–^{40}Ar$ dating, are correlated using the fingerprinted ash layers (see the Appendix for the detailed stratigraphic logs). In particular, Ti and Al concentrations and the Mg_V of biotite phenocrysts are clearly typical of each layer and can identify six pairs of the same tephra in the two stratigraphic sections. SiO_2 content in volcanic glass can also be useful for fingerprinting and recognizing one more pair of the same tephra layer (CLQT12/LB-T7). Granulometric parameters (primary and secondary mode, median, sorting) and shard morphology (shown in Table 12.1) are used to confirm these correlations. The identification of these correlated ash layers allows to increase the stratigraphic detail of a previous correlation based on chronostratigraphy (Di Celma et al. 2017). Taking into account $^{39}Ar–^{40}Ar$ ages in both localities (see Fig. 12.9) and the sedimentation rate calculated in Chapter 17, tephra correlation based on tephra fingerprinting allows stratigraphic reconstruction with resolution < 0.1 Ma.

By comparing Cerro los Quesos and Cerro la Bruja, we also observe that some tephra do not occur in both localities. The reason for that should be searched in some syn- or post-depositional disturbances in the depositional environment, such as marine currents and the shallow water context, which cause a laterally discontinuous deposition or preservation of tephra. In this work, we demonstrate that even in such a complex sedimentary environment, where the overall similar chemical composition of ashes could limit tephra discrimination and the action of marine currents could affect tephra lateral continuity and preservation, a petrographic and chemical fingerprinting can be applied successfully, even when dealing with pre-Quaternary successions. Secondly, we increase the chronostratigraphic detail and reconstruct a high-resolution stratigraphy in the Pisco

Formation, which hosts a marine vertebrate Fossil-Lagerstätte with a worldwide paleontological relevance. Finally, it is worth of note that forearc basins, such as the Pisco Basin, and in particular the diatomaceous sequences, represent an archive of distal Central Andes tephra, which can be used to increase the knowledge on the Central Andes volcanic activity.

This chapter is entirely modelled on the results and discussion of the paper "Chemical and petrographic fingerprinting of volcanic ashes as a tool for high-resolution stratigraphy of the upper Miocene Pisco Formation (Peru)" written by Giulia Bosio, Anna Gioncada, Elisa Malinverno, Claudio Di Celma, Igor M. Villa, Giuseppe Cataldi, Karen Gariboldi, Alberto Collareta, Mario Urbina and Giovanni Bianucci, which will be published by the Journal of the Geological Society in January 2019.

Chapter References

Abdel-Rahman, A.M. 1994. Nature of biotites from alkaline, calc-alkaline, and peraluminous magmas. Journal of Petrology, 35, 525-541.

Blott, S.J., Pye, K. 2001. Gradistat: a grain size distribution and statistics package for the analysis of unconsolidated sediments. Earth Surface Processes and Landforms, 26, 1237-1248.

Breitkreuz, C., de Silva, S. L., Wilke, H.G., Pfander, J.A., Renno, A.D. 2013. Neogene to Quaternary ash deposits in the Coastal Cordillera in northern Chile: Distal ashes from supereruptions in the Central Andes. Journal of Volcanology and Geothermal Research, 269, 68-82.

Cheilletz, A., Clark, A.H., Farrar, E., Arroyo Pauca, G., Pichavant, M. & Sandeman, H.A. 1992. Volcanostratigraphy and 40Ar/39Ar geochronology of the Macusani ignimbrite field: monitor of the Miocene geodynamic evolution of the Andes of southeast Peru. Tectonophysics, 205, 307-327.

D'Antonio, M., Mariconte, R., Arienzo, I., Mazzeo, F. C., Carandente, A., Perugini, D., Petrelli, M., Corselli C., Orsi G., Principato, M.S., Civetta, L. 2016. Combined Sr-Nd isotopic and geochemical fingerprinting as a tool for identifying tephra layers: Application to deep-sea cores from Eastern Mediterranean Sea. Chemical Geology, 443, 121-136.

De Silva, S. L., Francis, P. W. 1989. Correlation of large ignimbrites—two case studies from the Central Andes of Northern Chile. Journal of Volcanology and Geothermal Research, 37 (2), 133-149.

Di Celma, C., Malinverno, E., Cantalamessa, G., Gioncada, A., Bosio, G., Villa, I.M., Gariboldi, K., Rustichelli, A., Pierantoni, P.P., Landini, W., Tinelli, C., Collareta, A., Bianucci, G. 2016. Stratigraphic framework of the late Miocene Pisco Formation at Cerro Los Quesos (Ica Desert, Peru). Journal of Maps, 12, 1020-1028.

Di Celma, C., Malinverno, E., Bosio, G., Collareta, A., Gariboldi, K., Gioncada, A., Molli, G., Basso, D., Varas-Malca, R., Pierantoni, P.P., Villa, I.M., Lambert, O., Landini, W., Sarti, G., Cantalamessa, G., Urbina, M., Bianucci, G. 2017. Sequence stratigraphy and palaeontology of the upper Miocene Pisco Formation along the western side of the lower Ica valley (Ica desert, Peru). Rivista Italiana di Paleontologia e Stratigrafia (Research In Paleontology and Stratigraphy), 123, 255-274.

Engwell, S.L., Sparks, R.S.J., Carey, S. 2014. Physical characteristics of tephra layers in the deep sea realm: the Campanian Ignimbrite eruption. In: Austin, W. E. N., Abbott, P. M., Davies, S. M., Pearce, N. J. G. & Wastegard, S. (eds). Marine Tephrochronology. Geological Society, London, Special Publications, 398, 47-64.

Fisher, R.V., Schmincke, H.-U. 1984. Pyroclastic Rocks. Springer-Verlag, Berlin Heidelberg.

Gariboldi, K., Bosio, G., Malinverno, E., Gioncada, A., Di Celma, C., Villa, I.M., Urbina, M., Bianucci, G. 2017. Biostratigraphy, geochronology and sedimentation rates of the upper Miocene Pisco Formation at two important marine vertebrate fossil-bearing sites of southern Peru. Newsletter on Stratigraphy, 50 (4), 417-444.

Gilkes, R.J., Suddhiprakarn, A. 1979. Biotite alteration in deeply weathered granite. Clays and Clay Minerals, 27(5), 349-360.

Hart, D., Miller, D.J. 2006. Analysis and correlation of volcanic ash in marine sediments from the Peru margin, Ocean Drilling Program Leg 201: explosive volcanic cycles of the north-central Andes. In: Jørgensen, B.B., D'Hondt, S.L., and Miller, D.J. (Eds), Proceedings of the Ocean Drilling Program, Scientific Results, 201, 1-43.

Kay, S.M., Coira, B.L., Caffe, P.J., Chen, C.-H. 2010. Regional chemical diversity, crustal and mantle sources and evolution of central Andean Puna plateau ignimbrites. Journal of Volcanology and Geothermal Research, 198, 81–111.

Lebti, P.P., Thouret, J.-C., Worner, G., Fornari, M. 2006. Neogene and Quaternary ignimbrites in the area of Arequipa, Southern Peru: Stratigraphical and petrological correlations. Journal of Volcanology and Geothermal Research, 154, 251-275.

Lowe, D.J. 2011. Tephrochronology and its application: A review. Quaternary Geochronology, 6, 107-153.

Lowe, D. J., Pearce, N. J., Jorgensen, M. A., Kuehn, S. C., Tryon, C. A., Hayward, C. L. 2017. Correlating tephras and cryptotephras using glass compositional analyses and numerical and statistical methods: Review and evaluation. Quaternary Science Reviews, 175, 1-44.

Mamani, M., Worner, G., Sempere, T. 2010. Geochemical variations in igneous rocks of the Central Andean orocline (13°S to 18°S): Tracing crustal thickening and magma generation through time and space. Geological Society of America Bulletin, 122, 162-182.

Newhall, C.G., Self, S. 1982. The Volcanic Explosivity Index (VEI): An Estimate of Explosive Magnitude for Historical Volcanism. Journal of Geophysical Research, 87(C2), 1231-1238.

Owen, G. 2003. Load structures: gravity-driven sediment mobilization in the shallow subsurface. Geological Society, London, Special Publications, 216, 21-34.

Peccerillo, A., Taylor, S.R. 1976. Geochemistry of Eocene Calc-Alkaline Volcanic Rocks from the Kastamonu Area, Northern Turkey. Contributions to Mineralogy and Petrology, 58, 63-81.

Pedersen, G.K., Surlyk, F. 1977. Dish structures in Eocene volcanic ash layers, Denmark. Sedimentology, 24, 581-590.

Pichavant, M., Kontak, D.J., Valencia Herrera, J., Clark, A.H. 1988. The Miocene-Pliocene Macusani Volcanics. Mineralogy and magmatic evolution of a two-mica aluminosilicate-bearing ignimbrite suite. Contributions to Mineralolgy and Petrology, 100, 300-324.

Rieder, M., Cavazzini, G., D'yakonov, Y., Frank-Kamenetskii, V.A., Gottardi, G., Guggenheim, S., Koval, P.V., Muller, G., Neiva, A.M.R., Radoslovich, E.W., Robert, J., Sassi, F.P., Takeda, H., Weiss, Z., Wones, D.R. 1999. Nomenclature of the micas. Mineralogical Magazine, 63(2), 267-279.

Rose, W.I., Chesner, C.A. 1987. Dispersal of ash in the great Toba eruption, 75 ka. Geology, 15, 913-917.

Salisbury, M.J., Jicha, B.R., de Silva, S.L., Singer, B.S., Jiménez, N.C., Ort, M.H. 2011. 40Ar/39Ar chronostratigraphy of Altiplano-Puna volcanic complex ignimbrites reveals the development of a major magmatic province. Geological Society of America Bulletin, 123, 821-840.

Shane, P., Smith, V. & Nairn, I. 2003. Biotite composition as a tool for the identification of Quaternary tephra beds. Quaternary Research, 59, 262-270.

Shane, P., Nairn, I.A., Martin, S. B., Smith, V.C. 2008. Compositional heterogeneity in tephra deposits resulting from the eruption of multiple magma bodies: implications for tephrochronology. Quaternary International, 178(1), 44-53.

Smith, V.C., Pearce, N.J.C., Matthews, N.E., Westgate, J.A., Petraglia, M.D., Haslam, M., Lane, C.S., Korisettar, R., Pal, J.N. 2011. Geochemical fingerprinting of the widespread Toba tephra using biotite compositions. Quaternary International, 246, 97-104.

Thouret, J.-C., Worner, G., Gunnel, Y., Singer, B., Zhang, X., Souriot, T. 2007. Geochronologic and stratigraphic constraints on canyon incision and Miocene uplift of the Central Andes in Peru. Earth and Planetary Science Letters, 263, 151-166.

Thouret, J.-C., Gunnel, Y., Jicha, B.R., Paquette, J.L., Braucher, R. 2017. Canyon incision chronology based on ignimbrite stratigraphy and cut-and-fill sediment sequences in SWPeru documents intermittent uplift of the western Central Andes. Geomorphology, 298, 1-19.

Tosdal, R.M., Farrar, E., Clark, A.H. 1981. K-Ar geochronology of the late cenozoic volcanic rocks of the cordillera occidental, southernmost Peru. Journal of Volcanology and GeothermaI Research, 10, 157-173.

White, J.D.L., Houghton, B.F. 2006. Primary volcaniclastic rocks. Geology, 34 (8), 677-680.

Zanchetta, G., Sulpizio, R., Roberts, N., Cioni, R., Eastwood, W. J., Siani, G., Caron, B., Paterne, M., Santacroce, R. 2011. Tephrostratigraphy, chronology and climatic events of the Mediterranean basin during the Holocene: an overview. The Holocene, 21(1), 33-52.

PART II – INVERTEBRATE AND VERTEBRATE TAPHONOMY

Chapter 13. Exceptional preservation in the Pisco Fossil-Lagerstätte

Since the second half of the 20th century, the East Pisco Basin has been studied by researchers from all over the world because of the huge concentration of fossil marine vertebrates and their exceptional preservation.

The sedimentary strata outcropping in the Ica desert of Peru and belonging to the Pisco Formation have a widely recognized importance for the exceptional abundance in fossil marine vertebrates and for their extraordinary preservation. Due to this abundance and preservation, the Pisco Formation is now recognized as one of the most important Cenozoic marine Fossil-Lagerstätte worldwide (Seilacher 1970; Bianucci et al. 2016a, b; Brand et al. 2004; Collareta et al. 2015, 2017; Esperante et al. 2008, 2015; Gariboldi et al. 2015; Gioncada et al. 2016; Marx et al. 2017). The marine vertebrate assemblage, mainly hosted in diatomaceous mudstones, includes toothed and baleen-bearing whales, seals, marine slots, sea turtles, crocodiles, seabirds, and cartilaginous and bony fishes (Bianucci et al. 2016a, b c and references therein; Collareta et al. 2015, 2017; Di Celma et al. 2017; Gioncada et al. 2016; Lambert et al. 2015, 2017a, b; Landini et al. 2017a, b, in press; Marx et al. 2017; Marx & Kohno 2016; Stucchi et al. 2015, 2016).

In particular, the record of fossil marine vertebrates of the Pisco Formation is exceptional in terms of abundance of specimens, taxonomic diversity, ecomorphological disparity, and quality of preservation. Examples of remarkably preserved fossil remains featured in the Pisco Formation include phosphatized baleen plates and bristles of mysticete whales (Fig. 13.1) (Pilleri & Pilleri 1989; Brand et al. 2004; Esperante et al. 2008; Bisconti 2012; Gioncada et al. 2016; Marx & Kohno 2016; Marx et al. 2017), stomach contents and regurgitations of cetaceans and sharks (Fig. 13.2 and Fig. 13.3) (Collareta et al. 2015, 2017; Lambert et al. 2015), and articulated skeletons of cartilaginous fish (Fig. 13.3) (Ehret et al. 2009, 2012; Collareta et al. 2017).

By contrast, the knowledge on the fossil contents of the older deposits of the East Pisco Basin is still fragmentary, although including some specimens of extraordinary relevance, for both their evolutionary significance and their exceptional preservation (e.g., Clarke et al. 2010; Uhen et al. 2011; Lambert et al. 2017a; Martínez-Cáceres et al. 2017). Moreover, studies carried out in the last years highlighted an unexpected abundance of fossil vertebrates in the lower Miocene strata of the Chilcatay Formation (Di Celma et al. 2018; Landini et al. in press).

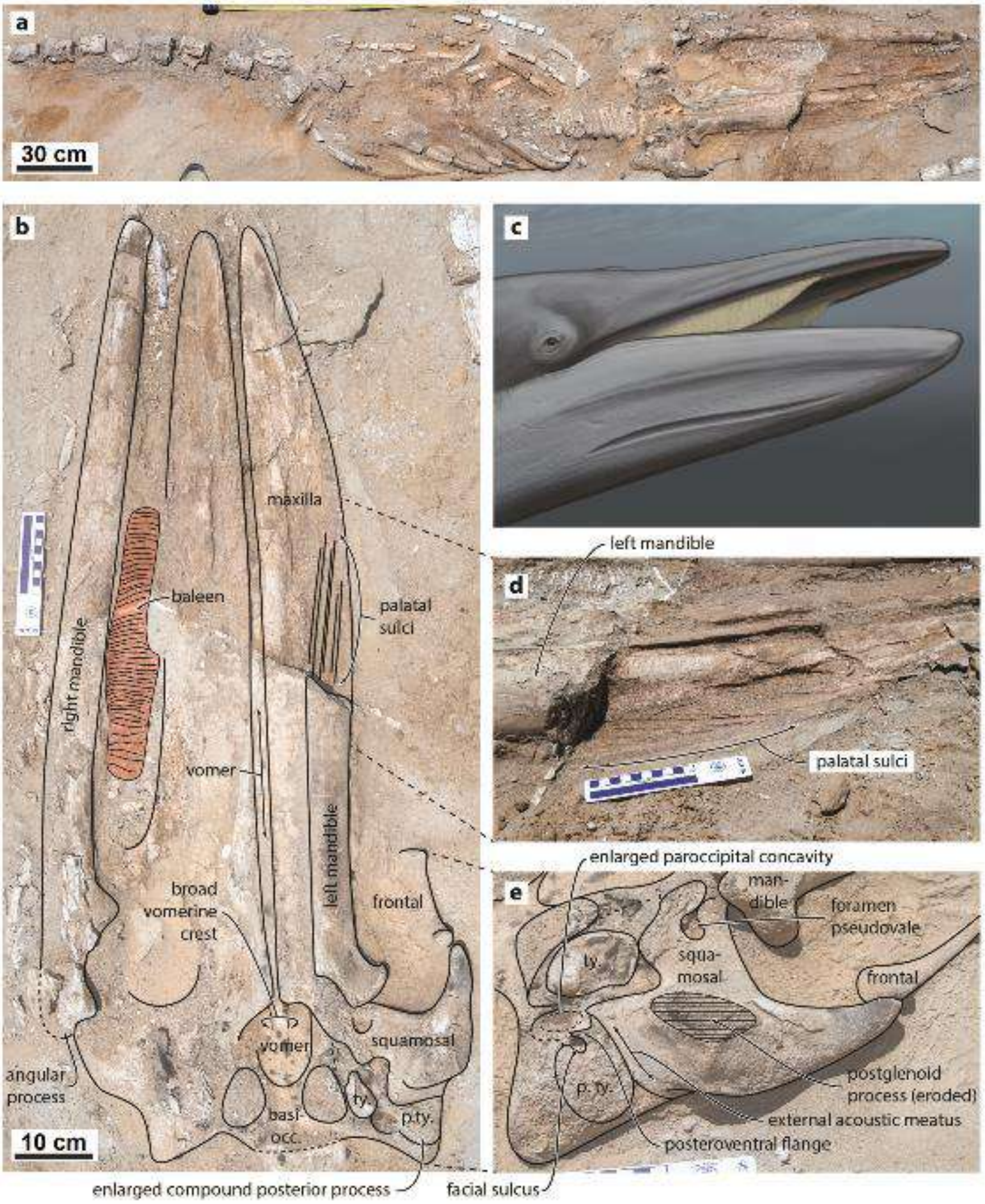

Figure 13.1. A specimen of *Piscobalaena nana* (MUSM 3292) preserving baleen. From Marx et al. (2017).

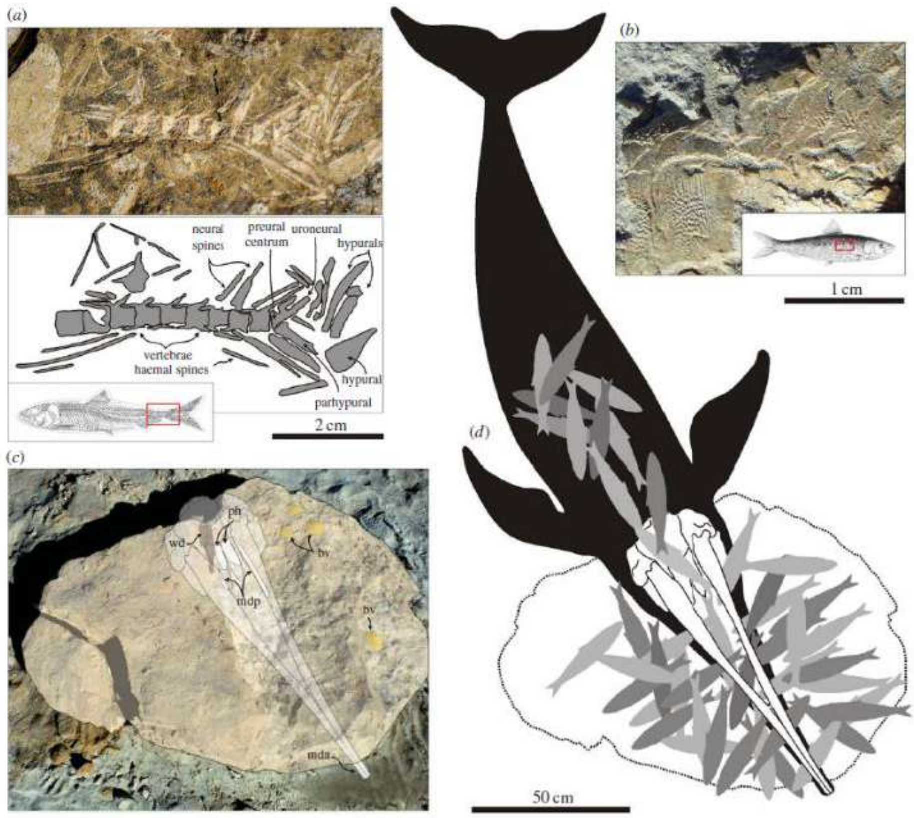

Figure 13.2. Fossil remains of the extinct beaked whale *Messapicetus gregarius* and associated clupeid fish *Sardinops* sp. cf. *S. sagax* found in Cerro Colorado. From Lambert et al. (2015).

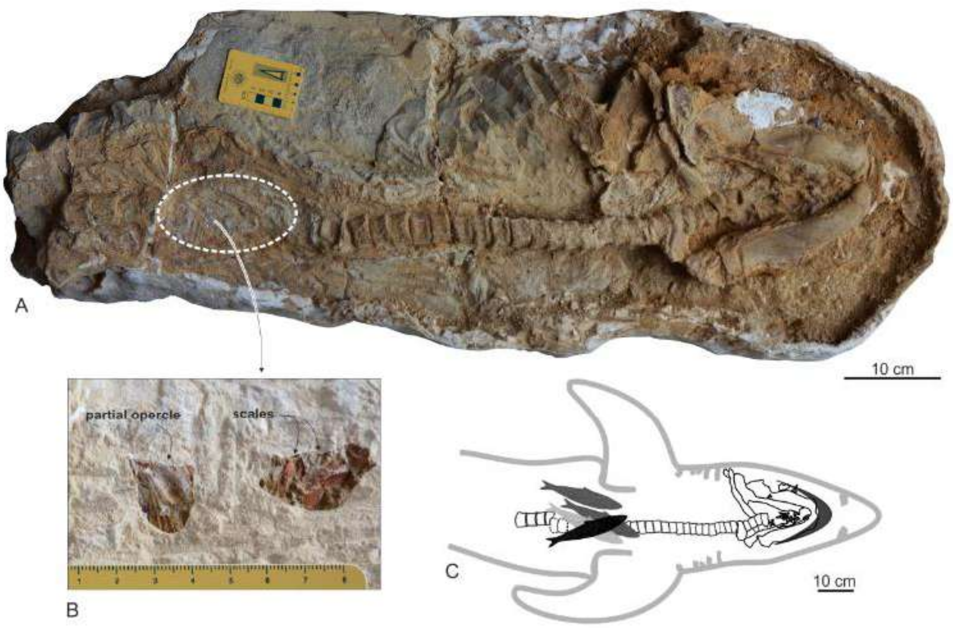

Figure 13.3. Fossil remains of the extinct mackerel shark *Cosmopolitodus hastalis* (specimen CPI-7899). From Collareta et al. (2017).

The extraordinary preservation characterized also the fossil invertebrates. The first description of the invertebrate fauna of the Pisco Formation has been realized in the Eighties by Muizon and DeVries (1985) and by DeVries (1988), and summarized more recently by DeVries and Frassinetti (2003) and DeVries (2007, 2016). A summary of the invertebrate content found in each allomember constituting the Pisco Formation has been presented in Di Celma et al. (2017), where the type of fossilization is mentioned for each mollusk accumulation. The taphonomy and the preservation of these fossils is still poorly studied in all the formations of the Pisco Basin.

In literature, it has been proposed that such an exceptional preservation in the Pisco Formation is due to a rapid burial, fast enough to cover whales on the sea-floor in weeks or months (Brand et al. 2004; Esperante et al. 2008, 2015). Brand et al. (2004) hypothesized a diatom accumulation of three to four orders of magnitude faster than today's rates (i.e., centimeters per week or month, rather than centimeters per thousand years. By contrast, recent studies explained in this dissertation (Chapter 17) show that the sedimentation rates in the Pisco Formation are similar to those of today's high-productivity coastal setting.

Such an outstanding accumulation of fossil vertebrates is currently regarded as the result of a complex interplay of different biotic and abiotic factors and processes, which concurred in creating an environmental setting where post-mortem preservation processes were, locally and at times, greatly facilitated. In particular, the widespread presence of dolomite concretions enclosing many fossil vertebrates of the Pisco Formation has been recently recognized (Fig. 13.4, Fig. 13.5) (Esperante et al. 2015; Gariboldi et al. 2015). Carbonate concretions enclosing fossils have been also described from many other deposits (e.g., Tarr, 1921; Weeks, 1957; Canfield & Raiswell 1991; Kaim et al. 2008; Danise et al. 2012; McCoy et al. 2015 and references therein).

Hypotheses on their relation with the decay processes have been proposed for both invertebrates and vertebrates (e.g., Briggs 2003; Danise et al. 2012). Information on the paleo-geochemical micro-environments related to the pre-burial decay and early diagenesis of fossil marine vertebrates has been gained by observations on modern shallow- and deep-water whale-fall communities (Allison et al. 1991; Goffredi et al. 2004; Treude et al. 2009; Little 2010). This subject is still a matter of discussion, in particular as regards: 1) the development of a sulphophilic stage supporting chemoautotrophic communities on shallow fossil whale falls (Dominici et al. 2009;

Danise et al. 2012, 2014); 2) the early vs. late diagenetic origin for carbonate cements precipitated within the skeletons (Kiel 2008; Shapiro & Spangler 2009).

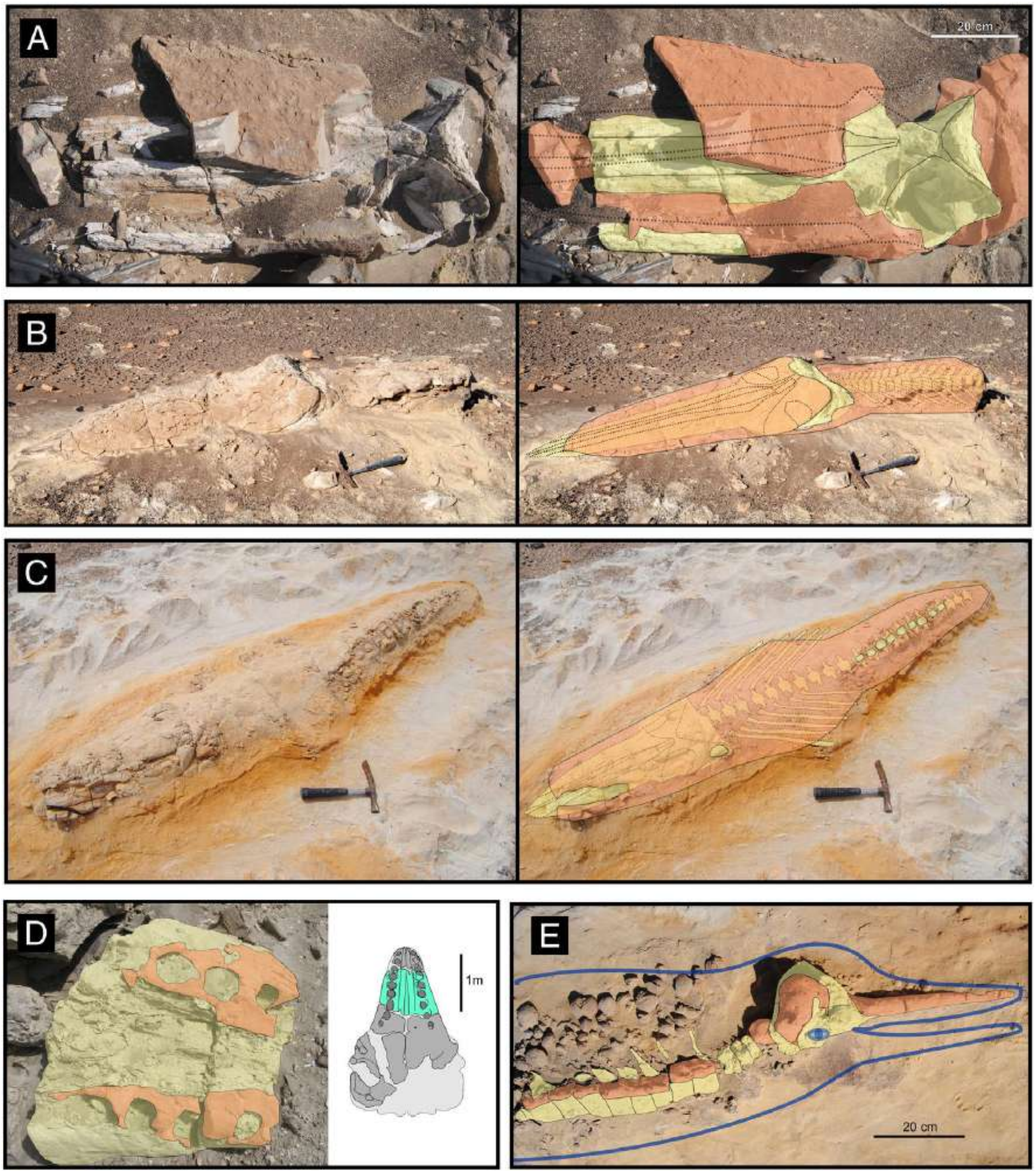

Figure 13.4. Carbonatic nodules enclosing fossils in the Pisco Formation.
From Gariboldi et al. (2015).

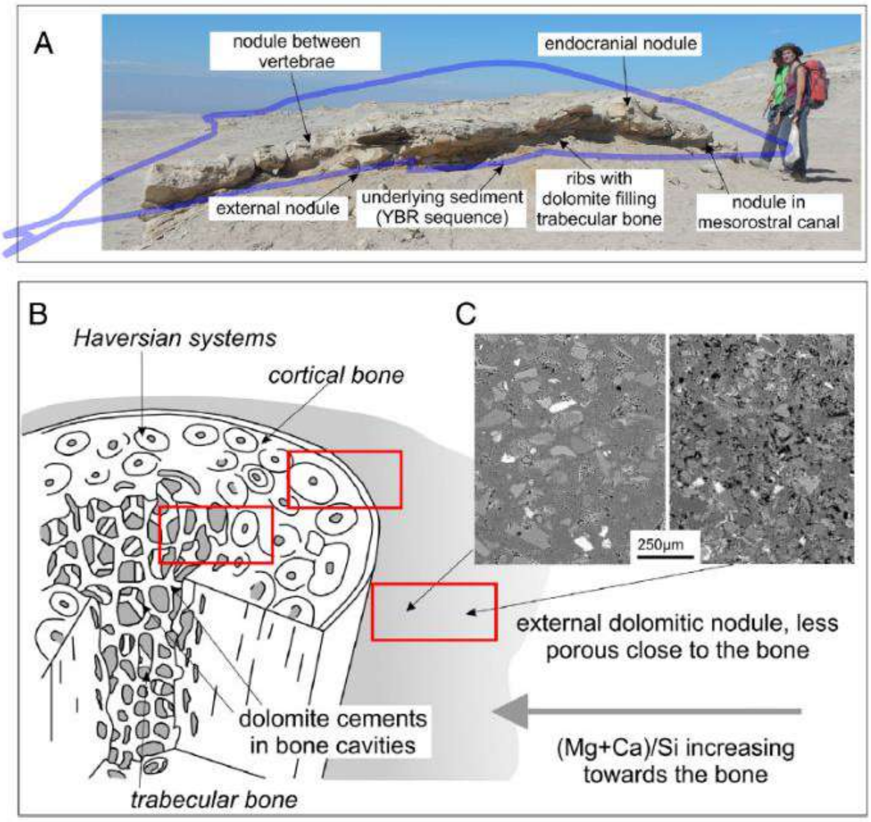

Figure 13.5. Concretion surrounding a mysticete skeleton and schematic section of a bone enclosed in a dolomitic nodule. From Gariboldi et al. (2015).

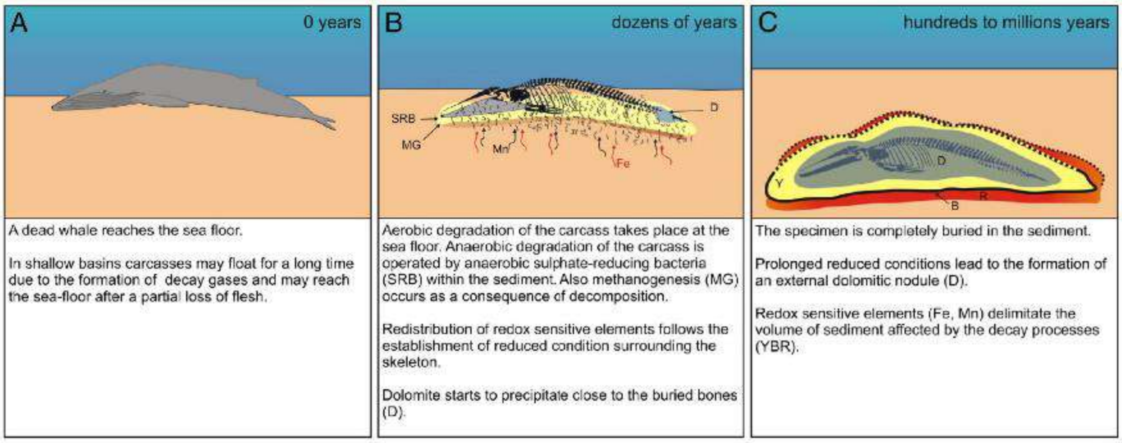

Figure 13.6. Dolomite formation reconstruction by Gariboldi et al. (2015).

The formation of mineral concretions during early diagenesis as a consequence of biomediated processes related to organic matter decay has been described elsewhere (McCoy et al. 2015; Yoshida et al. 2015). In the Pisco Formation, in case of a rapid burial, early precipitation of dolomite around vertebrate carcasses, although not always present, has been pointed out for its major contribution in allowing the preservation of complete and articulated skeletons, delicate anatomical structures, and even soft organic tissues (Fig. 13.6) (Gariboldi et al. 2015; Gioncada et al. 2016).

On the other hand, it is a matter of fact that this large vertebrate fossil record includes many skeletons that are not enclosed in carbonate concretions. Among these, it is possible to find very well preserved specimens, with good articulation and completeness and with highly mineralized bones and even soft tissues (e.g., Marx et al. 2017) as well as scarcely preserved bone remains. Observations indicate that the dolomite precipitation process affected especially large vertebrate carcasses (e.g., large-sized baleen whales), whereas it appears to have been less important (up to almost negligible) in correspondence of smaller carcasses (e.g., small-sized delphinidans and pinnipeds) whose often well-preserved remains constitute a large part of the fossil assemblages of the Pisco Formation (Gariboldi et al. 2015; Bianucci et al. 2016a, b; Di Celma et al. 2017).

To reconstruct a complete picture of this favorable fossilization environment, it is unavoidable to consider the fossilization path encountered by the vertebrate remains and the role of common diagenetic processes occurred after burial, involving dissolution and precipitation of minerals.

Some parts included in this chapter are the taken from the paper: "The dolomite nodules enclosing fossil marine vertebrates in the East Pisco Basin, Peru: Field and petrographic insights into the Lagerstätte formation" written by Karen Gariboldi, Anna Gioncada, Giulia Bosio, Elisa Malinverno, Claudio Di Celma, Chiara Tinelli, Gino Cantalamessa, Walter Landini, Mario Urbina and Giovanni Bianucci, published on Palaeogeography, Palaeoclimatology, Palaeoecology in 2015, Vol. 438, 81-95. In this paper, Giulia Bosio contributes to field data and sample collection, sample preparation, petrographic and mineralogical analyses, optical and electron microscopy and discussion about the dolomite formation.

Other parts are taken from introduction paragraph of the following papers: "Insights into the diagenetic environment of fossil marine vertebrates of the Pisco Formation (late Miocene, Peru) from mineralogical and Sr-isotope data" authored by Anna Gioncada, Riccardo Petrini, Giulia Bosio, Karen Gariboldi, Alberto Collareta, Elisa Malinverno, Elena Bonaccorsi, Claudio Di Celma, Marco Pasero, Mario Urbina and Giovanni

Bianucci, published on Journal of South American Earth Sciences in 2018, Vol. 81, 141-152. In this paper, Giulia Bosio contributes to sample collection and preparation, taphonomic analyses on vertebrates, invertebrate identification, diagenetic studies on mollusks and discussion on Sr-isotopes. "Taphonomy and palaeoecology of the lower Miocene marine vertebrate assemblage of Ullujaya (Chilcatay Formation, East Pisco Basin, southern Peru)" authored by Giovanni Bianucci, Alberto Collareta, Giulia Bosio, Walter Landini, Karen Gariboldi, Anna Gioncada, Olivier Lambert, Elisa Malinverno, Christian de Muizon, Rafael Varas-Malca, Igor Maria Villa, Giovanni Coletti, Mario Urbina and Claudio Di Celma, published in 2018 on Palaeogeography, Palaeoclimatology, Palaeoecology, Vol. 511, 256-279. In this paper, Giulia Bosio contributes to sample collection, measurement of the stratigraphic section and field mapping, optical microscope analyses on sediments, ex-pyrite framboid measurement, vertebrate taphonomy and microscopic analyses on bones, discussion on the paleoenvironment reconstruction and vertebrate taphonomy. "Looking for the key to preservation of fossil marine vertebrates in the Pisco Formation of Peru: new insights from a small dolphin skeleton" written by Anna Gioncada, Karen Gariboldi, Alberto Collareta, Claudio Di Celma, Giulia Bosio, Elisa Malinverno, Olivier Lambert, Jennifer Pike, Mario Urbina, Giovanni Bianucci, published in 2018 on Vol. 45(3) of Andean Geology. In this paper, Giulia Bosio contributes to the discussion on the bone mineralization and the chemical processes that contribute to the fossil preservation.

Chapter References

Allison, P.A., Smith, C.R., Kukert, H., Deming, J.W., Bennett, B.A. 1991. Deep-water taphonomy of vertebrate carcasses: a whale skeleton in the bathyal Santa Catalina Basin. Paleobiology, 17, 78-89.

Bianucci, G., Di Celma, C., Urbina, M., Lambert, G. 2016a. New beaked whales from the late Miocene of Peru and evidence for convergent evolution in stem and crown Ziphiidae (Cetacea, Odontoceti). PeerJ, 4:e2479.

Bianucci, G., Di Celma, C., Collareta, A., Landini, W., Post, K., Tinelli, C., de Muizon, C., Bosio, G., Gariboldi, K., Gioncada, A., Malinverno, E., Cantalamessa, G., Altamirano-Sierra, A., Salas-Gismondi, R., Urbina, M., Lambert, O. 2016b. Fossil marine vertebrates of Cerro Los Quesos:

Distribution of cetaceans, seals, crocodiles, seabirds, sharks, and bony fish in a late Miocene locality of the Pisco Basin, Peru. Journal of Maps, 12, 1037-1046.

Bianucci, G., Di Celma, C., Landini, W., Post, K., Tinelli, C., de Muizon, C., Gariboldi, K., Malinverno, E., Cantalamessa, G., Gioncada, A., Collareta, A., Salas-Gismondi, R., Varas-Malca, R.M., Urbina, M., Lambert, O. 2016c. Distribution of fossil marine vertebrates in Cerro Colorado, the type locality of the giant raptorial sperm whale Livyatan melvillei (Miocene, Pisco Formation, Peru). Journal of Maps, 12, 543-557.

Bisconti, M. 2012. Comparative osteology and phylogenetic relationships of Miocaperea pulchra, the first fossil pygmy right whale genus and species (Cetacea, Mysticeti, Neobalaenidae): Zoological Journal of the Linnean Society, 166(4), 876-911.

Brand, L.R., Esperante, R., Chadwick, A.V., Poma Porras, O., Alomía, M. 2004. Fossil whale preservation implies high diatom accumulation rate in the Miocene-Pliocene Pisco Formation of Peru. Geology, 32, 165-168.

Briggs, D.E.G. 2003. The role of decay and mineralization in the preservation of softbodied fossils. Annual Review of Earth and Planetary Sciences, 31, 275-301.

Canfield, D.E., Raiswell, R. 1991. Carbonate precipitation and dissolution: its relevance to fossil preservation. In: Allison, P.A., Briggs, D.E.G. (Eds.), Taphonomy: Releasing the Data Locked in the Fossil Record Geobiology 9. Plenum Press, New York, 337-387.

Clarke, J.A., Ksepka, D.T., Salas-Gismondi, R., Altamirano, A.J., Shawkey, M.D., D'Alba, L., Vinther, J., Devries, T.J., Baby, P. 2010. Fossil evidence for evolution of the shape and color of penguin feathers. Science, 330, 954-957.

Collareta A, Landini W., Lambert O., Post K., Tinelli C., Di Celma C., Panetta D., Tripodi M., Salvadori, P.A., Caramella, D., Marchi, D., Urbina, M., Bianucci, G. 2015. Piscivory in a Miocene Cetotheriidae: irst record of fossilized stomach content for an extinct baleen-bearing whale. Science of Nature, 102, 70.

Collareta, A., Landini, W., Chacaltana, C., Valdivia, W., Altamirano-Sierra, A., Urbina, M., Bianucci, G. 2017. A well preserved skeleton of the fossil shark Cosmopolitodus hastalis from the late Miocene of Peru, featuring fish remains as fossilized stomach contents. Rivista Italiana di Paleontologia e Stratigrafia (Research In Paleontology and Stratigraphy), 123, 11-22.

Danise, S., Cavalazzi, B., Dominici, S., Westall, F., Monechi, S., Guioli, S. 2012. Evidence of microbial activity from a shallow water whale fall (Voghera, northern Italy). Palaeogeography, Palaeoclimatology, Palaeoecology, 317-318, 13-26.

DeVries, T.J. 1988. Molluscs of the Pisco Basin. Pisco Basin guidebook. In: Dunbar, R.B., Baker, P.A. (Eds.), Cenozoic Geology of the Pisco Basin, IGCP, 156, 127-134.

DeVries, T.J. 2007. Cenozoic Turritellidae (gastropoda) from southern Peru. J. Paleontology, 81, 331-351.

DeVries, T.J. 2016. Fossil Cenozoic crassatelline bivalves from Peru: new species and generic insights. Acta Palaeontologica Polonica, 61, 661-688.

DeVries, T.J., Frassinetti, D. 2003. Range extensions and biogeographic implications of Chilean Neogene mollusks found in Peru. Boletín del Museo Nacional de Historia Natural de Chile 52, 119-135.

Di Celma, C., Malinverno, E., Bosio, G., Collareta, A., Gariboldi, K., Gioncada, A., Molli, G., Basso, D., Varas-Malca, R., Pierantoni, P.P., Villa, I.M., Lambert, O., Landini, W., Sarti, G., Cantalamessa, G., Urbina, M., Bianucci, G. 2017. Sequence stratigraphy and palaeontology of the upper Miocene Pisco Formation along the western side of the lower Ica valley (Ica desert, Peru). Rivista Italiana di Paleontologia e Stratigrafia (Research In Paleontology and Stratigraphy), 123, 255-274.

Di Celma, C., Malinverno, E., Collareta, A., Bosio, G., Gariboldi, K., Lambert, O., Landini, W., Pierantoni, P.P., Gioncada, A., Villa, I.M., Coletti, G., de Muizon, C., Urbina, M., Bianucci, G. 2018. Facies analysis, stratigraphy and marine vertebrate assemblage of the lower Miocene Chilcatay Formation at Ullujaya (Pisco basin, Peru). Journal of Maps, 14, 257-268.

Danise, S., Twitchett, R.J., Matts, K. 2014. Ecological succession of a Jurassic shallow-water ichthyosaur fall. Nature Communications, 5.

Dominici, S., Cioppi, E., Danise, S., Betocchi, U., Gallai, G., Tangocci, F., Valleri, G., Monechi, S. 2009. Mediterranean fossil whale falls and the adaptation of mollusks to extreme habitats. Geology, 37(9), 815-818.

Ehret, D.J., Hubbell, G., MacFadden, B.J. 2009. Exceptional preservation of the white shark C archarodon (Lamniformes, Lamnidae) from the early Pliocene of Peru. Journal of Vertebrate Paleontology, 29(1), 1-13.

Ehret, D.J., Macfadden, B.J., Jones, D.S., Devries, T.J., Foster, D.A., Salas-Gismondi, R. 2012. Origin of the white shark C archarodon (Lamniformes: Lamnidae) based on recalibration of the upper Neogene Pisco Formation of Peru. Palaeontology, 55(6): 1139-1153.

Esperante, R., Brand, L.R., Chadwick, A.V., Poma, O. 2015. Taphonomy and paleoenvironmental conditions of deposition of fossil whales in the diatomaceous sediments of the Miocene/Pliocene

Pisco Formation, southern Peru - a new Fossil-Lagerstatte. Palaeogeography, Palaeoclimatology, Palaeoecology, 417, 337-370.

Esperante, R., Brand, L.R., Nick, K.E., Poma, O., Urbina, M. 2008. Exceptional occurrence of fossil baleen in shallow marine sediments of the Neogene Pisco Formation, Southern Peru. Palaeogeography, Palaeoclimatology, Palaeoecology, 257, 344-360.

Gariboldi, K., Gioncada, A., Bosio, G., Malinverno, E., Di Celma, C., Tinelli, C., Cantalamessa, G., Landini, W., Urbina, M., Bianucci, G. 2015. The dolomitic nodules enclosing fossil marine vertebrates in the East Pisco Basin, Peru: field and petrographic insights into their genesis and role in preservation. Palaeogeography, Palaeoclimatology, Palaeoecology, 438, 81-95.

Gioncada, A., Collareta, A., Gariboldi, K., Lambert, O., Di Celma, C., Bonaccorsi, E., Urbina, M., Bianucci, G. 2016. Inside baleen: Exceptional microstructure preservation in a late Miocene whale skeleton from Peru. Geology, 44, 839-842.

Goffredi, S.K., Paull, C.K., Fulton-Bennett, K., Hurtado, L.A., Vrijenhoek, R.C. 2004. Unusual benthic fauna associated with a whale fall in Monterey Canyon, California. Deep-Sea Research Part I: Oceanographic Research Papers, 51(10), 1295-1306.

Kaim, A., Kobayashi, Y., Echizenya, H., Jenkins, R.G., Tanabe, K. 2008. Chemosynthesis based associations on Cretaceous plesiosaurid carcasses. Acta Palaeontologica Polonica, 53, 97-104.

Kiel, S. 2008. Fossil evidence for micro- and macrofaunal utilization of large nektonfalls: examples from early Cenozoic deep-water sediments in Washington State, USA. Palaeogeography, Palaeoclimatology, Palaeoecology, 267, 161-174.

Lambert, O., Bianucci, G., Muizon, C. de 2017a. Macroraptorial sperm whales (cetacea, odontoceti, physeteroidea) from the Miocene of Peru. Zoological Journal of the Linnean Society, 179, 404-474.

Lambert, O., Bianucci, G., Urbina, M., Geisler, J.H. 2017b. A new inioid (Cetacea, Odontoceti, Delphinidae) from the Miocene of Peru and the origin of modern dolphin and porpoise families. Zoological Journal of the Linnean Society, 179, 919-946.

Lambert, O., Collareta, A., Landini, W., Post, K., Ramassamy, B., Di Celma, C., Urbina, M., Bianucci, G. 2015. No deep diving: evidence of predation on epipelagic fish for a stem beaked whale from the late Miocene of Peru. Proceedings of the Royal Society B - Biological Sciences, 282, 20151530.

Landini, W., Collareta, A., Pesci, F., Di Celma, C., Urbina, M., Bianucci, G. 2017a. A secondary nursery area for the copper shark Carcharhinus brachyurus from the late Miocene of Peru. Journal of South American Earth Sciences, 78, 164-174.

Landini, W., Altamirano-Sierra, A., Collareta, A., Di Celma, C., Urbina, M., Bianucci, G. 2017b. The late Miocene elasmobranch assemblage from Cerro Colorado (Pisco Formation, Peru). Journal of South American Earth Sciences, 73, 168-190.

Landini, W., Collareta, A., Di Celma, C., Malinverno, E., Urbina, M., Bianucci, G. in press. The early Miocene elasmobranch assemblage from Zamaca (Chilcatay Formation, Peru). Journal of South American Earth Sciences.

Little, C.T.S. 2010. The prolific afterlife of whales; on the deep seafloor, the carcasses of the largest mammals give life to unique ecosystems. Scientific American, 302, 78-84.

Martínez-Cáceres, M., Lambert, O., Muizon, de C. 2017. The anatomy and phylogenetic affinities of Cynthiacetus peruvianus, a large Dorudon-like basilosaurid (Cetacea, Mammalia) from the late Eocene of Peru. Geodiversitas, 39, 7-163.

Marx, F., Collareta, A., Gioncada, A., Post, K., Lambert, O., Bonaccorsi, E., Urbina, M., Bianucci, G. 2017. How whales used to ilter: exceptionally preserved baleen in a Miocene cetotheriid. Journal of Anatomy, 231(2), 212-220.

Marx, F.G., Kohno, N. 2016. A new Miocene baleen whale from the Peruvian desert. Royal Society Open Science, 3(10), 160542.

McCoy, V.E., Young, R.T., Briggs, D.E.G. 2015. Sediment permeability and the preservation of soft-tissues in concretions: An experimental study. PALAIOS, 30, 608-612.

Muizon, C. de, DeVries, T.J. 1985. Geology and paleontology of late Cenozoic marine deposits in the Sacaco area (Peru). Geologische Rundschau, 74, 547-563.

Pilleri, G., Pilleri, O. 1989. Balaenoptera siberi, ein neuer balaenopterid (Cetacea) aus der Pisco-Formation Perus. In: Beitrage zur Palaeontologie der Cetaceen Perus I (Pilleri, G.; editor). Hirnanatomisches Institut der Universitat Bern Ostermundigen, 63-106, Bern.

Seilacher, A., 1970. Begriff und bedeutung der Fossil-Lagerstätten. Neues Jahrb. Geol. Palaontol. Abh. 1, 34-39.

Shapiro, R.S., Spangler, E. 2009. Bacterial fossil record in whale-falls: petrographic evidence of microbial sulfate reduction. Palaeogeography, Palaeoclimatology, Palaeoecology, 274, 196-203.

Stucchi, M., Emslie, S.D., Varas-Malca, R.M., Urbina, M., 2015. A new late Miocene condor (aves, Cathartidae) from Peru and the origin of South American condors. Journal of Vertebrate Paleontology, 35, e972507.

Stucchi, M., Varas-Malca, R.M., Urbina-Schmitt, M. 2016. New Miocene sulid birds from Peru and considerations on their Neogene fossil record in the Eastern Paciic Ocean. Acta Palaeontologica Polonica, 61, 417-427.

Tarr, W.A. 1921. Syngenetic origin of concretions in shale. Geological Society of America Bulletin, 32(4), 373-384.

Treude, T., Smith, C.R., Wenzhöfer, F., Carney, E., Bernardino, A., Hannides, A.K., Krüger, M., Boetius, A. 2009. Biogeochemistry of a deep-sea whale fall: sulfate reduction, sulfide efflux and methanogenesis. Marine Ecology Progress Series, 382, 1-21.

Uhen, M.D., Pyenson, N.D., Devries, T.J., Urbina, M., Renne, P.R. 2011. New middle Eocene whales from the Pisco Basin of Peru. Journal of Paleontology, 85, 955-969.

Weeks, L.G. 1957. Origin of carbonate concretions in shales, Magdalena Valley, Colombia. Geological Society of America Bulletin, 68(1), 95-102.

Yoshida, H.; Ujihara, A.; Minami, M.; Asahara, Y.; Katsuta, N.; Yamamoto, K.; Sirono, S.; Maruyama, I.; Nishimoto, S.; Metcalfe, R. 2015. Early post-mortem formation of carbonate concretions around tusk-shells over week-month timescales. Scientific Reports, 5, 14123.

Chapter 14. Methods applied for taphonomic studies

Taphonomic studies concern marine invertebrate and vertebrate fossils from both the Miocene units, the Chilcatay and the Pisco formations.

14.1. Methods applied for invertebrate taphonomy

In the field, fossil invertebrates have been collected in different localities and formations, paying attention to the stratigraphic position, the association with fossil vertebrates or the arrangement in accumulation levels. In the Chilcatay Formation, samples were collected mainly at Cerro Colorado, Ullujaya and Roca Negra. In the Pisco Formation, the main localities of sampling were Cerro los Quesos, Cerro Colorado, Cerro Blanco, Cerro la Bruja, the small unnamed cerro (called here Cerro Innominado) westward Cerros la Mama y la Hija, Cerro Submarino and Cerro Sombrero.

Invertebrate specimens were cleaned with an ultrasonic bath, named with initials and identified to the lowest possible taxonomic rank. Difficulties were encountered because of the poor preservation of the taxonomic features useful for the identification.

With the aim of reconstructing the diagenetic histories of both formations, mollusk and barnacle samples have been prepared for realizing thin sections from both Chilcatay and Pisco formations. Mineralogical analyses, integrated with taphonomic observations, enabled us to reconstruct the sequence of the diagenetic processes and to avoid the altered and diagenetic portions of carbonate shells for Sr-isotope stratigraphic analyses. Thin sections were prepared and petrographic analyses were carried out through Leica and Olympus optical microscopes. SEM-EDS Tescan VEGA TS Univac 5136XM was used for petrographic and morphological observations, also for checking evidence of dissolution in the shell structure. Thin sections were also analyzed through the cold cathode luminoscope for cathodoluminescence microscopy at the University of Milano, used for diagenetic investigation: cathodoluminescence could help in distinguish different mineral generations and the recrystallization of portions of the shells (Barbin 2013; Ullman & Korte 2015).

In the Pisco Formation, we decided to analyzed mollusks associated with vertebrates, because the minerals forming mollusk casts and internal molds may be of help in defining the sequence of minerals formation during diagenesis and in understanding the vertebrate preservation. All shells examined in the field and collected for analysis were found in situ, still partially included in the sediment. This excludes that the association of bivalves with cetaceans was due to recent erosion. The selected specimens of vertebrates, all belonging to cetaceans (C46, C47, O7 and M50, location in the fossil map of Bianucci et al. 2016), are from the fossil-rich interval within member F of the CLQ stratigraphic section (Bianucci et al. 2016). The samples collected for observations at the micro-scale and for isotopic and mineralogical analysis in correspondence of the four specimens include small fragments of mollusks, and fracture- and fault-filling veins. The mollusk samples were examined under a stereomicroscope, and some of them were sectioned to examine the filled internal cavity. Sediment components were inspected with the aid of smear slides for transmitted light microscopy. Fragments were carefully taken from the bivalve specimens. Some of them were mounted in resin and prepared as polished sections. After carbon-coating, the fragments were analyzed by scanning electron microscopy (SEMSEI, Secondary Electron Imaging, and BSEI, back-scattered electrons imaging) and EDS microanalysis, by means of a Philips XL30 equipped with a Dx4i microanalytical device at Earth Science Department of the University of Pisa. Analytical details were 20 kV filament voltage, 5 nA beam current, ZAF correction. XRPD data were collected for the different mollusk casts and internal molds and for gypsum veins.

For the Sr isotopic analysis on gypsum, bivalves were selected after visual inspection and following the mineralogical results in order to distinguish and include samples representative of different mineral formation processes (shell replacement, open-space filling). About 10 mg of sample were collected both in the inner shell parts and on superficial layers by means of a microdrill apparatus, taking care to avoid mixing. Sample GB30 was chemically treated using diluted ultrapure HCl on hot plate for dolomite dissolution; the remaining samples were handled for the total dissolution of gypsum. Sr isotope data were collected by solid-source thermal ionization mass spectrometry (TIMS) using a Finnigan MAT 262 mass spectrometer at the Earth Sciences Department of Sapienza University (Rome, Italy). The reported uncertainties represent in-run statistics at 2-s confidence level. Repeated analysis of the NBS 987 standard (n ¼ 10) gave an average $^{87}Sr/^{86}Sr$ value of 0.710245(9), and no correction was applied to the measured ratios for instrumental bias. An external error of ±0.000010 on the measured Sr isotopic composition has been assumed.

Special attention was given to the observation of fossil barnacle assemblages, focusing on their first-order taxonomic composition. Their taphonomic features and their distribution within the studied successions were investigated following Doyle et al. (1997), Nomura and Maeda (2008), and Nielsen and Funder (2003) methodologies, based on the fragmentation of the shells and whether or not the specimens are in life attitude. Representative rock samples were then collected for petrographic and paleontological analyses. A large number of barnacle specimens (including isolated opercular plates, shell fragments, complete shells and multi-individual aggregates) were also collected in the studied outcrops. The petrographic characteristics of the rocks and their skeletal assemblages where analyzed on polished thin sections. The different components were identified and quantified using point-counting method with a minimum of 400 hundred points per section (Flügel 2010). Barnacle taxa were studied by integrating information from both complete specimens (where available) and plates retrieved from the embedding rock. After studying them under a stereomicroscope, some selected specimens (including mural plates and complete shells) were prepared as thin sections to observe the internal microstructure of the shells, which can be useful for taxonomic identification (Cornwall 1956, 1958, 1962). As a result of the uncertainties inherent in fossil barnacle taxonomy, we elected to simply recognize and characterize the different morphotypes occurring in the investigated facies, with each morphotype reasonably corresponding to a single species, and vice versa.

14.2. Methods applied for vertebrate taphonomy

Fossil vertebrates for taphonomic considerations have been described in the field at the locality of Ullujaya for the Chilcatay Formation specimens and Pampa Corre Viento for the Pisco Formation fossil remains, respectively.

In the field, taphonomic observations on marine vertebrates at the locality of Ullujaya concerned the degree of preservation of the cortical bone and vertebral processes, as well as the presence/absence of: 1) bone abrasion; 2) bone fractures; 3) associated mollusk shells, remains of crabs and other invertebrates, teleostean and elasmobranch teeth; 4) associated remains of encrusting epibionts; and 5) traces of invertebrates and vertebrates. For microscopic taphonomic features, nine bone samples from seven cetacean specimens were prepared as polished thin sections cut orthogonally to the elongation of the bone. They were analyzed with Olympus BX50 and Leica Leitz Laborlux S transmitted light and Leica DM EP reflected light microscopes and with scanning electron microscopy and microanalysis (SEM-EDS; Tescan VEGA TS 5136 XM, University of Milano-Bicocca and the Philips-EDAX Genesis University of Pisa), obtaining semi-quantitative composition results. Smear slides of fine-grained sediments were analyzed with an Olympus BX50 polarized optical microscope in correspondence of big concentration of fossil vertebrates, in order to understand the paleoenvironmental conditions. The size distribution of relics of pyrite framboids was used as an indicator of redox conditions (Wilkin et al., 1996).

Providing a detailed and integrated characterization of the modes of fossilization of small-sized (i.e., less than 2.5 m in total length) vertebrates preserved in absence of dolomite concretions (McCoy et al. 2015; Gariboldi et al. 2015) is pivotal for understanding the genesis of the Pisco Formation Fossil-Lagerstätte. For this purpose, we investigated a well-preserved skeleton of a small pontoporiid dolphin from Pampa Corre Viento. This specimen is kept in the Museo de Historia Natural de la Universidad Nacional Mayor de San Marcos of Lima, Peru (hereinafter: MUSM) with accession number MUSM 887. Reflected-light optical microscopy and SEM-EDS analyses were performed on bones and sediments surrounding the specimen. X-rays Powder Diffraction analyses were carried out on sediments.

This chapter is resulted from the combination of papers, such as: "Taphonomy and palaeoecology of the lower Miocene marine vertebrate assemblage of Ullujaya (Chilcatay Formation, East Pisco Basin, southern Peru)" authored by Giovanni Bianucci, Alberto Collareta, Giulia Bosio, Walter Landini, Karen Gariboldi, Anna Gioncada, Olivier Lambert, Elisa Malinverno, Christian de Muizon, Rafael Varas-Malca, Igor Maria Villa, Giovanni Coletti, Mario Urbina and Claudio Di Celma, published in 2018 on Palaeogeography, Palaeoclimatology, Palaeoecology, Vol. 511, 256-279. In this paper, Giulia Bosio contributes to sample collection, measurement of the stratigraphic section and field mapping, optical microscope analyses on sediments, ex-pyrite framboid measurement, vertebrate taphonomy and microscopic analyses on bones, discussion on the paleoenvironment reconstruction and vertebrate taphonomy.

"Insights into the diagenetic environment of fossil marine vertebrates of the Pisco Formation (late Miocene, Peru) from mineralogical and Sr-isotope data" written by

Anna Gioncada, Riccardo Petrini, Giulia Bosio, Karen Gariboldi, Alberto Collareta, Elisa Malinverno, Elena Bonaccorsi, Claudio Di Celma, Marco Pasero, Mario Urbina and Giovanni Bianucci, published on Journal of South American Earth Sciences in 2018, Vol. 81, 141-152. In this paper, Giulia Bosio contributes to sample collection and preparation, taphonomic analyses on vertebrates, invertebrate identification, diagenetic studies on mollusks and discussion on Sr-isotopes.

"Looking for the key to preservation of fossil marine vertebrates in the Pisco Formation of Peru: new insights from a small dolphin skeleton" written by Anna Gioncada, Karen Gariboldi, Alberto Collareta, Claudio Di Celma, Giulia Bosio, Elisa Malinverno, Olivier Lambert, Jennifer Pike, Mario Urbina, Giovanni Bianucci, published in 2018 on Vol. 45(3) of Andean Geology. In this paper, Giulia Bosio contributes to the discussion on the bone fossilization and the chemical processes that contribute to the fossil preservation.

Methods applied for mollusk taphonomy are reported for the first time and will be included in future works. Methods for barnacle taphonomy are taken from the paper "Palaeoenvironmental analysis of the Miocene barnacle facies: case studies from Europe and South America" written by Giovanni Coletti, Giulia Bosio, Alberto Collareta, John Buckeridge, Sirio Consani and Akram El Kateb, in press on Geologica Carpathica. In this paper, Giulia Bosio contributes to sample collection of the Peruvian material, sample preparation and analyses, comparison among barnacle facies and the discussion.

Chapter References

Barbin, V. 2013. Application of cathodoluminescence microscopy to recent and past biological materials: a decade of progress. Mineralogy and Petrology, 107, 353-362.

Bianucci, G., Di Celma, C., Collareta, A., Landini, W., Post, K., Tinelli, C., de Muizon, C., Bosio, G., Gariboldi, K., Gioncada, A., Malinverno, E., Cantalamessa, G., Altamirano-Sierra, A., Salas-Gismondi, R., Urbina, M., Lambert, O. 2016a. Fossil marine vertebrates of Cerro Los Quesos: Distribution of cetaceans, seals, crocodiles, seabirds, sharks, and bony fish in a late Miocene locality of the Pisco Basin, Peru. Journal of Maps, 12, 1037-1046.

Cornwall, I.E. 1956: Identifying recent and fossil barnacles by the figures in the shell. Journal of Paleontology, 30, 3, 646-561.

Cornwall, I.E. 1958. Identifying recent and fossil barnacles. Canadian Journal of Zoology, 36(1), 79-89.

Cornwall, I.E. 1962. The identification of barnacles with further figures and notes. Canadian Journal of Zoology, 40(4), 621-629.

Doyle, P., Mather, A.E., Bennet, M.R., Bussel, M.A. 1997. Miocene barnacle assemblages from Southern Spain and their palaeoenvironmental significance. Lethaia, 29(3), 267-274.

Flügel, E. 2010. Microfacies of Carbonate Rocks: Analysis Interpretation and Application. Springer, New York, 1-1007.

Gariboldi, K., Gioncada, A., Bosio, G., Malinverno, E., Di Celma, C., Tinelli, C., Cantalamessa, G., Landini, W., Urbina, M., Bianucci, G. 2015. The dolomitic nodules enclosing fossil marine vertebrates in the East Pisco Basin, Peru: field and petrographic insights into their genesis and role in preservation. Palaeogeography, Palaeoclimatology, Palaeoecology, 438, 81-95.

McCoy, V.E., Young, R.T., Briggs, D.E.G. 2015. Sediment permeability and the preservation of soft-tissues in concretions: An experimental study. Palaios, 30, 608-612.

Nielsen, J.K., Funder, S. 2003. Taphonomy of Eemian marine mollusks and acorn barnacles from eastern Arkhangelsk region, northern Russia. Palaeogeography, Palaeoclimatology, Palaeoecology, 191, 139-168.

Nomura, S., Maeda, H. 2008. Significance of autochtonous fossil barnacles from the Miocene Natori Group at the Moniwa-Goishi area, northeast Japan. Paleontological Research, 12(1), 63-79.

Ullmann, C.V., Korte, C. 2015. Diagenetic alteration in low-Mg calcite from macrofossils: a review. Geological Quarterly, 59(1), 3-20.

Wilkin, R.T., Barnes, H.L., Brantley, S.L. 1996. The size distribution of framboidal pyrite in modern sediments: an indicator of redox conditions. Geochimica et Cosmochimica Acta, 60, 3897-3912.

Chapter 15. Mollusk taphonomy in both Chilcatay and Pisco formations

15.1. Chilcatay and P0 mollusk taphonomy

The Miocene Chilcatay and Pisco formations are well-known for the exceptional preservation of fossil marine vertebrates, but they are also characterized by the presence of fossil invertebrate fauna.

In the western side of the Ica River, these two formations exhibits two different preservation modes suggesting two distinct fossilization pathways. The results of mineralogical and geochemical analyses, integrated with taphonomic observations, enabled us to reconstruct the sequence of the fossilization and diagenetic processes for fossil invertebrates.

In the lower Miocene Chilcatay Formation, fossil invertebrates are common and well-preserved, but the assemblage is characterized by low biodiversity, with only few species of barnacles, echinoids, tube worms and bivalves (mainly pectinids and oysters). Overall, biogenic Ca-carbonates are well preserved. In the P0 allomember of the Pisco Formation, invertebrates show a very low preservation, but the Ca-carbonates are present, unlike in the younger P1 and P2 allomembers of the Pisco Formation.

The Chilcatay Formation mollusks were studied at the localities of Ullujaya and Roca Negra, where they show a high concentration but a low biodiversity. They are constituted essentially by bivalves, as pectinids and ostreids. The P0 assemblage was studied in Cerro Yesera de Amara, Cerro Submarino and Cerro Sombrero, and is constituted by a higher diversification, as oysters, *Dosinia ponderosa*, *Chionopsis*, *Miltha*, and specimens of Architectonicidae and Cypraeidae. Their preservation was studied in order to quantify the extent of diagenetic processes and therefore to assess if their shells are still pristine or not. This is important for Sr isotope analyses applied on carbonates to reconstruct the chronostratigraphy of the Chilcatay Formation and the P0 allomember (Chapter 8 and 11). Weathering and re-precipitated minerals after the death and the burial of the organism invalidate the final age calculation, altering the original $^{87}Sr/^{86}Sr$ of the shell.

Figure 15.1. a) Photo of a very big oyster specimen, found in Chilcatay Formation at Roca Negra. b) Photo of pectinids found in Chilcatay Formation at Ullujaya.

Mollusk shells are mainly made by calcite, which is abundant in this formation, differently from the youngest allomembers of the Pisco Formation. At the macroscale, we can assert that fossil shell remains of Chilcatay mollusks are constituted by Ca-carbonates and show a quite good preservation (Fig. 15.1a, b). Oysters are usually bioturbated and show predation traces of sponges and big borings of other predator mollusks. In several cases, they show layers of unaltered nacre. Pectinids are well preserved, with small borings and some barnacles still attached on their shells.

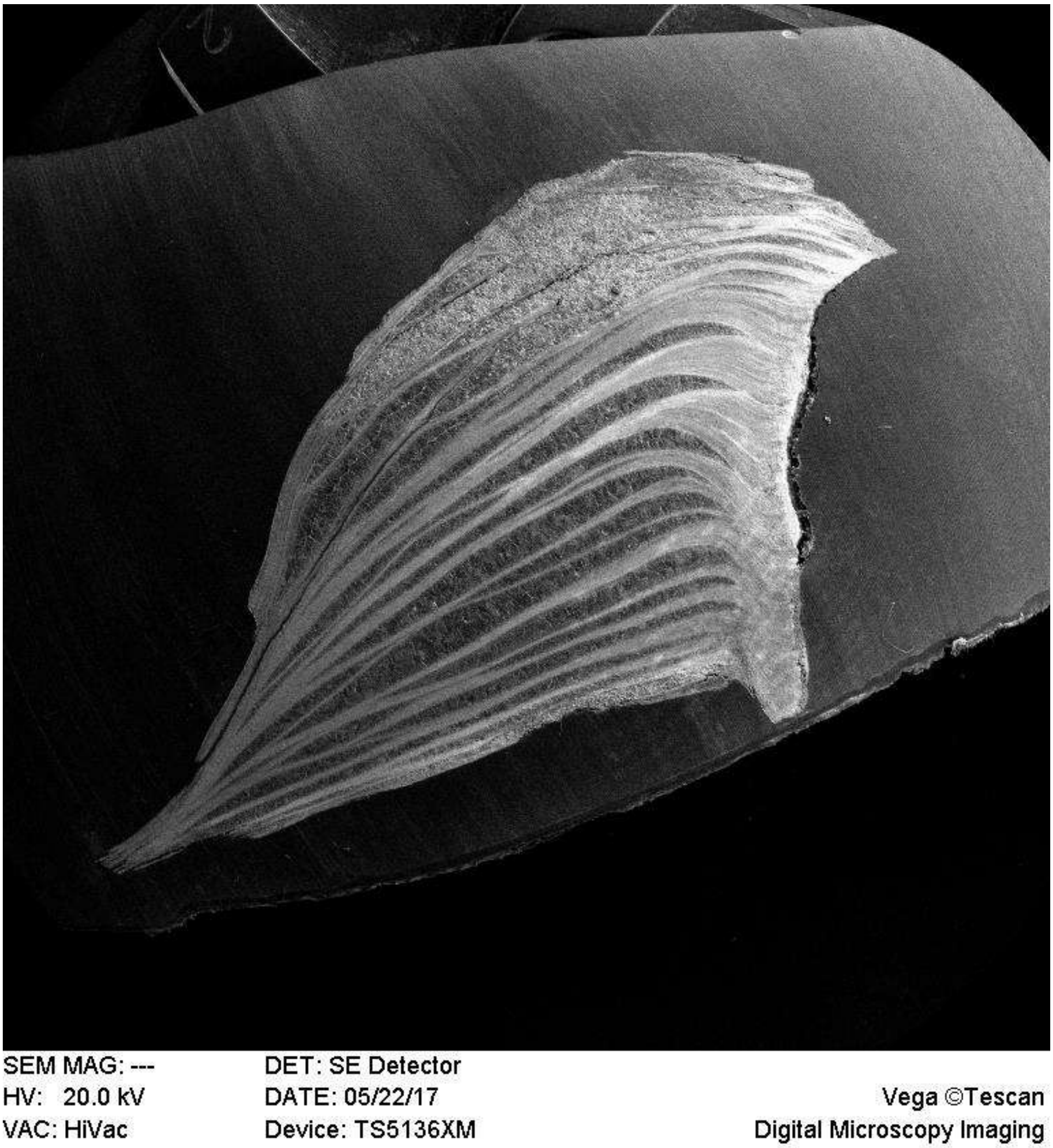

Figure 15.2. SE image of YA-SOT oyster sample showing an alternation of prismatic and chalky layers.

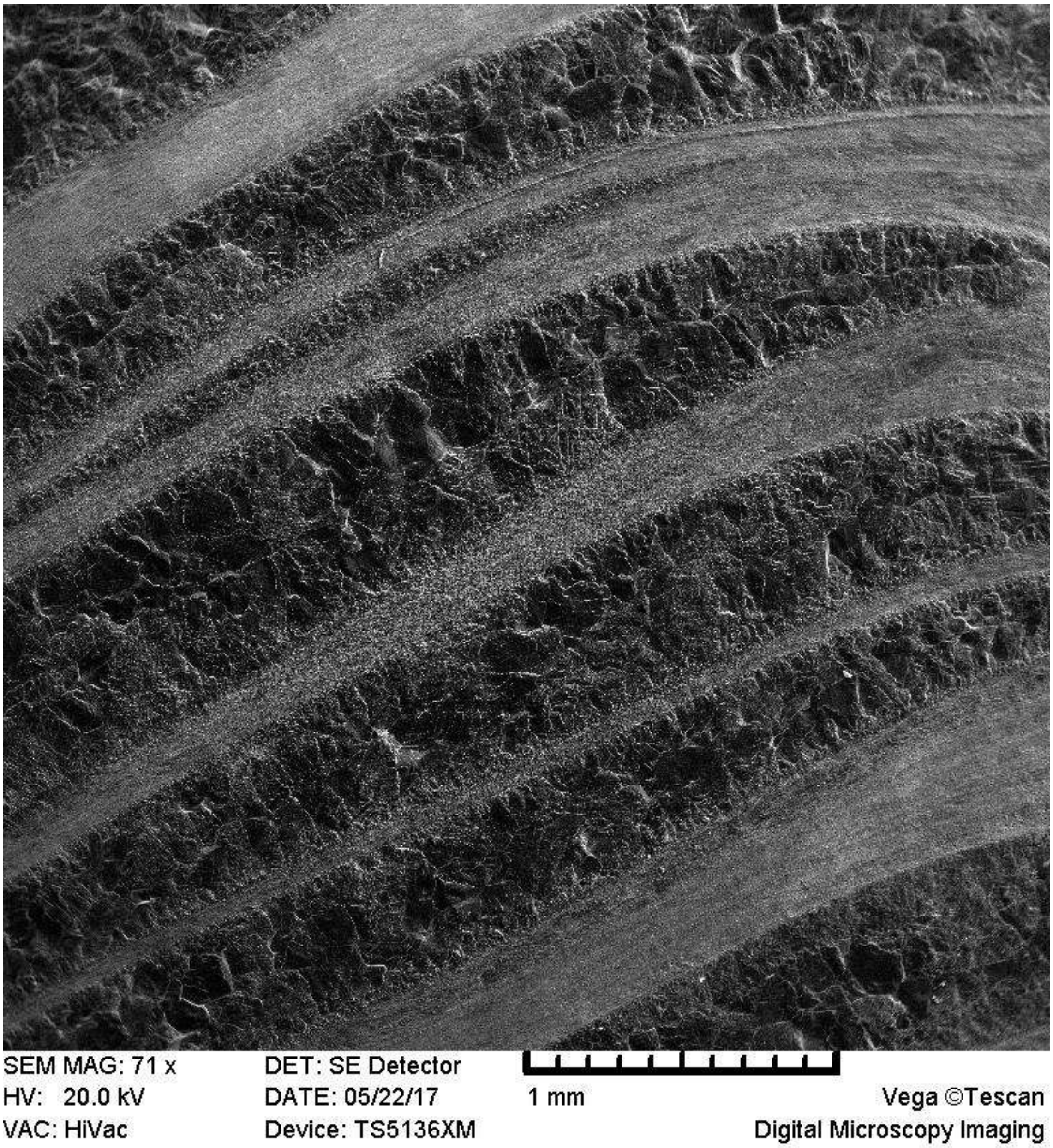

Figure 15.3. Zoom of chalky layers alternating with prismatic layers in YA-SOT oyster.

Many samples of ostreids and pectinids have been analyzed through the optical and SEM-EDS microscope in order to establish the degree of alteration that affected the shell (Scasso et al. 2001). Images through the detection of secondary electrons from different ostreids specimens show an alternation of prismatic and chalky (or sparry) layers in many specimens (Fig. 15.2 and Fig. 15.3). SE images show, in some cases, a well preserved and intact structure of the pristine prismatic layer of oysters that suggests a low degree of alteration (Fig. 15.4). Several oyster samples showing an intact prismatic layer were selected for Sr isotope analyses, as UL-D4 (from a layer in *Ct1a* facies association at Ullujaya) and PN-OST (few meters above the base of the Chilcatay Formation in Roca Negra) samples. In few cases, this prismatic layer is almost unrecognizable, very irregular and seems dissolved (Fig. 15.5), proving that alteration occurred. The specimens showing this feature were discarded from Sr isotope analyses, as oysters from the level UL-D18. All the minerals analyzed through EDS show a Ca-carbonate composition.

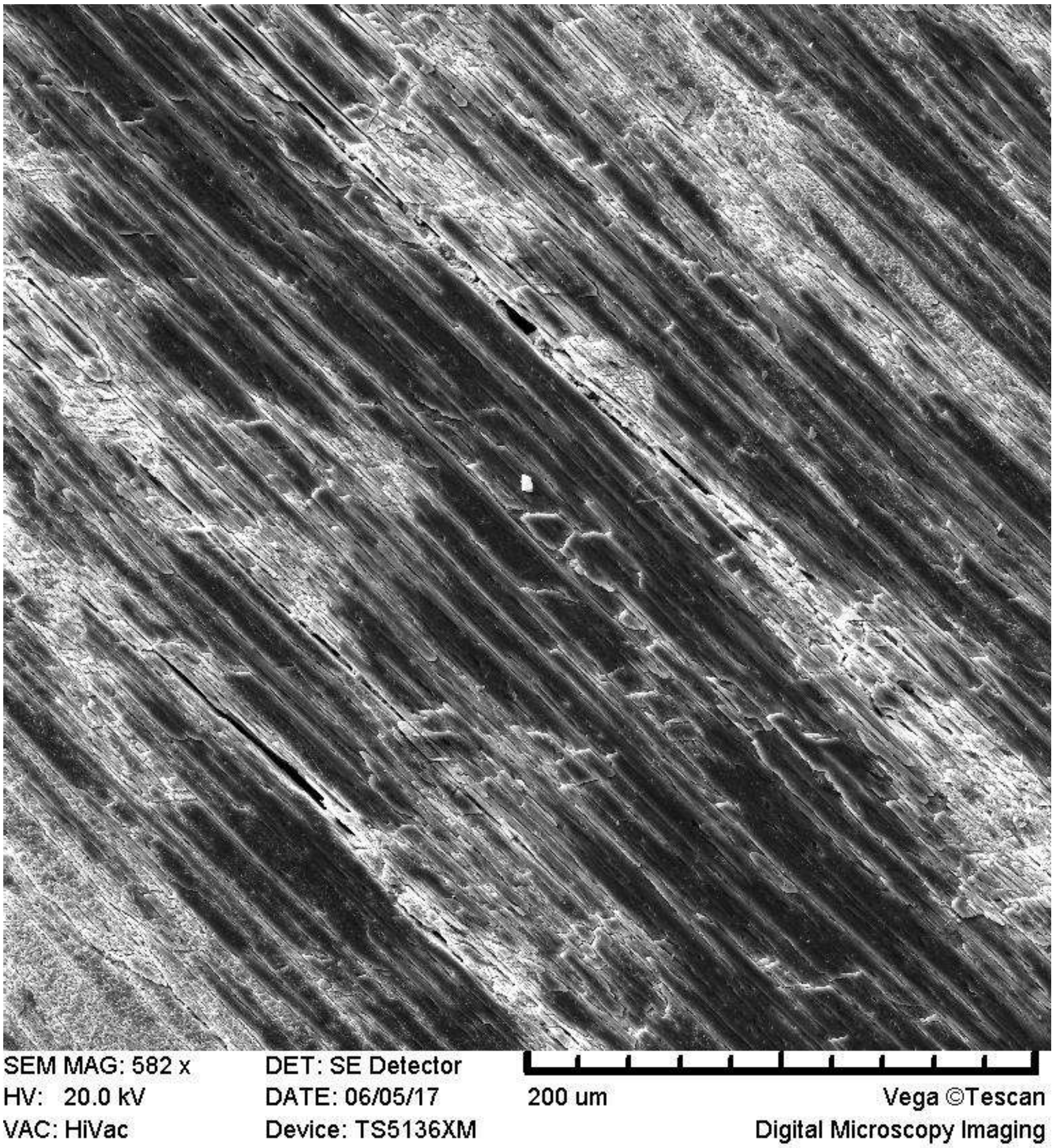

Figure 15.4. SE image of UL-D4 oyster showing a well preserved prismatic layer.

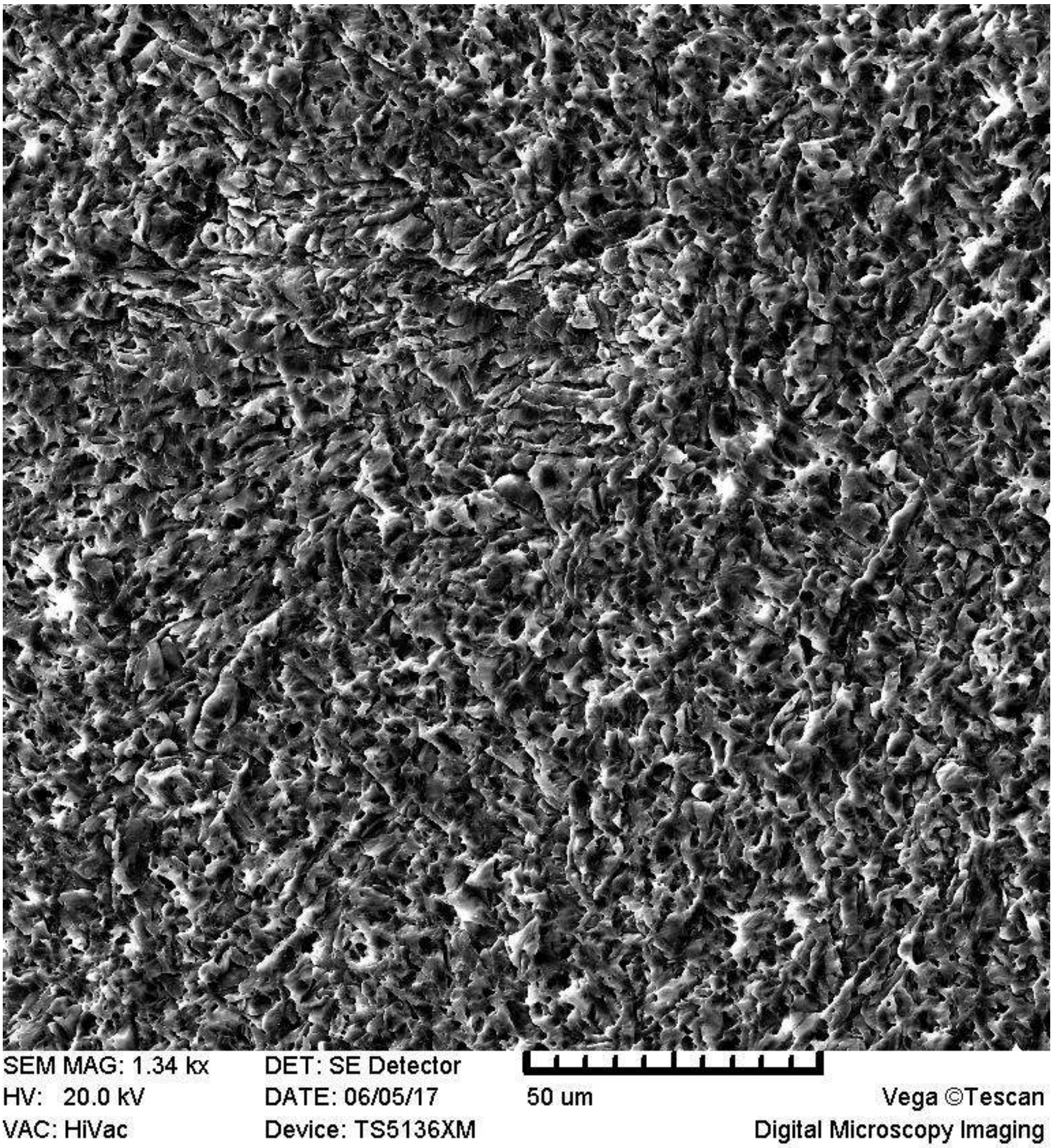

Figure 15.5. SE image of the oyster UL-D18 showing a badly preserved prismatic layer.

The oysters that show a well-preserved structure of the prismatic layer and the pectinids that show an intact crossed foliated microstructure were selected for further investigations. Thin sections of these samples were analyzed through cathodoluminescent microscopy in order to distinguish different generations of calcite. Cathodoluminescence analyses reveal that these fossils usually have layers that show different kind of luminescence response. Pectinids have a quite homogeneous and low luminescence, as shown in Figure 15.6, showing a low alteration degree.

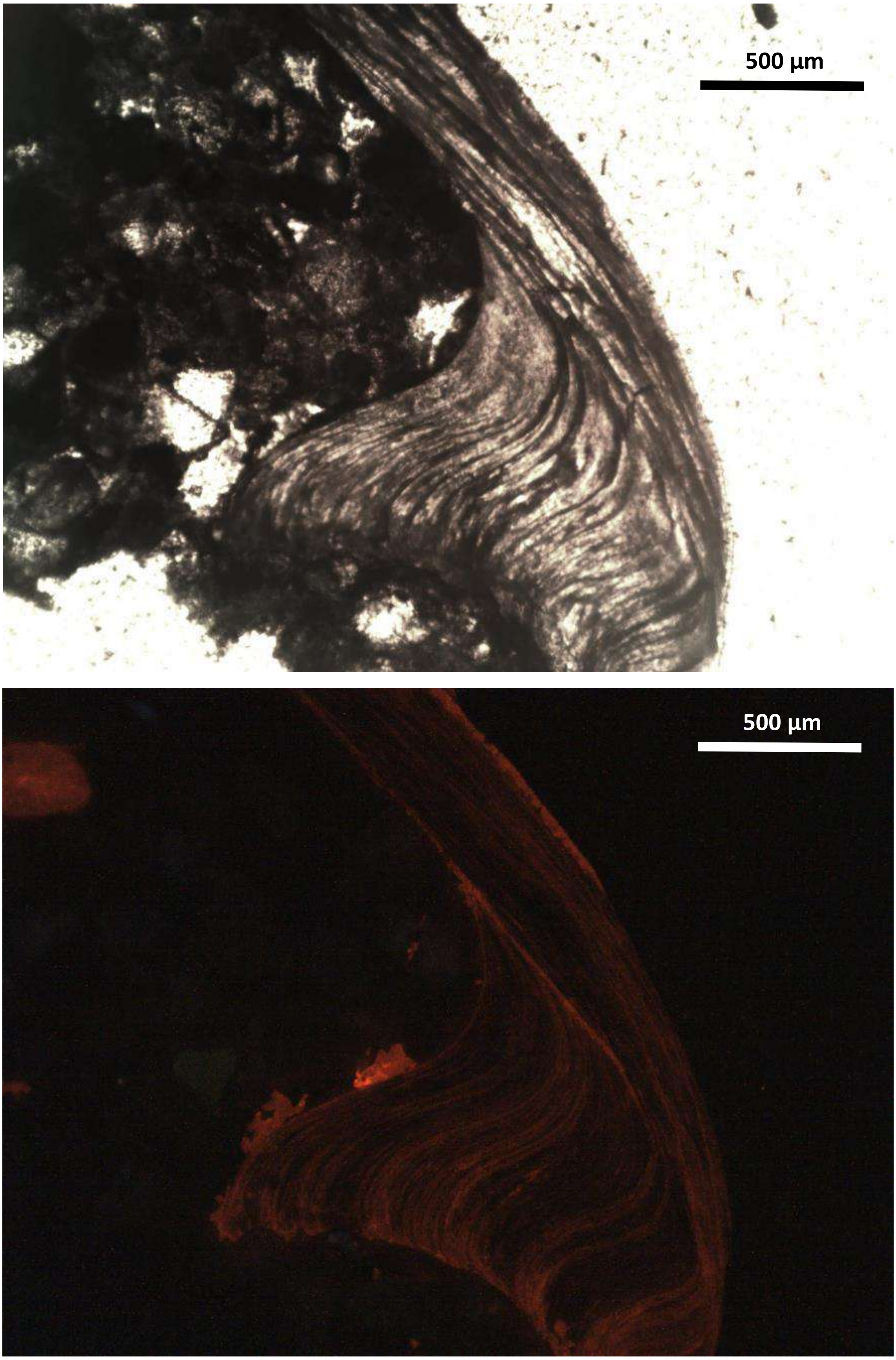

Figure 15.6. Optical and cathodoluminescent image of a pectinid found at Ullujaya.

Thin sections of selected oysters from both Ullujaya and Roca Negra localities show well-preserved pristine carbonate layers, characterized by a low and homogeneous luminescence. However, there are also luminescent zones characterized by diagenetic calcite reprecipitation (Fig. 15.7). As shown by Crippa et al. (2016), fossil ostreids can exhibit layers of sparry calcite replacing the old and original aragonitic layers, suggesting an alteration of the bivalve shell. In some cases, it is easy to recognize some microborings made by other organisms. These can be filled by a cement of late calcite (Fig. 15.8), which must be avoided during sampling for Sr isotope analyses, or show an infill of terrigenous grains (Fig. 15.9) that could modify the Sr isotope content.

Several oysters from Chilcatay and P0 allomember show a low luminescence, but in some cases, they are characterized by luminescent layers, which are not the ones filled by chalky (sparry) calcite (Fig. 15.10). To explain this feature that is present also in modern oysters, Barbin (1991, 2013) affirms that cathodoluminescence is not a reliable indicator of diagenetic alteration for oysters, because the absorption of Mn^{2+} by benthic organisms depends on various factors, as growth rate, ontogeny, open sea conditions, bathymetry and salinity.

For eliminating any doubt about the alteration that affected these fossils, we avoid oyster samples that show an irregular prismatic layer at secondary electron microscopy, an alternation of chalky (sparry) calcite layers, diffuse microborings and a high and heterogeneous luminescence, as YA-SOT and UL-D18.

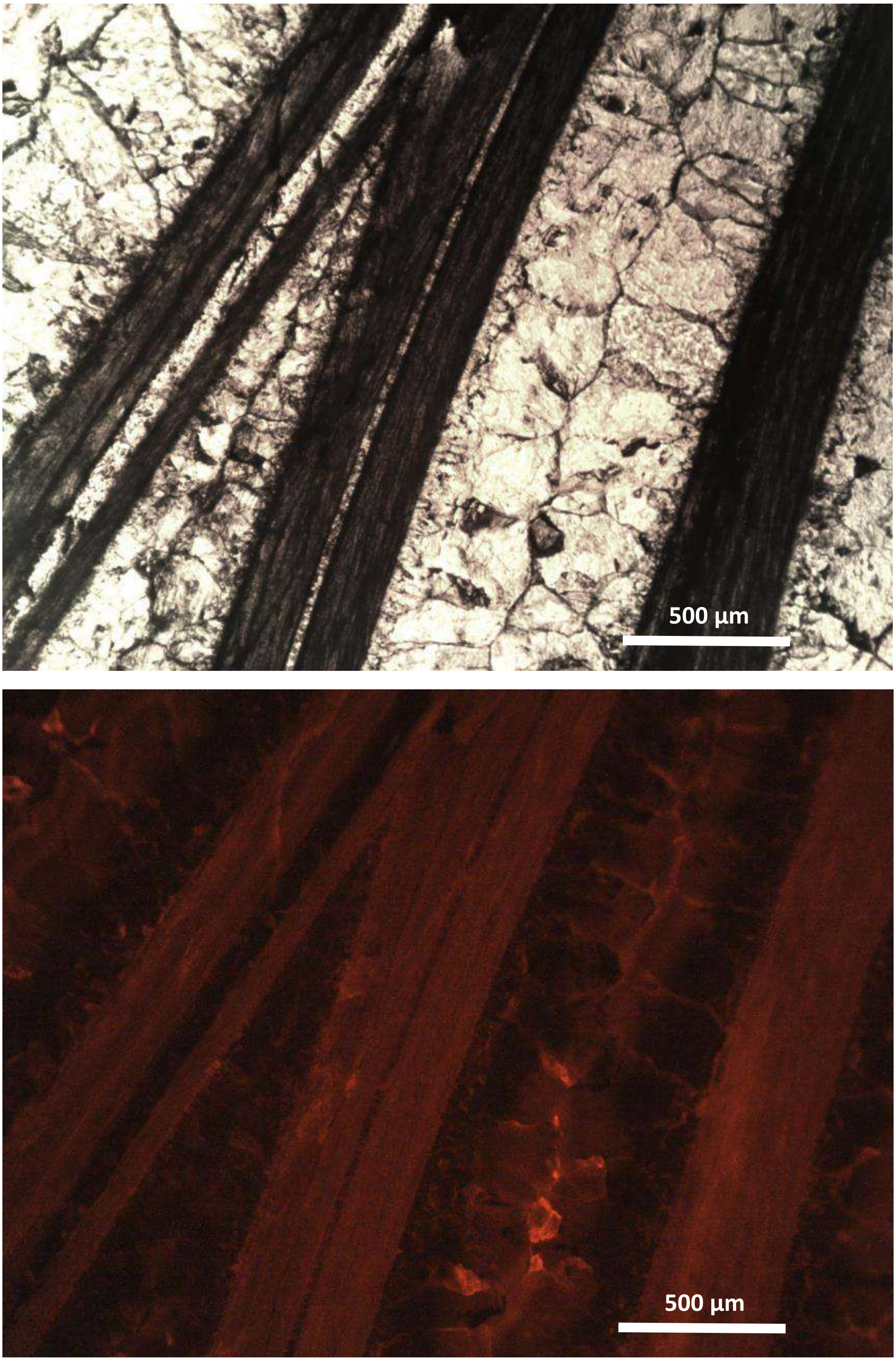

Figure 15.7. Optical and cathodoluminescent image of YA-SOT oyster showing sparry calcite layers.

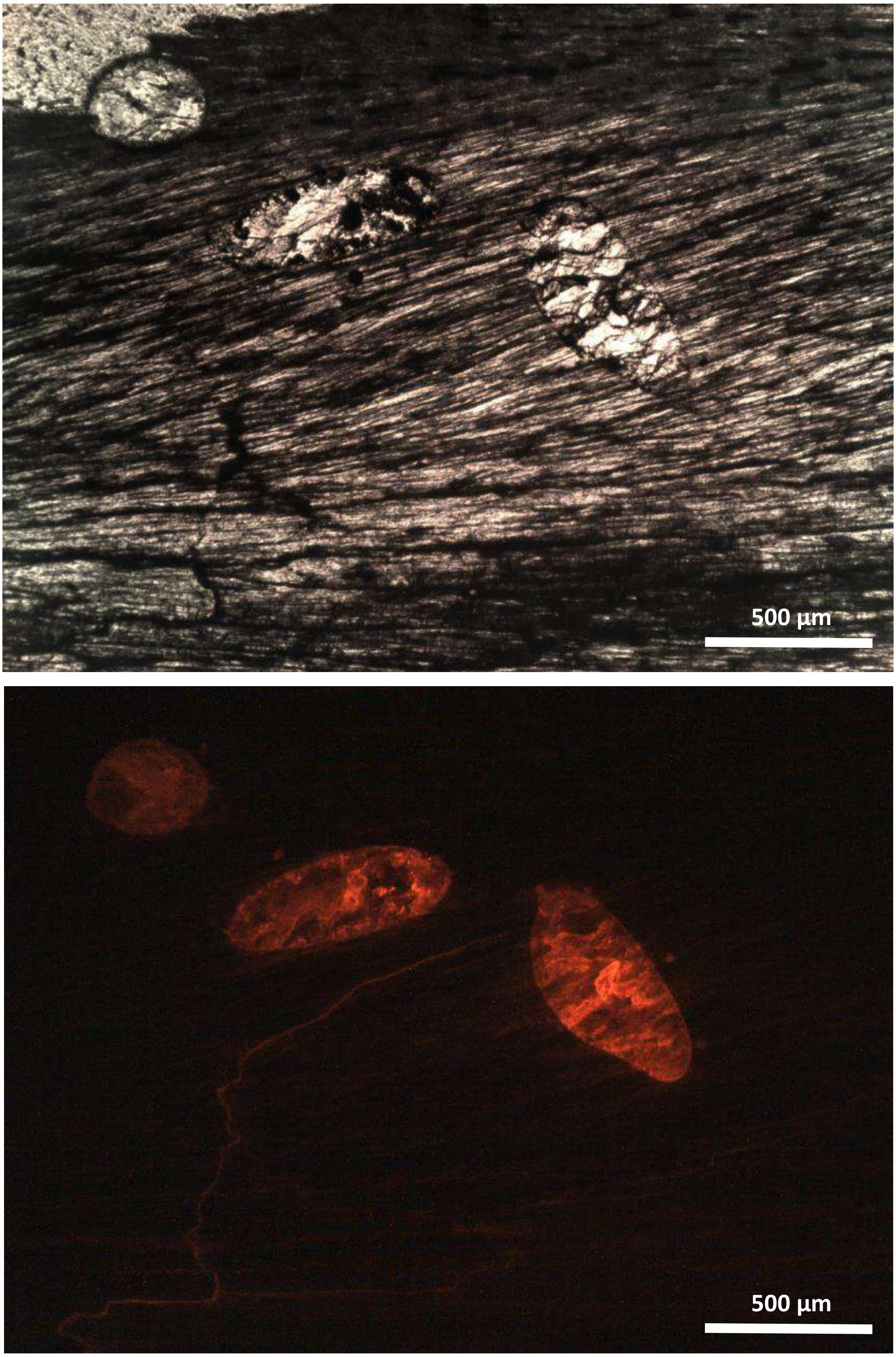

Figure 15.8. Optical and cathodoluminescent image of a UL-D4 oyster showing microborings filled by diagenetic calcite.

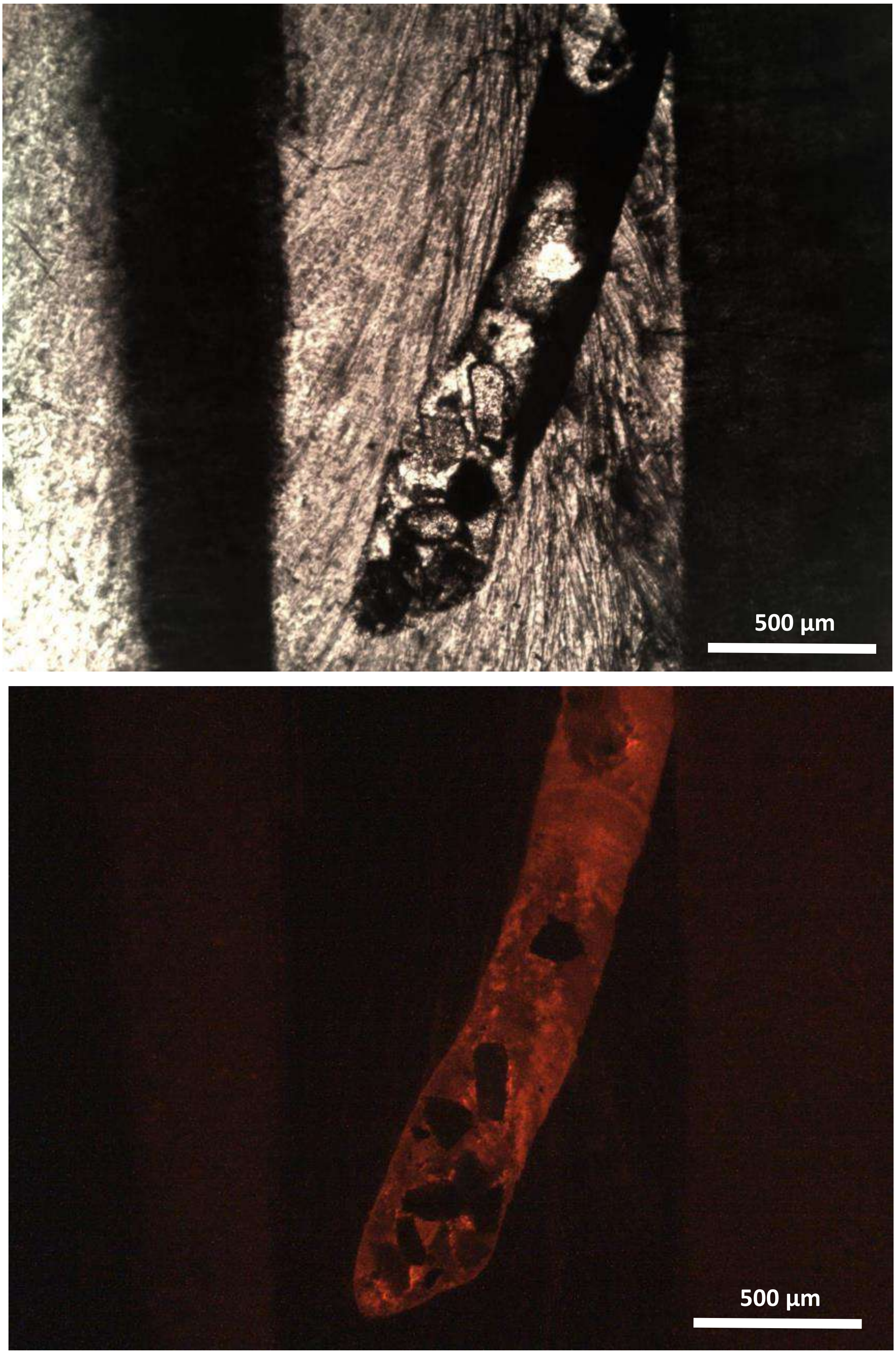

Figure 15.9. Optical and cathodoluminescent image of the UL-D18 altered oyster showing microborings filled by terrigenous minerals and a diagenetic cement.

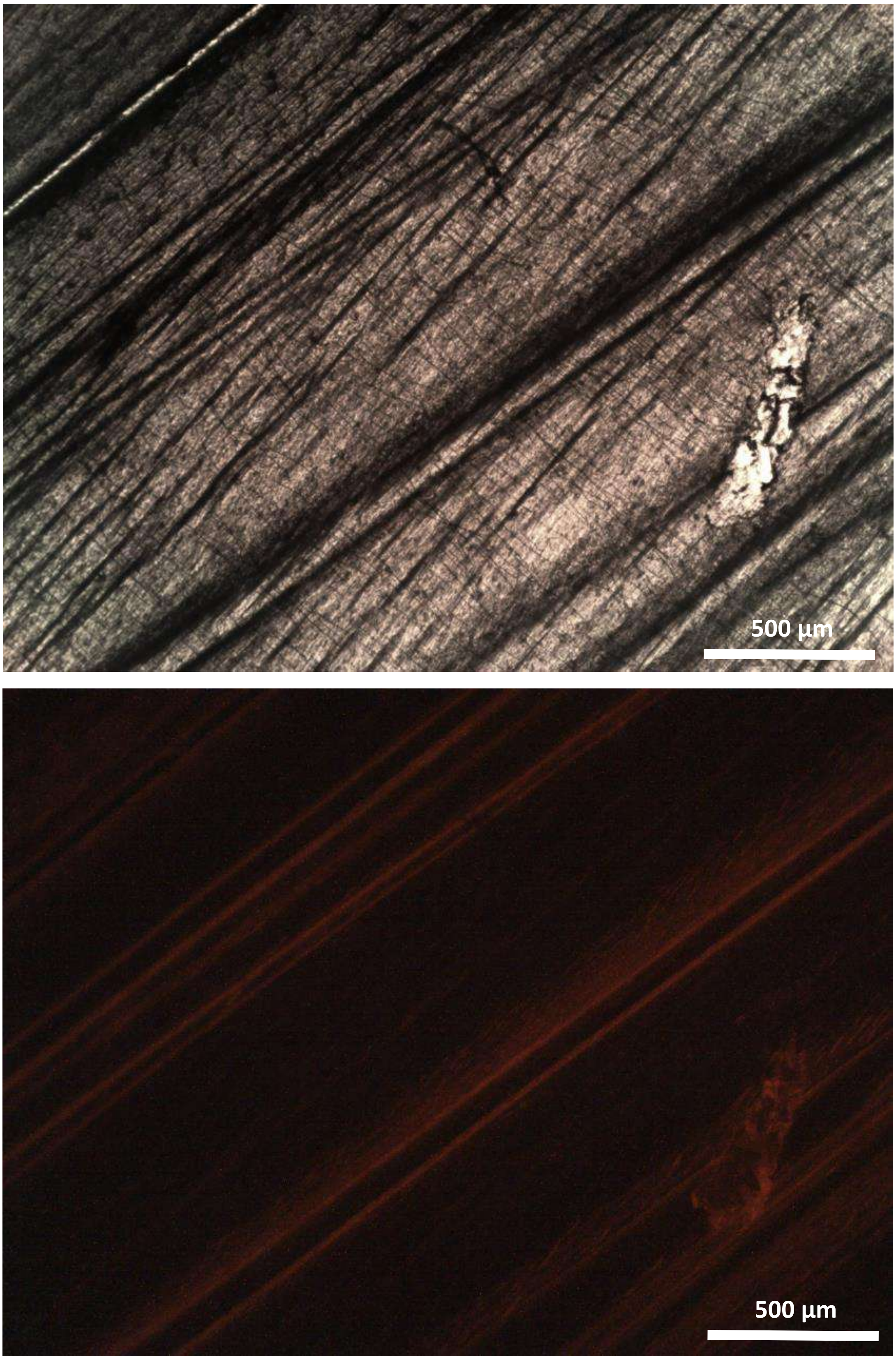

Figure 15.10. Optical and cathodoluminescent image of PN-OST oyster showing a low cathodoluminescence with thin layers with higher luminescent.

15.2. P1 and P2 mollusk taphonomy

P1 and P2 allomembers show mollusk-rich layers characterized by low biodiversity and high dominance (DeVries 1988). Mollusks are commonly preserved only as gypsum casts or dolomite/gypsum internal molds. Pristine mollusk shells are rare and pure Ca-carbonates are only occasionally observed, especially in the P0 allomember. In very few cases, bivalves are observed associated to fossil vertebrates, but they seem not to be typical of the Miocene whale-fall communities (Smith et al. 2015).

The P1 allomember is characterized by a relatively abundant and varied mollusk assemblage, especially at its base, where all the specimens are internal molds composed of dolomite. At the base, which crops out at Cerros Cadenas de los Zanjones, bivalves belong to the genera *Dosinia* (*D.* cf. *ponderosa*), *Hybolophus*, *Miltha* and *Trachycardium*. At Cerro Sombrero, the most common bivalves are *Chionopsis* sp.; at the same level, tonnoid gastropods also occur. A particular assemblage has been found southeast of Cerro Colorado: at one level, a few meters above the base of the P1 allomember, large dolomite molds occur, as the bivalve genera *Panopea* and *Trachycardium*, along with specimens of different sizes of *Dosinia* cf. *ponderosa*, and fossil molds of barnacles. At Cerro Colorado, many dolomite molds and gypsum-replaced shells of *Anadara sechurana* and *Dosinia* sp. have been found at the same level of a kentriodontid-like delphinidan fossil, where strata of the P1 allomember crop out. At Cerro los Quesos, immediately to the west of the present study area, a level characterized by dolomitic internal molds of *Hybolophus* sp. is present. Near Cerros Cadenas de los Zanjones, the mollusk assemblage is composed of many dolomitic molds of *Dosinia* cf. *ponderosa*; *Miltha* sp. and *Hybolophus* sp.; gastropods of the superfamily Tonnoidea and the turritellid *Incatella hupei*. Finally, near Cerro La Bruja the mollusk assemblage includes *Hybolophus* sp., *Turritella varicosta*, *Trachycardium* sp., *Anadara sechurana* and *Dosinia* sp. with specimens differing from *D. ponderosa* for size, shape and ornamentation of the shell.

The mollusk assemblage found in a P1 level (Fig. 15.11 and Fig. 15.12) southeast of Cerro Colorado tells an interesting taphonomic history. Specimens of the infaunal *Panopea*, reaching more than one meter in depth under the seafloor, co-existed with specimens of *Trachycardium, Anadara* and *Dosinia* cf. *ponderosa*, which live at lower depth in the sediment. As shown in Figure 15.13, the specimens of *Panopea* are dolomite molds with casts of the muscles and the pallial line, articulated, with evident traces of worms and barnacles that lived on the inner part of the shell (Fig. 15.14).

Figure 15.11. Bivalve accumulation level southeast of Cerro Colorado.

Figure 15.12. Detail of the accumulation level with *Panopea* and *Trachycardium*.

Figure 15.13. *Panopea* specimen found in the accumulation level in P1 sediments.

Figure 15.14. Detail of barnacle molds and casts on the internal mold of a *Panopea* specimen.

We found all the bivalve species together, as an accumulation level, without maintaining the life position but preserving the articulation. We hypothesizes that a storm event or strong currents have brought the *Panopea* specimens at the surface, with the other species, but without entirely exhuming them. Most of the specimens, indeed, are completely articulated, so they have been filled by the sediment without being subject to strong currents at the seafloor. After the death of the *Panopea* individuals, the inner part of the shell was colonized by different organisms, representing a hard substrate and a place shielded from the high hydrodynamism. After this colonization, the shell was completely filled by the sediment, and dolomite precipitated, probably because of the high concentration of organic matter (Gariboldi et al. 2015) within a narrow place. After the dolomite precipitation, secondary circulation of fluids caused the dissolution of the calcite shell, leaving only the molds of these organisms.

The macro-invertebrate content of P2 is characterized by the disappearance of *Anadara sechurana* and *Miltha* sp. In the study area, at the base of this allomember, mollusks occur as dolomite internal molds of the bivalves *Dosinia ponderosa* and *Hybolophus* sp., and dolomite molds with gypsum replaced shells of *Incatella hupei*. Above this base, at an unnamed cerro (called here Cerro Innominado) in the north-northwest of Cerros la Mama y la Hija, a level yielded abundant specimens of *Hybolophus* sp. replaced by gypsum and, in some cases, filled by a dolomitized sediment, with well-preserved hinge and ornamentation; these remains probably belong to the species *H. maleficae* or *H. nelsoni* described by DeVries (2016). At Cerro los Quesos, a particular concentration of gypsum-replaced mollusks is present in the upper part of the stratigraphic succession (Member F of Di Celma et al. 2016). The mollusks belong to the genus *Hybolophus* and regularly occur adjacent to the vertebrate fossils. At Cerro la Bruja few specimens of *Dosinia* sp. also occur as internal molds. Finally, at Cerro Blanco the P2 allomember shows the presence of barnacle plates and dolomite internal molds of mussels (*Mytilidae*), the latter never found in the previously described allomembers nor at other localities where the Pisco Formation crops out.

The process of mollusk fossilization in the P2 allomember is very dissimilar to that of the Chilcatay Formation and the P0 allomember. Mollusks are usually preserved as internal molds, or recrystallized shells. At the macroscale, we can observe that the original shell of mollusks has disappeared and Ca-carbonates are absent or occasionally present. The mineralogical phases are generally represented by dolomite and gypsum. Manganese frequently cemented sediments in the proximity of the bivalves. In a particular level, found at the base of P2 near Cerro la Mama y la Hija, some gypsum replaced bivalves of the genus *Hybolophus* showing a very particular geopetal structure (Fig. 15.15).

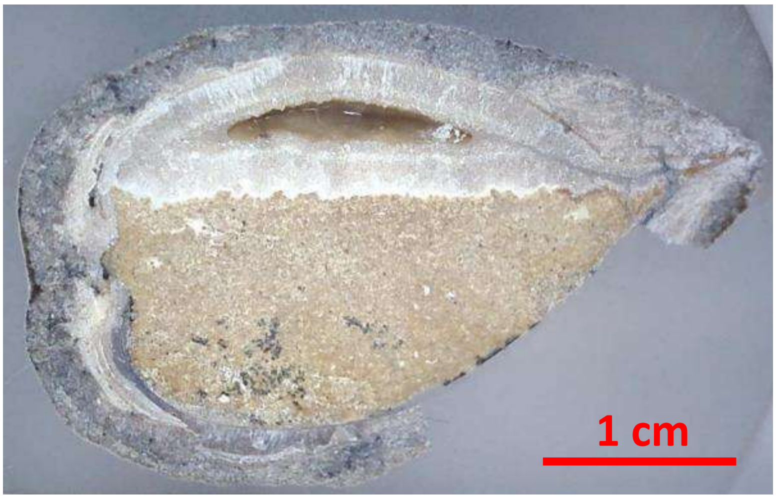

Figure 15.15. Inner core of a *Hybolophus* specimen showing a geopetal structure with different mineralogical phases.

The sketch of this structure is shown in Figure 15.16, where all the identified mineralogical phases are specified.

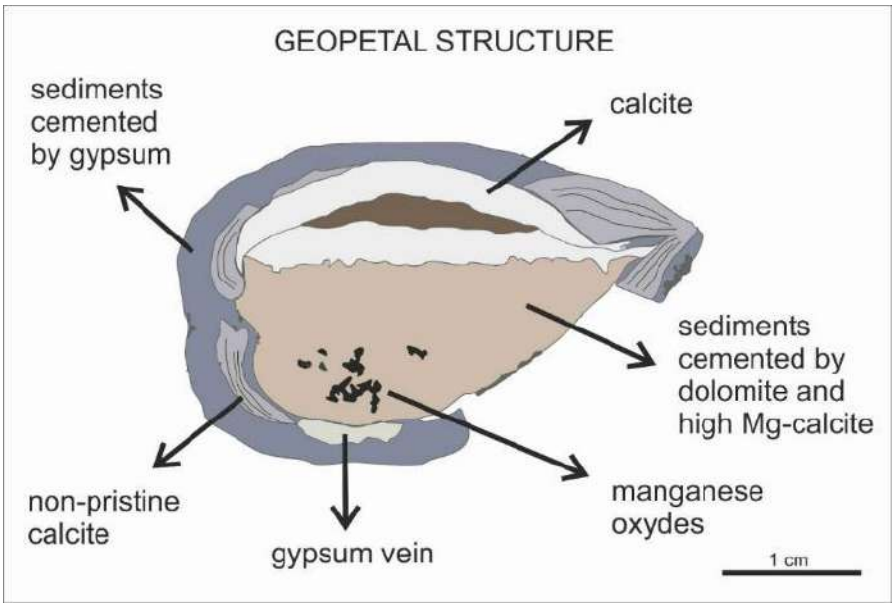

Figure 15.16. Sketch of the geopetal structure of Figure 15.15.

Optical microscopy, SEM-EDS and Raman analyses reveal that bivalves were first buried and filled by sediments, later cemented by Ca-carbonates; Mn-oxides precipitated cementing adjacent zones (Fig. 15.17); then different generations of calcite precipitated in the cavity, completing the geopetal structure (Fig. 15.18); at that point, the shell was being dissolved and a new calcite re-precipitated, replacing the pristine one; finally, two generations of gypsum have been observed, as a cast of the bivalve and as late veins.

Furthermore, cathodoluminescence analyses were performed on a particular specimen, in order to distinguish the different cement generations, helping understand the complex diagenetic history of these mollusks. Cathodoluminescence, indeed, confirm that the calcite is interested by diagenetic processes also in cases where the pristine structure of the shell seems to be preserved under the optical microscope. The lamellar structure is completely replaced by sparry calcite and shows a very high luminescence (Fig. 15.19). Furthermore, we can easily distinguish almost three different generations of calcite precipitating in the cavity of the geopetal structure, which show different luminescent response (Fig. 15.20).

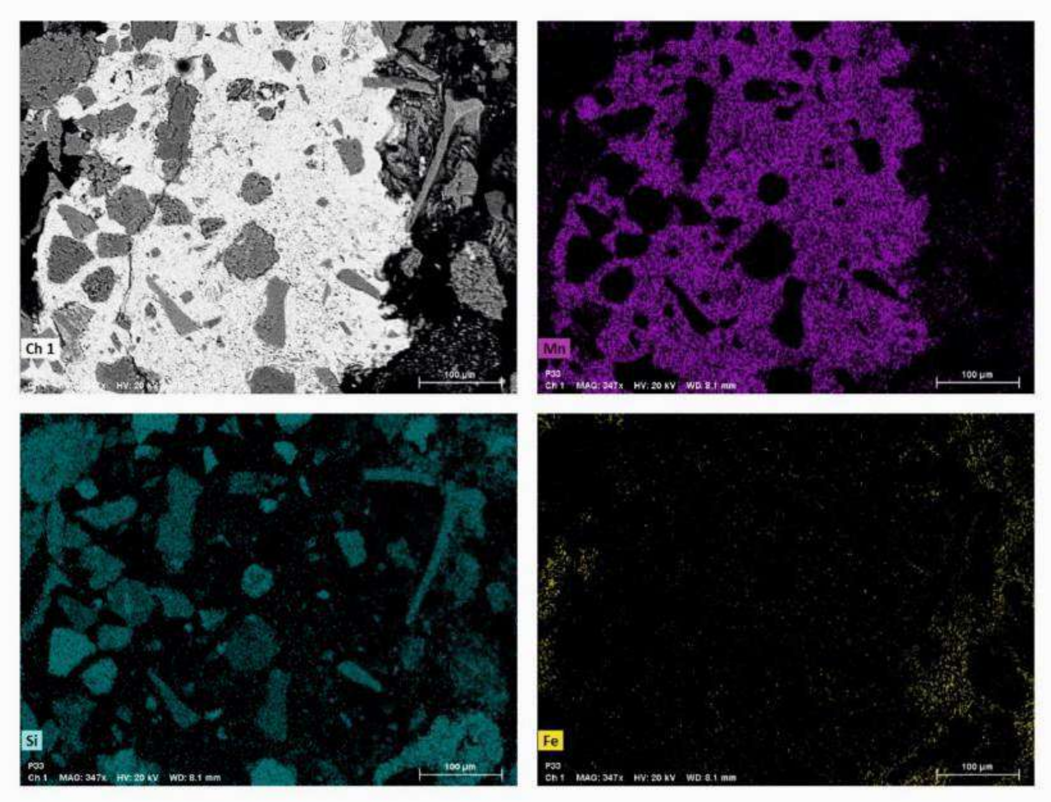

Figure 15.17. Elemental compositional maps realized with SEM-EDS showing manganese cementing sediments adjacent to bivalves.

Figure 15.18. BSE image of the geopetal structure showing different calcite generations filling the empty space.

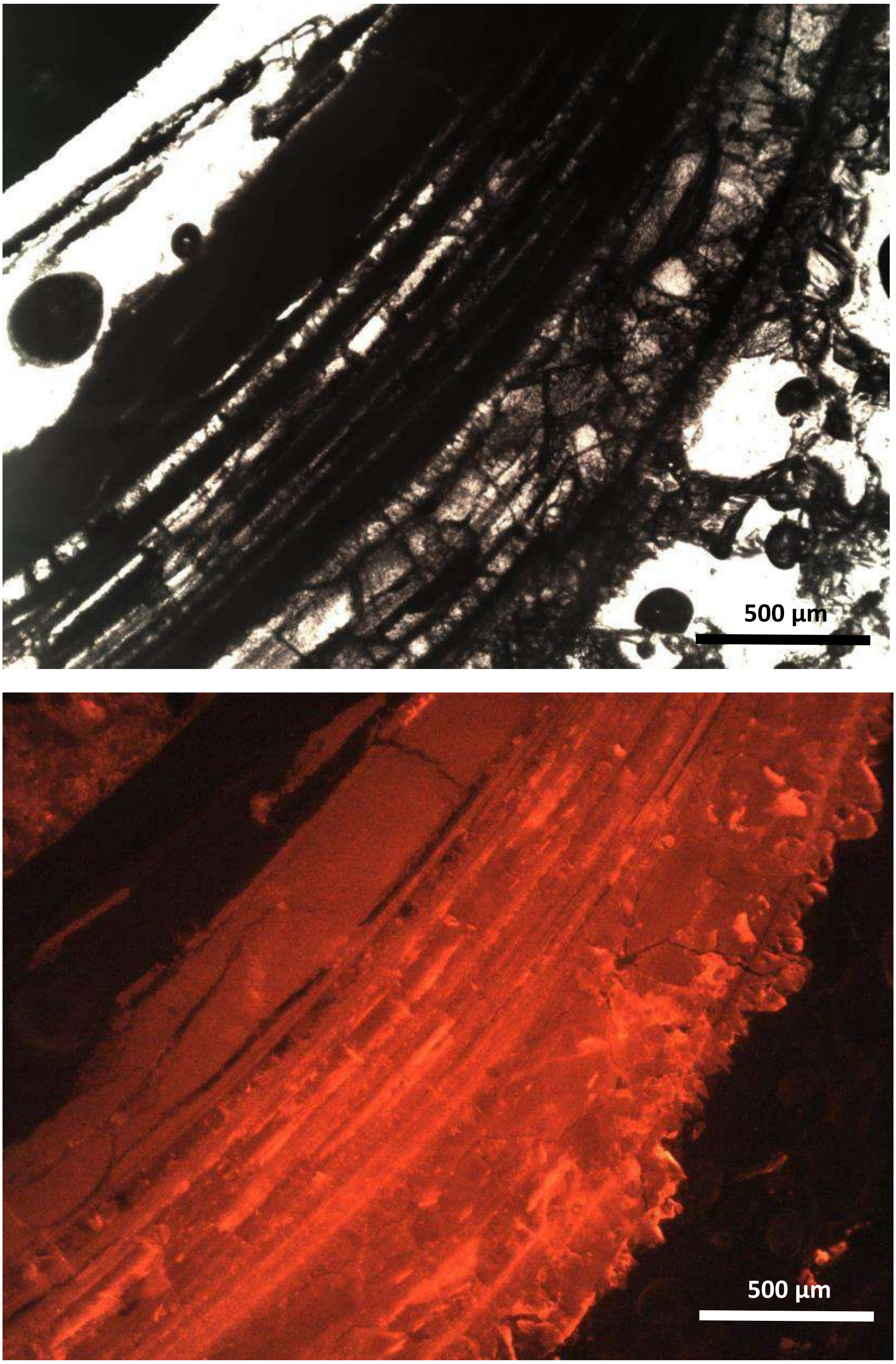

Figure 15.19. Optical and cathodoluminescent image of the lamellar portion of the *Hybolophus* shell.

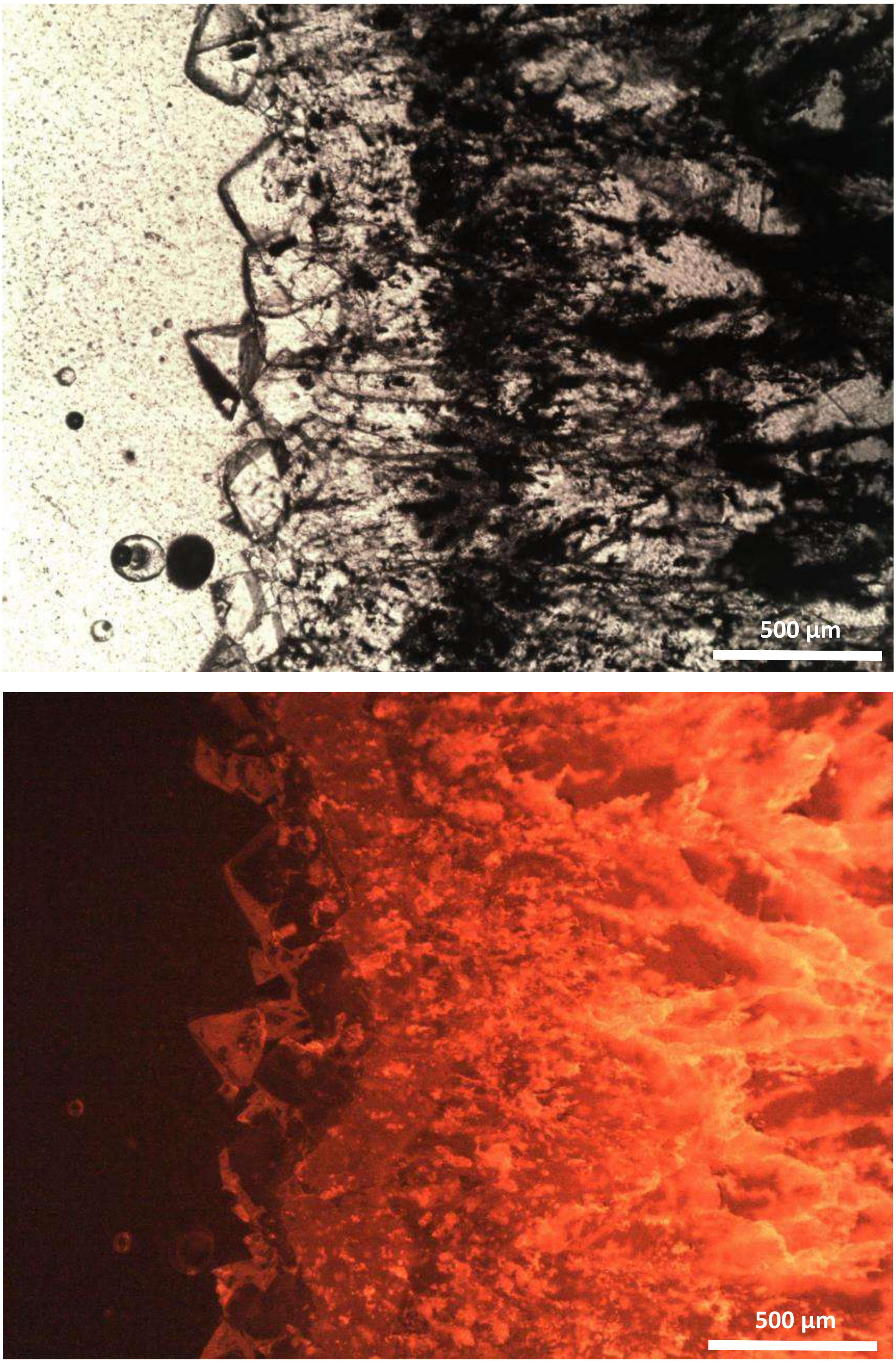

Figure 15.20. Optical and cathodoluminescent image of the calcite filling. Detail of different calcite cement generations.

Therefore, the pristine Ca-carbonate shell of *Hybolophus* specimens is not preserved, but is completely dissolved or recrystallized. The paleoenvironment of the youngest Pisco Formation do not allow the preservation of the shells, proving that the diagenesis greatly conditioned the type of fossilization of these mollusks.

A peculiar mollusk concentration is noticed also in the upper part of the succession, in correspondence of a few meters thick interval within the fossil-rich portion of member F (Di Celma et al. 2016), typically occurring as heaps near five partial skeletons of cetaceans (Fig. 15.21). None of these specimens is attributable to any genus that usually characterizes the whale-fall communities (Smith et al. 2015). Instead, all the identified specimens belong to the genus *Hybolophus*, a semi-infaunal suspension feeder; they have been identified by means of comparison with the morphology of some better preserved specimens from the Pisco Formation.

Figure 15.21. *Hybolophus* specimens in life position, associated to cetacean bones.

At Cerro los Quesos, O7, M50, C46, and C47 (see Table 1) are the sole vertebrate specimens that display associated mollusk bivalves. Indeed, mollusks (and, more in general, invertebrate remains) strictly associated to fossil vertebrates are rare in the Pisco Formation. The bivalves collected are not very well preserved and do not maintain their pristine shell, making hard their identification. Comparing some of these bivalves to other specimens from the Pisco Formation in different localities, we observed some similarities that allow us to identify some individuals as belonging to the genus *Hybolophus*. Hand samples of some of the mollusks are shown in Figure 15.22.

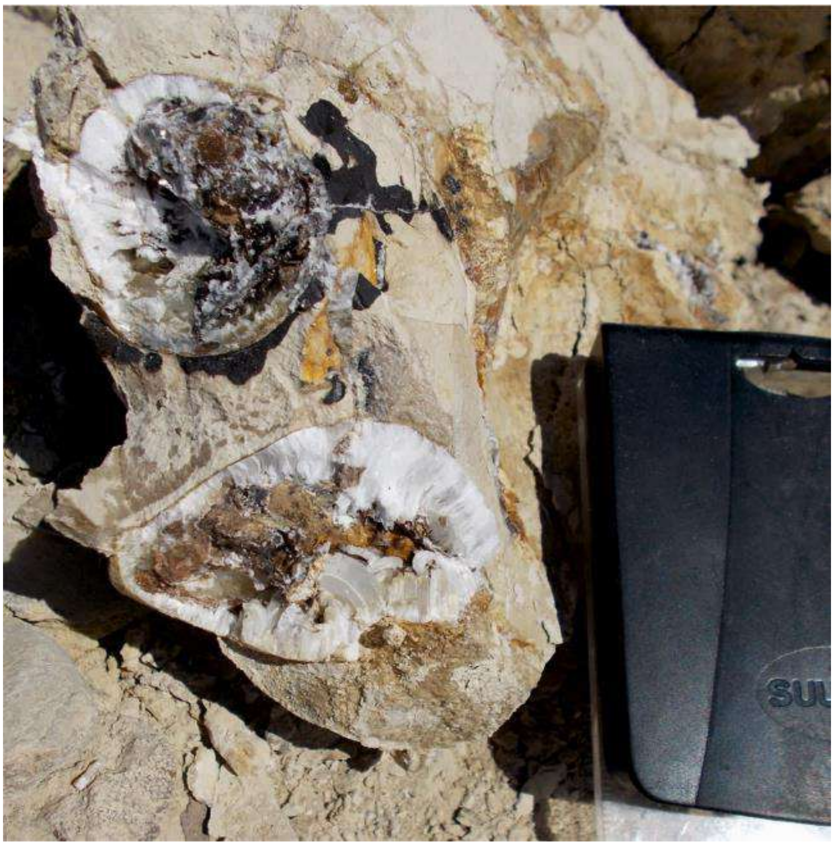

Figure 15.22. *Hybolophus* specimens filled by gypsum and surrounded by manganese.

Identification of the diagenetic minerals by XRPD is reported in Table 15.2. The bivalve specimen GB38, found near the vertebrae of O7, is preserved as one single valve replaced by microcrystalline gypsum and partially filled by lithified sediment (Fig. 15.23a; Tables 15.1 and 15.2). Other two specimens found associated to this fossil vertebrate show a preserved hinge that allows us to identify these specimens as *Hybolophus* sp.

Fossil specimen[(1)]	Geographical coordinates	Systematic determination	Short description and field taphonomic features	Host sediment	Field evidence of early diagenetic processes[(2)]	Sample	Sample short description	Reference to figures
O7	14° 31′ 30.4″ S 75° 42′ 56.6″ W	Phocoenidae indet.	Disarticulated but associated skeleton of an immature (unfused epiphyses of vertebrae) phocoenid consisting of a fragment of skull (rostrum), several vertebrae and rib fragments; incompleteness and breakings partially due to recent erosion.	diatomaceous mudstone	no external concretion; no Fe–Mn-rich boundary	O7-GY	vein of fibrous gypsum, 1 cm thick	Fig. 3A, E
						GB38A	gypsum-replaced bivalve shell, outer part	
						GB38B	gypsum-replaced bivalve shell, interior part	
M50	14°31′29.4″ S 75°42′55.4″ W	Misticeti indet.	Skull and articulated mandibles upside down of a relatively small balaenopterid (bizygomatic width: 1.5 m: estimated body length: ca 13 m): specimen partially destroyed by recent erosion.	diatomaceous mudstone	dolomite concretion filling cranium, with Fe–Mn concentrations; no external concretion; no Fe–Mn-rich boundary	GB47	gypsum-replaced bivalve shell	Fig. 2A and B
C46	14° 31′ 19.2″ S 75° 43′ 00.6″ W	Cetacea indet.	Several disarticulated but associated lumbar and caudal vertebrae of an immature (unfused epiphyses) small size cetacean.	lithified diatomaceous mudstone	no external concretion, but hard sediment; minor dolomite within bone porosity and as interior mold of bivalves; traces of a Fe–Mn-rich boundary	GY3	vein of fibrous gypsum, 1.5 cm thick	Fig. 2C, D, E, F; 3B, C; 4C
						GB30	dolomite inner mold of a gypsum-replaced bivalve	
						GB35	bivalve replaced and filled by fibrous gypsum, shell outer part	
						GB36	bivalve replaced and filled by fibrous gypsum, interior	
C47	14° 31′ 29.9″ S 75° 42′ 56.1″ W	Cetacea indet.	Several disarticulated but associated vertebrae and ribs of an adult (fused epiphyses) small size cetacean; one tooth belonging to a juvenile *Cosmopolitodus hastalis* shark was found near the ribs.	diatomaceous mudstone; volcanic ash just below the specimen	no external concretion; traces of a Fe–Mn-rich boundary	C47-GY	vein of fibrous gypsum, 0.5–1 cm thick	Fig. 2G and H, 4A, 4B
						GB45A	bivalve filled by fibrous gypsum, outer part	
						GB45B	bivalve filled by fibrous gypsum, interior	

(1) see Bianucci et al. (2016a); (2) we considered field evidence of early diagenetic processes, related to the decay of the whale organic matter, the presence of dolomite concretions and of concentrations of iron and manganese (= redox-dependent elements).

Table 15.1. Fossil vertebrates list and the mollusk and vein samples in correspondence of each of them. Figs. referred to Gioncada et al. (2018).

The specimen GB47 is a replaced single shell found near the specimen M50 (Table 15.1). The original Ca carbonate has been replaced by anhydrite and gypsum (Table 15.2). This bivalve is the only one found near the skull of M50 and is not enough well preserved to be identified. The mollusks found near the vertebrae of the cetacean specimen C46 are in life-position (Fig. 15.21, Table 15.1). This supports that the bivalves lived near the cetacean bones rather than the bone mollusk association was due to post-mortem transport. Possibly, the partial cementation of the diatomaceous sediment hosting the remains preserved the infaunal bivalves in their original vertical position.

Fossil specimen	*sample*	*description*	*diagenetic/vein minerals*	*detrital minerals*
O7	C07-GY	*vein*	gypsum, anhydrite	
	GB38A	*shell*	gypsum, traces of anhydrite	quartz
	GB38B	*inner mold*	gypsum, anhydrite	
M50	GB47	*shell*	gypsum, anhydrite	quartz
C46	GY3	*vein*	gypsum, anhydrite	quartz
	GB30	*inner mold*	dolomite	
	GB35	*shell*	gypsum, minor anhydrite	
	GB36	*inner mold*	gypsum, traces of anhydrite	traces of quartz
C47	C47-GY	*vein*	gypsum, anhydrite	quartz
	GB45A	*shell*	gypsum	
	GB45B	*inner mold*	gypsum	

Table 15.2. XRPD results of the analyses of the post-burial minerals collected in correspondence of the selected vertebrates.

Some of the mollusks associated with C46 are preserved as a perfect carbonate internal mold consisting of a dolomite nodule (Table 15.2). All the well preserved specimens found near this cetacean remains show similarities in morphology with those of the genus *Hybolophus*. The dolomite mold of GB30 shows the scars of two equal adductor muscles and an intact pallial line, and is partially surrounded by microcrystalline gypsum, probably remnant of the gypsum-replaced shell. Most shells, instead, are apparently entirely replaced and filled by gypsum (e.g. GB35, GB36), showing a slight ornamentation with concentric ribs. XRPD data indicate that gypsum is often accompanied by anhydrite (Table 15.2). When sectioned, these specimens reveal a core consisting of a dolomite nodule of variable size, with the remaining space filled almost completely by fibrous crystals of gypsum growing inward from the original valves (Fig. 15.23c). The fibers bend where touching the internal nodule (Fig. 15.23c). The dolomite internal nodules are yellowish to dark brown in color, and dark brown to black is also the color of the lithified host sediment just outside several mollusks (Fig. 15.23c, d). SEM-EDS inspections reveal that the dolomite nodules consist mainly of dolomite, as indicated by XRPD data (Table 15.2), containing scattered biogenic and terrigenous clasts with cavities completely cemented by finely crystallized dolomite; the blackened portions correspond to concentrations of manganese, probably present as a fine cementing oxydroxide phase together with dolomite. Several mollusk bivalves are associated to the fossil vertebrae and ribs of the cetacean specimen C47 and are mostly entirely replaced and/or filled by gypsum. Among these, the shell GB45 has been sampled for analysis and consists entirely of gypsum (Tables 15.1 and 15.2). The external part of the shell of this mollusk shows concentric, poorly preserved ribs.

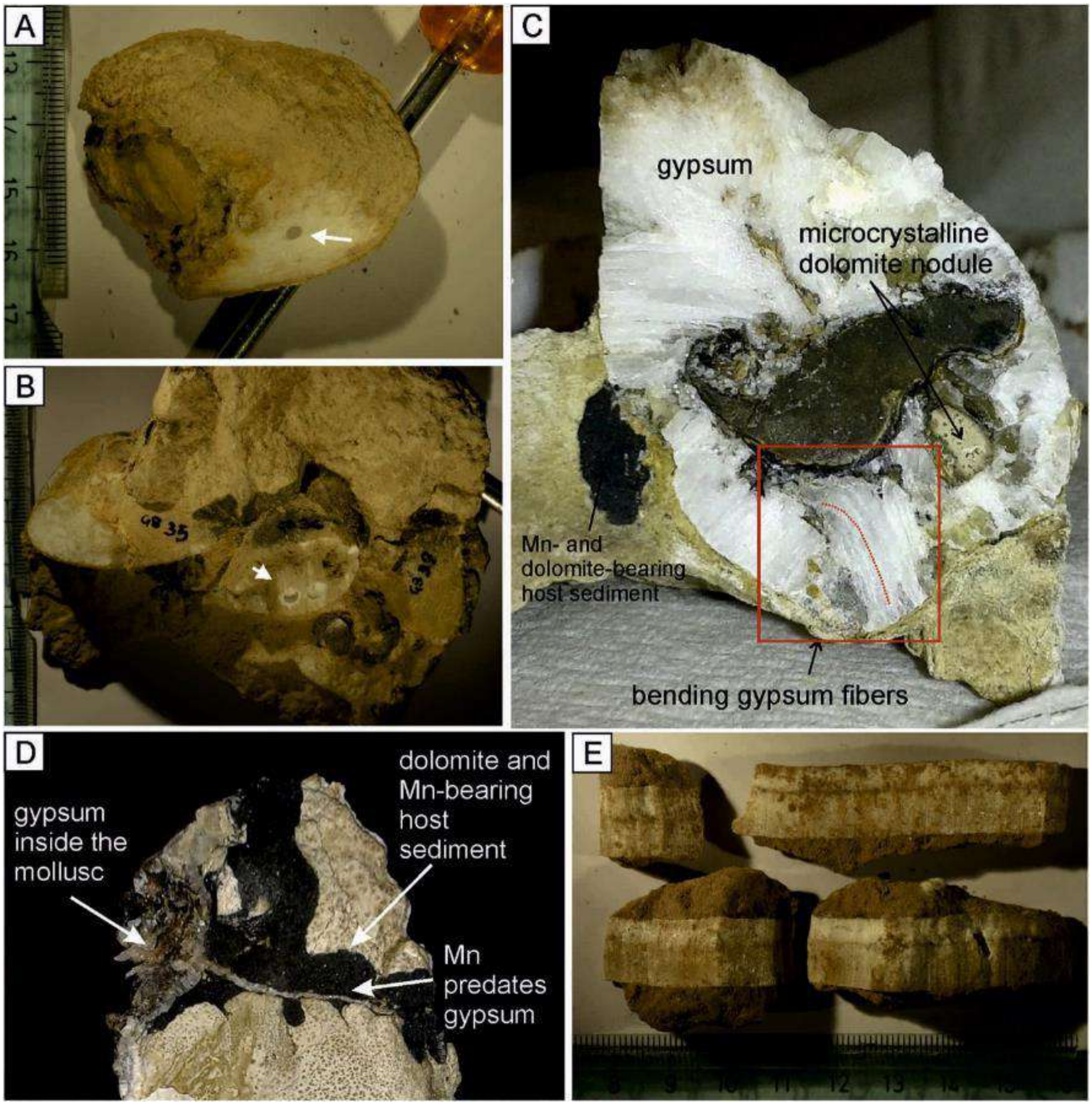

Figure 15.23. a) Mollusk valve GB38 (associated with the cetacean specimen O7) with microdrilling hole (arrow); the internal cavity of the bivalve is filled by lithified sediment. b) Mollusks GB35 and GB36 (associated with the cetacean specimen C46). c) Mollusk specimen GB35 (associated with the cetacean specimen C46) after sectioning,

showing the complex internal filling structure and the external Mn concentrations; the dotted line highlights the fibers of gypsum bending where touching the pre-existing nodule. d) Manganese concentrations out of a mollusk specimen cut by a gypsum veinlet. e) Example of gypsum veins.

Dolomite formed small nodules inside the internal cavities of the articulate bivalves. The microcrystalline texture of dolomite, together with its occurrence in nearly closed, protected environments, having abundant decaying organic matter and scarce exchange with the surrounding seawater (the still articulated and closed shells of bivalves), strongly suggest that dolomite formed with a localized process analogous to that forming carbonate concretions enclosing fossil specimens. The latter process has been described as linked to anaerobic organic matter decay through bacterial sulfate reduction, providing the alkalinity for carbonate precipitation (Berner 1981; Gariboldi et al. 2015; McCoy et al. 2015; Yoshida et al. 2015). In particular, for dolomite concretions, biomediated sulfate reduction has been proposed to counteract the inhibiting effect of sulfate on dolomite primary precipitation in a marine environment (Baker & Kastner 1981).

Since, in some cases, the dolomite concretion has completely filled the internal cavity of the articulated shells of the bivalves, forming an internal mold replicating the internal features, it is possible to assume that the calcium carbonate shell was still present when dolomite formed. However, no or negligible calcium carbonate is currently present in the studied samples, where biogenic calcite is replaced by gypsum. The above depicted processes allow to suggest a possible explanation for calcite dissolution. In fact, the resuming oxygenated conditions around and within bivalves (after the organic matter decay), besides causing the precipitation of Mn, caused the oxidation of the previously formed iron sulfides, or of the sulfide produced by sulfate reduction, leading to a reduction of pH (Coleman et al. 1985). The resulting local acidification can be proposed as a cause for the dissolution of the calcium carbonate shells, similarly to what has been proposed in other carbonate-bearing sedimentary environments (Lin et al. 2016; Pirlet et al. 2010). The same authors suggest that the resulting elevated Ca concentration in porewater and the availability of sulfate can also play a role in the formation of authigenic gypsum; however, in our case, this mostly disagrees with the Sr isotopic composition of gypsum (see below). Moreover, although it cannot be excluded that part of the gypsum forming the mollusks was early diagenetic (in some cases, more than one phase of gypsum is suggested by inspection of texture within replaced mollusks), a formation of gypsum extended to late diagenesis at CLQ is indicated by the abundant veins and cavities filled by gypsum with fibrous texture, which would not be explained by the above process alone.

The minerals replacing and filling the bivalves have been analyzed through $^{87}Sr/^{86}Sr$ method, in order to understand the chronologic order of each diagenetic process. The $^{87}Sr/^{86}Sr$ ratio measured on mollusks and veins is reported in Table 15.3. As regards the mollusks, the dolomite inner mold (mollusk GB30) has $^{87}Sr/^{86}Sr$ ratio of 0.70899; for the gypsum replacing and filling mollusks, the Sr isotopic ratio ranges between 0.70858 and 0.70906, and no systematic differences are observed between external and internal parts and/or among the different fossil specimens. Gypsum from veins is in the range 0.70864-0.71111, the most radiogenic values being measured in the O7-GY sample. Despite the limited number of data, the $^{87}Sr/^{86}Sr$ data in mollusks and veins in Table 3, clustering at 0.708925-0.709060 and at 0.708587-0.708766, clearly suggest the contribution of Sr from mainly two isotopically distinct sources (Fig. 15.24), besides additional isotopic heterogeneities.

Fossil specimen	*Sample*	$^{87}Sr/^{86}Sr$	*abs. error*[a]
O7	O7-GY	0.711110	0.000008
	GB38A	0.708582	0.000007
	GB38B	0.708650	0.000008
M50	GB47	0.708645	0.000009
C46	GY3	0.708644	0.000009
	GB30	0.708992	0.000008
	GB35	0.708925	0.000007
	GB36	0.708587	0.000009
C47	C47-GY	0.708766	0.000007
	GB45A	0.708714	0.000009
	GB45B	0.709060	0.000009

[a] In-run statistics at 2-s confidence level.

Table 15.3. Sr isotope composition of the post-burial minerals collected in correspondence of the selected vertebrates.

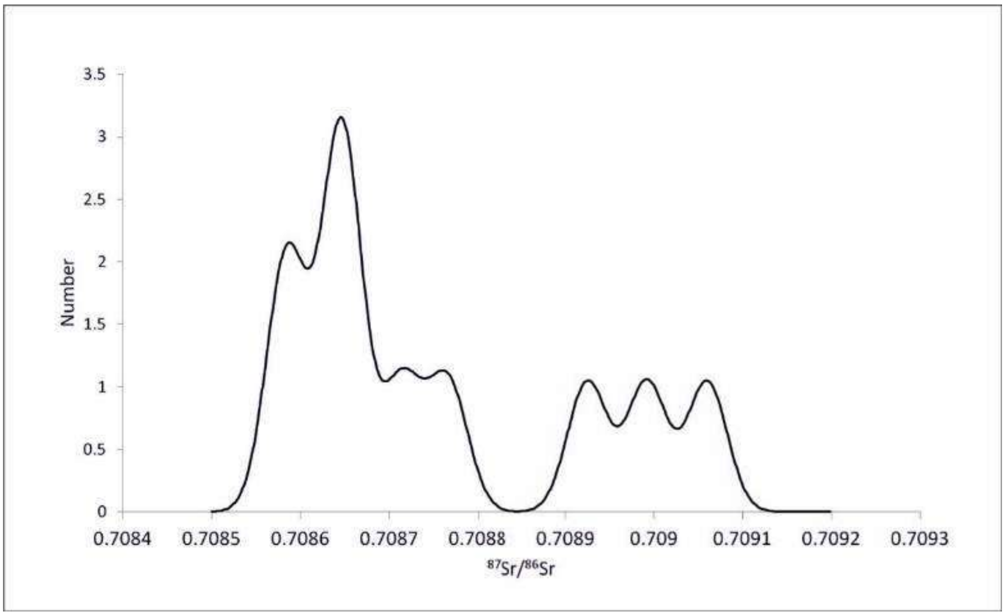

Figure 15.24. $^{87}Sr/^{86}Sr$ distribution plot of mollusks and veins showing a bimodal distribution.

In the studied mollusk samples, the original carbonate shell is not preserved and has been replaced by gypsum; the inner mold is made of dolomite. Following the Sr-isotope chronostratigraphy (McArthur et al. 2001), the $^{87}Sr/^{86}Sr$ ratio measured in the dolomite filling of the GB30 specimen (C46 fossil whale) yields a numerical age of 6.2 ± 0.4 Ma. Such date is consistent with the absolute radiometric age of 6.93 ± 0.09 and ≥ 6.71 ± 0.02 Ma obtained by ^{39}Ar–^{40}Ar analyses (Chapter 10) on biotite from tephra layers about 10 m below and 40 m above, respectively. This overall correspondence is in agreement with a formation of dolomite as an early seawater precipitate during the Messinian, favored by the local increase of porewater alkalinity due to organic matter oxidation and sulfate reduction (Bontognali et al. 2014; Vasconcelos et al. 1995), confirming the hypothesis of Gariboldi et al. (2015) of early dolomite precipitation for the formation of the nodules wrapping fossil marine vertebrates in the Pisco Formation. With similar mechanisms, the occurrence of dolomite layers in sediments from the Peru Margin has been related to the conditions established at shallow depth below the seafloor during early diagenesis, at the sulfate reduction-methanogenesis boundary in the sedimentary column (Meister et al. 2007). The $^{87}Sr/^{86}Sr$ ratio of gypsum from mollusks deviates from the isotopic value of dolomite, towards a lower isotopic composition (with the exception of sample GB45B which is slightly higher), in some cases overlapping with the $^{87}Sr/^{86}Sr$ ratio measured in gypsum veins. A possible explanation is that the $^{87}Sr/^{86}Sr$ ratio of gypsum reflects a pre-Miocene seawater-derived brine as a source for Sr, characterized by a lower $^{87}Sr/^{86}Sr$ ratio, entrapped in the sediment pores of the shelf sites for a long time (Kastner et al. 1990; Meister et al. 2007). The migration of these brines and their interaction with the sediments, possibly modifying their isotopic composition, is able to explain the variability of the gypsum Sr-isotope data and is in agreement with the observation that gypsum formation post-dates of an undetermined interval of time the early diagenetic minerals (dolomite, Mn minerals). A role for old evaporitic layers in providing a saline fluid component to these brines cannot be excluded. Despite the common occurrence of gypsum-filled faults and fractures (Rustichelli et al. 2016), no evaporitic successions or layers of primary gypsum have been observed along the sedimentary sections exposed at Cerro los Quesos (Di Celma et al. 2016); however, in the Pisco Formation, evaporites have been reported by Marocco and Muizon (1988), indicating that local evaporitic basins formed during sedimentation of the Pisco Formation. We suggest weathering in the hot and arid desert climate as a cause for the presence of anhydrite in the outcropping veins of the Pisco Formation. Alternatively, we propose that the circulation of high-salinity brines in the subsoil could have favored the partial dissolution of gypsum and precipitation of anhydrite, prior to exhumation. Anhydrite could have survived without rehydrating to gypsum due to the arid environment encountered after exhumation (see Pueyo et al. 2001 for anhydrite associated to evaporitic gypsum in the Atacama Desert).

The clear difference between the preservation of invertebrate fossils in these two formations is probably due to the very distinct depositional environments. The Chilcatay Formation is composed of sandstones and siltstones interbedded with cobble layers. It is characterized by a shallow marine environment (i.e., *Ct2a*) with a paleo-depth of 0-15 m, a slightly deeper clinoformed sediments dominated by carbonate factories that underwent transport (15-20 m; i.e., *Ct1b*) and a deeper facies with a paleo-depth of 15-70 m (i.e., *Ct1a* and *Ct2b*). In the whole formation, the Ca-carbonates are preserved. Instead, the Pisco Formation is mainly siliceous organized in allomembers with sandstone at the base, with a paleo-depth of 0-15 m, and diatomaceous siltstones at the top, characterized by a paleo-depth of 15-70 m. Here the Ca-carbonates are hardly preserved.

This chapter is partially unreleased. Some parts are based on specific paragraphs from the paper "Sequence stratigraphy and paleontology of the upper Miocene Pisco Formation along the western side of the lower ica valley (Ica Desert, Peru)" written by Claudio Di Celma, Elisa Malinverno, Giulia Bosio, Alberto Collareta, Karen Gariboldi, Anna Gioncada, Giancarlo Molli, Daniela Basso, Rafael M. Varas-Malca, Pietro Paolo Pierantoni, Igor Maria Villa, Olivier Lambert, Walter Landini, Giovanni Sarti, Gino Cantalamessa, Mario Urbina and Giovanni Bianucci, printed in 2017 on Rivista Italiana di Paleontologia e Stratigraia (RIPS), Vol. 123(2): 255-273. In this paper, Giulia Bosio contributes to measurement of the stratigraphic section and field mapping, sample collection, identification and description of the invertebrate fauna, reconstruction of the chronostratigraphic framework and discussion.
And from the paper "Insights into the diagenetic environment of fossil marine vertebrates of the Pisco Formation (late Miocene, Peru) from mineralogical and Sr-isotope data" authored by Anna Gioncada, Riccardo Petrini, Giulia Bosio, Karen Gariboldi, Alberto Collareta, Elisa Malinverno, Elena Bonaccorsi, Claudio Di Celma, Marco Pasero, Mario Urbina and Giovanni Bianucci, published on Journal of South American Earth Sciences in 2018, Vol. 81, 141-152. In this paper, Giulia Bosio contributes to sample collection and preparation, taphonomic analyses on vertebrates, invertebrate identification, diagenetic studies on mollusks and discussion on Sr-isotopes.
However, several results are still unpublished and they will be developed for a paper on mollusk taphonomy.

Chapter References

Baker, P.A., Kastner, M. 1981. Constraints on the formation of sedimentary dolomite. Science, 213, 214-216.

Barbin, V., Ramseyer, K., Debenay, J.P., Schein, E., Roux, M., Decrouez, D. 1991. Cathodoluminescence of recent biogenic carbonates: an environmental and ontogenetic fingerprint. Geological Magazine, 128(1), 19-26.

Barbin, V. 2013. Application of cathodoluminescence microscopy to recent and past biological materials: a decade of progress. Mineralogy and Petrology, 107, 353-362.

Berner, R.A. 1981. Authigenic mineral formation resulting from organic matter decomposition in modern sediments. Fortschritte der Mineralogie, 59, 117-135.

Bontognali, T.R.R., McKenzie, J.A., Warthmann, R.J., Vasconcelos, C. 2014. Microbially influenced formation of Mg-calcite and Ca-dolomite in the presence of exopolymeric substances produced by sulphate-reducing bacteria. Terra nova, 26, 72-77.

Coleman, M.L., Berner, R.A., Durand, B., Meadows, P.S., Eglinton, G. 1985. Geochemistry of diagenetic non-silicate minerals kinetic considerations. Philosophical Transaction of the Royal Society A, 315, 39-56.

Crippa, G., Angiolini, L., Bottini, C., Erba, E., Felletti, F., Frigerio, C., Hennissenb, J.A.I., Leng, M.J., Petrizzo, M.R., Raffi, I., Raineri, G., Stephenson, M.H. 2016. Seasonality fluctuations recorded in fossil bivalves during the early Pleistocene: Implications for climate change. Palaeogeography, Palaeoclimatology, Palaeoecology, 446, 234-251.

DeVries, T.J. 1988. Molluscs of the Pisco Basin. Pisco Basin guidebook. In: Dunbar, R.B., Baker, P.A. (Eds.), Cenozoic Geology of the Pisco Basin, IGCP, 156, 127-134.

DeVries, T.J. 2016. Fossil Cenozoic crassatelline bivalves from Peru: new species and generic insights. Acta Palaeontologica Polonica, 61, 661-688.

Di Celma, C., Malinverno, E., Cantalamessa, G., Gioncada, A., Bosio, G., Villa, I.M., Gariboldi, K., Rustichelli, A., Pierantoni, P.P., Landini, W., Tinelli, C., Collareta, A., Bianucci, G. 2016. Stratigraphic framework of the late Miocene Pisco Formation at Cerro Los Quesos (Ica desert, Peru). Journal of Maps, 12, 1020-1028.

Gariboldi, K., Gioncada, A., Bosio, G., Malinverno, E., Di Celma, C., Tinelli, C., Cantalamessa, G., Landini, W., Urbina, M., Bianucci, G. 2015. The dolomitic nodules enclosing fossil marine vertebrates in the East Pisco Basin, Peru: field and petrographic insights into their genesis and role in preservation. Palaeogeography, Palaeoclimatology, Palaeoecology, 438, 81-95.

Gioncada, A., Petrini, R., Bosio, G., Gariboldi, K., Collareta, A., Malinverno, E., Bonaccorsi E., Di Celma, C., Pasero M., Urbina, M., Bianucci, G. 2018. Insights into the diagenetic environment of fossil marine vertebrates of the Pisco Formation (late Miocene, Peru) from mineralogical and Sr-isotope data. Journal of South American Earth Sciences, 81, 141-152.

Kastner, M., Elderfield, H., Martin, J.B., Suess, E., Kvenvolden, A., Garrison, R.E. 1990. Diagenesis and interstitial water chemistry at the Peruvian continental margins- major constituents and strontium isotopes. In: Suess, E., von Huene, R. (Eds.), Initial Report Ocean Drilling Program, 112(B), 413-440.

Lin, Q., Jiasheng, W., Thomas, J.A., Pibo, S., Gaowei, H. 2016. Formation mechanism of authigenic gypsum in marine methane hydrate settings: evidence from the northern South China Sea. Deep-Sea Research I, 115, 210-220.

Marocco, R., Muizon, C. de 1988. Le Bassin Pisco, bassin cenozoïque d'avant arc de la cote du Perou central: analyse geodynamique de son remplissage. Geodynamique, 3, 3-19.

McArthur, J.M., Howarth, R.J., Bailey, T.R. 2001. Strontium isotope stratigraphy: LOWESS version 3. Best-fit line to marine Sr-isotope curve for 0 to 509 Ma and accompanying look-up table for deriving numerical age. Look-up table. The Journal of Geology, 109, 155-169.

McCoy, V.E., Young, R.T., Briggs, D.E.G. 2015. Sediment permeability and the preservation of soft-tissues in concretions: An experimental study. PALAIOS, 30, 608-612.

Meister, P., Mckenzie, J.A., Vasconcelos, C., Bernasconi, S., Frank, M., Gutjahr, M., Schrag, D.P. 2007. Dolomite formation in the dynamic deep biosphere: results from the Peru Margin. Sedimentology, 54, 1007-1032.

Pirlet, H., Wehrmann, L.M., Brunner, B., Frank, N., Dewanckele, J., van Rooij, D., Foubert, A., Swennen, R., Naudts, L., Roone, M., Cnudde, V., Henriet, J.P. 2010. Diagenetic formation of gypsum and dolomite in a cold-water coral mound in the Porcupine Seabight, off Ireland. Sedimentology, 57, 786-805.

Pueyo, J.J., Chong, G., Jensen, A. 2001. Neogene evaporites in desert volcanic environments: Atacama Desert, Northern Chile. Sedimentology, 48, 1411-1431.

Rustichelli, A., Di Celma, C., Tondi, E., Baud, P., Vinciguerra, S. 2016. Fibrous gypsum veins as diffuse features and within fault zones: the case study of the Pisco Basin (Ica Desert, Southern Peru). Journal of the Geological Society, 173, 405-418.

Scasso, R.A., McArthur, J.M., del Río, C.J., Martínez, S., Thirlwall, M.F. 2001. 87Sr/86Sr Late Miocene age of fossil molluscs in the "Entrerriense" of the Valdés Peninsula (Chubut, Argentina). Journal of South American Earth Sciences, 14, 319-329.

Smith, C.R., Glover, A.G., Treude, T., Higgs, N.D., Amon, D.J. 2015. Whale-fall ecosystems: recent insights into ecology, paleoecology, and evolution. Annual Review of Marine Science, 7, 571-596.

Vasconcelos, C., McKenzie, J.A., Bernasconi, S., Grujic, D., Tiens, A.J. 1995. Microbial mediation as a possible mechanism for natural dolomite formation at low temperatures. Nature, 377, 220-222.

Yoshida, H., Ujihara, A., Minami, M., Asahara, Y., Katsuta, N., Yamamoto, K., Sirono, S., Maruyama, I., Nishimoto, S., Metcalfe, R. 2015. Early post-mortem formation of carbonate concretions around tusk-shells over week-month timescales. Scientific Reports, 5, 14123.

Chapter 16. Barnacle taphonomy

16.1. Skeletal assemblage and mineralogical composition

In the lower allomember (Ct1) of the Chilcatay Formation, two slightly different barnacle facies can be recognized in *Ct1a* and *Ct1b* facies associations, respectively (Fig. 16.1a-b).

The barnacle facies of *Ct1a* consists of poorly-sorted coarse-sandstones to conglomerates with siliciclastic and bioclastic elements (Fig. 16.1a, c-e); the barnacle-bearing horizons alternate with medium- to fine-grained sandstones, almost devoid of bioclasts (Fig. 16.1a). The rock is massive, porous and poorly cemented. Barnacles are very common, occurring as clusters of shells, isolated individuals and large shell fragments (Fig. 16.1d, e). According to thin section analysis, barnacles dominate the skeletal assemblage (Table 16.1; Fig. 16.1f, g). Echinoids are also very common; mollusks are less abundant and mainly represented by ostreids and pectinids (Table 16.1). Benthic foraminifera are very rare (mainly *Cibicides* Montfort, 1808, *Peneroplis* Montfort, 1808 and *Nonion* Montfort, 1808; Table 16.1). Serpulids are uncommon in the skeletal assemblage, but occasionally they occur in large clusters. Bryozoans are very rare (Table 16.1). The siliciclastic fraction is important and accounts for more than half of the components (Table 16.1; Fig. 16.1f, g). It consists of fragments of igneous rocks from the basement and ash-flow tuffs.

The barnacle facies of *Ct1b* is organized into clinobeds of well-sorted, coarse-grained mixed siliciclastic-bioclastic deposits, which are more cemented and less porous than those of the lower facies (Fig. 16.1a). On a macro-scale at the outcrop, barnacles dominate the bioclastic fraction (occurring as clusters, isolated individuals and shell fragments), but bivalves also occur (Fig. 16.1h-j). In thin section, barnacle remains are the most abundant group of skeletal grains; however, the common presence of sparite-filled molds suggests that mollusks were also important (Table 16.1; Fig. 16.1k-l). Among the few preserved bivalve specimens, ostreids and pectinids are dominant. Echinoids are also abundant (Table 16.1). Benthic foraminifera are less common (mainly *Cibicides* and *Peneroplis*; Table 16.1). Rare calcareous tubes also occur (Table 16.1). Based on point-counting analyses, siliciclastic components are slightly more important than bioclasts and they mainly consist of pebbles and granules of igneous basement rocks (Table 16.1; Fig. 16.1f, g, k-l).

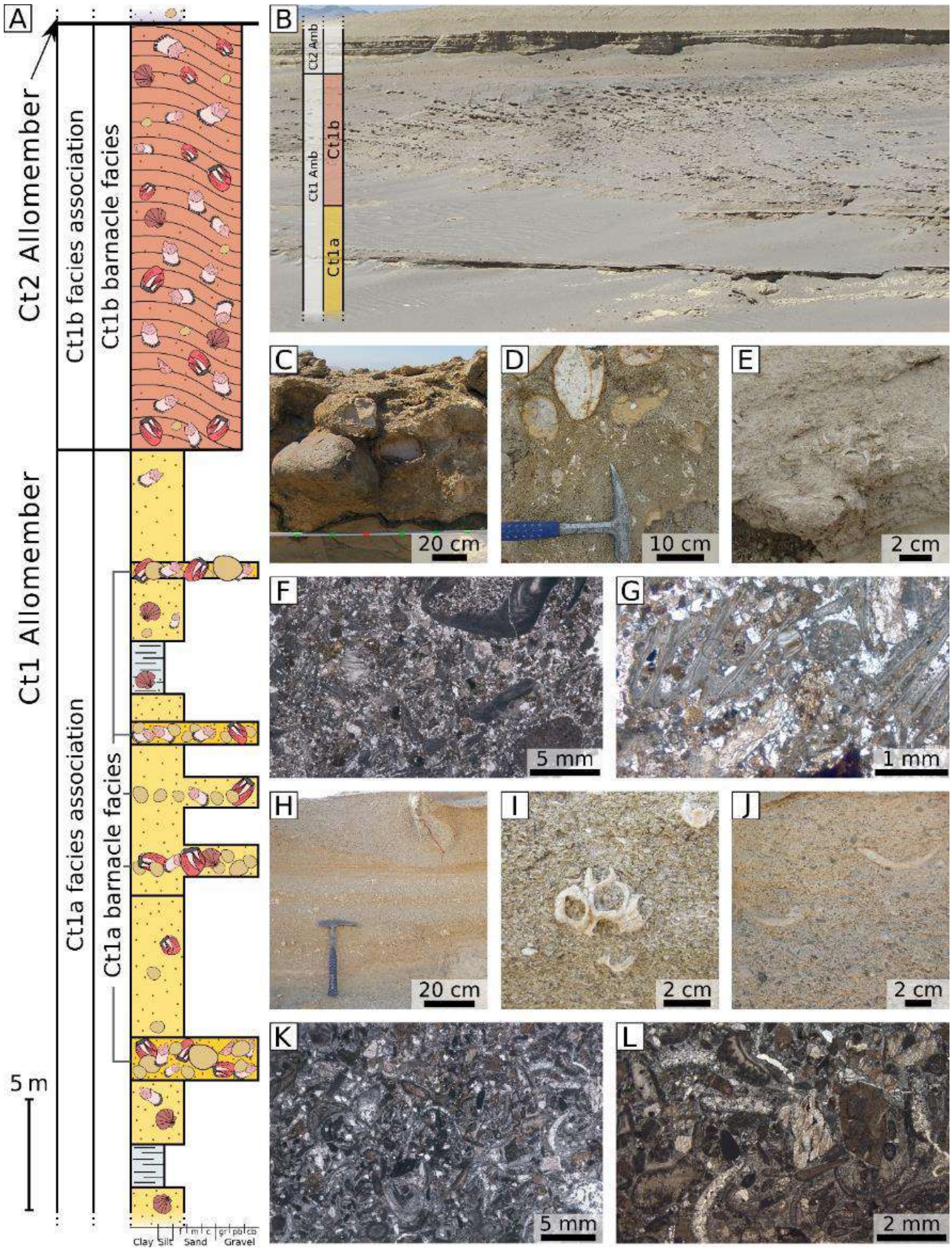

Figure 16.1. Barnacle facies of the Chilcatay Formation (Ullujaya, Peru). a) Simplified stratigraphic column of the barnacle facies of the Chilcatay Formation. b) Overview of the Ullujaya outcrop including a simple stratigraphic column highlighting the different facies. c) Macroscopic texture of the barnacle facies of *Ct1a*. d) Detail of the texture and

clast composition of the *Ct1a* barnacle facies. e) Detail of the texture and composition of the *Ct1a* barnacle facies. f) Thin section of a sample of the *Ct1a* barnacle facies. g) Detail of sample of the *Ct1a* barnacle facies with barnacles and foraminifera. h) Macroscopic texture of the *Ct1b* barnacle facies. i) Detail of the texture and bioclastic composition of the *Ct1b* barnacle facies. j) Detail of the texture and composition of the *Ct1b* barnacle facies. k) Thin section of a sample of the *Ct1b* barnacle facies. l) Detail of the abundant sparite-filled molds in the *Ct1b* barnacle facies. From Coletti et al. (in press).

	Chilcatay Formation	
	Lower barnacle facies	Upper barnacle facies
Petrographic composition		
Bioclastic components	22.0%	24.0%
Terrigenous components	65.0%	30.5%
Sparite	10.0%	41.0%
Micrite	3.0%	4.5%
Detail of the bioclastic fraction		
Barnacles	71.5%	80.0%
Molluscs	8.5%	7.5%
Echinoids	18.5%	8.0%
Bryozoans	<0.5%	///
Coralline algae	///	///
Benthic foraminifera	1.0%	4.0%
Other	<0.5%	<0.5%

Table 16.1. Petrographic composition and skeletal assemblage of the examined barnacle facies made by point counting (following Flügel 2010).

16.2. Barnacle preservation

In both facies, the cirripede remains occur as displaced clusters, displaced complete shells and wall plate fragments (Fig. 16.2). Unlike the barnacle-coralline facies, the clusters are generally detached from their original substrate (Type C of Nomura & Maeda 2008; displaced clusters of Doyle et al. 1997).

Complete specimens are generally moderately well-preserved, but display evidence of abrasion and lack the opercula (Fig. 16.2). The best preserved specimens retain their pigmentation (Fig. 16.2a, d). The shells are often filled by sand. In the barnacle facies of Ct1a, this filling is remarkably rich in bioclastic fragments and has less abundant mineral grains than the rock embedding the specimens. Disarticulated plates are often abraded (Grade 1 of Nielsen & Funder 2003). Opercula are rare - only a couple of abraded and fragmented scuta have been recovered.

16.3. Barnacle identification

Based on macroscopic features of the wall plates and on their internal microscopic structure, three barnacle taxa have been recognized: cf. *Austromegabalanus* sp., Balanidae indet., and Concavinae indet. (Fig. 16.2).

The specimens identified as cf. *Austromegabalanus* sp. have a shell diameter approaching 4 cm (Fig. 16.2a-c); they are comprised of six wall plates with broad, well-developed radii plus a calcareous, tubiferous, basis (Fig. 16.2a). The best preserved specimens are longitudinally striped, with pink-purple bands alternating with white (Fig. 16.2a). In thin section, the radii are tubiferous and their sutural edges bear transversely oriented septa with secondary denticles on the lower side only (a diagnostic character of the megabalanine genera included in the tribe Austromegabalanini; Newman 1979; Buckeridge 2015). The interlaminate figures present an almost straight main axis with many transverse branches characterized by multiple arrow-shaped terminations (Fig. 16.2b, c). *Austromegabalanus* Newman, 1979 is known to occur along the coasts of southern Peru and in the Miocene sediments of the Pisco Basin (e.g., Newman 1991; Carriol et al. 1987).

The specimens referred to Balanidae indet. are medium- to large-sized shells, comprised of six wall plates and characterized by a longitudinally striated outer wall with spiny-bulging protuberances creating a rough and irregular external surface (Fig. 16.2d-f). Some individuals display a pink color on the plates (Fig. 16.2d). In the lowermost portion of the shell the basal edges of the wall plates become inflected, and grow horizontally inwards, thus producing an inward-tapering calcareous membrane. This feature is often incomplete (i.e., a hole is present at the center of the basal calcareous membrane). In juvenile individuals that were overgrown by adults the basal calcareous membrane is not developed. The parietes of the wall plates are porous and multiple rows of tubes are present (Fig. 16.2e). Large pores occur also in the sheath (Fig. 16.2e). The radii are solid. Interlaminate figures are arborescent, with a long straight axis and short transverse branches with crescent-moon to kidney-shaped terminations (Fig. 16.2f). Based on the general architecture of the six-plated shell and the presence of complex interlaminate figures, these specimens are provisionally identified as indeterminate balanids. Among Balanidae, a porous sheath characterizes *Titobustillobalanus tubutubulus* Carriol & Álvarez-Fernández, 2015 from the latest Pleistocene of Spain and various species of the amphibalanine genus *Fistulobalanus* Zullo, 1984.

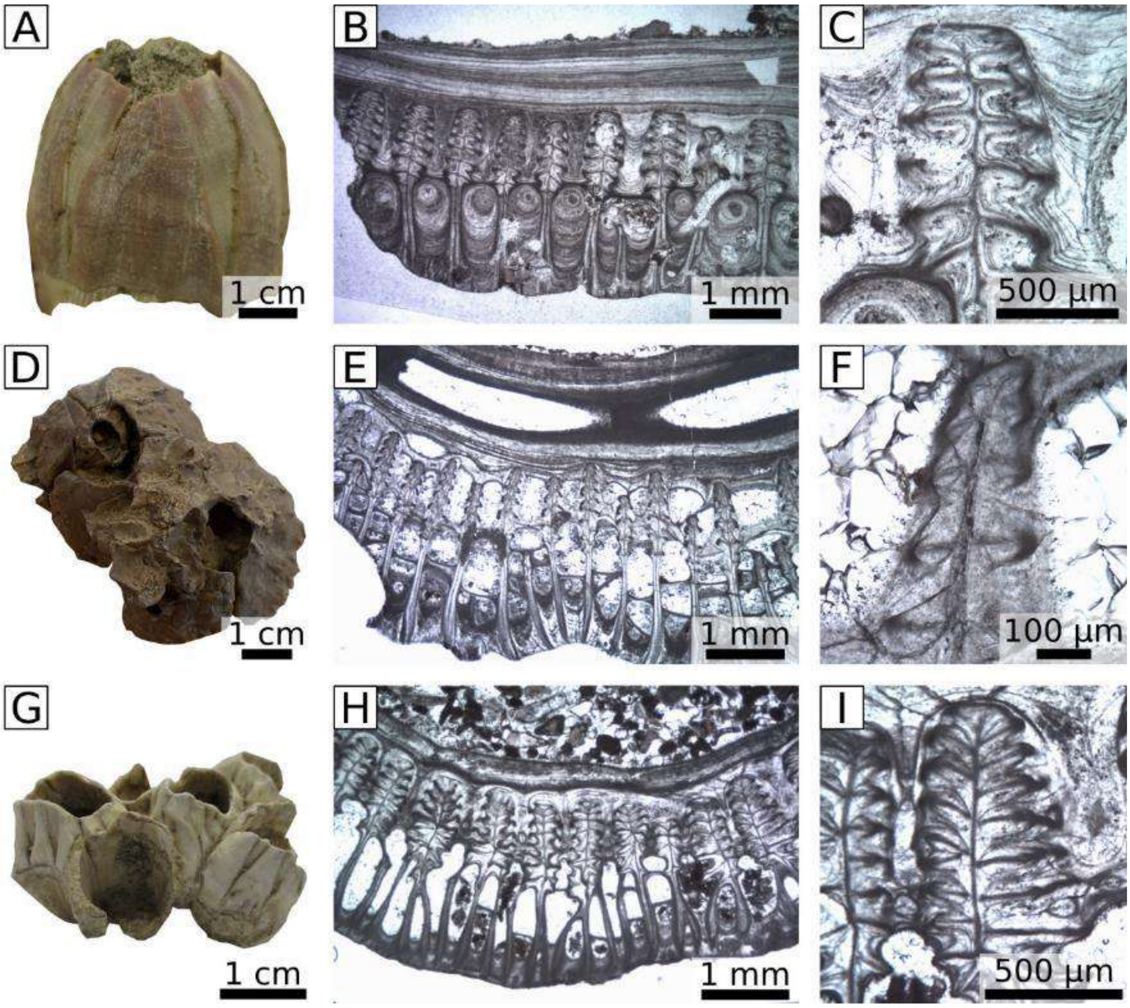

Figure 16.2. Barnacles of the barnacle facies of Ullujaya. a) First morphotype, complete shell (Lower barnacle facies). b) First morphotype, interlaminate figures of (Lower barnacle facies). c) First morphotype, detail of the interlaminate figures (Lower barnacles facies). d) Second morphotype, cluster of shells (Lower barnacle facies). e) Second morphotype, interlaminate figures (Lower barnacle facies). f) Second morphotype, detail of the interlaminate figures (Lower barnacle facies). g) Third

morphotype, cluster of shells (Upper barnacle facies). h) Third morphotype, interlaminate figures (Lower barnacle facies). i) Third morphotype, detail of the interlaminate figures (Lower barnacle facies). From Coletti et al. (accepted).

The specimens identified as Concavinae indet. are medium- to small-sized, six-plated shells with a basal diameter ranging between 1 and 2 cm (Fig. 16.2g-i). They appear to have been strictly cluster-forming organisms, since even displaced single individuals show an elongated, tubiferous, basal plate tapering downwards (a morphology that is typically associated with a gregarious growth habit, e.g., Newman & Ross 1976). Some specimens display a faint pink to purple pigmentation. The wall plates are porous and display a single row of tubes divided by frequent transverse septa (Fig. 16.2h). Interlaminate figures have a long and straight axis with numerous, closely-spaced transverse branches characterized by arrow-shaped terminations (Fig. 16.2i). These branches are often organized in pairs, stemming from the same point of the main axis (Fig. 16.2i). The very rare opercula retrieved in the sieved material may be attributed to this group of specimens due to their size. They consist of triangular scuta characterized by transverse growth lines.

A further, currently unidentified, barnacle taxon was observed only once in the *Ct1a* facies association. It is represented by small-sized individuals (around 0.5 cm in basal diameter) forming a cluster which partially encrusts a pectinid shell. These small-sized barnacles could also represent juveniles of one of the afore-mentioned taxa. The common occurrence of pectinids with small barnacle attachment scars (*Anellusichnus circularis* Santos, Mayoral & Muñiz, 2005) on the outer surface could indicate that this type was less uncommon than suggested by body fossils alone.

16.4. Facies interpretation

Both examined barnacle facies can be related to a relatively shallow-water, high-energy, environment, in agreement with the paleoenvironment of the Chilcatay at Ullujaya, as exposed in Chapter 6 (Part I). Although in situ reworking and downslope sediment transport might have somewhat affected them, they still clearly retain their shallow-water, high-energy, signature (i.e. coarse- to extremely-coarse grain-size; faunal composition entirely and overwhelmingly dominated by shallow-water taxa).

Both barnacle facies of the Chilcatay Formation have a "low diversity" skeletal assemblage, with barnacle and mollusks (mainly epifaunal bivalves like ostreids and pectinids) accounting for > 75 % of the skeletal fragments (Table 16.1). It should be noticed that mollusk abundance was probably reduced by selective dissolution during diagenesis; this particularly applies to the barnacle facies of *Ct1b*, where mollusk- shaped, sparite-filled molds are common. The abundance of barnacles and epifaunal bivalves points toward an exposed setting since both groups are favored by high water energy (Farrow et al. 1978; Nebelsick 1992). A setting favorable for barnacles is also supported by the diverse barnacle assemblage with at least three common taxa. The preservation of barnacles in both facies is similar. Whole individuals are present (either as displaced clusters or single shells) and always separated from their substrate. Some specimens still preserve their pigmentation but the majority of them do not. Opercula are extremely rare. These characteristics suggest significant reworking, compatible with a setting above fair-weather wave-base, more severe compared to other barnacle-coralline facies (Pietra da Cantoni Group; Coletti et al. 2015), probably causing the loss of pigmentation in many specimens and the definitive loss of the opercula. Such features are compatible with reworking in above fair-weather wave-base setting. As said in Chapter 6 (Part I), we interpreted *Ct1b* as a shoreface deposit, probably formed at a water depth of 15–20 m (assuming a storm-wave base around 15–20 m in accordance with the models of Hernández-Molina et al. 2000; Massari & Chiocci 2006). We interpreted *Ct1a* as an offshore deposit resulting from the downslope transport of shoreface material (below 30–40 m of water depth since the height of the clinoforms is about 15–20 m). Since both facies have the same signature, it is likely that most of reworking occurred in the shoreface environment, with the downslope movement only mildly affecting the association. This is also supported by the sediment preserved within the shells of the *Ct1a* barnacles, which is similar in composition to that of *Ct1b* (more bioclasts and less siliciclastic particles).

The analysis of both modern and fossil barnacle facies suggests that the major factors controlling the development of a barnacle-dominated carbonate factory are: the availability of hard-substrate, hydrodynamic energy and nutrient availability. As a consequence, the most favorable setting for a barnacle-dominated carbonate factory is probably an inshore rocky substrate, characterized by high-energy conditions and abundant nutrient-supply. This situation can lead to the formation of the typical barnacle-rich facies, where abundant barnacles are associated with other hard-substrate organisms, like ostreids, pectinids and echinoids. They represent the most common type of barnacle-dominated facies.

This chapter is a part of the paper "Palaeoenvironmental analysis of the Miocene barnacle facies: case studies from Europe and South America" written by Giovanni Coletti, Giulia Bosio, Alberto Collareta, John Buckeridge, Sirio Consani, Akram El Kateb, in press on Geologica Carpathica. In this paper, Giulia Bosio contributes to sample collection of the Peruvian material, sample preparation and analyses, comparison among barnacle facies and the discussion.

Chapter References

Buckeridge, J.S. 2015. Revision of Southern Hemisphere taxa referred to Fosterella (Crustacea: Cirripedia), and their extinction in response to Pleistocene cooling. Integrative Zoology, 10, 6, 555-571.

Carriol, R.P., Álvarez-Fernández, E. 2015. Balanomorphs from late Upper Pleistocene and Holocene caves in northern Spain, with a new genus and species, and their palaeoclimatological implications. Annales de Paléontologie, 101, 1, 21-27.

Coletti, G., Basso, D., Frixa, A., Corselli, C. 2015. Transported rhodoliths witness the lost carbonate factory: a case history from the Miocene Pietra da Cantoni limestone (NW Italy). Rivista Italiana di Paleontologia e Stratigrafia (Research In Paleontology and Stratigraphy), 121(3), 345-368.

Doyle, P., Mather, A.E., Bennet, M.R., Bussel, M.A. 1997. Miocene barnacle assemblages from Southern Spain and their palaeoenvironmental significance. Lethaia, 29(3), 267-274.

Farrow, G.E., Cucci, M., Scoffin, T.P. 1978. Calcareous sediments on nearshore continental shelf of western Scotland. Proceedings of the Royal Society of Edinburgh, 76B, 55-76.

Flügel, E. 2010. Microfacies of Carbonate Rocks: Analysis Interpretation and Application. Springer, New York, 1-1007.

Hernández-Molina, F.J., Fernández-Salas, L.M., Lobo, F., Somoza, L., Díaz-del-Río, V., Alveirinho Dias, J.M. 2000. The infralittoral prograding wedge: a new large-scale progradational sedimentary body in shallow marine environments. Geo-Marine Letters, 20(2), 109-117.

Massari, F., Chiocci, F. 2006. Biocalcarenite and mixed cool-water prograding bodies of the Mediterranean Pliocene and Pleistocene: architecture, depositional setting and forcing factors. In: Pedley H.M. & Carannante G. (Eds.): Cool-water carbonates: depositional systems and palaeoenvironmental controls. Geological Society, London, Special Publications, 255, 95-120.

Montfort, P.D. de 1808. Conchyliologie systématique et classification méthodique des coquilles, Vol. 1. Schoell, Paris, 1-409.

Nebelsick, J.H. 1992. Components analysis of sediment composition in Early Miocene temperate carbonates from the Austrian Paratethys. Palaeogeography, Palaeoclimatology, Palaeoecology, 91, 59-69.

Newman, W.A. 1979. On the biogeography of balanomorph barnacles of the Southern Ocean, including two new balanid taxa; a subfamily, two genera and three species. In: Proceedings of the International Symposium on Marine Biogeography and Evolution in the Southern Hemisphere. New Zealand Department of Scientific and Industrial Research Information Series, Auckland, 137, 279-306.

Newman, W.A., Ross, A. 1976. Revision of the balanomorph barnacles; including a catalogue of the species. Mem. Transactions of San Diego Society of Natural History, 9, 1-108.

Nielsen, J.K., Funder, S. 2003. Taphonomy of Eemian marine mollusks and acorn barnacles from eastern Arkhangelsk region, northern Russia. Palaeogeography, Palaeoclimatology, Palaeoecology, 191, 139-168.

Nomura, S., Maeda, H. 2008. Significance of autochtonous fossil barnacles from the Miocene Natori Group at the Moniwa-Goishi area, northeast Japan. Paleontological Research, 12(1), 63-79.

Santos, A., Mayoral, E., Muñiz, F. 2005. Bioerosion scars of acorn barnacles from the southwestern Iberian Peninsula, upper Neogene. Rivista Italiana di Paleontologia e Stratigrafia (Research In Paleontology and Stratigraphy), 111(1), 181-189.

Zullo, V.A. 1984. New genera and species of balanoid barnacles from the Oligocene and Miocene of North Carolina. Journal of Paleontology, 58, 5, 1312-1338.

Chapter 17. Bone preservation in both Chilcatay and Pisco formations

17.1. Vertebrate taphonomy in the Chilcatay Formation

The reason that leads such an exceptional preservation of fossil marine vertebrates in the Pisco Basin is still not completely understood.

For investigating vertebrate preservation in the Chilcatay Formation, macroscopic taphonomic data were collected both in the field and at the Museo de Historia Natural de la Universidad Nacional Mayor de San Marcos (MUSM) by examining fossils collected over the past years from the Ullujaya locality. Field observations were limited by the fact that most of the exposed specimens are still included in partially lithified sediment that has not been removed to avoid damaging the bones.

Excluding twelve specimens that were not found in situ (due to recent erosion and subsequent dislocation), all the fossil vertebrate skeletons whose stratigraphic collocation is known display various degrees of disarticulation and are incomplete (Fig. 17.2 and Fig. 17.2). The associated bones of the disarticulated skeletons exhibit a random arrangement without any preferential orientation. Among the sixteen cetacean crania found in situ, nine (56.2%) are arranged dorsal side-up and seven (43.8%) are arranged ventral side-up position (Fig. 17.1a). For most of the studied specimens, all skeletal elements are found within a single sediment layer, and evidence of sinking into the substratum are generally absent. Disarticulated vertebrae are typically observed with their epiphyseal surfaces parallel to the subjacent stratification, an arrangement that would prove very stable for a vertebra resting for a prolonged time on a relatively compact soft substrate, which does not allow sinking (Fig. 17.1b-e). The few exceptions include disarticulated vertebrae with transverse processes stuck into the underlying sediment (Fig. 17.2f, g) and a partly articulated vertebral column that moderately sank into the substratum (Fig. 17.2h, i).

Considering all the cetacean specimens that were found in situ, twenty-five of them (48.1%) consist of just one isolated anatomical element (e.g., cranium, vertebra, rib; Fig. 17.1a), thirteen (25.0%) of a few fully disarticulated bones (ca 25% of the skeleton being preserved; Fig. 17.1b-e), eleven (21.2%) of a few partially articulated bones (e.g., a few articulated vertebrae and ribs, with the remaining bones being disarticulated; Fig. 17.1f, g), two (3.8%) of fully disarticulated partial skeletons (ca 50% of the skeleton being preserved; Fig. 17.1h, i), and one (1.9%) of a fully articulated small portion of the skeleton (seven vertebrae; Fig. 17.1j, k).

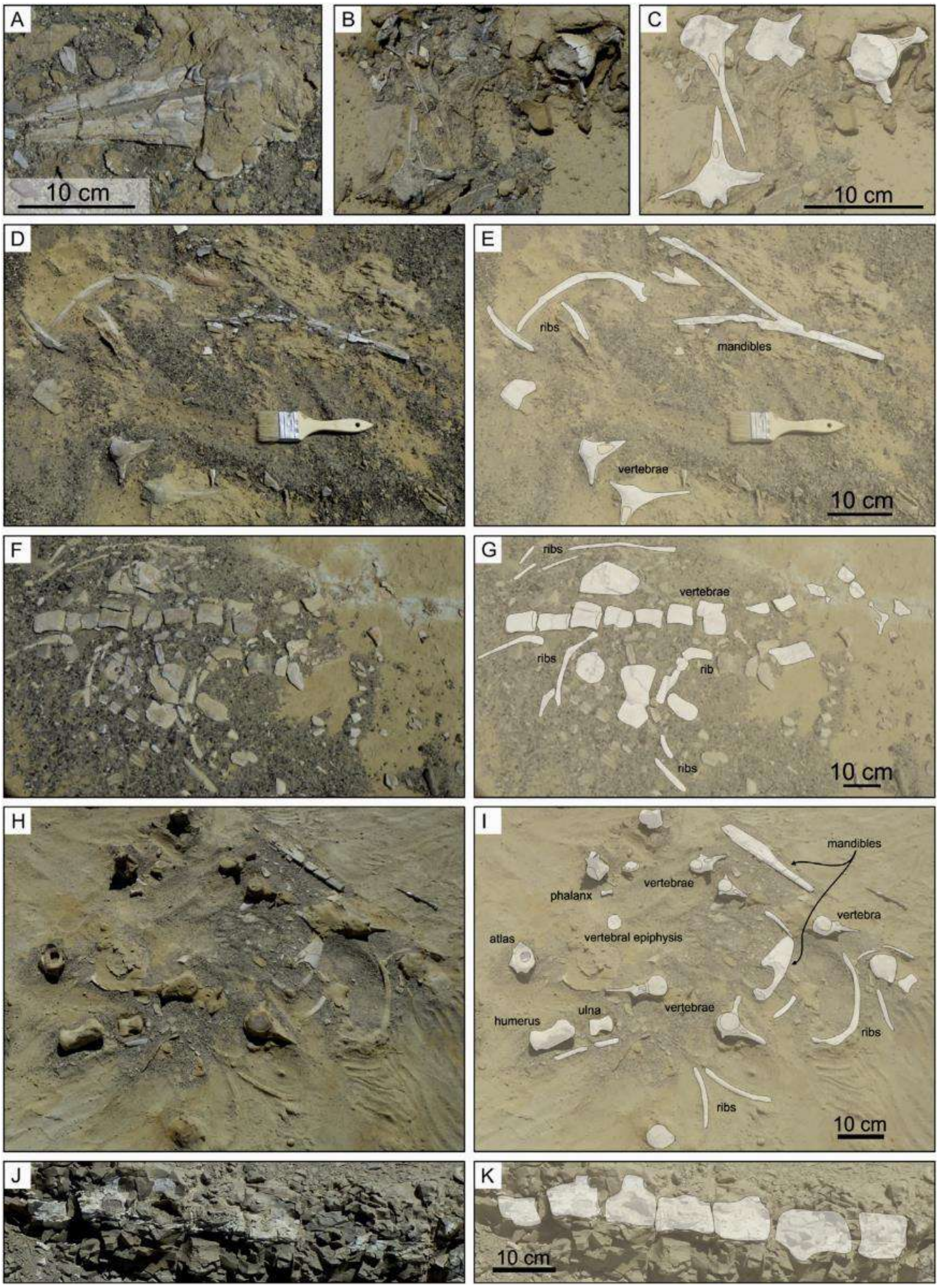

Figure 17.1. Bedding view of fossil cetaceans from Ct1a of the Chilcatay Formation exposed at Ullujaya. a) Isolated cranium of *Kentriodon* sp. disposed ventral side-up

position (field number: O7). b) Four associated and disarticulated vertebrae of aff. Odontoceti indet. (O57) and c) corresponding explanatory line drawing. d) Few associated and disarticulated bones (including mandibles and some vertebrae and ribs) of Odontoceti indet. (O29) and e) corresponding explanatory line drawing. f) Partial skeleton (including articulated vertebrae and disarticulated ribs and other fragmentary bones) of aff. Odontoceti indet. (O59) and g) corresponding explanatory line drawing. h) Fully disarticulated partial skeleton (including mandibles, humerus, ulna, vertebrae, and ribs) of Squalodelphinidae indet. (O4) and i) corresponding explanatory line drawing. j) Seven articulated vertebrae of aff. Odontoceti indet. (O38) and k) corresponding explanatory line drawing. From Bianucci et al. (2018).

The articulation vs completeness bivariate bubble plot obtained with the above data (Fig. 17.3) highlights the high number of specimens whose completeness and articulation equal to zero. As a consequence, the T value is also very low (0.30), thus supporting biostratinomic conditions and processes favoring the disarticulation of the carcasses and the dispersal of the bony elements. The low value (0.08) of Pearson's r^2 and the moderate (0.47) value of rs indicate that articulation and completeness are not firmly related to each other, as also evidenced by the observation of fully disarticulated skeleton with different degree of completeness.

Out of the thirteen cetacean skulls collected for systematic study, only one of them retains the mandible (but only the right ramus) articulated, only one has both periotics (ear bones) articulated, one displays all the teeth in anatomical position, and six lack all teeth in their alveoli.

The smaller sample of non-mammalian vertebrates preserved as skeletal elements (one sea turtle and ten bony fish) confirms the taphonomic pattern observed for the cetaceans, all the detected skeletons being more or less incomplete and articulated. In particular, among bony fish, the most complete specimen (referred to aff. *Makaira* sp.) consists of an articulated, significant portion of the vertebral column with several skeletal elements scattered in a few square meters. The other fish specimens consist of six isolated portions of partly articulated vertebral columns (Fig. 17.2d, e), one fully articulated caudal fin (Fig. 17.2c), one isolated cranium, and two fragmentary portions of skulls.

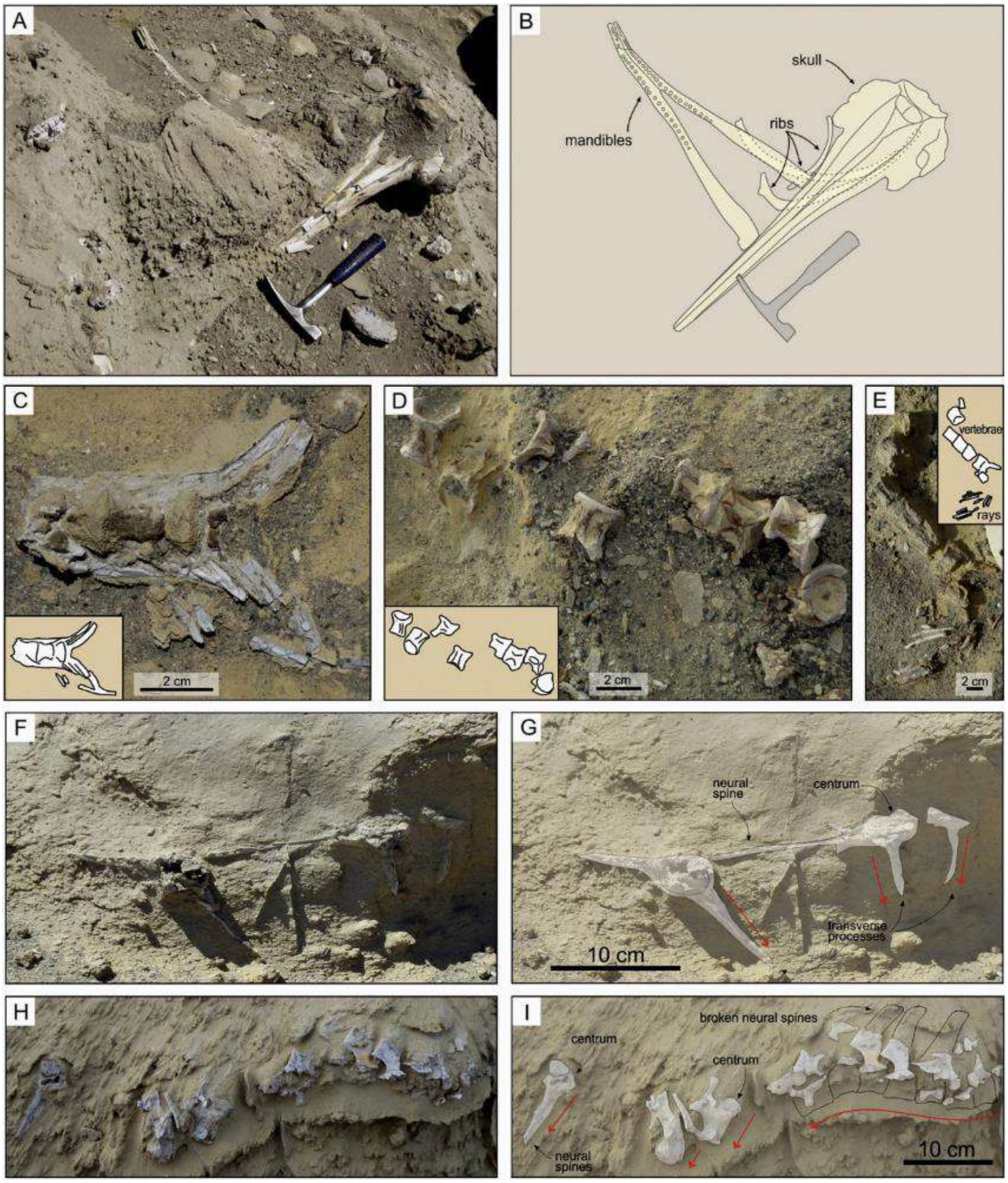

Figure 17.2. Fossil cetaceans (a–b, f–i) and tuna-like bony fish (c–e) from *Ct1a* of the Chilcatay Formation exposed at Ullujaya. a) Disarticulated cranium, mandibles, and two ribs of an undescribed specimen of *Chilcacetus cavirhinus* (field number: O5; catalogue number: MUSM 2527) and b) corresponding explanatory line drawing. c) Fully articulated caudal fin (T2). d) Some associated and partially disarticulated vertebrae (T5). e) Few associated and partially disarticulated vertebrae and rays (T6). f) Three associated and disarticulated vertebrae of aff. Odontoceti indet. (O40) with sunk transverse processes and g) corresponding explanatory line drawing. h) Partially

articulated vertebral column of aff. Odontoceti indet. (O50) that moderately sank and i) corresponding explanatory line drawing. Red arrows indicate sinking of the bones.

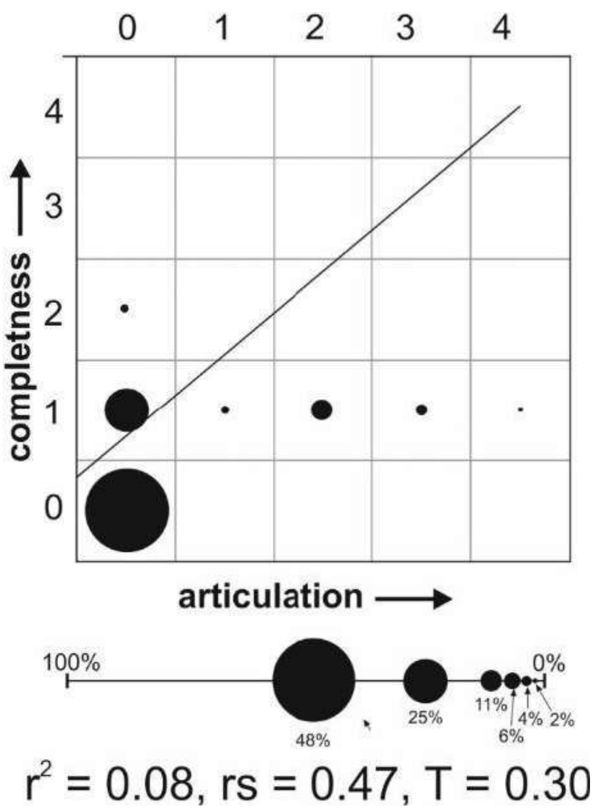

Figure 17.3. Bubble plot of articulation versus completeness for the marine vertebrate assemblage from *Ct1a* of the Chilcatay Formation exposed at Ullujaya. Abbreviations: r^2=Pearson's r-squared value; rs=Spearman rank-order correlation coefficient; T=intersect of the best-fit linear trend line with the completeness axis. For more details, see Bianucci et al. (2018) and Beardmore et al. (2012).

Mollusks, barnacles, worm tubes, and other invertebrate remains, as well as shark teeth, are never found strictly associated to the bones. Bioerosion due to macro-invertebrates is never observed on the fossil bones, whereas shark bite marks are occasionally encountered. Bioturbations caused by the bone-eating worm *Osedax* (Kiel et al. 2010) and other evidences of whale fall communities (Smith et al. 2015) have not been observed. None of the detected specimens was found included and/or associated to carbonate concretions, unlike what has been observed in the overlying Pisco Formation (Gariboldi et al. 2015; Gioncada et al. 2016). Furthermore, macroscopic evidence of adhering phosphate crusts or envelopes has not been observed.

Macroscopically, most of the bones preserved within the sediment have a reddish color and appear well mineralized. SEM-BSE observations on representative samples (Table 17.2) indicate that the bone tissue is rather dense (Fig. 17.4a, b), confirming a good degree of mineralization, with well-preserved bone structures. Under the optical microscope, in both the compact and the cancellous bone, Haversian canals and medullary cavities may exhibit cementation (Table 17.2 and Fig. 17.4c-f). In one of the samples, Ca-phosphate partially fills osteon porosity, indicating incipient permineralization. In several cases (Table 17.2), the Haversian canals of the compact bone and the larger medullary cavities of the cancellous bone are totally or partially filled by Ca-Mg carbonates. Several generations of carbonate cement are observed, having different Ca/Mg ratios. Furthermore, in several samples, sediment grains fill some of the bone cavities, thus providing evidence that the bone went broken before diagenesis occurred. In some cases, Fe-oxides/hydroxides fill the Haversian canals in the reddish portions of the bone. Gypsum can also fill partly the bone cavities.

When the external part of the bone is preserved, it can be intact, partly dissolved, or affected by microborings. Two of the four examined specimens having bones not decorticated exhibit microborings of the B-type (sensu Gariboldi et al. 2015) (Table 17.2). In these cases, borings are a few μm wide and can be filled by gypsum, apatite, or Fe-oxyhydroxides. The boundary between the bone tissue and the sediment is cemented by Fe-oxyhydroxides causing the bone surface to appear reddish.

Field evidence of abrasion and fracturing of the exposed bones is often not easy to interpret due to the erosion in the present-day desert. In this respect, the analysis of thirteen partial skeletons collected for systematic study has proven more useful. Most of these fossils lack evidence of abrasion, having their cortical bone well preserved (e.g., the *Chilcacetus cavirhinus* MUSM 1401 and the *Huaridelphis raimondii* MUSM 1403). However, weak abrasion is observed in some crania of the MUSM collections (e.g., the *Kentriodon* MUSM 2431 and MUSM 631), but that could be due to recent erosion. Fracturing is clearly observed in one cranium (MUSM 631) referred to *Kentriodon*, having its posterior portion damaged. In all the other collected skulls, fractures (if present) are minor and do not generate significant distortion of the bones (e.g., in the holotype skull MUSM 1396 of *Huaridelphis raimondii*). Delicate bone elements, such as the hamular processes and the laminae of the pterygoid, are preserved in several crania. With regard to the postcranial remains, most bones are broken and fragmentary (in part, because of recent erosion), although some vertebrae exhibit a good state of preservation of the narrow and elongated neural spine and transverse processes.

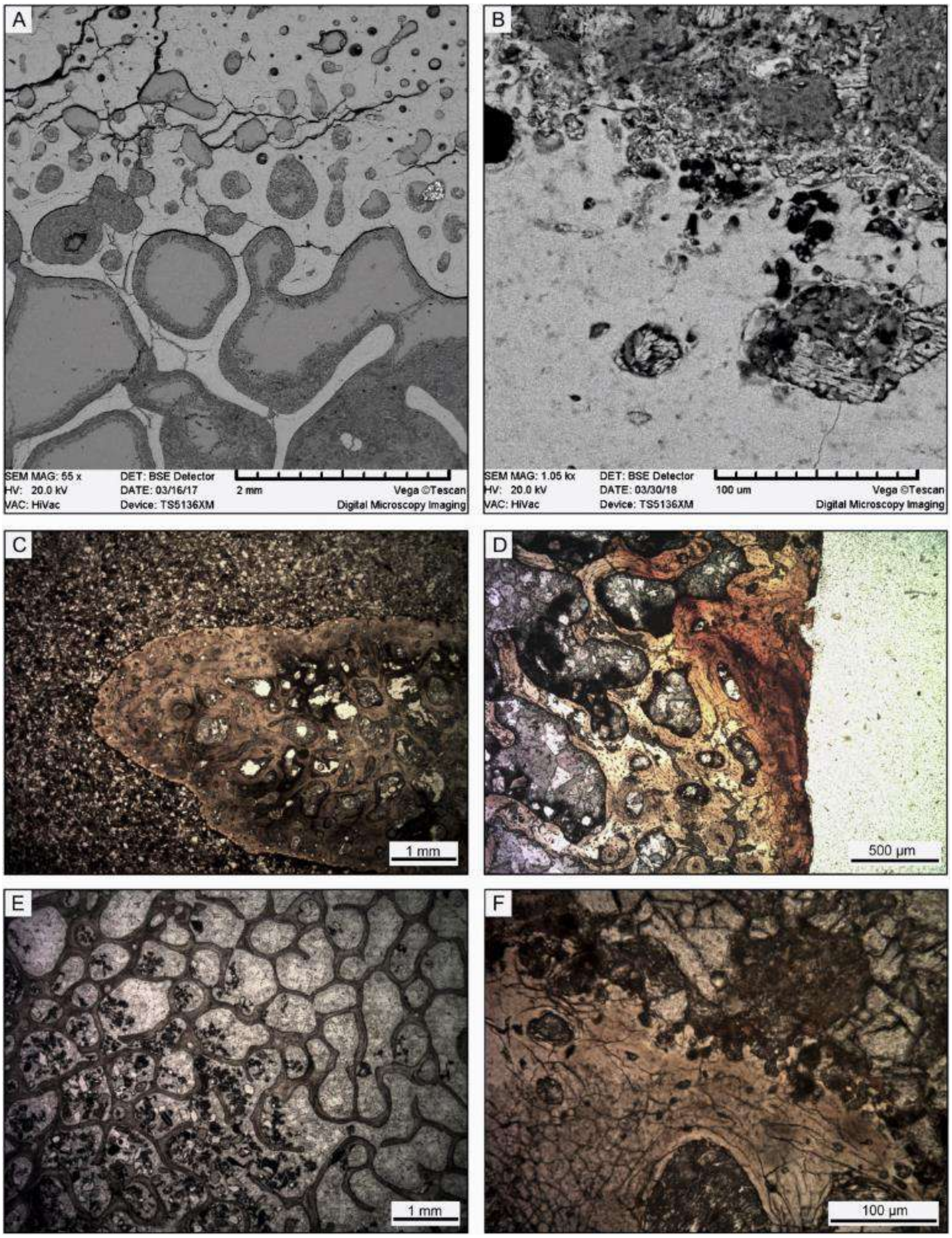

Figure 17.4. Optical photos (a, b) and backscattered Scanning Electron Microscope images (c, f) of fossil marine mammal bones from Ct1a of the Chilcatay Formation exposed at Ullujaya. a) Detail of calcite cementing both the cancellous and the compact bone cavities of specimen O5; note that calcite started to grow from the surface of the bone trabecolae. b) Microborings on the bone surface of specimen O3. c) Transverse thin section in transmitted light of a rib from specimen O3; both cancellous and

compact bone are visible. d) Reddish color of the bone surface of specimen O52 caused by the presence of Fe-oxyhydroxides. e) Cancellous bone of a rib of specimen O5 showing an infill of sediment in some marrow cavities cemented by calcite. f) Microborings of the B-type (sensu Gariboldi et al. 2015) on the surface of a rib of specimen O3. From Bianucci et al. (2018).

Number	Height abs (m)	Determination	Analysed bone elements	Bone colour	Bone surface	Bone permineralization
O3	15.0	*Huaridelphis raimondii*	Rib	Reddish	Partially dissolved, with borings	Minor, Fe-oxides/hydroxides
O5	9.7	*Chilcacetus cavirhinus*	Ribs	White to brownish	Intact, no borings	High, calcite and dolomite
O16	15.0	*Kentriodon* sp.	Rib	Pinkish	Intact, no borings	–
O29	15.0	Odontoceti indet.	Bone fragment	Reddish	Partially dissolved, with borings	Moderate, Ca-Mg carbonates
O41	26.2	aff. Odontoceti indet.	Vertebra	White	Worn out[a]	Moderate, Ca-Mg carbonates
O52	25.9	aff. Odontoceti indet.	Vertebra	Reddish to black	Worn out[a]	Moderate, Ca-Mg carbonates
O53	27.4	aff. Odontoceti indet.	Vertebra	Brownish	Worn out[a]	Minor, Ca-phosphate and Fe-oxides/hydroxides

[a] The presence/absence of borings cannot be assessed due to the lack of bone surface.

Table 17.2. General prospect of the vertebrate specimens selected for the microscopic analyses, with a summary of the macro- and microscopic taphonomic features of the bones. From Bianucci et al. (2018).

Our taphonomic observations suggest prolonged flotation and repeated movements through the water mass of the marine vertebrate carcasses before their final deposition on the seafloor (Schäfer 1972). During this long-time floating phase, the carcasses were subject to biogenic and physical processes of partial destruction, as supported by the shark bite marks (at least part of them indicating scavenging action) and by the overall low degrees of completeness and articulation of the specimens. The high number of isolated crania of cetaceans may record the separation of the relatively heavy head from the rest of the body during the early phases of the flotation of the carcasses, as observed by Schäfer (1972) for extant dolphins and already hypothesized for fossil cetaceans from the upper Miocene of the East Pisco Basin by Bianucci et al. (2010). Further disarticulation could have occurred during the period when the carcasses laid exposed on the seafloor, due to the fluidization of the remaining soft tissues and consequent gravitational collapse (Reisdorf et al. 2014). In some cases, the presence of sediment infilling some bone cavities proves that the micro-breakages of the bones occurred before diagenesis and those bones were exposed on the seafloor after the carcass deposition, as a consequence of the early body dismemberment.

Bottom currents can be discarded as a cause of disarticulation due to the lack of preferential orientation of the disarticulated remains and the lack of sedimentary structures, considering also that the aforementioned evidence of euxinic conditions supports water stagnation close to the seafloor. Together with the scarcity of breakage and abrasion marks on the bones, the preservation of delicate bone structures further supports the absence of transport due to bottom currents. Scavenging action as a cause of disarticulation can be discarded due to the lack of fossil traces on the bones (with the notable exception of those left by sharks) and of closely associated macroinvertebrate remains (whose absence is probably due to the euxinic conditions of the bottom waters, see above).

The hypothesis of a prolonged flotation in this paleoenvironment cannot be applied to the "classical" Pisco Formation, where complete and fully articulated skeletons are more abundant, especially in the diatomitic portions. In the Pisco paleoenvironment, the carcasses of the whales sank in the soft muddy sediments, with a high porosity, being partially covered. This sinking did not allowed the rising of the carcasses to the surface, preventing a carcass flotation that is hypothesized for the Chilcatay vertebrates in Ullujaya (Reisdorf et al. 2012).

Bones often exhibit a reddish color on the surface, visible at both macro- and micro-scale (Fig. 17.4c-f). This feature is probably due to the oxidation of Fe, available for the formation of abundant pyrite framboids in anoxic bottom water and within the sediments. Bone cavities, such as Haversian canals and medullary cavities, show in some cases a Ca-phosphate filling that occurred during early diagenesis and a later cementation of carbonates (spatic calcite and subordinate Mg-Ca carbonates) or gypsum. Differing from what has been recorded at various sites of the Pisco Formation, micritic clotted dolomite filling the bone cavities and dolomite envelopes have not been observed with fossil vertebrates at Ullujaya. In the deposits of the Pisco Formation, dolomite concretions grew around vertebrate carcasses during the very early phases of diagenesis, as a consequence of anaerobic degradation processes of organic matter leading to cementation of the surrounding matrix (Gariboldi et al. 2015; Gioncada et al. 2016). Therefore, the formation of dolomite nodules requires an early covering of the vertebrate carcass by sediment (e.g., via sinking into a soupy substrate or rapid burial by high rates of sediment deposition) (Gariboldi et al. 2015; Gioncada et al. 2016). Moreover, microbially mediated degradation processes inducing dolomite precipitation are more likely to be efficient if the amount of decaying organic matter is large and permeability of the embedding sediment is low, both conditions favoring a locally anoxic environment. At Ullujaya, taphonomic and sedimentological evidence accounts against rapid sinking and/or burial of the vertebrate carcasses, supporting instead the hypothesis that their deposition occurred after substantial defleshing and the consequent exposure of the bones on the seafloor. Such a prolonged biostratinomic journey likely contributed to prevent the formation of dolomite envelopes around the Ullujaya marine vertebrate remains.

The fine-quality preservation of the bones, the absence of adhering phosphate crusts or nodules, and the above reported sedimentary evidence also exclude the interpretation of the *Ct1a* vertebrate assemblage as a condensed deposit due to hiatal and/or lag concentration consequent to low sedimentation rates or erosion (see Pyenson et al. 2009; Boessenecker et al. 2014).

17.2. Pyrite framboid distribution and anoxic events in the Chilcatay Formation

During microscopic observations of the *Ct1a* sediments, abundant, subspherical framboidal aggregates of Fe-oxyhydroxide microcrystals, representing relic textures of pyrite framboids were detected through the sediment, which consists of small rhombohedral crystals of dolomite terrigenous clasts, and biogenic fragments (Fig. 17.5). Following Wilkin et al. (1996), the diameter of the framboids was measured in five samples from *Ct1a*, selected between 22 and 28.5 m above the base of the measured section (abbreviated: abs), where a high concentration of fossil vertebrates was found (Fig. 17.6). Framboids from 22 m abs, 23.5 m abs, 26 m abs, and 28.5 m abs exhibit a mean diameter of 4.6 ± 2.0 μm (as 1σ), 5.1 ± 1.9 μm, 5.3 ± 2.2 μm, and 5.0 ± 1.9 μm, respectively. Sample UL-D3 (25 m abs) exhibits a higher mean diameter of 8.3 ± 4.8 μm. Framboids having a diameter >10 μm are 3.8% at most except for sample UL-D3 having a high percentage of large framboids (32.5%). Irregularly-shaped framboids are rare and concentrated in sample UL-D3.

According to Agbi et al. (2015), the size distribution of framboidal pyrite could be used for distinguishing between oxic-dysoxic and euxinic conditions in the paleo-bottom water, using the method applied by Wilkin et al. (1996) in modern sediments. Wilkin et al. (1996) noticed that pyrite framboids from euxinic environments are generally smaller and less variable in size than those from sediments underlying oxic or dysoxic bottom water, and related this feature with the different formation mechanisms of pyrite (Raiswell

& Berner 1985), which is syngenetic in euxinic settings and diagenetic in sediments underlying oxic water columns. In the *Ct1a* sediments exposed at Ullujaya, the size distribution of ex-pyrite framboids suggests an alternation of periods characterized by euxinic and oxic-dysoxic conditions (Fig. 17.7).

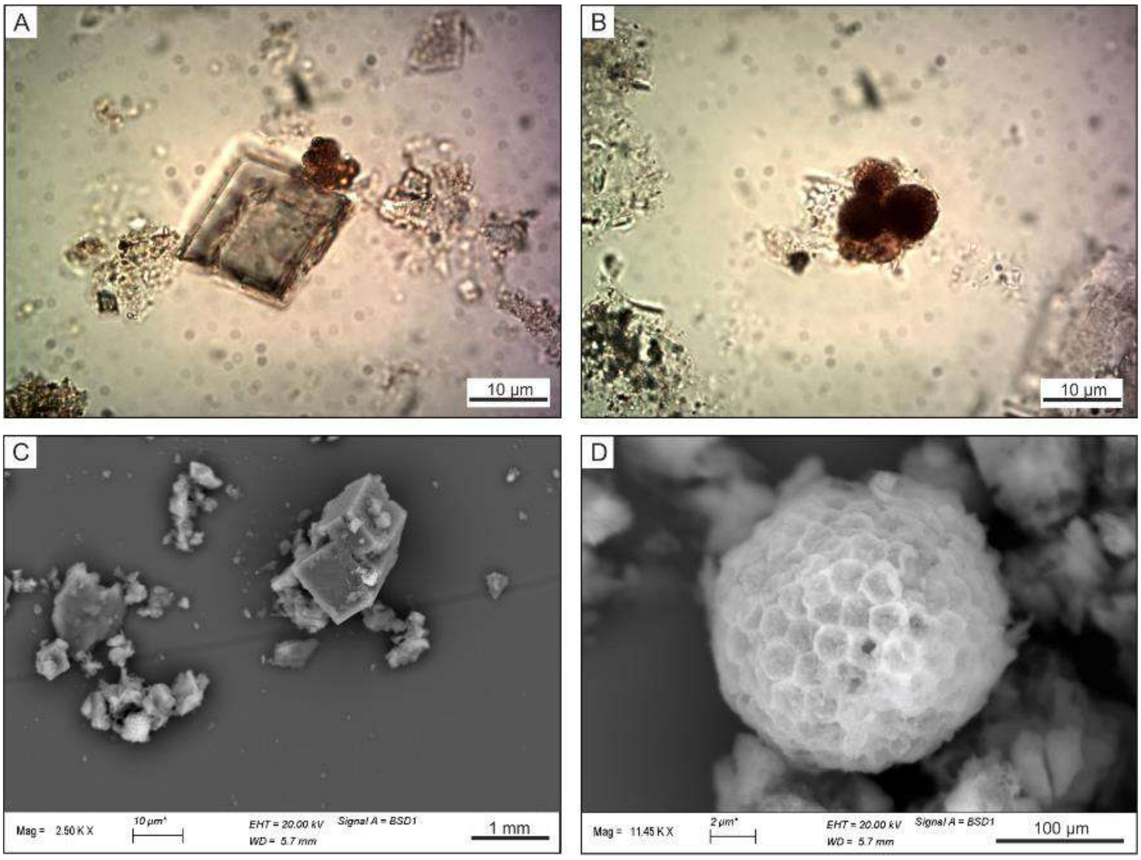

Figure 17.5. Optical photos (a, b) and backscattered Scanning Electron Microscope (c, d) images of pyrite relics from the sediments of Ct1a. a) Rhombohedral crystals of dolomite associated with relics of pyrite framboids. b) Spherical relics of pyrite framboids. c) Rhombohedral crystals of dolomite. d) Detail of the framboidal texture of a pyrite relic. From Bianucci et al. (2018).

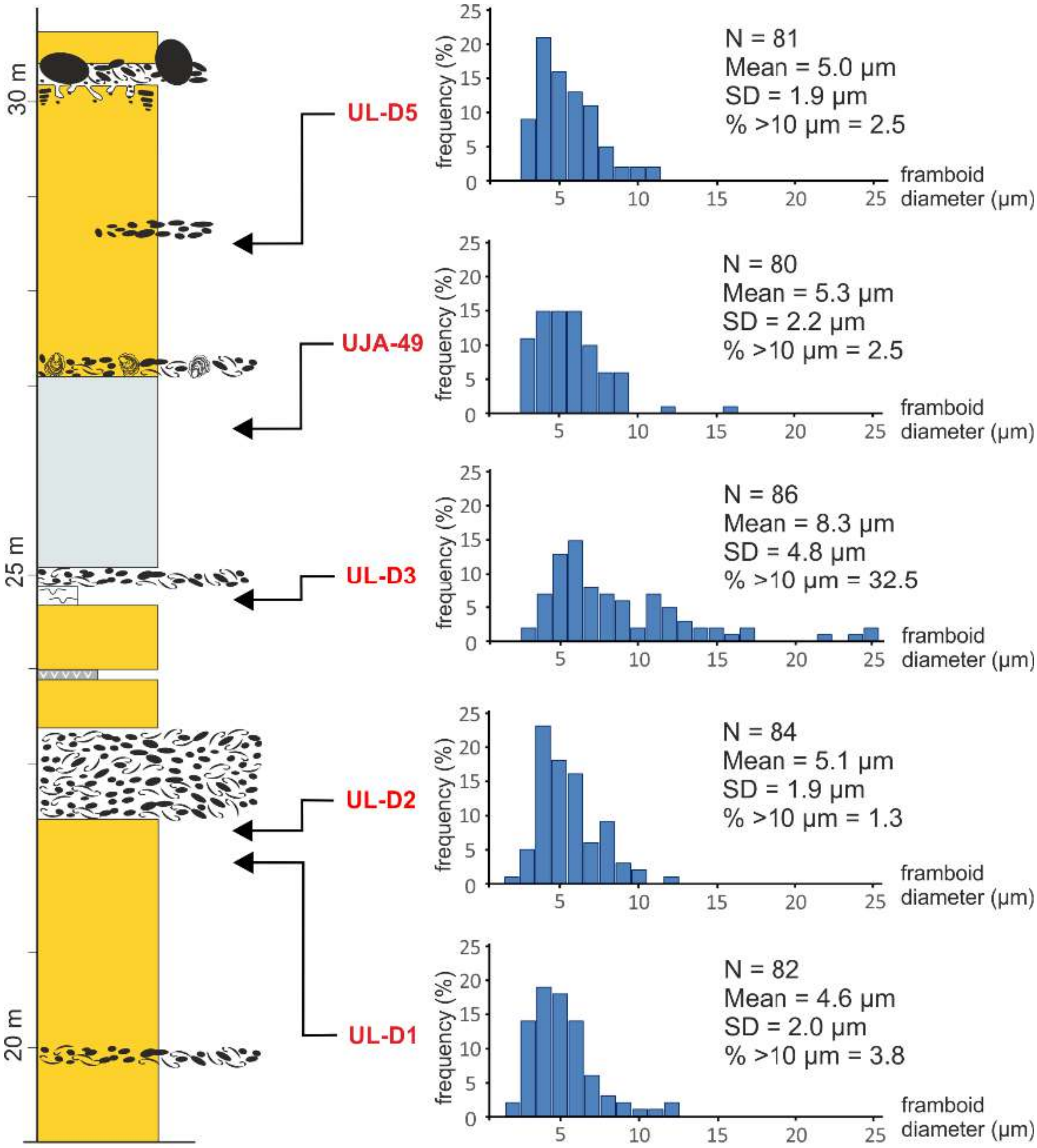

Figure 17.6. Histograms of the size distribution of framboids in *Ct1a*, between 22 and 28.5 m abs. The number of pyrite framboids relics (N), the mean of framboid diameter, the Standard Deviation (SD) of the mean, and the percentage of framboids with a diameter >10 µm are shown for each sample. Note the different distribution in the UL-D3 histogram with respect to the other samples. From Bianucci et al. (2018).

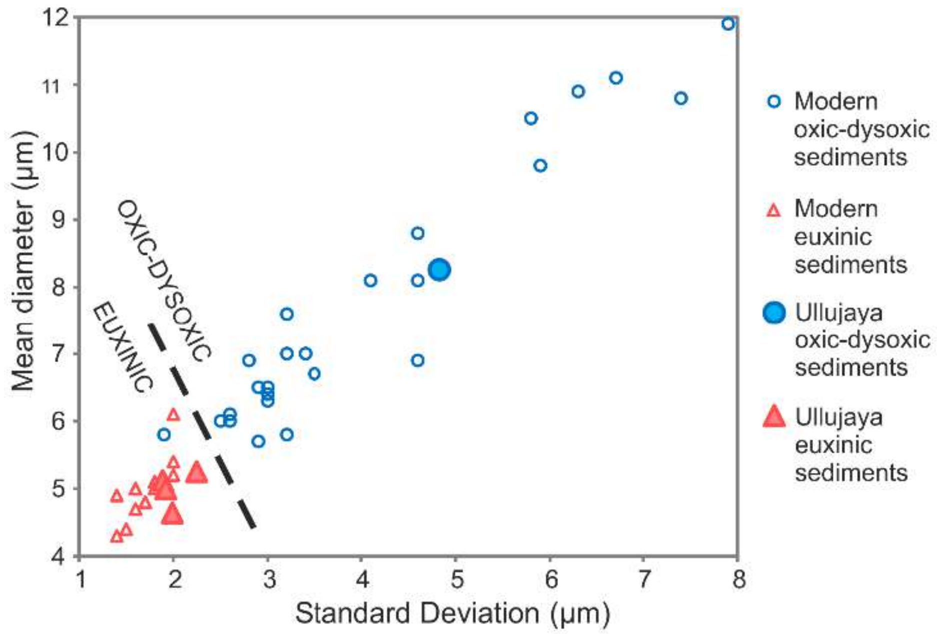

Figure 17.7. Diagram of framboid size distribution as a result of euxinic or oxic-dysoxic conditions. Data on modern euxinic and oxic-dysoxic environments are from Wilkin et al. (1996). Following the example of Agbi et al. (2015), these literature data are compared with our results. Samples from Ct1a provide evidence of the alternation of euxinic and oxic-dysoxic conditions at the seafloor. From Bianucci et al. (2018).

As recorded in the modern euxinic environments (Wilkin et al. 1996), framboids from samples UL-D1, UL-D2, UJA-49, and UL-D5 exhibit a mean diameter close to 5.0 ± 1.7 µm and large (i.e., >10 µm) framboids are scarce, accounting for < 4% of the measured aggregates. Indeed, framboids from sample UL-D3 exhibit a mean diameter of 8.3 µm (± 4.8) and > 30% of them is large-sized, in agreement with the description of pyrite aggregates from modern oxic-dysoxic environments, with a mean of 7.7 ± 4.1 µm and 10-50% of framboids >10µm (Wilkin et al. 1996). Therefore, the *Ct1a* paleoenvironment of Ullujaya was interested by some euxinic events; on the other hand, the marine fossil assemblages found in the Ct1 allomember, including bivalves and barnacles in the shallow-water *Ct1b* and fish and cetaceans in the inner shelf *Ct1a*, suggest normal oxygenation in nearshore areas, where breaking waves efficiently mixed oxygen from the atmosphere into the water.

Further supporting the hypothesis of poorly oxygenated bottom waters, is the presence of *Thalassinoides*-*Gyrolithes*-burrowed intervals documented within *Ct1a* (Chapter 6, Part I) resembling the "doomed pioneers trace fossil assemblages" documented by Föllmi and

Grimm (1990). In their doomed pioneer hypothesis, the authors argued that ichnofabrics beneath gravity-flow event beds deposited in generally inhospitable environments (e.g., benthic oxygen-deficiency) may be the product of adult allochtonous crustaceans that probably grew up in the well-oxygenated marginal areas and survived exhumation, transport by gravity-driven sediment flows, and re-deposition into deeper-water, oxygen-depleted depositional sites. Based on their interpretation, the displaced callianassid tracemakers are versatile enough to live and feed under the new oxygen-deficient bottom conditions for a short period of time before dying from suffocation and, therefore, may successfully penetrate the substrate to create conspicuous dwelling burrow networks. Accordingly, the systematic absence of additional ichnogenera and autochthonous body fossils of shelled benthic organisms throughout *Ct1a* supports the possibility that the *Thalassinoides*-*Gyrolithes*-burrowed intervals reflect short-term burrowing activity of doomed pioneers in an otherwise oxygen-deficient sea-bottom environment normally inhibiting benthic life (Föllmi & Grimm 1990).

A key role in the development of oxygen-deficient conditions on the sea floor was probably played by local factors, such as the semi-enclosed nature of the East Pisco Basin during deposition of the Chilcatay strata and the likely presence of a nearby upwelling zone where deep, nutrient-enriched water raised towards the surface, causing increased organic productivity and high oxygen demand on the shelf, as observed along the present-day Eastern Pacific margin (Pickering et al. 1989). As a matter of fact, however, diatom forms that are typical of upwelling settings (e.g., *Thalassionema*) do not occur in Ct1, but they are present in the overlying deposits of the Ct2 allomember.

17.3. Vertebrate taphonomy in the Pisco Formation

For understanding if the sedimentation rates had played a role in the preservation in the Pisco Formation as suggested by Brand et al. (2004) and Esperante et al. (2008, 2015), we estimated the sedimentation rates in the Pisco Formation at the locality of Cerro los Quesos taking into account both diatom bioevents and radiometric ages (Fig. 17.8).

We found out a value of ca. 32 cm/ka (0.32 mm/a), similar to those of modern environments and two to four orders of magnitude lower than those proposed by Brand et al. (2004). Therefore, although high sedimentation rates may have played a role, the exceptional preservation of fossils of the Pisco Formation is likely to be due to some additional cause.

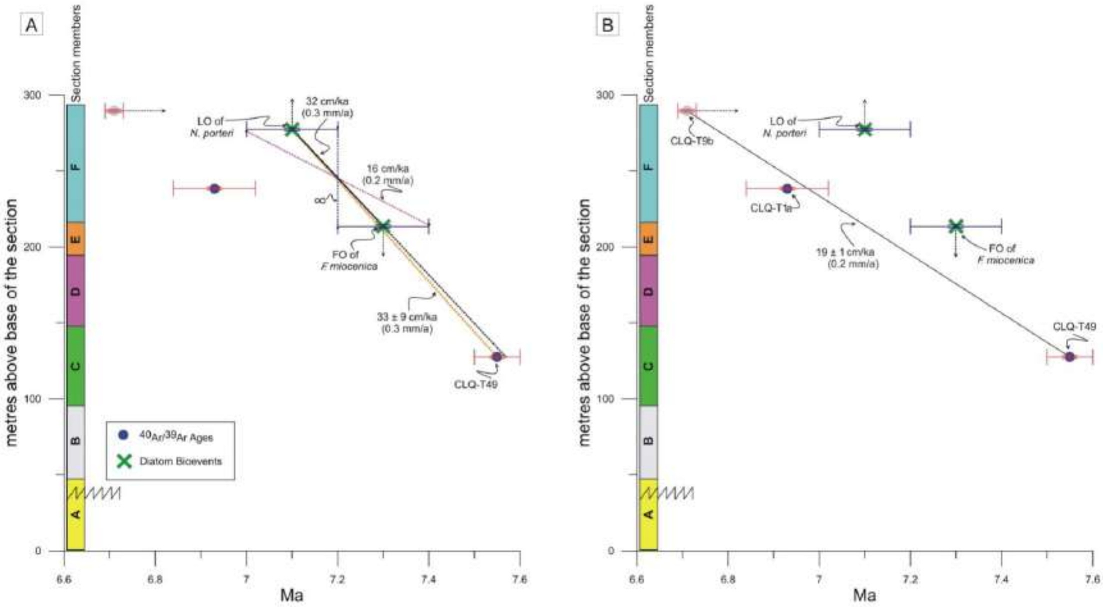

Figure 17.8. Cerro Los Quesos age models taking into account diatom bioevents and radiometric ages. Modified from Gariboldi et al. (2017).

These results support other explanations for the exceptional preservation, such as the formation of dolomite nodules enclosing entirely or partially the fossil vertebrates in the Pisco Formation, as hypothesized by Gariboldi et al. (2015). However, as explained in Chapter 13, not all the specimens are found within carbonate nodules or with inner nodules in the cavities, especially for the small-sized vertebrates.

Consequently, providing a detailed and integrated characterization of the modes of fossilization of small-sized (i.e., less than 2.5 m in total length) vertebrates preserved in absence of dolomite concretions is pivotal for understanding the genesis of the Pisco Formation Fossil-Lagerstätte. For this purpose, we investigated a well-preserved skeleton of a small pontoporiid dolphin, *Brachydelphis mazeasi*, from Pampa Corre Viento, a locality in the Ica Desert (7.5 km north-northeast of Cerro los Quesos) where upper Miocene beds of the Pisco Formation are exposed. This specimen is kept in the Museo de Historia Natural de la Universidad Nacional Mayor de San Marcos of Lima, Peru (hereinafter: MUSM) with accession number MUSM 887. Although this specimen is not enclosed within a dolomite concretion, it is surrounded by an evident dark boundary, suggesting that the processes involved in fossilization left their traces in the form of diagenetic minerals around the cetacean skeleton. Examples of similar dark boundaries around remains of larger-sized vertebrates have been observed in the field within the

Pisco Formation at the localities of Cerro los Quesos and Cerro Colorado (Gariboldi et al. 2015). With the aim of shedding light on the fossilization processes that affected well-preserved skeletons of small-sized vertebrates in the Pisco Formation, we undertook a taphonomic, petrographic, and mineralogical study of MUSM 887 and of its “nodule”, thus adding a new piece to the comprehension of this renowned Fossil-Lagerstätte.

The overall organization of the *Brachydelphis mazeasi* MUSM 887 in two distinct blocks (Fig. 17.9), each of which is comprised of anatomically coherent and rather articulated bones, suggests an early burial of the carcass by soft sediment, followed by gravitational collapse of the body due to decay-related fluidization of the soft tissues, and consequent loss of connectivity of the skeletal elements (e.g., Reisdorf et al. 2014). Moreover, a moderate degree of deformation and bone displacement during diagenetic compaction of the host sediment (e.g., Reisdorf et al. 2012) cannot be excluded, as possibly supported by the observation of load fracturing on the left scapula of MUSM 887 (see Fig. 17.9). Although early burial due to the action of bottom currents (possibly concurring to bone displacement and re-clustering) or to small submarine landslides cannot be excluded, these hypotheses could not be validated in the field. Detachment of portions of the appendicular skeleton before complete burial should also be considered, as suggested by the lack of bony elements of the left forelimb distal to the humerus.

The bones are very well preserved. The microscopic and microanalytical investigations indicate a good degree of mineralization of the bone tissue, now consisting of fluorapatite. Such a degree of mineralization suggests that the post-mortem degradation of collagen within bone tissues was followed, during the early stages of diagenesis, by recrystallization of the original hydroxylapatite, increase of crystallite size, and a consequent reduction of porosity (Trueman & Tuross 2002; Keenan 2016). The new Ca-phosphate phase, namely fluorapatite or carbonated fluorapatite (Pfretzschner 2004; Wopenka & Pasteris 2005), produced by recrystallization of bone hydroxylapatite has been demonstrated to be more stable, even in aqueous solutions at relatively low pH or low phosphorus concentrations (Keenan 2016). Therefore, the presence of environmental conditions facilitating bone recrystallization during early diagenesis was a predominant parameter for the preservation of this beautiful specimen.

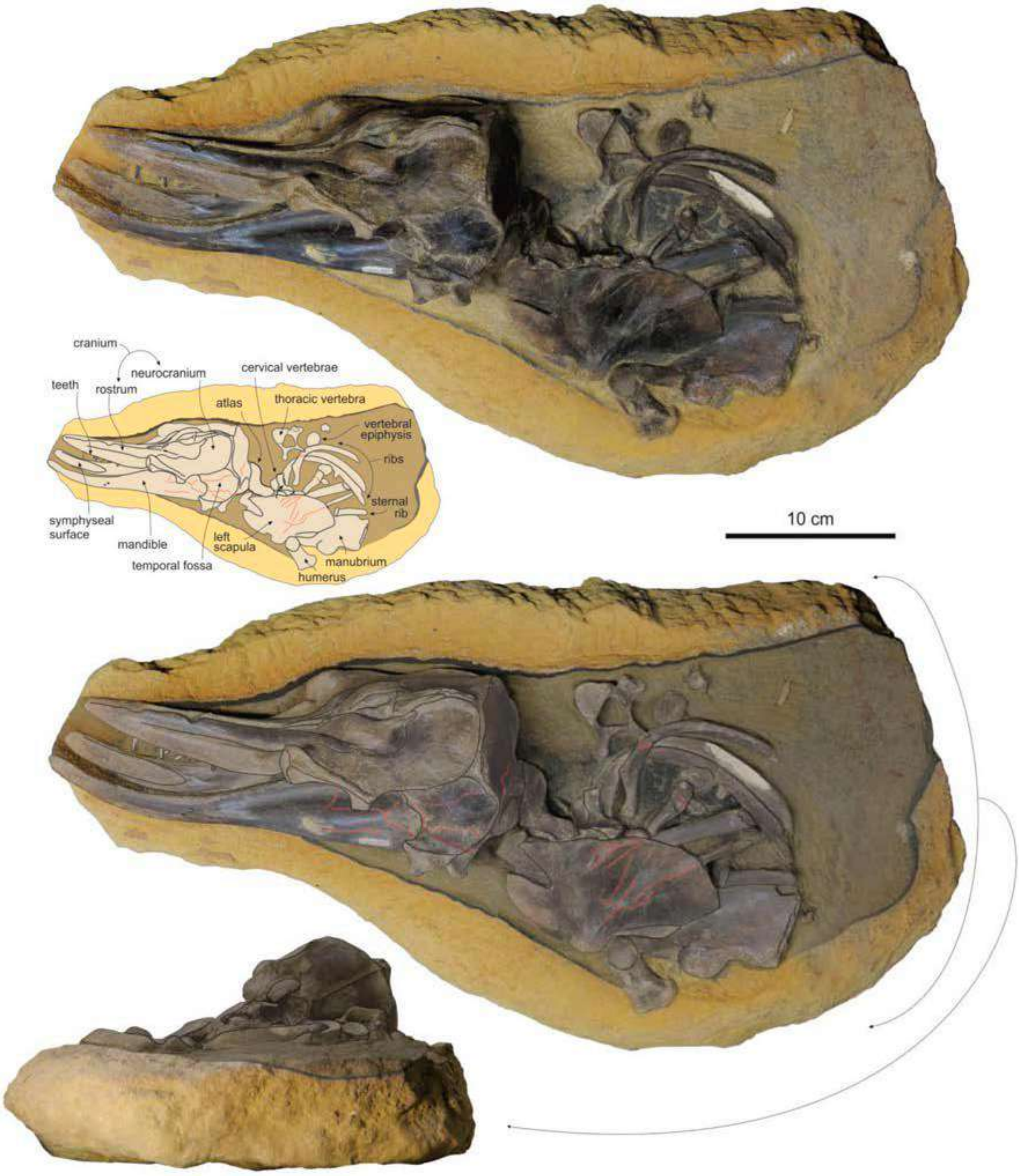

Figure 17.9. The block containing the remains of the skull, bony thorax, and left forelimb of the small dolphin *Brachydelphis mazeasi* MUSM 887, with corresponding line drawings indicating the different elements preserved. Modified from Gioncada et al. (2018).

The presence of the Mn layer below MUSM 887 seemingly encloses the fossil specimen (Fig. 17.9). Several similar examples have been observed in the field, suggesting the same relationship. Therefore, it can be suggested that the formation or preservation of the Mn-cemented dark boundary is strictly related to the presence of the carcass: it delimits the volume of sediment that was affected by chemical conditions differing from the contemporary surrounding sea bottom as a consequence of the decay of the odontocete carcass. Mn-rich layers may form by precipitation of Mn-minerals from seawater at a redox boundary, located below or at the sediment-water interface, as a consequence of the redox-dependent behavior of this element. The sedimentary paleoenvironment of the highly fossiliferous sandstones that constitute the basal beds of the P2 allomember was a shallow-marine upper shelf environment (Di Celma et al. 2017) with an oxic water column and no evidence of anoxic conditions at the seafloor. Therefore, the oxidation front was located below the sediment-water interface, favoring the formation of a concentration of Mn in the upper sediment layer (Fig. 17.10a).

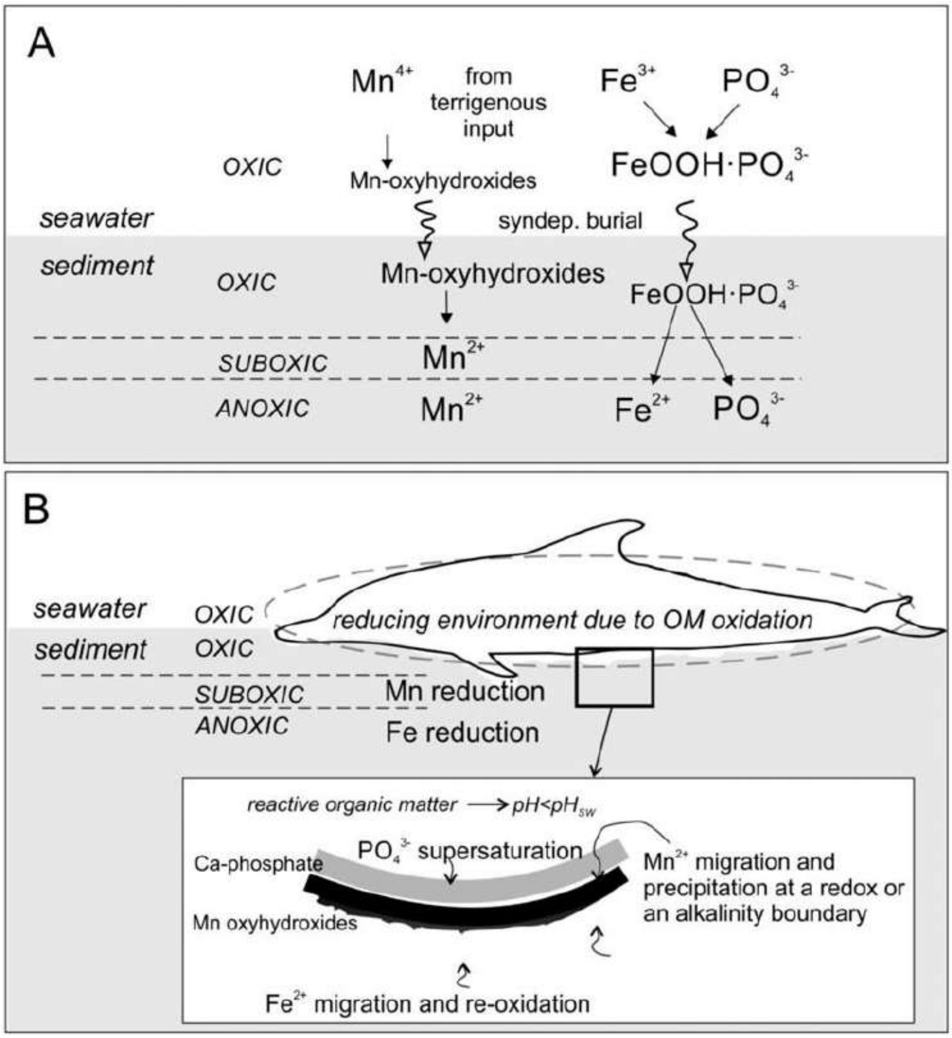

Figure 17.10. a) Manganese, iron and phosphorus behavior at an oxic sea bottom (modified from Cui et al. 2016), OM: organic matter. b) Schematic model summarizing

the hypothesized formation of the mineral pattern around the Corre Viento pontoporiid skeleton under study. From Gioncada et al. (2018).

We can suppose that, after the death of a marine vertebrate, aerobic remineralization of organic matter was the main, although not the sole, mechanism as long as the remains were exposed on the seafloor. In case of large-sized marine vertebrate falls, the oxygen recharge may be locally insufficient for organic matter oxidation, even if the conditions at the seafloor are generally oxic (Allison 1988), and a microbial ecosystem of whale-fall may formed (Allison et al. 1991; Shapiro & Spangler 2009; Danise et al. 2012). In the case of small-size marine vertebrates, such as the pontoporiid specimen MUSM 887, organic matter degradation on the seafloor may be accomplished mainly by aerobic processes.

In the locally anoxic environment created by the decay of the Corre Viento cetacean carcass at the sea bottom, and in case of Mn availability within bottom sediment, Mn-reduction could have been one of the most prominent mechanisms for organic matter remineralization. Additionally, the lowering of pH due to bacterial decay of soft tissues favored Mn solubility. As a consequence, the increased Mn concentration in porewater resulted in the precipitation of Mn minerals at the anoxic-oxic interface and/or at an alkalinity interface, representing the boundary above which porewater was chemically affected by the processes of degradation of the carcass (Fig. 17.10b). Indeed, this Mn-rich layer would not have developed in case of deposition of the dolphin carcass on an anoxic sea bottom.

With an oxic water column and in conditions of high primary productivity such as those of the Corre Viento shelf depositional environment, dissolved phosphate is vehiculated to the seafloor together with Fe^{3+} (as $FeOOH \cdot PO_4^{3-}$) and is then released to the porewater following Fe-reduction in anoxic conditions below the water-sediment interface (Kim et al. 1999; Cui et al. 2016). In the case of the studied pontoporiid, anoxic conditions were induced in correspondence of the carcass by decay processes. Consequently, Fe reduction processes and, possibly, the decay of the carcass itself, released P increasing its concentration in porewater close to the pontoporiid remains, inducing authigenic calcium phosphate precipitation at the boundary with suboxic conditions (Fig. 17.10). The presence of Ca-phosphate immediately below the specimen is, thus, an evidence of availability of P in porewater during the very early diagenesis: this is a factor of prime importance for bone apatite recrystallization and, consequently, for preservation (Keenan 2016; Keenan & Engel 2017). Therefore, the geochemical environment in which the pontoporiid was set once the labile tissues were decayed (probably on a timescale of weeks) can explain the high degree of mineralization observed for the compact bone of the ribs.

Differently from several specimens in the Pisco Formation, in the case here studied, the fossil is not enclosed in a dolomite concretion. Dolomite formation is inhibited by the high dissolved sulfate ion concentration in seawater (Baker & Kastner 1981). The microbially mediated sulfate reduction is able to lower the sulfate ion inhibitory effect and, concomitantly, increases alkalinity (e.g., Compton 1988). In agreement with the lack of dolomite, we did not find evidence of former pyrite framboids, typically a result of sulfate reduction, associated to the bones. We speculate that the Corre Viento sandy sediments allowed the porewater below the water-sediment interface to exchange with seawater in a rather efficient way. Therefore, even with sulfate reduction, the moderate permeability of the sediment enclosing the pontoporiid carcass, coupled with the small body size of the specimen, would have prevented the concentration of dissolved sulfate (inhibiting dolomite formation) to decrease enough (or for long enough) for allowing extensive dolomite formation (Vasconcelos et al. 1995; Meister 2013). Interestingly, the neurocranium of MUSM 887 is well preserved and barely deformed (Fig. 17.9). This could be explained by hypothesizing that the inside of the brain cavity is filled by early-formed diagenetic minerals, very likely dolomite, as it is commonly observed in fossil vertebrates of the Pisco Formation, including small-sized animals (Gariboldi et al. 2015; Gioncada et al. 2016).

As a general consideration, the observation of regular and recurrent patterns for the distribution of diagenetic minerals in the sediment enclosing fossil vertebrates, without or with limited carbonate concretions, gives insights into the early taphonomic history of these remains, just as dolomite concretions do. In the case of the pontoporiid skeleton here investigated, this pattern reveals a situation favorable to preservation, with early burial and the establishment of local anoxic/suboxic porewater environment, even if the surrounding seafloor environment and water column were characterized by fully oxic conditions.

The part of this chapter about the vertebrate taphonomy in the Chilcatay Formation is based on some paragraphs of "Taphonomy and palaeoecology of the lower Miocene marine vertebrate assemblage of Ullujaya (Chilcatay Formation, East Pisco Basin, southern Peru)" authored by Giovanni Bianucci, Alberto Collareta, Giulia Bosio, Walter Landini, Karen Gariboldi, Anna Gioncada, Olivier Lambert, Elisa Malinverno, Christian de Muizon, Rafael Varas-Malca, Igor Maria Villa, Giovanni Coletti, Mario Urbina and Claudio Di Celma, published in 2018 on Palaeogeography, Palaeoclimatology, Palaeoecology, Vol. 511, 256-279. In this paper, Giulia Bosio contributes to sample collection, measurement of the stratigraphic section and field mapping, optical microscope analyses on sediments, ex-pyrite framboid measurement, vertebrate taphonomy and microscopic analyses on bones, discussion on the paleoenvironment reconstruction and vertebrate taphonomy.

Regarding the Pisco Formation vertebrate taphonomy, the chapter refers to "Biostratigraphy, geochronology and sedimentation rates of the upper Miocene Pisco Formation at two important marine vertebrate fossil-bearing sites of southern Peru" written by Karen Gariboldi, Giulia Bosio, Elisa Malinverno, Anna Gioncada, Claudio Di Celma, Igor M. Villa, Mario Urbina and Giovanni Bianucci, published on Newsletters on Stratigraphy in 2017, Vol. 50/4 (2017), 417-444. In this paper, Giulia Bosio contributes to sample collection, volcanic ash analyses, ^{39}Ar–^{40}Ar geochronology, discussion on the previous dating and the new results, comparison of data and calculation of sedimentation rates. It also refers to the paper "Looking for the key to preservation of fossil marine vertebrates in the Pisco Formation of Peru: new insights from a small dolphin skeleton" written by Anna Gioncada, Karen Gariboldi, Alberto Collareta, Claudio Di Celma, Giulia Bosio, Elisa Malinverno, Olivier Lambert, Jennifer Pike, Mario Urbina, Giovanni Bianucci, published in 2018 on Vol. 45(3) of Andean Geology. In this paper, Giulia Bosio contributes to the discussion on the bone fossilization and the chemical processes that contribute to the fossil preservation.

Chapter references

Agbi, I., Ozibo, B., Newton, R. 2015. Pyrite framboid size distribution of the Grey Shales (Yorkshire UK) as an indication of redox conditions. IOSR Journal of Applied Geology and Geophysics, 3, 36-42.

Allison, P.A. 1988. The decay and mineralization of proteinaceous macrofossils. Paleobiology, 14, 139-154.

Allison, P.A., Smith, C.R., Kukert, H., Deming, J.W., Bennett, B.A. 1991. Deep-water taphonomy of vertebrate carcasses: a whale skeleton in the bathyal Santa Catalina Basin. Paleobiology, 17, 78-89.

Baker, P.A., Kastner, M. 1981. Constraints on the formation of sedimentary dolomite. Science 213(4504), 214-216.

Bianucci, G., Collareta, A., Bosio, G., Landini, W., Gariboldi, K., Gioncada, A., Lambert, O., Malinverno, E., Muizon, de C., Varas-Malca, R., Villa, I.M., Coletti, G., Urbina, M., Di Celma, C. 2018. Taphonomy and palaeoecology of the lower Miocene marine vertebrate assemblage of Ullujaya (Chilcatay Formation, East Pisco Basin, southern Peru)". Palaeogeography, Palaeoclimatology, Palaeoecology, 511, 256-279.

Bianucci, G., Lambert, O., Post, K. 2010. High concentration of long-snouted beaked whales (genus Messapicetus) from the Miocene of Peru. Palaeontology, 53, 1077-1098.

Beardmore, S.R., Orr, P.J., Manzocchi, T., Furrer, H., Johnson, C. 2012. Death, decay and disarticulation: modelling the skeletal taphonomy of marine reptiles demonstrated using Serpianosaurus (Reptilia; Sauropterygia). Palaeogeography, Palaeoclimatology, Palaeoecology, 337, 1-13.

Boessenecker, R.W., Perry, F.A., Schmitt, J.G. 2014. Comparative taphonomy, taphofacies, and bonebeds of the Mio-Pliocene Purisima Formation, Central California: strong physical control on marine vertebrate preservation in shallow marine settings. PLoS ONE, 9, e91419.

Brand, L., Esperante, R., Chadwick, A.V., Porras, O. P., Alomía, M. 2004. Fossil whale preservation implies high diatom accumulation rate in the Miocene–Pliocene Pisco Formation of Peru. Geology, 32(2), 165-168.

Compton, J.S. 1988. Degree of supersaturation and precipitation of organogenic dolomite. Geology, 16(4), 318-321.

Cui, H., Xiao, S., Zhou, C., Penge, Y., Kaufman, A.J., Plummer, R.E. 2016. Phosphogenesis associated with the Shuram Excursion: Petrographic and geochemical observations from the Ediacaran Doushantuo Formation of South China. Sedimentary Geology, 341, 134-146.

Danise, S., Cavalazzi, B., Dominici, S., Westall, F., Monechi, S., Guioli, S. 2012. Evidence of microbial activity from a shallow water whale fall (Voghera, northern Italy). Palaeogeography, Palaeoclimatology, Palaeoecology, 317-318, 13-26.

Di Celma, C., Malinverno, E., Bosio, G., Collareta, A., Gariboldi, K., Gioncada, A., Molli, G., Basso, D., Varas-Malca, R., Pierantoni, P.P., Villa, I.M., Lambert, O., Landini, W., Sarti, G., Cantalamessa, G., Urbina, M., Bianucci, G. 2017. Sequence stratigraphy and paleontology of the upper Miocene Pisco Formation along the western side of the lower Ica Valley (Ica Desert, Peru). Rivista Italiana di Paleontologia e Stratigrafia (Research In Paleontology and Stratigraphy), 123(2), 255-273.

Esperante, R., Brand, L., Nick, K., Poma, O., Urbina, M. 2008. Exceptional occurrence of fossil baleen in shallow marine sediments of the Neogene Pisco Formation, Southern Peru. Palaeogeography, Palaeoclimatology, Palaeolecology, 257, 344-360.

Esperante, R., Brand, L. R., Chadwick, A.V., Poma, O. 2015. Taphonomy and paleoenvironmental conditions of deposition of fossil whales in the diatomaceous sediments of the Miocene/Pliocene Pisco Formation, southern Peru – a new Fossillagerstätte. Palaeogeography, Palaeoclimatology, Palaeoecology, 417, 337-370.

Föllmi, K.B., Grimm, K.A. 1990. Doomed pioneers: gravity-flow deposition and bioturbation in marine dysaerobic environments. Geology, 18, 1069-1072.

Gariboldi, K., Gioncada, A., Bosio, G., Malinverno, E., Di Celma, C., Tinelli, C., Cantalamessa, G., Landini, W., Urbina, M., Bianucci, G. 2015. The dolomite nodules enclosing fossil marine vertebrates in the East Pisco Basin, Peru: field and petrographic insights into the Lagerstätte formation. Palaeogeography, Palaeoclimatology, Palaeoecology, 438, 81-95.

Gioncada, A., Collareta, A., Gariboldi, K., Lambert, O., Di Celma, C., Bonaccorsi, E., Urbina, M., Bianucci, G. 2016. Inside baleen: exceptional microstructure preservation in a late Miocene whale skeleton from Peru. Geology, 44, 839-842.

Keenan, S.W. 2016. From bone to fossil: A review of the diagenesis of bioapatite. American Mineralogist, 101, 1943-1951.

Keenan, S.W., Engel, A.S. 2017. Early diagenesis and recrystallization of bone. Geochimica et Cosmochimica Acta, 196, 209-223.

Kiel, S., Goedert, J.L., Kahl, W.-A., Rouse, G.W. 2010. Fossil traces of the bone-eating worm Osedax in early Oligocene whale bones. Proceedings of the National Academy of Sciences, 107, 8656-8659.

Kim, D., Schuffert, J.D., Kastner, M. 1999. Francolite authigenesis in California continental slope sediments and its implications for the marine P cycle. Geochimica et Cosmochimica Acta, 63(19-20), 3477-3485.

Meister, P. 2013. Two opposing effects of sulfate reduction on carbonate precipitation in normal marine, hypersaline, and alkaline environments. Geology, 41(4), 499-502.

Pfretzschner, H.U. 2004. Fossilization of Haversian bone in aquatic environments. Comptes Rendus Palevol, 3, 605-616.

Pickering, K.T., Hiscott, R.N., Hein, F.J. 1989. Deep-marine Environments: Clastic Sedimentation and Tectonics. Unwin Hyman, London.

Pyenson, N.D., Irmis, R.B., Lipps, J.H., Barnes, L.G., Mitchell Jr., E.D., McLeod, S.A. 2009. Origin of a widespread marine bonebed deposited during the middle Miocene Climatic Optimum. Geology, 37, 519-522.

Raiswell, R., Berner, R.A. 1985. Pyrite formation in euxinic and semi-euxinic sediments. American Journal of Science, 285, 710-724.

Reisdorf, A.G., Anderson, G.S., Bell, L.S., Klug, C., Schmid-Röhl, A., Röhl, H.J., Jung, M., Wuttke, M., Maisch, M.W., Benecke, M., Wyler, D., Bux, R., Fornaro, P., Wetzel, A. 2014. Reply to "Ichthyosaur embryos outside the mother body: not due to carcass explosion but to carcass implosion" by van Loon (2013). Palaeobiodiversity and Palaeoenvironments, 94, 487-494.

Reisdorf, A.G., Bux, R., Wyler, D., Benecke, M., Klug, C., Maisch, M.W., Fornaro, P., Wetzel, A. 2012. Float, explode or sink: postmortem fate of lung-breathing marine vertebrates. Palaeobiodiversity and Palaeoenvironments, 92(1), 67-81.

Schäfer, W. 1972. Ecology and Palaeoecology of Marine Environments. University of Chicago Press, Chicago.

Shapiro, R.S., Spangler, E. 2009. Bacterial fossil record in whale-falls: petrographic evidence of microbial sulfate reduction. Palaeogeography, Palaeoclimatology, Palaeoecology, 274, 196-203.

Smith, C.R., Glover, A.G., Treude, T., Higgs, N.D., Amon, D.J. 2015. Whale-fall ecosystems: recent insights into ecology, paleoecology, and evolution. Annual Review of Marine Science, 7, 571-596.

Trueman, C.N., Tuross, N. 2002. Trace elements in recent and fossil bone apatite. Reviews in Mineralogy and Geochemistry, 48, 13-49.

Vasconcelos, C., McKenzie, J.A., Bernasconi, S., Grujic, D., Tien, A.J. 1995. Microbial mediation as a possible mechanism for natural dolomite formation at low temperatures. Nature, 377, 220-222.

Wilkin, R.T., Barnes, H.L., Brantley, S.L. 1996. The size distribution of framboidal pyrite in modern sediments: an indicator of redox conditions. Geochimica et Cosmochimica Acta, 60, 3897-3912.

Wopenka, B., Pasteris, J.D. 2005. A mineralogical perspective on the apatite in bone. Materials Science and Engineering C, 25, 131-143.

FINALE

Chapter 18. General discussion

18.1. Evolution and cycles of the East Pisco Basin during the Miocene

Measuring and mapping the Miocene sedimentary successions in the western side of the Ica River, we noticed that the thickness of the exposed successions increases from the north-northwest to the south-southeast (Fig. 18.1). In particular, the Pisco Formation can be considered a wedge of sediment that thins to the northeast, a trend present also within each of the three Pisco allomembers in which it is subdivided. Therefore, the East Pisco Basin has its depocenter in the south of our study area (see Fig. 18.1) and the coastline was settled northeastward.

Our studies on these Miocene successions of the East Pisco Basin reveal a cyclic pattern in sedimentation. Chilcatay and Pisco formations are bounded by regionally extended unconformities characterized by basement clasts, shark teeth, polished bones and phosphoritic nodules, sometimes accompanied by ostreids. These unconformities are locally accompanied by angular unconformities and, therefore, they would be better defined as alloformations referring to allostratigraphy (NACSN, 2005). In turn, as described in Chapter 6 and Chapter 9 of this dissertation, we subdivided both Chilcatay and Pisco formations in unconformity-bounded allomembers, which represent transgressive phases interrupted by regressive events (Fig. 18.1 and Fig. 18.2). These unconformities are the result of the subaerial exposure during periods of lowered sea level. In the Pisco Formation, we observed that the three unconformities converge landwards into a main single surface representing the lowest boundary of the Pisco Formation. The lower part of each allomember exhibits a fining-upward and deepening-upward succession, with medium-grained sandstones at the base, and siltstones, mudstones or diatomaceous siltstones at the top of the allomember (see Fig. 18.1 and Fig. 18.2). The lithology suggests a transgressive facies for each allomember. In turn, the regressive events are not registered, because either there is no deposition during regression events or because erosion took the regressive deposits away during the periods of subaerial exposure.

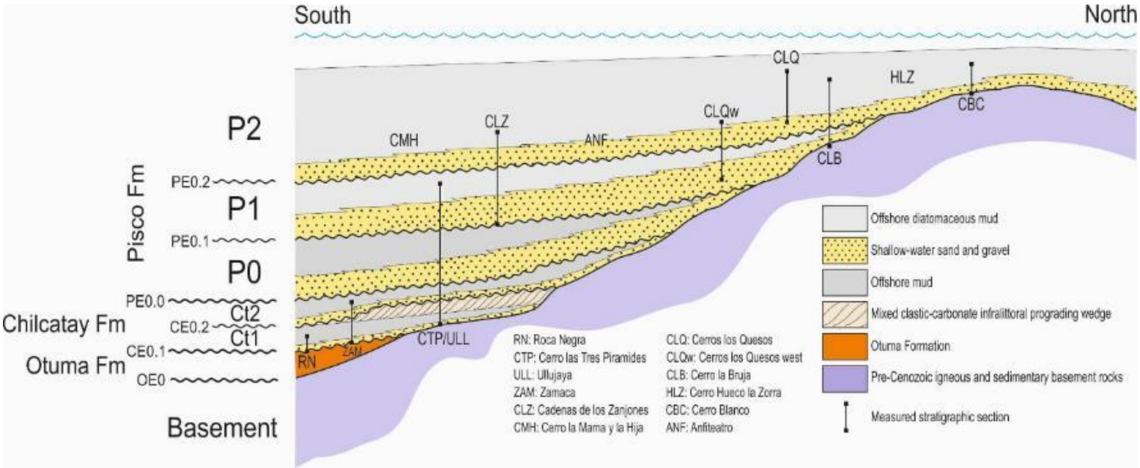

Figure 18.1. Reconstruction of the East Pisco Basin sedimentation. Modified from Di Celma et al. (2017).

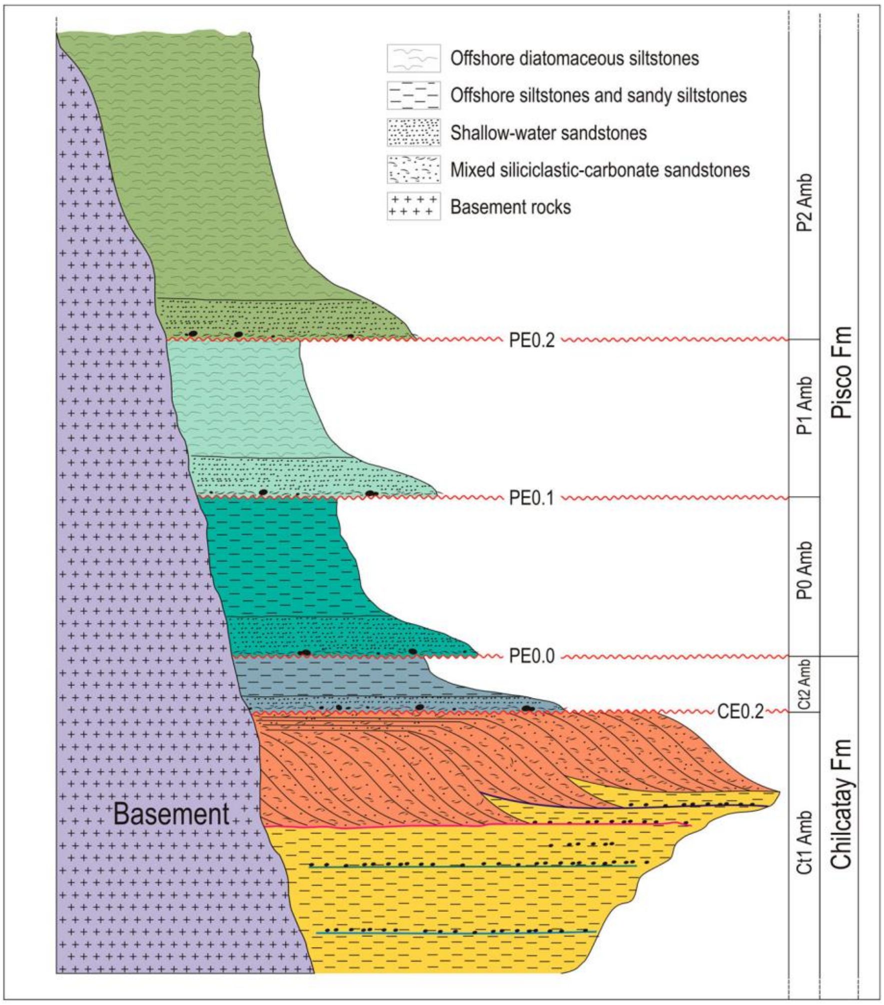

Figure 18.2. Schematic stratigraphic section of Chilcatay and Pisco formations. Modified from Di Celma et al. (2018).

The age constrains obtained by different methods in our chronostratigraphic studies gave the possibility of assigning an age to these transgressive cycles and unconformities. Both Chilcatay and Pisco formations exposed in the western side of the Ica River exhibit a Miocene age: the Chilcatay Formation is Burdigalian, constrained between 19.25 and 18.02 Ma (base of the Ct1 allomember and top of the Ct2 allomember, respectively); the P0 allomember is Langhian – Serravallian, the oldest obtained age is 14.80 Ma and the youngest is 12.60 Ma; the P1 allomember is entirely Tortonian, from 9.46 to 8.60 Ma; and the P2 allomember is Tortonian – Messinian, between 8.39 and 6.71 Ma.

Thanks to this chronostratigraphic framework, we can try to reconstruct the origin of these transgressive cycles. Despite the tectonic activity affecting the East Pisco Basin through the Cenozoic, a comparison between the ages estimated for each Pisco Basin unconformities and the Mi-events identified by Miller et al. (1991) based on the deep-sea oxygen isotopic record as a proxy of glacio-eustatic fluctuations can be hypothesized, as attempted by Di Celma et al. (2018). A cooling phase characterized by several short-lived periods of glaciations started during the Miocene (Zachos et al. 2001). These periods can be identified with the Mi-Events of Miller et al. (1991), in which the lowering of the sea level is related to the increase of the continental ice volume on Antarctica.

For all the formations, the boundaries are time-transgressive; therefore, the base of the formations can be diachronous, as stated for the Chilcatay Formation. In the study area, the base of the Chilcatay Formation is assigned to ca. 19.25 Ma, but in other localities, such as at Cerros Las Salinas and Cerro La Virgen about 100 and 70 km northwest of Ullujaya, the lowermost strata have been dated to the late Oligocene by DeVries and Jud (2018). In the study area, the CE0.1 unconformity, separating the Chilcatay Formation from the underlying Otuma Formation, can correlate with the Mi1aa oxygen isotope maximum dated at ca. 20.0 Ma by Browning et al. (2013). Considering the fact that the base of the Chilcatay Formation can be older in other localities, this unconformity can be assigned to the Mi1 dated at ca. 23.2 Ma by Browning et al. (2013) (see Fig. 18.3). Within the Chilcatay Formation there is another unconformity, CE0.2, which divides the Ct1 allomember from the overlying Ct2 allomember. This unconformity can be related to the Mi1ab, dated at ca. 18.7 Ma (Browning et al. 2013, see Fig. 18.3), even an age at the top of Ct1 or at the base of Ct2 is not still obtained.

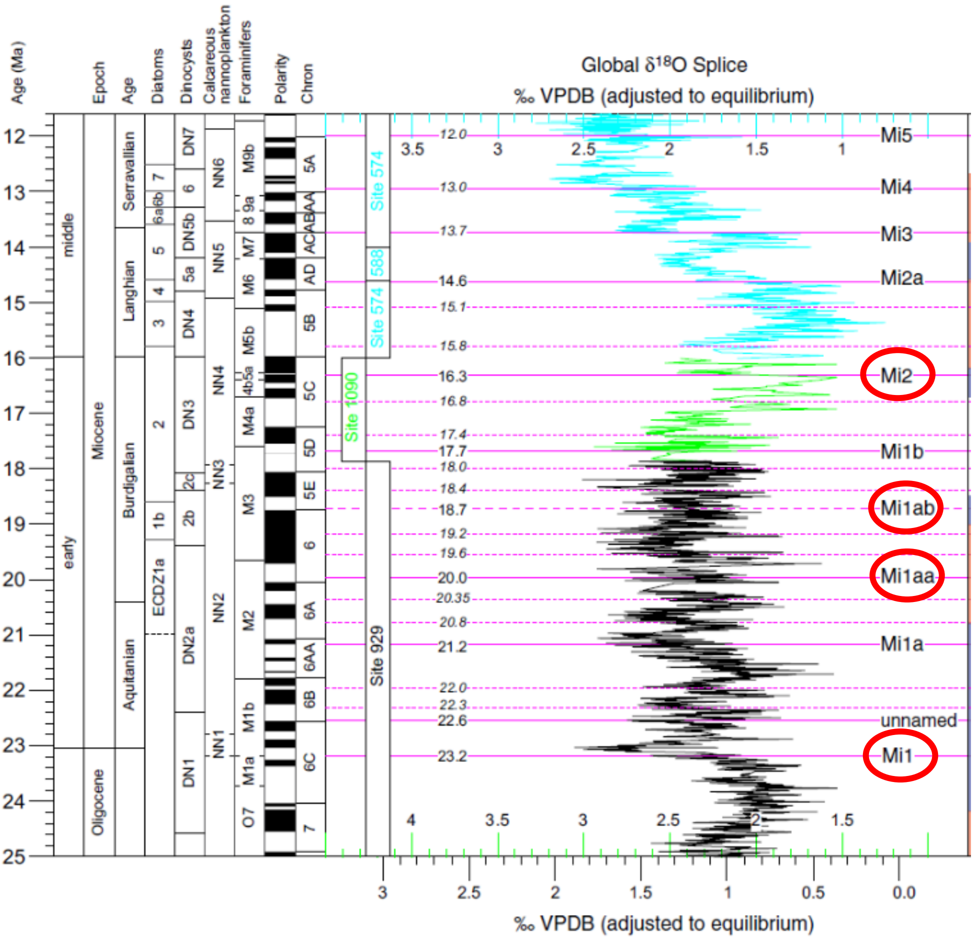

Figure 18.3. Ages for Mi-events from the Integrated Ocean Drilling Program Expedition 313. Modified from Browning et al. (2013).

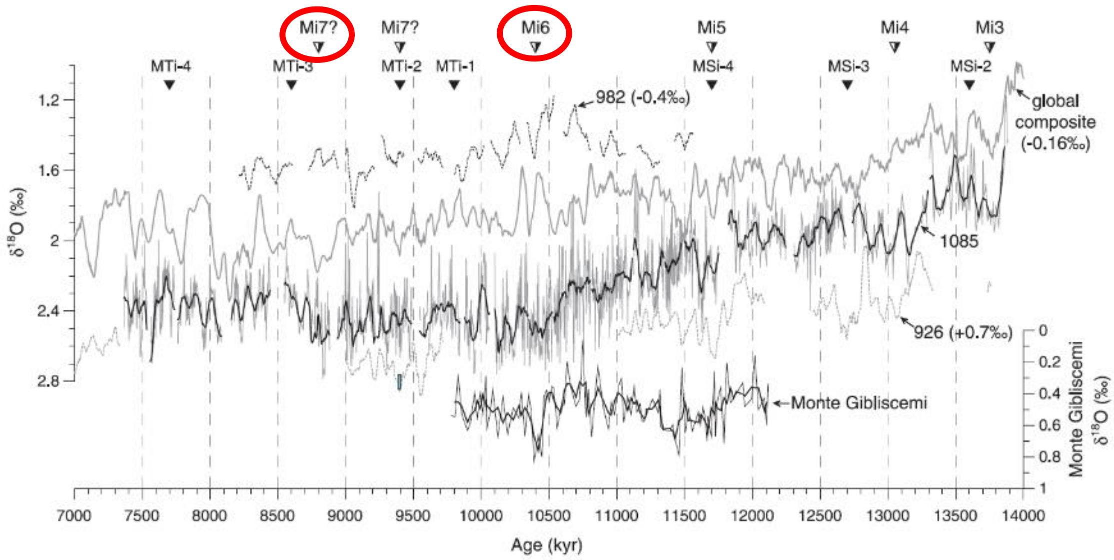

Figure 18.4. Comparison between the long-term trends in the benthic stable oxygen isotope record from ODP Site 1085 (solid black line), ODP Site 926 (dashed gray line),

ODP Site 982 (dashed black line), the global deep sea composite of Zachos et al. (2001a) (solid grey line), and the Monte Gibliscemi record (thin black line; Turco et al., 2001). Modified from Westerhold et al. 2005.

Unconformities	Allomembers	Mi-events	Ages (Ma)
	P2		
PE0.2		Mi7	8.7
	P1		
PE0.1		Mi6	10.3
	P0		
PE0.0		Mi2	16.3
	Ct2		
CE0.2		Mi1ab	18.7
	Ct1		
CE0.1		Mi1aa / Mi1	20.0 / 23.2

Table 18.1. Attempt of correlating Miocene Pisco Basin unconformities and the Mi oxygen isotopic maximum events of Miller et al. (1991). Ages are referred to Browning et al. (2013), Miller et al. (1998), Turco et al. (2001) and Westerhold et al. (2005).

The PE0.0 unconformity, between the Chilcatay Formation and the lowest allomember of the Pisco Formation, P0, can correlate with the Mi2 oxygen isotope maximum dated at ca. 16.3 Ma (Browning et al. 2013), differently from what hypothesized in Chapter 10, without the Sr isotope results (Fig. 18.3). Finally, as hypothesized in Chapter 10, the PE0.1 unconformity separating P0 from P1 allomembers can be related to the Mi6 oxygen isotopic maximum dated at 10.3 Ma by Miller et al. (1998), and astronomically dated at 10.4 Ma by Turco et al. (2001) and Westerhold et al. (2005) (Fig. 18.4). Finally, the PE0.2 unconformity between P1 and P2 allomembers can be assigned to the Mi7 isotopic maximum dated at 8.7 Ma by Miller et al. (1998) and Westerhold et al. (2005) (Fig.18.4), as stated in Chapter 10. This correlation, summarized in Table 18.1, will be efficient if these breaks in deposition in the East Pisco Basin reflect the eustatic (global) sea level variations or have a tectonic (local) origin.

In addition to these transgressive cycles recognizable in the Chilcatay and Pisco formations, we could also hypothesize a cyclic pattern in lithology, in a more vast scale, considering also the other Eocene – Oligocene units.

Generally speaking, the middle to upper Eocene Paracas Group (Los Choros and Yumaque formations) is dominated by a mainly calcareous and poorly silicic sedimentation, instead the uppermost Eocene – lower Oligocene Otuma Formation comprises fine-grained sediments and characterized by a diatomaceous facies (Dunbar et al. 1990; DeVries 1998, 2017; DeVries et al. 2017; DeVries & Jud 2018). Thus, the Chilcatay and Pisco formations are equally differentiated. The Chilcatay Formation is dominated in the Ct1 allomember by a shallow water sedimentation of mixed siliciclastic-carbonate deposits, enriched in mollusk, echinoid and barnacle fragments, proving that a shallow-marine carbonate factory must have been situated towards the northeast of the locality of Ullujaya, but is no longer preserved or exposed. Moreover, the siltstones of the Ct2 allomember are predominantly rich in carbonate microfossils (calcareous nannofossils and planktonic foraminifera) but become rich in siliceous microfossils (diatoms and silicoflagellates) in the upper portion. This change to the siliceous composition becomes evident in the Pisco Formation, in particular in the youngest P1 and P2 allomembers. In turn, the P0 allomember shows a rather shallow water deposition and a terrigenous sedimentation (no microfossils were observed in this allomember). The carbonate fragments of mollusk and barnacle shells are still present in the P0 allomember, in contrast with P1 and P2 allomembers. We can observe a great change in sediment composition moving to P1 and P2; both units show sandstones at the base and a progressively thinning of grain-size of the sediment, exhibiting diatomaceous siltstones at the top. These siliceous organisms substituted the calcareous one.

It seems, therefore, that the basin passed through different phases of sedimentation during the Cenozoic, with a dominance of the diatom ooze in the late Miocene (and before, in the uppermost Eocene – lower Oligocene Otuma Formation). The siliceous predominance of the late Miocene Pisco Formation could be related to two events: i) the local increase of the primary production in the basin due to the late Miocene cooling and the strengthening of the Humboldt current, already active in the Miocene (Amiot et al. 2008);

ii) the global differentiation of diatom species that causes an increase of the diversity of whales (Marx & Uhen 2010) (Fig. 18.5).

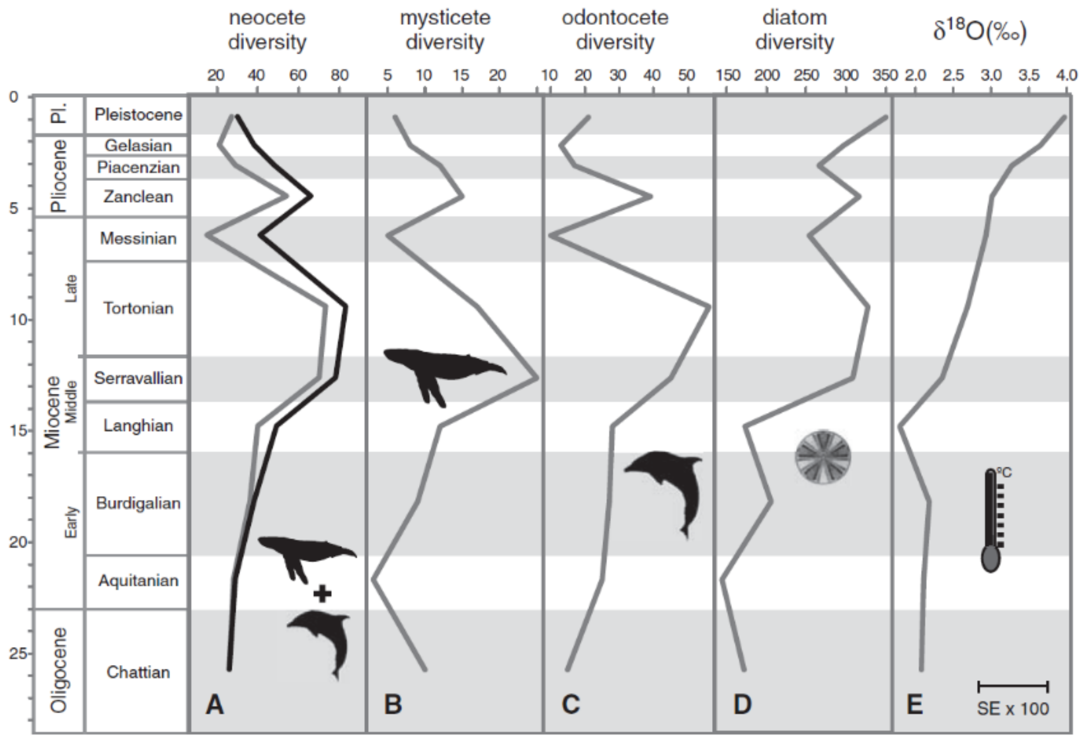

Figure 18.5. Comparison of neocete (a), mysticete (b), and odontocete (c) paleodiversity with diatom paleodiversity (d) and global δ^{18}O values (e). From Marx and Uhen (2010).

18.2. Paleontological and paleoecological implications

The chronostratigraphic reconstruction of the Chilcatay and the Pisco formations produced some consequences in both invertebrate and vertebrate paleontology. Moreover, the P0 allomember, as seen for the lithology and the shallow-water paleoenvironment, seems to be closer to the Chilcatay Formation also in the paleontologic content, regarding both the vertebrate and invertebrate fauna.

First of all, regarding mollusks, *Dosinia* cf. *ponderosa* is the only species found in all of the three component allomembers. The most important faunal change in the Pisco Formation has been observed to occur through the PE0.1 unconformity, between P0 and P1 allomembers, characterized by the appearance of a new fauna (e.g. *Anadara sechurana*, *Incatella hupei*, and species of *Hybolophus*, *Panopea* and *Trachicardium*), showing affinities with the Miocene Panamic fauna rather than with that of the lower to middle Miocene Navidad Formation of Chile (DeVries & Frassinetti 2003). Confirming these observation, the P0 allomember has been attributed to the Langhian – Serravallian (middle Miocene). Moreover, the finding of specimens of Cypraeidae and Architectonicidae, specimens of *Ficus distans* (DeVries pers. comm.), together with the finding of the only coral colony ever noticed in the Pisco Basin, suggest a warm water paleoenvironment (see Fig. 18.6), differently from the other Pisco allomembers. This hypothesis is supported by the presence of fossil teeth belonging to the extinct tropical shark *Hemipristis serra* reported in Collareta (2017).

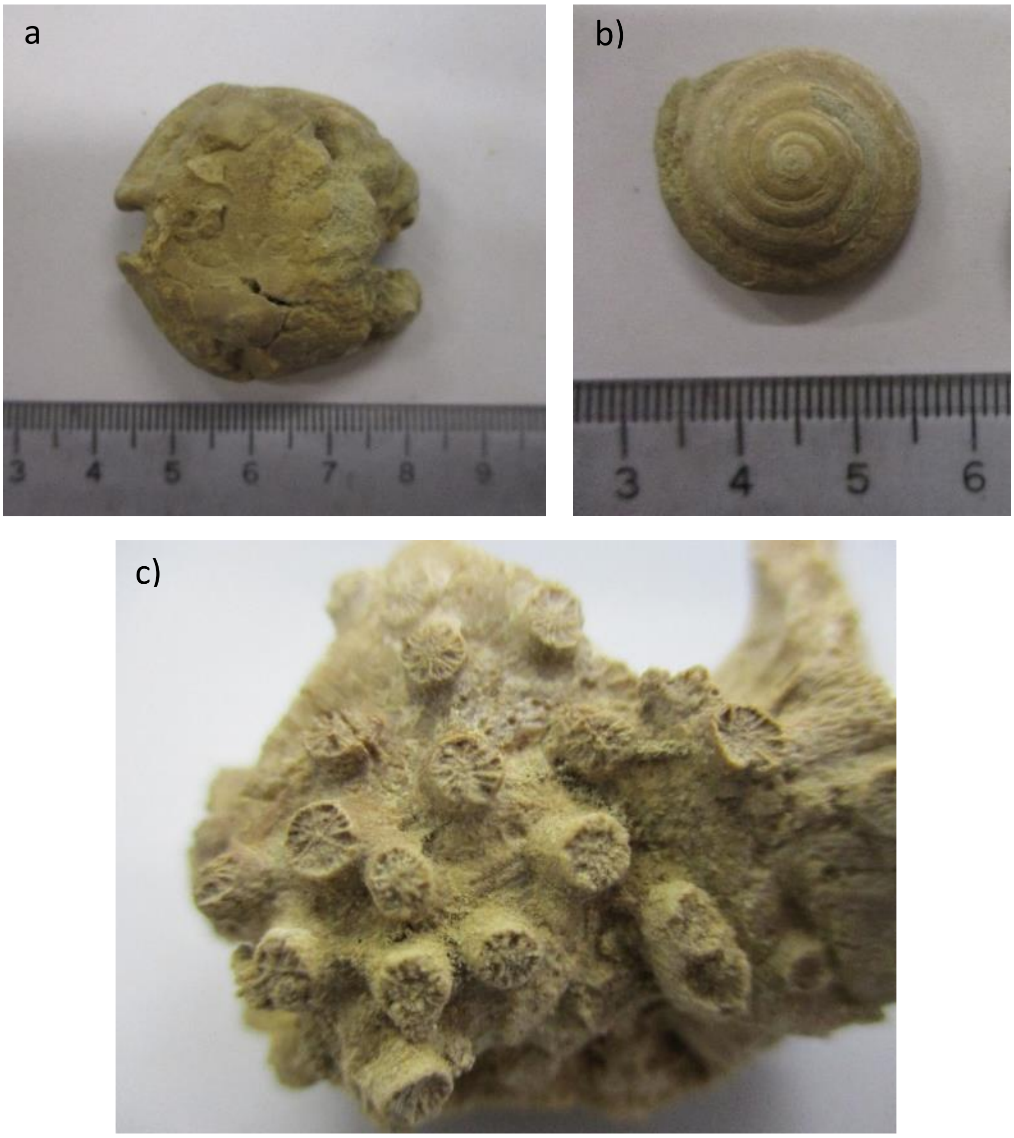

Figure 18.6. Fossil invertebrates found in P0 allomember. a) Specimen of Cypraeidae. b) Specimen of Architectonicidae. c) Coral colony on barnacles. Total length: 5 cm.

Another consideration is the presence of *Anadara sechurana* in the upper part of the P1 allomember, above the ash layer dated at 9.10 ± 0.04 Ma (Chapter 10). As *A. sechurana* was considered not younger than middle Miocene, its occurrence was used consequently in following studies to constrain outcrops of the Pisco Formation (e. g. Bianucci et al. 2010). However, recent researches highlighted that the range of *A. sechurana* is not limited to the middle Miocene and may extend into the early Tortonian. In the Gatun Formation (Panama), for instance, this species ranges from 11.6 to 10.4 Ma (Austin Hendy pers. comm.) and its disappearance is likely related to local unfavorable environmental conditions rather than to a real extinction (Austin Hendy pers. comm.). For these reasons, we suggest that *A. sechurana* extends its range in the late Miocene. Both *A. sechurana* and *Miltha* sp. seem to disappear above the PE0.2 surface, where we observed this smaller change in the molluskan fauna.

Regarding fossil vertebrates, the vertebrate content of P0 is still scarcely known; nevertheless, based on observations in Chapter 9, it clearly differs from that of the overlying P1 allomember, especially with regard to the cetacean assemblage. Therefore, even in the vertebrate fauna, the greatest change in the assemblage took place in correspondence with the PE0.1 unconformities, between P0 and P1 allomembers, and not the PE0.0 unconformity between the Chilcatay and the Pisco formations. This implied that the invertebrate and vertebrate fauna registered a change between the middle and the late Miocene, when the global cooling increased and the Humboldt Current, and the consequent upwelling, became stronger.

Finally, the application of the tephrostratigraphy in the P2 allomember has different implication in the vertebrate paleontology of the Pisco Basin. Taking into account ^{39}Ar–^{40}Ar ages in Cerro los Quesos and Cerro la Bruja localities (see Chapter 12) and the sedimentation rates calculated in Chapter 17, tephra correlation based on tephra fingerprinting allows stratigraphic reconstruction with resolution < 0.1 Ma. The tephrostratigraphic framework provided in the present thesis also helps in clarifying the relationships between two of the most prominent fossil-bearing localities of the Pisco Formation, namely, Cerro la Bruja (e.g., Muizon 1988; Lambert et al. 2014, 2017) and Cerro los Quesos (e.g., Bianucci et al. 2016a, b, and references therein; Lambert et al. 2017; Gioncada et al. 2018b). At Cerro la Bruja, the basal sandy beds of the P2 allomember (i.e., the “CLB vertebrate level” sensu Muizon & DeVries 1985 and Muizon 1988) are particularly rich in fossil vertebrates (Di Celma et al. 2017). At Cerro los

Quesos, in turn, most of the fossil vertebrates are found in the fine-grained sediments that comprise the highest portion of the P2 beds there exposed, i.e., "member F" sensu Di Celma et al. (2016) (Bianucci et al. 2016a). Based on the long-distance correlation presented in Chapter 12, the diatomaceous strata of member F at Cerro los Quesos are clearly geologically younger than the basal sandy beds of the P2 allomember at Cerro la Bruja, and as such, they bear two temporally distinct fossil vertebrate assemblages. The taxonomic compositions of these assemblages are largely overlapping (e.g., Di Celma et al. 2017) and some of the observed differences likely reflect different paleoenvironmental conditions (e.g., the shallow-water sandstones of the CLB vertebrate level feature abundant remains of seals, which in turn are much rarer in the offshore mudstones of member F); nevertheless, in the light of our results, various taxonomic novelties recorded from member F can be interpreted as evidence that some faunistic turnover occurred, involving the disappearance - i.e., local or global extinction - of the pontoporiid dolphin *Brachydelphis mazeasi* (an extinct species closely related to the extant La Plata river dolphin, Gioncada et al. 2018a) and the appearance - i.e., first arrival or origination - of phocoenids (porpoises) and kogiids (pygmy sperm whales).

18.3. Fossilization in the Miocene sedimentary successions

Fossil preservation and diagenetic processes in the Chilcatay Formation are very different from those of the Pisco Formation. Both formations are characterized by an abundant and exceptional concentration of both fossil vertebrates and invertebrates, despite the differences in lithologies and paleoenvironments.

Miocene invertebrates are preserved as pristine shells and have a good preservation in the Chilcatay Formation, where carbonate is still present and the siliceous composition only comprises the siliciclastic and terrigenous material, aside from the top of the Ct2 allomember, where few siltstone samples enriched in siliceous microfossils were found. Ostreids, pectinids, echinoids and barnacles are well preserved and show a calcite pristine composition, with the exception of some specimens showing a calcite recrystallization. In the Pisco Formation, invertebrates are badly preserved, with some exception in the P0 allomember. The latter shows mollusks and barnacles not very well preserved but, in some cases such as oysters layers or barnacle sheaths, calcite is still present. Calcite or dolomite molds of invertebrates are frequently found within recrystallized shells (not pristine). In the youngest allomembers, P1 and P2, invertebrates are very badly preserved and the original calcite or aragonite shell is not present anymore. The mollusks found in these allomembers are only constituted of gypsum casts or dolomite/gypsum internal molds, precipitated during the early or late diagenesis. No calcite or other carbonates different from dolomite are preserved in these units but casts or molds of calcite organisms were found, therefore calcite dissolution occurred after cast/mold formation within the sediment. The diverse degree of calcite preservation is probably due to the differences in paleoenvironments and diagenetic processes in those successions. A possible explanation for calcite epipelagic dissolution (in the water column) in this shallow marine environment can be the great abundance of organic matter. Biologically mediated processes such as dissolution within the guts and fecal pellets of grazers and the microbial oxidation of organic matter lead to calcite dissolution in shallow waters (Milliman et al. 1999; Pfeifer et al. 2002). Calcite dissolution can occur as a result of oxic respiration, organic matter degradation and reoxidation processes, so high supply of organic matter combined with low rates of sulfate reduction lead to an intense dissolution of calcite in surface environment (up to 90%) (Pfeifer et al. 2002). Moreover, Milliman et al. (1999) assert that the calcite removal is higher in areas of coastal and equatorial upwelling, such as the diatomaceous sediments of the Pisco Formation. For mollusk casts and molds, instead, the calcite dissolution must occurred within the sediment, after the mold formation. A possible explanation for this process, but we do not exclude other hypothesis, is the decrease of pH because of the oxidation of pyrite. In fact, the resuming oxygenated conditions after the anaerobic organic matter degradation around and within bivalves in the sediments caused the oxidation of the previously formed iron sulfides, or of the sulfide produced by sulfate reduction, leading to a reduction of pH (Coleman et al. 1985).

The extraordinary vertebrate preservation is reknown in both the formations, even the best and exceptional findings have been discovered in the Pisco Formation, especially in the P1 and P2 allomembers (e.g. Esperante et al. 2008; Lambert et al. 2010; Collareta et al. 2015). The reasons of this exceptional fossilization are still scarcely known, but recently the taphonomy of vertebrate remains of both the formations have been investigated. In the Chilcatay Formation, cetacean bones are well preserved and exhibit a good degree of apatite mineralization. Despite the absence of carbonate nodules, in contrast with those of the Pisco Formation, bone cavities are locally filled by Ca-Mg carbonates. Only in few cases microborings of the B-type (sensu Gariboldi et al. 2015) occurred in the compact bone, but larger borings caused by benthic invertebrates, such as *Osedax*, are not observed. No remains of whale-fall communities are present. The reason of such a good preservation would be the occurrence of anoxic events. The size distribution of pyrite framboid relics in the Ct1 fine sediments at Ullujaya revealed indeed some fluctuations of euxinic and oxic-dysoxic conditions at the seafloor. Therefore, the fossil vertebrate preservation was favored by the oxygen-deficient bottom conditions that inhibited the action of benthic invertebrates and macro-scavengers and the formation of a developed whale-fall community. In the Pisco Formation, the reason of the exceptional preservation was first attributed to the rapid burial, but is not the only process that comes in (see Chapter 17). One of the explanation was proposed by Gariboldi et al. (2015), who illustrated how the carbonate nodules, especially dolomite concretions, could prevent the degradation of the bones and diagenetic compression of skeletons during burial, and the erosion of fossils after exhumation (see Fig. 18.7). This process is mainly observed for the carcasses of big dimensions, but small specimens, as odontocetes, usually do not have a concretion around the skeleton. At the sea bottom, indeed, the fall of small-sized cetacean carcass did not induce a local chemical variation of the environment strong enough to reach conditions favorable to the carbonate precipitation. For understanding the preservation of small cetaceans, a small pontoporiid dolphin was analyzed (see Chapter 17, Part II) and we found out that a rapid burial of the specimen is pivotal for the bone preservation, allowing the early establishment of anoxic processes for degradation of organic matter. The presence of a permeable sediment without any dolomite nodule, together with the availability of P released from the Fe-reduction processes and the carcass decay in anoxic environment, favored the recrystallization of bone apatite, allowing excellent bone tissue preservation (see Fig. 18.8).

Thus, we demonstrate that a good preservation is possible in such different environments, both anoxic and oxic/dysoxic, and in very different sediments, because of the diverse and multiple diagenetic processes that come in after the deposition of the whale carcass on the seafloor. The fossilization processes and the reasons of this exceptional abundance and extraordinary preservation must continue to be studied in depth for understanding how a Fossil-Lagerstätte such as that of the Pisco Basin could be formed.

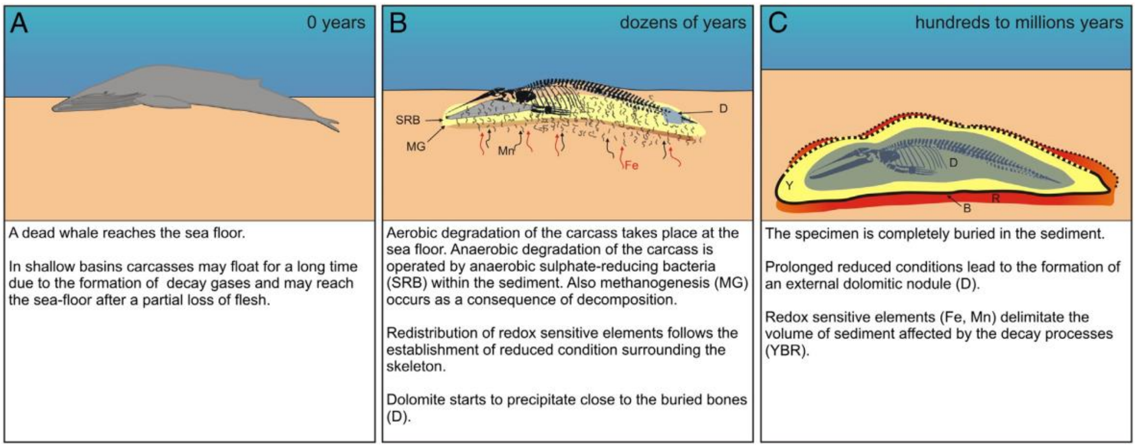

Figure 18.7. Dolomite formation reconstruction. a) Marine vertebrate deposited at the sea floor. b) The consumption of the soft tissue is rapid compared to lipid degradation. Rapid burial affected the skeleton. Sulphate reducing bacteria are represented. c) The sediment surrounding the skeleton is permanently modified by the consequences of decay. From Gariboldi et al. (2015).

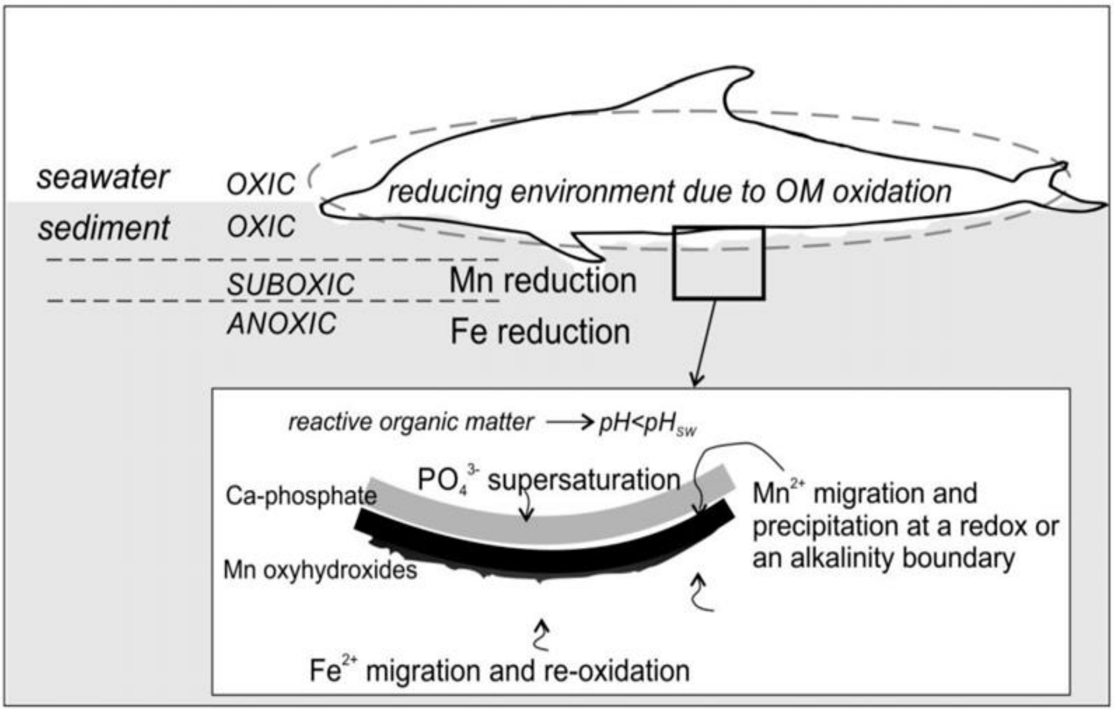

Figure 18.8. Schematic model summarizing the formation of the mineral pattern around a small-sized cetacean carcass. Modified from Gioncada et al. (2018a).

Chapter References

Amiot, R., Gohlich, U.B., Lécuyer, C., Muizon, de C., Cappetta, H., Fourel, F., Héran, M.-A., Martineau, F. 2008. Oxygen isotope compositions of phosphate from Middle Miocene–Early Pliocene marine vertebrates of Peru. Palaeogeography, Palaeoclimatology, Palaeoecology, 264, 85-92.

Bianucci, G., Lambert, O., Post, K. 2010. High concentration of long-snouted beaked whales (genus Messapicetus) from the Miocene of Peru. Palaeontology, 53, 1077-1098.

Bianucci, G., Di Celma, C., Collareta, A., Landini, W., Post, K., Tinelli, C., de Muizon, C., Bosio, G., Gariboldi, K., Gioncada, A., Malinverno, E., Cantalamessa, G., Altamirano-Sierra, A., Salas-Gismondi, R., Urbina, M., Lambert, O. 2016a. Fossil marine vertebrates of Cerro Los Quesos: Distribution of cetaceans, seals, crocodiles, seabirds, sharks, and bony fish in a late Miocene locality of the Pisco Basin, Peru. Journal of Maps, 12, 1037-1046.

Bianucci, G., Di Celma, C., Urbina, M. & Lambert, O. 2016b. New beaked whales from the late Miocene of Peru and evidence for convergent evolution in stem and crown Ziphiidae (Cetacea, Odontoceti). PeerJ, 4:e2479.

Browning, J.V., Miller, K.G., Sugarman, P.J., Barron, J., McCarhy, F.M.G., Kulhanek, D.K., Katz M.E., Feigenson, M.D. 2013. Chronology of Eocene–Miocene sequences on the New Jersey shallow shelf: Implications for regional, interregional, and global correlations. Geosphere, 9(6), 1434-1456.

Coleman, M.L., Berner, R.A., Durand, B., Meadows, P.S., Eglinton, G. 1985. Geochemistry of diagenetic non-silicate minerals kinetic considerations. Philosophical Transactions of the Royal Society A, 315, 39-56.

Collareta, A. 2017. Paleoecological reconstruction of the marine vertebrate fauna of the Pisco Formation (Peru): a multidisciplinary approach. PhD thesis, Pisa, Italy.

Collareta A, Landini W., Lambert O., Post K., Tinelli C., Di Celma C., Panetta D., Tripodi M., Salvadori, P.A., Caramella, D., Marchi, D., Urbina, M., Bianucci, G. 2015. Piscivory in a Miocene Cetotheriidae: irst record of fossilized stomach content for an extinct baleen-bearing whale. Science of Nature, 102, 70.

Dunbar, R.B., Marty, R.C., Baker, P.A. 1990. Cenozoic marine sedimentation in the Sechura and Pisco basins, Peru. Palaeogeography, Palaeoclimatology, Palaeoecology, 77, 235-261.

DeVries T.J. 1998. Oligocene deposition and Cenozoic sequence boundaries in the Pisco Basin (Peru). Journal of South American Earth Sciences, 11, 217-231.

DeVries, T. J. 2017. Eocene stratigraphy and depositional history near Puerto Caballas (East Pisco Basin, Peru). Boletín de la Sociedad Geológica del Perú, 112, 39-52.

DeVries, T.J., Jud, N.A. 2018. Lithofacies patterns and paleogeography of the Miocene Chilcatay and lower Pisco depositional sequences (East Pisco Basin, Peru). Boletín de la Sociedad Geológica del Perú, Volumen Jubilar 8, 124-167.

DeVries, T.J., Urbina, M., Jud, N.A. 2017. The Eocene- Oligocene Otuma depositional sequence (East Pisco Basin, Peru): Paleogeographic and paleoceanographic implications of new data. Boletín de la Sociedad Geológica del Perú, 112, 14-38.

Di Celma, C., Malinverno, E., Bosio, G., Collareta, A., Gariboldi, K., Gioncada, A., Molli, G., Basso, D., Varas-Malca, R., Pierantoni, P.P., Villa, I.M., Lambert, O., Landini, W., Sarti, G., Cantalamessa, G., Urbina, M., Bianucci, G. 2017. Sequence stratigraphy and palaeontology of the upper Miocene Pisco Formation along the western side of the lower Ica valley (Ica desert, Peru). Rivista Italiana di Paleontologia e Stratigrafia (Research in Paleontology and Stratigraphy), 123, 255-274.

Di Celma, C., Malinverno, E., Bosio, G., Gariboldi, K., Collareta, A., Gioncada, A., Landini, W., Pierantoni, P.P., Bianucci, G. 2018. Intraformational unconformities as a record of Late Miocene eustatic falls of sea level in the Pisco Formation (southern Peru). Journal of Maps, 14(2), 607-619.

Esperante, R., Brand, L. R., Nick, K. E., Poma, O., Urbina, M. 2008. Exceptional occurrence of fossil baleen in shallow marine sediments of the Neogene Pisco Formation, Southern Peru. Palaeogeography, Palaeoclimatology, Palaeoecology, 257, 344-360.

Gariboldi, K., Gioncada, A., Bosio, G., Malinverno, E., Di Celma, C., Tinelli, C., Cantalamessa, G., Landini, W., Urbina, M., Bianucci, G. 2015. The dolomitic nodules enclosing fossil marine vertebrates in the East Pisco Basin, Peru: field and petrographic insights into their genesis and role in preservation. Palaeogeography, Palaeoclimatology, Palaeoecology, 438, 81-95.

Gioncada, A., Gariboldi, K., Collareta, A., Di Celma, C., Bosio, G., Malinverno, E., Lambert, O., Pike, J., Urbina, M., Bianucci, G. 2018a. Looking for the key to preservation of fossil marine vertebrates in the Pisco Formation of Peru: new insights from a small dolphin skeleton. Andean Geology, 45(3).

Gioncada, A., Petrini, R., Bosio, G., Gariboldi, K., Collareta, A., Malinverno, E., Bonaccorsi, E., Di Celma, C., Pasero, M., Urbina, M., Bianucci, G. 2018b. Insights into the diagenetic environment of fossil marine vertebrates of the Pisco Formation (late Miocene, Peru) from mineralogical and Sr isotope data. Journal of South American Earth Sciences, 81, 141-152.

Lambert, O., Bianucci, G., Post, K., Muizon, C. de, Salas-Gismondi, R., Urbina, M., Reumer, J. 2010b. The giant bite of a new raptorial sperm whale from the Miocene epoch of Peru. Nature, 466, 105-108.

Lambert, O., Bianucci, G., Beatty, B.L. 2014. Bony outgrowths on the jaws of an extinct sperm whale support macroraptorial feeding in several stem physeteroids. Naturwissenschaften, 101(6), 517-521.

Lambert, O., Bianucci, G., Muizon, C. de. 2017. Macroraptorial sperm whales (Cetacea, Odontoceti, Physeteroidea) from the Miocene of Peru. Zoological Journal of the Linnean Society, 179, 404-474.

Marx, F.G., Uhen, M.D. 2010. Climate, Critters, and Cetaceans: Cenozoic Drivers of the Evolution of Modern Whales. Science, 327, 993-996.

Miller, K.G., Wright, J.D., Fairbanks, R.G. 1991. Unlocking the Ice House: Oligocene-Miocene Oxygen Isotopes, Eustasy, and Margin Erosion. Journal of Geophysical Research, 96, 6829-6848.

Miller, K.G., Mountain, G.S., Browning, J.V., Kominz, M., Sugarman, P.J., Christie-Blick, N., Katz, M.E., Wright, J.D. 1998. Cenozoic global sea level, sequences, and the New Jersey transect: results from coastal plain and continental slope drilling. Reviews of Geophysics, 36(4), 569-601.

Milliman, J.D., Troy, P.J., Balch, W.M., Adams, A.K., Li, Y.-H., Mackenzie, F.T. 1999. Biologically mediated dissolution of calcium carbonate above the chemical lysocline. Deep-sea Research I, 46, 1653-1669.

Muizon, C. de 1988. Les Vertébrés de la Formation Pisco (Pérou). Troisième partie: Les Odontocètes (Cetacea, Mammalia) du Miocène. Travaux de l'Institut Français d'Études Andines, 42, 1-244.

Muizon, C. de, DeVries, T.J. 1985. Geology and paleontology of late Cenozoic marine deposits in the Sacaco area (Peru). Geologische Rundschau, 74(3), 547-563.

Turco, E., Hilgen, F.J., Lourens, L.J., Shackleton, N.J., Zachariasse, W.J. 2001. Punctuated evolution of global climate cooling during the late Middle to early Late Miocene: High-resolution planktonic foraminiferal and oxygen isotope records from the Mediterranean. Paleoceanography, 16, 405-423.

NACSN 2005. North American stratigraphic code. AAPG Bulletin, 89, 1547-1591.

Pfeifer, K., Hensen, C., Adler, M., Wenzh¨Ofer, F., Weber, B., Schulz, H.D. 2002. Modeling of subsurface calcite dissolution, including the respiration and reoxidation processes of marine sediments in the region of equatorial upwelling off Gabon. Geochimica et Cosmochimica Acta, 66, 24, 4247-4259.

Westerhold, T., Bickert, T., Röhl, U. 2005. Middle to late Miocene oxygen isotope stratigraphy of ODP site 1085 (SE Atlantic): New constrains on Miocene climate variability and sea-level fluctuations. Palaeogeography, Palaeoclimatology, Palaeoecology, 217, 205-222.

Zachos, J. C., Shackleton, N. J., Revenaugh, J. S., Pälike, H., Flower, B. P. 2001. Climate response to orbital forcing across the Oligocene-Miocene boundary. Science, 292, 274-278.

Chapter 19. Conclusions

The multidisciplinary work carried out in these years in the western side of the Ica River resulted in a stratigraphic, paleoecologic, taphonomic and chronostratigraphic studies of the Miocene sedimentary successions such as the Chilcatay and Pisco formations.

The stratigraphic reconstruction of the Chilcatay Formation at Ullujaya shows a shallow-water paleoenvironment, characterized at the base by the *Ct1a* facies association recording the coeval deeper parts of the basin (offshore setting) receiving bypass suspended fines from the shallower ramp, and the *Ct1b* facies association recording a distally steepened mixed siliciclastic-bioclastic ramp. Above the Ct1 allomember, above the surface CE0.2, the Ct2 allomember consists of two major facies associations comprising shoreface sandstones (*Ct2a*) and offshore silty facies (*Ct2b*). The main part of the fossil vertebrates, mainly consisting of odontocete bones and shark teeth, came from the *Ct1a* facies association, and comprises a coastal community, dominated by mesopredators, representative of a warm-temperate, sheltered embayment connected with riverine and openocean environments. Considering chronostratigraphic results, given by biostratigraphy, ^{39}Ar–^{40}Ar dating on tephra and Sr isotope analyses, the whole Chilcatay Formation in the study area is assigned to the Burdigalian (early Miocene), precisely between 19.25 and 18.02 Ma (or 17.08 Ma following only the diatom biostratigraphy). This results are tentatively correlated to the Mi-events, the oxygen isotopic maxima in the Miocene: the Chilcatay Formation would be deposited between the Mi1 or Mi1aa (dated at 23.2 or 20.0 Ma, respectively) and the Mi2 event (dated at 16.3 Ma), with a gap in correspondence of the Mi1ab (dated at 18.7 Ma) that would correspond to the CE0.2 unconformity between Ct1 and Ct2 allomembers. Taphonomic studies in the Chilcatay Formation reveal that mollusks and barnacles are usually well preserved and maintained their pristine Ca-carbonate shell. Fossil vertebrates are disarticulated but almost complete, and their bones show a good preservation, probably due to the fluctuation of euxinic and oxic-dysoxic conditions at the seafloor.

The youngest Pisco Formation is divided stratigraphically in three allomembers, P0, P1 and P2, due to recognition of three basin-wide unconformities (called PE0.0, PE0.1 and PE0.2). In each allomember, shallower-water sand-rich deposits rest unconformably on deeper, diatomite-rich deposits (aside for P0), representing transgressive cycles. Fossil vertebrates are present in all these allomembers, and a difference from the P0 assemblage and that of the overlying P1 allomember, especially with regard to the cetacean assemblage, is noticed. In P1 allomember, baleen-bearing whales are mainly represented by medium-sized cetotheriids, whereas larger balaenopterids dominate the P2 allomember. Compared to the Chilcatay Formation studied in Ullujaya, the Pisco Formation paleoenvironment seems to be deeper and less protected. Chronostratigraphic results from biostratigraphy, ^{39}Ar–^{40}Ar dating on tephra and strontium isotope stratigraphy assigned the Pisco Formation to the middle – late Miocene. In particular, Sr isotope analyses on carbonates and phosphates suggest a Langhian – Serravallian age for the P0 allomember (from 14.8 to 12.6 Ma). The P1 allomember was instead assigned entirely to the Tortonian (from 9.46 to 8.60 Ma) and the P2 allomember was dated to the Tortonian – Messinian (from 8.39 to 6.71 Ma). The application of the tephra fingerprinting to the P2 deposits allow to build a high-resolution stratigraphy and to correlate sediments exposed in different localities, with important implications for the vertebrate paleontology. The chronostratigraphic framework allows an attempt of correlation with the Mi-events: the Pisco Formation would be deposited after the Mi2 (dated at 16.3 Ma) correlated to PE0.0. Within the formation, the PE0.1 unconformity can correspond to the Mi6 (10.3 Ma in age) and the PE0.2 unconformity can be related to the Mi7 (dated at 8.7 Ma). Taphonomic studies in the Pisco Formation show a very bad preservation for fossil invertebrates, with some exceptions in the P0 allomember, where few carbonate shells are still found, but in some cases they are completely recrystallized. In the youngest allomembers, invertebrate shells are absent or completely substituted by gypsum, and mollusks are only present as dolomite/gypsum internal molds or casts. Vertebrate taphonomy shows an exceptional concentration of fully articulated and completed specimens and the preservation of delicate tissues, as baleen. Bones are well-preserved and show a good permineralization or phosphatization. This extraordinary preservation is due to a rapid burial, an early diagenetic carbonate nodule formation, but especially to the diagenetic processes going on in the sediment enclosing vertebrate remains in the early stages after the burial.

Acknowledgements

This thesis is the result of my exciting work on the Pisco Basin, started in 2014 and carried forward until 2018. I would like to express my heartfelt thanks to my supervisor Elisa Malinverno, for giving me this wonderful opportunity and for sharing with me her enthusiasm about this research: thank you for trusting me in any situation. I am very grateful to my co-tutor Anna Gioncada, who looked after me through my studies, helping me out with all the problems I have encountered and encouraging me during tough times. Special thanks to my other co-tutor Giovanni Bianucci, for being a great Principal Investigator in our expeditions and for transmitting to me his boundless passion for studying fossils in the Ica Desert. Particular thanks go to Claudio Di Celma, who taught me everything he knows while on the field and incited me to persevere with my work even when the results were not as we expected them to be. I want to also thank my tutor Igor Villa for giving me the chance to learn how a wonderful instrument such as the noble gasses mass spectrometer is used, and for sharing with me his knowledge on Ar-Ar dating. Particular thanks go to Karen Gariboldi, without whom this project and my work would not have been possible, thank you for teaching me everything I know on diatoms; and particular thanks go to Alberto Collareta as well, for his constant support and for sharing with me lots of adventures and experiences. I also wish to thank everyone else who has shared with me the desert experience, in particular Giancarlo Molli, Walter Landini, Felix Marx, Olivier Lambert, Pietro Paolo Pierantoni, Christian de Muizon, Chiara Tinelli, Gabriella Bagnoli and Gino Cantalamessa. I greatly appreciate the hospitality of the Museo de Historia Natural (UNMSM) in Lima and I would like to thank our Peruvian colleagues Mario Urbina, Rafael Varas-Malca and Walter Aguirre. Thanks to Thomas DeVries, who shared his knowledge about Pisco mollusks with me, and helped me in identifying some specimens.

I am also grateful to Daniela Basso, who patiently helped me in my studies on mollusks and share her enthusiasm with me, and to Mariano Parente, who taught me the basis of strontium stratigraphy. Special thanks to Valentina Barberini for spending full days measuring together and for sharing with me the secrets of the spectrometer, and to Nicoletta Fusi for kindly supporting me in my lab experience. I want to thank also Andrea Risplendente, for his friendliness while assisting me during the microprobe analyses, and

Fabrizio Berra, for the cathodoluminescence analyses. Thanks to Dieter Buhl, for making Sr analyses in Bochum, and to Sergio Andò, for the attempts with the Raman spectroscopy. I am truly grateful to my evaluators Felix Marx and Sebastian Watt for the perseverance and patience necessary to examine my dissertation.

I wish to thank all my colleagues, especially Giovanni, who always championed me, Agostino, the best office companion a person could hope for, and Fabio, Valentina, Chiara. Particular thanks go to all the students that helped me in my work in these years, especially to Raffaella, Stefania and Carolina.

Last but not least, I would like to thank all my wonderful friends that have been cheering for me all this time, especially Chiara, who is like a sister to me, Silvia, Valentina, Sara, Federica, Maila and Carla; and all the other friends who have been close to me, you know who you are: thank you. The greatest thanks go to my family, especially to my parents Domenica and Vittorio, who always supported me in all my peculiar passions and decisions.

Thanks to the Ica Desert, where I left a piece of my heart.


HOSTAL
BOULEVARD

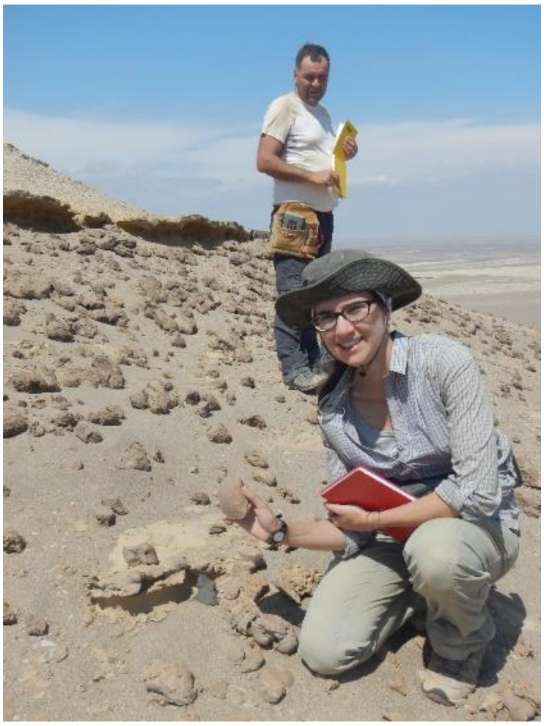

Appendix

Symbols legend
Burrows
Skolithos
Gyrolithes
Thalassinoides
Sedimentary structures and lithologies
Swaley cross-stratification
Planar cross-stratification
Trough cross-stratification
Large-scale gutter casts
Low-angle planar lamination with small-scale gutter casts
Plane parallel lamination
Slump folds
Laminated diatomites
Volcanic ash
Dolomite-cemented beds
Large nodules
Mollusc shell debris
Mollusc molds and casts
Dolomite clasts with Gastrochaenolites-type borings
Pebble-size phosphate nodules
Pebble- to cobble-size basement clasts
Pebble- to boulder-size basement clasts
Igneous basement
Erosional unconformity
Cerro Colorado
Cerro Blanco
Toro Chico
Cerro Los Quesos
Cerro Los Quesos west
Cerro La Bruja
Cadenas de Los Zanjones
Ullujaya
P2
P1
Chilcatay-P1
Orange 3
Orange 2
Orange 1
Chilcatay Unlimo
Superficie A
Livello B
Livello C
Livello D